



MONASH University

Multiscale Characterisation of Reduced Graphene Oxide Assemblies

Ashley Beth Roberts

B.S.Phy., M.S.Phy.Eng., M.B.A.

A thesis submitted for the degree of Doctor of Philosophy at
Monash University in 2017
Faculty of Engineering, Department of Materials Science and Engineering
Clayton, Victoria, Australia

Copyright Notice

© Ashley Beth Roberts (2017).

I certify that I have made all reasonable efforts to secure copyright permissions for third-party content included in this thesis and have not knowingly added copyright content to my work without the owner's permission.

Abstract

This work investigates the structure of reduced graphene oxide (rGO) assemblies from the sub-nm to macro-scale, relating morphology to material performance reported in the literature. A wet processing method allows the chemistry of rGO sheets to be specifically tailored, and further modification to the anisotropic pore structure of layered assemblies can be achieved through controlled hydration, resulting in a unique type of porous carbon. There continues to be intense interest in graphene-based materials, with many exceptional properties for separation and energy storage being reported, yet experimental methods to investigate the specific structure-property relationships are not well developed. Thus, addressing this gap in knowledge is urgently needed to advance the development of rGO-based functional materials.

While rGO materials are typically evaluated using graphene as a reference, this work judiciously evaluates X-ray photoelectron spectroscopy, Raman spectroscopy, and X-ray diffraction data in context to more disordered carbon materials. An innovative and practical methodology is clearly outlined, with this approach being able to extract a significant amount of qualitative and quantitative information at the microscale, obtaining substantial insight on disorder and aromaticity from the less utilized spectral features. At the mesoscale, small and wide angle scattering (SANS, SAXS, WAXS) proved to be ideally suited for characterizing the pore network in both dried and hydrated rGO assemblies, offering the additional advantage of operating in ambient conditions and extending across a wide size range.

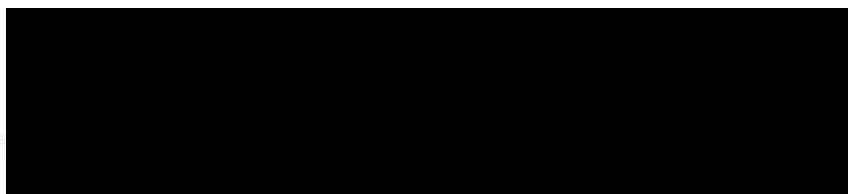
The results of this work show a correlation between the synthesis procedure of the original GO and the chemical composition of rGO, which could be used to control the conductivity, reactivity, and pseudocapacitance in the bulk material. These rGO sheets were used to design a microscale physical model to act as a basic structural unit (BSU). The BSU was found to be a turbostratic cluster consisting of approximately seven rGO layers with an (hk) coherence length extending across 6 nm with smaller, 1 nm, aromatic domains. The BSU was then used to evaluate rGO assemblies at the meso- and macroscale, and results show that while the size of these BSUs remains relatively constant, processing conditions will impact disorder and resultant stacking density, which is directly linked to the accessible surface area and ensuing pore network within the bulk.

Many different processing conditions are examined, with a specific focus on the influence of oxidation and drying. Further, the role of water in rGO hydrogels is explored using *in situ* experimental methods to measure the impact of hydration on the pore structure. The insight gained from the results of this work can be directly applied in order to improve performance of rGO materials now that processing methods have been clearly linked to the explicit chemical and morphological features at both the micro- and mesoscale. The final aspect of this work expands on the methods developed for dry and hydrogel films to design *in situ* X-ray scattering experiments to uncover the dynamics of ion transport in rGO assemblies used for energy storage.

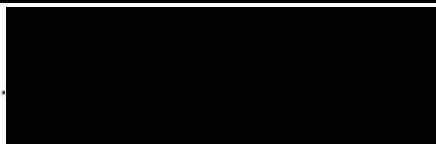
Declaration

This thesis contains no material which has been accepted for the award of any other degree or diploma at any university or equivalent institution and that, to the best of my knowledge and belief, this thesis contains no material previously published or written by another person, except where due reference is made in the text of the thesis.

Signature:

A large black rectangular box redacting the signature.

Print Name:

A black rectangular box redacting the printed name.

Date:

March 26, 2017

Acknowledgements

Acknowledgement for financial support:

I acknowledge generous support through the Monash Faculty of Engineering International Postgraduate Research Scholarship (FEIPRS) to cover the costs of my tuition, and the Australian Research Council Discovery Project (DP1312512) which covered project costs and paid my living stipend throughout PhD candidature. The Australian Institute of Nuclear Science and Engineering (AINSE) postgraduate award supported the use of facilities and services as well as a top-up scholarship, and generous travel allowance to enable my work at ANSTO facilities. Additionally, I received travel support from the Monash Centre for Atomically Thin Materials (MCATM), the Asia-Oceania Neutron Scattering Association (AONSA), and the German Academic Exchange Service (DAAD) to attend conferences and access research facilities in Australia, Japan, and Germany.

Acknowledgement of professional support:

I acknowledge my supervisors at Monash University, Prof Dan Li and Prof George Simon, for their professional guidance and financial support, as well as my ANSTO supervisor, Dr Chris Garvey, for his guidance on small angle scattering techniques and access to facilities. In addition, Dr Garvey facilitated my attendance and participation at numerous conferences, symposiums, and training programs in Australia and Europe which added significantly to postgraduate experience and professional network. I would also like to acknowledge Prof David Officer, whose time and effort in evaluating the final version of this work enhanced the scientific value and readability of the thesis.

Acknowledgement for expertise and experimental support:

I acknowledge the work of Dr Bing Huang who prepared all of the original GO precursor materials used in this study. Further, many people assisted with the long hours required for shifts during the beamtime experiments, namely Dr David Cheng, Jing Xiao, and Diyan Liu with a special thanks to Dr Chris Garvey and Dr Vikram Raghuvanshi who were most generous with their time during the experiments as well as discussions on data analysis. Dr Zai-quan Xu provided access to the Raman spectroscopy instrument used in this work.

For the design of the *in situ* sample holders, Lee Dumas did the CAD drawings and 3D printing for the rotation stage and humidity delivery system while Dr Tony Pandolfo provided expert guidance in designing the SAXS ion transport set-up. The local technicians at the Australian Synchrotron also helped tremendously by machining the specialized sample holder designed for the *in situ* experimentation. Further, Dr Norman Booth was very generous with his time and skills during the SANS experiments at ANSTO, assisting with the complex sample environments for the rGO hydrogels.

Acknowledgement for beamtime:

In Chapter 4, this research was undertaken on the soft X-ray spectroscopy beamline at the Australian Synchrotron, Victoria, Australia. A special acknowledgement to Dr Yulin Zhong who wrote the proposal and the instrument scientist, Dr Bruce Cowie, who assisted with the beamtime.

In Chapter 6, this research was undertaken on the SAXS/WAXS beamlines at the Australian Synchrotron, Victoria, Australia. A special acknowledgement to the instrument scientists assisting with my beamtime, Dr Stephen Mudie, Dr Tim Ryan, and Dr Adrian Hawley.

Also in Chapter 6, I acknowledge the support of the Australian Centre for Neutron Scattering, Australian Nuclear Science and Technology Organisation, Lucas Heights, Australia, for providing access

to the neutron research facilities used in this work. More specifically, the assistance from instrument scientists: i) Dr Christine Rehm and Dr Liliana de Campo on KOOKABURRA, the Ultra-Small-Angle Neutron Scattering beamline; iii) Dr Chris Garvey on QUOKKA, Small-Angle Neutron Scattering beamline; and iii) Dr Helen Maynard-Casely on WOMBAT, the High-Intensity Powder Diffractometer. I also thank Helmholtz-Zentrum Berlin (HZB) for the allocation of neutron radiation beamtime. Measurements were carried out at the Membrane Diffractometer instrument on the V1 beamline at Research Reactor BER II, Wannsee, Germany, under the assistance of Thomas Hauß.

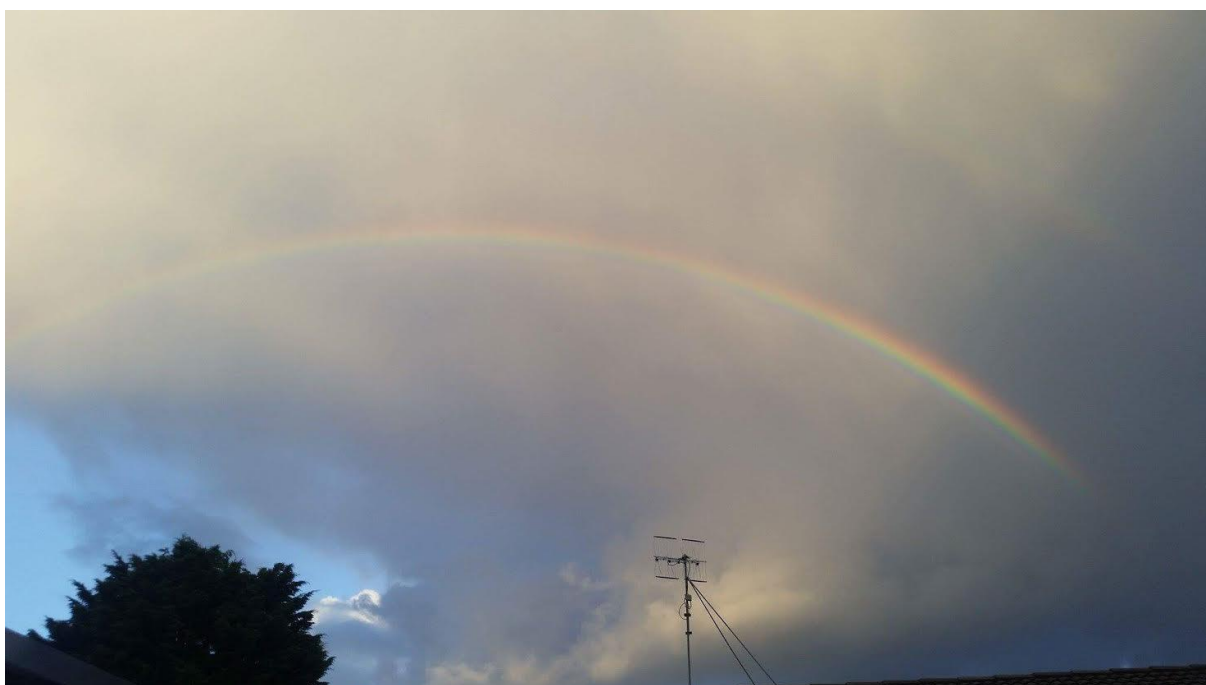
Acknowledgement for access to facilities:

For assistance with the TEM sample preparation and imaging in Chapter 5, I acknowledge use of the facilities and the assistance of Dr Emily Chen and Dr Tim Williams at the Monash Centre for Electron Microscopy.

In the EDS results of Chapter 4 and FIB/SEM results of Chapter 6, this work was performed in part at the Melbourne Centre for Nanofabrication (MCN) in the Victorian Node of the Australian National Fabrication Facility (ANFF).

Acknowledgement of emotional support and encouragement:

I would not have been able to complete this project without the support of my family and friends. Each contributed to my life in unique and beautiful ways and there are no words that could properly acknowledge their actions. My life is eternally indebted to Din, whose ultimate sacrifice changed my life forever. A special expression of gratitude is offered to my mom who gave her body and independence to bring me into the world, and to both of my parents, my grandparents, and my brother who have been with me through it all, while allowing me to grow into who I am today.



*In my experience, I have found that the solutions to all of life's most intractable problems
are not found through any form of intellect or cleverness.*

They are solved simply by moving on.

– Carl Gustav Jung

Contents

List of Tables x

List of Figures xii

List of Abbreviations..... xxvi

Chapter 1.	Introduction to rGO Assemblies as a Unique Type of Porous Carbon	1
1.1	Statement of the Problem and Significance of the Study	1
1.2	Background of the Problem	2
1.3	Purpose of the Study and Primary Research Questions.....	7
1.4	Outline of the Thesis	9
1.5	Assumptions, Limitations, and Scope.....	10
1.6	Definition of Terms.....	11
1.6.1	Specific nomenclature for graphene-based materials	11
1.6.2	Specific nomenclature for structural features along graphene layers.....	13
Chapter 2.	Literature Review	15
2.1	Description of rGO Sheets and Assemblies	15
2.1.1	Significance of graphene and rGO in materials engineering.....	15
2.1.2	Structure of GO and rGO sheets.....	15
2.1.2.1	Chemical composition	15
2.1.2.2	Structure.....	24
2.1.3	Three-dimensional architecture of rGO assemblies.....	30
2.1.4	Outstanding research questions related to rGO assemblies.....	32
2.2	rGO Assemblies Viewed as a Unique Type of Porous Carbon.....	32
2.2.1	General properties of layered and porous carbons	32
2.2.1.1	The graphene layer.....	33
2.2.1.2	Oriented lamellar carbons.....	34
2.2.1.3	Complex porous carbons.....	36
2.2.2	Structure-property relationships in porous carbons.....	37
2.2.3	<i>In situ</i> investigation into ion transport in porous carbons	40
2.3	Structural Characterization of Ordered Carbons	41
2.3.1	Short history of the investigation into carbon microstructure	41
2.3.2	Wide angle scattering of ordered lamellar carbons.....	42
2.3.2.1	Basic diffraction and scattering concepts.....	42
2.3.2.2	Diffraction theory in graphite and turbostratic carbon powders	43
2.3.2.3	Causes of line broadening	46
2.3.2.4	Geometric considerations for layered turbostratic thin films.....	47
2.3.2.5	Geometric considerations for porous assemblies.....	50
2.3.3	Small angle scattering of porous carbons	51
2.3.3.1	Basic small angle scattering concepts	51

2.3.3.2	Structural information obtained from the scattering curve	54
2.4	Concluding Remarks	59
Chapter 3.	Materials and Methods	60
3.1	Materials.....	60
3.1.1	Preparation of graphene oxide precursor	60
3.1.2	Reduction of graphene oxide to rGO	61
3.1.3	Filtration of rGO hydrogel and dried assemblies	62
3.2	Specialized Sample Holders.....	66
3.3	Experimental Methods.....	67
3.3.1	rGO materials used in each experimental chapter	67
3.3.1.1	Chapter 4 rGO materials.....	69
3.3.1.2	Chapter 5 rGO materials.....	69
3.3.1.3	Chapter 6 rGO materials.....	70
3.3.2	Electron microscopy and microanalysis	70
3.3.3	Photon spectroscopy, diffraction, and scattering	71
3.3.4	Neutron diffraction and scattering.....	73
3.4	SAS Data Treatment	75
Chapter 4.	The Chemical Structure of GO and rGO Sheets.....	76
4.1	Introduction: Chemical Composition of GO and rGO Sheets	76
4.2	X-ray Photoelectron Spectroscopy.....	76
4.2.1	XPS applied to rGO assemblies.....	76
4.2.2	Results and discussion.....	78
4.2.2.1	Full spectral scan results.....	78
4.2.2.2	High resolution scans of C1s, O1s, and N1s regions.....	82
4.2.2.3	High resolution valence band (VB) spectra	97
4.3	Energy Dispersive Spectroscopy.....	103
4.3.1	EDS applied to rGO assemblies	103
4.3.2	Results and discussion.....	105
4.4	Conclusions.....	108
Chapter 5.	The Basic Structural Unit of rGO Assemblies	110
5.1	Introduction: Concept of a Basic Structural Unit in the Microporous Region (<2 nm).....	110
5.2	Transmission Electron Microscopy.....	112
5.2.1	TEM applied to rGO assemblies	112
5.2.2	Results and discussion.....	114
5.3	Raman Spectroscopy	122
5.3.1	RMS applied to rGO assemblies	122
5.3.1.1	Raman spectra for graphene.....	122

5.3.1.2	Raman spectra for carbon materials	124
5.3.2	Results and discussion	135
5.3.2.1	Consistency of results	135
5.3.2.2	Comparison of spectral shapes for GO and rGO	135
5.3.2.3	Raman peak fitting	138
5.3.2.4	Interpretation of peak fitting	143
5.3.2.5	RMS of rGO hydrogel assemblies	152
5.3.3	Concluding remarks	156
5.4	X-ray Diffraction	157
5.4.1	XRD applied to rGO assemblies	157
5.4.2	Results and discussion	159
5.5	Conclusions	162
Chapter 6.	rGO Assemblies as Bulk Porous Carbons	167
6.1	Introduction: rGO Assemblies as a Bulk Porous Carbon Material	167
6.2	Direct Imaging	169
6.2.1	Optical imaging	169
6.2.2	Electron imaging	173
6.3	X-ray and Neutron Scattering	182
6.3.1	WAXS, SAXS, and SANS applied to rGO assemblies	182
6.3.2	WAXS and SAXS results and discussion	188
6.3.2.1	General analysis of WAXS and SAXS features in GO and rGO assemblies	188
6.3.2.2	Drying conditions and heat treatment	200
6.3.2.3	Oxidation level	207
6.3.2.4	Electrolyte-mediated-rGO	208
6.3.2.5	Hydration level	214
6.3.3	Neutron results and discussion	218
6.4	Conclusions and Future Work	222
Chapter 7.	Conclusions and Future Work	226
7.1	Overall Outcome: rGO Assemblies as a Unique Type of Porous Carbon	226
7.2	Main Findings	227
7.2.1	Chemical composition of rGO sheets	227
7.2.2	Microscale features and properties	228
7.2.3	Mesoscale features and properties	229
7.2.4	Macroscale features and properties	230
7.3	Future research directions	231
7.3.1	Impacts on rGO sheet chemistry resulting from GO processing conditions	231
7.3.2	Quantitative analysis of the pore network	231

7.3.3	Homogeneity of the bulk material	231
7.3.4	Hydration and water transport	231
7.3.5	Further <i>in situ</i> investigations on ion transport in rGO assemblies.....	232
7.3.6	Suggestions for innovative rGO bulk materials	232
References	233	

List of Tables

Table 1. Procedures for synthesizing GO with varied degrees of oxidation and the corresponding sample names reported in this work.	61
Table 2. Comparison of the mass for each of the dried rGO assemblies made from GO precursors of different oxidation levels. It should be noted the thickness measurements are obtained with a micrometre and lack high precision, so while the variance in the mass per unit area values is $\pm 6\%$, the variance in mass density is much larger at $\pm 30\%$	64
Table 3. Matrix indicating which experimental methods were applied to specific rGO assemblies and the corresponding chapters containing the results.	68
Table 4. Chemical species present in rGO and the corresponding binding energy (BE) for the peak centre assigned to that particular bond as measured by XPS.	77
Table 5. Elemental composition and corresponding atomic percentage of each rGO assembly as determined by XPS full spectral scans. Results for the material in the original state is compared to that after further thermal reduction at 250°C and 550°C. Standard deviation in atomic percentage is 2% for carbon, 0.5% for oxygen, and 0.6% for nitrogen. The carbon to oxygen ratio (C/O) is also presented to compare with EDS data presented in the next section.	80
Table 6. Bands identified in the VB spectra labelled A-K in Figure 20 are assigned with physical meaning and compared with literature values for binding energies in the C2s and C2p region for carbon materials.	103
Table 7. Comparison of XPS and EDS results for the rGO samples prepared from the highest and lowest oxidized GO. The table includes the atomic percentage calculated from spectra peaks of carbon and oxygen as well as the resulting C/O atomic ratio.	106
Table 8. Atomic percent concentrations of carbon and oxygen in GO and corresponding rGO assemblies prepared using GO synthesized with variations of the Hummer's method to modify oxidation degree.	106
Table 9. Results from fitting the SAED pattern to determine bond length, order, and alignment in the rGO assembly.	116
Table 10. Corresponding values for $d_{(hkl)}$ from the SAED pattern of rGO assemblies compared to those of graphite, with the L_c values highlighted for (002) and (004) reflections being the most accurate measurement for the coherence length of the BSU along the c-axis, as discussed in the text.	118
Table 11. Comparison of peak parameters and corresponding real-space values for data taken from the curve fitting or directly from the reduced SAED spectra, with the values in the final column being the most accurate assessment of L_a , as discussed in the text.	119
Table 12. Comparison of the main peak parameters in the region from 1100 cm^{-1} to 1700 cm^{-1} for GO and rGO assemblies prepared from GO solutions with different oxidation levels.	137
Table 13. Relevant parameters extracted from the peak fitting procedure applied to all rGO assemblies.	142
Table 14. Relevant peak ratios extracted from the fitting procedure applied for all rGO assemblies.	146
Table 15. Results for L_a based on different calculation methods. Three are based on the I_D/I_G ratio, including the original Tuinstra-Koenig model [255], modified T-K relation for Stage Two carbons from Ferrari and Robertson [170], and the graphene activation area model developed by Lucchese [266]. These are compared to results from an alternative model using the broadening of the G-band proposed by Mallet [268].	148

Table 16. Relevant parameters extracted from the peak fitting procedure applied for all rGO assemblies.	155
Table 17. Results of the XRD (002) peak fitting for π - and γ -band components in rGO assemblies to assess the aromaticity of the material and determine the length of the coherent domains.....	160
Table 18. Comparison of the slope of the linear regions for pump dried GO and rGO assemblies with values of high-q and low-q regions in rGO listed individually, while GO is measured across the full q-range (*90° rotaion is the only GO curve with two Porod regions and the value listed is at high-q).	193
Table 19. Results of the surface fractal and paracrystalline lamellar model applied to the through-the-edge scattering curve of the pump dried rGO assembly. Colours match the individual components which fit the curve in Figure 155.....	199
Table 20. Structural parameters evaluated directly from the Bragg peak taken from WAXS curves for the rGO assemblies as measured through-the-edge along the (002) peak profile.	204
Table 21. Structural parameters evaluated using SASfit software to fit the combined SAXS and WAXS reduced scattering curves of the rGO assemblies with a fractal or paracrystalline model, as measured through surface or edge, as indicated.	205
Table 22. Fit of the Porod region for through-the-surface SAXS results for rGO assemblies of varied oxidation level.....	207
Table 23. Structural parameters evaluated from WAXS of the EM-rGO assemblies as measured through-the-edge along the (002) peak profile.	212

List of Figures

Figure 1. Timeline to highlight the number of graphene publications and significant achievements during the first ten years after discovery [4].	1
Figure 2. Illustration of the filtration process to produce layered rGO assemblies from aqueous dispersions where the corrugation of the sheets has been influenced by hydrothermal treatment at 100°C, 150°C, and 180°C to produce different pore networks in the bulk (A). The rGO assemblies can be kept hydrated as free-standing hydrogels (B) or dried to form rGO paper (C with scale bar 1 µm) that can be further annealed to increase the alignment of rGO layers, as shown in XRD (D). These structural differences have clear impacts on the performance of rGO assemblies as electrochemical capacitors with results for the hydrogels (E) and dried papers (F) prepared with hydrothermal treatment showing marked differences, especially at higher scanning rates. Further differences are also seen in the annealed rGO assemblies (G). Reproduced from [17].	3
Figure 3. Free standing rGO assembly (A) where the pore network has been tuned using non-volatile liquid (sulfuric acid) of 79 vol% (B) and 27 vol% (C) to form EM-rGO assemblies. The only structural evidence of the pores is provided by SEM (with scale bar 2 µm), showing the overall thickness of the assembly is strongly impacted, but actual structural differences are not known. The thickness was used to calculate the mass density which is used to gauge performance of the assemblies, which show marked differences at scan rates of 50 mV/s (D) and 500 mV/s (E) with the gravimetric capacitance (F) being attributed to differences in the pore size. From two figures published in reference [24].	4
Figure 4. Comparison of commonly applied radiation (electron, photon, and neutron) and penetration characterization methods for porous materials and the corresponding detectable pore size range for each technique.	6
Figure 5. Description of the experimental methods used to characterize the pore structure within rGO assemblies from the micro- to meso- and macro- scale.	8
Figure 6. Optical images (used in this work) of the same CCG membrane when fully hydrated (Wet) and after drying (Dry) show clear structural changes with varied features.	9
Figure 7. Original structural model of graphitizable and non-graphitizable carbon proposed by Franklin in 1950 (top from [46]). Description given by Marsh of the major structural changes that occur as a carbon goes through the graphitization process from 1000-3000°C (bottom from [32]).	12
Figure 8. Examples of corrugation (A), intra-sheet defects (B), and inter-sheet pores (C). Reproduced from [48, 49].	14
Figure 9. Schematic diagram showing the chemical evolution during the oxidation process of graphite to produce GO. Reproduced from [57].	16
Figure 10. The Lerf-Klinowski model for the structure of graphene oxide is presently the most accepted (from [62]).	18
Figure 11. Monitoring of the evolution of the surface chemistry of GO is shown by <i>in situ</i> XPS measurements, while thermally reducing the films at 200°C intervals up to 1000°C. The corresponding TGA results compare pyrolytic graphite (PG) with GO and each mass loss corresponds with water (100°C), oxygen groups decompose while releasing CO and CO ₂ from holes in the graphene sheet (200°C), simultaneous removal and recombination as epoxy and carbonyl aid the formation of phenolic groups (300-500°C) (from [66]).	19
Figure 12. Depiction of the impact different levels of oxidation in the original GO will have on the resulting structure of rGO. The structures are the result after rapid, high temperature reduction of GO with 20% oxygen (left) and 33% oxygen (right). The grey atoms are carbon, red are oxygen, and white are hydrogen in both hydroxyl and phenol groups (from [65]).	20

- Figure 13. Variations in schematic structures of GO and nitrogen-doped rGO produced by hydrazine-assisted solvothermal reduction (temperature range of 80-180°C) showing numerous graphitic (purple), pyridinic (pink), and pyrrolic (green) nitrogen species (left from [77]), compared with hydrazino alcohols, hydrazides, and hydrazones (right from [75])...... 21
- Figure 14. Variations in schematic structures of nitrogen-doped rGO produced interactions with ammonia gas at high temperatures (A from [86]) or urea in a hydrothermal environment (B from [87])...... 22
- Figure 15. Schematic A (at top) depicts the typical oxygen containing acidic and basic functionalities on the edges of carbonaceous solids (from [92]). Schematic B (at bottom) depicts types of nitrogen surface functional groups often present in activated carbons: (a) pyrrole, (b) primary amine, (c) secondary amine, (d) pyridine, (e) imine, (f) tertiary amine, (g) nitro, (h) nitroso, (i) amide, (j) pyridone, (k) pyridine-N-oxide, (l) quaternary nitrogen (from [93])...... 23
- Figure 16. Diagrams depicting the aromatic domain size L_a as a function of the sp^3 bonding from residual oxygen groups as GO is reduced at different temperatures is shown in A (from [104]) and the AFM image of rGO shown in B confirms the relative size of aromatic and oxygenated domains (from [70]). Both of these studies reveal the transport (hopping or percolation) is determined by the sp^2 fraction, which is itself related to the oxygen content, as shown in C. 25
- Figure 17. Structure of pure graphene (A), graphene oxide (B), and reduced graphene oxide (C) where aromatic domains are coloured in yellow, oxygen functionalities in red, and holes in purple. The corresponding description of how the residual oxygen groups disturb the planar structure along the carbon lattice, with surface roughness being related to the variance in defect concentration from high oxidized areas (D), individual oxygen bonds (E), and aromatic domains (F). Scale bar is 1 nm (from [106]). 26
- Figure 18. Natural planar fluctuations in suspended graphene sheets (corrugation) was measured by the broadening of crystalline diffraction spots, as shown in A and B (from [48]), where the deviation from a perfectly flat, 2D crystal disrupts the periodicity and results in reciprocal space features like that of narrow cones instead of perfect rods (as shown in the diagram). Defects in the carbon lattice result in curvature that influences the stacking of carbon layers within a pyrocarbon (C) and the geometry of defect configurations will lead to curvatures with specific shapes, as shown in D (from [111] and [110], respectively). 27
- Figure 19. SEM images of wrinkled (top A) and highly crumpled (bottom B) graphene sheets along with the corresponding atomistic modelling results and water contact angle (from [112]). 27
- Figure 20. Distribution of bond and elastic energy (A) along with van der Waals energy (B) in stable crumpled sheet configurations for graphene of sheet length 18 nm and 24 nm (C). Diagrams showing the different structural features in crumpled graphene (D) and GO (E) along with an illustration showing the prevalence of crosslinking in sheets that contain more defects (F) (from [113]). Simulations performed using the LAMMPS package [114] based on the adaptive intermolecular reactive empirical bond order (AIREBO) potential function [115] where both covalent bonds and van der Waals interactions are included. This method has been validated by predicting consistent structural and mechanical properties of graphitic structures, including bending rigidity and surface energy..... 28
- Figure 21. Structural depiction of how a graphene sheet of length L crumples when constrained within a sphere of radius r (A-D). Results show regardless of the original sheet length L_0 (or corresponding confinement sphere with radius r_{eq}), the fractal dimension of a purely crumpled sheet is 2.358. Depending on if the graphene sheet is more crumpled or folded, there will be a specific percentage of van der Waals (VdW) stacking present (F) which directly corresponds to the solvent accessible surface area (SASA) of the sheet (from [116]). 29

Figure 22. Hierarchical structure and corresponding size regime making up the bulk of a GO paper, where individual sheets form clusters of a lamellar form which in turn form what is termed a “super” lamellae (A) proposed by Wood et al. [119]. Model for a more disordered 3D rGO porous assembly that shows in-plane defects and a high degree of corrugation (B) proposed by Zhang et al. [120]. Molecular level model proposing how water and ions move within the “cascading slit-shaped pores” of rGO hydrogels with tuned pore size (C) proposed by Cheng et al. [26].	31
Figure 23. The unit cell (A) and band structure (B) of a sheet of pure graphene, followed by diagrams showing how the unit cell (C) stacks to form Bernal stacking in graphite (D, E, and F). The corresponding reciprocal space unit cell shows the BZ with high symmetry points and lines in pure graphene (G) alongside the BZ for 3D graphite (H), as described by Dresselhaus [53].	33
Figure 24. Atomistic model of a RL pyrocarbon looking through the edge (c-direction in A) and along the sheet (ab-plane in B) showing carbon vacancies and rips alongside hexagonal bonding in light grey and carbon defect bonds in black. The coloured spheres result from hydrogen bonding. TEM images of the stacking structure along the c-direction for RL (C) and ReL (D) pyrocarbons with insets depicting the degree of alignment between the layers measured as the mean orientation distance (MOD) [49].	35
Figure 25. Schematic of a carbon cluster where the solid lines represent graphene layers with total length L_2 aligned along an orientation with tilt given by γ . The coherent domains are shown in the shaded zones with parameters L_a and L_c , with the latter equating the number of layers, N , making up the stack. L_1 is equivalent to L_a and defines the defect free portion of L_2 . Reprinted from [133].	35
Figure 26. Schematic drawings of the differing internal structure of porous carbon materials used in energy storage devices. A comparison between carbon black (A), mesoporous carbon (B), carbon nanotubes (C), and graphene platelets (D) shows the main features of both the carbon matrix and resulting pore structure [135].	36
Figure 27. Sketch of a typical graphene plane in a carbon fibre (A) with aromatic domains and in-plane defects (by Fourdeux in 1971 but printed in [30]). Artist's conception of graphene layers within a porous fibre (B), showing the different types of order that may be present and how that impacts the internal pore network. These fibres typically have an outer layer of about 100 nm that is highly aligned with the structure becoming much more disordered in the core [138].	37
Figure 28. A structural schematic detailing the different pore structures in a typical porous carbon that has an overall stacked structure that is made up of particles with micro- and meso- pores. The main models used to describe capacitance are the electric double layer (EDLC) model, with ions adsorbing along the surface of the pore, and the slit/pore model, which acts like a parallel plate. Reproduced from [143].	38
Figure 29. Advanced computer models by Biggs et al. [148] showcase the complex relationship between carbon structures and the molecular adsorbates within them [148]. Adsorption was simulated by the cavity biased grand canonical Monte Carlo (GCMC) method of Mezei [149] where chemical potential, temperature, and volume are constants. The solid carbon structure was based on the models developed by Oberlin et al. [150-156].	39
Figure 30. Depiction of the main features of a graphene sheet in solution (A), considering that the edge geometry (top) and through-plane surface combine to have a disk-like structure which would yield the slope of -2 seen in the SANS profile. <i>In situ</i> SAXS investigating the structure of ions in microporous carbon (B), showing the changes in scattering intensity for the three different electrolytes as the voltage is changed to draw anions/cations into the pores. Reproduced from [162] and [163].	41

Figure 31. Hexagonal crystal structure of graphene layers, showing the corresponding bond length, S , and diffraction planes, d_1 and d_2	44
Figure 32. Interference peaks in the reciprocal lattice of graphite (A) with the size of the spots representing intensities and the dashed arcs show the volume of reciprocal space available to CuK_α and MoK_α radiation. Comparatively, interference maxima for turbostratic carbon (B) shows spots for the $(00l)$ reflections and lines for (hk) . Typical radially averaged powder diffraction pattern from a turbostratic carbon (C) showing independent contributions from I_{inter} , I_{intra} , and I_{incoh} along with a description of asymmetric broadening of the (hk) contribution (D). Reproduced from [177] and [176].	45
Figure 33. Transmission (A and B) and reflection (C) orientations for a turbostratic carbon with all graphene layers oriented along one plane. In (A), the reflections along the c -axis are not visible in the diffraction pattern, but they appear as the sample is rotated (45° rotation in (B)). Reflection geometry through the c -plane reveals both the $(00l)$ and (hk) intensities separately, with the (hk) reflection exhibiting a broadened, fan-like shape shown in the contour diagram. Reproduced from [183].	48
Figure 34. Real space structure of graphene layers in turbostratic carbons along with the resulting reciprocal space features detected in diffraction measurements. One layer has crystalline spots in the a^*b^* plane (A) while a turbostratic pole results in a series of rods and additional spots in c^* (B). A full turbostratic assembly has randomly rotated graphene layers in all directions, creating rings in a^*b^* and pronounced peaks along c^* (C). Reproduced from [31].	49
Figure 35. X-ray diffraction patterns of ex-PAN fibres exhibiting different levels of alignment of the graphene layers, where the most disordered turbostratic structure is seen in (A) and the microstructure becomes progressively more ordered until the partially graphitized form is shown in (D). The overall alignment of the graphene layers can be measured with the azimuthal intensity spread across the (002) peaks marked with arrows, and the result is shown in (E) where more aligned planes produce pronounced peaks and diffuse peaks have a broadened profile characterised by the FWHM which is used to define the orientation angle. Reproduced from [30].	50
Figure 36. Schematic of the dimensions (a , b , and c) and alignment (ϕ in red) of a pore within a carbon fibre (A) alongside the overall coherent domains within the carbon matrix (L_a in yellow and L_c in orange) (B). The alignment of the porous turbostratic clusters within the bulk fibre are shown in (C) alongside rotational considerations that can be used to measure the overall order within the turbostratic layers and resulting pore network (D). The main geometric considerations for the anisotropic features are detailed in (D) where #1 has graphene layers aligned parallel with the incoming electron beam (e^-) which can be rotated about the X -axis (ϕ in red) as shown in #2 or about the Z -axis (ψ shown in green) as shown in #3. Reproduced from [30] and [154].	51
Figure 37. Representation of how the scattering vector, q , is determined from the scattering pattern gathered by the detector and then translated into a curve of scattering intensity vs q for analysis from [186].	52
Figure 38. Description of how the scattering cross section varies for different elemental species. The X-ray scattering scales directly with the number of electrons while neutron scattering is more dependent on the mass of the nucleus and packing density. The schematic on the right shows how adjusting the scattering length density of the solvent can be used to mask out particular features in the material.	53
Figure 39. An examples of reduced and combined SANS and USANS data on an absolute intensity scattering curve. The insets are schematic representations of the structural features that are characterized at each q -range. Reproduced from [188].	54

Figure 40. Description of the form factor of a cylinder, showing the different regions along a scattering correlate with the dimensions of this elongated object with two distinct Guinier radii. The intermediate slope between these regions is related to $q^{-\alpha}$ where the value of α is related to the interface between the scattering object and matrix. Reproduced from [186].	55
Figure 41. Diagram of shapes showing how the slope in the Porod region Q^{-D} is described by the dimensionality of a surface, (D values 1 through 4), and is related to the structural features in the material as visualized within a given q-window outlined by the red circle (from [186]).	57
Figure 42. The diagram of an elongated pore with dimensions a, b, and c along with the OA, ϕ , in relation to the fibre axis is shown to understand how these structural parameters can be deduced from the resulting anisotropic scattering pattern (details are given in the text). Reproduced from [30].	58
Figure 43. UV-vis absorbance curves showing the unique features of GO (green) and rGO (black) to ensure the solutions are completely reduced.	62
Figure 44. Diagram of a basic filtration set-up, where the rGO dispersion is poured into the funnel at the top and the resulting assembly is formed on top of the Anodisk membrane while the water is drawn into the filtration flask below when under vacuum (from [205]).	63
Figure 45. Photographs of the rGO dispersion before filtration and the resulting stable hydrogel assembly stored in water (left) along with a comparison of the pump-dried GO and rGO assemblies. The hydrogel is a dark black colour, while the dried GO is dark brown, and the dried rGO is grey with a very pearly lustre (camera flash is incident on the rGO assembly to highlight the reflectance properties – it is not white in colour, see Figure 46).	64
Figure 46. Comparison of rGO assemblies that were pump dried, air dried, or vacuum dried, showing the tendency of the material to shrink under different conditions. All assemblies shown here have the same mass.	65
Figure 47. The CAD drawings used to 3D print the sample holder used to obtain a full 90° rotation, going from through the surface (0°) to 45° in the holder, which is shown within the blue box and from 45° to through the edge (90°) in the holder shown within the orange box.	66
Figure 48. Sample mount to function as a humidity delivery system and rotation stage where output from a controllable humidifier enters the base and passes through to the sample area mounted at top (red arrow). The vapour passes through a humidity sensor that is placed inside the cavity marked in orange. The entire apparatus is secured to a rotation stage at the base, allowing it to be fully rotated (indicated by blue arrow).	67
Figure 49. CAD design and photographs of the sample holder designed to tightly secure the rGO assemblies while drying and also functions as an electrochemical testing cell for rGO.	67
Figure 50. Photographs of the SAXS/WAXS beamline at the Australian Synchrotron. The photos show the configuration for the maximum (seven meter) camera length, with the numbers 1, 2, and 3 (top) corresponding to the three configurations reported in this work. The lower left image shows the back of the Pilatus 1M and the lower right image indicates the region where the sample is placed, with the X-ray beam passing through the sample before entering the nose-cone.	73
Figure 51. Diagram of the multiple-reflection crystal system used in the KOOKABURRA USANS instrument at ANSTO (from [210]).	75
Figure 52. Full spectral scans at 1486 eV of rGO at room temperature, 250°C and 550°C showing the prevalence of oxygen functional groups on GO of varying oxidation levels. Each scan shows characteristic peaks for oxygen, nitrogen and carbon.	79
Figure 53. XPS results from the full spectral scan, showing changes in elemental composition as rGO is further reduced at high temperatures.	81

Figure 54. XPS high resolution scans for HOPG, at 80° and 140° with respect to the analyser, yield an ideal carbon sp^2 signal that was used to optimize the C1s peak fitting procedure for the rGO materials using a Donald Sunjic (DS) function.	83
Figure 55. Nitrogen functional groups typically present in carbonaceous materials and the corresponding binding energy, highlighting the impossibility of assigning unique species based on the peak position alone. Reproduced from [99].	84
Figure 56. High resolution C1s (a), O1s (b), and N1s (c) XPS results and peak deconvolution showing the percent area for each bond type within the rGO samples HO8, HO4, LOD, and LOX at room temperature.	86
Figure 57. High resolution C1s (a), O1s (b), and N1s (c) XPS results and peak deconvolution for rGO sample HO8 at room temperature (RT) and after further thermal reduction at 250°C and 550°C.	87
Figure 58. High resolution C1s (a), O1s (b), and N1s (c) XPS results and peak deconvolution for rGO sample HO4 at room temperature (RT) and after further thermal reduction at 250°C and 550°C.	88
Figure 59. High resolution C1s (a), O1s (b), and N1s (c) XPS results and peak deconvolution for rGO sample LOD at room temperature (RT) and after further thermal reduction at 250°C and 550°C. The O1s and N1s spectra are not as smooth in the LO- materials (compared to HO-) because the lower oxygen and nitrogen content results in a smaller signal to noise ratio.	89
Figure 60. High resolution C1s (a), O1s (b), and N1s (c) XPS results and peak deconvolution for rGO sample LOX at room temperature (RT) and after further thermal reduction at 250°C and 550°C. The O1s and N1s spectra are not as smooth in the LO- materials (compared to HO-) because the lower oxygen and nitrogen content results in a smaller signal to noise ratio.	90
Figure 61. Results from the N1s high resolution XPS peak fitting showing the prevalence of associated nitrogen peaks within each rGO sample and the evolution of each species after heating to 250°C and then to 550°C. The N4 contribution is omitted from this comparison because it is only present in extremely small concentrations.	91
Figure 62. Results from the O1s high resolution XPS peak fitting which demonstrates the prevalence of specific oxygen bonding within each rGO sample and the evolution of each species after heating to 250°C, and then to 550°C.	93
Figure 63. Results from the O1s high resolution XPS peak fitting showing the evolution of the specific oxygen functionalities at RT and after heating to 250°C and then to 550°C.	94
Figure 64. Percentage of sp^2 bonds as determined by fitting the C1s high resolution XPS spectra and the corresponding total sp^2 C-C content found from taking the sp^2 percentage of total carbon present in each sample.	95
Figure 65. Percentage of total sp^3 C-C content present in each sample.	97
Figure 66. Valence band spectra showing a unique “signature” for each rGO sample at room temperature and after further thermal reduction at 250°C and 550°C. VB spectra here have been overlaid in order to compare peak intensities for different valence band energy regions described in the text, and the features are more clearly explained within the figures to follow (spectra for HO4 at 550°C is not available).	98
Figure 67. Enlarged view of the valence band spectra at the Fermi level for each sample at room temperature. The slope at 0-2 eV corresponds to the DOS, with the feature at 3 eV associated with C2p- π bands in all carbon materials. The black arrow highlights 0 eV and shows all spectra are slightly shifted to 0.20-0.13 eV.	98
Figure 68. The evolution of valence band spectra at the Fermi Edge for all rGO materials at RT and after further thermal reduction at 250°C and 550°C. The ordinate axis is kept constant across each temperature, in order to highlight changes in the slope at low binding energy.	99

Figure 69. Overlapping valence band spectra for each of the rGO samples HO8, HO4, LOD, and LOX at room temperature to show the different “signature” patterns for each material.	100
Figure 70. Overlapping valence band spectra for each of the rGO samples HO8, HO4, LOD, and LOX after further thermal reduction at 250°C, to demonstrate how the different “signature” patterns have changed after removal of oxygen and nitrogen groups.	100
Figure 71. Overlapping valence band spectra for each of the rGO samples HO8, HO4, LOD, and LOX after further thermal reduction at 550°C to show how the different “signature” patterns have changed after removal of oxygen and nitrogen groups (spectra for HO4 at 550°C is not available).	101
Figure 72. Deconvolution of the VB spectra for HO4 at room temperature, showing distinct peaks that are applied to LOX at RT and after heating to 550°C to highlight the features most strongly impacted by oxygen and nitrogen bonding which impact the electronic structure of the carbon lattice. ...	102
Figure 73. Monte Carlo simulations to estimate the interaction volume of the layered films for GO (top) and rGO (bottom) using an electron beam with accelerating voltage of 5 keV (left) or 10 keV (right). Each box has a height of 2 μm and length of 3 μm	104
Figure 74. EDS for GO (left) and rGO (right) materials showing the elemental composition present.	106
Figure 75. Atomic percent concentrations oxygen (top) alongside the carbon/oxygen ratio (bottom) for GO and rGO assemblies prepared from GO with modifications to the oxidation process	107
Figure 76. Diagram to represent the elements making up the basic structural unit for different types of carbons, as proposed by Oberlin et al. [156]. The BSU of total length, L_a , is composed of stacked, graphene-like layers with aromatic domain length (l , in pink) and corrugation from stacking faults, defects (white rings), and oxygenated edge groups (dots) which impact the stacking order along L_c (left). These units are assembled to form the larger, bulk carbon structure which may consist of larger meso- and macropores and contain a given degree of order between different BSUs (right).	110
Figure 77. The TEM image (left) and SAED pattern (right) of the cross-section of a dry rGO assembly show crystalline coherent domains along with meso-scale disorder in inter-sheet alignment (radial intensity spread of (002) ring).	112
Figure 78. Method to measure the orientation angle (OA) of the (002) plane in layered carbons using the SAED, where the FWHM can be used to classify material into one of four levels of texture (from [247]).	114
Figure 79. The fringe analysis technique measures fluctuations in intensity along a linear region of interest (shown in the red box on left image). A series of peaks is used to measure the distance between points of maximum intensity, which correspond to the interlayer distance (right).	115
Figure 80. Diagram relating the rings seen in the SAED pattern to the unit cell of graphite (from [248]). The outer rings (marked A in blue) result from the intra-sheet carbon bonds while the inner ring and bright spots (marked B in orange) result from inter-sheet stacking of multiple basal planes.	115
Figure 81. Inter-sheet lamellar stacking has enhanced intensity in sectors 1 and 3 (orange), while intra-sheet bonding is slightly enhanced in sectors 2 and 4 (blue). Radial intensity curves for each sector are plotted alongside the full 360° radial average to illustrate peak intensity is dependent on orientation. Peak fitting for the full 360° as well as sectors 1&3 and 2&4 was performed to obtain the values listed in Table 9.	116
Figure 82. Measurement of intensity flections along the (002) ring are used to classify the long-range alignment of the rGO layers (region between orange rings). This azimuthal intensity scan has been	

fitted with two Gaussians and the FWHM of 72° is a direct measure of the orientation angle (OA) used to classify layered carbon systems.	117
Figure 83. The maximum peak height was used to determine the location of the peak centre and breadth of the (002), (100), and (110) planes from the SAED pattern. The full 360° radial average is shown on the left and a comparison between sectors 1&3 (dotted) to sectors 2&4 (solid) is shown on the plot to the right.....	119
Figure 84. Measurement of the anisotropic SAED pattern across a very narrow range (5° spread between the pink and blue arrows) which corresponds to the (<i>hk</i>) reflections allows for the (10) and (11) peaks to be analysed without broadening due to the “fountain-like” spread from two-dimensional crystals. The sharp feature at 2.51 nm^{-1} is an artefact from the TEM support grid and is ignored in the rGO structural analysis.	120
Figure 85. Original TEM image (top left) that was then modified using ImageJ [254] to highlight the stacked aromatic regions (top right). The image was further modified and then measurements were taken to quantify the domain length and number of stacked layers (bottom).	121
Figure 86. Edge-on images of rGO assemblies from TEM (left) can be better interpreted alongside high-resolution SEM (right) imaging which shows the very small lattice fringe lengths in TEM ($< 5 \text{ nm}$) are due to disorder and stacking faults as SEM shows the size of rGO sheets extends to hundreds of nanometres.	122
Figure 87. Example of Raman spectra for pristine graphene (top) and defective graphene (bottom), highlighting the main features used for structural analysis and interpretation (from [124]).	123
Figure 88. Comparison of the 2D (also termed G') Raman band taken with 2.41 eV laser energy for HOPG and 1-4 layers of graphene with Bernal stacking [125].	125
Figure 89. Evolution of first- and second-order Raman spectrum for HOPG and graphite crystallites of decreasing size, highlighting the presence of the D-band (1355 cm^{-1}) and broadening in second-order peaks as L_a decreases (from [260]).	126
Figure 90. Raman spectra for various noncrystalline, mainly graphitic, amorphous carbons (left) compared with those for crystalline graphitic carbons (right) [261].	127
Figure 91. Graphic depiction of the sp^2 and sp^3 configurations in the three stage amorphization trajectory from graphite, to nanocrystalline graphite, to amorphous carbon (a-C) and tetrahedral amorphous carbon (ta-C) proposed by Ferrari and Robertson [171].	128
Figure 92. Three-stage model for the amorphization trajectory of carbons proposed by Ferrari and Robertson [170]. The position of the G band as well as the intensity ratio of the D to G band is related to the amount of sp^3 carbon present in graphite, nanocrystalline graphite, amorphous carbon (a-C), and tetrahedral amorphous carbon (ta-C).	129
Figure 93. Relationship between the $I(\text{D})/I(\text{G})$ peak ratio and aromatic domain length, L_a , for graphitic material (labelled nc-G where the TK equation holds) and amorphous carbons (labelled a-C where the TK relationship is no longer valid) [170].	130
Figure 94. Work by Lucchese et al. [266] created a full model of the I_D/I_G dependence to the density of defects and inter-defect distance, L_D , from micro down to sub-nm scale. The new model defined both a “structurally disordered” region, r_s , alongside “activated” region, r_a , from which the D band arises (A). Depending on the defect density, the activated regions will overlap and the D band intensity will be influenced accordingly (B-E).	131
Figure 95. Cancado et al. [267] extended the model relating I_D/I_G with the inter-defect distance, L_D , to apply at different excitation energies by adjusting the coefficient, C_A , as shown in the inset with solid curve is given by $C_A = 160 \cdot E_L^{-4}$ (A). Relationship between the FWHM of the D and 2D bands to	

L_D at different excitation energies (B). Comparison of the FWHM of the G band to L_D at different excitation energies (C).....	132
Figure 96. Early work of Ferrari and Robertson showing the relationship between the FWHM of the G band to known L_a values for a variety of carbon materials [263].	133
Figure 97. Mallet-Ladeira et al. [268] argue for using the HWHM of the G band to determine L_a in pyrocarbons and cokes, citing the distinct relationship in the 2-10 nm region (A) and independence from excitation energy (B) as advantages over the I_D/I_G ratio.	133
Figure 98. Typical Raman spectra features for graphite, activated carbon (AC), and thermally reduced GO (TRGO) (A) taken from reference [137]. A similar comparison of pyrocarbon (PyC) and graphite (Gr) Raman spectra (B) with the suggested curve fitting (C) taken from reference [273].	134
Figure 99. Raman map of D/G peak ratio across the surface of the HO8-rGO assembly, showing a homogeneous distribution of sp^2 domains and defects across the sample surface.....	135
Figure 100. Raman spectra for GO (bottom) and rGO (top) samples prepared with various levels of oxidation.	136
Figure 101. Comparison of the values from the table above, showing clear trends in the peak parameters for GO and rGO assemblies prepared from GO solutions with different oxidation levels.	137
Figure 102. Raman spectra for rGO assemblies normalized to the G-peak intensity highlights the differences in all other peaks directly relates to the oxidation level.....	138
Figure 103. Summary of curve fitting options outlined by Seong on spectra of soot: (a) 2 Lorentzian and 1 Gaussian, (b) 3 Lorentzian, (c) 3 Lorentzian and 1 Gaussian, (d) 4 Lorentzian, (e) 4 Lorentzian and 1 Gaussian, (f) 5 Lorentzian [257].	139
Figure 104. Example of fitting second-order spectral features for graphene materials with various degrees of defects and disorder (from [276])......	140
Figure 105. Details of the fitting procedure are labelled for the LOX assembly showing the BFW (G), Gaussian (D''), and three Lorentzian (I, D, D') peaks for the first-order spectral region (top) and the three Lorentzian ($D+I$, $2D$, $D+G$) and one Gaussian (combination of $2D'$ and $G+D'$) peaks for the second-order spectral region (bottom).....	141
Figure 106. Peak fitting for the first- (left) and second-order (right) regions of the Raman spectra for rGO assemblies. All fits converged with a χ^2 tolerance value of $1E-6$ reached (reduced χ^2 ranged from $8.9E-6$ to $4.4E-5$ and adjusted $R^2 > 0.999$).....	142
Figure 107. Comparison of D, G, and $2D$ peak positions for all rGO assemblies.	143
Figure 108. Comparison of D, G, and $2D$ FWHM values for all rGO assemblies.	144
Figure 109. Comparison of the D, G, D' , I, and D'' peak area values for all rGO assemblies.	145
Figure 110. Graphene and HOPG with different types of defects are compared to show a relationship between $I_{D'}/I_G$ and I_D/I_G that translates into $I_D/I_{D'}$ values that can differentiate boundary-, vacancy-, and sp^3 -like defects – each shown by the data points of black hexagons (graphite edge), stars (ion induced holes), and red dots (chemical bonding), respectively (from [278]).	147
Figure 111. Comparison of the $I_D/I_{D'}$ and $A_D/A_{D'}$ peak ratios for all rGO assemblies.....	147
Figure 112. Comparison of the calculated L_a results, based on different models for GO and rGO assemblies.....	149
Figure 113. Calculation of L_a based on Lucchese's model [266] with error bars to account for possible variance due to estimation of defect size.	150
Figure 114. Data and linear fit that Mallet's model [268] is based on compared with results for rGO and GO using L_a values resulting from Lucchese's model [266].	150

Figure 115. Comparison of GO and rGO assemblies with nano-graphitic carbons investigated by Mallet [268] and Ganesan's work [216] on both Stage One and Stage Two nano-graphitic carbons in a similar size region.....	151
Figure 116. Comparison of the I_{2D}/I_{D+G} and I_{2D}/I_G peak ratios for all rGO assemblies	152
Figure 117. Optical images of the rGO hydrogels used for Raman analysis, showing both of the hydrated films prepared at 100°C (A) and 180°C (B) have a very smooth surface which becomes very rough as the water evaporates (C). The blue scale bars indicate 20 μm	153
Figure 118. Full RMS spectra for HO4 rGO hydrogel assemblies prepared at different reduction temperatures. The inset highlights the higher order region which exhibits different properties than the dried assemblies, most notably the enhanced feature at 2450 cm^{-1}	154
Figure 119. Comparison of the Raman spectra for the HO4 hydrogel and LOX pump dried assembly, both reduced at 100°C, to highlight the dry and hydrogel assemblies show very similar spectral features.	154
Figure 120. Fitting procedure applied to the first order RMS region for HO4 hydrogel assemblies prepared at the different reduction temperatures of 100°C and 180°C.	155
Figure 121. Raman results from the rGO assemblies are marked on the three-stage model for the amorphization trajectory of carbons proposed by Ferrari and Robertson [170] showing rGO materials are most likely in Stage Two and contain 5-10% sp^3 bonds.....	157
Figure 122. Example of fitting the (002) peak for XRD in coal to quantify aromatic and aliphatic contributions to the inter-layer reflection from [284] and corresponding structural diagram developed in 1961 by Yen et al. [109].....	158
Figure 123. Peak profile of the (002) reflection for pump-dried rGO assemblies. To emphasize differences in peak shape, the spectra have been normalized to give peak height of one and offset for clarity.	159
Figure 124. Fitting results for the XRD (002) peak profile, consisting of the π -band and γ -band components. All fits converged with a χ^2 tolerance value of 1E-6 reached (reduced χ^2 ranged from 62 to 142 and adjusted $R^2 > 0.97$).	160
Figure 125. XRD profile for the LOH GO and rGO assemblies highlighting the marked change in (002) peak depending on the drying method used.	161
Figure 126. XRD profile for the HO8 GO and rGO assemblies showing the non-existent (002) peak for hydrogel assemblies.	162
Figure 127. The elements of the BSU for dried rGO assemblies fit well with the micro- to mesoscale structural model for a lamellar pyrocarbon developed by Farbos et al. [49] which are shown on the left and compared to SEM images of pump dried rGO assemblies showing the macro-scale features as seen "through-the-surface" and "through-the-edge".....	166
Figure 128. General description of how the different structural elements of the rGO sheets will influence the scattering pattern, depending on if the wide- and small- angle scattering measurements are taken through-the-surface or through-the-edge of the assembly. The SEM images and schematic of the scattering geometry indicate how the sample is oriented with respect to the incoming beam to produce the 2D scattering results shown at right.	168
Figure 129. Optical images comparing the surface topology of HO3 rGO assemblies dried under different conditions (all scale bars are 100 μm).	169
Figure 130. Optical images showing the surface topology of a wet HO3 rGO hydrogel (all scale bars are 10 μm).	170

Figure 131. Optical images of EM-rGO assemblies treated with different concentrations of sulfuric acid (0.2 M, 0.5 M, 1.0 M, and 2.0 M) as indicated.	171
Figure 132. Optical images comparing the surface topology of HO3 rGO assemblies dried under different conditions to EM-rGO prepared with different concentrations of intercalated sulfuric acid and then vacuum dried (all scale bars are 100 μ m).	172
Figure 133. SEM images of the surface of GO assemblies of different oxidation levels.	174
Figure 134. SEM images of the surface of pump dried rGO assemblies prepared from GO precursors of different oxidation levels.	175
Figure 135. Higher resolution SEM images of the surface of pump dried rGO assemblies prepared from GO precursors of different oxidation levels, showing density fluctuations along the surface.	176
Figure 136. High resolution SEM image of the surface of the HO3 rGO assembly, showing density fluctuations as well as wrinkles, folds, and corrugation along the surface.	177
Figure 137. SEM image of the surface of the HO3 rGO assembly after low-dose ion irradiation to selectively ablate regions of the carbon matrix depending on the density of the bulk. The images show progressive damage to the surface, where area 1 has not been exposed to the ion beam while areas 2, 3, and 4 have been irradiated for increasing amounts of time.	178
Figure 138. High resolution SEM image of the edge of the HO3 rGO assembly, showing a high degree of corrugation and waviness within the stacked graphene layers.	179
Figure 139. TEM image of the edge of the HO3 rGO assembly, showing the graphene layers are much more turbulent at the mesoscale than that indicated from microscale features in SEM.	180
Figure 140. Comparison of TEM (left) and SEM (right) images of the total cross section of the HO3 rGO assembly at the macroscale.	180
Figure 141. High resolution SEM images of the cross section of two pump dried HO3 rGO assemblies from within the bulk, where a focused ion beam was first used to cut away the bulk material in thin sections and resulted in a smooth surface of the carbon matrix that is imaged with the electron beam. The blue line represents the horizontal surface of the rGO assembly with the area below it being the carbon matrix and voids, and the area above it being a layer of platinum deposited to protect the bulk material during the ion milling process.	181
Figure 142. A comparison of isotropic and anisotropic scattering patterns from carbon fibres with different pore structures. The result of reducing the scattering pattern by taking a radial average of an isotropic sample is also highlights the fact that many porous carbons have rather featureless curves (from [136]).	183
Figure 143. SEM image and assumed structural model for EM-rGO materials tuned with sulphuric acid of different concentrations. Reproduced from [17].	185
Figure 144. Schematic of the effect of sheet layering on the shape of the SAS curve when the incident beam is parallel to the layering plane (through-the-edge). The striped boxes represent the layers and the solid elongated objects represent the SAS pattern. The length of the scattering feature (black arrow) indicates the smallest periodic size in the c-axis, while the widening (green bracket) is related to the extension of periodic order along the a-axis. Periodicity creates a more uniform width while size distribution decreases long-range ordering and results in a fan-shaped pattern where the intensity spread (orange line) is related to the prevalence of scatterers within a given range. ...	186
Figure 145. WAXS results for bulk water in ambient conditions showing two characteristic features (reproduced from [286]).	187
Figure 146. Schematic of how the rGO assemblies are placed in respect to the incoming X-ray beam in order to produce isotropic (through surface) and anisotropic (through edge) WAXS patterns. The	

wavy lines represent the edges of layered rGO sheets and the solid plane represents the surface. The 2D image is evaluated in sectors, where the blue region corresponds to intra-sheet features along the ab-plane and the yellow region can evaluate the inter-sheet stacking and pores along the ac-plane independently as the sample is rotated from 0° to 90° to align through-the-edge.	188
Figure 147. WAXS and SAXS patterns for pump dried GO and LOD rGO layered assemblies probed through-the-surface (isotropic patterns) or through-the-edge where the Bragg peak and pore alignment are clearly visible in the anisotropic patterns.	189
Figure 148. Reduced scattering curves for pump dried GO and rGO taken from the horizontal sector shown in yellow in Figure 146 where the Bragg peak emerges when the X-ray beam is aligned through-the-edge. The main features of the curve used for analysis are marked on the figure, where the dotted and solid lines indicate which regions are used to calculate the slope (Porod region) and the arrow indicates the scattering feature associated with a larger inter-sheet structure.	190
Figure 149. Sector analysis in the horizontal and vertical sections of the 2D scattering pattern for pump dried GO (top) and the resulting rGO (bottom) assembly across a full 90° rotation.	191
Figure 150. A comparison of the Porod regions in the reduced scattering curves for pump dried rGO taken in the horizontal sector show very different power law relationships for through-the-edge (ac-plane) and through-the-surface (ab-plane) with the value of -3 to -4 being characteristic of a rough interface and the value of -2.6 relating to a fractal dimension describing the density distributions and features of the pore network in the bulk (a mass or pore fractal).	192
Figure 151. Kratky plot of the pump dried rGO assembly which more clearly identifies scattering features within the edge and surface curves.	194
Figure 152. Fit of the linear region in a plot of $q^3 I(q)$ versus q^2 for the through-the-edge curve (blue) and the through-the-surface curve (green) and dotted lines indicating the onset of scattering resulting from interlayer fluctuations in the stacking distance between graphene planes (note maximum q^2 of $0.008 \text{ \AA}^{-2} \approx 7 \text{ nm}$).	195
Figure 153. Schematic of the stacking disorder described by paracrystalline theory where the displacements in the layer positions result in a structure function that decays across longer-range order (left). The structure factor applied here is displayed in the plot on the right, showing how different physical parameters (number of layers, N, layer spacing, d, and the variance in layer spacing, Δ) impact the resulting function (right). Reproduced from the SASfit user guide [214].	196
Figure 154. Full fit of the through-the-edge scattering pattern of the pump dried rGO assembly with the raw data in yellow and the black line is the fit to data after applying a paracrystalline, multi-lamellar structure factor combined with a power law at low-q. The portions of the curve related to surface scattering, D_s , cluster height, L_c , and interlayer distance, $d_{(002)}$ are labelled on the curve along with arrows highlighting deviations from the raw data discussed in the text.	197
Figure 155. Results of the surface fractal and lamellar models shown individually on the through-the-edge scattering curve.	198
Figure 156. Sector plot of the horizontal region (across the (002) reflection) when the assembly is rotated through-the-edge (90°), at 45°, and through-the-surface (0°). The corresponding 90° and 0° WAXS patterns are shown above the SAXS patterns at 90° and smaller rotation to 75° for the pump dried rGO assembly.	201
Figure 157. Sector plot of the horizontal region (across the (002) reflection) when the assembly is rotated through-the-edge (90°), at 45°, and through-the-surface (0°). The corresponding 90° and 0° WAXS patterns are shown above the SAXS patterns at 90° and smaller rotation to 75° for the vacuum dried rGO assembly.	201

Figure 158. Sector plot of the horizontal region (across the (002) reflection) when the assembly is rotated through-the-edge (90°), at 45°, and through-the-surface (0°). The corresponding 90° and 0° WAXS patterns are shown above the SAXS patterns at 90° and smaller rotation to 75° for the air dried rGO assembly.	202
Figure 159. Sector plot of the horizontal region (across the (002) reflection) when the assembly is rotated through-the-edge (90°), at 45°, and through-the-surface (0°). The corresponding 90° and 0° WAXS patterns are shown above the SAXS patterns at 90° and smaller rotation to 75° for the hydrothermal rGO assembly.	202
Figure 160. Sector plot of the horizontal region (across the (002) reflection) when the assembly is rotated through-the-edge (90°), at 45°, and through-the-surface (0°). The corresponding 90° and 0° WAXS patterns are shown above the SAXS patterns at 90° smaller rotation to 75° for the annealed rGO assembly.	203
Figure 161. Comparison of the (002) peak profiles for rGO assemblies that underwent heat treatment (annealing or hydrothermal) or various drying conditions (pump, vacuum, or air). The π -band and γ -band components are indicated by the dotted lines and the small arrow highlights the emergence of a graphitic peak in the annealed assembly.	204
Figure 162. The reduced through edge scattering curves and shape of the SAXS and WAXS patterns (top) are used to design a structural diagram of ordered and disordered domains within the annealed and air dried assemblies (bottom), indicating how these structural elements can impact the pore network surrounding these turbostratic clusters. The grey brackets and arrows highlight that the larger volumes within the assembly contribute to the small angle scattering, and these regions consist of both open pore space and also the coherent domains of turbostratic clusters, as indicated in green. The interlayer space, $d_{(002)}$, within the clusters is the source of the wide-angle peak (green arrows). The pink line shows how L_a is measured with Raman and the blue line represents how L_a is measured with XRD.	206
Figure 163. Plot of the through-the-surface combined WAXS and SAXS results for pump dried rGO assemblies of varied oxidation level. Curves are offset for clarity with arbitrary intensity values.	207
Figure 164. SAXS results for as-prepared EM-rGO assemblies taken at different locations along the surface of 2.0 M (top) and 0.1 M (bottom) samples.	208
Figure 165. Comparison of through edge SAXS patterns of the freeze dried method (with and without pre-treatment of 0.1 M sulfuric acid) to other drying methods which produced more aligned rGO sheets.	209
Figure 166. Comparison of through-the-edge SAXS patterns for hydrated EM-rGOs prepared with different concentrations of sulfuric acid at 90° (edge), 45°, and 0°(surface).	210
Figure 167. Through-the-edge WAXS patterns for hydrated EM-rGOs and a typical rGO hydrogel (far right) with identical intensity scaling. The intensity at the highest q -values (at and beyond the Bragg peak shown in diffuse red) is due to scattering from water.	210
Figure 168. Reduced through-the-edge WAXS patterns for the EM-rGO materials tuned with different amounts of sulfuric acid as compared to a hydrogel assembly without modification.	211
Figure 169. Comparison of the through-the-edge and through-the-surface WAXS results for 1.0 M EM-rGO.	213
Figure 170. Through-the-surface scattering curves for 1.0 M and 5.0 M EM-rGO show the presence of bulk water at high- q	213

Figure 171. WAXS patterns for rGO hydrogels showing the peak for bulk water is present in both through-the-surface and through-the-edge images, where a faint (002) feature is visible in the latter.	214
Figure 172. Through-the-surface <i>in situ</i> WAXS patterns for hydrogel assemblies from a fully wet to a fully dry state (left to right), with the intermediate structure undergoing a pronounced transition, as referenced in the text.	214
Figure 173. Through-the-edge <i>in situ</i> WAXS patterns for hydrogel assemblies from a fully wet to a fully dry state (top left to bottom right), with the intermediate structure undergoing a pronounced transition, as referenced in the text.	215
Figure 174. Reduced horizontal sector for the through-the-edge WAXS results of an rGO hydrogel as it goes from a completely hydrated ($V_{\text{rGO}}:V_{\text{H}_2\text{O}}$ of 1:20) (top, black curves) to a completely dry ($V_{\text{rGO}}:V_{\text{H}_2\text{O}}$ of 1:0.05) (lower, rainbow curves) state. The arrows indicate the major structural changes that are discussed in the text.	216
Figure 175. Plot of the reduced <i>in situ</i> hydrogel curves from Figure 174 with the number index on the y-axis and the colours corresponding to the relative intensity (orange highest, dark blue lowest). The insets correspond with q-ranges of interest discussed in the text (shown with grey brackets and black arrows pointing to the q-range indicated), with orange dashed lines corresponding to the index number where a pronounced shift occurs.	217
Figure 176. Reduced through-the-surface SAXS results for an rGO hydrogel as it goes from a completely hydrated (drying time of zero) to a completely dry (drying time >18 minutes) state with the slope of the low-q SAS range (red arrow) plotted to show the transition over time (on left).	218
Figure 177. Combined USANS, SANS, and neutron diffraction plot on an absolute intensity scale for HO3 rGO. Defined structural regions are indicated with orange lines on the plot and are referenced in the text.	219
Figure 178. Kratky plot of the combined USANS, SANS, and neutron diffraction results for HO3 rGO with the regions of interest highlighted in green and defined features indicated with the arrows.	220
Figure 179. Guinier plot of the SANS region corresponding to the feature seen in the mid-q range for HO3 rGO with a fit of the linear region to obtain the slope which can be related to the radius of gyration of the scattering particle.	221
Figure 180. SANS curves for as-prepared, dried EM-rGO assemblies as compared to a pump dried sample that was not tuned with sulfuric acid.	222
Figure 181. Depiction of how carbon orientation and pore alignment can be measured at the microscale (wide angle at left) and mesoscale (small angle at right) based on the approach for pore characterization via WAXS and SAXS analysis in carbon fibres as outlined by Dresselhaus [30] and discussed in Chapter 2.	224
Figure 182. Depiction of the individual structural elements making up the scattering curve for rGO assemblies. This figure highlights the findings of this work, showing the influence of orientation and scale on the particular structural element within the rGO assembly. The through-the-surface fractal network is consistent throughout the bulk, while the through-the-edge lamellar structure is composed of different size entities. From right to left: the Bragg peak at high-q measuring the interlayer distance between the stacked aromatic domains; the broad feature at mid-q relating to the size of the turbostratic clusters; the Porod region at low-q arising from the surface roughness of aligned and elongated rGO sheets; these features continue across the entire 4.5 μm length of the bulk assembly.	227

List of Abbreviations

AC	activated carbon
BE	binding energy
BSU	basic structural unit
EDS	energy dispersive spectroscopy
EM-rGO	electrolyte mediated reduced graphene oxide
FIB	focused ion beam
FWHM	full width half maximum
GO	graphene oxide
HO-	high degree of oxidation
HR-SEM	high-resolution scanning electron microscopy
<i>l</i>	aromatic length
L_a	(<i>hk</i>) coherent length or aromatic length (as outlined in the text)
L_c	(<i>00l</i>) coherent length
LO-	low degree of oxidation
macro	size region > 50 nm
meso	size region 2 nm to 50 nm
micro	size region < 2 nm
OA	orientation angle at microscale
Phi (ϕ)	alignment angle to layer axis at mesoscale
PSD	pore size distribution
PT	paracrystalline theory
rGO	reduced graphene oxide
RMS	Raman spectroscopy
SAED	selected area electron diffraction
SANS	small angle neutron scattering
SAS	small angle scattering
SASA (ASA)	solvent accessible surface area
SAXS	small angle X-ray scattering
SEM	scanning electron microscope
TEM	transmission electron microscopy
TK	Tuinstra Koenig relation
USANS	ultra-small angle neutron scattering
VB	valence band
WAXS	wide angle X-ray scattering
XPS	X-ray photoelectron spectroscopy
XRD	X-ray diffraction

Chapter 1. Introduction to rGO Assemblies as a Unique Type of Porous Carbon

1.1 Statement of the Problem and Significance of the Study

With the explosion of graphene related research since the reports of its unusual electronic properties in 2004 [1, 2] and award of the Nobel Prize in Physics in 2010, the field now contains many thousands of articles focused on graphene-based materials that range from scientific studies of defect-free graphene sheets to engineered composite materials which combine graphene-like sheets of carbon with just about anything. The growing number of publication is shown in Figure 1, and this trend continues into the present year where it is estimated that graphene related publications from China increase more than 70% annually [3]. To narrow the focus, this project investigates reduced graphene oxide (rGO) assemblies created by a solution-based reduction of graphene oxide (GO) using chemical means (can also be referred to as chemically converted graphene, CCG). While rGO can generally be described as a two-dimensional sheets of carbon atoms arranged in a honeycomb-shaped lattice, they differ from pure graphene (produced through mechanical exfoliation or chemical vapor deposition) in a variety of important ways which will be discussed in detail throughout this work.

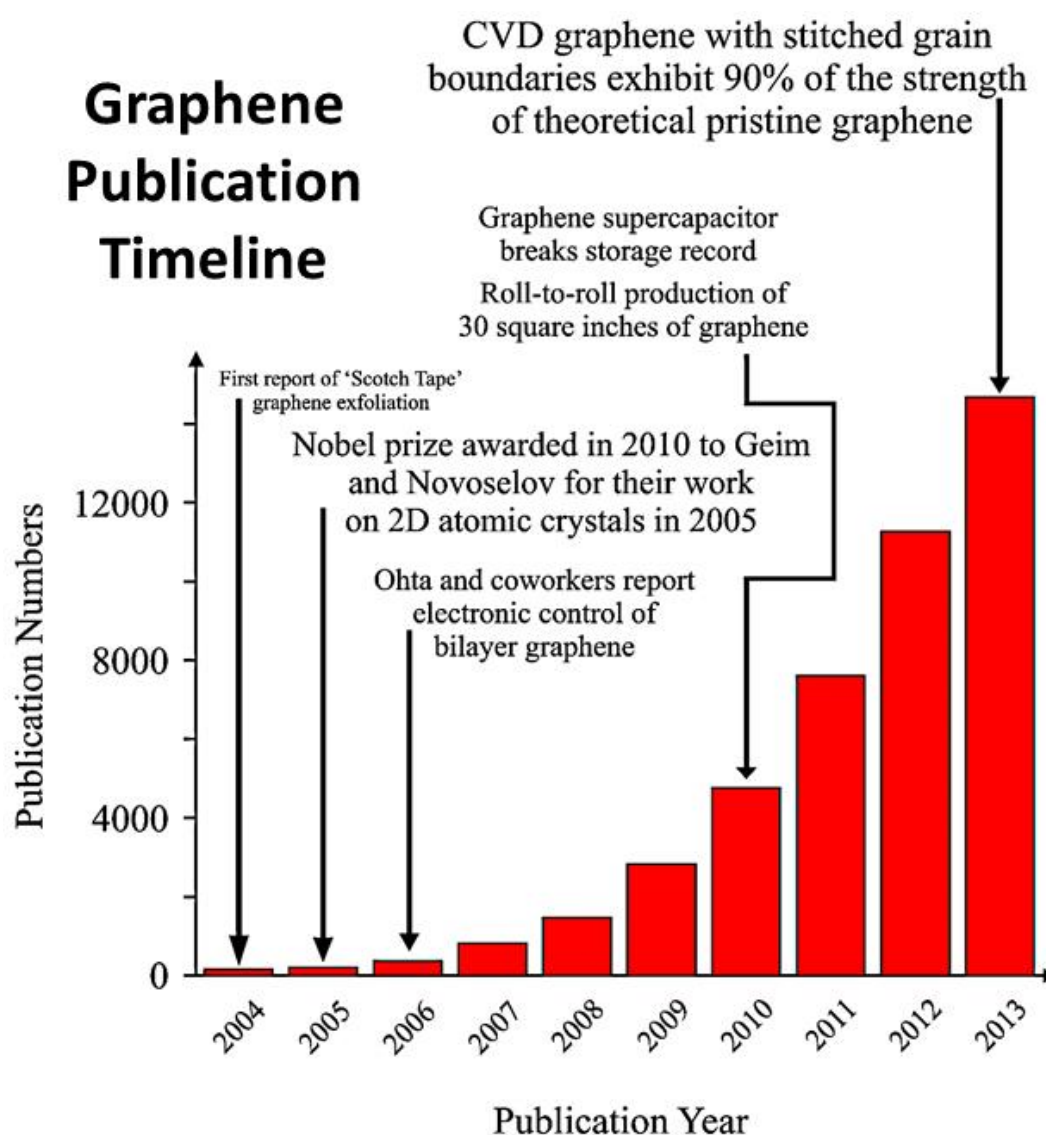


Figure 1. Timeline to highlight the number of graphene publications and significant achievements during the first ten years after discovery [4].

The past decade of graphene research has contributed a vast body of scientific knowledge outlining the unique properties of this two dimensional crystal and promising many potential applications across a range of fields including energy storage, electronics, sensors, and medical technologies. Scientists, engineers, entrepreneurs, and industrial giants are all eager to translate these findings into practical devices and drive new economic development based on the enhanced material properties graphene appears to offer [5-8] [9]. The most promising method for scalable production of graphene is through the reduction of graphene oxide, which results in carbon sheets that retain the desirable properties of high strength and conductivity, but unlike defect-free graphene, rGO materials have inherent variations in structure and chemistry [10]. While new and improved performance from graphene-based materials is reported at an exponential rate, in-depth fundamental studies to characterize and correctly interpret the underlying mechanisms driving the performance have not kept pace. This gap is especially prominent with rGO materials, and the aim of this work is to fully characterize the structure of rGO layered assemblies.

While this work has limited the scope to investigate layered rGO assemblies prepared from filtration of aqueous dispersions reduced with hydrazine (later detailed in section 3.1: Materials), it is expected that the large research community focusing on graphene-based assemblies can use the methods and models developed in the results of this thesis to draw conclusions about structure-property relationships for other types of rGO systems. It is important that the methods used can quantify structural elements across a very broad size range because features at the micro-, meso-, and macroscale play specific roles for different types of transport (gasses, liquids, and ions), where characteristics at larger length scales may not be indicative of the nanoscale properties or morphology. Because the chemical and structural features of rGO assemblies control the structure-property relationships in these materials, existing experimental methods need to be expanded upon in order to understand these interactions.

While there are many published works detailing specific structural elements of rGO materials and unique aspects of their corresponding material performance, this work qualitatively and quantitatively analyses the structure from the chemical level all the way up to the resulting bulk assemblies. Further, an in-depth analysis of radiative characterization methods applied to the rGO assemblies is offered in tandem in order to provide much needed insight on how best to interpret data for this relatively new type of porous carbon. This work also introduces new techniques that are especially applicable for hydrated rGO materials used in energy storage applications.

1.2 Background of the Problem

Currently, rGO assemblies are much less understood than their close relatives of graphene and graphite, and these new materials occupy a unique place within the porous carbon family. While there is a large and growing body of work devoted to investigating rGO materials, a full description of the structure of rGO assemblies is still not known, and given the chemical variance within rGO materials, it is likely that an all-encompassing, fixed description may not be possible. Because of the variations in chemical composition and anisotropic pore structure, experimental procedures to investigate these layered rGO materials are not well developed – this is especially true for the hydrogel assemblies where *in situ* investigations on hydration and energy storage are critically needed, but are hindered by additional experimental challenges. By first recognizing that rGO assemblies are more closely related to porous carbons than pure graphene, this work draws upon the rich history of carbon research and applies both traditional and new characterization methods to outline a best-practice approach for experimental work and data analysis.

Scalable and cost-effective production of graphene-based materials is necessary in order for them to be relevant in most markets. The wet chemistry route of first synthesizing GO from graphite flakes

and then reducing it to rGO is widely believed to be the most promising method for large scale production. There is a need for standardization and characterization of these materials, as the major hurdles for industrial adoption hinge on the specific properties of the rGO sheet as well as those of the final bulk assembly [10] – these aspects can often have trade-offs, as will be discussed in the text. While the overall surface chemistry of GO has been studied for many years, there are innumerable variations in rGO materials because so many factors will contribute to the final structure [11, 12]. The original graphite material, along with the specific conditions of both the oxidation and reduction processes, will have large impacts on the structure of rGO sheets that subsequently influence the performance of the resulting bulk material, as reported for many types of porous carbons [13, 14]. The work here follows the method developed by Li et al. [15] to produce stable, water-based dispersions of rGO reduced using hydrazine which has now become widely applied in both research and industry, being well regarded as an effective method for producing low-cost, bulk rGO materials [7, 10, 16].

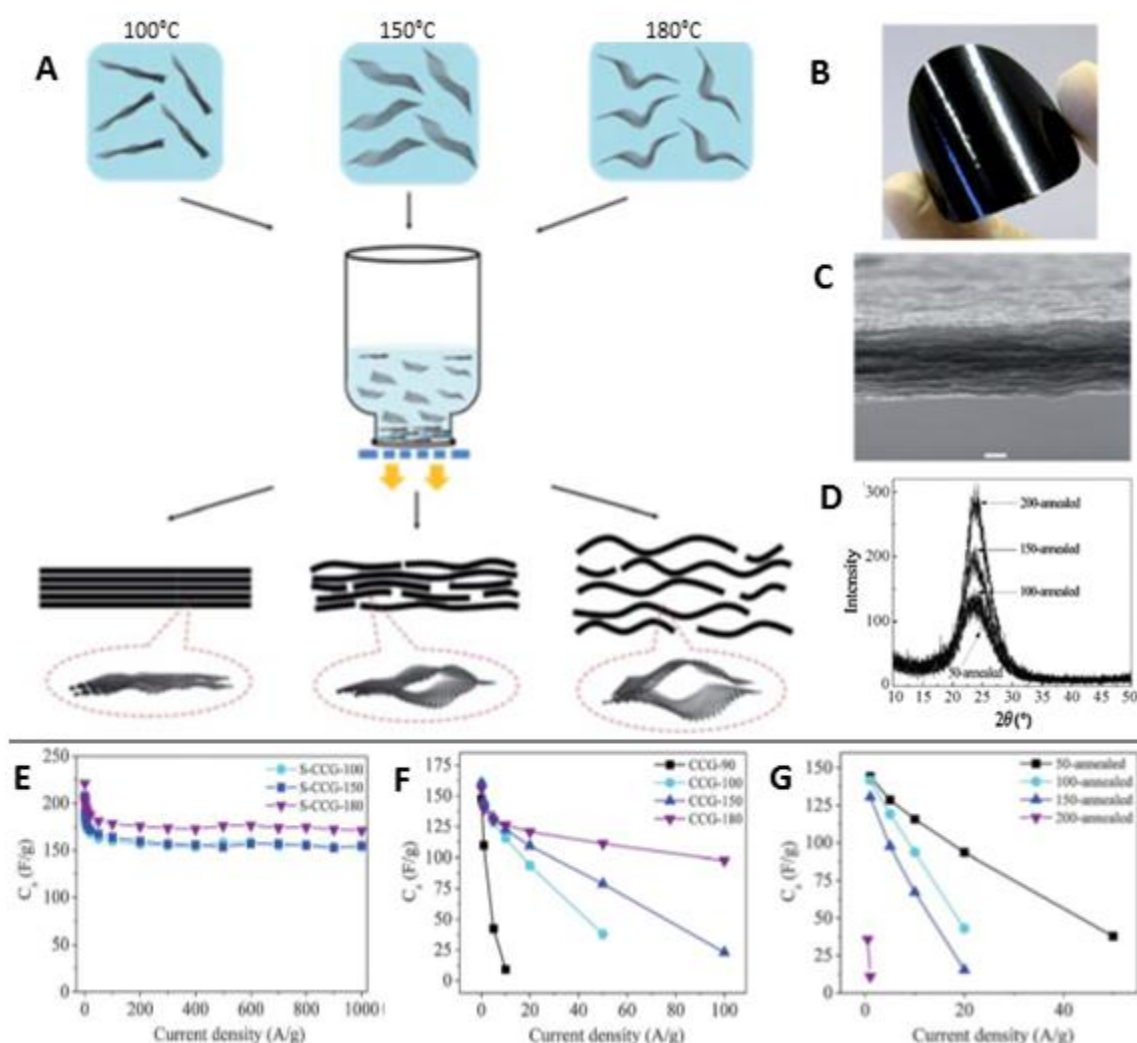


Figure 2. Illustration of the filtration process to produce layered rGO assemblies from aqueous dispersions where the corrugation of the sheets has been influenced by hydrothermal treatment at 100°C, 150°C, and 180°C to produce different pore networks in the bulk (A). The rGO assemblies can be kept hydrated as free-standing hydrogels (B) or dried to form rGO paper (C with scale bar 1 μm) that can be further annealed to increase the alignment of rGO layers, as shown in XRD (D). These structural differences have clear impacts on the performance of rGO assemblies as electrochemical capacitors with results for the hydrogels (E) and dried papers (F) prepared with hydrothermal treatment showing marked differences, especially at higher scanning rates. Further differences are also seen in the annealed rGO assemblies (G). Reproduced from [17].

To put this work in context, while graphene oxide was first reduced to form stable aqueous dispersions by Boehm et al. in 1962 [5, 18, 19], it was not until more recently that it became an area of popular research resulting from the pursuit of scalable graphene processing. This thesis follows closely with the work of Li et al. who has published much work on dry, layered rGO paper [20] as well as rGO hydrogel films [21] where the structure of these materials has been modified using different temperatures and reaction times to influence sheet corrugation [22, 23], as illustrated in Figure 2. The structural differences were shown to have large impacts on the material's performance as a supercapacitor, as specified in plots E, F, and G of the figure. Much of the research on rGO assemblies is focused on their potential application as supercapacitors, and this work aims to address open questions in the field, relating the results of published reports on material performance to the new findings on pore structure and chemical composition presented in this work. It is expected that researchers from this field will be the main readers of this work, and it is for this reason that multiple references to rGO-based supercapacitors are made throughout this thesis.

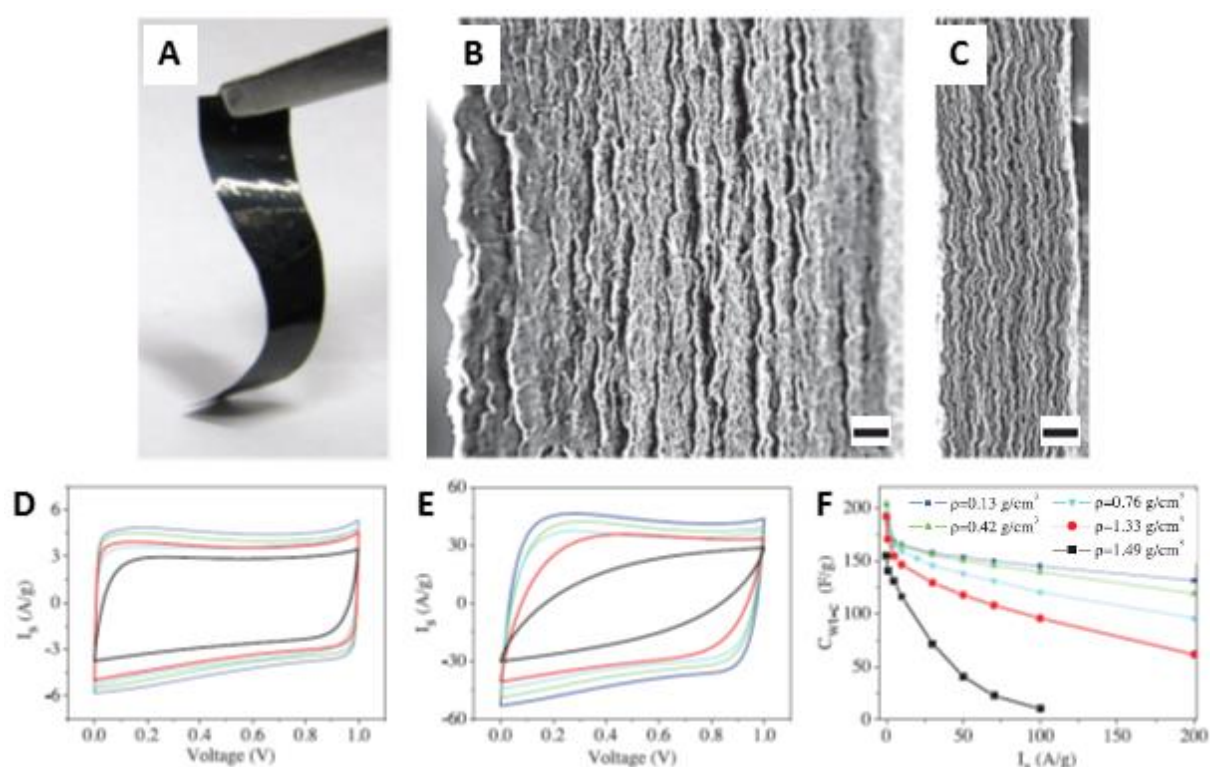


Figure 3. Free standing rGO assembly (A) where the pore network has been tuned using non-volatile liquid (sulfuric acid) of 79 vol% (B) and 27 vol% (C) to form EM-rGO assemblies. The only structural evidence of the pores is provided by SEM (with scale bar 2 μm), showing the overall thickness of the assembly is strongly impacted, but actual structural differences are not known. The thickness was used to calculate the mass density which is used to gauge performance of the assemblies, which show marked differences at scan rates of 50 mV/s (D) and 500 mV/s (E) with the gravimetric capacitance (F) being attributed to differences in the pore size. From two figures published in reference [24].

Additionally, Li's group was able to show it is possible to effectively prevent collapse of the porous structure using water [25] and non-volatile liquids [24], further exploiting this method to tune the pore structure within the rGO assemblies which are termed "electrolyte mediated" rGO (EM-rGO), as shown in Figure 3. While these materials have shown unique properties and excellent performance in membrane separation [22], ion transport [26], and energy storage [24], there has not been a detailed characterization of the pore structure within these assemblies, which is needed in order to understand the fundamental processes underlying these promising results. In addition to the work of Li's group mentioned here, there has been extremely widespread interest in graphene-based assemblies and composites over the past decade [27], but experimental methods to investigate the porous structure

and define structure-property relationships are not well developed. This is especially true for the hydrogel systems and *in situ* studies where ambient conditions are required.

The novelty of rGO assemblies created a need for this work because, unlike other porous carbon materials, rGO assemblies are unique in their *lamellar geometry and pore structure* as well as the *wet processing method* used to fabricate them. Numerous studies have reported exceptional properties of rGO assemblies, yet the mechanisms behind these phenomena are not clearly understood. This study investigates possible links between the chemical composition and pore structure of both dried and hydrated rGO assemblies from the sub-nano- to macro-scale and ties these findings to published reports on material performance. Not only pore size, but aspects of pore size distribution and pore connectivity will determine the performance of rGO assemblies, and this work aims to address this gap in knowledge.

As mentioned, a main feature of an rGO assembly that differentiates it from other porous carbon materials is that it can be prepared as a wet, soft-material using solution-based chemistry which allows the resultant assembly to remain hydrated. Other porous carbons are produced through thermal (selective gasification) or chemical (acidic intercalation) activation processes to create pores in solid carbon precursors such as graphite or plant-based organic material, and while they can later be hydrated, the structure (and thus performance) is evaluated in a dry state [28]. Most of the typical methods, like gas adsorption, cannot be effectively applied to rGO assemblies, especially in the case of hydrogels, which leaves a large gap in a full characterization of the structure of these unique materials. Dynamic electrosorption analysis (DEA) has been proposed as an effective method to measure how different structural features impact the transport of ions within the bulk [17], but there has not yet been any direct structural characterization developed to substantiate this. In order to fully characterize these hydrated rGO assemblies, which are also termed “solvated graphenes” [29], innovative experimental methods have been applied to these systems and the interpretation of the results is developed through this work.

Despite the fact that the material processing methods are quite different, activated carbons (ACs) and rGO solution-based assemblies are very similar structurally, both consisting of porosity (space) enclosed by carbon atoms. Specific structural details of the carbon/space assembly, such as pore-size, pore-size distribution, and the composition of the carbon surface, will determine the performance of porous carbons, no matter what methods were used to fabricate the materials. Therefore, this work draws upon the well-established characterization methods and nomenclature within the field of carbon research in order to effectively investigate these innovative rGO assemblies as a porous carbon.

The main features of porous carbons can be characterized within the two focus areas of *chemical bonding within the carbon matrix* and *the structure of the pores contained within it*. The pore structure of porous carbons is known to encompass an extremely broad length scale, requiring extensive experimentation to determine the structural features of the three IUPAC defined regions: micropores (0-2 nm), mesopores (2-50 nm), and macropores (>50 nm). Existing models for other porous carbons (ACs, pyrocarbons, coal, etc.) have been well researched and developed [13, 30-32], and these results can be adapted and applied to new graphene-based assemblies.

The simplest definition of porosity is the fraction of void volume over total volume of the material, but this measure does not serve to adequately describe the actual pore size or shape nor does it give any information on the interconnectedness of the pore network. This “void” space is very difficult to quantify and because it can span many orders of magnitude in length, there is not one experimental method that can adequately cover this enormous range. Figure 4 compares the most widely applied methods to characterize porous materials, and these can be broken down into the two major approaches of radiative and penetration/invasion techniques. Referencing the analysis methods in the figure, because the pores in rGO assemblies are typically less than 10 nm in size, it would seem the

penetration methods would be well suited for this study, however, this is not the case and the reasons that radiation methods were chosen for this work are discussed here.

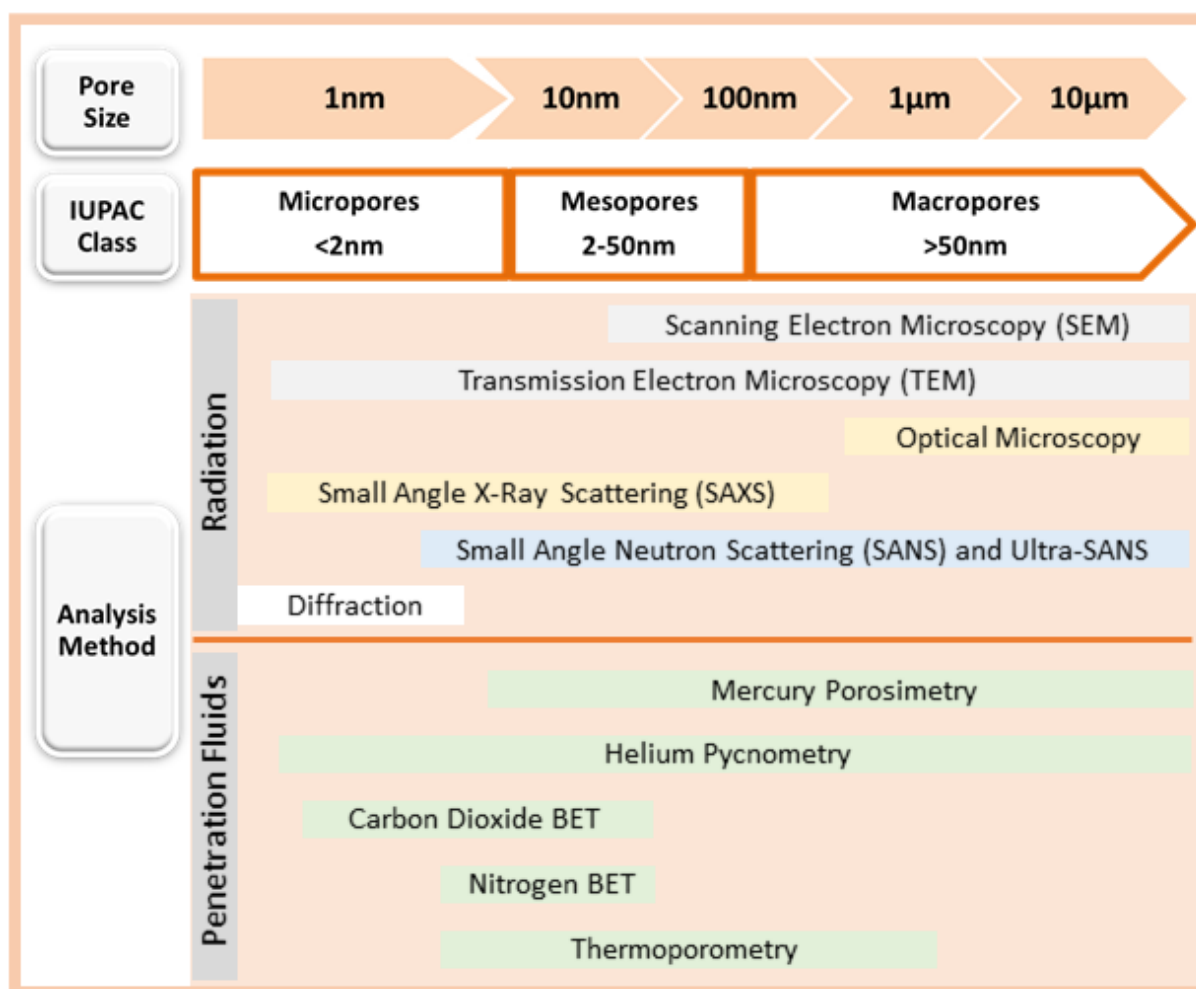


Figure 4. Comparison of commonly applied radiation (electron, photon, and neutron) and penetration characterization methods for porous materials and the corresponding detectable pore size range for each technique.

Fluid invasion (or gas adsorption) is most typically employed with high-pressure mercury while low-pressure adsorption uses nitrogen or carbon dioxide. Intrusion methods have been long used in the study of porous carbon, and it was not until more recently that unique interactions within micropores were discovered and this brought the validity of intrusion techniques into question. It is now generally accepted that nitrogen adsorption, which is the most commonly used technique, is not suitable for small micropores (especially < 0.7 nm) and investigation into the use of other adsorptives, such as helium and carbon dioxide, was more widely explored [28]. While helium is very accurate, the experimental conditions requiring temperatures of 4.2K are not easily attained. Carbon dioxide can be used at 273K or 293K and is a good alternative, with the main disadvantage is the need to apply very high pressures to the system in order to cover the full range of porosity. In any case, even if pore size is identified, because of the special features of the interaction between the adsorbate and adsorbent in micropores, there are no intrusion methods that can definitively identify the pore size distribution (PSD) in microporous materials. Therefore, not only are the intrusion methods unfit to characterize the rGO assemblies because of the discrepancies for small micropores, but these methods also significantly disturb the material structure because of the extreme pressures and temperatures required. Furthermore, intrusion methods are performed on static and dry systems, rendering them useless for the rGO hydrogels and dynamic materials.

Radiation methods can use focused beams photons (optical light, X-rays), neutrons, or electrons exploiting both particle (direct imaging) and wave (diffraction and small angle scattering) properties. SAXS and SANS are very useful experimental techniques because they can be performed in ambient conditions, cover such a broad length scale, and act across a larger surface area to yield results characteristic of the bulk. Unlike penetration methods, it is important to note that SAXS and SANS will resolve the surface of *all* pores, including those that are isolated or inaccessible and would not contribute to transport properties within the assemblies. By utilizing small angle scattering and diffraction techniques, the characterization of the morphology of both dried and hydrogel materials is possible, but some knowledge of the physical shape of the scattering features as well as the overall structure of the pore network is a prerequisite for accurate data interpretation. TEM has been historically used for the characterization of mesoscale carbon structures, but again this is limited due to the sample preparation constraints and vacuum conditions. Further, the small section of material examined with TEM may not be characteristic of the bulk. SEM has similar sample constraints and a lower resolution, but combining the direct imaging methods of optical microscopy, SEM, and TEM with diffraction and scattering techniques allows for a full characterization of the dominant structural elements within rGO assemblies, including the total porosity, pore architecture, and internal surface characteristics of these materials.

1.3 Purpose of the Study and Primary Research Questions

Currently, no definitive models exist to describe the structure of multi-layer graphene-based materials. A complete characterization requires that both the surface chemistry and the morphology of individual rGO sheets be elucidated and these findings can then be used as basic building blocks to construe the structure of bulk assemblies. This work characterizes the structure of rGO assemblies under both static and dynamic/responsive conditions in order to more fully understand transport properties of the materials. The work presented here shows promising results about the main factors influencing the chemistry and aromaticity of rGO sheets and then combines this with suggestions on how to best interpret the experimental results in order to link morphology to the material properties of the bulk assemblies. This can be done using a combination of electron microscopy with X-ray/neutron diffraction and scattering techniques to quantify the surface corrugation and interlayer spacing of the graphene-based sheets and the pore structure within the rGO assemblies.

This study expands on research methods used for other porous carbon systems in order to understand the chemical and structural make-up of rGO assemblies. The reason rGO assemblies are desirable materials is not only because of the high surface area and tuneable pore size (as other ACs already exhibit these properties), but the difference is due to the lamellar pore network and wet processing conditions. These features require different characterization methods than those used for ACs. *Thus, the main purpose of this study is two-fold:*

- i) **To explore the application of radiative experimental techniques in order to determine how chemical and structural data for rGO assemblies can be best obtained and interpreted**
- ii) **To use these results in order to define the chemical and structural make-up of dried and hydrated bulk rGO materials prepared by filtration of aqueous dispersions reduced via hydrazine**

Of all materials, porous carbons have the largest extended pore network known, with the size range of structural elements spanning over five orders of magnitude [33, 34]. Specific features within each scaling region (micro-, meso- and macro-) will have unique impacts on the material properties. Thus, in order to fully characterize the morphology of rGO assemblies, there is a need to define the structure across a very large length scale and employ a variety of techniques, as demonstrated in Figure 5. A critical assessment of the most commonly used characterization methods used for porous carbons was used to determine what experimental conditions will yield the desired knowledge of rGO chemistry and pore structure. Most existing experimental methods to investigate nano-scale structures are not

suitable for a full characterization of porous rGO assemblies, especially solvated graphenes. In order to fully evaluate the chemical composition and structure of these materials across a very broad length scale, this work has employed a variety of complex procedures, with a specific emphasis on neutron and X-ray scattering techniques in order to perform *in situ* studies on hydrated CCG assemblies to quantify:

- the surface corrugation and interlayer spacing of the graphene-based sheets
- the pore structure within the membrane material
- the role of water in shaping the structure of graphene-based assemblies

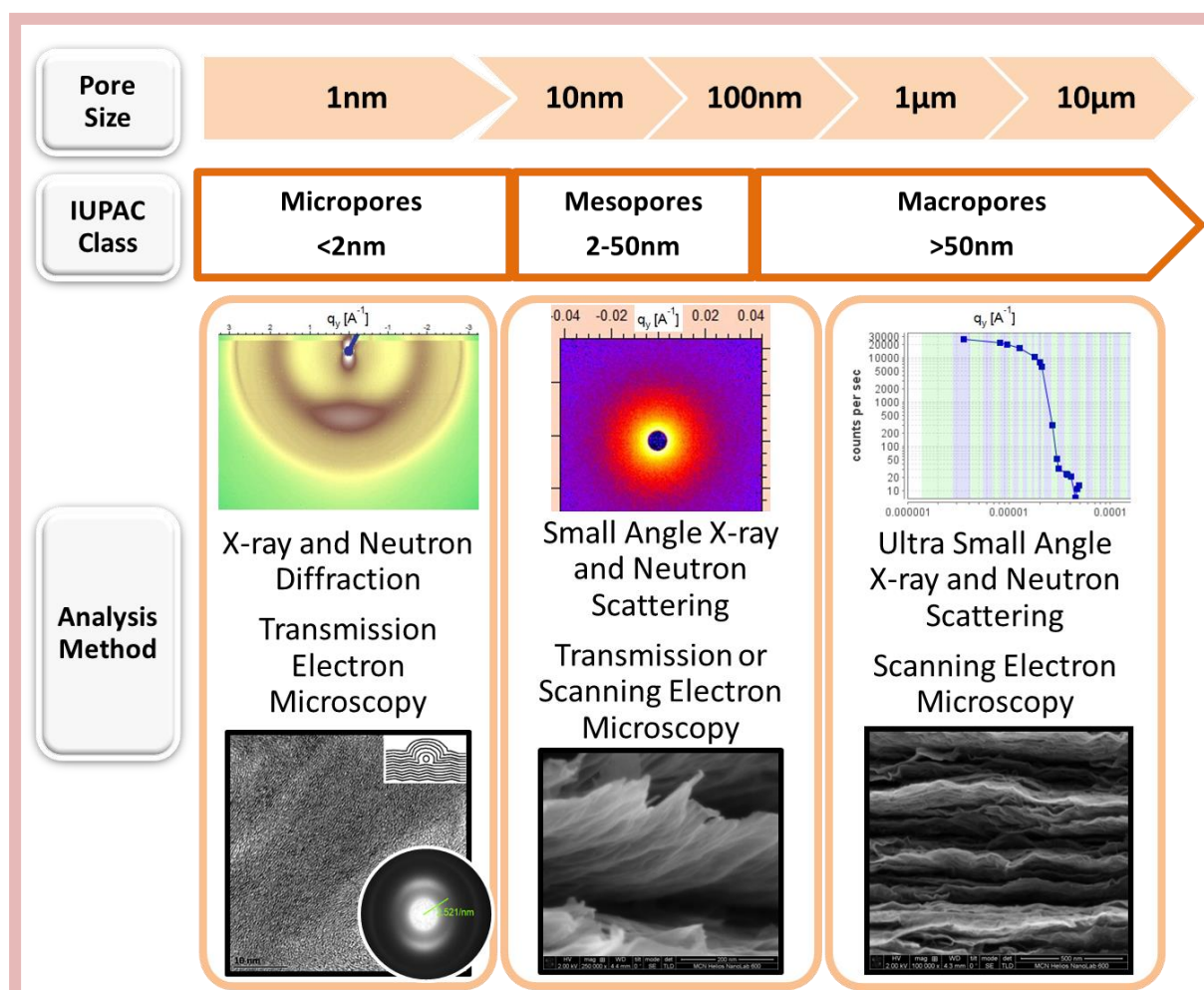


Figure 5. Description of the experimental methods used to characterize the pore structure within rGO assemblies from the micro- to meso- and macro- scale.

It has been shown that the pore size, pore size distribution, and the structure of the overall pore network all play a role in determining the energy storage capacity for supercapacitors [35-42]. As rGO assemblies have shown promise in this area [12, 25], the final aspect of this work expands on the structural characterization methods developed for dry and hydrogel films to design experimental methods for *in situ* X-ray scattering that can uncover structure-property relationships for rGO assemblies used for energy storage.

Firstly, aspects of various GO processing conditions that impact the resulting rGO chemistry were investigated to determine what role, if any, residual oxygen groups and nitrogen doping play in impacting the structure of rGO assemblies. Then, other aspects of processing, such as reduction temperature and drying methods were explored to see how these conditions will influence both the rGO sheet properties at the micro-scale and the bulk assembly structure at the meso- and macro- scale. Both the original hydrogels, resulting dried films, and EM-rGO assemblies with varied pore structure

are investigated in order to get an authentic depiction of the material, as it would be used in an actual device. A main focus of the work is to understand the role of water in rGO hydrogels and the structural impacts hydration and drying methods have on the pore structure, which are clearly evident in differences in material performance and obvious structural changes, like those shown in Figure 6, but have not yet been defined through experiment. To accomplish this, *in situ* experimental methods needed to be developed and applied.

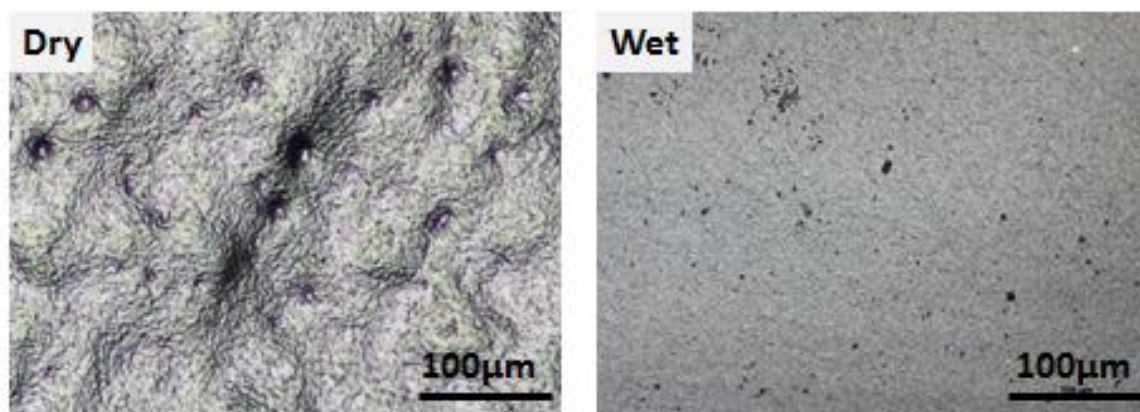


Figure 6. Optical images (used in this work) of the same CCG membrane when fully hydrated (Wet) and after drying (Dry) show clear structural changes with varied features.

1.4 Outline of the Thesis

The material properties will depend on the structure at the micro-, meso-, and macro- scale because both the individual pores and the overall pore network will impact performance. These parameters are highly dependent on the chemistry within, and surface forces between, rGO sheets. Thus, this thesis is broken into three main experimental sections to determine the structure of rGO assemblies at a molecular level (Chapter 4), at the most basic structural unit (Chapter 5), and as a porous carbon network spanning from the sub-nm to μm range (Chapter 6). The main questions under investigation within each chapter are also noted here.

The **Literature Review** begins with an in-depth discussion on the main properties of rGO assemblies and then provides an overview of the material properties and unanswered questions in the field. There is a brief discussion on the most widely applied characterization methods, including the drawbacks and limitations of these methods, along with fundamental theoretical and applied knowledge about how the structure of carbon materials is determined. This section finishes with a detailed account of more recent work using small angle scattering (SAS) to probe the structure and dynamic properties in porous carbons.

The details of all experimental methods, including sample preparation, are given within **Chapter 3**. The specific aspects of GO synthesis and the detailed settings used in all experimental techniques is clearly outlined. However, because the adaptation of these experimental techniques is one of the main purposes of this work, discussion on the specific approaches to data analysis for rGO assemblies is incorporated within the experimental results in the chapters that follow.

In **Chapter 4**, the chemical nature of rGO assemblies in regard to the processing conditions of the original GO is investigated. The specific type of nitrogen doping in rGO and the thermal stability of residual oxygen groups gives a more complete picture of rGO sheets as the individual building blocks of the assemblies. These building blocks then combine to form a “basic structural unit” (BSU), which

is defined in **Chapter 5**. These micro-size features can be used to describe the dimension of the pores which result from the inter- and intra- layer configuration and disorder. A detailed analysis of the most widely applied methods (Raman and X-ray diffraction (XRD)) is given to highlight common misconceptions and suggest improved approaches to the analysis. Discussion on how stacking disorder and inter-sheet defects impact the electronic and mechanical properties, as well as the implications for accessible surface area, is included.

More specifically, the aim of **Chapter 4** and **Chapter 5** is to investigate:

- What is the structure and composition of the rGO sheets?
 - Does the chemical composition of rGO relate to that of the GO precursor?
 - What is the structure of the intra-sheet carbon bonding (sp^2/sp^3 regions)?
 - What is the structure of the inter-sheet carbon bonding (002 lamellar stacking)?
 - What are the best methods to obtain this information experimentally?

Chapter 6 uses the BSU developed in Chapter 5 to interpret the results from wide angle X-ray scattering (WAXS) and small angle X-ray scattering (SAXS) patterns, which are used to expand the structural model to the micro, meso- and macro- scale, describing not only the structure of the pores, but the overall pore network as well. Knowledge of diffraction and small angle scattering in other porous carbon materials is modified to design new methods for both the experimental set-up and data analysis. Details on how SAS is used to investigate porous carbon materials is followed by discussion on choosing a structural model and how to interpret the scattering curves. In dried assemblies, the specific impacts that drying and annealing have on the porosity are investigated, while the pore structure of hydrated, electrolyte mediated rGO (EM-rGO) materials is fully revealed. Further, *in situ* drying of hydrogel assemblies provides novel insights into how water impacts the pore network, with specific correlations between hydration and accessible surface area being drawn. A combination of neutron diffraction, small angle neutron scattering (SANS), and ultra-small angle neutron scattering (USANS) is then used to obtain a scattering curve that ranges a length scale over five orders of magnitude.

More specifically, the aim of **Chapter 6** is to investigate:

- What is the pore structure within the rGO assemblies?
 - Can sheet spacing, alignment, and corrugation be used to describe the pore structure?
 - How do these feature impact pore size, pore size distribution, and the pore network?
 - Are the bulk assemblies homogeneous and what is the role of structural distributions?
- Is it possible to design experimental methods to directly investigate hydration *in situ*?
 - What physical processes occur upon drying?
 - What is the role of water in these systems?
 - How can the control of intercalated water impact accessible surface area?

The main conclusions are presented in **Chapter 7**, and these are then followed by promising initial results for future work designing *in situ* experiments to investigate charging dynamics of rGO assemblies used as supercapacitors to determine if SAXS is a viable technique to investigate ion transport within rGO assemblies.

1.5 Assumptions, Limitations, and Scope

While the specifics of the materials used here are described in detail within the Literature Review and Methods, the scope of this work only tests rGO prepared using one type of reduction method. The specific features of the GO precursor were not independently explored, and all conclusions drawn about the resulting rGO assemblies were based on other published works, as presented in the Literature Review. While the main conclusions of this work will hold true for many rGO materials, there will be differences for rGO reduced using thermal or other chemical methods. This is mostly relevant in the results of Chapters 4 and 5, but in any case, the experimental methods developed will

apply to work on all types of rGO assemblies and should act as a useful guide for future researchers, regardless of the specific preparation methods employed.

It should also be noted that it is possible to utilize a wide variety of chemical techniques to assess the surface chemistry of rGO assemblies (titration, gravimetric, etc), but this work limited the focus to X-ray photoemission spectroscopy (XPS) because it is widely reported in literature and can uniquely identify all the bond types using a single method. Further, this work aims to act as a practical reference for others in the field, and it is hoped that through a clear and detailed analysis of the data, XPS results can be better utilized in understanding rGO materials. Similarly, many other experimental methods could have been used throughout the work, but holding to the main aim of acting as a practical guide and helping to clarify some of overlooked features in the most widely used methods, the choice of detailed analysis with Raman and XRD should prove to be most applicable in the field. Finally, because SAS is not a widely utilized tool for structural characterization in rGO materials, the usefulness of these methods (especially for hydrated material and *in situ* experimentation), along with a practical approach to interpreting data was thought to offer a great deal of new insight that could be more broadly applied.

In regard to the SAS analysis specifically, it should be noted that this is a fairly specialized field that relies on rather complex mathematical and computational models that could be much more deeply developed and expanded on than what is included here. To offer the most practical and adoptable approach, this work does not delve into the more fundamental aspects of scattering theory, and instead limits the results and discussion to extractable parameters that are most relevant in determining the overall structure and performance of rGO materials. Major factors and features are identified, which should pave the way for more in-depth mathematical and computational models incorporating chemical bonding and intermolecular forces should others choose to focus on the scattering theory more holistically.

1.6 Definition of Terms

There can be much confusion in the literature based on inaccurately applied terminology. In an attempt to use the most accurate labelling while also familiarizing the reader with nomenclature used throughout the text, the major features used to describe the structural elements of rGO assemblies are described here. These terms are taken from publications on the standardization of graphene [43] and sp^2 carbon nanomaterials [44] as well as well-regarded textbooks in the field of layered and porous carbons [32, 45]. As these are definitions, some are taken verbatim from the sources listed above.

1.6.1 Specific nomenclature for graphene-based materials

Graphene – A single-atom-thick sheet of hexagonally arranged sp^2 bonded carbon atoms. The sheet itself must be isolated and freely suspended, but the lateral dimensions of graphene can vary from nanometers to the macroscale. Other members of the 2D graphene family cannot technically be called graphene if they have carbon defects/vacancies, bonded chemical groups, or consist of more than an isolated monolayer.

Graphene layer – A single-atom-thick sheet of hexagonally arranged sp^2 bonded carbon atoms occurring within a carbon material structure. This term can be used regardless of whether the material has 3D order (graphitic) or not (turbostratic or disordered). This term is a conceptual structural unit long-used for aromatic and layered ordering within many types of carbon materials.

Multi-layer graphene (MLG) – A 2D sheet-like material that consists of a small number (2-10) well-defined, countable, stacked graphene layers that can be free standing or substrate-bound. If the stacking is known, additional terms such as “Bernal-stacked” or “rotationally faulted” should be added

to the description of the MLG. If the material does not consist of well-defined layers with an extended lateral direction, the term “carbon thin film” should be used instead of MLG.

Few-layer graphene (FLG) – A subset of MLG consisting of only 2-5 graphene layers.

Graphite – This term requires the existence of 3D order and is commonly misused in publications about carbon materials, especially multi-layered graphene materials. Graphite, along with the similar terms of graphitic, graphite nanosheets, graphite nanoplatelets, and graphite nanocrystals all require the presence of ABA or ABCA stacking between the graphene layers. Thus, graphitic materials always contain 3D crystalline order (Miller indices of hkl reflections). It should also be noted that the term crystallite, as in carbon- or graphite-crystallite, should only be used to refer to 3D crystallinity, hence the term “graphene-crystallite” is not structurally possible. Further, to use the prefix nano- for these materials requires the lateral dimension is less than 100 nm.

Turbostratic carbon – A three dimensional hexagonally arranged sp^2 bonded carbon structure where there is no special relationship between different graphene layers. The name is derived from “turbo” (rotated) and “strata” (layer) and can also be called rotationally faulted. Thus, it is essentially a layering of 2D crystals without a correlated third crystalline axis (Miller indices of $hk0$ only, no hkl reflections). A turbostratic structure is common in carbon materials prepared at low temperatures, but it has been cautioned not to mistakenly correlate turbostratic structure with other properties of carbons, as this structural term is very broad, indicating only that there is some type of layer structure present and there is no three dimensional crystalline order within it.

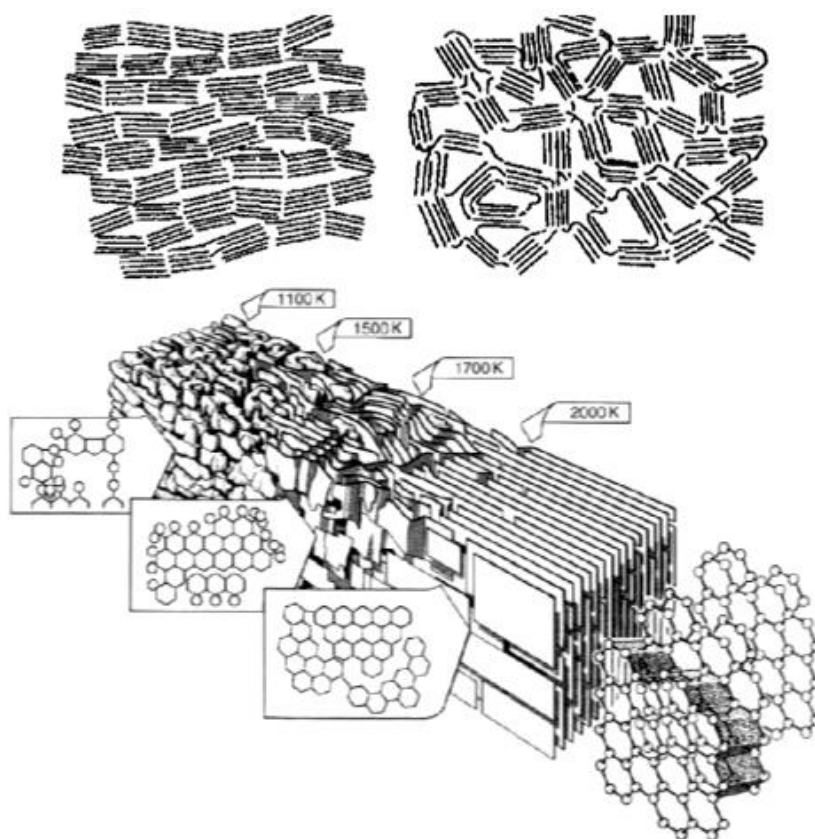


Figure 7. Original structural model of graphitizable and non-graphitizable carbon proposed by Franklin in 1950 (top from [46]). Description given by Marsh of the major structural changes that occur as a carbon goes through the graphitization process from 1000-3000°C (bottom from [32]).

Graphitization – The process of the development of 3D crystalline order (ABA or ABCA) either through a direct growth process or by applying high temperature to a previously disordered carbon, as detailed in Figure 7. Bulk carbon materials can be broken into the broad classes of graphitizable (soft) and non-

graphitizable (hard) to describe the overall bonding within the carbon matrix, as specific types of disorder will not allow the graphene layers to move freely for this alignment process to take place. Carbon materials can also be labelled as partially-graphitized, and a ratio can be assigned to the portion of 3D graphitic material compared to disordered content.

Graphite oxide – A bulk solid made by functionalizing the basal plane of graphite through oxidation. Graphite oxide can be fully exfoliated to produce graphene oxide (GO) or partially exfoliated to produce few-layer GO (FLGO).

Graphene Oxide (GO) – A chemically modified graphene material prepared by the oxidation and exfoliation of graphite flakes or powders. This chemical process results in significant modification to the edge groups and basal plane of graphene, producing a monolayer material with a typical carbon to oxygen ratio of 2:1. GO can have varied lateral dimensions and in-plane carbon defects, with the main defined feature is it must have a C:O atomic ratio less than 3:1.

Reduced graphene oxide (rGO) – GO that has been reduced by thermal, chemical, microwave, photo-chemical, photo-thermal, or bacterial methods. As so many different methods can be employed, the specific reduction conditions should be noted before comparing results from rGO prepared using various processing methods.

Graphene-based materials – Broad term that can describe materials consisting of multilayered graphene, chemically modified graphene (GO or rGO), as well as other assemblies using some type of graphene material as a precursor. Specifics of the particular material should be better defined using the terms outlined above.

Hydrogel [47] – Specific definitions of a hydrogel system will vary, but the most common of these is that it is a linked 3D polymeric network that exhibits the ability to swell and retain a significant fraction of water within its structure, but will not dissolve in water. Water fills the space between macromolecules, with the mass fraction of water being much higher than the mass fraction of polymer.

1.6.2 Specific nomenclature for structural features along graphene layers

Defects – A broad term used to describe any deviation from the pristine sp^2 lattice. Specific features of the defect, such as carbon vacancy, edge, or chemical bond, should be included to specify the defect type whenever it is known.

In-plane or intra-sheet vacancy defects – There are not considered pores, as such, but do allow for transport through the graphene layer because of carbon vacancies. Depicted visually in Figure 8 (B).

Inter-sheet pores – The typical description of porous media where the pore results from expanded lamellar space wherever graphene layers are effectively separated. Depicted visually in Figure 8 (C).

Disorder – Used to evaluate the degree of misalignment from idealized crystal structure.

Functionalized – A broad term used to describe chemical bonding along the graphene layer.

Stacking – Considering the graphene sheet is in the xy plane, stacking occurs along the z plane. There may or may not be order present in the stacking arrangement – graphitic, turbostratic, or disordered materials all contain some type of stacking.

Collapsed – The distance between two otherwise separated points on a surface is reduced to that of the interlayer spacing of graphite (van der Waals interaction). When the graphene layers collapse, the surface area between is no longer considered accessible surface area.

Clustered – Aggregates of nanoforms with no long- or short- range order besides that of the objects themselves.

Mosaic crystal – An idealized model of an imperfect crystal, imagined to consist of numerous small crystallites that are to some extent randomly misoriented and dispersed. The mosaicity is commonly equated with the standard deviation of this distribution.

Mosaic cluster – Same principle as that of mosaic crystal described above, but containing clusters rather than crystallites.

In-plane fluctuations – Can include corrugation, wrinkles, folds, or curling.

Folded – When the graphene layer folds over on itself. This is a specific type of stacking.

Wrinkled – When the graphene layer has a perturbation at the surface that results in a bi-layer formation.

Corrugated – The graphene layer surface undulates without changing the overall mono-layer shape (no wrinkling or folding). The size of the undulations is less than the dimensions of the nanoform itself. Depicted visually in Figure 8 (A).

Wavy – The nanoform itself undulates and this undulation is on a larger scale than the corrugated nanoform.

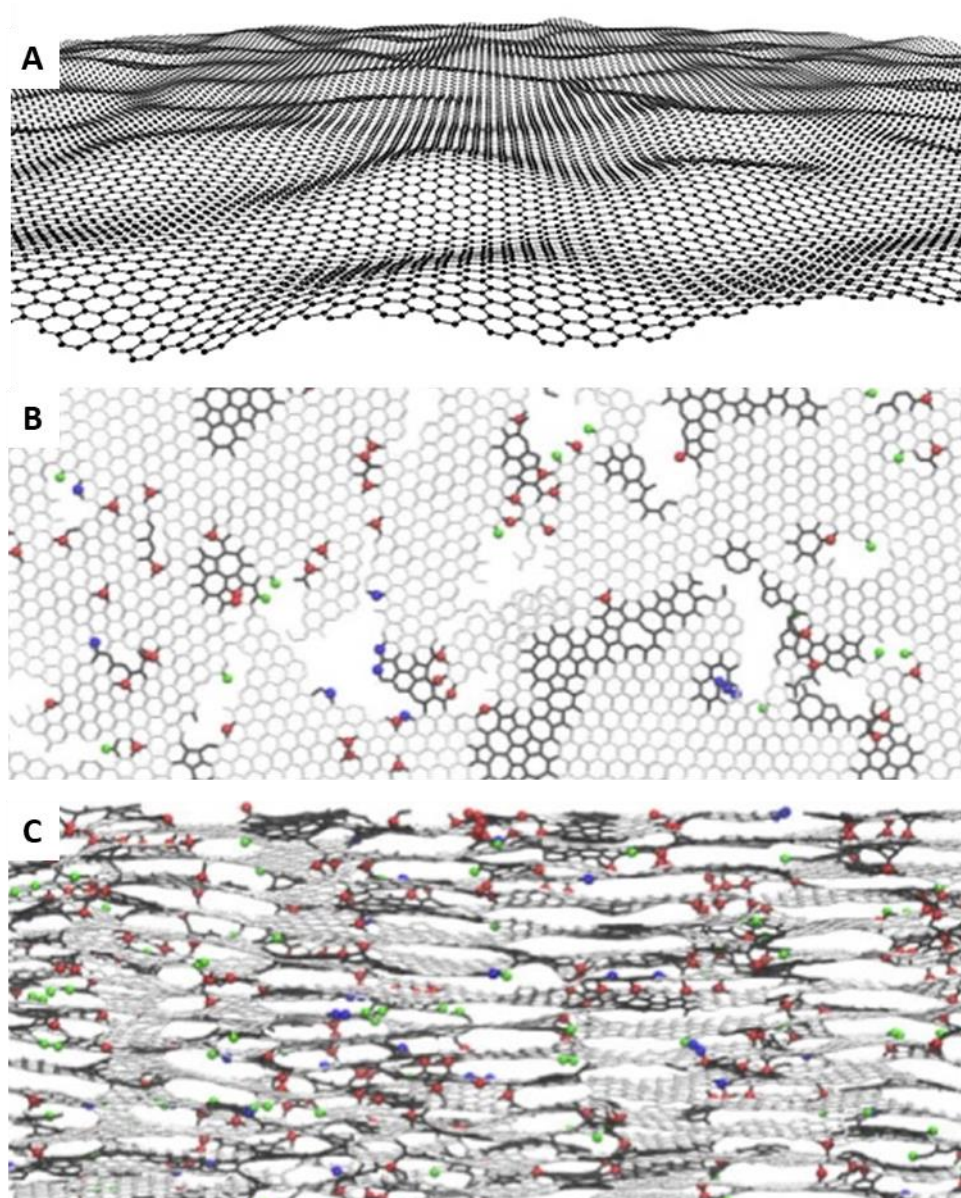


Figure 8. Examples of corrugation (A), intra-sheet defects (B), and inter-sheet pores (C). Reproduced from [48, 49].

Chapter 2. Literature Review

2.1 Description of rGO Sheets and Assemblies

2.1.1 Significance of graphene and rGO in materials engineering

While reports of its existence have been around since the 1960s [19], graphene-related research did not reach “gold-rush” status until it was popularized in 2004 [1, 2], receiving the Nobel Prize in Physics in 2010 and interest growing exponentially ever since. After their ground-breaking reports on the unique properties of the first stable two-dimensional crystal, Geim and Novoselov gave a detailed overview of graphene’s brief history and offered suggestions for practical applications ten years ago, in 2007 [8]. Here they outline the unique properties of graphene and argue the material is not a trending fad, but has obvious advantages for applications in material science that could be readily realized in industry. Since that time, this intense focus on discovering new graphene-based material has indeed laid claim to many marketable products [12, 50-53]. Geim and Novoselov [8] highlighted electronics, composites, energy storage, flexible displays, and sensors as the most promising graphene-based products – all of which have now been realized in an experimental setting and many are making their way to market, with economic reports (by IDTechEx and other market research firms) forecasting the global graphene market is expected to reach \$200-300 million by 2020, at a massive growth rate of over 40% from 2015 to 2020.

Given the seemingly boundless potential for both fundamental research and creating new materials, the literature currently published on graphene is far too broad to discuss all aspects in the field, and this Literature Review will focus only on graphene materials made from the bulk processing method of firstly synthesizing graphene oxide (GO) from graphite, followed by the removal of most of the oxygen functionalities to obtain a stable aqueous dispersions of reduced graphene oxide (rGO) [15]. Like graphene, these rGO materials are essentially a two-dimensional sheet of carbon atoms arranged in a honeycomb-shaped lattice, but they differ from pure graphene (produced through mechanical exfoliation or chemical vapor deposition) in a variety of important ways which will be discussed. The processing methods for GO and rGO vary widely, and there is much current research focused on optimizing scalable processing methods in order to develop industrially viable techniques to produce graphene materials, with many reviews devoted to this subject [6, 7, 27]. This is a significant area of research, as scalability and functionality are key for wide adoption of graphene-based materials. Presently there is a lack of understanding of how processing conditions impact the structure of rGO assemblies and thus influence the material performance.

2.1.2 Structure of GO and rGO sheets

2.1.2.1 *Chemical composition*

In the work reported in this thesis, the procedure for synthesizing the original graphite oxide solutions was varied in order to measure the impact changes in reaction temperature and reaction time have on the structure of the resulting reduced graphene oxide sheets. The focus is specifically on the final rGO assemblies, with limited attention paid to the original GO material other than determining if the adjusted oxidation conditions will impact the properties of the resulting rGO. The reduction procedure used here is kept constant and is based on the early work of Boehm et al. [5, 18], later popularized by Wallace [15], where aqueous suspensions of GO are reduced with hydrazine at elevated temperatures (100°C, 140°C, and 180°C) in a basic aqueous solution. A broad overview of GO and resulting rGO is provided here in order to provide a context in which the thesis aims can be understood, highlighting the main aspects of GO processing and reduction conditions that could influence the chemical composition of rGO sheets and subsequent performance of rGO materials. This is then followed with details on the specific aspects of rGO assemblies directly related to the focus of this work.

The chemical exfoliation of graphite is a very old technique [54], and was traditionally accomplished by opening up the graphite layers to create what is termed a graphite intercalated compound (GIC) by soaking graphite flakes in mixtures of nitric and sulfuric acid for an extended period of time. It is important to distinguish between a GIC, graphite oxide, and graphene oxide, as the number of layers making up each platelet will determine how effective the method is in producing reduced, single-layer graphene-like sheets. In this work, the label GO will only be used to describe single sheet, graphene oxide.

The most common methods to synthesize oxidized graphite directly are those of Brodie [54] and, later, Hummers [55], where the graphite oxide is fully exfoliated to single GO sheets using sonication or other mechanical methods. While sonication is necessary to fully exfoliate the platelets, it should be recognized that these harsh mechanical processes damage the sheets, resulting in GO with a sheet size significantly smaller than the starting material (from many microns reduced to several hundred nanometres) [56]. Thus, the size of the GO sheet is largely dependent on the starting graphite material and processing conditions (sonication power and time) while the size of the aromatic islands along the sheets is due to the degree of oxidation and method of reduction (chemical processes).

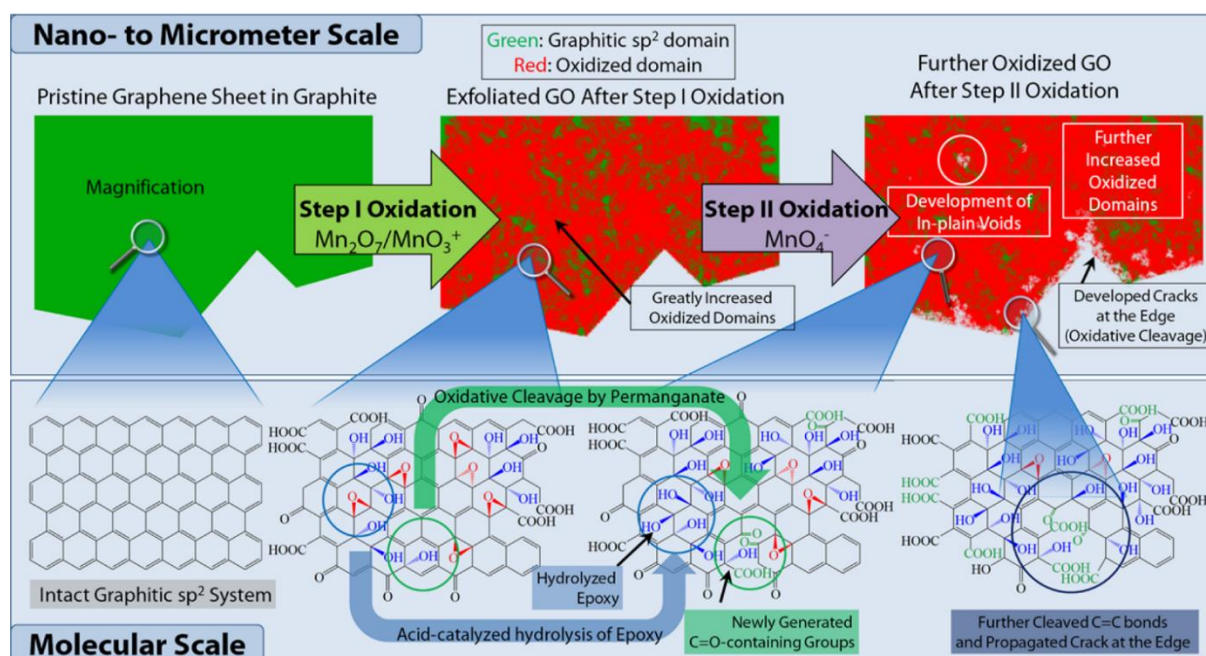


Figure 9. Schematic diagram showing the chemical evolution during the oxidation process of graphite to produce GO. Reproduced from [57].

A full understanding of the chemical composition and morphology of GO and rGO sheets continues to be an area of focused research, and many aspects are not yet fully understood. Since the modified Hummers method [55, 58] is used to produce the GO in this work, it is useful to give a brief background on the chemical process in order to better interpret the resulting rGO structure. This discussion is largely centred on the more recent work of Kang [57] and Shao [58], and the reader is directed there for a more complete description of the chemical processes underling GO processing. The process of oxidizing graphite can be broken down into two main steps, which can be termed *Step 1 oxidation*: KMnO_4 and *Step 2 oxidation*: *hydrolysis*, as shown in Figure 9 [57]. First, graphite flakes are soaked in a water-free mixture of concentrated sulfuric acid and sodium nitrate before *Step 1 oxidation* introduces potassium permanganate to obtain fully exfoliated graphite oxide. Shao et al. [58] showed that the temperature of this reaction step plays a large part in the resulting GO chemistry, with more thermally stable, less oxidised GO with a larger aromatic content being obtained at less than 50°C reaction temperature. It was found that holding this step at a higher temperature produced over-

oxidized material with more defects and less favourable properties. Thus, *Step 1 oxidation: KMnO_4* can result in GO sheets with fewer defects by using low temperature conditions, but allowing the reaction to run for slightly longer time periods. Very recently, Kang et al. [57] uncovered the mechanisms behind *Step 2 oxidation: hydrolysis* showing, similarly, that the time and temperature conditions for this stage of the oxidation process also strongly impacts the resultant chemical composition of GO. Kang's work showed that holding this reaction at temperatures below 50°C was able to preserve the aromatic structure of the GO sheets as less tears and holes were produced during the oxidation. Comparatively, reactions at 70°C and 90°C had significant and irreparable damage to the graphene lattice. Further, the type of oxygen groups bound to the basal plane were impacted by the temperature of *Step 2 oxidation: hydrolysis*, with the ratio of hydroxyl to epoxy groups increasing at higher temperatures. This results in significantly diminished electrical conductivity, as the hydroxyls are most resistant to reduction, preserving the sp^3 carbon network and hampering electric conduction in rGO. For both oxidation steps, increasing the reaction time allows for GO to be further oxidized, especially at higher temperatures with increased hydroxyl and epoxy units along the basal plane and additional carboxyl groups forming at edges [57].

The edge carboxyl groups, as well as the hydroxyl and epoxide groups along the basal plane allow for stable colloidal dispersions of GO, as each layer is effectively a charged macro-anion. The oxidation reaction is terminated by the addition of more water and hydrogen peroxide, and excess ions are removed through a subsequent purification step. The resulting GO can be dried or stored in water, as the GO platelets automatically repel each other because of the electrostatic repulsion, forming stable dispersions. Due to the extremely hydrophilic nature of GO, it can be stored as an aqueous dispersion for long periods of time, diluted to any desired concentration, and/or readily mixed with other compounds. The water of hydration in GO and rGO, as well as the amount of water adsorption in dried GO and rGO flakes, is directly related to the level of oxidation and thus provides useful insight on surface forces and chemistry present in the material [59, 60]. Once GO has been reduced, the loss of hydrophilic groups and resulting aromatic domains result in a more hydrophobic suspension, and this hydrophilic/hydrophobic nature must be considered in order to tailor material properties for specific applications and performance.

The resulting physical and chemical structure of GO is highly dependent on the starting graphite material and the oxidation procedure – both of which will contribute to the resulting GO surface chemistry and morphology. It should be noted that while four main oxygen groups are known to be present in GO ($-\text{O}-$, $-\text{OH}$, $-\text{C}=\text{O}$, and $-\text{COOH}$) [5], unlike small molecules, crystalline solids, or an otherwise homogeneous material, there can never be an exact structure for GO as there are too many variables in processing [56]. Ever since Brodie [54] and Staudenmaier [61] first began to study oxidized graphite materials, researchers have continued to notice the large variance in GO structure and chemistry which results from both the source of the graphite and reaction conditions. Experimentally obtained results for the chemical composition of GO can vary across a large range from $\text{C}_8\text{H}_{1.6}\text{O}_{2.1}$ to $\text{C}_8\text{H}_{2.5}\text{O}_{3.9}$ to $\text{C}_8\text{H}_{4.6}\text{O}_{6.7}$, which are just some of the examples of the wide variance of compositions resulting from different processing conditions [6]. Nevertheless, much work has been done to more clearly define the types of oxygenated functional groups present and the location of these groups along the carbon lattice (very precise review given by Dreyer et al. [56] and theoretical insight by Gao et al. [16]). From these, the Lerf-Klinowski model has arisen as the most accepted model to describe distribution of oxygen groups on graphene [62, 63]. A visual depiction of the surface chemistry of GO based on this model is shown in Figure 10.

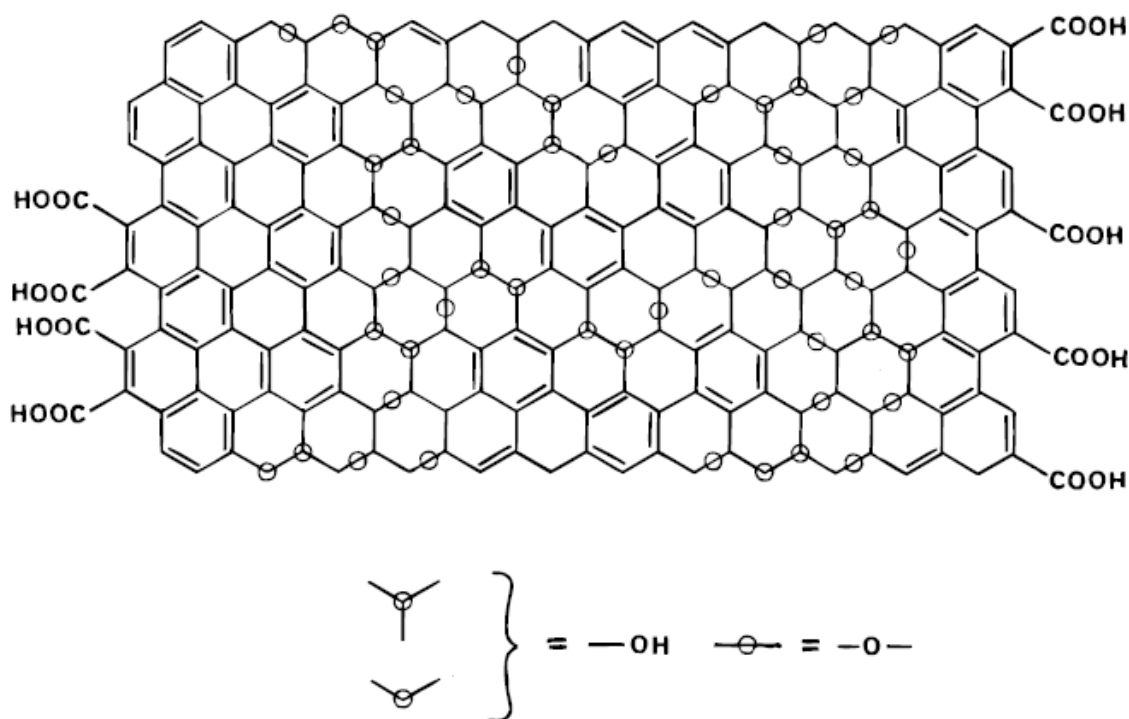


Figure 10. The Lerf-Klinowski model for the structure of graphene oxide is presently the most accepted (from [62]).

Lerf et al. [62] were the first to propose what is now the most generally accepted model of GO, where epoxide (-O-) and hydroxyl (-OH) groups are in close proximity to each other and randomly dispersed across the planar surfaces of the graphene sheet, while carbonyl (-C=O) and carboxyl (-COOH) groups are located along the edges. There are alternative models for the structures of GO, mostly related to the presence of basal plane carbonyl (>C=O) groups, with notable published work by Dekany [59] and Ajayan [64], who claim that C=O species can exist in GO along the basal plane. The existence of carbonyl groups has since been supported by computational models [65] and verified in a number of experimental works [66].

Most models describe a slightly corrugated structure consisting of two distinct regions: (1) variable-sized *aromatic islands* of pure sp^2 carbon that are separated by (2) aliphatic six-membered rings bonded to oxygen functional groups. Within the aliphatic region, regions containing double bonded oxygen and epoxide groups are expected to remain flat, while regions with -OH functionalities lead to a slightly distorted tetrahedral configuration (where corrugation of the graphene layers is induced) [59, 62, 67]. There are typically one and a half times more epoxy groups than hydroxyl groups contributing to the sp^3 carbon bonds, but this can vary depending on the level of oxidation. Lerf et al. postulated that the relative size of the aromatic domains is dependent on the level of oxidation [63], and an understanding of the mechanisms behind this were put forth through computer simulations. Boukhvalov and Katsnelson showed the specific surface chemistry of GO is also dependent on the oxidation level, with the ratio of epoxides to alcohols increasing with increased oxidation [68]. The simulation results matched all known experimental data for the oxygen content in the materials and showed the most energetically favourable oxidation conditions result in 75% coverage along the carbon sheet with both oxygen and hydroxyl groups being present. Calculations showed GO becomes conducting once this coverage is reduced to 25%, and it is relatively easy to further reduce the oxygen content to a C:O ratio of 16:1 but any reduction beyond this is much more difficult. Bagri et al. [65] carried this further to show the chemistry of the resulting rGO is highly dependent on this epoxy-hydroxyl configuration, determining the proximity of these groups during thermal reduction tends to result in the formation of carbonyl and phenol pairs accompanied by a hole in the carbon lattice. The

resilience of these thermally stable phenol groups in rGO has also been reported experimentally [16, 66, 69], as shown in Figure 11 where carboxyl, carbonyl, and epoxy species diminish while an increase in –OH groups is detected from 200°C–400°C. Oxygen groups resistant to thermal reduction remain even at temperatures approaching 1000°C, demonstrating the limitations to completely restoring the structure of rGO to that of pure graphene.

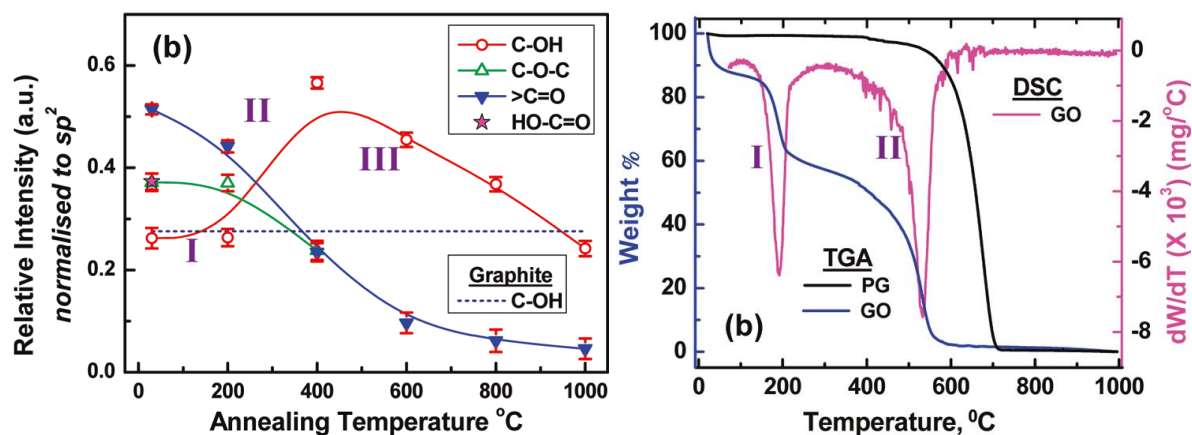


Figure 11. Monitoring of the evolution of the surface chemistry of GO is shown by *in situ* XPS measurements, while thermally reducing the films at 200°C intervals up to 1000°C. The corresponding TGA results compare pyrolytic graphite (PG) with GO and each mass loss corresponds with water (100°C), oxygen groups decompose while releasing CO and CO₂ from holes in the graphene sheet (200°C), simultaneous removal and recombination as epoxy and carbonyl aid the formation of phenolic groups (300–500°C) (from [66]).

Various means can be employed for reduction of GO to rGO, but each method will have specific impacts on both the resulting chemistry and structure of the rGO sheet. Specific aspects of the chemical composition will be discussed below, but regardless of the reduction method used, the electrical conductivity of rGO will be about five orders of magnitude higher than GO, but about 10 times lower than that of pristine graphite powders. It was found that the electrical transport of rGO sheets is dominated by electron hopping [70], indicating the conductive aromatic domains are linked by nonconductive regions where defects, edges, and/or oxygen groups are located [70]. While rGO sheets can never fully attain the idealized mechanical and electronic properties of pure graphene sheets, they offer the advantage of easy, cost effective, and scalable processing with many opportunities for functionalization using the reactive edge sites and residual oxygen groups.

Discussion of all possible reduction methods applied with rGO materials is outside the scope of this work. Thus the discussion here will focus on chemical reduction using hydrazine in a basic aqueous solution [15] with some additional comments regarding thermal reduction, especially when these methods are employed in combination. It is noted that fairly complete outline of the major experimental and theoretical work investigating reaction pathways for various reduction methods is provided by Gao et al. [16]. Further, there are multiple chemical methods that can effectively reduce GO, each with specific advantages. The discussion here is limited to reduction via hydrazine because it is the method applied in this work and offers a low-cost solution for large-scale aqueous processing, differing from most strong reductants which have a severe reaction with water. Overall, hydrazine is effective in restoring conductivity and having a relatively low impact on disrupting of the carbon-carbon bonding along the graphene sheets. Further, because the by-product of the reduction is gas, it is naturally removed from the system.

The effective reduction of GO using hydrazine was first reported by Boehm et al. [18, 19], and later popularized by Stankovich [71], with resulting rGO having a carbon to oxygen ratio as high as 10.3:1 (methods slightly vary in temperature and gas vs. liquid reduction). It was found that effective reduction of the oxygen groups is highly dependent on the reaction temperature [72, 73], with higher

temperatures (95°C) being necessary for a more complete reduction, yielding rGO with a carbon oxygen ratio of up to 15:1. The conductivity and sheet resistance will show a range, depending on the form of the bulk rGO used for testing, with the highest values in the range of 2400 S m⁻¹, close to that of graphite (2500 S m⁻¹) [56]. This demonstrates the effectiveness of hydrazine reduction at restoring aromatic domains with high conductivity. It has also been observed that the BET surface area of hydrazine reduced GO assemblies can range from 450-750 m² g⁻¹ [56, 74], which is far lower than the idealized value for exfoliated graphene of 2620 m² g⁻¹ and highly depended on the residual oxygen content, sheet morphology, and interlayer-spacing within the bulk assembly. Li et al. demonstrated the production of aqueous suspensions of rGO that were stabilized via surface forces in a basic solution which greatly improved opportunities for scalability, functionalization, and simple bulk processing of rGO materials [15].

The surface chemistry and morphology of rGO sheets remains an area of current interest as these properties will determine the performance of rGO bulk materials. The mechanism of hydrazine reduction has been shown to act mostly on the basal bound epoxy groups (which restores the aromatic domains and increases sp² content), but is rather ineffective at removing hydroxyl and carboxyl groups [71, 73]. There are contradicting reports as to whether hydrazine can [73, 75] or cannot [16] remove carbonyl species, but this may be due to differences in reaction temperature. At temperatures greater than 95°C, the effectiveness at removing basal-plane epoxy groups improves while at the same time carboxyl groups begin to reduce, further enhancing the overall reduction process. Wang et al. [75] showed this effect could be significantly enhanced through a solvothermal hydrazine reduction process at 180°C which significantly increased the conductivity of rGO layered assemblies (also termed graphene paper in some literature) to values of 2720 S m⁻¹, compared to the typical 95°C treatment yielding 580 S m⁻¹. It is the general consensus that basal hydroxyl groups are the most difficult to remove, and edge bound species of hydroxyl, carboxyl, and carbonyl remain in rGO reduced using hydrazine [5]. As discussed previously with thermally reduced GO, the density of oxygen groups on the basal plane will also be a factor in the resultant surface chemistry of rGO, and the specific mechanisms underpinning hydrazine reduction show the same trend. A higher density of epoxy groups on the basal plane will still result in smaller sp² domains after reduction [76], most likely due to the recombination of neighbouring epoxy and hydroxyl groups to form phenols.

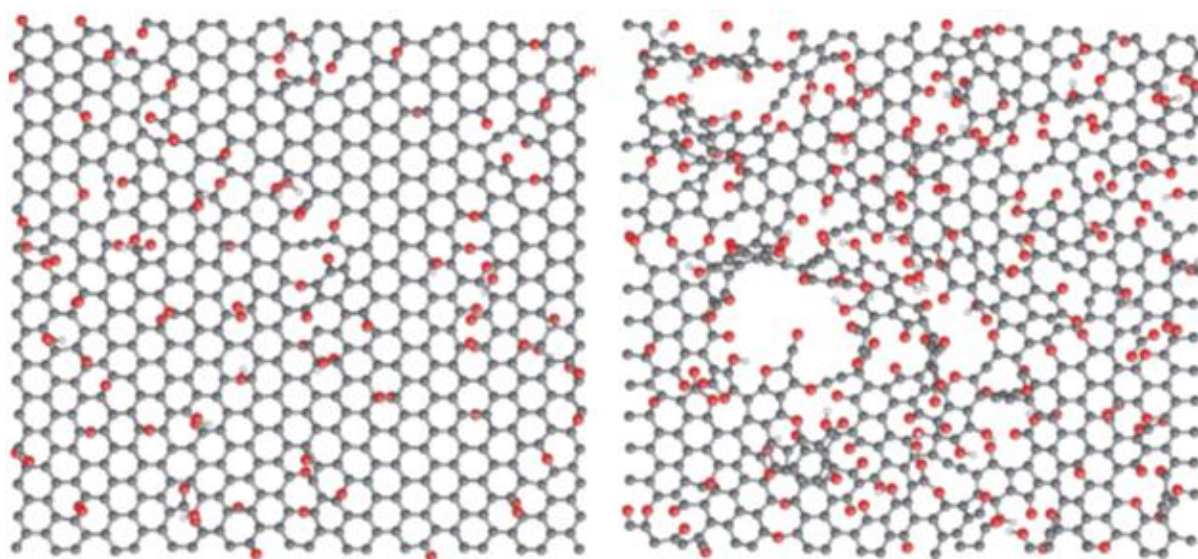


Figure 12. Depiction of the impact different levels of oxidation in the original GO will have on the resulting structure of rGO. The structures are the result after rapid, high temperature reduction of GO with 20% oxygen (left) and 33% oxygen (right). The grey atoms are carbon, red are oxygen, and white are hydrogen in both hydroxyl and phenol groups (from [65]).

The original oxidation level of the GO sheets, as well as the particular reduction conditions, will also have impacts on defects within the carbon lattice. Generally, higher oxidized material will lead to more in-plane carbon defects, with higher temperatures and faster reduction rates being the most destructive. As shown in Figure 12, GO with original oxygen content of 20% and 33% results in rGO with very different levels of oxidation and defect density [65]. These computational models show the effect of rapid, high temperature reduction at 1200K, so there are many more defects introduced to this carbon lattice than there would be in the case of hydrazine, which would be more like the low oxygen content figure on the left. The initial configuration of hydroxyl and epoxy groups is expected to drive the formation of carbonyl and phenol groups, where the formation of holes within the basal plane is energetically favourable in all cases. Gao et al. [16] also shows that hydroxyl groups are not stably bound to the basal plane, and in order to remain stable require a neighbouring epoxy, migration to an edge site, or conversion to phenol. The conversion to phenol is the preferable route, as other options result in sp^3 carbon bonds, which leads to an increase in sheet resistance.

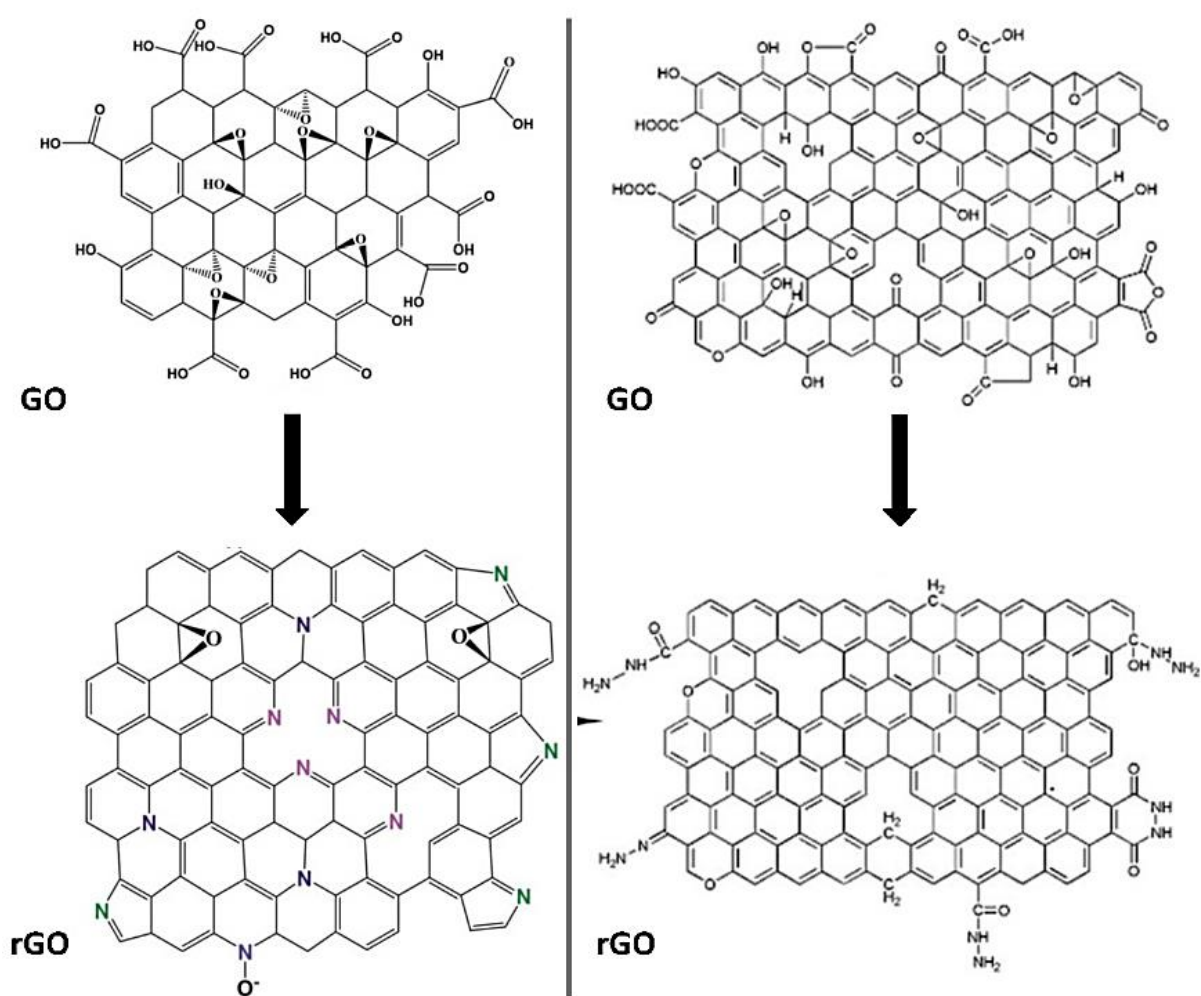


Figure 13. Variations in schematic structures of GO and nitrogen-doped rGO produced by hydrazine-assisted solvothermal reduction (temperature range of 80-180°C) showing numerous graphitic (purple), pyridinic (pink), and pyrrolic (green) nitrogen species (left from [77]), compared with hydrazino alcohols, hydrazides, and hydrazones (right from [75]).

The impact hydrazine has on the presence of nitrogen in rGO has been the matter of debate, but some degree of nitrogen doping in the resultant rGO is always reported [5] – typically at values of around three atomic percent. Previous reports have shown the nitrogen bonding primarily occurs at the edge sites, while the degree of N-doping scales with the degree of oxidation or concentration of defects in the graphene lattice [78], specifically with the amount of epoxy and carbonyl groups [73]. The reaction

mechanism is attributed to reduction of the epoxy groups as well as interactions with the carbonyl and carboxyl groups [75], but consensus on the resulting species has still not been reached, with accounts of be sp^2 or sp^3 hybridized environments all being reported. Examples of these nitrogen groups reported in the literature are as follows: amino aziridine [71]; hydrazino alcohol, hydrazide, and/or hydrazone [73, 75, 76]; “pyrrole-like” (pyrazole and/or pyrazoline) species [79-82]; or a combination of pyridinic, pyrrolic, and graphitic types [77, 83]. Two of the reported structures for nitrogen-doped rGO are shown in Figure 13, and it is clear very different bond types have been assigned, with the left side of the figure depicting only nitrogen groups incorporated into carbon rings, while the structure on the right shows “amine-like” functionalities of hydrazino alcohols, hydrazides, and hydrazones. An accurate determination of the nitrogen bonding is important because this has significant impacts on the conductivity of the rGO sheets, with the site of the nitrogen bonding being the main determinant of enhanced capacitance for N-doped rGO supercapacitors [60, 84, 85].

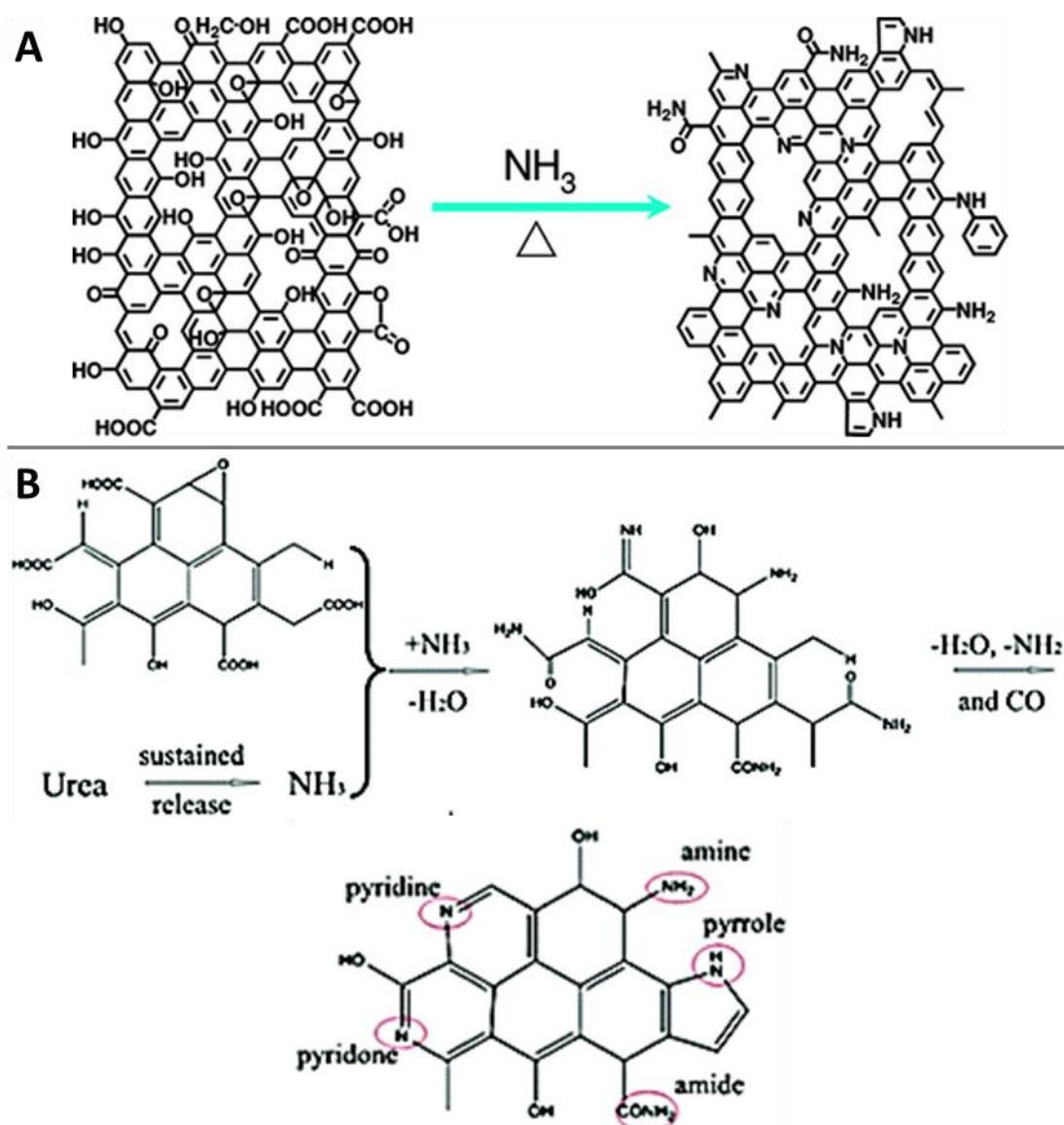


Figure 14. Variations in schematic structures of nitrogen-doped rGO produced interactions with ammonia gas at high temperatures (A from [86]) or urea in a hydrothermal environment (B from [87]).

Interestingly, solvothermal conditions (also a method used in this work), optimised at $180^\circ C$, significantly enhanced the hydrazine reduction process by way of a Wolff-Kishner-Huang [88] reaction to reduce carbonyl groups while also facilitating additional reactions with carboxylic groups to form

hydrazino alcohols [75]. Along with the role of hydrazine, additional nitrogen doping can result when rGO is prepared via hydrothermal reduction in aqueous dispersions with ammonia (method used in this work). This has been shown to contribute to the formation of residual amines after reactions with acidic groups on GO, including carboxyl, hydroxyl, and epoxy groups [75, 86, 89, 90], and a similar effect has been reported for interactions with urea [87, 91]. Two of the proposed chemical structures are depicted in Figure 14, where further incorporation of the nitrogen groups into aromatic rings is thought to occur under particular reaction conditions [86, 87].

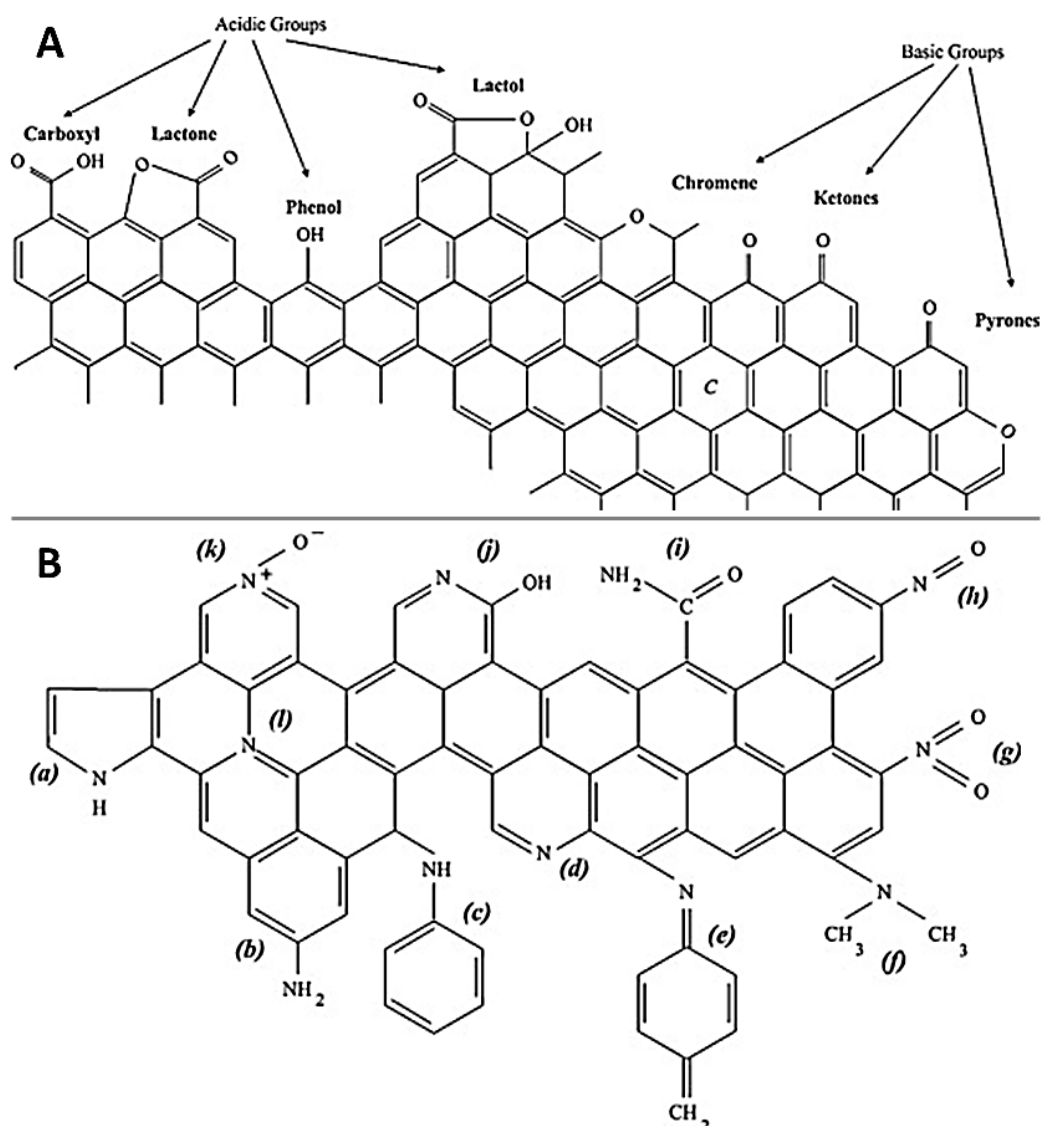


Figure 15. Schematic A (at top) depicts the typical oxygen containing acidic and basic functionalities on the edges of carbonaceous solids (from [92]). Schematic B (at bottom) depicts types of nitrogen surface functional groups often present in activated carbons: (a) pyrrole, (b) primary amine, (c) secondary amine, (d) pyridine, (e) imine, (f) tertiary amine, (g) nitro, (h) nitroso, (i) amide, (j) pyridone, (k) pyridine-N-oxide, (l) quaternary nitrogen (from [93])

The nitrogen bonds on rGO materials can occur at both basal and edge sites, but more favourable bonding occurs along the graphene edges. In addition to the works mentioned above on rGO materials, there has been a vast amount of research conducted on the identification of chemical species within other types of nitrogen containing carbonaceous solids [92, 94], including activated carbon [95, 96] [93], carbon fibers [97, 98], chars [99], and hydrothermal carbon [100]. In these materials, preferential bonding also occurs along edge sites, and the typical acidic/basic oxygen functionalities found in carbonaceous solids are shown in Figure 15(A). In low temperature reactions, ammonia reacts with the stronger acidic groups (carboxylic, anhydrides, lactones) to form amide, imide, imone, amine,

and/or nitrile, while at higher temperatures, ammonia can also decompose weak acids (carbonyl, phenol, quinone) and more thermally stable groups located in aromatic rings are formed (pyrrolic- and pyridinic-like) [95]. Figure 15(B) shows the multitude of nitrogen functionalities that are typically found in activated carbons [93], many of which are similar to what would be expected in nitrogen-containing rGO materials.

In summary, to enhance the conductivity of the rGO sheets, it is desirable to remove as many of the oxygen groups as possible and restore the sp^2 carbon network. However, upon reduction, along with the removal of oxygen functional groups, the graphene sheets undergo other physical and chemical changes, resulting in a material that is markedly different from defect-free graphene. The work presented here focuses on rGO produced using a hydrothermal chemical reduction process utilizing hydrazine [15], and the sheets produced with this method contain in-plane defects, residual oxygen groups, and nitrogen doping, all of which will influence conductivity and impart a large degree of structural disorder [56, 76]. Published experimental results and molecular modelling show that the epoxide groups attached to the aromatic domains are the most easily removed, but epoxides and hydroxyls attached to edges and defects will remain even after treatment at very high reduction temperatures [66]. Also, edge sites with carbonyl groups are strongly bound, yet edge sites with carboxyl are unstable and can be removed at slightly elevated temperatures. It has also been shown that phenol groups can be produced during thermal deoxygenation because the epoxide and C-OH groups are in close proximity along the planar surface, facilitating localized bonding at temperatures up to 400°C, where these moieties begin to slowly decompose [66]. Additionally, rGO reduced using hydrazine is usually suspended in an aqueous solution stabilized with ammonia [15]. Under these conditions, the nitrogen from both hydrazine and ammonia can bond to the defect regions produced during the reduction process, creating nitrogen-doped rGO sheets [73, 76, 77, 90, 101].

2.1.2.2 Structure

The residual chemical groups on the rGO sheets have important structural implications on the size and connectivity of the aromatic domains along the carbon lattice [102]. The electronic properties of carbon materials depend not only on the chemical composition, but also on the morphology, which is not necessarily linked to a particular physical structure. For example, Stankovich [103] noted that while glassy carbon is a pure sp^2 carbon matrix, it contains very tiny aromatic domains because of its amorphous-like structure, with the dimension of these domains similar to an activated carbon with approximately 11% residual oxygen, where the small aromatic domains result from oxygen groups and defects in the carbon lattice. In spite of large differences in structure and properties, both glassy and activated carbon materials typically exhibit aromatic domains with length, L_a , of about 1.5 nm. Based on the structural diagrams of Ellis mentioned previously [80], GO with 50% oxygen would have an L_a less than 1 nm, and the prevalence of remaining basal bound groups in rGO would indicate the size of aromatic domains will vary, but should be close to 1 nm in rGO with a 10% oxygen content [80].

The size and connectivity of the aromatic domains in rGO sheets will determine the resistivity of the material, with distinct types of transport being dependant on the sp^2 fraction and oxygen content in the material, as shown in Figure 16. Hopping is dominant if there is more than 20% residual oxygen present (corresponds to less than 60% sp^2 bonding), which is common during the initial stages of reduction [70]. Mattevi et al. [104] showed that further reduction is able to connect the sp^2 clusters so that percolative transport can occur, with reduction above 450°C being equivalent to chemical reduction with hydrazine. As previously discussed, it is not possible to fully reduce GO, and thus some sp^3 bonding is always present due to residual oxygen groups and carbon defects which creates “conduction bottlenecks” between the clusters and limits the maximum conductivity of the material.

It should be noted that the diagrams in Figure 16 also correspond to a physical morphology resulting from carbon bonding and residual oxygen groups which will now be discussed.

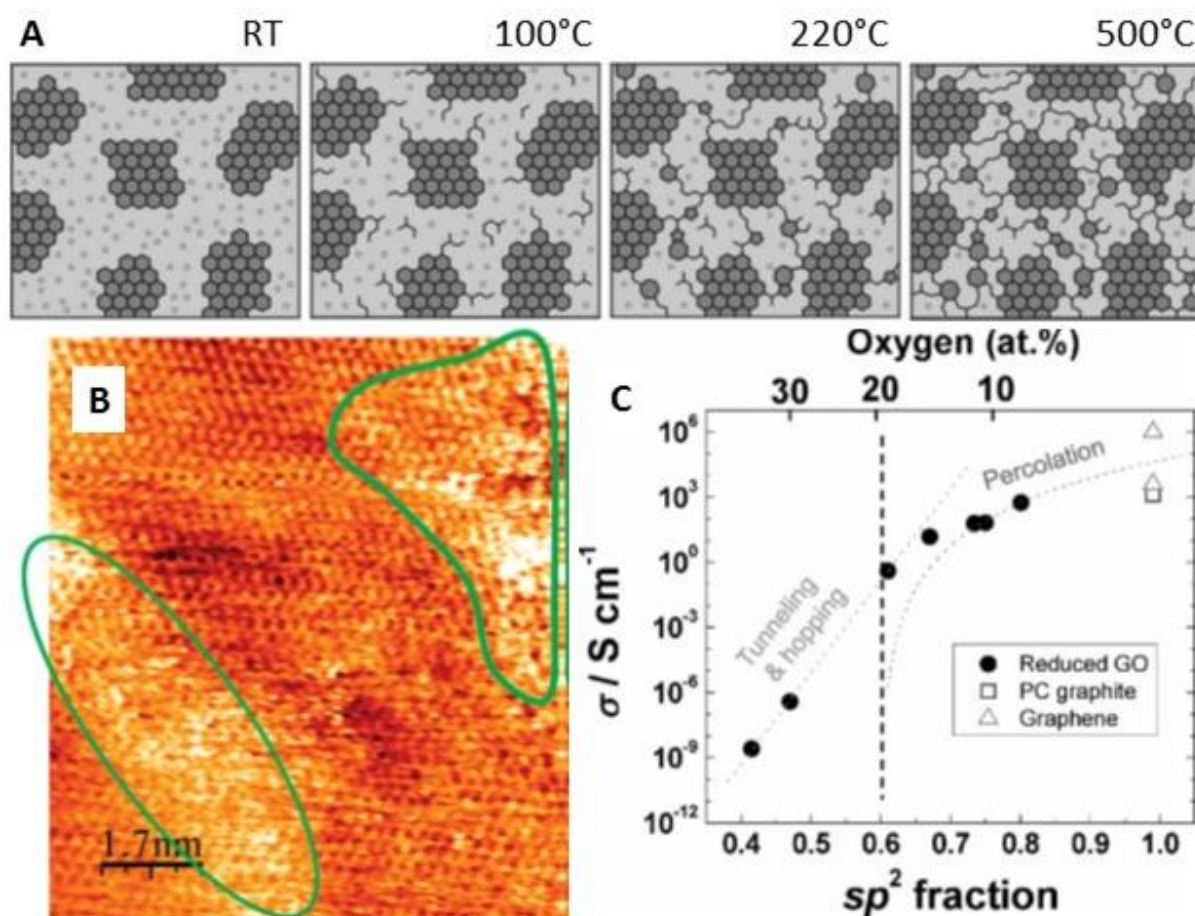


Figure 16. Diagrams depicting the aromatic domain size L_a as a function of the sp^3 bonding from residual oxygen groups as GO is reduced at different temperatures is shown in A (from [104]) and the AFM image of rGO shown in B confirms the relative size of aromatic and oxygenated domains (from [70]). Both of these studies reveal the transport (hopping or percolation) is determined by the sp^2 fraction, which is itself related to the oxygen content, as shown in C.

In addition to the electronic considerations mentioned above, it is important to recognize that the dimension and shape of rGO sheets will impact the resulting material properties of rGO assemblies just as much as, or perhaps even more than, the chemistry, depending on the application. For example, in an electrochemical supercapacitor, the amount of ions that can be stored in the pore depends on the total accessible surface area, as well as the size of the micropore, yet this relationship is not trivial as there is not a true linear correlation between surface area and capacitance. In practice, there is an optimal micropore size that correlates with a specific electrolyte system within a given voltage window [41]. Furthermore, the uniformity of the pore sizes, usually described by the PSD, as well as the way the pores are interconnected has a large impact on capacitor performance. The morphology of rGO sheets will impact the overall stacking within rGO assemblies and, thus, determine many important properties of the bulk material, such as permeability, accessible surface area, and these pore size considerations. The residual oxygen groups and sheet corrugation will be the main determinants of the structural features mentioned here.

GO sheets have been found to have an average surface roughness of 0.6 nm resulting from the distortions of sp^2 bonds to sp^3 C-O bonds, and this roughness is also, then, proportional to the electronic structure of GO as oxygen bonding increases resistance due to bond configurations [6, 105]. It can be expected that the residual oxygen groups bound to the basal plane of rGO retain a similar level of roughness, and the variance in defect concentration along the sheets was shown clearly with

ultra-high-resolution transmission electron microscopy (TEM) [106], as shown in Figure 17. Thus, the structure of individual rGO sheets can be used to infer the structure of stacked assemblies, where aromatic domains allow for restacking due to the planar surface and Van der Waals bonding (Figure 17(F)) and oxygenated domains contain protruding bonds that result in increased stacking distance between rGO layers (Figure 17(D,E)). This would result in two distinguishable regions, with interlayer distance related to aromatic (sp^2) or aliphatic (sp^3) bonding, typical features seen in oxygenated carbons like coal [46, 107-109].

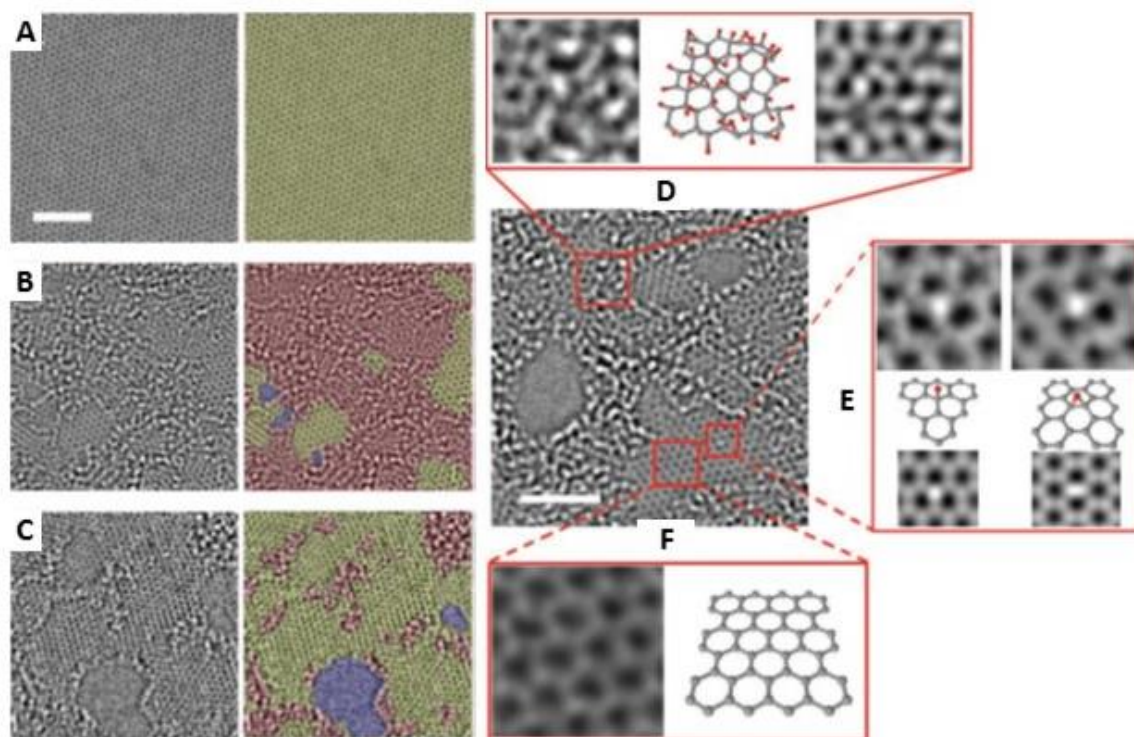


Figure 17. Structure of pure graphene (A), graphene oxide (B), and reduced graphene oxide (C) where aromatic domains are coloured in yellow, oxygen functionalities in red, and holes in purple. The corresponding description of how the residual oxygen groups disturb the planar structure along the carbon lattice, with surface roughness being related to the variance in defect concentration from high oxidized areas (D), individual oxygen bonds (E), and aromatic domains (F). Scale bar is 1 nm (from [106]).

Even with pure sp^2 bonding, suspended graphene has microscopic ripples, or surface corrugation, because of thermal fluctuations and is essential for the structural stability of two-dimensional carbon sheets, as shown comparatively in Figure 18(A) and (B) [48]. These results were taken from graphene suspended on a TEM grid under high vacuum, and it can be assumed that the surface forces between the sheet and surrounding media will play a large role in determining the overall corrugation, with rGO in aqueous media exhibiting different features than that of freely suspended pure graphene. It is also known that defects and dislocations will result in shrinkage and local deformations that add to sheet corrugation and increase strain in graphene [6]. Two-dimensional graphene systems have been shown to exhibit long-range out-of-plane buckling that results from specific defects along the lattice [110], as shown in Figure 18 (D). Pentagon-heptagon defect pairs are normally detected along a grain boundary and can relax to an unperturbed graphene lattice. However, hole-like defects are assumed to be more prevalent in rGO layered structures, and these will increase corrugation along the sheet and add to overall disorder within the stacking of the sheets, like that seen in smooth lamellar pyrocarbons, and depicted in in Figure 18 (C) [111].

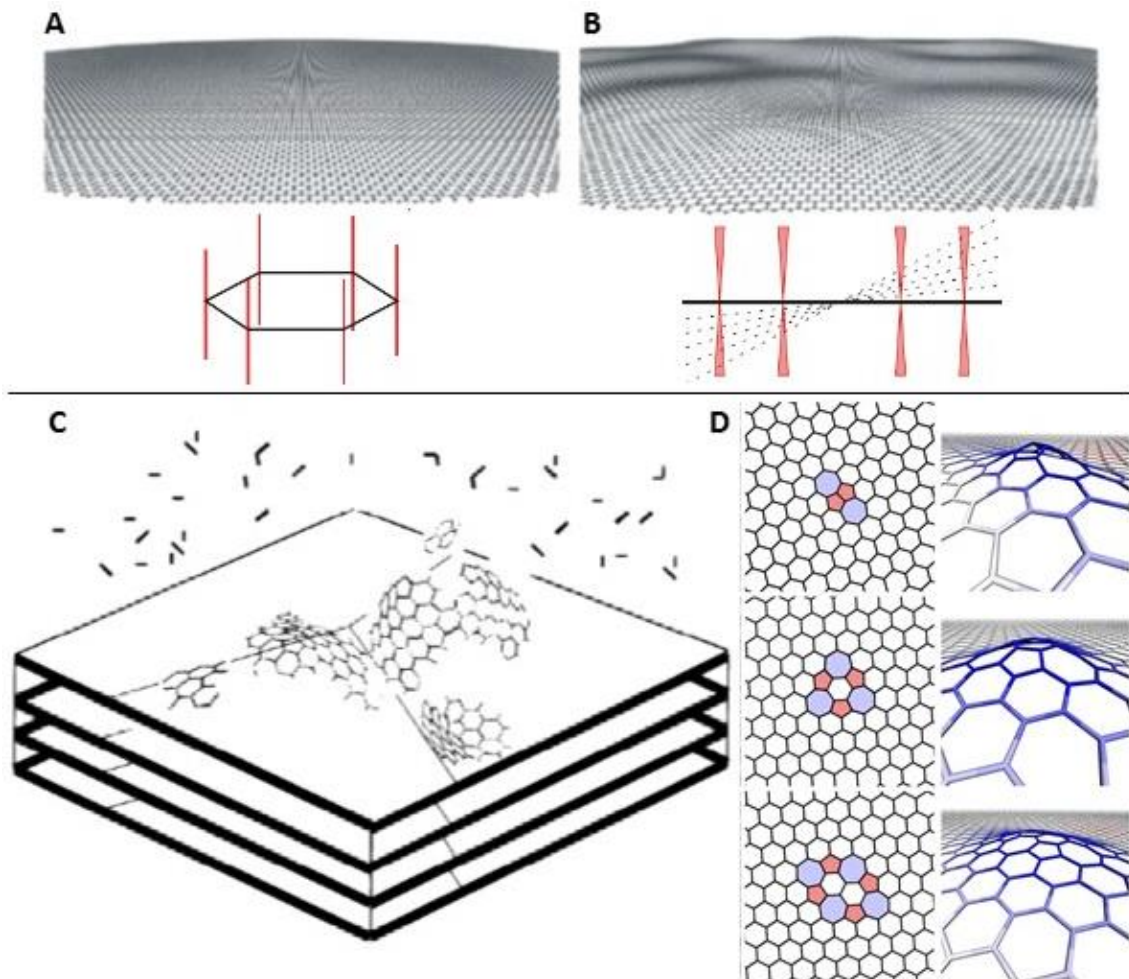


Figure 18. Natural planar fluctuations in suspended graphene sheets (corrugation) was measured by the broadening of crystalline diffraction spots, as shown in A and B (from [48]), where the deviation from a perfectly flat, 2D crystal disrupts the periodicity and results in reciprocal space features like that of narrow cones instead of perfect rods (as shown in the diagram). Defects in the carbon lattice result in curvature that influences the stacking of carbon layers within a pyrocarbon (C) and the geometry of defect configurations will lead to curvatures with specific shapes, as shown in D (from [111] and [110], respectively).

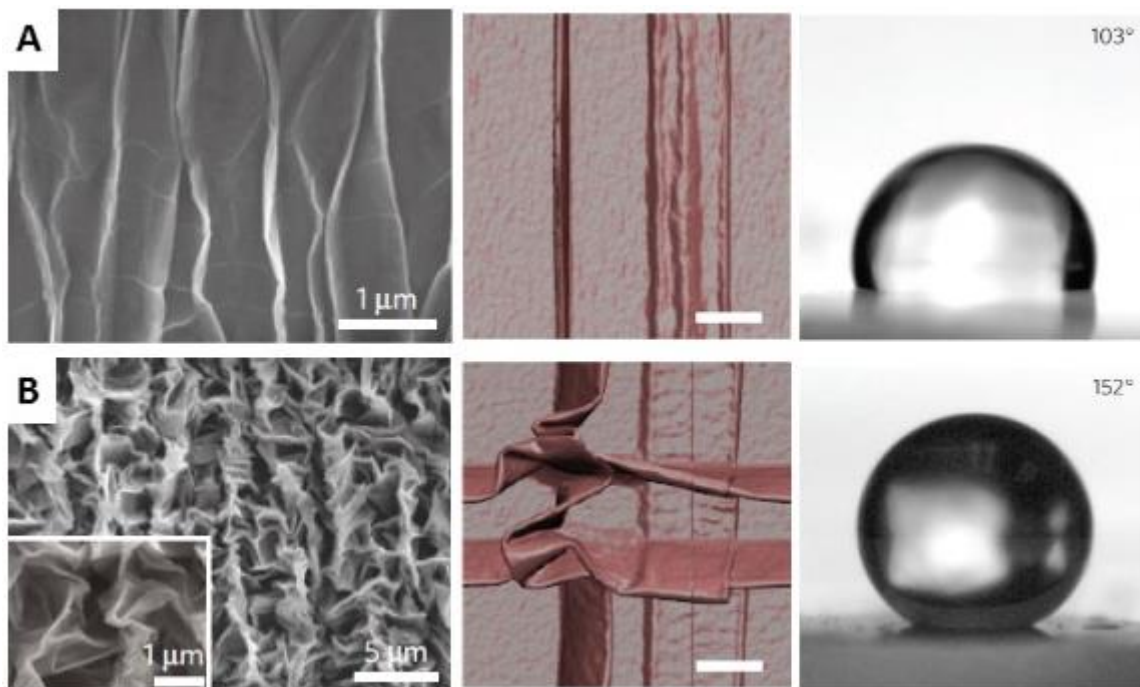


Figure 19. SEM images of wrinkled (top A) and highly crumpled (bottom B) graphene sheets along with the corresponding atomistic modelling results and water contact angle (from [112]).

In addition to corrugation and curvature due to defects, graphene and rGO will undergo wrinkling in response to confinement or controlled crumpling (applied pressure or mechanical stress). The presence of these wrinkles, like those shown in Figure 19, impact the wettability, transparency, reactivity, and mechanical properties of the material [112]. It is difficult to assign a direct measurement to this crumpling because it is highly disordered and statistically variable. Again, similar to the chemical structure of rGO, the morphology is also best described using a statistical distribution characterized by the major factors of surface roughness and aromatic domain size, with the material properties acting as an indirect measurement of these same features.

These wrinkles and folds will also act to stabilize graphene sheets, and multiples studies have found that graphene and rGO sheets will fold in precise and predictable ways, related to the defects, dangling bonds, and interlayer van der Waals cohesion forces which also act to stabilize the resulting folded structure [113]. The same forces that act along a single sheet will also act between different sheets, so an understanding of what factors will determine sheet morphology is of the utmost importance to forming an accurate structural model of highly complex rGO assemblies. Figure 20(A-C) shows the difference in van der Waals cohesion between a graphene sheet that is relatively free of defects and folded in half compared to a sheet that has more folds and crumples. It is clear that a higher amount of crumpling is effective at reducing the stacked regions which will be inaccessible to gasses and ions. Figure 20(D-E) shows the main structural features which can act to stabilize the folded graphene sheets with covalent crosslinks, ridges, and oxygen bonds effectively overcoming the van der Waals forces. Figure 20(E) further highlights that more defective graphene sheets will have more crosslinking and surface corrugation which can help stabilize the crumpled structure.

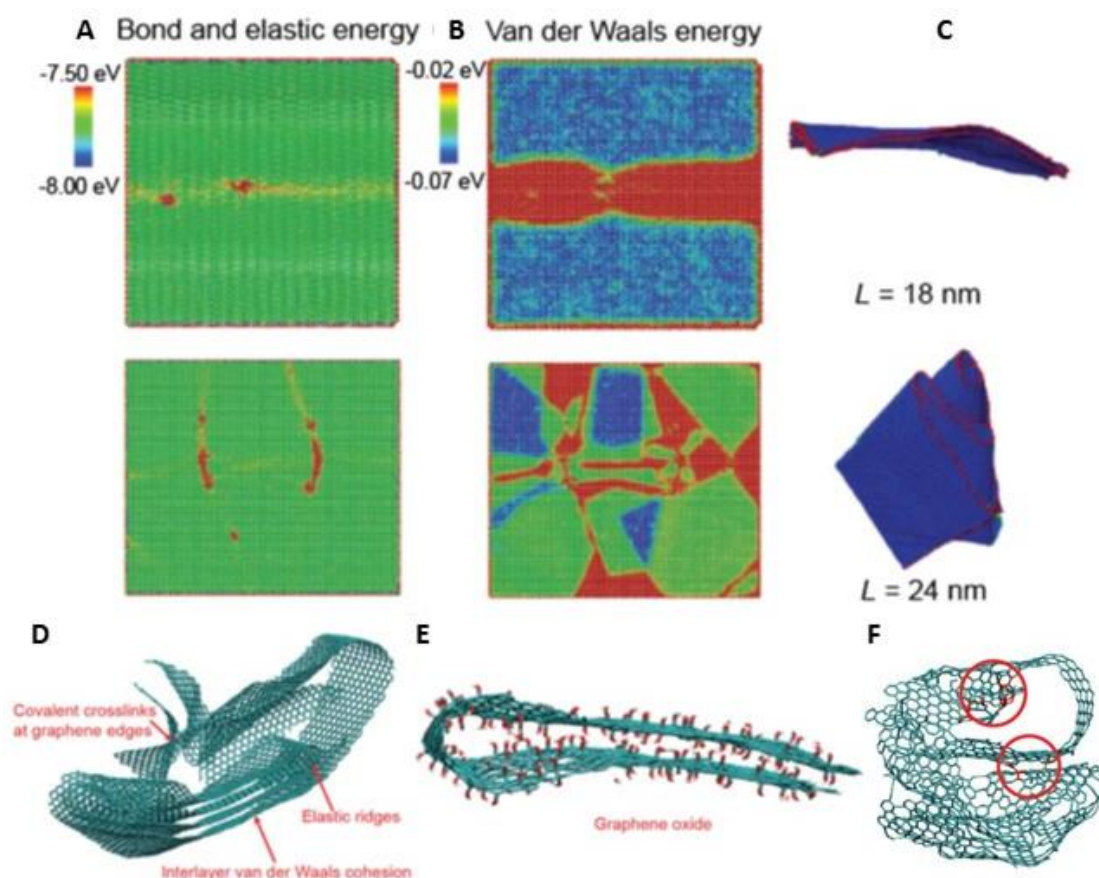


Figure 20. Distribution of bond and elastic energy (A) along with van der Waals energy (B) in stable crumpled sheet configurations for graphene of sheet length 18 nm and 24 nm (C). Diagrams showing the different structural features in crumpled graphene (D) and GO (E) along with an illustration showing the prevalence of crosslinking in sheets that contain more defects (F) (from [113]). Simulations performed using the LAMMPS package [114] based on the adaptive intermolecular reactive empirical bond order (AIREBO) potential function [115] where both covalent bonds and van der Waals interactions are included. This method has been validated by predicting consistent structural and mechanical properties of graphitic structures, including bending rigidity and surface energy.

Similar work was done to assign a quantitative value to the crumpling of graphene sheets and further relate this to the solvent accessible surface area (SASA) along the sheet [116]. Figure 21 shows the major findings of this work where a graphene sheet of length L is crumpled by constraining it within a sphere of radius r , and no matter what the sheet or confinement size is, a purely crumpled sheet will have a fractal dimension of 2.358. This fractal dimension can then be directly related to the amount of crumpling versus folding, where more folded sheets will have fractal dimension greater than 2.358 which signals the loss of SASA because more van der Waals stacking is present. These results have a significant impact on the rGO assemblies under investigation, and allow for interpretation of the sheet morphology as it relates to material performance, especially in regard to supercapacitors which rely heavily on a high SASA.

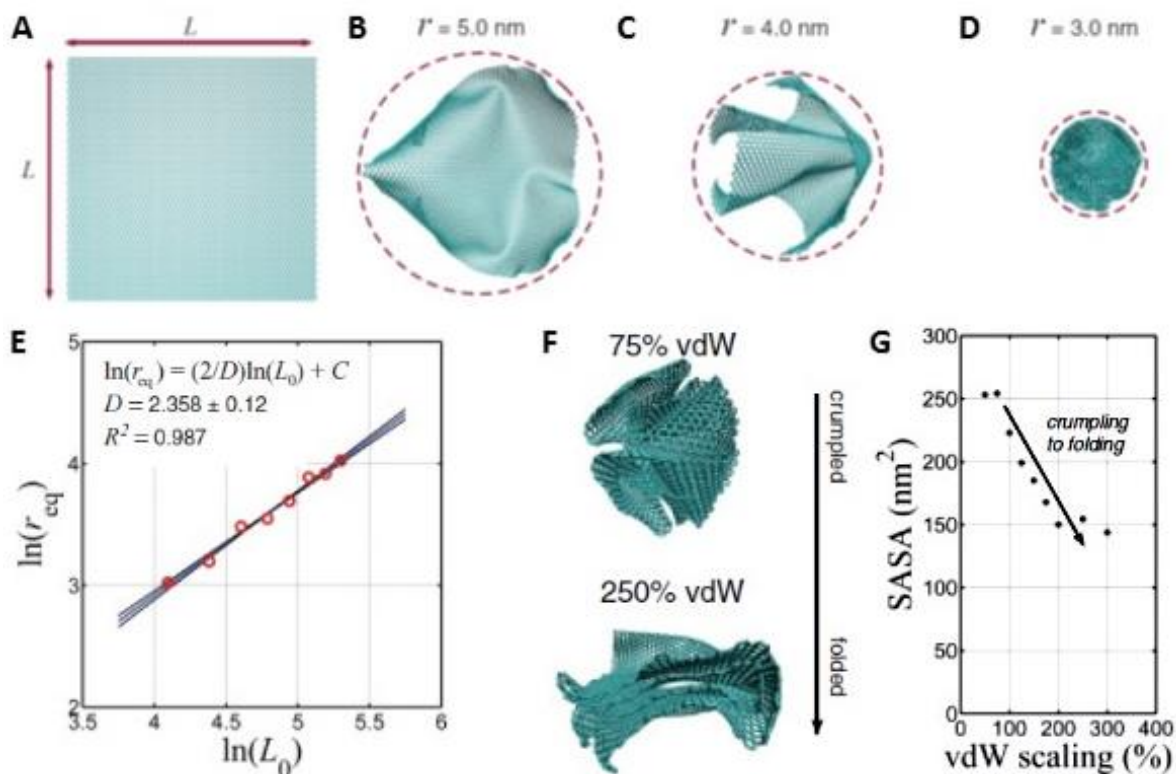


Figure 21. Structural depiction of how a graphene sheet of length L crumples when constrained within a sphere of radius r (A-D). Results show regardless of the original sheet length L_0 (or corresponding confinement sphere with radius r_{eq}), the fractal dimension of a purely crumpled sheet is 2.358. Depending on if the graphene sheet is more crumpled or folded, there will be a specific percentage of van der Waals (VdW) stacking present (F) which directly corresponds to the solvent accessible surface area (SASA) of the sheet (from [116]).

Thus, the three dimensional nanostructure of layered rGO assemblies contain accessible surface area that is directly related to the residual oxygen groups, corrugation, and crumpling that exists within each individual sheet. As these sheets accumulate to form bulk assemblies, the structural perturbances will ultimately create the individual pores and overall pore network by the prevention of stacking wherever the π - π interactions are weakened. It has been shown that removal of these perturbations leads to a significantly reduced surface area in rGO assemblies, especially in sub-nm pores [74]. It should also be mentioned that because of the different surface chemistry and crumpling conditions for various rGO materials, the measured surface area for these materials has been reported across a wide range of $723 \text{ m}^2 \text{ g}^{-1}$ [74], $425 \text{ m}^2 \text{ g}^{-1}$ [56], and $300 \text{ m}^2 \text{ g}^{-1}$ [69].

2.1.3 Three-dimensional architecture of rGO assemblies

Graphene-based materials come in all forms, from single sheet to very advanced 3-dimensional architectures [38]. Furthermore, there are countless composite materials that can be created by incorporating nanoparticles or polymers into a graphene-based matrix where the rGO sheets can comprise either the majority or the minority material [27]. As mentioned, one of the largest challenges in creating a scalable processing method from graphene-based materials is to prevent agglomeration or restacking of the sheets after they have been reduced from GO. Further, in order to obtain rGO bulk materials that can be used for specific applications, it is necessary to effectively control both the surface chemistry and structural properties of the pores. Stable solutions of solvated graphene offer unique opportunities for functionalization and tailoring the structure and are very promising materials, particularly in the fields of energy storage and biomedical devices (particularly in the hydrogel form) [29].

The previous introductory chapter of this work highlighted the specific applications where these rGO assemblies have shown promise alongside the relevant research questions that remain. The focus of this work is aimed at determining the structure of rGO assemblies, and these results are then discussed in the context of addressing the knowledge gap that remains from previous research, especially as it relates to how the structure of these porous rGO assemblies is likely to impact ion transport [26] and supercapacitor performance [24]. Ultimately, it is the large surface-to-volume ratio and high conductivity of porous carbons and graphene-based materials that yields the well-known advantages, but solvated graphene also goes much further as the low-temperature, aqueous processing conditions allow for unique opportunities. Robust assemblies composed of multi-layer rGO sheets can be fabricated with various thickness using solution based filtration method [15], and added features of controllable corrugation [22, 23] and adjustable packing density [24] have shown promise in separation and energy storage technologies.

While these rGO assemblies show immense promise, direct measurement of the pore structure has not yet been accomplished. Accurately tuning the pore size while retaining a consistent pore network is of great interest, however accurate characterization is quite complex as the performance will depend on not only individual pore size, but also pore size distribution, interconnectivity of pores (ASA), total porosity, as well as wettability and specific aspects of the surface chemistry [39, 117, 118]. As discussed in the introduction, these factors require full characterization to extend across a large length scale and employ a multitude of techniques. This is further complicated with hydrated and dynamic systems, and structural features can be inferred based on performance, but no direct measurement has been done to corroborate these reports. It should also be noted that the expected size range of the pores in rGO assemblies ranges from sub-nm up to about 15 nm, or perhaps more, and this particular size range lies in a range where most experimental methods are not optimised – either focusing on sub-nm diffraction measurements or larger structures of over 100 nm. TEM is an exception to this, but the sample conditions are not well suited for rGO materials, particularly hydrogels.

Figure 22 shows a hierarchical structural model put forth for GO and rGO bulk assemblies at the micro- and macro-scale. While these models are supported by indirect analysis of material properties, no direct structural data verifies these claims, especially in the size regime below the resolution of SEM imaging, which is typically used as the only experimental tool for this aim. Much information can be gained in the sub-nm region using X-ray diffraction, but not in the case of the disordered and solvated materials. Thus, a large gap remains in creating a complete structural model of rGO assemblies based on direct evidence which incorporates aspects of the individual rGO sheets, micro-clusters, and meso-lamellar features that will define the overall pore structure.

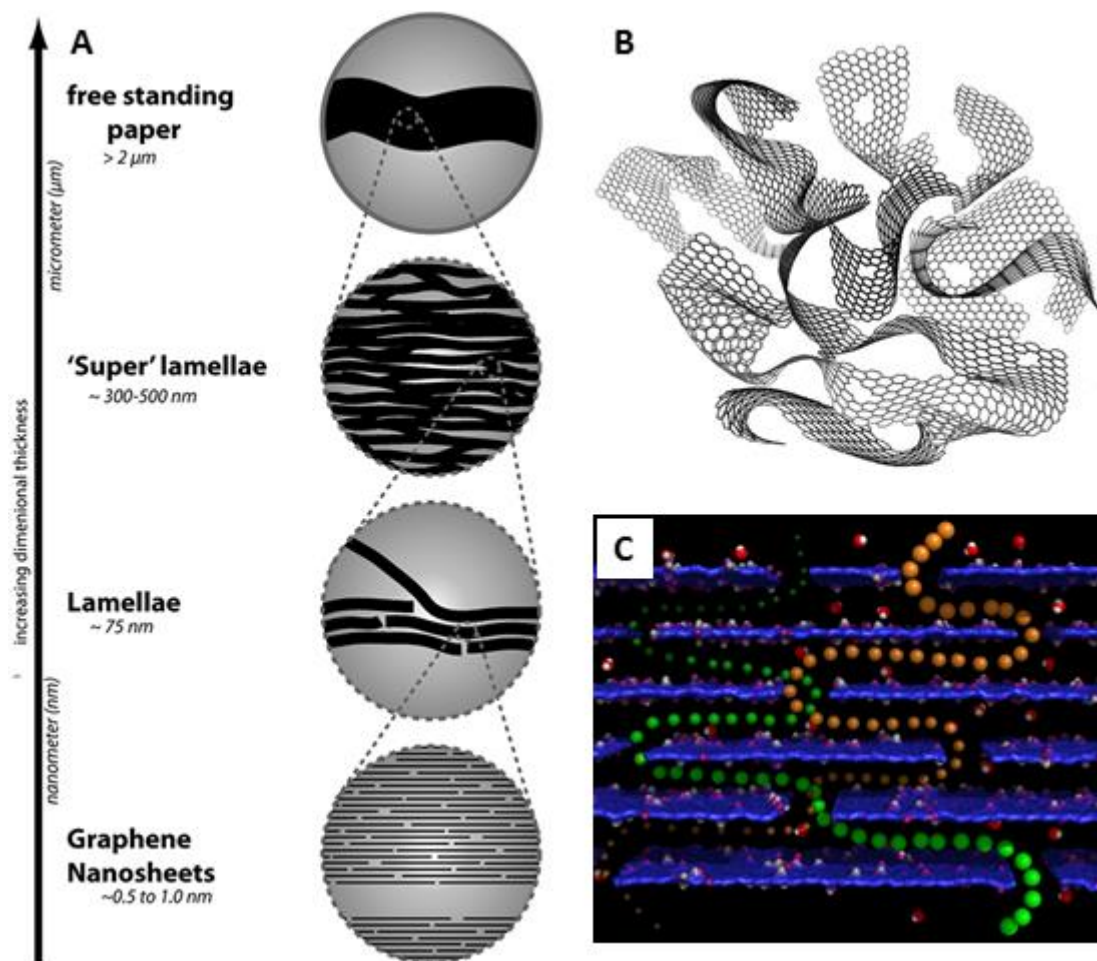


Figure 22. Hierarchical structure and corresponding size regime making up the bulk of a GO paper, where individual sheets form clusters of a lamellar form which in turn form what is termed a “super” lamellae (A) proposed by Wood et al. [119]. Model for a more disordered 3D rGO porous assembly that shows in-plane defects and a high degree of corrugation (B) proposed by Zhang et al. [120]. Molecular level model proposing how water and ions move within the “cascading slit-shaped pores” of rGO hydrogels with tuned pore size (C) proposed by Cheng et al. [26].

One of the most promising indirect measurements of how the pore structure influences performance has been shown to be dynamic electrosorption analysis (DEA), as reported by Cheng et al. [17]. This technique overcomes many of the issues related to other penetration methods and uses ionic species to directly probe the surface of rGO assemblies. The size and affinity of the ions can be tailored so that differences in the charging behaviour can be seen, and these differences are then used to draw conclusions about the total accessible surface area, as well as the accessibility of the pores or dynamic resistance. While no direct structural evidence is attained, the advantages of this method is that it is can easily performed in specific conditions that better match that of the actual device (as an energy storage material). The work presented in this thesis builds on the performance measurements presented in the DEA analysis, using the same preparation methods for rGO assemblies so that the newly identified, direct structural results can be compared to the DEA results.

The basic premise for investigating porous carbons with a combined DEA and structural analysis is to identify the structures that cause specific, measureable phenomena that occur during the charge/discharge process in rGO electrodes with aqueous electrolytes. The main factors investigated with DEA were three-fold: i) at low charging rates, the ions are able to overcome the impedance and enter confined pores to yield the total accessible surface area, as measured by the maximum capacitance; ii) at higher charging rates, there is a significant amount of energy loss that stems from the impedance which is influenced by the overall pore structure, and the capacity drop reflects features causing this resistance such as overall tortuosity and the prevalence of small micropores

(<2 nm); iii) applying electrochemical impedance spectroscopy (EIS) [121] to measure the resistor-like behaviour at high frequencies and capacitor-like behaviour at low frequencies where the characteristic time constant, τ_0 , can be deduced and measure how fast an ion can transport within the pore network. Using the DEA method, it was found that rGO assemblies prepared with different reduction temperatures, drying conditions, and annealing temperatures must have very different pore structures, and this thesis suggests relevant links between the structural features of rGO assemblies and these ion transport measurements reported in these other works.

2.1.4 Outstanding research questions related to rGO assemblies

As discussed, it is likely there must be trade-offs in performance when particular reduction conditions are applied. For example, removal of basal plane oxygen groups will enhance conductivity, but could also reduce accessible surface area due to restacking of rGO sheets. The additional performance impacts from wettability, pseudocapacitance, nitrogen doping, and aromaticity are all factors that require surface chemistry be precisely accounted for. Currently, there have been no direct relationships made between the synthesis conditions of the original GO precursor and the structure of the resulting rGO sheets.

There is clearly a significant gap in knowledge related to both the surface chemistry of rGO sheets and the porous structure of rGO assemblies. While a large number of publications exist showcasing the unique properties of graphene-based assemblies [12, 27, 29], the fundamental analysis of structural elements underpinning the performance is in its infancy [36, 74, 122]. The work with DEA highlights that pronounced difference in the structure must be there, yet until now there has been no direct determination of the structure. This is the same for publications on sheet corrugation [22], as the only validation of the structure was made based on filtering particles of different size through the assembly. While assumptions can be inferred from the indirect results, there is no way to differentiate what factors could be due to a specific pores size or if they are more related to the overall pore connectivity. As noted throughout the literature, there is a need for new methods to be developed that can quantitatively assess the complex structure of rGO assemblies, especially as this related to changes in pore size and ions in confinement [123]. Further, it is of interest to allow these new methods to be adaptable for *in situ* experimentation to track both the structure of the rGO material as well as liquids and ions confined within the porous network.

2.2 rGO Assemblies Viewed as a Unique Type of Porous Carbon

2.2.1 General properties of layered and porous carbons

Because the two main structural features of interest for rGO assemblies are that they are: i) layered in the c-direction, with the defective graphene 2D crystal laying along the ab plane; and ii) porous, with what are assumed to be slit-like pores formed between the rGO layers, also along the c-direction. Thus, one of the main considerations resulting from this particular type of structural ordering is that rGO assemblies will be a highly anisotropic material, likely to also exhibit anisotropic transport properties. This requires specific experimental conditions in order to obtain data along two, very different planes (the ab-plane and the c-axis stacking direction). This is not the case for most porous carbon materials, as they contain an isotropic pore structure and can be measured using the typical powder diffraction methods. Therefore, with rGO assemblies, an approach that considers both the disordered pore network and the layered, anisotropic structure must be applied. Since the rGO assemblies are not pure crystals, but contain a significant amount of disorder both along the rGO sheets and within the lamellar stacking direction, the structural features like corrugation and residual functional groups

along the *ab* plane are also expected to have an impact on the stacking structure in the *c*-direction where the majority of the pore network lies.

This section gives a brief account of the main structural features in layered and porous carbons, starting from the most basic level of a graphene sheet up to more complex porous carbon forms. It will be followed by an explanation of how these main features impact the properties of the bulk carbon material and then outline the best methods to measure and characterize these important structural features.

2.2.1.1 The graphene layer

The most basic level of the layered carbon structure is the individual graphene layer. As shown in Figure 23, the unit cell of graphene contains only two atoms (marked **A** and **B** in (A) and (C)) which are connected by a carbon-carbon bond a_{c-c} that is 0.142 nm in length. When these sheets stack to form graphite, the stacking perpendicular to the layer plane usually occurs in what is referred to Bernal stacking (ABAB alignment shown in (D), (E), and (F)) where the centre of a hexagon in one layer is followed by a corner carbon atom in the next layer. Thus, graphite with AB stacking is defined as a crystal with a unit cell containing four atoms, two from each adjoining graphene plane, and has lattice constants of $a=0.246$ nm and $c=0.670$ nm, where the inter-layer distance between two graphene sheets in graphite is 0.335 nm. The high symmetry points of the unit cell in reciprocal space are also shown in Figure 23. As for any hexagonal lattice system, the Brillouin zone (BZ) of graphene shows the Γ point is at the zone centre, M points are at the centre of each side, and K and K' are points on the corners (shown in (B), (G), and (H)).

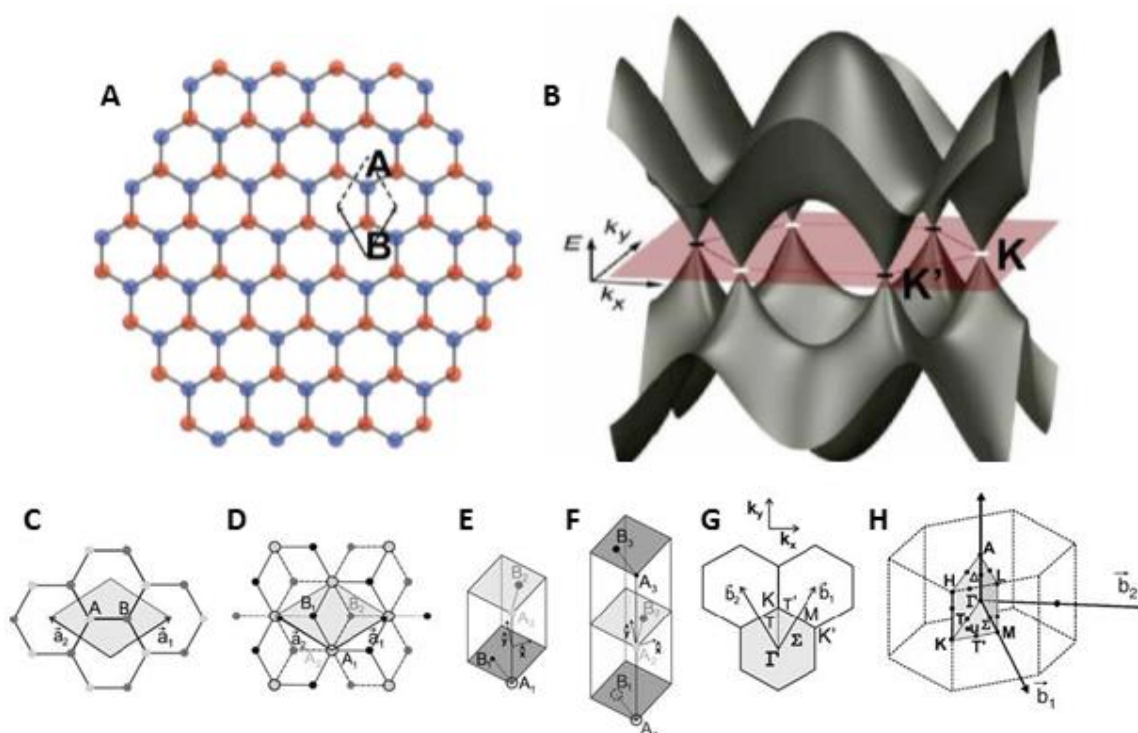


Figure 23. The unit cell (A) and band structure (B) of a sheet of pure graphene, followed by diagrams showing how the unit cell (C) stacks to form Bernal stacking in graphite (D, E, and F). The corresponding reciprocal space unit cell shows the BZ with high symmetry points and lines in pure graphene (G) alongside the BZ for 3D graphite (H), as described by Dresselhaus [53].

An understanding of the crystal structure of graphene is needed to assist with interpretation of the results from XRD and Raman spectroscopy. The main feature that should be noted is the highly anisotropic qualities of graphene, where the properties along the plane (described as the *ab* direction in Figure 23) are very different than those perpendicular to the graphene plane. The carbon-carbon

bonds making up the hexagonal lattice are extremely strong, while the van der Waals forces holding stacked sheets together is quite weak. Further, the thermal and electronic properties are highly directionally dependent. There are numerous reviews and reports on the unique properties of graphene and the specific features related to the 2D crystal structure and symmetry [1, 6, 53, 124, 125].

2.2.1.2 *Oriented lamellar carbons*

As the graphene layers stack to form bulk materials, the structure can range from the most crystalline state of graphite to a purely turbostratic assembly, with intermediate forms typically found in the wide variety of pyrocarbons. The main features of layered carbons relates to the order along the graphene plane (aromatic structure) as well as the degree of graphitization [46] between the layers. It has been shown with X-ray photoelectron spectroscopy that the electronic structure of rGO is similar to that of graphite [126]. The main features of these layered materials can be simplified, as there are only two main bond configurations, where the σ -bonds form covalent bonds between the hexagonal carbons along the sheet and the π -bonds lead to the forces holding adjacent sheets together as well as contributing the electrons that lead to graphene's extreme conductivity. It should be noted that the peculiar nature of electron transport in graphene is still under investigation, and while most published work will claim van der Waals forces are the cause for stacking in layered carbons, there is a growing body of evidence that this is actually a semi-metallic bond [127] and the affinity between graphene layers is a combined metallic and van der Waals type of bonding [128, 129]. Despite this, throughout the thesis, the restacking in rGO materials will be referred to as a result of van der Waals forces, since the electronic structure of rGO is not a main focus of the work and the more widely accepted van der Waals model can help to stabilize the discussion.

Pyrocarbons come in different forms, but highly oriented layered structures are common and the characterization methods have been well developed over many years [130-132]. The three main types of pyrocarbons are smooth laminar (SL), rough laminar (RL), and regenerative laminar (ReL) defined by the measured anisotropy and graphitizability. All of them contain some level of disorder, with crystalline lengths of only a few nanometres. While more disordered than graphite, many pyrocarbons retain a highly lamellar structure, and may serve as a good model for rGO assemblies in the dried state. As shown in Figure 24, the structure is clearly identified based on the combination of an atomistic model in (A) and (B) along with TEM images showing the alignment of graphene planes based on the dark fringes and corresponding mean orientation distance in (C) and (D) [49].

It is apparent there are differences along and between graphene layers depending on if the material is RL or ReL, and these differences are attributed to the amount of structural defects. The structure can be defined by the main physical features of clustered hexagonal aromatic domains connected by grain boundaries, inter-layer crosslinking (screw dislocations), and hydrogen saturated edges [31, 49, 111], all of which are expected to be present in rGO assemblies (plus the additional residual oxygen and nitrogen bonds). The texture is determined from the graphene layers, with RL materials having flatter, more extended fringes as well as more parallel stacking than that exhibited by ReL and SL. For all low-temperature pyrocarbons (below graphitization temperatures), the length of the aromatic domains along the graphene layers is quite short, with about 60% of fringes having a length of 0-1 nm, 30% at 1-2 nm, and the remaining 10% trails off exponentially with only a few layers measuring 5-7 nm being found in RL materials. Also, the typical stacking height, measured in the c-direction, is typically 1.5-2 nm which equates to about 5-6 stacked layers.

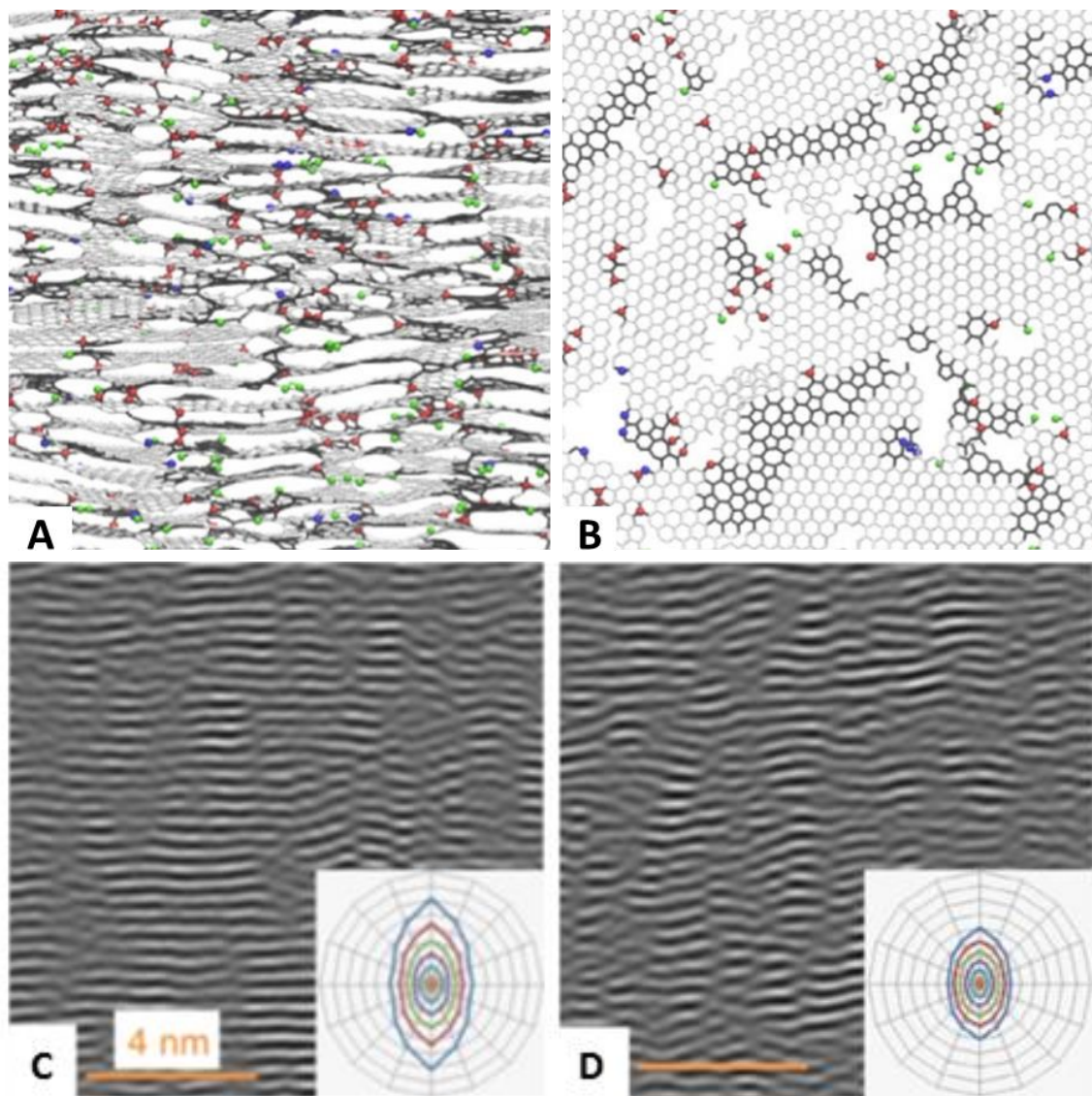


Figure 24. Atomistic model of a RL pyrocarbon looking through the edge (c-direction in A) and along the sheet (ab-plane in B) showing carbon vacancies and rips alongside hexagonal bonding in light grey and carbon defect bonds in black. The coloured spheres result from hydrogen bonding. TEM images of the stacking structure along the c-direction for RL (C) and ReL (D) pyrocarbons with insets depicting the degree of alignment between the layers measured as the mean orientation distance (MOD) [49].

The main features defining the layering within the carbon matrix can thus be defined by the simplified parameters shown in Figure 25. Measurements for the orientation angle, total graphene layer length, dimensions of the coherent domain, and the number of layers in the stack will be used throughout this text in order to characterize the layer structure of rGO assemblies.

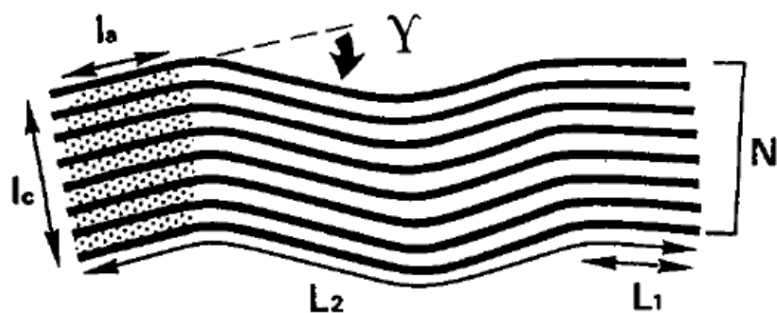


Figure 25. Schematic of a carbon cluster where the solid lines represent graphene layers with total length L_2 aligned along an orientation with tilt given by γ . The coherent domains are shown in the shaded zones with parameters L_a and L_c , with the latter equating the number of layers, N , making up the stack. L_1 is equivalent to L_a and defines the defect free portion of L_2 . Reprinted from [133].

2.2.1.3 Complex porous carbons

There are a countless number of different types of porous carbons, each with rather unique structures [28, 30-32, 134]. The main features that define a porous carbon relate to the purity (percentage of carbon compared to other elements, most often oxygen and hydrogen) and the physical structure of the carbon matrix and resulting pores. As depicted in Figure 26, porous carbons can have a particle-like structures with varied densities (A and B), rod-like carbon tubes or fibres (C), or larger graphene-sheets assembled into 3D clusters (D) with each material having very different surface area, density, and energy storage capacity [135]. There can be further structural evolution as these assemblies are heated, falling into the broad classes of hard carbon (non-graphitizable) and soft carbon (graphitizable), as mentioned in the Introduction.

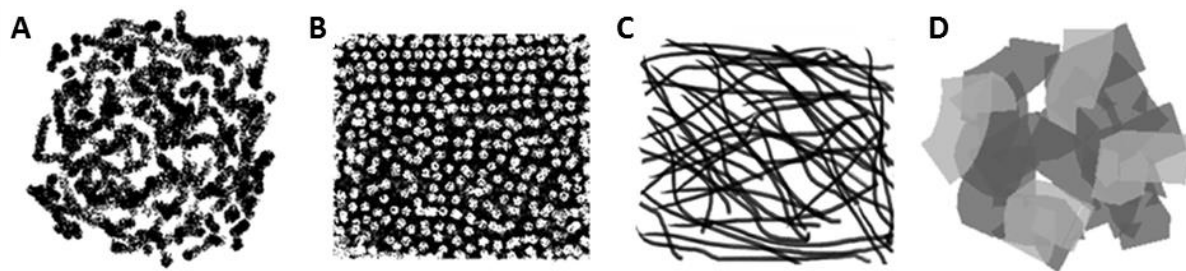


Figure 26. Schematic drawings of the differing internal structure of porous carbon materials used in energy storage devices. A comparison between carbon black (A), mesoporous carbon (B), carbon nanotubes (C), and graphene platelets (D) shows the main features of both the carbon matrix and resulting pore structure [135]

Dresselhaus is well known for her work on carbon fibres [30], and for a full and detailed account of many types of carbon materials, the reader is directed to her work. However, it is worth noting that that carbon fibres show many similarities to rGO assemblies, due to similar dimensions of the bulk assembly and mechanical properties as well as the complex physical structure created by the graphene layers making up the materials. While not a true layered carbon, carbon fibres do show a high degree of structural order, while also exhibiting some inhomogeneity within the fibre, as well as anisotropic features [28, 136], as shown in Figure 27. The basic structural unit of a carbon fibre is assumed to be a planar network of benzene rings forming graphene layers of various dimensions [30]. The defective graphene planes of varied size cluster together to form fibres with typical thickness around 7 μm , equal to that of dried rGO assemblies when filtered to have a surface density of 1 mg cm^{-2} . These graphene planes then form the complex, porous structures depicted below.

Similarities between the structure and properties of rGO assemblies and amorphous carbons have been reported, with both materials having a very similar aromatic domain size, sp^2 carbon content, and oxygen containing groups [137]. This thesis attempts to highlight this fact, as most of the current publication on rGO try to compare it with the work done on pure graphene even though it is probable that rGO bulk materials share more similarities with forms more akin to coal and carbon black. These other carbon forms are not as popular in current publications, but this work draws upon the vast history of solid science and discovery built over many years, especially in the field of activated carbon [32]. The complexity of these structures is highlighted here in order to put this work with rGO in context, as an extensive review of the various forms of porous carbons and how these features can best be measured by different experimental techniques was necessary to complete this work. The main aspect that makes rGO material differ from these other carbon forms is the wet processing conditions. Thus, the hydrogel assemblies are quite different than the porous carbon materials mentioned here.

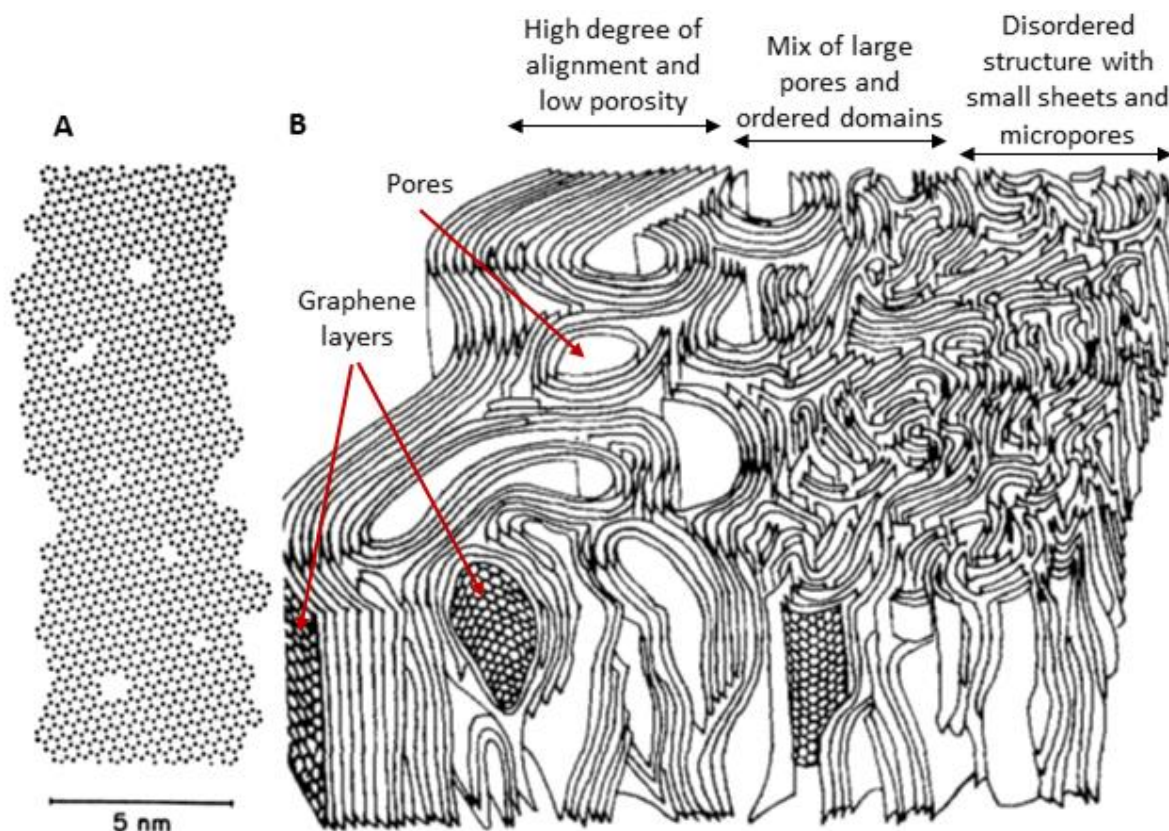


Figure 27. Sketch of a typical graphene plane in a carbon fibre (A) with aromatic domains and in-plane defects (by Fourdeux in 1971 but printed in [30]). Artist's conception of graphene layers within a porous fibre (B), showing the different types of order that may be present and how that impacts the internal pore network. These fibres typically have an outer layer of about 100 nm that is highly aligned with the structure becoming much more disordered in the core [138].

The main features defining the porous content within the carbon matrix can thus be defined by the overall porosity, accessible surface area, and structure of the pore network which includes the pore size distribution and individual pore sizes and shape. Porous materials are classified by the pore size, with the IUPAC standard notation being the widely accepted method for classification of porous carbon materials. Using these standards, microporous materials have pore diameters of less than 2 nm, mesoporous materials have pore diameters between 2 nm and 50 nm and macroporous materials have pore diameters of greater than 50 nm. In most cases, the material is composed of a range of pore sizes and complete description of the porous nature is based a number of combined factors including size, PSD, shape, alignment, surface roughness, and surface chemistry. The pore network can be described in different ways, but it is typically measured as a fractal dimension [28, 34, 139] which can correlate with the surface roughness, PSD, and overall tortuosity of the transport experienced by the species moving within the pores. Measurement that can somehow quantify these features are of importance in order to fully characterize the pore structure of rGO assemblies.

2.2.2 Structure-property relationships in porous carbons

As mentioned, the two basic features of a porous carbon are the carbon matrix itself and the porous surface area contained within this matrix. An account of what is understood about the chemical composition and sheet structure of rGO based on the current literature to date was given previously, so this section first addresses some relevant points about the stacking nature of the carbon and then focuses more specifically on the pores and pore network.

A good example of how the structural features of carbon impact performance can be obtained by comparing different types of carbon black. An important finding made by Bourrat [133] in his study comparing the structure of different carbon blacks to their accessible surface area and conductivity,

was that the layer length of the graphene sheet (L_2) in Figure 25 played a more influential role than the coherent domain lengths, L_a and L_c . By comparing the structural elements making up the carbon matrix, Bourrat was able to apply fundamental characterization methods to industrial carbon black samples in order to separate them into five distinct types of turbostratic carbon forms. Even though the coherent domain size was equal for carbons of different types, they exhibited marked differences in performance which were clearly related to the overall graphene layer length, L_2 , where longer layers could be directly correlated with higher specific surface area and decreased resistance. Further, these better performing carbons with longer layer lengths had less fractal surfaces, with a lower value for the mass-fractal dimension (a fractal dimension closer to two than three). Thus, both long and short range structures were equally important, with a longer layer being advantageous in both situations as the length improved conductance as well as more effectively “covering” the surface and imparting more porosity. Thus, while the coherence domains will translate as a measure of the overall defect density within the carbon, these features are not responsible for influencing the main aspects of performance in carbon blacks.

The two major applications for porous carbons, rGO in particular, are for in the fields of separation science and energy storage. The separation and transport of liquids, particularly water, is a current topic of interest for GO and rGO membranes as they have shown very unique properties with promising applications in this area [140, 141]. This is because of the nanoscale confinement between the sheets as well as chemical properties due to the functional groups. Simulation work has shown very interesting phenomena that support the theory linking water transport in nano-confined GO pores to an ice-like packing structure governed by the interlayer distance and initiated from highly hydrophilic environments [142]. Many types of carbon-based membranes display ultrafast permeation for selective liquids and gasses, all due to the combination of pore size and surface chemistry of the material. Thus, it should be possible to create a material tailored for whatever type of application desired, with rGO showing good potential in this area because of the low temperature, aqueous, scalable processing conditions.

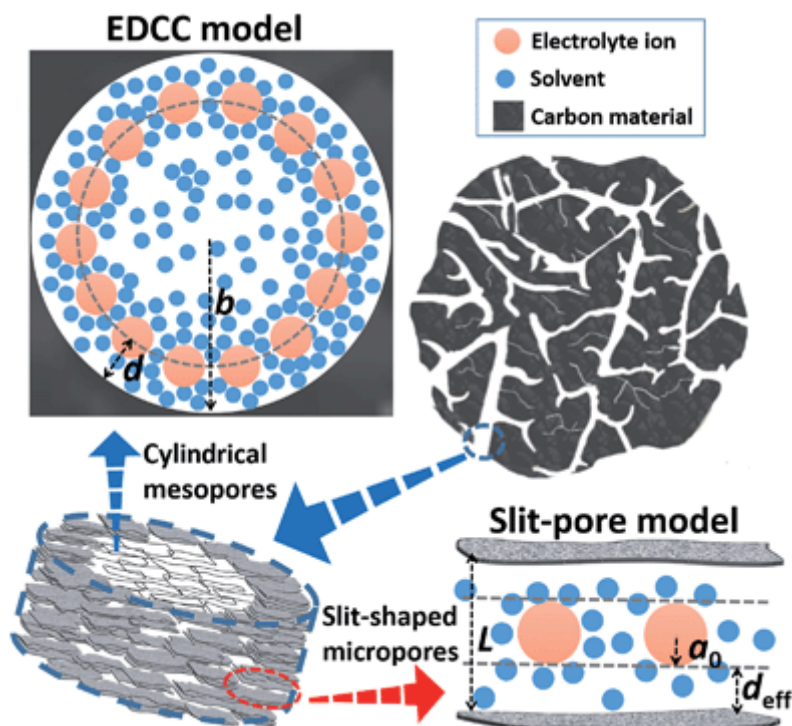


Figure 28. A structural schematic detailing the different pore structures in a typical porous carbon that has an overall stacked structure that is made up of particles with micro- and meso- pores. The main models used to describe capacitance are the electric double layer (EDLC) model, with ions adsorbing along the surface of the pore, and the slit/pore model, which acts like a parallel plate. Reproduced from [143].

The most reported topic for application of multilayer-graphene based assemblies is in the area of energy storage, with the most promising application being as the electrode material in supercapacitors [14, 37, 144]. In all capacitive materials, the size, geometry, and distribution of pores within the device will determine its performance; thus, the control and characterization of porosity is of the utmost importance [35]. A generalized schematic of the most fundamental aspects of the mechanism behind electrolytic capacitance within the carbon pores is shown in Figure 28. In order to improve the performance of supercapacitors, it is necessary to have the highest power density possible which can only be achieved when the electrolyte has fast access to the surface of the electrode material. Thus, the power density is determined by the material's physical structure and can be improved by increasing the accessible surface area, but there is a trade-off when additional resistance is encountered within very narrow pores [145]. Thus, while a microporous assembly will have the greatest surface area per unit volume, the ions may not be able to access these surfaces quickly, thus decreasing the power and supercapacitor performance. This relationship is not trivial, as there is not a simple linear correlation between surface area and capacitance. In practice, there is an optimal micropore size that correlates with a specific electrolyte system within a given voltage window [41]. Furthermore, the uniformity of the pore sizes, pore geometry, as well as the way the pores are interconnected has a large impact on capacitor performance [41, 146, 147]. There have been many strategies employed to control both pore size and hierarchical pore architecture in carbon materials, as well as a large amount of modelling and simulation work directed toward understanding ion storage in nano-porous carbon materials [40, 42]. An example of more complex models to probe the longer-range mechanisms in porous carbon capacitors is shown in Figure 29, where the overall pore network, and resulting flow within it, becomes much more disordered than that compared with individual pores.

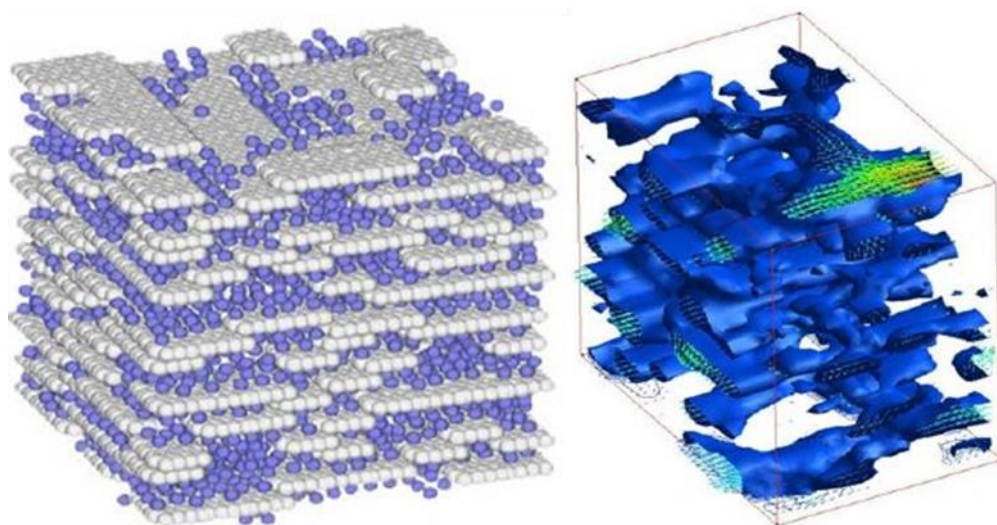


Figure 29. Advanced computer models by Biggs et al. [148] showcase the complex relationship between carbon structures and the molecular adsorbates within them [148]. Adsorption was simulated by the cavity biased grand canonical Monte Carlo (GCMC) method of Mezei [149] where chemical potential, temperature, and volume are constants. The solid carbon structure was based on the models developed by Oberlin et al. [150-156].

Since the development of new or improved energy storage materials is such an important area of research, it follows that investigation into the processes governing ion transport would be of much interest. The recent discoveries showing capacitance increase in carbon materials with hydrophilic surface groups, specific PSD features, and pores of less than 1 nm in size have refocused research efforts toward understanding ion confinement in nanopores. Recent studies have shown that long held theories about the nature of ions in electrolytic capacitors don't hold true at the nanoscale [36]. Normalized capacitance will decrease with pore size until a critical value of approximately 1 nm is reached, and even though the size of the solvated ion is larger than the pore, experimental results

confirm pores smaller than 1 nm greatly enhance the double layer charge storage [157]. Results also show that the maximum capacitance is obtained when the ion size matches the carbon pore size, which again challenged the traditional understanding on the physics of capacitance, as only one ion could fit into a pore of this size, making it impossible to have ions adsorbed on both pore walls, which has always been the traditional description of electric double layer capacitor materials [146].

In general, the results from more traditional activated carbons and coals show that the capacitance is not directly related to the BET specific surface area. A thorough review by Frackowiak [158] outlines the main features that can be used to form an ideal supercapacitor. Firstly, the carbon must be tailored to fit the specific ionic radii used in the electrolyte. Further, having a smaller pore size at the positive electrode compared to that at the negative one will enhance capacitance and decrease resistance. A wider PSD in the micropore range yields a higher capacitance overall, and the presence of pores less than 0.7 nm will enhance the specific capacitance when small ionic species are used. Thus, an adequate pore size is more important than high surface area, as the additional porosity is useless if it cannot be adequately accessed. Along with the micropores, there needs to be an adequate distribution of mesopores to allow for rapid transport of the ions through the pore network. It was found an optimal proportion of mesopores is between 20-50%. As mentioned previously, the role of the carbon matrix must also be considered, as the conductivity of the carbon can strongly limit the capacitor performance. Further, the presence of oxygen functional groups can be advantageous as they can contribute to pseudocapacitance and/or wettability. Thus, an optimal structure has: i) a high surface area of ultramicropores (usually less than 1 nm) that fit to the size of the ions in the electrolyte; ii) a well-balanced micro-/mesopore ratio to reduce internal resistance; iii) the carbon structure encasing this network is highly conductive; iv) the carbon surface can be further enhanced with oxygen functional groups if applicable. Based on this, it is clear that the chemistry and processing conditions of rGO offer unique opportunities to build highly tailored supercapacitor electrode materials that can yield high performance.

2.2.3 *In situ* investigation into ion transport in porous carbons

Ideally, experiments that were able to track the physical progressions that take place inside the carbon pores while the separation and/or energy storage process was carried out would be able to provide the best insight into the fundamental principles driving the unique performance in specific porous carbons. Since it is possible to control so many aspects of rGO materials (either along the sheet through controlling the surface chemistry or attaching polymer functionalities, or in the bulk by controlling the packing density and pore size), these assemblies also offer opportunities to use them for research into the more fundamental aspects of transport in nano-confinement.

While different options for *in situ* characterization of these rGO assemblies are possible, by far the most comprehensive approach is with small angle scattering of X-rays (SAXS) or neutrons (SANS) [159-161]. The details of these techniques is discussed in the next section, but some of the most recent work in the field will be discussed briefly here. In the final chapter of this thesis, future work is outlined for applying these methods to rGO materials, with initial experimental results showing the viability of investigating ion transport in rGO using *in situ* SANS and SAXS. Two of the more recent works that will be highlighted briefly are by Milner et al. on graphene platelets in solution [162] and Prehal et al. on bulk porous carbon electrodes [163], as shown in Figure 30. As shown in the structural diagram and corresponding reduced scattering curve in part (A) of the figure along with the changes in scattering intensity as the voltage is ramped, it is possible to both probe the nature of graphene sheets and the ion transport within the pores while changing the environmental conditions influencing the structural behaviour. These methods offer a plethora of opportunities to study both the rGO assemblies and the gasses or liquids interacting within the pore network. It is noted that there has been significant other

work published in the field, with some examples being the development of pores in activated carbons [164] and the structure of ionic liquids inside carbon micropores [165, 166].

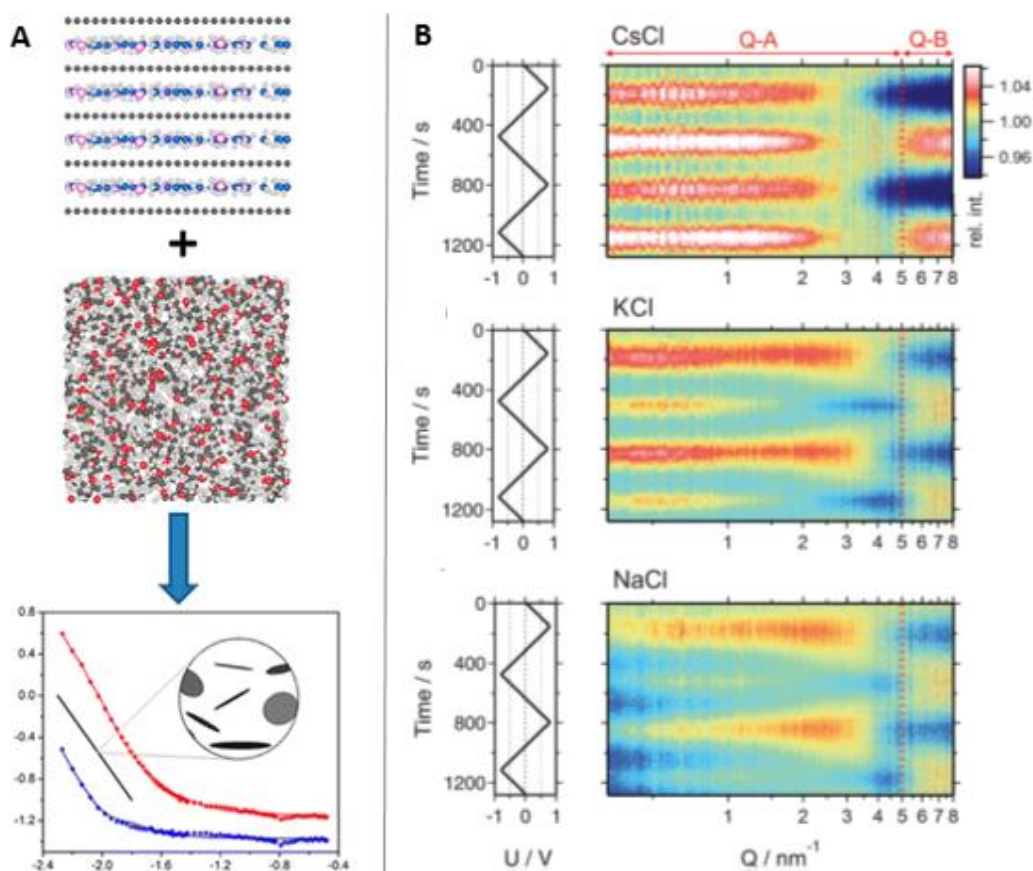


Figure 30. Depiction of the main features of a graphene sheet in solution (A), considering that the edge geometry (top) and through-plane surface combine to have a disk-like structure which would yield the slope of -2 seen in the SANS profile. *In situ* SAXS investigating the structure of ions in microporous carbon (B), showing the changes in scattering intensity for the three different electrolytes as the voltage is changed to draw anions/cations into the pores. Reproduced from [162] and [163].

2.3 Structural Characterization of Ordered Carbons

2.3.1 Short history of the investigation into carbon microstructure

The study of the structure of carbons, especially graphite and related layered assemblies, has a long and rich history. Warren was the first to show the existence of single graphene layers in non-crystalline carbon in 1934 and went on to fully characterized the rotational and translational disorder in 1941 [167]. He demonstrated that a disordered structure leads to the absence of (hkl) reflections and instead consists of the two separate features: (hk) -reflections along the 2D graphene sheet and $(00l)$ -reflections from the inter-sheet stacking of the layers. Franklin then expanded on this model and in 1951, showed that there was non-crystalline carbon bonded to the edges of graphene layers that could act as a cross-linker between graphene sheets, and the specific features of this disorder and crosslinking would determine how graphitizable a given carbon would be [46, 168]. The results of Warren and Franklin showed there were no 3D graphite crystals present in these disordered carbons, but unfortunately, the term “crystallite” is often inaccurately applied throughout the literature. In this work, this important distinction is taken into account, and instead use the terms coherent domain, graphene-layer clusters, or restacked regions to define the presence of more ordered, turbostratic parallel-layer groups [169]. IUPAC also recognizes these distinctions clearly, terming “non-graphitic”

carbons materials that have long range 2D crystal order along the graphene layers (hk), but no measurable order in a third direction other than the nearly parallel layered stacking, further applying Warren's nomenclature of "turbostratic" stacking. Another important distinction is to that of "amorphous carbon", a term that is also often incorrectly applied, where the material does not have any long-range crystallinity in any direction.

The theory and methods gained from Warren and Franklin's work are given in the following section, as X-ray diffraction and wide angle scattering were the most widely used tools to characterize the structure of carbons at that time. The extensive work of Warren on carbon blacks [169] has been greatly expanded by combining XRD with other techniques. Over the past fifty years, other experimental methods have been developed to deal specifically with the carbon microstructure, most notably TEM and Raman spectroscopy, with Dresselhaus providing detailed insight on Raman spectroscopy for carbon fibres [30], nanotubes [134], and more recently graphene [125]. Ferrari has also made significant contributions advancing the understanding of Raman spectroscopy in more disordered carbons, developing methods to characterize specific types of bonding and disorder in graphitic, diamond, and amorphous materials [170, 171].

Advances in the characterization of pyrocarbons have been largely attributed to Bourrat [31]. He has shown that using a measure of anisotropy and coherent domain length found using diffraction methods was not sufficient to truly differentiate between similar layered carbon materials [130]. Bourrat combined anisotropy with the total sheet length and fringe lengths as measured by TEM with the size of coherent clusters measured by XRD and overall disorder measured with Raman. This gave a more complete story, which could also tie structure to the measured material properties. The ReL pyrocarbons showed fringes with many short corrugation distortions while the RL had fringes that were very flat and extended. Further, the SL pyrocarbons had fringes with much more pronounced corrugation and curvatures. Raman spectroscopy was able to differentiate this ordering even more clearly, with the broadening of the D-band (described in detail in Chapter 5) able to give the best estimate for the amount of structural defects. This combination of anisotropy, measured by the orientation angle and density of defects identified with Raman was able to effectively classify different samples as RL, ReL, or SL. Since rGO assemblies share many structural features with these layered carbons, it is desirable to apply the same techniques. However, because rGO assemblies are very thin and flexible, the microtoming and polishing necessary to measure anisotropy with polarized light microscopy or create high quality TEM specimens is not possible. That is one reason why slight adaptations and different methods have been used in the present work.

2.3.2 Wide angle scattering of ordered lamellar carbons

2.3.2.1 Basic diffraction and scattering concepts

Diffraction has long been the most widely utilized technique for the characterization of ordered domains and defects in many carbon materials and is described in detail within many textbooks. Only a brief overview is provided here in order to understand the main experimental implications for rGO assemblies. Considering a monochromatic source with wavelength, λ (photons, electrons, and neutrons are used in this work, but the diffraction principle is the same), the wave-vector in a given unit vector direction can be defined for the incident wave as:

$$\mathbf{k}_0 = \frac{2\pi\hat{\mathbf{k}}_0}{\lambda} \quad 2.1$$

Whilst the scattered wave it is defined as:

$$\mathbf{k}_s = \frac{2\pi\hat{\mathbf{k}}_s}{\lambda} \quad 2.2$$

Diffraction occurs when the relationship below is satisfied:

$$\Delta k \equiv |k_s - k_0| = q \quad 2.3$$

where Δk is the change in wave vector that occurs during the scattering event and q is any reciprocal lattice vector, typically denoted as the (hkl) lattice points. The dimension of q is given in inverse length (typically \AA^{-1} or nm^{-1}), and the scattering pattern is described as the structure in reciprocal space while the particles making up the massive object have structure in real space, measured in units of length.

As the scattered waves will interact through constructive or destructive interference, the resulting scattered intensity will fluctuate. Thus, the measured coherent scattering is given by the intensity, I , defined broadly as:

$$I \propto P(q)S(q) \quad 2.4$$

where $P(q)$ is the typically referred to as the form factor and results from the scattering of a given particle, which can be made up of many atoms. The scattering pattern oscillates in a particular fashion which is related to the characteristic shape (hence the name *form* factor) of the particle, which could be a sphere, rod, cylinder, etc. The term $S(q)$ is typically referred to as the structure factor, defined as the sum over the n atoms in the unit cell:

$$S(q) = \sum_{j=1}^n e^{iq \cdot r_j} \quad 2.5$$

where r_j gives the vector coordinates in the unit cell. The structure factor corresponds to the Fourier transform of the scattering density within the real space structure. Thus, the structure factor contains information about the position of the atoms within the particles, and will also apply to densely packed systems when the distances between individual particles is of the same order of magnitude as the atomic distances within the particles. This relationship becomes evident in small angle scattering where a decrease in intensity is typical of repulsive particles and an increased intensity suggests attractive interactions, like that of aggregation.

The relation described here holds for scattering at both small and wide angles, typically referred to as scattering and diffraction, respectively.

2.3.2.2 Diffraction theory in graphite and turbostratic carbon powders

The crystal structure and resulting diffraction planes from an individual graphene layer is shown in Figure 31. The real space carbon-carbon bond length in the hexagonal structure is 0.142 nm and the resulting diffraction planes within the ab -plane are indicated as d_1 and d_2 , which form the (hk) diffraction spots. In graphite, each adjacent layer will build up along the c -plane in specified ABAB or ABCA stacking order to result in a 3D (hkl) lattice. As an infinite crystal with all atoms in periodic positions, the Fourier transform of the scattering density (electron density with X-ray and electron beams or nuclei with neutron beam) would consist of a specific set of points with the placement of graphitic (hkl) spots shown in Figure 32(A). Comparatively, if the graphene layers are stacked with a random rotation of the sheets, as in turbostratic carbons, the randomly rotated (hk) lattice positions will result in rods instead of spots in (hk) , while more diffuse spots will show the alignment of the expanded layer spacing in $(00l)$, as shown in Figure 32(B). Another factor to consider with turbostratic layering is that the lattice cell constant in the c -direction for ABAB graphite of 0.670 nm (twice the interlayer spacing of 0.335 nm) is no longer applicable. It should be clearly recognized that the

interlayer separation distance in turbostratic carbon does not represent a lattice constant, only a representation of the average physical distance separating the graphene planes within the coherent cluster.

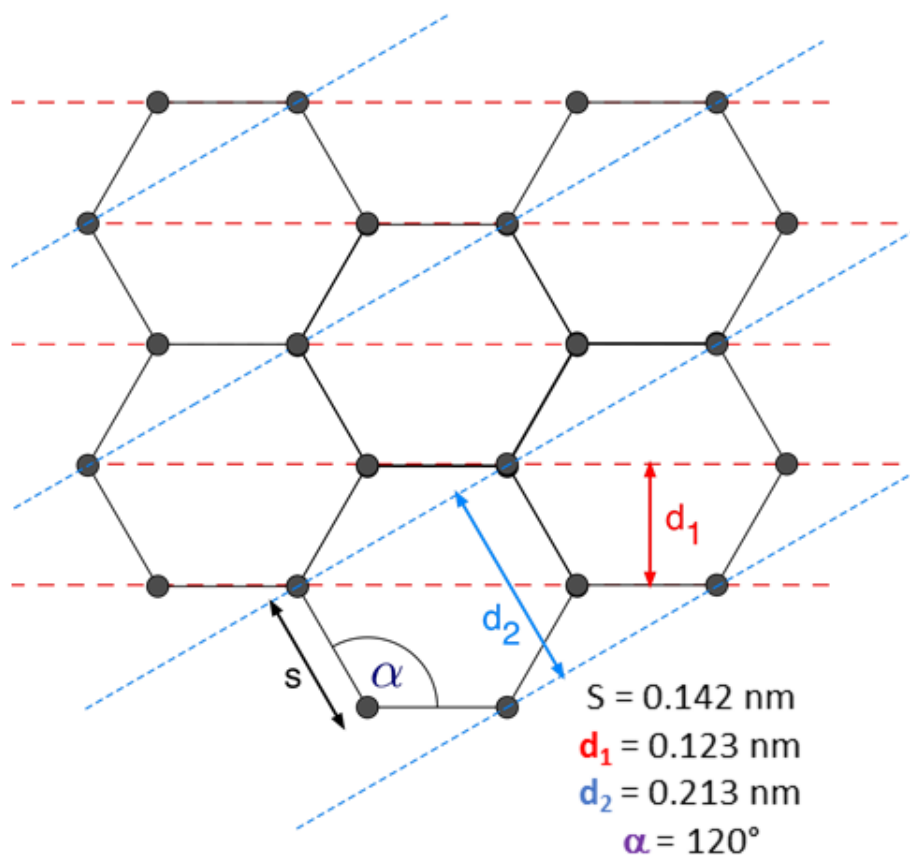


Figure 31. Hexagonal crystal structure of graphene layers, showing the corresponding bond length, S , and diffraction planes, d_1 and d_2 .

Application of XRD or WAXS traditionally covers the length scale of atomic crystals, ranging from the smallest atomic spacing up to about 1 nm depending on the wavelength of the incident beam and experimental configuration. Usually, the technique used to identify Bragg peaks [172] associated with the atomic crystal configuration is referred to as XRD, while WAXS is a more general term that differentiates itself from SAXS in that it extends to wider angles, identifying features of smaller size, including that of Bragg peaks. In a typical polycrystalline powder diffraction experiment, it is assumed all crystals are distributed randomly, so the resulting diffraction pattern is dispersed across all possible directions, resulting in rotationally averaged, smooth rings with radial distance equal to that of the (hkl) spots. The measured angle between the incident wave vector and the resulting coherently scattered intensity ring is referred to as the scattering angle. The Bragg equation has long been used to correlate the angle of diffraction (θ_{hkl}) from crystal planes with a real-space periodicity (d_{abc}) through:

$$\lambda = 2d_{abc}\sin(\theta_{hkl}) \quad 2.6$$

for each of the crystal diffraction planes. These intensity fluctuations can be collected using a point detector in the traditional Bragg-Brentano geometry, or all diffraction spots and rings can be visualized together using a 2D plate-type detector. In either case, the resulting radial averaged scattering profile for a powder sample is like that shown in Figure 32(C), with contributions from: i) I_{inter} , the inter-sheet spacing (002) and (004); ii) I_{intra} , the intra-sheet 2D crystallinity (10) and (11); iii) I_{incoh} , the background from incoherent and elastic scattering from unorganized atoms (carbon defects or impurities); and iv)

instrumental background or broadening effects due to experimental conditions (can easily be measured and subtracted in most cases).

For more disordered and oxygen containing carbons, the contribution to the background incoherent intensity can be significant, and this can be used to evaluate the amorphous nature of rGO materials. Franklin [173] and Ergun [174], showed that the intensity contribution from amorphous carbon is relatively constant over the whole scattering range which is very useful as it can be easily subtracted from the coherent intensity and also be used to directly measure the fraction of amorphous carbon present. Computational methods to calculate the amorphous fraction as well as other parameters contributing to the peak broadening described below are detailed in [108, 175, 176], but the description here is limited to the more generalized considerations.

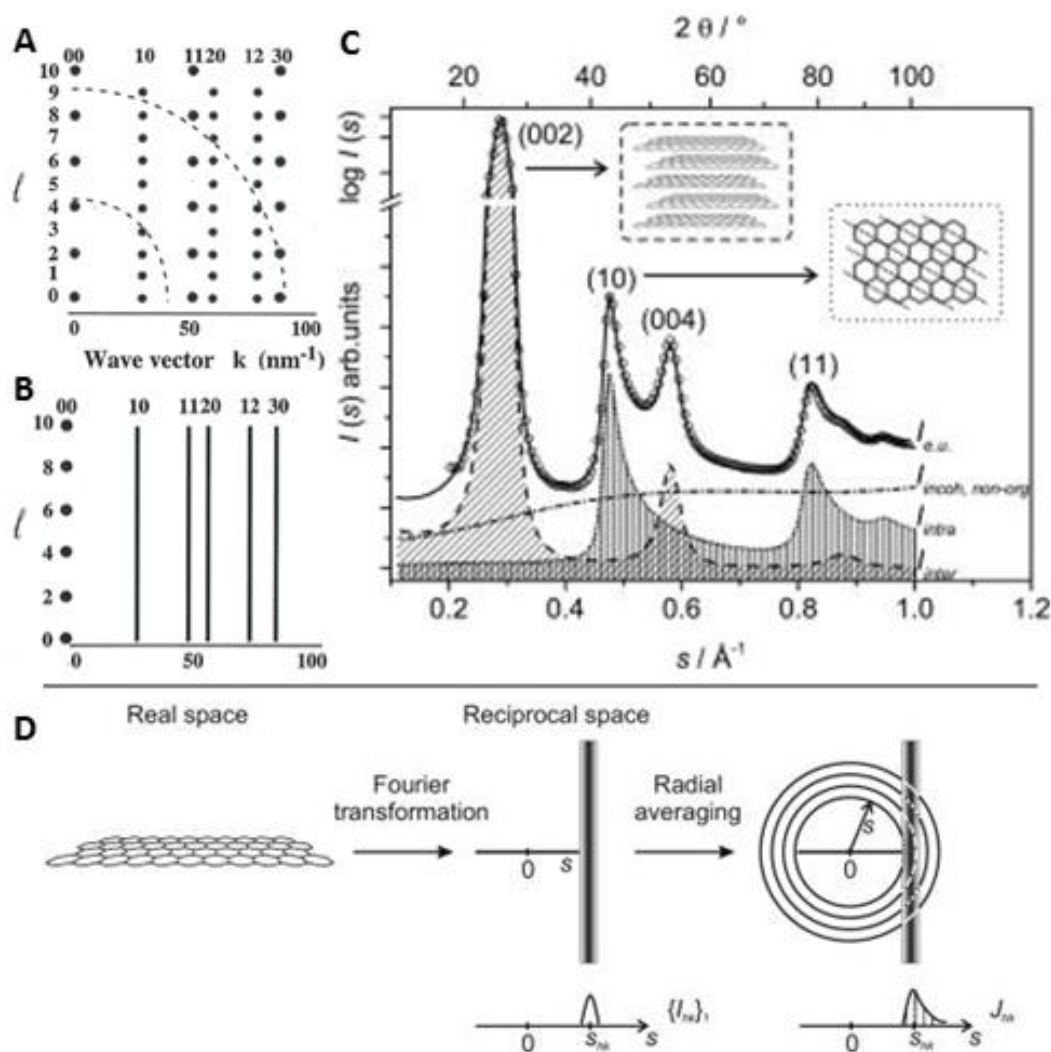


Figure 32. Interference peaks in the reciprocal lattice of graphite (A) with the size of the spots representing intensities and the dashed arcs show the volume of reciprocal space available to $\text{CuK}\alpha$ and $\text{MoK}\alpha$ radiation. Comparatively, interference maxima for turbostratic carbon (B) shows spots for the (00l) reflections and lines for (hk). Typical radially averaged powder diffraction pattern from a turbostratic carbon (C) showing independent contributions from I_{inter} , I_{intra} , and I_{incoh} along with a description of asymmetric broadening of the (hk) contribution (D). Reproduced from [177] and [176].

Peak asymmetry is an important consideration when fitting peak profiles, and as a result of the radial averaging, there is a high degree of broadening toward low-angles, as shown in Figure 32(D). These are particularly pronounced in layered materials like graphite and porous carbons resulting from the additional asymmetry caused by the two dimensionality of the (hk) crystals. The two dimensional nature of the (hk) reflection in relation to the instrumental geometry and radial averaging, results in

asymmetric (10) and (11) peaks that are also shifted slightly toward larger angles, as shown by Biscoe and Warren [169]. The magnitude of the shift in diffraction angle is given by:

$$\Delta(\sin\theta) = \frac{0.16\lambda}{L_a} \quad 2.7$$

This displacement is related to the wavelength of the incident beam, and for this work, is not relevant based on the methods employed. For example, considering results from typical Cu K α X-ray diffraction measurements, the shift equates to about 0.7°, but the hk reflections analysed here only appear in higher energy X-ray (8keV or above) and electron diffraction patterns, so this displacement effect has been ignored.

2.3.2.3 Causes of line broadening

Diffraction from a perfect infinite crystal is close to that of a Dirac delta function (infinite line without any width), but in fact yields Bragg peaks with extremely narrow widths, as determined by Darwin [178]. However, in reality the experimental data contains much wider peaks, with the instrument and sample both contributing to line broadening. Therefore, to determine the specific microstructural parameters of the sample itself, the physically broadened profile must be analysed independently from the total observed intensity profile. First, an empty background measurement is taken to subtract any intensity not related to the sample itself, and is usually a fairly straightforward procedure. Next, instrumental broadening can be measured using a standard crystal sample (traditionally quartz). Each instrumental profile is distinct, but will depend most on wavelength distributions and geometrical aberrations. For materials with rather pronounced peaks, distinguishing the exact contribution from instrumental broadening is paramount. However, in more disordered materials that have characteristically broad peaks, as in rGO assemblies, the instrumental broadening contribution is irrelevant and can often be ignored when using modern instrumentation. This is the case with the rGO assemblies, and instrumental broadening does not need to be considered unless otherwise specified in the text.

Thus, the broadening features in rGO assemblies are useful because they contain detailed information on important parameters of the coherent domains. Because the broadening of diffraction peaks can be directly related to structural features within the material itself when instrumental and geometric factors are minimized and/or accounted for. More specifically, the FWHM or integral breadth can be used to measure both crystallite size and microstrain in disordered materials. Scherrer first used this method of relating diffraction peak broadening to very small coherent regions (sub-micron crystallites) in 1918 and it has been expanded on ever since [179]. The basic form of the Scherrer equation can be written as:

$$\beta(2\theta) = \frac{K\lambda}{L_{(2\theta)}\cos\theta} \quad 2.8$$

where $\beta(2\theta)$ is the line broadening (in radians) for a given Bragg peak at 2θ after subtracting the instrumental broadening, K is a dimensionless constant that is dependent on the shape of the crystal, λ is the wavelength of the incident beam, $L_{(2\theta)}$ is the average size of the coherent domain along the given axis associated with that Bragg peak, and θ is the Bragg angle for the given peak. The Scherrer constant, K , is dependent on the shape of the crystal, and Warren [167] established the need for two distinct constants in random layer lattices (as are turbostratic graphitic materials) because (hk) is effectively an independent, two dimensional particle, as discussed in detail in the previous section. Thus, the coherence lengths along the ab- or c-directions (see Figure 25 for diagram of these

dimensions where intra-sheet L_a is for (hk) and inter-sheet L_c is for $(00l)$ reflections) are found independently with:

$$L_a = \frac{1.84\lambda}{\beta(2\theta)_{(hk)}\cos\theta} \quad \text{or} \quad L_c = \frac{0.89\lambda}{\beta(2\theta)_{(00l)}\cos\theta} \quad 2.9$$

This serves as a lower limit for the size of coherent domains because there are many other factors that can contribute to line broadening in turbostratic carbons, such as impurities. It is clear the Scherrer equation relates peak broadening to both the size of the coherent domain as well as the Bragg angle, and it is important to note that broadening resulting from small crystallite size is independent from the reflection order. Thus, knowing the length of the coherent domain does not change, any difference in broadening seen between peaks of different order must be attributed to other factors – most notably microstrain.

Small crystallites can divide into smaller incoherently scattering domains as a result of dislocations which also produce strains within the coherent domains. Unlike size broadening, strain broadening is angle dependent and the two causes can thus be distinguished. Stokes and Wilson [180] defined the *apparent strain* for the distribution of tensile strains perpendicular to the reflecting planes as:

$$\eta = \beta(2\theta)\cot\theta \quad 2.10$$

The measurement of the strain using this equation is dependent on the direction of the coherent domain making up the broadening of the given peak, so shape effects need to be considered for carbon materials with a high degree of alignment in the planes (not power distribution of reflections) and independent $(00l)$ and (hk) reflections.

There are two basic approaches to the quantitative analysis of diffraction broadening [181]. The first, and most rigorous, is to apply the Stokes deconvolution method combined with the Warren and Averbach analysis. The alternative approach is to apply simplified integral-breadth methods which are much easier to use and adequate to obtain the necessary parameters in most cases. The integral-breadth methods are used in this work, and Voigt-type profiles (combination of Gaussian and Cauchy-Lorentz) are applied to represent the function as contributions from size and strain influence the peak shape in different ways. Voigt functions have been applied to measure size and strain contributions to broadening [182] to yield the volume-weighted domain size and upper limit of strain, which is more than adequate for non-crystalline materials such as rGO assemblies where there is such a large size dispersity and high degree of disorder.

2.3.2.4 Geometric considerations for layered turbostratic thin films

The earliest work using diffraction to characterize the structure of carbons considered only powder patterns from randomly oriented small crystals. In 1941, White and Germer [183] were the first to analyse electron diffraction patterns from turbostratic carbon samples with a marked degree of preferential orientation (this work was later expanded on by Ruland et al. using oriented carbon fibres [184]). They tested over 100 different carbon films in both transmission and reflection orientations to look at the rotation patterns (rocking-curve) from single “crystals” (actually turbostratic structures with (hk) graphene planes all aligned in ab -plane and stacked with rotational faults in the c -plane). The results are shown in Figure 33, along with a schematic that details how the diffraction bands and spots are shifted as the sample orientation is changed.

In transmission geometry where the graphene layers are arranged directly perpendicular to the incoming beam, the high degree of alignment of the (002) and corresponding higher order reflections results in infinite spots that cannot be seen in the resulting diffraction pattern. Thus, the two rings

seen in Figure 33(A) are solely due to the randomly rotated (hk) reflections. As the sample is rotated, contributions from both the (hk) 2D crystals and highly oriented ($00l$) inter-sheet spacing are seen on the detector plate, with the (hk) arcs becoming significantly broadened with a fan-like shape. This broadening is depicted in the contour diagram calculated by White and Germer [183]. Contributions from specific lattice parameters can thus be evaluated independently depending on the geometry of the experimental set-up. In reflectance geometry where the graphene layers are arranged roughly parallel to the incoming beam, as in the edge-on geometry that will be used in this work evaluating rGO assemblies, there is a clear distinction between the (hk) and ($00l$) features as well as information about the overall alignment of the planes.

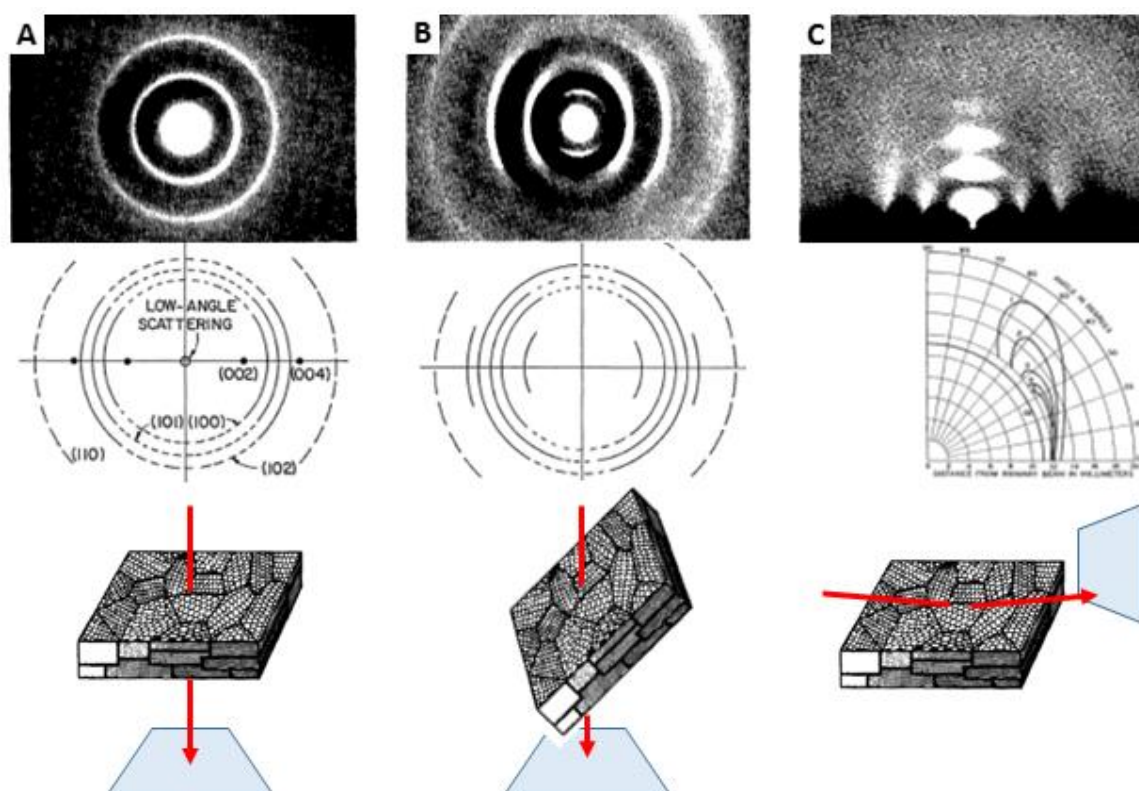


Figure 33. Transmission (A and B) and reflection (C) orientations for a turbostratic carbon with all graphene layers oriented along one plane. In (A), the reflections along the c -axis are not visible in the diffraction pattern, but they appear as the sample is rotated (45° rotation in (B)). Reflection geometry through the c -plane reveals both the ($00l$) and (hk) intensities separately, with the (hk) reflection exhibiting a broadened, fan-like shape shown in the contour diagram. Reproduced from [183].

This shows there are geometric distinctions that must be made between analysing the diffraction and scattering pattern of a polycrystalline powder sample (random lattice orientations in all directions) compared to that of a bulk layered turbostratic carbon (separation of the two distinct ab - and c -planes). The smearing of the (hk) intensity lines in an oriented film can be more easily accounted for using a 2D detector and measuring an intensity profile only over specific regions (azimuthal intensity). Reasons for this are shown more clearly in Figure 34. Here, the distinct ($00l$) spots run up the centre (shown as c^*) and the randomly oriented (hk) spots forming the rings within the ab -plane (shown as a^* and b^*). Placing a 2D plate-like detector centred at the origin makes it possible to measure the vertical ($00l$) and horizontal (01) and (11) scattering angles independently and without the need for radial averaging.

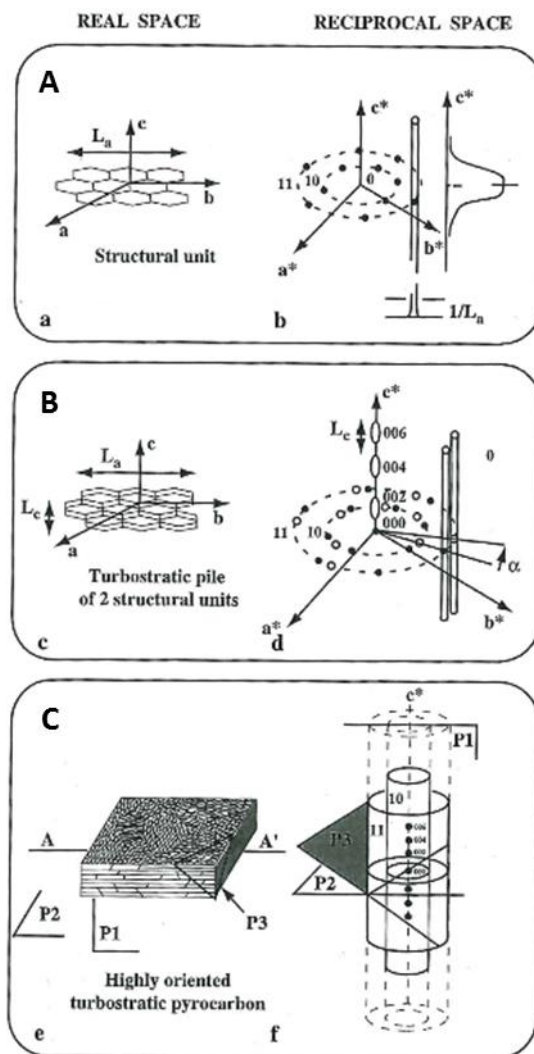


Figure 34. Real space structure of graphene layers in turbostratic carbons along with the resulting reciprocal space features detected in diffraction measurements. One layer has crystalline spots in the a^*b^* plane (A) while a turbostratic pole results in a series of rods and additional spots in c^* (B). A full turbostratic assembly has randomly rotated graphene layers in all directions, creating rings in a^*b^* and pronounced peaks along c^* (C). Reproduced from [31].

Experimental examples of this can be clearly seen in work done on carbon fibres that have more or less ordering of the graphene layers. Figure 35 shows the progression of structural order in an ex-PAN fibre prepared under different conditions [30]. The diffraction pattern in (A) is most disordered and the level of alignment increases in (B) and (C) until the structure of (D) clearly reveals graphitic, 3D crystals are present in the material. The alignment is characterized by measuring the intensity spread across the (002) peaks at a set distance from the beam centre, known as an azimuthal intensity spread. The overall broadening of the azimuthal intensity of the (002) peak feature is used to characterize the orientation of graphene planes within the material, where the FWHM value equates to the widely applied structural parameter, orientation angle (OA). Thus, carbon materials with sharper (002) peaks have a smaller orientation angle which correlates with a higher level of alignment between graphene planes. The OA is sometimes referred to as *misorientation* angle in order to be more representative of the actual structure, but OA is used throughout this thesis and is defined by the geometric considerations discussed here and in the following section.

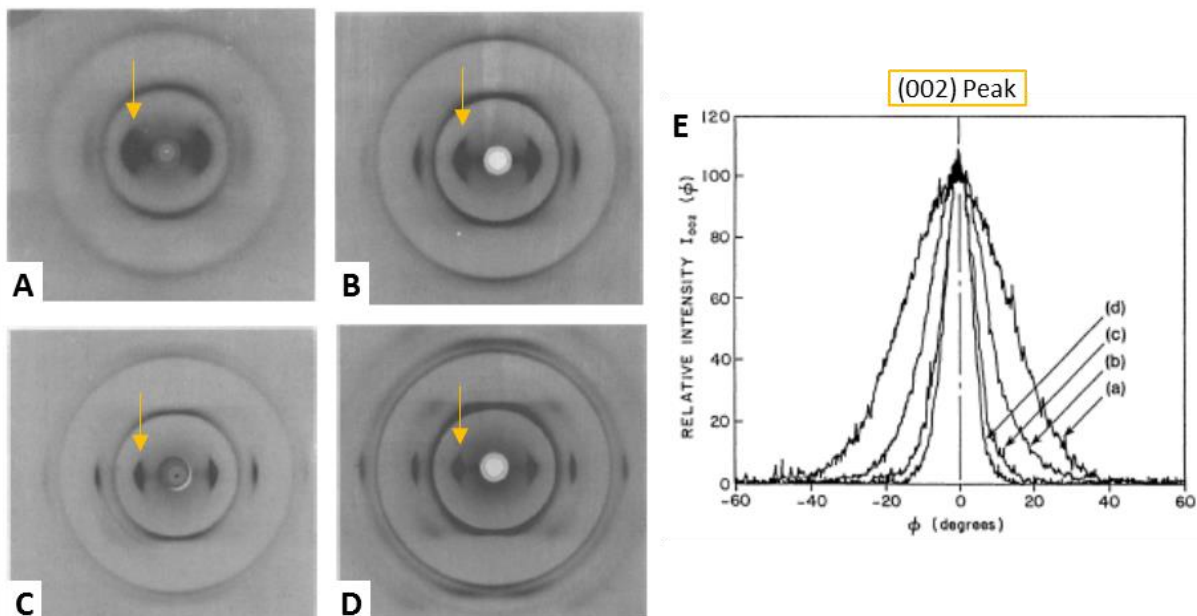


Figure 35. X-ray diffraction patterns of ex-PAN fibres exhibiting different levels of alignment of the graphene layers, where the most disordered turbostratic structure is seen in (A) and the microstructure becomes progressively more ordered until the partially graphitized form is shown in (D). The overall alignment of the graphene layers can be measured with the azimuthal intensity spread across the (002) peaks marked with arrows, and the result is shown in (E) where more aligned planes produce pronounced peaks and diffuse peaks have a broadened profile characterised by the FWHM which is used to define the orientation angle. Reproduced from [30].

2.3.2.5 Geometric considerations for porous assemblies

The technicalities discussed above can also be applied to the slightly larger structural units within these layered carbons. These larger structures will scatter at smaller angles where the pores and coherent domains within the carbon layers also form a somewhat periodic structure that will cause constructive and destructive interference. These features are clearly seen in work done on carbon fibres, which provide good reference materials when analysing rGO assemblies. As shown in Figure 36, the structure of individual pores within these layered materials has discrete dimensions in the a-, b-, and c-directions. The pores, along with the carbon matrix consisting of turbostratic clusters, are aligned with a particular orientation, here depicted as ϕ , along the fibre length. This angle is also referred to as either the orientation angle (OA) [131] or misorientation angle [30], with this thesis using the term OA. The overall size and orientation of these structural features in all directions can be measured by varying the graphene plane alignment with respect to the incoming beam where there will be a polar distribution of the (002) spots in reciprocal space. All of these structural features combine to form the overall bulk assembly, which includes both the carbon matrix and larger pore network. Building on the understanding of how these small features combine to form a complex bulk material, leads to the next section where a more complete discussion on small angle scattering in porous carbons is given.

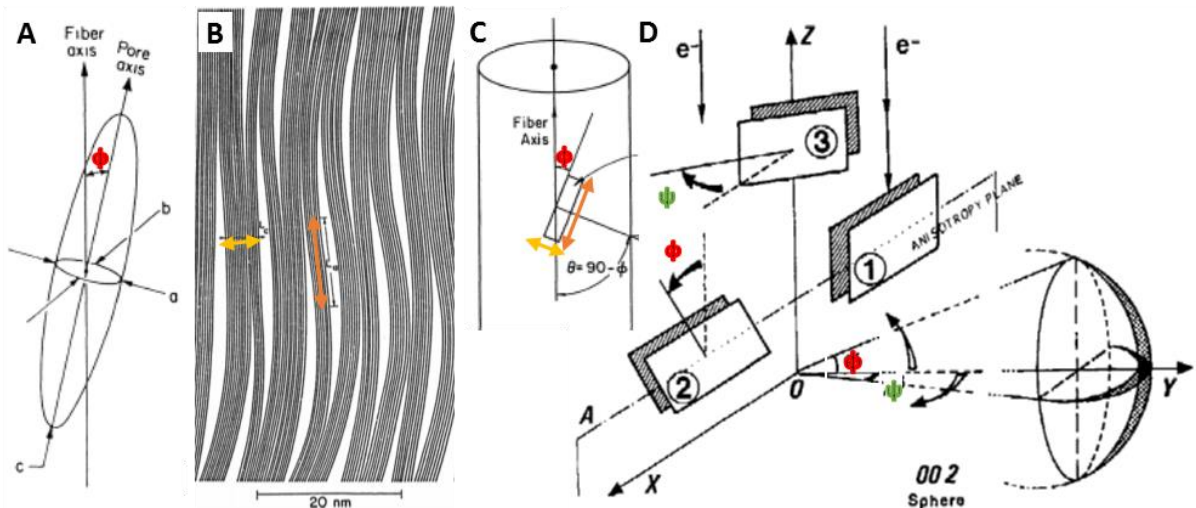


Figure 36. Schematic of the dimensions (a , b , and c) and alignment (ϕ in red) of a pore within a carbon fibre (A) alongside the overall coherent domains within the carbon matrix (L_a in yellow and L_c in orange) (B). The alignment of the porous turbostratic clusters within the bulk fibre are shown in (C) alongside rotational considerations that can be used to measure the overall order within the turbostratic layers and resulting pore network (D). The main geometric considerations for the anisotropic features are detailed in (D) where #1 has graphene layers aligned parallel with the incoming electron beam (e^-) which can be rotated about the X-axis (ϕ in red) as shown in #2 or about the Z-axis (ψ shown in green) as shown in #3. Reproduced from [30] and [154].

2.3.3 Small angle scattering of porous carbons

2.3.3.1 Basic small angle scattering concepts

Scattering, especially using high flux beams with a wide range of camera lengths, is a very attractive method for studying porous carbons because it is possible to characterize the structure across a very broad length scale. SAS has been used to characterize the complex pore structure in carbons covering pore sizes from sub-nm to microns, and can be further extended using ultra-small angle (USAXS or USANS) equipment for structures up to $\sim 10 \mu\text{m}$ [160]. Another important point is that while direct imaging is the domain of electron microscopy, SAXS and SANS can provide comprehensive statistics on particle sizes, shapes, and distributions averaged over a complete macroscopic sample. Small-angle scattering is rarely able to solve a problem on its own, and is typically used in conjunction with a number of other techniques in order to verify the mathematical models chosen to represent the material are correct. Porous carbons can be quite difficult to characterize because they do not produce clearly defined scattering patterns like a perfect crystal would, but are instead composed of very complicated pore geometry and a wide range of size distributions which produces a scattering pattern with less conclusive features.

Scattering theory has an extremely broad range of applications and there are many textbooks that cover the theories and derivations in detail [185]. Only a very brief description is included here for a basic understanding. The majority of the discussion and equations below follow the text on the porous texture of carbons written by Lozano-Castello et al. [28]. The main technique is outlined in Figure 37, where an incident beam is transmitted through the sample of interest. As outlined in the earlier diffraction section, an incident beam, \mathbf{k}_i , of wavelength, λ , will either be absorbed, transmitted, or scattered when passing through the sample. Scattering results from density variations within the sample, and if there is porosity or other sources of heterogeneity in the material, a small fraction of the incident beam that is scattered away from the transmitted beam in a solid angle increment of $\Delta\Omega$ to hit the detector. The scattered beam is defined as vector \mathbf{k}_s , at an angle from the incident beam (defined as 2θ in the diagram). To evaluate the scattering pattern, the change in wave vector $\mathbf{k}_s - \mathbf{k}_i$, termed the scattering vector, \mathbf{q} , is determined by the interaction with the detector.

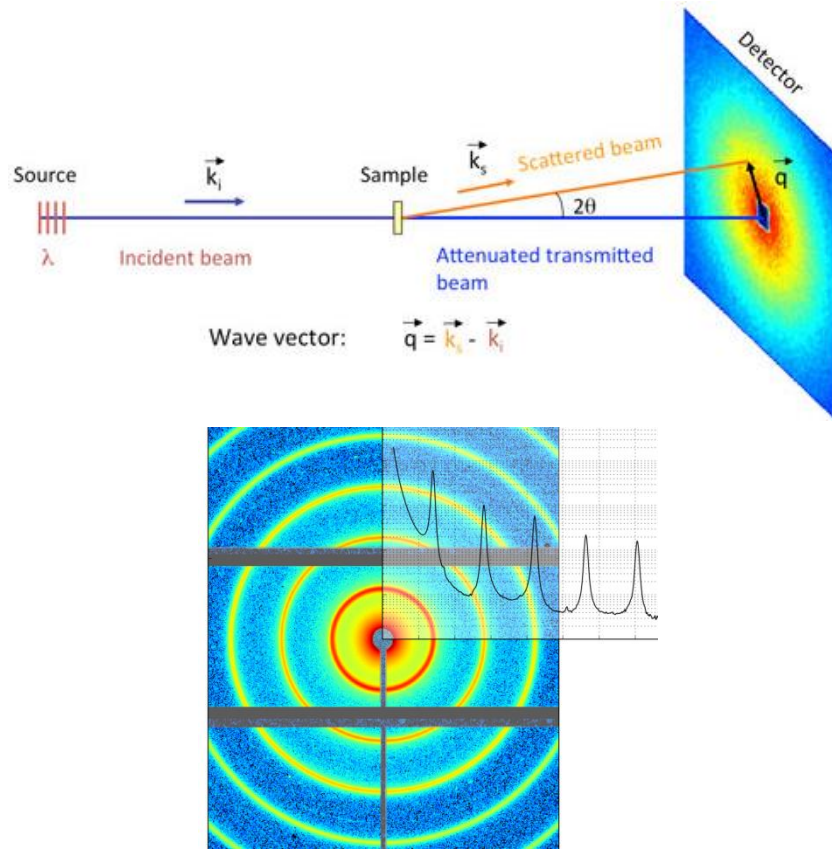


Figure 37. Representation of how the scattering vector, q , is determined from the scattering pattern gathered by the detector and then translated into a curve of scattering intensity vs q for analysis from [186].

The magnitude for elastic scattering is used for analysis, simplified as:

$$q = 2|\vec{k}_s| \sin \theta \quad 2.11$$

Using the magnitude of the incident beam as $|\vec{k}_s| = 2\pi/\lambda$ leads to the familiar relationship used to evaluate scattering patterns:

$$q = \frac{4\pi \sin \theta}{\lambda} \quad 2.12$$

The scattering vector can be easily related to real space length scales by using Bragg's Law which describes the distance between scattering particles, $n\lambda = 2d \sin \theta$, to show:

$$q = \frac{2\pi}{d} \quad 2.13$$

for peaks and features related to periodic structures. It is important to notice that q is inversely proportional to the size of an object; thus, at high q , scattering is from smaller objects and at low q , scattering is from larger structures. The way in which the scattering intensity varies with q is directly related to the structure, where contrast between surfaces will arise if there is a difference in scattering length density at that particular increment of Δq . A conceptual way to visualize the method is equivalent to observe the system through a $2\pi/q_0$ diameter "window" or "yard-stick" in real space and think about what would be seen.

To expand on the previous discussion of diffraction and scattering in carbons, the flux of the radiation scattered, $I(\theta, \lambda)$, at a given solid angle $\Delta\Omega$ is defined by:

$$I(\theta, \lambda) = I_0(\lambda) \Delta\Omega \eta(\lambda) T V \frac{d\sigma(q)}{d\Omega} \quad 2.14$$

Where $I_0(\lambda)$ is the incident flux, $\eta(\lambda)$ is the detector efficiency at a given wavelength, T is the sample transmission, and $d\sigma(q)/d\Omega$ is known as the differential cross section. It is the differential cross section which gives all the desired structural information about the material and it is defined by:

$$\frac{d\sigma(q)}{d\Omega} = N_p V_p^2 (\Delta\rho)^2 P(q) S(q) + B_{inc} \quad 2.15$$

Where N_p is the number of scattering bodies (p for particles), V_p is the volume of one scattering body, and $\Delta\rho$ is the contrast term defined by the difference in scattering density. $P(q)$ is the form factor and $S(q)$ is the structure factor with the added B_{inc} accounting for the incoherent background signal. The differential cross section has units of inverse length and is usually expressed in units of cm^{-1} . During the SAS measurement, the intensity is recorded across many values of q , and fluctuations are due to the specific structural features in the sample resulting from variations in density. The average coherent scattering length density is found by summing each of the scattering bodies (atoms of type i) over a given unit volume, described by:

$$\rho = \sum_i \frac{b_i}{\Delta V} = \sum_i b_i \frac{DN_A}{M_w} \quad 2.16$$

Where D is the mass density, N_A is Avogadro's number ($6.022 \times 10^{23} \text{mol}^{-1}$), and M_w is the molecular weight.

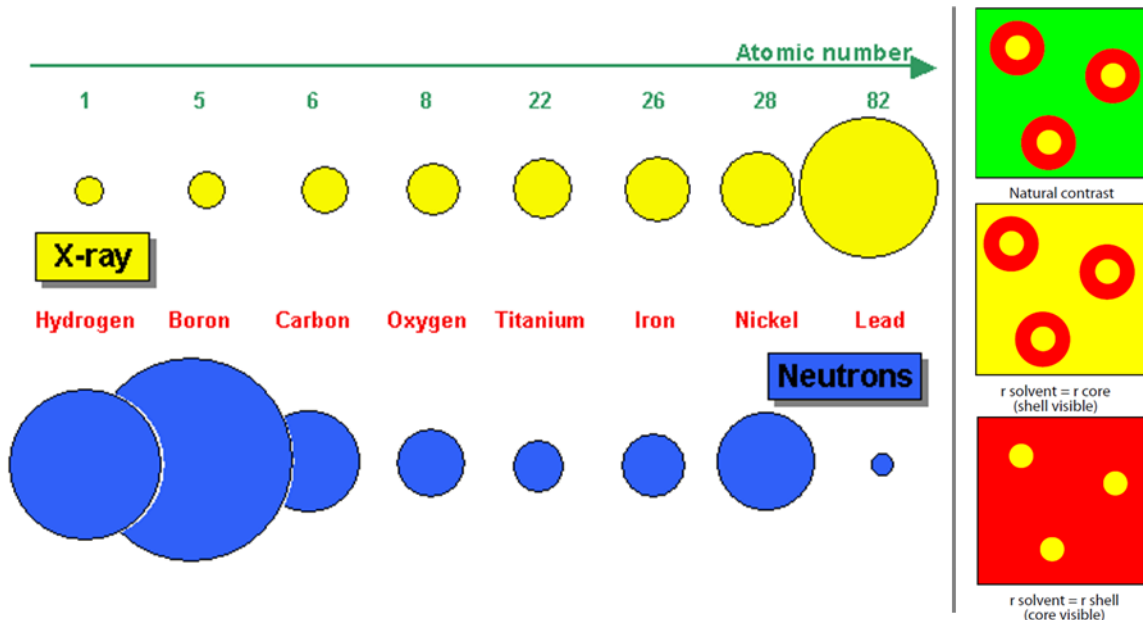


Figure 38. Description of how the scattering cross section varies for different elemental species. The X-ray scattering scales directly with the number of electrons while neutron scattering is more dependent on the mass of the nucleus and packing density. The schematic on the right shows how adjusting the scattering length density of the solvent can be used to mask out particular features in the material.

Some general aspects of scattering length density are described in Figure 38. There are important distinctions between SAS of X-rays and neutrons, particularly when dealing with light elements [160]. Contrast matching in SAXS experiments on carbon fibres has been effective at characterizing both the accessible porosity and percentage of micropore volume [187]. Neutron scattering can be particularly useful in characterizing the structure of light elements because there is such a large variance in scattering length density. Further, contrast matching can be easily employed in aqueous materials (like the rGO hydrogel assemblies) by adjusting the H₂O:D₂O ratio. Contrast matching is suggested as follow up to the results shown in Chapter 6, and is discussed in future work.

2.3.3.2 Structural information obtained from the scattering curve

There are differences in scattering from monodisperse colloidal particles, bulk aggregate systems, polydisperse mediums, and aligned assemblies, and each require specific experimental and analytical considerations. However, there are some general scattering principles that hold true for most any materials under investigation. Thus, a discussion on the major features of a scattering curve along with the specific plots used to assess specific structural features will be presented here, since most of these methods are applied to data acquired with rGO assemblies.

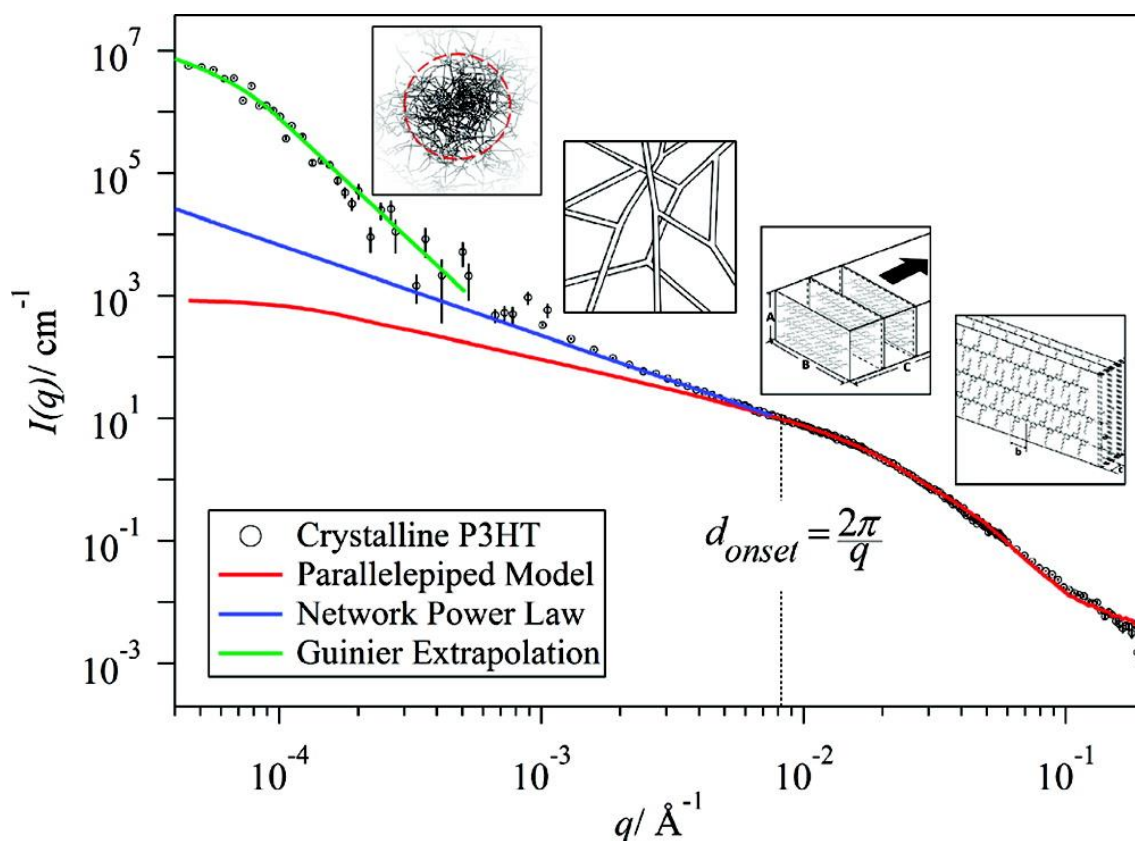


Figure 39. An examples of reduced and combined SANS and USANS data on an absolute intensity scattering curve. The insets are schematic representations of the structural features that are characterized at each q -range. Reproduced from [188].

Examples of the various regions on a combined SANS and USANS scattering curve are shown in Figure 39, with insets representing the specific features characteristic of that size range, as shown by d_{onset} . It is clear how the individual molecules seen at the largest q -values arrange to form lamellar stacks in the intermediate SANS range (red curve). These stacks then form a branched rod-like network measured at higher q (blue curve), that are then characterized as larger clusters with USANS (green curve).

Using Figure 39 as reference, these features will now be described in mathematical terms so quantitative structural information can be derived from the scattering curve. The first region at lowest q , shown in green, is used to determine the Guinier radius [189], R_g , of a scattering object which holds when $q \cdot R_g < \sqrt{3}$. If the material consists of monosized particles in a two-phase system, the relationship is defined as:

$$I(q) = I_0 \exp \left[\frac{-R_g^2 q^2}{3} \right] \quad 2.17$$

where R_g is the radius of gyration and can be obtained directly from slope, $R_g^2/3$, of the linear region on a the Guinier Plot of $\ln(I)$ vs q^2 in the range $qR_g < \sqrt{3}$ which occurs when the probed range ($2\pi/q$) is larger than the particle size. The particle size measured is independent of the absolute intensity, I_0 , and of any physical/shape model, but polydispersity and interparticle effects can strongly influence the measurement of R_g , so care must be taken in the interpretation of this parameter unless the material is monodisperse and very dilute. When structural information about the particle or aggregate shape is known, R_g can be further analysed for the specific measurements of:

$$\text{sphere with radius, } r: R_g^2 = r^2 \frac{3}{5} \quad 2.18$$

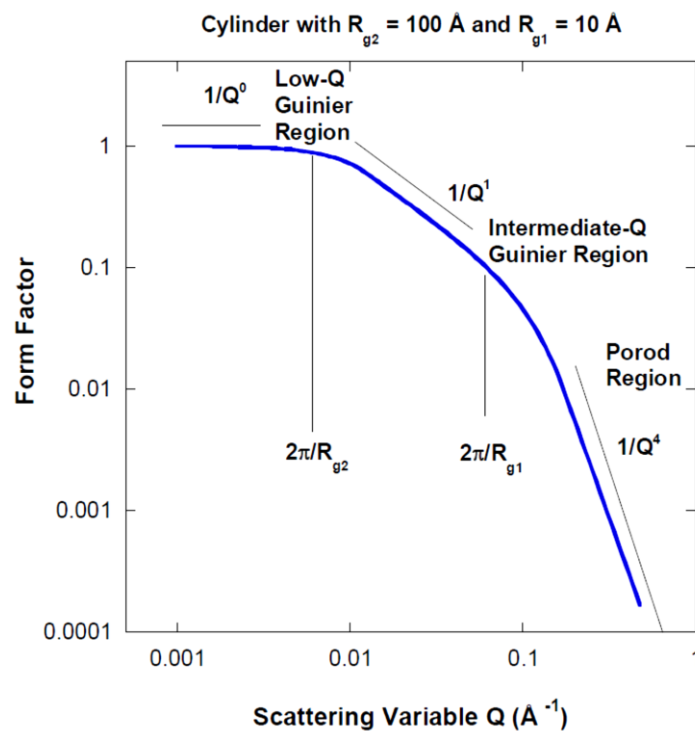


Figure 40. Description of the form factor of a cylinder, showing the different regions along a scattering correlate with the dimensions of this elongated object with two distinct Guinier radii. The intermediate slope between these regions is related to $q^{-\alpha}$ where the value of α is related to the interface between the scattering object and matrix. Reproduced from [186].

However, the relationship needs to be adjusted when materials have elongated objects, because the lengths along the shape can vary greatly in size, as shown in Figure 40. For example, a cylinder may have a length of 10s of nanometres, but a radius of only a few. Further, flat lamellar objects could extend across a long length scale, but be extremely thin (as in the case of graphene layers). In these cases, the Guinier plot is modified to accommodate an intermediate- q region representing the smaller size scatterer as shown in:

$$\text{cylinder with length, } L, \text{ and radius, } r: R_g^2 = \frac{L^2}{12} + \frac{r^2}{2} \quad 2.19$$

where the small r component can be found with the adjustment:

$$I(q) = \frac{I_0}{q} \exp \left[\frac{-R_g^2 q^2}{2} \right] \quad 2.20$$

and again:

$$\text{flat lamella of thickness, } t: R_g^2 = \frac{t^2}{12} \quad 2.21$$

where the small thickness component, t , can be found with the adjustment:

$$I(q) = \frac{I_0}{q^2} \exp \left[\frac{-R_g^2 q^2}{1} \right] \quad 2.22$$

Thus, a plot of $\ln(I(q) \cdot q^2)$ vs q^2 in the region of $2\pi/L^{0.5} \leq q \leq 1/R_t$, where L is the cross section of the lamella and R_t is the radius of gyration of the thickness, can be used to calculate the thickness of slit-shaped pores. The linear portion of this plot will yield a slope of $-R_t^2$, and the equation above for the thickness of a lamella equates to the width of pores in that range.

At the highest q region in Figure 39 marked in red, scattering features corresponding to the smallest ordered structure existing in the material are observed. This is representative of the size of the smallest building blocks and could result from structures such as small particles, micelles, lamellar spacing, bi-layers, or pores. Extending the q range even further would eventually resolve any atomic spacing as seen in the wide angle scattering discussed in the previous section. Porod [190] showed this high- q region depends on the fine structure of the particle, scaling with the physical attributes of the interface and providing information about the interfacial area between the two phases of the system. In a two phase system with smooth boundaries at the interface, the scattering limit at high- q will relate to the total interfacial area, A , between the two phases of varied density ($\Delta\rho$), defined as:

$$I(q) = 2\pi A(\Delta\rho)^2 q^{-4} \quad 2.23$$

Through the application of the Porod Law, the Porod Invariant (PI) can be obtained. This is a useful parameter for analysing porous materials, and is defined by:

$$PI = \int q^2 I(q) dq \quad 2.24$$

The Porod Invariant is related to the void fraction, ϕ , in a porous material and can be related to the overall volume, V , to yield the porosity through:

$$\frac{1}{V} PI = 2\pi(\Delta\rho)^2 \phi(1 - \phi) \quad 2.25$$

More generally, within the Porod region, a power law is applied to the decay rate of scattering intensity. The simplified premise describing the decay of the intensity as a power law with α defining the slope is given as:

$$I(q) \propto q^{-\alpha} \quad 2.26$$

The Porod Law relates the total scattering surface to the volume of material in the beam, and the slope of the $\text{Log}(I)$ vs $\text{Log}(q)$ plot can be related to the total scattering surface area. Within this q range, the scaling of intensity is a continuum description in terms of scattering density, and for a system composed of distinct mesoscopic particles or pores, all small-angle scattering can be understood as arising from surfaces or interfaces. In a two-phase media with a sharp perfectly smooth boundary or surface, the slope of the scattering curve in the Porod region of a $\text{Log}(I)$ vs $\text{Log}(q)$ plot will have a slope of -4. The Porod law neglects any fluctuations or variations in the density within one of the phases, and it is common that porous carbon materials deviate from this law [30]. In general, fluctuations along the surface will contribute a term in $I(q)$ proportional to q^{-D} , where D is the dimensionality of the fluctuations.

Porod's Law is a useful conceptual framework for the interpretation of SAS measurements, which effectively describes the dimension of scattering objects' local structure. Factors which influence this power law can be from the structure of the interface, density fluctuations in the material, and extensive surface roughness or curvature [191, 192]. Deviations from this smooth surface result in values of D ranging from 1 to 4, and this decrease in the magnitude of the slope is indicative of increased internal surface causing increased scattering and scattering at wider angles. For the extremes, a Porod slope of -1 is typical for scattering of rigid rods while -4 represents a perfectly smooth interface between two phases, as shown in Figure 41.

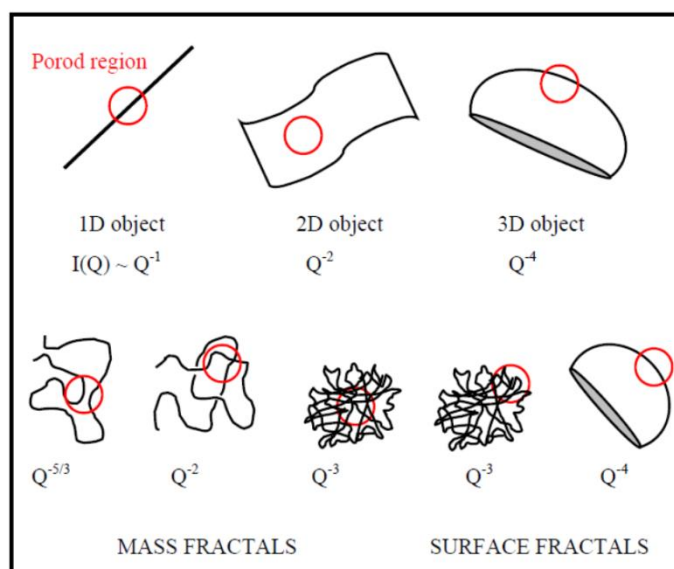


Figure 41. Diagram of shapes showing how the slope in the Porod region Q^{-D} is described by the dimensionality of a surface, (D values 1 through 4), and is related to the structural features in the material as visualized within a given q -window outlined by the red circle (from [186]).

For many years, researchers have found that disordered carbon materials often exhibit properties suggesting non-integer fractal dimensionality [30]. These relationships are shown visually in Figure 41. A general definition for a fractal system is that the total mass of a system will depend on its size with

$M=L^D$, indicating that a fractal material has a density that decreases with increasing size. Bale and Schmidt [193] defined how this can relate to fractal surfaces in porous materials where a slope between -3 and -4 is indicative of the rough surface within a pore. This surface fractal dimension can be equated to $D=6-\alpha$ ($I(q)$ scales with $q^{-(6-D)}$), where a smooth surface has a dimension of 2, yielding the typical Porod relationship of q^{-4} . For rougher surfaces, the fractal dimension will be greater than 2, resulting in a slope between -3 and -4. Correspondingly, values of q^{-2} to q^{-3} are typical for a mass fractal structure such as those in branched systems (gels) or networks, where a value of D closer to 2 is considered more two-dimensional and D values closer to 3 is more three dimensional, or uniformly filling space. For other complex systems, like polymer coils, the Porod slope is related to excluded volume parameter, V , with $\alpha=1/V$. A comparison can also be made for polymer chains where swollen coils scale with $q^{-5/3}$ or q^{-3} for collapsed polymer coils, while q^{-2} indicates Gaussian chains in a dilute solution [186]. There are many comprehensive investigations of fractal theory applied to small angle scattering [194-196] with Pfeifer and Avnir et al. [34, 197-200] being well-known in the field along with specific computational forms outlined by Cherney et al. [201-203].

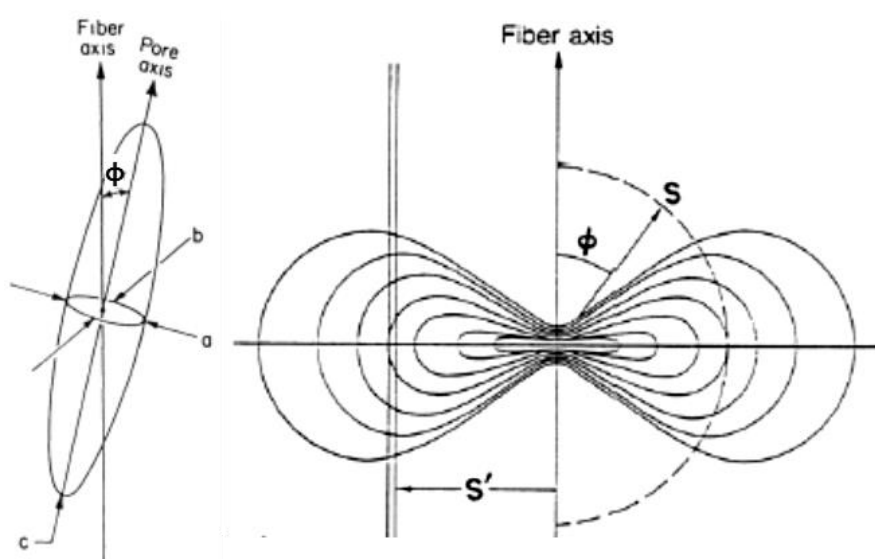


Figure 42. The diagram of an elongated pore with dimensions a , b , and c along with the OA , ϕ , in relation to the fibre axis is shown to understand how these structural parameters can be deduced from the resulting anisotropic scattering pattern (details are given in the text). Reproduced from [30].

A final comment will specifically address carbons with highly aligned pores, building on the concepts of the previous section on diffraction and extending the main parameters of interest to small angles. Again, carbon fibres are used as an example because the structure and geometric considerations are similar to that of rGO assemblies. In fibres, where the graphene sheets are preferentially aligned along the fibre axis (as was shown in Figure 36), the resulting small angle scattering pattern will display anisotropic features corresponding to the alignment of the $(00l)$ lattice points and resulting pore structure between the graphene-layer clusters. The diagram of the elongated pore in Figure 42 is the typical shape produced within the aligned carbon fibre matrix, and the distinctive fan-shape scattering pattern will result from this oriented, layered structure. As previously described, the measure of the OA can describe the overall orientation of the pores across different length scales and also be used to analyse the evolution of porosity in carbon materials [28, 136]. It should be noted that there can be differences in the OA measured at wide and small angles depending on the carbon microstructure [30]. When interpreting a scattering pattern from a carbon fibre with graphene sheets aligned along the direction of the fibre axis and pores with the dimension of a , b , and c , as shown, the azimuthal intensity

$I(\phi)$ can be measured across a constant value of q to obtain the arc marked **S** [30]. The specific features of the pore can be analysed with:

$$q^2 B_{obs}^2 = q^2 B_{\phi}^2 + c^{-2} \quad 2.27$$

where B_{obs} is the measured width of the distribution (FWHM) and B_{ϕ} is the width of the orientation distribution of the pores. This relationship is quite useful because the alignment of the pores can be easily obtained from the slope of plot of $q^2 B_{obs}^2$ versus q^2 while the intercept can be equated with the pore length, c .

Additionally, the slit pattern on the left hand side can be used to obtain the a/b pore dimensions directly, as the intensity measured along the profile $S=S'$ can be analysed using the equation:

$$I(S') = \exp \left[\frac{-(a^2 + b^2)\pi^2 S'^2}{6} \right] \quad 2.28$$

In the case that a and b are not equal (non-spherical pore width), if there is a significant difference in the size ($a > b$), the contributions from the two pore widths can be separated. It is common to have carbon fibres with c/a ratios of 1.5 to 3.5 and c/b ratios of 4 to 24 [30].

2.4 Concluding Remarks

This literature review was meant to outline the main features of interest in carbon materials as they relate to the characterisation of the structure of rGO assemblies and identifying the mechanisms driving structure-property relationships in these unique materials. The discussion here attempted to lay the groundwork for designing the approach to the experimental analysis in this thesis, beginning with the most fundamental units of rGO sheet chemistry and ending with the overall features of bulk porous carbons. The remainder of this thesis follows accordingly, with results for the chemical composition and carbon bonding in rGO sheets followed by constructing a basic structural unit (BSU) at the micro-scale and finally an analysis of the overall bulk assembly. Each experimental chapter builds upon the elements of structure identified in the chapter before to create a finished work that extends across the entire length scale of rGO assemblies.

The overall significance of this work is closely tied with identifying specific structural features that can impact the resulting performance of rGO materials. As discussed in this Literature Review, it is not yet known what impact the chemical composition of the original GO sheets has on the composition of the resulting rGO. A deeper understanding of these conditions is crucial in order for large-scale processing to become viable. Further, there has hitherto been no direct measure of the pore structure in rGO assemblies. All of the promising technologies discussed here, especially those related to separation science and energy storage, cannot be fully understood or improved without a clear understanding of the physical structure in these layered, porous rGO materials. Characterizing the pore structure in these assemblies should prove relevant to those working in the field, as many assumptions made using indirect methods can then be validated or refuted.

Chapter 3. Materials and Methods

3.1 Materials

3.1.1 Preparation of graphene oxide precursor

All analytical grade chemicals were purchased from Sigma-Aldrich Co., Merck KGaA (EMSURE®), or Thermo Fisher Scientific Inc. (Ajax Finechem UNIVAR®), unless otherwise specified in the text.

The raw graphite material plays a large role in determining the resulting GO and rGO structure. Graphite powder from Alfa Aesar of 325 mesh (flake, natural, 99.8%, Lot#C15Z023) was used for all GO preparation other than LOX which was synthesized from 100 mesh (powder, natural, briquette grade, 99.9995%, Lot#J11X001). Graphite powder is available in different mesh sizes, which is a method of categorizing a particle size by running the powder through a specific sized screen, typically for materials greater than 44 microns (325 mesh). The mesh number equates to the number of holes a standard area is broken into, with larger mesh number meaning smaller openings to sieve the powder through. To determine the powder's particle size distribution, more than one screen needs to be applied when separating the particles in the powder, but this is not always done. Therefore, most powders with a - 325 mesh rating have a range of particle sizes, all measuring less than 44 microns, but with many of the particles being considerably less than 44 microns.

Graphite oxide was synthesized from the abovementioned 325 and 100 mesh graphite powders using the modified Hummers method [55, 58, 204]. Graphite flakes were soaked in a water-free mixture of concentrated sulfuric acid (H_2SO_4) and sodium nitrate (NaNO_3), with one gram of graphite powder mixed with 0.5 g of NaNO_3 and concentrated sulfuric acid. The volume of sulfuric acid was adjusted to yield different graphite to acid ratios in order to control the viscosity during the oxidation process (as indicated in Table 1). This ratio is adjusted because the higher oxidized graphite flakes are greatly expanded, causing the suspensions to be too thick if confined to a smaller volume. The process of oxidizing graphite can be broken down into two main steps, which can be termed *Step 1: oxidation* with potassium permanganate (KMnO_4) and *Step 2: hydrolysis* with water. Variations in the oxidation level were controlled by adjustments in oxidation time and temperature, as indicated in Table 1.

The graphite powder (1 g) and sodium nitrate (0.5 g) was stirred in 23, 24, or 46 mL of sulfuric acid, as indicated, at a temperature of 0°C for 45 minutes. During *Step 1: oxidation*, KMnO_4 (3 g) was slowly and carefully added while the temperature was kept constant at 0°C. After mixing, the temperature was kept at 10 °C or 35°C for the time given in Table 1. While the difference in sulfuric acid volume may have minor impacts on the oxidation level, the active species controlling the reaction is diamanganese heptoxide which is formed from the reaction of potassium permanganate with sulfuric acid [56]. The amount of potassium permanganate and raw graphite material are kept constant for all samples, so any impacts from adjusting the volume of sulfuric acid will be minor.

To begin *Step 2: hydrolysis*, deionized water (at twice the volume of H_2SO_4) was slowly added while the temperature of the reaction was kept at 90°C, unless otherwise indicated in Table 1. The reaction was held at constant temperature for the time listed before adding 500 mL of deionized water along with 20 mL 30% hydrogen peroxide to terminate the reaction. The graphite oxide dispersion was then repeatedly washed with 5% HCl aqueous solution and then deionized water, followed by centrifugation, according to the Hummers method [55]. A further dialysis process was applied for one week to ensure any remaining metal contaminants were removed.

The concentration of each graphite oxide dispersion was determined by first diluting and sonicating a controlled volume of the graphite oxide to produce a dispersion of GO which was then filtered into a dry, thin GO paper. The GO paper was allowed to further dry in a low temperature (50°C) oven for 24 hours before weighing in order to remove water adsorbed within the GO layers. The resulting mass of

GO paper was used to calculate the concentration of the original graphite oxide dispersion which was then reduced to produce the rGO dispersions and assemblies tested in this work.

Thus, the samples used in this work are assumed to be in an oxidation series, and are labelled from highest to lowest oxidation level, as indicated in Table 1.

Table 1. Procedures for synthesizing GO with varied degrees of oxidation and the corresponding sample names reported in this work.

Oxidation degree	Reference in Thesis	Size of Graphite Flakes	M(graphite): V(H ₂ SO ₄)	Step 1: Oxidation of Graphite (KMnO ₄)		Step 2: Hydrolysis of Graphite Oxide (H ₂ O)	
				temp	time	temp	time
Extra Low	LOX	100 mesh 150 μ m	1:24	10°C	16 hours	10°C	6 hours
Low-A	LOA	325 mesh 45 μ m	1:23	35°C	2 hours	10°C	15 min
Low-D	LOD	325 mesh 45 μ m	1:23	35°C	2 hours	90°C	15 min
Low-H	LOH	325 mesh 45 μ m	1:23	35°C	2 hours	>125°C	15 min
High-3	HO3	325 mesh 45 μ m	1:46	35°C	3.5 hours	90°C	1.5 hours
High-4	HO4	325 mesh 45 μ m	1:46	35°C	8 hours	90°C	1.5 hours
High-7	HO7	325 mesh 45 μ m	1:46	35°C	18 hours	90°C	1.5 hours
High-8	HO8	325 mesh 45 μ m	1:46	35°C	3.5 hours	90°C	4 hours

3.1.2 Reduction of graphene oxide to rGO

This process follows the methods outlined by Li et al. [15]. The concentration of the graphite oxide dispersion described above was diluted in ultrapure water to yield a concentration of 1.0 mg/mL in order to ensure that the rGO does not agglomerate during the reduction process. This dispersion was placed in an ice bath and sonicated for thirty minutes to produce a stable GO dispersion. The GO was then centrifuged at 3000 rps for 30 minutes in order to remove any possible agglomerates, but all dispersions were found to be quite homogeneous with only a few larger agglomerates being drawn to the bottom of the tube and removed. The GO dispersion was a light tan colour. The resulting stock solution of GO was then poured into a 100 mL volumetric flask and concentration was verified with a pre-determined UV-vis calibration curve.

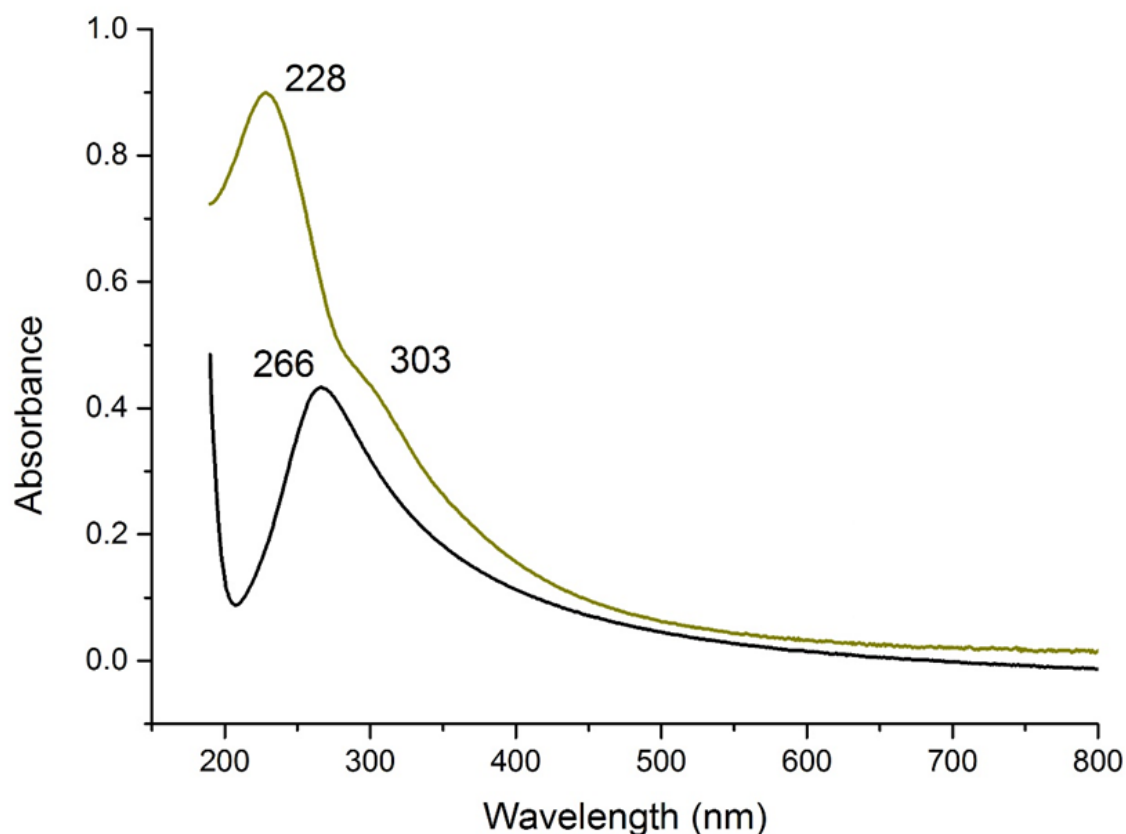


Figure 43. UV-vis absorbance curves showing the unique features of GO (green) and rGO (black) to ensure the solutions are completely reduced.

To reduce GO, 28wt% ammonia (NH_3) was first added as the stabilizing agent at a $V_{\text{NH}_3\text{H}_2\text{O}}:V_{\text{GOH}_2\text{O}}$ ratio of 7:2000, which equates to 350 μL in the 100 mL flask. Then, 35 wt% hydrazine (N_2H_4) hydrate was added as the reduction agent at a mass ratio of $M_{\text{N}_2\text{H}_4}:M_{\text{GO}}$ of 7:10, which equates to 200 μL of 35wt% N_2H_4 in the 1.0 mg/mL GO stock solution. The flask was then mixed and placed in a boiling water bath to hold the reaction temperature at 100°C for three hours. Upon reduction, the stable aqueous suspension of rGO is black, with no light passing through the dispersion. After further dilution of the dispersions, UV-vis absorbance data, such as that shown in Figure 43, was obtained to ensure the GO was completely reduced.

Hydrothermally-reduced rGO was prepared by the same method as described above, but the GO, hydrazine, and ammonia solution was placed in a Teflon-lined autoclave vessel that was held at 180°C for three hours and then allowed to cool to room temperature before filtration.

3.1.3 Filtration of rGO hydrogel and dried assemblies

In order to produce rGO assemblies with mass density of approximately 1 mg for every cm^2 area of the thin films, using the estimate that for all GO materials, roughly 60% of the mass from the original GO dispersion will remain after reduction (~40% loss due to the removal of oxygen groups), the following procedure was applied. Figure 44 shows the basic set-up where circular Anodisk alumina filters with 200 nm pore size (Whatman™, GE Healthcare, Buckinghamshire, UK) were used as the support for all rGO assemblies. Pouring the rGO dispersion into the funnel at top resulted in assemblies with diameter of 37 mm, producing bulk, thin-films with a surface area of 10.75 cm^2 . Thus, 20 mL of the rGO stock suspensions were vacuum filtered to produce oriented thin films with mass indicated in Table 2. The mass of each pump dried assembly was weighed after drying in a low temperature (50°C) oven for 24 hours to ensure water content was minimized, before calculating the mass density after reduction. It is clear that the amount of mass lost during the reduction process is highly variable depending on the

original GO material, with lower oxidized GO being more readily reduced using the hydrazine method. Further, it was determined that dried rGO assemblies will hold additional water when left in ambient conditions, and this adsorbed water equates to approximately 5-10% of the total assembly weight. More highly oxidized samples had an overall higher average water content ($10\pm2\%$) while lower oxidized samples had slightly less ($9\pm2\%$) and the extra low oxidized having only $5\pm1\%$.

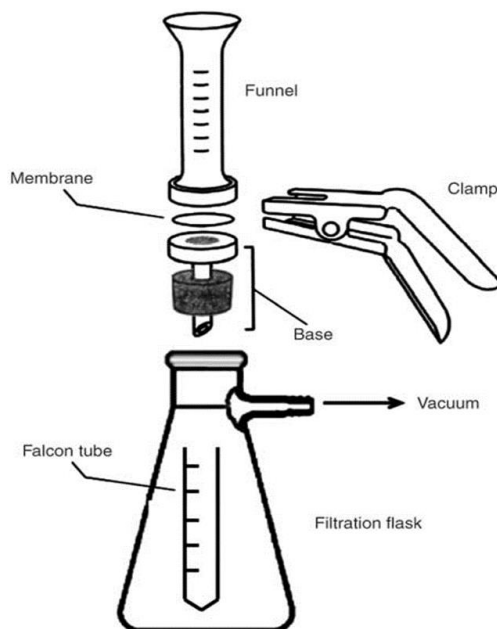


Figure 44. Diagram of a basic filtration set-up, where the rGO dispersion is poured into the funnel at the top and the resulting assembly is formed on top of the Anodisk membrane while the water is drawn into the filtration flask below when under vacuum (from [205]).

A micrometer was used to obtain an estimate for the thickness of the films, with the dry assemblies demonstrating an average thickness of 6-7 μm , but showing a rather large lateral variance even within the same film ($\sim 20\%$). Thus, the average volume of a full pump dried assembly is approximately 6.45 mm^3 , resulting in the mass density values shown in Table 2. Overall, there was a range in thickness of 4-9 μm for different dried assemblies. The hydrogel films were even more variable, ranging from 110-180 μm for different assemblies, with an average of about 150 μm . These hydrogel assemblies also showed a higher degree of variance than the dry materials, especially within the same film, due to the high water content and “soft” nature of these materials. Using the micrometer, the accuracy of these thickness measurements is hard to define given the low precision (especially in the dried assemblies which are less than 10 μm thick) and mechanical pressure applied (especially in the hydrogel assemblies which are quite soft). Thus, more precise measurements are presented in Chapter 6 results using SEM. In spite of this, the measurements from micrometer readings serve as a close estimate, and also show that the hydrogels are swollen to thicknesses over 20 times that of dried films. It should be noted that the large difference in thickness for the dried and hydrated materials is solely due to the water content, as they will contain the same amount/mass of rGO, as determined by the concentration and volume of the rGO dispersion filtered to make the resulting assembly.

Table 2. Comparison of the mass for each of the dried rGO assemblies made from GO precursors of different oxidation levels. It should be noted the thickness measurements are obtained with a micrometre and lack high precision, so while the variance in the mass per unit area values is $\pm 6\%$, the variance in mass density is much larger at $\pm 30\%$.

Oxidation degree	Reference in Thesis	Mass Dried rGO Assembly		Mass per cm^2	Mass Density
		(mg)	+/-	(mg/cm^2)	(mg/mm^3)
Extra Low	LOX	6.5	0.2	0.60	1.0
Low-A	LOA	7.6	0.1	0.71	1.2
Low-D	LOD	8.5	0.1	0.79	1.3
Low-H	LOH	9.5	0.2	0.88	1.5
High-3	HO3	9.2	0.3	0.86	1.4
High-4	HO4	9.3	0.3	0.87	1.4
High-7	HO7	10.3	0.3	0.96	1.6
High-8	HO8	9.8	0.3	0.91	1.5

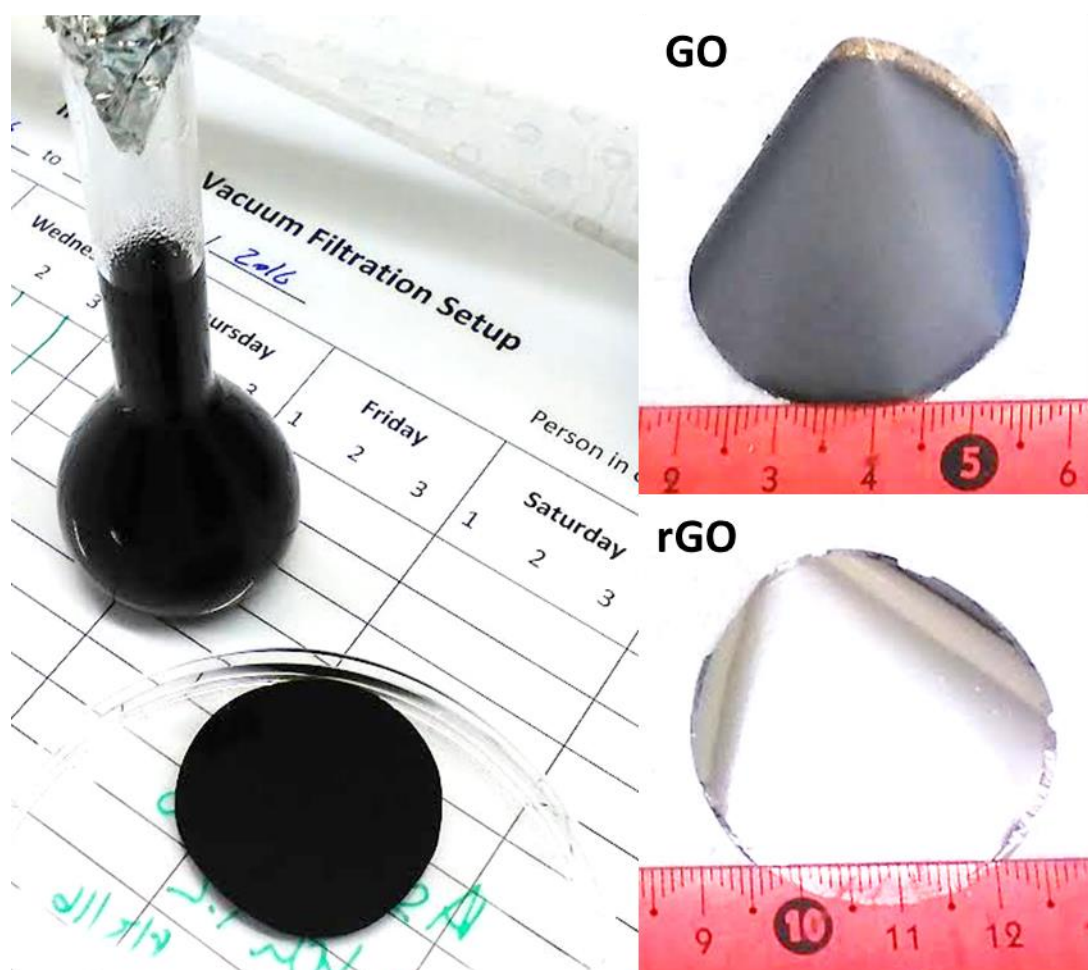


Figure 45. Photographs of the rGO dispersion before filtration and the resulting stable hydrogel assembly stored in water (left) along with a comparison of the pump-dried GO and rGO assemblies. The hydrogel is a dark black colour, while the dried GO is dark brown, and the dried rGO is grey with a very pearly lustre (camera flash is incident on the rGO assembly to highlight the reflectance properties – it is not white in colour, see Figure 46).

Figure 45 shows the rGO pre-filtered dispersion along with a resulting hydrogel assembly, where the assembly is removed from the filtration set-up after the dispersion has been completely filtered, but the film is still wet. This hydrogel is compared to pump dried GO and rGO films where they have been left on the filtration set-up with constant vacuum applied until all the water is removed from the films (overnight process). The difference in the colour and lustre of each material is clearly observed in the photographs.

To assess the impact of drying, filtered assemblies were either:

- removed from the filter while still wet and then stored in ultrapure water to produce a stable hydrogel films,
- removed from the filter while still wet and then transferred to a freeze drier to fully dry while attempting to preserve the hydrated pore structure,
- removed from the filter while still wet and then dried under vacuum (same freeze dry process, but without low temperature),
- removed from the filter while still wet and then allowed to air dry in a low temperature oven (50°), or
- removed only after completely dried on the pump to produce a very shiny, graphitic like paper.

It is clear from Figure 46 that the different drying methods also shrink the rGO assemblies considerably, impacting the mass density values shown in Table 2. The pump dried assembly is kept stable on the filter support with the constant pressure from the vacuum, resulting in a smooth surface. The air dried and vacuum dried assemblies were removed from the filtration set-up while wet, clamped between two Teflon plates, and then allowed to fully dry under the specified conditions.



Figure 46. Comparison of rGO assemblies that were pump dried, air dried, or vacuum dried, showing the tendency of the material to shrink under different conditions. All assemblies shown here have the same mass.

The final procedure applied to the rGO materials follows the previous work to tailor the pore size of rGO assemblies used as supercapacitors [24], where stable hydrogel membranes made from GO precursors were immersed in 5.0 M, 2.0 M, 1.0 M, 0.5 M, or 0.1 M sulfuric acid for three hours while mixing. The electrolyte mediated rGO (EM-rGO) assemblies were then immediately freeze dried under vacuum for two days to remove all water content, leaving behind the non-volatile sulfuric acid to stabilize the pore network. The day before testing (24 hours), the dried EM-rGO films were washed with water repeatedly to remove the sulfuric acid and stored in ultrapure water as a stable EM-rGO hydrogel film. Previously, all assumptions about the pore structure of these materials were made on the dried films containing intercalated sulfuric acid, but here they are tested in the aqueous state because it is most similar to the operating conditions as a supercapacitor. These EM-rGO materials were examined by techniques outlined in Chapter 5 and Chapter 6, but because no differences were measurable, only results acquired from HO3 or HO4 rGO assemblies are reported.

3.2 Specialized Sample Holders

The X-ray scattering results taken from a wide angular rotation, as well as the *in situ* experiments of hydration (Chapter 6), required specific sample holders be built. Figure 47 shows how the dried rGO assemblies were mounted in the rotation holders in order to obtain scattering results across the entire surface-to-edge range of 0° to 90°. For the through the edge samples, very thin strips of the rGO assemblies were cut (≤ 1 mm) to ensure high transmission through the sample (thicker samples can introduce effects from multiple scattering). The two sides of the holders were held together with o-rings and then mounted on top of a humidity delivery system (shown in Figure 48) that was attached to a rotation stage at the SAXS/WAXS beamline. The results presented in Chapter 6 utilize the mounting and rotation functions of this design, but the apparatus is able to extend its functionality to act as a controlled humidity chamber. In this case, a humidifier is attached to the sample mount so that water content within the rGO assemblies can be controlled while the structural impacts are measured. To enclose the top insert where the sample is located, a thin film that is transparent to X-rays is wound around the circular holder and held securely with the o-rings. An additional cavity was included so that a humidity sensor can be inserted in order to determine if the relative humidity at the sample varied from that at the output of the humidifier, accounting for possible variations after traveling through the delivery tube.

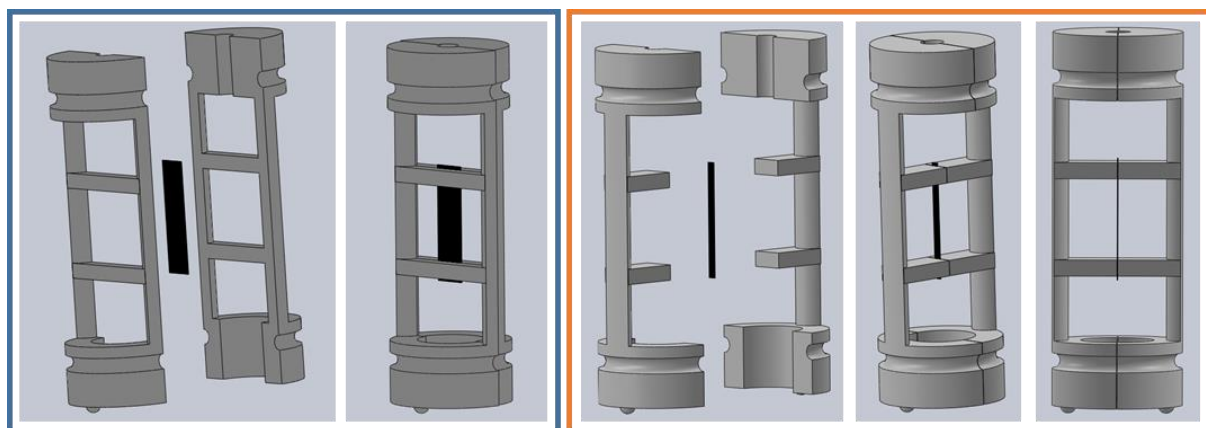


Figure 47. The CAD drawings used to 3D print the sample holder used to obtain a full 90° rotation, going from through the surface (0°) to 45° in the holder, which is shown within the blue box and from 45° to through the edge (90°) in the holder shown within the orange box.

For the *in situ* drying results presented in Chapter 6, the sample holder shown in Figure 49 was used. Since the rGO assemblies tend to curl and rip upon drying, in order to keep the samples aligned and intact, the thin films needed to be tightly secured and mounted while the SAXS/WAXS results were acquired. The photographs show that rGO assemblies mounted so the incident beam went through the surface (left) as well as those mounted so the beam went through the edge (right, in yellow), retained structural integrity throughout the drying process. This is especially difficult to achieve with the samples mounted through-the-edge, as the thin strips (≤ 1 mm) must be prevented from ripping or twisting, and this sample holder functioned very well, ensuring high quality results. In addition, this design was intended to extend its functionality and also act as an electrochemical cell for *in situ* measurements on the rGO assemblies as they function as a supercapacitor. In this instance, the holder is enclosed, the window is sealed with X-ray transparent film, and a positive/negative bias is applied to the top/base plate. The holder shown here was made of stainless steel, and even though the contacts were coated with a platinum foil, the high resistance from the bulk metal did not allow for good cyclic voltammetry (CV) results to be obtained.

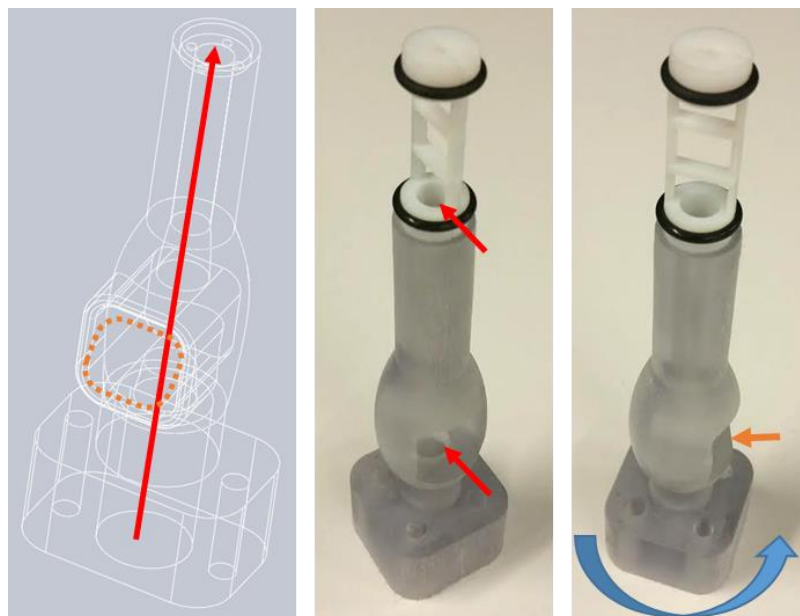


Figure 48. Sample mount to function as a humidity delivery system and rotation stage where output from a controllable humidifier enters the base and passes through to the sample area mounted at top (red arrow). The vapour passes through a humidity sensor that is placed inside the cavity marked in orange. The entire apparatus is secured to a rotation stage at the base, allowing it to be fully rotated (indicated by blue arrow).

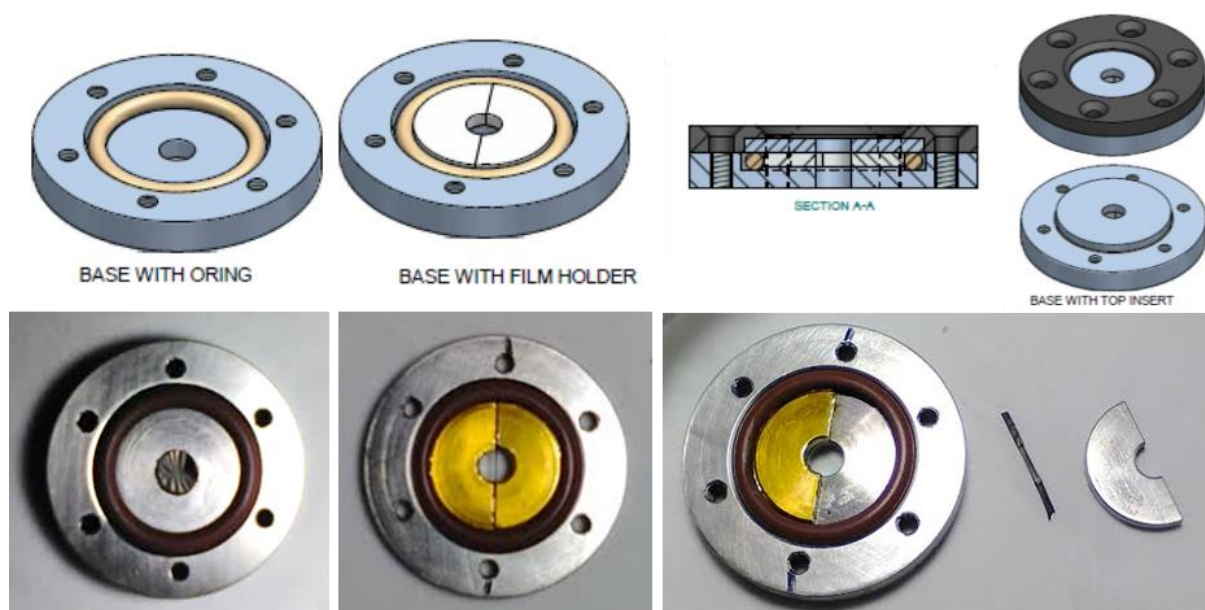


Figure 49. CAD design and photographs of the sample holder designed to tightly secure the rGO assemblies while drying and also functions as an electrochemical testing cell for rGO.

3.3 Experimental Methods

3.3.1 rGO materials used in each experimental chapter

For all results reported in this work, graphite oxide was synthesized from graphite powder using a modified Hummers method [206] with the variations in oxidation level were controlled by slight differences in oxidation time and temperature, during the Step 1 and Step 2 oxidation processes, as discussed in Section 3.1.1 and outlined in Table 1. Because not all rGO materials were investigated for each experimental method, a general explanation for the choice of materials is given here, with more details given in the sub-sections to follow. Samples LOD and HO3 were synthesized using the most widely-used reaction conditions for GO, and serve as examples of standard oxidation levels typically

reported in the literature. In contrast to this, LOX has the most unique synthesis method, and not only was it desirable to investigate the chemical composition of this extremely low-oxidised material, it was not yet known if these low temperature conditions would result in exfoliated GO suspensions and stable rGO assemblies. HO8 represents the other end of the spectrum, with the extended reaction time during Step 2 thought to lead to the highest level of oxidation. Thus, for experimental results that were focused on comparing different rGO materials, LOX and HO8 were always used to represent the extremes, and these were then compared with more moderate oxidation conditions, like those used for LOD and HO3.

It should be noted that because not all materials are compared directly using each experimental technique, there are limitations to the conclusions that can be made regarding the specific impacts that these slight variations in GO synthesis have on the resulting rGO materials. However, it was considered useful to investigate the range of rGO materials in order to determine if any patterns or trends emerge. If so, trends could then be followed up with more detailed investigations using rGO assemblies prepared from a wider range of GO reaction conditions. Similarly, if no differences were measurable by the given technique (as is the case with data presented in Chapter 6), this also provides useful information for planning further studies.

Table 3. Matrix indicating which experimental methods were applied to specific rGO assemblies and the corresponding chapters containing the results.

Reference in Thesis	Experimental Method									
rGO-	Chapter 4		Chapter 5			Chapter 6				
	XPS	EDS	Raman	XRD	TEM	Optical	SEM	SAXS	WAXS	Neutron
LOX	✓	✓	✓	✓			✓	✓		
LOA			✓					✓		
LOD	✓	✓					✓	✓	✓	
LOH			✓	✓				✓		
HO3		✓			✓	✓	✓	✓		✓
HO4	✓							✓		
HO7		✓						✓		
HO8	✓	✓	✓	✓			✓	✓		

For all experimental results, each GO solution was reduced with hydrazine in ammonia [15] to produce stable aqueous suspensions of rGO, as detailed in Section 3.1.2. These were then vacuum filtrated to produce the oriented thin films investigated in this work. Table 3 indicates which rGO assemblies were used to obtain the given experimental results in each chapter, while relevant discussion on the choice of rGO samples used provided throughout this section. Following this, the experimental preparation methods and the instrument settings are thoroughly outlined within Section 3.3.2, Section 3.3.3, and Section 3.3.4.

In addition, because a large focus of this thesis is to identify and optimize characterisation methods (experimental procedures and corresponding data analysis), there is a significant amount of discussion included within the results chapters to supplement the content presented in this section. The reader is directed to areas of the thesis titled “[method] applied to rGO assemblies” for more details on the

experimental concepts, which are given in Section 4.2.1, 4.3.1, Section 5.2.1, Section 5.3.1, 5.4.1, and Section 6.3.1.

3.3.1.1 *Chapter 4 rGO materials*

Chapter 4 centres on the chemical composition of rGO sheets, and XPS was used to investigate two low-oxidised and two high-oxidised rGO materials for comparison. Access to the XPS instrumentation was limited, so four materials were chosen for comparison as follows: LOX and HO8, the two materials thought to have the largest difference in oxygen content, were compared along with two materials with more moderate oxidation conditions, LOD and HO4. Further, HO4 was selected to see if there was any measurable difference in the chemical composition of rGO materials that had undergone a longer reaction time during the Step 1 oxidation procedure.

EDS was then used to supplement the results from XPS. While not able to identify the precise bond types available with XPS, EDS was used to determine if the chemical composition was homogeneous as a much larger surface area and volume can be examined with this method. Again, the extreme oxidation conditions of LOX and HO8 were compared with more moderate conditions in LOD and HO3. In addition, the HO7 sample was selected, again to see if there was any measurable difference resulting from the long Step 1 oxidation procedure. Because EDS is less sensitive than XPS, it was thought HO7 would be more likely to show a measureable difference than HO4.

Other than the special case of LOX, for all materials tested in Chapter 4, during the GO synthesis the temperature for both oxidation steps was kept constant, but the reaction time varied.

3.3.1.2 *Chapter 5 rGO materials*

Chapter 5 focusses on the microstructural elements of the rGO sheets and assemblies, and TEM was used to obtain a general physical description of the rGO assemblies, both for its own sake and also to verify the accuracy of results obtained from scattering and spectroscopic methods such as Raman, XRD, and SAXS used to develop the detailed structural models. Because of the significant sample preparation challenges posed for TEM applied to rGO assemblies, only one sample was used to obtain TEM results, and HO3 was chosen because it is most characteristic of a typical rGO material (standard GO synthesis procedures). Specifics about the limitations for TEM with rGO assemblies are discussed in Section 5.2.1.

Raman Spectroscopy was used to compare rGO prepared using variations in the low-oxidised conditions to the extreme high-oxidized conditions of HO8. Again, LOX and HO8 are used to represent the overall range of possible rGO materials resulting from the variations in GO processing. Because Raman is able to quantify the length of the aromatic regions in rGO sheets, as well as indicate the overall defect density for the materials, the low-oxidized materials were most interesting for comparison since they would be used in applications requiring less defective sheets with larger aromatic domains. Thus, results were expected to show if the changes in temperature during Step 2 would have any impacts on the defect density of the rGO materials. In contrast, a material with very small aromatic domains would be expected to result from highly oxidized materials, and the results for HO8 would be indicative of the impacts of longer reaction times. The results of the dry rGO assemblies were compared with two HO4 hydrogels reduced under hydrothermal conditions at 100°C (typical) and 180°C (elevated) in order to determine if there were large differences resulting from hydration and/or reduction temperature.

For the XRD results, LOX and HO8 were again used and then compared to the more moderately oxidized materials of LOH and HO3. Other rGO materials were tested with XRD, but identification of any structural details was limited for all materials other than LOX (discussed in Section 5.4.2), and presentation of results was thus limited to four materials to better simplify the discussion.

3.3.1.3 Chapter 6 rGO materials

Chapter 6 builds on the microstructural elements of rGO assemblies identified in previous chapters to design a meso- and macro-scale model for these materials using direct imaging combined with scattering methods. Optical imaging is presented using HO3-rGO material in order to provide information on the overall macrostructure of the material (similar purpose as that of TEM discussed above at the microscale). For this purpose, HO3 was again used because it serves as a reference for a standard rGO material. Other samples were also tested, but there were no discernible differences at the macroscale, so only results from HO3 are shown in order to simplify discussion and keep the focus on the different features resulting from various drying methods. In addition, EM-rGO materials are used in this section to highlight the macroscale inhomogeneity seen in materials prepared from different concentrations of sulfuric acid.

All reported EM-rGO results were obtained using HO3 or HO4 rGO materials. Various oxidation levels were used to prepare the EM-rGO materials investigated using SAXS, and similar to the optical imaging results, there was no difference detected in materials prepared from different oxidation levels. Thus, these meso- and macrostructural differences are dominated by the electrolyte mediated conditions, not the oxidation level of the GO used, so these materials are referred to only as EM-rGO within the text (excluding reference to HO3 or HO4 precursors).

Both GO and rGO materials were investigated using SEM, and again, there were no detectable structural features that could be attributed to the oxidation levels. While more materials were imaged with SEM, only results for two high-oxidised and two low-oxidized materials are shown (again including LOX and HO8) in order to provide some comparison and report results across a larger total surface area. All four materials are shown in order to demonstrate that the features in the images are characteristic of the material, not individual anomalies from a small, select region.

Since the SAXS results were obtained from a high-flux synchrotron source, data acquisition could be performed in just seconds, which made it possible to examine the entire range of rGO materials and easily report directly comparable data from the reduced scattering curves in a simple graph. This acts as a useful reference because it adds experimental evidence to the claim that there are no meso- or macroscale structural differences resulting from varied GO processing conditions, except for the extreme case of LOX (this is not the case at the microscale). Thus, these SAXS results support the limited reporting of results for the other methods applied in this chapter. Correspondingly, the large amount of SAXS and WAXS data presented on the angular rotation of rGO assemblies and the *in situ* hydration measurements are only reported from the LOD-rGO assembly.

Neutron data takes a very long time to acquire because of the low number of interaction events, so only three samples were tested with these techniques: LOD, HO3, and HO4. Again, there was no detectable difference between any of these materials, and the data reported here was taken using HO3.

3.3.2 Electron microscopy and microanalysis

Scanning electron microscopy (SEM) images and energy dispersive spectroscopy (EDS)

Samples were prepared by cutting small sections from the centre region of the rGO films with a scalpel. These were affixed to an SEM stub using carbon tape only at the edges of the film so that the region of interest would not be impacted by the surface roughness of the tape. The rGO films were thus slightly elevated from the SEM stub (≈ 1 mm) because of the thickness of the carbon tape, and there would be no influence from the aluminium content of the stub in the EDS results. Neither GO or rGO materials were coated prior to imaging. Results were obtained on a FEI Helios Nanolab 600 Dual FIB-SEM with Genesis EDX. All SEM images were taken with low operating voltage of 2 or 5 KeV and a

current of 43 pA. Secondary electrons images were acquired with an ETD or a through-the-lens detector (high resolution) at a working distance of 4.1 mm. The electron and ion beams are offset by 52°. Milling with the FIB was performed using a 30 KeV gallium beam with current of 9.7 pA and a short dwell time of 0.1 us to reduce damage. A thin strip of platinum was deposited at the cut site to reduce curtaining and other potential artefacts, and a cleaning cross section was applied before a finer cut was used to obtain the smooth surface seen in the SEM images of the cross sectional surfaces presented in Chapter 6. The EDS results were obtained at 5 and 10 KeV with current of 86pA and a dwell time of 400 us.

Transmission electron microscopy (TEM)

Samples were prepared by ultramicrotoming 50 nm cross sections using Leica EM UMC7 cryo-ultramicrotome after embedding the rGO assembly in resin. The embedding medium was prepared using a Procure 812 Embedding Kit from ProSciTech Pty Ltd. In this process, a mixture of 5 mL Procure 812 was prepared from mixing 2.25 mL DDSA (dodecenyl succinic anhydride) and 3 mL NMA (nadic methyl anhydride) and then placed in a 60°C vacuum oven for ten minutes and allowed to outgas. The fixative agent of 0.3 mL BDMA (benzyl dimethylamine) was then added, and the mixture was again placed in a 60°C vacuum oven for ten minutes and allowed to outgas where it then turned amber in colour. Thin strips (1 mm) of the pump dried rGO assembly were placed in a fixative well plate and covered with the embedding medium and allowed to cure for 60 hours. Conventional imaging and diffraction analysis were taken using a FEI Tecnai G2 T20 operating at 200 kV with a LaB6 emitter. Images were acquired with an Orius SCD200D wide-angle CCD camera (diffraction capable) and Orius SC600 high-resolution CCD camera.

3.3.3 Photon spectroscopy, diffraction, and scattering

Raman spectroscopy

Samples were prepared by cutting small sections from the centre region of the rGO films with a scalpel. These were laid flat on a glass slide for imaging and data acquisition. Raman spectra were taken on a Witec Instrument 300R with 532 nm excitation wavelength (Si band used to calibrate the wavelength, no instrument broadening). The laser probe with power of 1.25 mW for CCG and 0.40 mW for GO. Actual power at the sample will be 1/8 these values because of objectives and apertures (0.16 mW and 0.05 mW for CCG and GO, respectively). The spot size is 500 nm with approximately 50 nm penetration (for 532 nm wavelength). All scans were taken with a 5 sec integration time. Image scanning area is 21 μm^2 and Raman maps were taken with 70 spots per line.

X-ray photoelectron spectroscopy (XPS)

Samples were prepared by cutting small sections from the centre region of the rGO films with a scalpel. These were affixed to the stub using two mechanical pins, held only at the edges of the film so that sample was held flat and secured against the stub. The pump dried rGO samples used in this work are extremely smooth, and no difference in XPS signal was detected at various regions along the sample surface, indicating surface roughness did not impact the data. Samples were placed into the ultra-low vacuum chamber and all thermal reduction steps were done in the chamber, without removing the samples at any point. The carbon, oxygen, and nitrogen chemical species of the CCG films were characterized by XPS on the Soft X-ray Spectroscopy Beamline of the Australian Synchrotron. Quantitative XPS spectra were obtained at 1486.7 eV and used for elemental composition, while high resolution spectra were taken at 600 eV and used for the spectral line fitting to determine the type of bonding present. A gold standard was used as a reference for calibrating the 600 eV spectra. Valence band scans were taken at 150 eV.

X-ray diffraction (XRD)

Samples were prepared by cutting small sections from the centre region of the rGO films with a scalpel. These were laid flat on a single crystal quartz slide for data acquisition. The single crystal quartz was positioned so no diffraction signal would be produced, which would overshadow the weak signal of the broad rGO peak (note that amorphous material, such as fused quartz, cannot be used). An X-ray reflectometer was used for the results in Chapter 5. A Panalytical X'Pert Pro instrument operating at tube voltage of 45 kV with Cu K α sealed tube source. A slit was used to limit beam divergence to 1/2degree and sample were mounted on a motorised XYZ, Phi sample stage. XRD results were measured across the 2 θ range of 4°-60° with a step size of 0.001 and measurement time of 0.5 seconds per step.

Wide- and small angle scattering (WAXS/SAXS)

Samples were prepared by cutting small sections from the centre region of the rGO films with a scalpel. These were placed in specialized sample holders to allow for structural investigation across a large angular range, as detailed in Section 3.2. More details on sample preparation and conditions of data acquisition are also provided in Section 6.3.2. All WAXS and SAXS data was collected on the SAXS/WAXS beamline at the Australian Synchrotron. There are significant advantages to performing these characterization measurements on this beamline, namely the high flux source and extended q-range. In addition, the small beam size (FWHM of 250 μm horizontal \times 150 μm vertical) allows scattering data to be taken both through the surface and through-the-edge of the thin rGO assemblies. The SAXS/WAXS beamline is capable of utilising X-rays in the range of 5.2 to 20 KeV, and the camera length can be adjusted to optimize the accessible q-range. The results of this work combine three camera lengths and also make use of the ability to adjust the wavelength of the incident beam in order to obtain scattering data from a very large q-range. As shown in Figure 50, settings at location #1 of 0.425 m (20 KeV, $\lambda=0.62$ Å), #2 of 1.529 m (12 KeV, $\lambda=1.03$ Å), and #3 of 7.262 m (12 KeV, $\lambda=1.03$ Å) result in a total q-range of 2×10^{-3} Å $^{-1}$ to 3 Å $^{-1}$. For both WAXS and SAXS data acquisition, the Pilatus 1M detector was used because it offers a much larger solid angle than the typical WAXS detector (seen mounted above the beamline in the top photo). The Pilatus 1M has very low noise, a large dynamic range, and rapid data collection over a large active area. The 2D scattering patterns were acquired in 'gapless mode', where the dead space due to the inter-module gaps of the detector is eliminated by summation of three concurrent images taken with the detector slightly translate (offset). The discussion here is limited because the specifics of the SAXS/WAXS data acquisition and reduction are discussed in much detail within the text of Chapter 6.

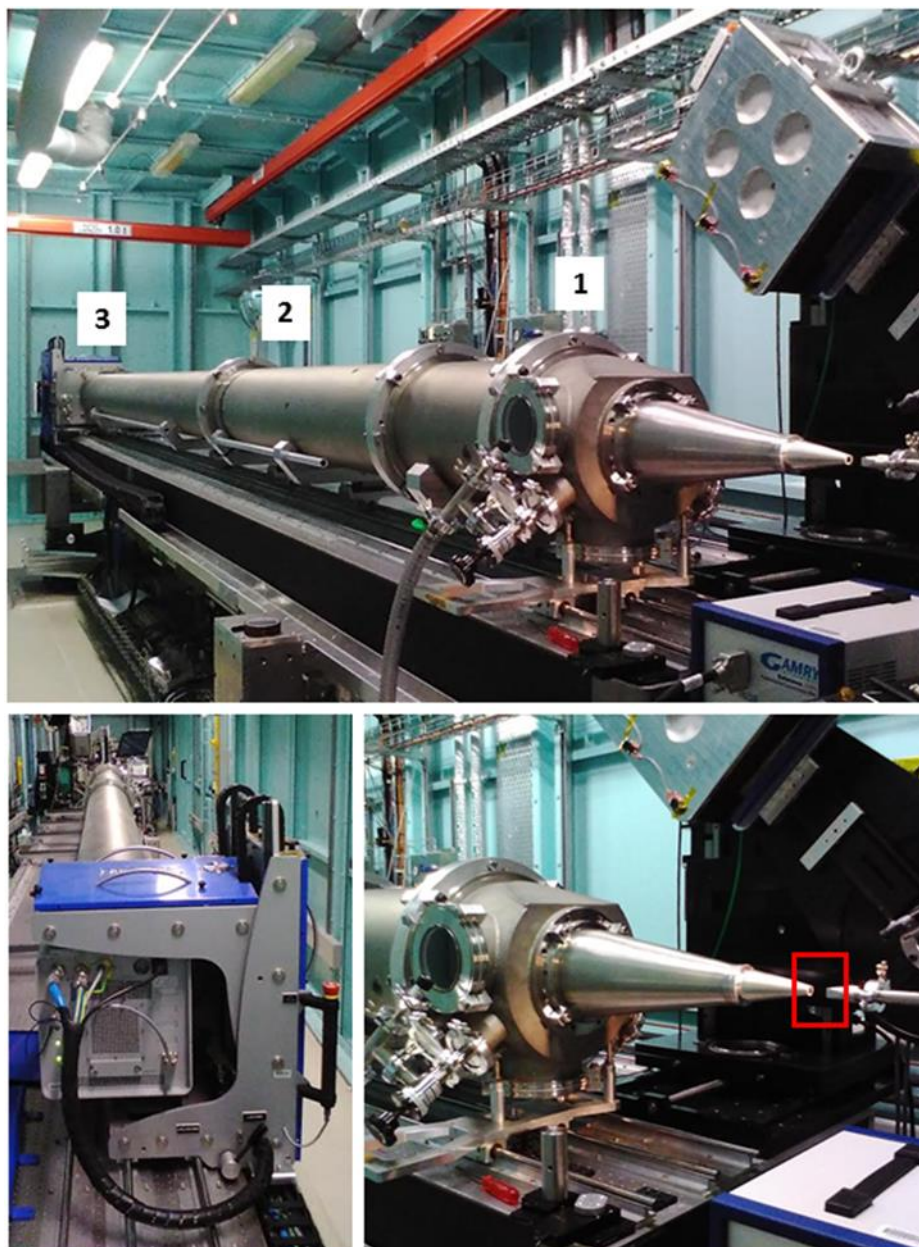


Figure 50. Photographs of the SAXS/WAXS beamline at the Australian Synchrotron. The photos show the configuration for the maximum (seven meter) camera length, with the numbers 1, 2, and 3 (top) corresponding to the three configurations reported in this work. The lower left image shows the back of the Pilatus 1M and the lower right image indicates the region where the sample is placed, with the X-ray beam passing through the sample before entering the nose-cone.

3.3.4 Neutron diffraction and scattering

Samples were prepared by cutting 2-3 cm wide sections from the the rGO films with a scalpel. Due to the small number of interaction events, multiple rGO films were stacked in order to have adequate sample in the beam. The data was adjusted to account for differences in thickness, and accuracy was verified by the fact that the adjusted, absolute scattering intensity for different samples was equal at high q -values (further details provided within Section 6.3.1 and Section 6.3.3). Materials were placed within specialized sample holders designed for each particular beamline.

Neutron diffraction

Neutron diffraction was performed on Wombat, a high intensity neutron diffractometer beamline running off the OPAL Neutron Guide Hall at the Bragg Institute at the Australian Centre for Neutron Scattering (ANSTO) [207]. Vertically focussing Ge 115 and 113 monochromator was configured to deliver a high flux neutron beam with wavelength 2.95 \AA and q -range of $0.9\text{-}4.7 \text{ \AA}^{-1}$ (desirable to

overlap with QUOKKA SANS instrument with q -range up to 0.57 \AA^{-1}). Data is acquired on a continuous detector bank consisting of eight curved panels with no gap between them, producing 120° of continuous coverage. The panels have a spatial resolution of about 1.5 mm, and are 2D position sensitive along the curved and vertical direction. Because the number of scattering events is much lower for neutrons than X-rays, six rGO films were stacked to obtain the neutron diffraction data in order to reduce the necessary acquisition time. The instrument-specific, Gumtree data processing program was used to reduce the data using the 'WombatReductionUI' script. The general reduction procedure first normalizes the frames in the input data file according to monitor counts, subtracts a pre-defined background, applies an efficiency correction, and then sums the resulting frame(s) vertically to obtain a 1D spectral pattern.

Small angle neutron scattering (SANS)

SANS was performed on QUOKKA in the OPAL Neutron Guide Hall at the Bragg Institute at the Australian Centre for Neutron Scattering (ANSTO) [208]. QUOKKA offers a high neutron flux ($4 \times 10^7 \text{ cm}^2 \text{ s}^{-1}$) due to a brilliant cold source, relatively large beam cross-section, and a velocity selector of short rotor length and high transmission. The extended range of the guide-to-sample distance can be continuously adjusted from 1 to 20 m, together with focussing optics, resulting in a tremendous q -range of $6 \times 10^{-4} \text{ \AA}^{-1}$ to 0.7 \AA^{-1} when focusing lens optics are employed. Typically measurements are made using wavelengths of 5 Å or 8 Å, and QUOKKA possesses a large solid angle area detector (active area 960 x 960 mm).

Because of the lower incident flux and weaker interaction of neutrons with matter compared to that of X-rays, six rGO films were stacked to obtain the neutron scattering data in order to reduce the necessary acquisition time, resulting in transmission of 95% (>90% ensures no effects from multiple scattering). A neutron beam of wavelength 5 Å and camera lengths of 20 m (q -range $1.0 \times 10^{-3} \text{ \AA}^{-1}$ to $20 \times 10^{-3} \text{ \AA}^{-1}$), 14 m (q -range $3.6 \times 10^{-3} \text{ \AA}^{-1}$ to $42.6 \times 10^{-3} \text{ \AA}^{-1}$), and 1.3m (q -range $6.8 \times 10^{-2} \text{ \AA}^{-1}$ to $48.0 \times 10^{-2} \text{ \AA}^{-1}$) were used to obtain the SANS results presented in Chapter 6. Only data from scattering through-the-surface of the rGO assemblies was acquired with SANS because the beam size is too large, and rGO assemblies too thin, to make measurements of scattering through-the-edge possible using the neutron beam. Through-the-surface scattering results in an isotropic scattering pattern, and the 2D data from each camera length was firstly normalized for the detector response to a flat scatterer (plexiglass) and then the incident neutron beam intensity, the intensity from a blocked beam subtracted (dark current measurement) and then finally the empty cell scattering (scaled by the transmission). This reduced two dimensional image was finally radially averaged and then combined with the other camera lengths for the continuous data set across the extended q -range. The instrument-specific Gumtree graphical user interface was used to set instrument conditions and collect data, while data was visualized and reduced to an absolute intensity scale using the Igor Pro macros from NIST [209] which has been modified to accept Quokka data. Igor Pro is propriety software published by Wavemetrics Inc.

Ultra-small angle neutron scattering (USANS)

USANS was performed on KOOKABURRA in the OPAL Neutron Guide Hall at the Bragg Institute at the Australian Centre for Neutron Scattering (ANSTO) [210]. The KOOKABURRA instrument significantly extended the small-angle range from that of QUOKKA, with the combination of USANS and SANS at ANSTO allowing for the characterisation of microstructure over 4 orders of magnitude in size (1 nm to 10 μm). KOOKABURRA is based on the classical Bonse–Hart method [211], which consists of using two multiple-reflection crystal systems arranged in a nondispersive geometry to achieve a steep decrease in the tails of the perfect crystal diffraction curves. When a sample is inserted between these two components, small-angle scattering spreads the peak from that of the ideal crystal, and this broadening is representative of the sample material, quantified by the difference between the two rocking curves

of the analyser, with and without sample. As shown in Figure 51, the first crystal (premonochromator) is highly-oriented pyrolytic graphite (HOPG), aligned at a fixed Bragg angle of 45° , to provide neutrons of 4.74 \AA , and the monochromator and analyser channel-cut perfect crystals are silicon with selection of reflection planes Si(111) at a fixed Bragg angle of 49.1° . During data acquisition, the analyser crystal is rotated and data is collected at one value of q at a time, with this point-by-point measurement being performed in discrete angular steps, making the raw data one-dimensional (compared to that of the 2D detector images which are subsequently reduced).

Again, because the number of scattering events is much lower for neutrons than X-rays, six rGO films were stacked to obtain the neutron scattering data in order to reduce the necessary acquisition time, resulting in transmission of 98% (>90% ensures no effects from multiple scattering). Using the Si(111) reflection, a neutron beam of wavelength 4.74 \AA was used to acquire data shown in Chapter 6, resulting in the extension of the q -range down to $3 \times 10^{-5} \text{ \AA}^{-1}$. USANS measurement has excellent horizontal resolution but very poor vertical resolution and results in a slit smearing [211] which is a particular type of instrumental convolution [212]. The smeared data could be simply fit as-is by using smeared models [209], but because it is desirable to link the USANS data to that of SANS, the desmearing process accounts for the different effects for slit-smeared USANS and pinhole-smeared SANS data, allowing data sets taken from the different instruments to be combined on one scattering curve. Desmearing of the USANS data was done using the NIST IGOR macro [209] which is based on Lake's iterative method [213].

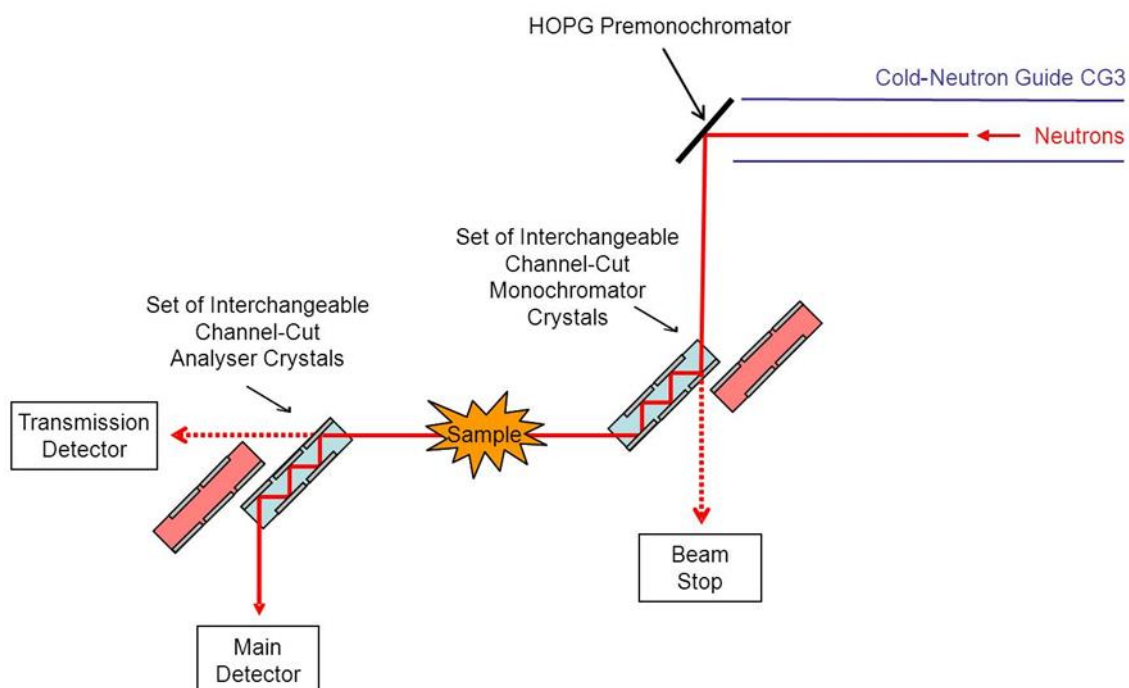


Figure 51. Diagram of the multiple-reflection crystal system used in the KOOKABURRA USANS instrument at ANSTO (from [210]).

3.4 SAS Data Treatment

Specific parameters and theoretical approach to the X-ray and neutron scattering data are detailed in Chapter 6. The main programs used to reduce the 2D data from the scattering images were site-specific, with *Scatterbrain* being developed by the SAXS/WAXS beamline at the Australian Synchrotron and Gumtree control system coupled with the IGOR Pro macro for reduction and desmearing developed by NIST [209]. Model fitting to the SAXS data was performed using SASfit [214].

Chapter 4. The Chemical Structure of GO and rGO Sheets

4.1 Introduction: Chemical Composition of GO and rGO Sheets

Each batch of prepared GO can vary greatly in both the sheet length and chemical composition. Since it is these sheet-like particles that become the building blocks for the dried and hydrogel rGO assemblies, it is necessary to ascertain how the chemical composition and structural features of the GO precursor impacts the resulting rGO bulk materials, if it is intended to have some control over the resulting material performance. Regardless of the processing methods employed, these particulate systems result in a statistical distribution of properties, with a range of chemical compositions and sheet sizes. While exact parameters for individual rGO sheets are not representative of the bulk assembly, as would be the case for a typical polymer or crystalline material, understanding statistically significant parameters that influence the resulting rGO properties, structure, and chemical composition are of great importance in the field. For example, a typical dried film with thickness of 4 μm and inter-sheet spacing of 4 \AA equates to a total of 10,000 rGO sheets stacked within the plane, illustrating the complexity of this layered system which is dependent on the structure and chemical composition of each unique rGO sheet. A thorough analysis to determine the chemistry and electronic structure of the rGO sheets is necessary in order to go forward with interpretations of performance in the bulk porous assembly.

The specific objectives of this chapter are thus to: determine the atomic concentration of carbon, oxygen, and nitrogen in different rGO samples; investigate if the original GO precursor has an impact on the chemical composition of the resulting rGO; and attempt to reveal connections between specific oxygen and nitrogen functional groups and the aromatic domains (sp^2/sp^3 ratio) within the rGO sheets. To these ends, high resolution XPS was used to determine the precise concentration and type of carbon, oxygen, and nitrogen bonds present on the surface and edges of rGO films prepared from GO synthesized with variations in temperature and reaction time, which are thought to impact the degree of oxidation [57, 58]. The evolution of both nitrogen and oxygen species in rGO will largely depend on reduction conditions and temperature. Thus, changes in these chemical groups were monitored after further thermal reduction in order to evaluate the impact additional removal and/or evolution of oxygen and nitrogen groups has on the sp^2/sp^3 carbon bonds. As discussed in the Literature Review (2.1.2.1), there is a range of debate regarding the type of nitrogen bonding present in hydrazine reduced rGO, and the results presented in this work highlight the limitations of assigning a distinct species based on the results of XPS alone. Since XPS is a surface analysis technique (with a penetration depth ≈ 10 nm), energy dispersive X-ray spectroscopy (EDS or EDX) was also employed to quantify the elemental content to depths of over 1 μm and look for variation within the bulk rGO assembly.

4.2 X-ray Photoelectron Spectroscopy

4.2.1 XPS applied to rGO assemblies

X-ray photoelectron spectroscopy (XPS) is a commonly-used surface analysis technique to allow for the identification of the elements within a material and the type of bonding present [215]. It has the added advantages of high resolution and quantification for light elements, with carbon, oxygen and nitrogen content being easily assessed. Elements present in the surface region of a sample will produce unique peaks on a full spectral scan, across all binding energies (0 to 1500 eV) and these peaks can be used to quantify the chemical species present. Once these elements are identified, high resolution scans can then be used to retrace the peaks from the full spectral scan to discern a precise peak shape that relates to specific bonds for a given element.

Table 4. Chemical species present in rGO and the corresponding binding energy (BE) for the peak centre assigned to that particular bond as measured by XPS.

Bond	BE	Comments on Peak Parameters
Carbon		
C-C sp ²	284.5 eV	Peak fit with Donald Sunjic function
C-C sp ³	285.0 eV	Disordered sp ³ bonds broaden C-C peak
C-N C-OH Hydroxyl	285.8 eV	Similar binding energies are combined into one peak (C-N 285.9 eV and C-OH 285.5-285.7 eV)
C-O-C Epoxy	286.7 eV	Literature range 286.3-286.7 eV
C=O Carbonyl	287.8 eV	Literature range 287-288 eV
C(O)OH Carboxyl	288.9 eV	Literature range 288.9-289.1 eV
π-π* satellite	290.4 eV	Broader satellite feature from sp ² C-C bonds
Oxygen		
C=O Carbonyl	531.0 eV	Oxygen doubly bonded to aromatic carbon
C(O)OH Carboxyl C-O-C Epoxy C-OH Hydroxyl	532.2 eV	Oxygen singly bonded to aliphatic carbon
C-OH Phenol	533.4 eV	Oxygen singly bonded to aromatic carbon
Chemisorbed Water	534.7 eV	None was present in the samples
Nitrogen		
N1	398.7 eV	Two-coordinated and bound to at least one sp ² carbon
N2	399.9 eV	Three-coordinated with sigma bonds (sp ³ carbon)
N3	401.1 eV	Quaternary nitrogen/substituted at graphitic site
N4	402.7 eV	Nitrogen oxides

The high resolution XPS spectra for C1s, O1s, and N1s regions is particularly useful in analysing bonding in rGO films because it can distinguish the type of carbon bonds present in the material, making quantitative analysis of both sp²/sp³ carbon content and residual oxygen groups possible. The type of bonding present in rGO depends on both the initial oxidation conditions and the reduction process. In this work the rGO materials are reduced using hydrazine, ultimately exhibiting the possible bond configurations outlined in Table 4. It should be noted that fitting high resolution XPS spectra in GO and rGO materials is highly subjective, and due to the overlapping nature of the peaks, the assignment of specific chemical species is dependent on the choice of parameters applied to the peak fitting. Much of the current literature draws conclusions about rGO performance based on XPS data, yet complications arise from conflicting reports for peak placement and variations in fitting methods applied with studies on GO- and rGO-based materials [66, 69, 71, 73, 216]. Due to this uncertainty, the results presented here include a detailed discussion about the method used for peak fitting with the logic behind this explained in detail, resulting in an accurate and reproducible assessment of specific oxygen and nitrogen bonding present in the rGO materials. Table 4 lists the peak placement applied in this work, with the values for binding energy being based on the peak profile of these XPS results, extensive literature review of rGO XPS spectra [66, 69, 71, 73, 81, 93, 94, 96, 97, 100, 216-218], and knowledge of existing structural models for GO and rGO, as outlined in Section 2.1.2.1.

The valence band (VB) for rGO assemblies is also evaluated in order to gain insight on the conductivity and reactivity differences resulting from the varied elemental content measured in the full spectrum and high resolution XPS scans. The VB scan is a complex composite spectra consisting of many overlapping component peaks. It is commonly referred to as the “signature” or “fingerprint” for a material, and for carbon-based materials, the region below 20 eV is the main area of interest. Due to the complexity of factors contributing to slight peak shift and the fact that spectra for oxidized or doped carbons is highly dependent on the atomic composition [219], it is not possible to quantitatively evaluate bonding using the VB spectra alone. As the precise peak placements are highly convoluted and depend on the excitation energy used, VB spectra are unlike the typical XPS results in that they cannot directly be compared with standards. However, combining other knowledge about the material composition, changes in the shape of the valence band and analysis of the unique “signature” can be used to qualitatively evaluate binding affinities in the material. Further, the VB can be directly related to density of states (DOS) calculations and the band structure of materials [66, 219, 220], providing further insight on how chemical differences will impact performance, especially in regard to resistivity and reactivity.

4.2.2 Results and discussion

4.2.2.1 *Full spectral scan results*

The spectral scans shown in Figure 52 are from rGO assemblies prepared from GO that was synthesized to produce sheets with various oxidation degree, as outlined in Chapter 3 (Methods and Materials). The area of each carbon, oxygen, and nitrogen 1s peak was used to produce the quantitative atomic percentage comparisons for each rGO assembly, as listed in Table 5. The oxygen content in the as-prepared rGO assemblies is similar to that reported from high temperature thermal reduction [69], and shows the hydrazine method used here was effective in reducing most oxygen species, without the need for high temperatures.

The results of the full spectral scans clearly show that the synthesis conditions for the original GO precursor has a significant impact on the resultant rGO materials. Data from Figure 52 is listed in Table 5 and shows that both high oxidized (HO-) samples contained less than 90% carbon before further thermal reduction, while both low oxidized (LO-) samples had an initial carbon content above 90%. Both of the high oxidized samples contain the same amount of oxygen ($\approx 11\%$) which is almost twice that of both low oxidized samples ($\approx 6.5\%$). Even after heating to 550°C , the only sample that was able to achieve high purity ($>95\%$ carbon) was the rGO prepared from the extra low oxidation GO precursor (LOX). Nitrogen is the least prevalent atomic species, but it is also the most variable between samples and is not directly related to the overall residual oxygen content.

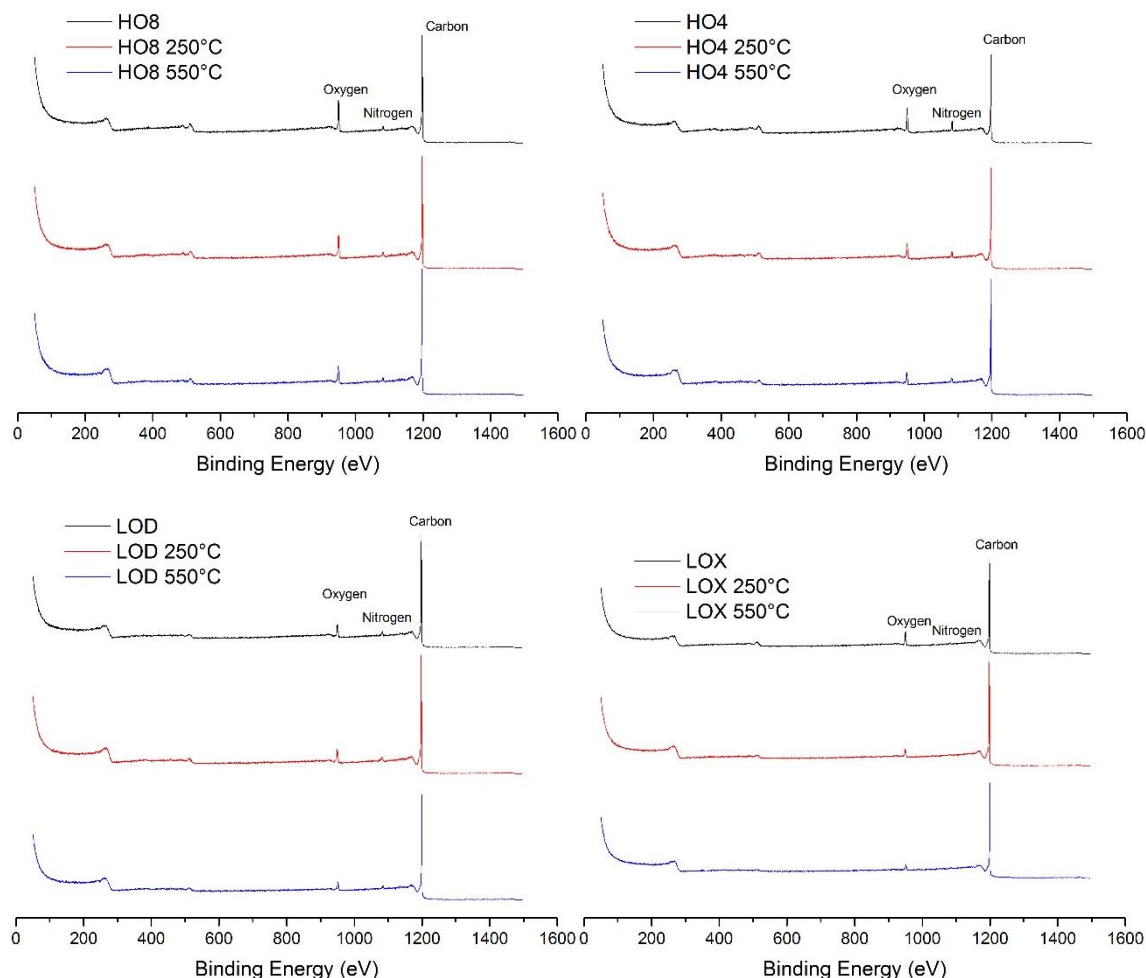


Figure 52. Full spectral scans at 1486 eV of rGO at room temperature, 250°C and 550°C showing the prevalence of oxygen functional groups on GO of varying oxidation levels. Each scan shows characteristic peaks for oxygen, nitrogen and carbon.

On initial inspection, this indicates that during the GO synthesis process, the temperature as well as the time for both oxidation processes will carry over to strongly impact the resulting rGO chemical composition. Section 2.1.2.1 of the Literature Review discussed the structure of GO and rGO sheets and outlines the oxidation process as described by Kang et al. [57]. *Step 2: hydrolysis* is suspected to result in significantly larger defect density when the time and temperature in this step is increased. The results here show that this also translates to more residual oxygen content remaining in the resulting rGO after reduction. This is likely to be due to the prevalence of exposed edges (from higher defect density) where oxygen functional groups most resistant to the initial hydrazine treatment are found. In addition, *Step 1: oxidation* was much longer for HO4, and the published work showing that over-oxidation leads to increased epoxy and hydroxyl groups with an enhanced epoxy to hydroxyl ratio [68] offers an explanation for the higher nitrogen content in this sample when these changes in GO chemical composition are then related to the knowledge of the hydrazine and ammonia reduction process presented in detail within Section 2.1.2.1. It is thought that the reaction mechanism for nitrogen doping in hydrazine-reduced GO can be attributed to interactions with epoxy groups [71, 73, 76, 79, 80], with additional impacts from ammonia reacting with acidic groups [87, 90, 96]. In this case, the prolonged, eight hour over-oxidation conditions from *Step 1: oxidation* would be expected to increase epoxy content which could be the cause of increased nitrogen content in the HO4 assembly.

Table 5. Elemental composition and corresponding atomic percentage of each rGO assembly as determined by XPS full spectral scans. Results for the material in the original state is compared to that after further thermal reduction at 250°C and 550°C. Standard deviation in atomic percentage is 2% for carbon, 0.5% for oxygen, and 0.6% for nitrogen. The carbon to oxygen ratio (C/O) is also presented to compare with EDS data presented in the next section.

<i>Sample</i>	<i>C1s</i>	<i>O1s</i>	<i>N1s</i>	<i>C1s %</i>	<i>O1s %</i>	<i>N1s %</i>	<i>C/O Ratio</i>
<i>Original</i>							
<i>HO8</i>	1	0.1292	0.0347	86	11.1	3.0	7.7
<i>HO4</i>	1	0.1279	0.0625	84	10.7	5.2	7.9
<i>LOD</i>	1	0.0683	0.0253	92	6.2	2.3	15
<i>LOX</i>	1	0.0725	0.0112	92	6.7	1.0	14
<i>250°C</i>							
<i>HO8</i>	1	0.0998	0.0186	89	8.9	1.7	10
<i>HO4</i>	1	0.0746	0.0396	90	6.7	3.6	13
<i>LOD</i>	1	0.0606	0.0292	92	5.6	2.7	16
<i>LOX</i>	1	0.0424	0.0071	95	4.0	0.7	24
<i>550°C</i>							
<i>HO8</i>	1	0.0699	0.0141	92	6.4	1.3	14
<i>HO4</i>	1	0.0563	0.0303	92	5.2	2.8	18
<i>LOD</i>	1	0.0421	0.0161	95	4.0	1.5	24
<i>LOX</i>	1	0.0251	0.0018	97	2.4	0.2	40

Using thermal reduction to better ascertain what type of residual oxygen groups are most prevalent and persistent in rGO indicates that major differences can be seen in the type and concentration of oxygen functional groups relative to the GO precursor. The progressive reduction of the rGO assemblies can be seen more clearly in Figure 53. The rGO samples were heated to 250°C and then 550°C under vacuum to assess the impact that further thermal reduction has on existing oxygen and nitrogen functional groups, as well as monitoring changes in sp^2/sp^3 carbon bonding. As discussed in Chapter 2, the oxygen groups along the edges are much more strongly bound than those along the basal plane. Knowing that the initial reduction conditions of hydrazine treatment at 100°C will act mostly to reduce epoxy groups (a chemical reaction with hydrazine) and carboxyl groups (low temperature thermal reaction) [73, 76], it is of interest to determine which oxygen groups persist in rGO and if this can be effectively modified through further thermal treatment. Previous work [66] has shown that significant changes in basal-plane oxygen functionalities occur within the temperature regions applied here, specifically a large mass loss at 250°C and 550°C attributed to: i) reduction temperatures between 200-400°C quickly reduce carboxyl and epoxy, while concurrent formation of additional phenol groups on the basal plane can occur due to the close proximity of epoxy and hydroxyl groups and ii) reduction temperatures between 400-600°C further remove carbonyl moieties and some hydroxyl, yet many hydroxyl groups will persist even up to 1000°C.

The extra low oxidation sample (LOX) had a significantly lower level of nitrogen doping occur during the reduction process. While results show the initial GO oxidation level could impact the amount of nitrogen doping that occurs, this cannot be confirmed with the limited sample set and is contradicted by HO8 and LOD having very similar nitrogen concentrations. This makes it clear that a measure of the total oxygen content alone is not sufficient to explain the nitrogen species present. Results of the specific bonding with the rGO assemblies, as determined by the high-resolution XPS results, are also required. A typical nitrogen concentration of 3% is found in rGO that has been reduced with hydrazine

or doped separately using chemical and thermal processes [221]. HO8 and LOD follow this trend, but HO4 and LOX have significantly higher and lower levels, respectively. Literature reports vary in the assessment of which type of nitrogen doping occurs in rGO, and depending on the type of bond, the nitrogen content may or may not diminish upon further thermal treatment [76, 79, 91, 95, 96, 99, 100, 222]. The results presented here show that nitrogen groups are removed from the rGO at temperatures below 250°C, indicating they are not strongly bound. Accurate determination of the nitrogen bonding is important because this has significant impacts on the conductivity of the rGO sheets and resulting assemblies. For example, the bond type and location of the nitrogen (basal plane or edge) is the main determinant of enhanced capacitance for N-doped rGO supercapacitors and catalysis [84, 222-224].

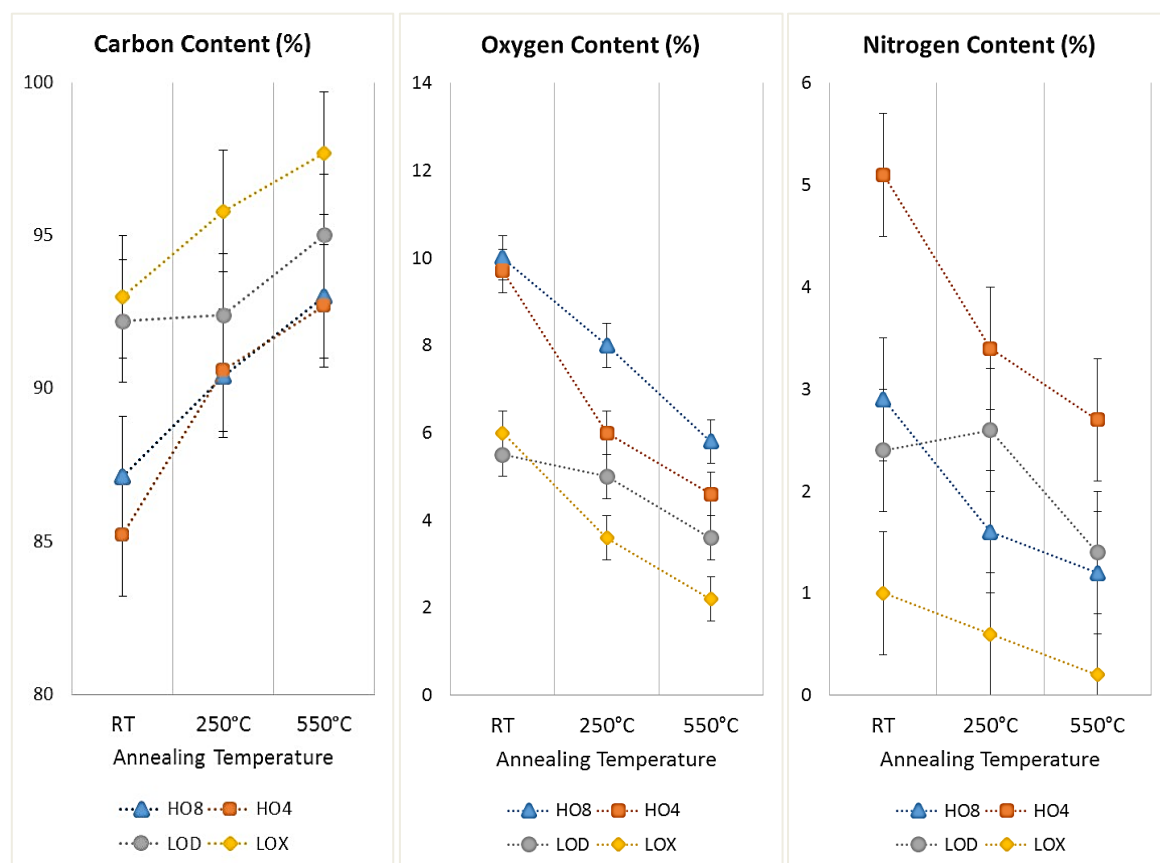


Figure 53. XPS results from the full spectral scan, showing changes in elemental composition as rGO is further reduced at high temperatures.

Both the high and low oxidation samples follow the expected trend of decreased oxygen content after exposure to higher thermal reduction temperatures, demonstrating that all rGO samples can be further reduced. In general, there was an average of 3% decrease in functional groups for each temperature step, with two exceptions: (i) the HO4 sample had an initial nitrogen content much higher than that seen in other samples and showed a greater loss of functional groups upon heating to 250°C; (ii) the LOD sample showed very little loss of functional groups upon heating to 250°C. Because specific functional groups are removed at different temperatures, these slight differences in oxygen and nitrogen content after further thermal reduction requires a more quantitative assessment of exactly what functional groups are present in rGO assemblies and how they impact bonding within the carbon matrix. This determination of the specific species present can be obtained by investigating differences in the binding energy within the carbon, oxygen, and nitrogen high resolution XPS spectra, and is discussed below.

4.2.2.2 High resolution scans of C1s, O1s, and N1s regions

4.2.2.2.1 Details of the high resolution peak fitting procedure

Figure 56 to Figure 60 show high resolution C1s (a), O1s (b), and N1s (c) XPS results and peak deconvolution for the rGO assemblies. As mentioned, correct quantitative analysis of the XPS results is highly dependent on the profile fitting applied to the spectra, and thus a detailed discussion on the parameters is provided here. Additional speculation has been minimized by rigorous cross-referencing with the literature to determine that changes in peak parameters follow known trends, while also tracking any changes across the different 1s spectra for each given bond during the peak fitting procedure. Even after considering that there will be unavoidable discrepancies in the precise deconvolution scheme applied, the results clearly confirm major trends that correlate the specific functional groups and sp^2/sp^3 carbon with the original GO processing condition. This knowledge, along with the details on further thermal reduction process in rGO, does give much insight and assists in answering the persistent research questions related to the performance of rGO materials.

Unless otherwise mentioned, the fitting procedure was constrained to yield equivalent FWHM values of 1 eV for all species except for the highest energy C1s bond for C-O(OH), which broadened slightly to 1.3 eV. The specific peak positions held constant for all profiles (peaks centred at the binding energies indicated in Table 4), with standard deviations less than 0.10 eV for C1s spectra and 0.17 eV for O1s and N1s spectra. With the exception of the carbon-carbon peak, all spectra were deconvoluted using a Voigt peak shape with Gaussian–Lorentzian components (70:30) after performing a Shirley background subtraction using CasaXPS.

The only exception to the Voigt (70:30) line shape is seen in the C1s carbon-carbon peak which, after extensive review of literature and fine adjustment to these peak parameters [216, 225], was broken into three different components.

- I. The carbon sp^2 peak was fitted with a Donald Sunjic function (DS), with an asymmetry parameter of 0.04 and convolution width of 210 centred at 284.5 eV. The DS peak shape parameters were determined by fitting an XPS high resolution scan of highly oriented pyrolytic graphite (HOPG) taken on the same beamline, as shown in Figure 54. The DS peak shape is far superior to a pure Voigt-type function and yields the best fit for the main carbon sp^2 peak. The only deviation between the DS fit and the carbon data is at the higher binding energy asymptote (above 286.5 eV), which somewhat overestimates this region of the line profile and is a probable cause for the slightly low estimates of C-O(OH) bonding, which is discussed later in this section.
- II. Fitting the carbon-carbon peak of the rGO with a DS profile alone was not sufficient for rGO assemblies because it characterizes the ordered, aromatic bonding within the carbon layers. The high level of disorder and presence of defects in rGO creates a second component to the carbon-carbon peak that is not related to pure, flat aromatic layering. As with other porous and layered carbons discussed in the Literature Review, the oxygen groups, corrugation, and edges disturb the sp^2 structure; thus, the peak also contains a significant contribution from disordered carbon and sp^3 bonding. The fitting process was optimized by adding an additional peak at 285 eV with adjusted Gaussian–Lorentzian components (10:90) with an exponential blend factor for tail broadening of 1.6 to account for the disordered carbon component of the profile.
- III. Finally, a $\pi-\pi^*$ satellite feature (often referred to as the sp^2 shake-up peak in the literature) was added at 290-291 eV with a broadened FWHM of 2 eV. This peak is only seen in graphite-like less defective rGO materials and is directly related to prevalent aromatic domains.

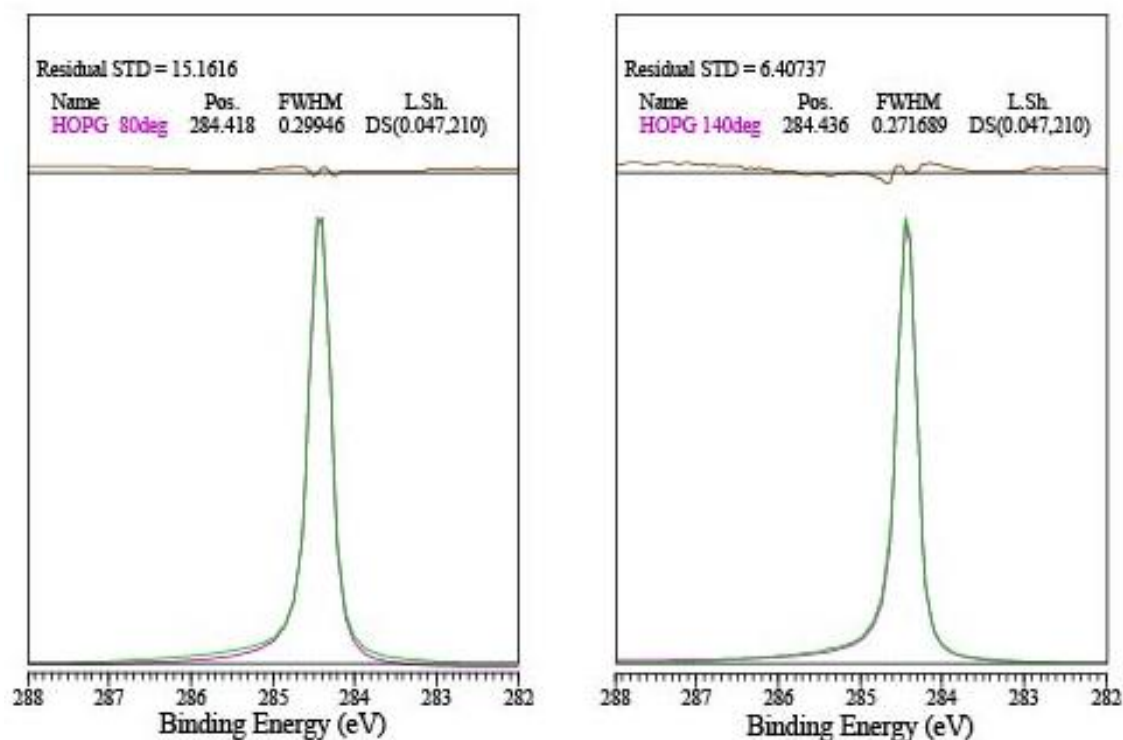


Figure 54. XPS high resolution scans for HOPG, at 80° and 140° with respect to the analyser, yield an ideal carbon sp^2 signal that was used to optimize the C1s peak fitting procedure for the rGO materials using a Donald Sunjic (DS) function.

Despite slightly differing reports in the literature, this work follows the most straightforward and generally accepted deconvolution scheme for O1s core level for all rGO assemblies, which suggests the three components at 531.0, 532.2, and 533.4 eV. Thus, the lowest binding energy corresponds to doubly-bonded oxygen (carbonyl) and other components at higher BE corresponding to singly-bonded oxygen. This second category can be further broken into the two different components of oxygen groups bound to aliphatic carbon (which include carboxyl, hydroxyl, and epoxy) or oxygen groups bound to aromatic carbon (from basal bound phenol). The shape of the O1s profile of rGO matches well with this fitting method, showing distinct changes in peaks assigned at these values that follows the main trends of thermally reduced GO [66, 69]. Further, the O1s peak components were combined with results from the atomic concentration determined in the full spectral scan to ensure the low intensity, overlapping carbon-oxygen bonds in the C1s spectra were accurately apportioned.

Assignment of the nitrogen peaks was based on XPS databank assignments [226] and a detailed literature review. A main peak at 400 eV is typically dominant in almost all nitrogen containing carbonaceous solids [94] and is consistent for nitrogen in an sp^3 bonding environment, which can be associated with both pyrrolic and amine forms [93, 101], making precise chemical determination difficult [227]. Often, pyrrolic-N formation is attributed to nitrogen doped graphene [77, 83, 91], but the 400 eV peak has also been attributed more broadly to “pyrrole-like” species [82, 100], and has been more thoroughly characterized as an “amine-like” pyrazoline in rGO reduced with hydrazine [79-81]. Analysis of chemical pathways based on calculations for reaction mechanisms and computer models predict the formation of hydrazino alcohols and/or amino aziridine [71, 76]. The ammonia used during the reduction process is also known to react with GO, where the oxygen groups act as strong binding sites [90]. Further, in rGO reacted with ammonia or urea, nitrogen content has been attributed to amine, amide, and imide [86, 95] which can then undergo dehydration to pyridine or pyridine [87]. These amine-like groups have also been shown to be prevalent in carbon fibers reacted with ammonium ions at the carbon surface [98].

Reference to these bond types and methods of formation in rGO was discussed in the Literature Review (Section 2.1.2.1), and many of the possible nitrogen-carbon bonds shown there are coupled with the corresponding binding energies shown in Figure 55. This highlights the impossibility of assigning a specific nitrogen group based on the position of the XPS peaks alone [99].

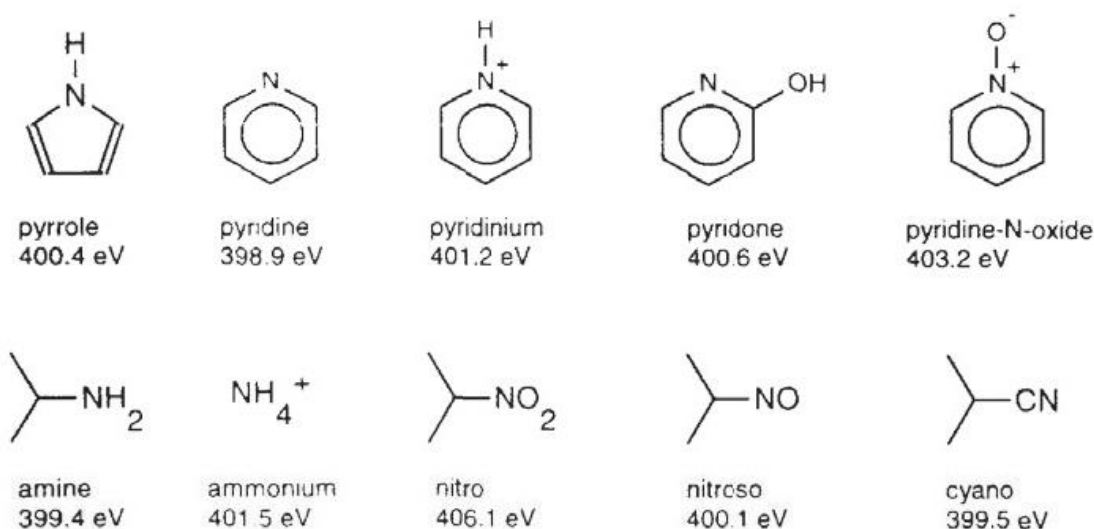


Figure 55. Nitrogen functional groups typically present in carbonaceous materials and the corresponding binding energy, highlighting the impossibility of assigning unique species based on the peak position alone. Reproduced from [99].

The formation of both nitrogen and oxygen bonds in rGO will largely depend on reaction conditions and temperature, and knowledge of this can be used to help distinguish which species is present. Jansen et al. [96] used XPS to study the surface groups on several types of nitrogen-containing activated carbons. This work showed that amide, amine, imide and lactams are the principal nitrogen-containing groups at low temperatures (< 400°C), while at high temperatures, nitrogen groups that are incorporated into the aromatic surface structure of the carbon (pyridine- and pyrrole-type groups) are more abundant and remain stable up to 900°C. Further, amides were shown to be rather unstable and converted to pyrroles and pyridine or decomposed at temperatures above 400°C. The main XPS peak at 400 eV is associated with lactam, imide, and/or amine, and the loss in total nitrogen content combined with a change in peak shape, showed these species decompose and/or convert to more stable structures during a temperatures increase from 200°C to 400°C.

For the peak assignments for the N1s data presented here, the convention outlined by Titantah et al. [217] has been used because it is very flexible for use in different types of carbon materials and is discussed in context to the nitrogen atom bonding environment for clarity, as reported in Table 4. These peak assignments match well with the various bond types for specific nitrogen functional groups reported in literature and discussed above, but allow for greater flexibility during the data presentation, leaving the specific groups to be discussed after the presentation of results. Here, the main N1s peaks occur at ≈ 398 -399 eV (labelled as N1) for a nitrogen that is two-coordinated and bound to at least one sp^2 carbon, ≈ 399 -400 eV (labelled as N2) for a nitrogen that is three-coordinated with sigma bonds (bound to sp^3 carbon), ≈ 400 -402 eV (labelled as N3) for a quaternary nitrogen such as ammonium ions or a three-coordinated nitrogen substituted at a graphite site (graphitic), and ≈ 402 -403 eV (labelled as N4) for nitrogen oxides. The fitting method made a slight adjustment to the nitrogen oxide assignment of Titantah, instead adopting the peak assignments from publications on rGO [81, 101] and activated carbon [93]. In any case, the contribution from nitrogen-oxygen bonding was very small (less

than 0.5% of overall bonds which is detectable), and is not quantifiable within the error bounds of these measurements), so it has been largely ignored in further analysis.

4.2.2.2.2 Presentation of high resolution XPS scans

Firstly, a comparison of each rGO material in its original state at room temperature is shown in Figure 56. Some general features of the materials are noticeable, with the most obvious being that the sp^2 carbon content is much higher for rGO assemblies made from the low oxidized GO precursor, and results indicate the aromatic regions along the rGO sheets are better preserved and contain less defects when prepared from LO-GO, compared with those reduced from HO-GO. Comparing HO- and LO- materials, a major difference appears in the carboxyl feature in the C1s spectra which is much more prevalent in the HO- materials, and suggests that the prolonged reaction time in *Step 2: hydrolysis* allows for more carboxyls to remain in the rGO, again indicating that more edges and defects are present.

Looking at the O1s spectra for LO- materials, there is a fairly even distribution of oxygen functional groups that follows a ratio of $\approx 25:40:35$ for C=O, C-O(OH), and C-O bonds present. This suggests that rGO prepared from LO-GO precursors will result in a well predicted and stable distribution of specific oxygen groups. Conversely, while both high oxide samples, HO8 and HO4, have the same overall oxygen content, the high resolution scans show distinct differences in the type of functional groups present. The HO4 material exhibits unique features when compared to the other samples, with spectra showing a much higher contribution from phenol, epoxy, hydroxyl, and C-N bonds, further supporting the idea that the distinct processing conditions of prolonged time in *Step 1: oxidation* used to prepare HO4-GO strongly impacts both the basal bound phenol and epoxy/hydroxyl content as well as the resulting nitrogen doping. It can also be seen from the N1s spectra that the nitrogen bonding is dominated by the 400 eV feature in all samples, regardless of the initial oxidation conditions.

The successive figures follow changes in the high resolution spectra for HO8 (Figure 57), HO4 (Figure 58), LOD (Figure 59), and LOX (Figure 60) after heating to 250°C, and then 550°C. The results of the nitrogen, oxygen, and carbon bonding are then discussed in the corresponding sections below.

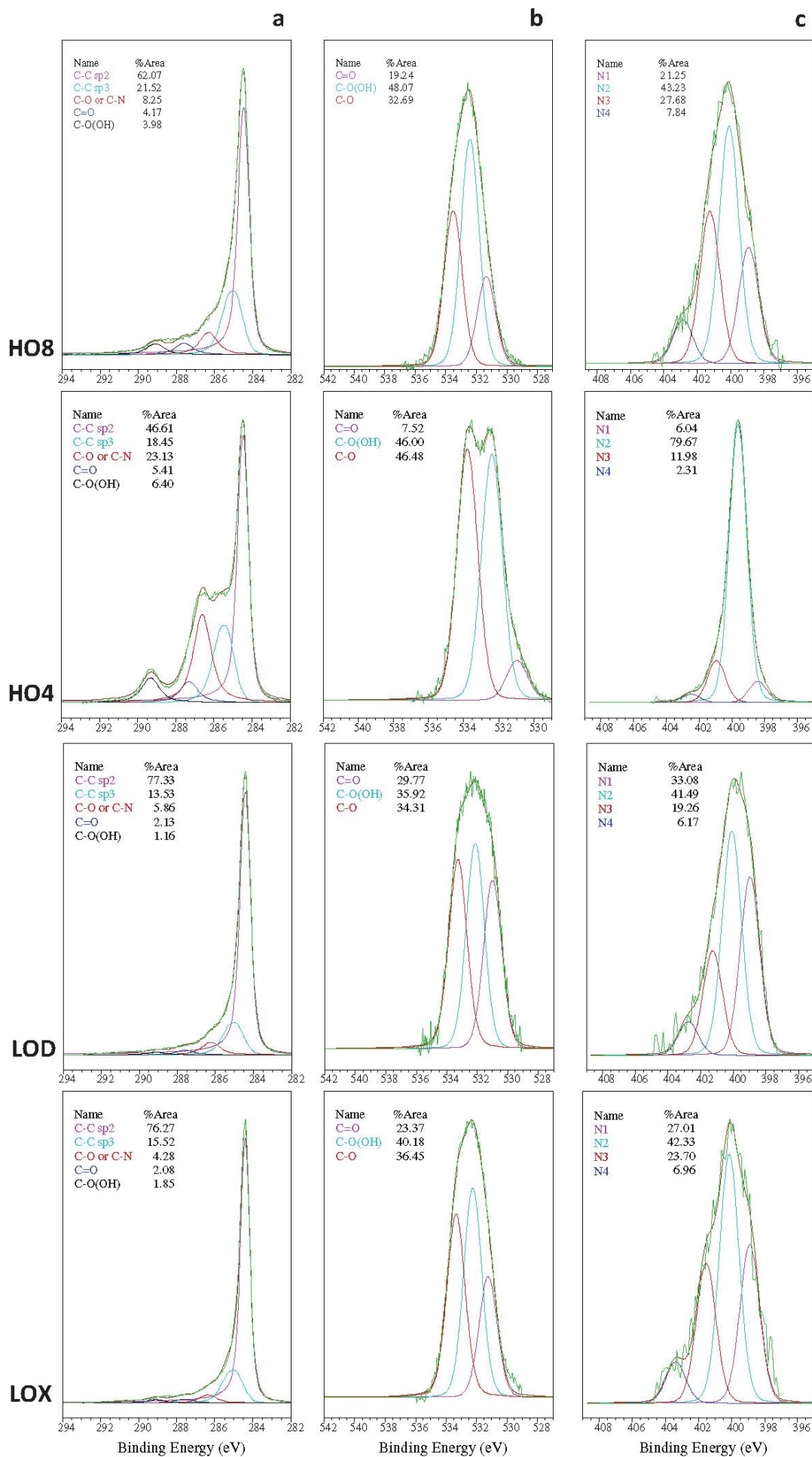


Figure 56. High resolution C1s (a), O1s (b), and N1s (c) XPS results and peak deconvolution showing the percent area for each bond type within the rGO samples HO8, HO4, LOD, and LOX at room temperature.

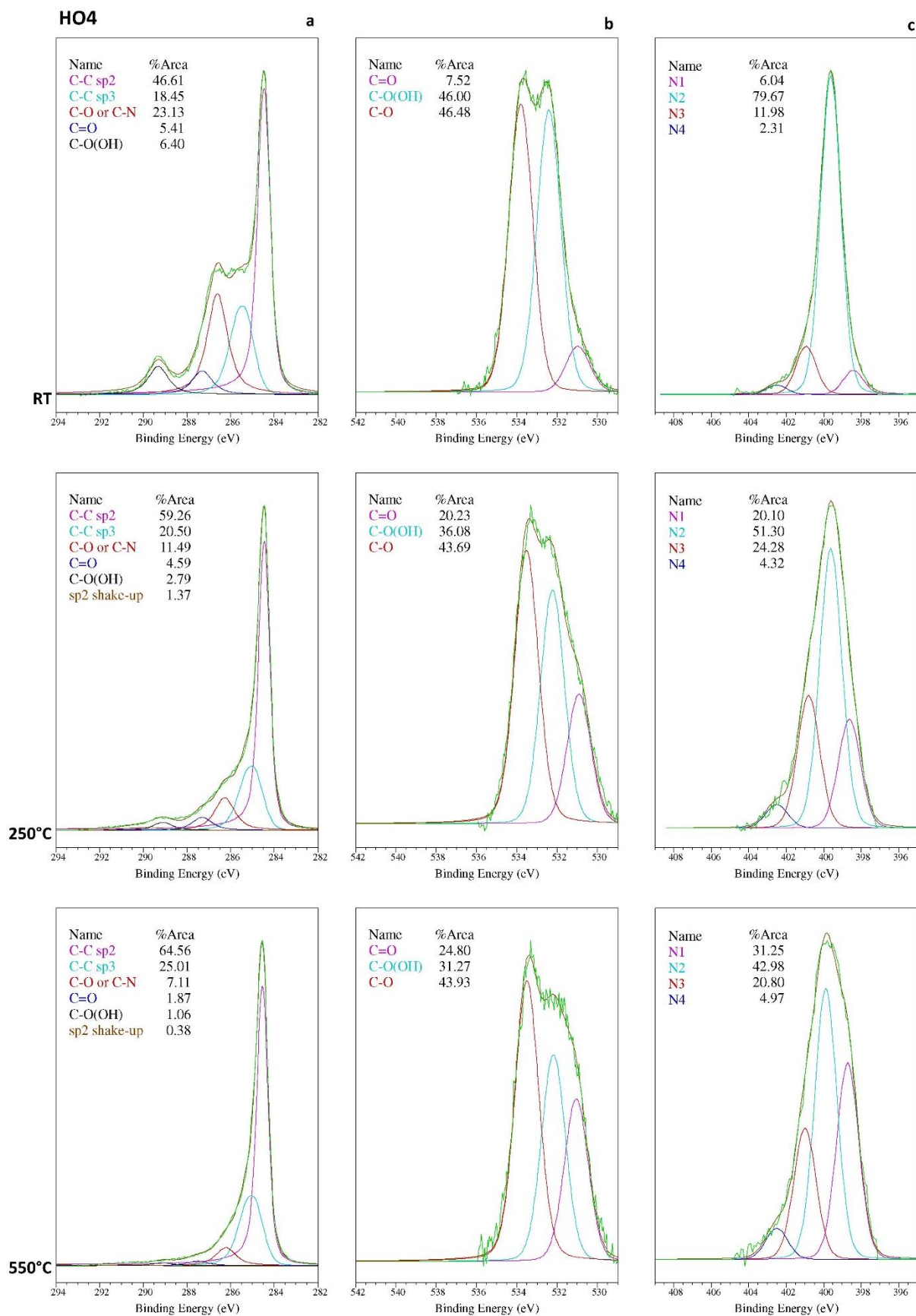


Figure 58. High resolution C1s (a), O1s (b), and N1s (c) XPS results and peak deconvolution for rGO sample HO4 at room temperature (RT) and after further thermal reduction at 250°C and 550°C.

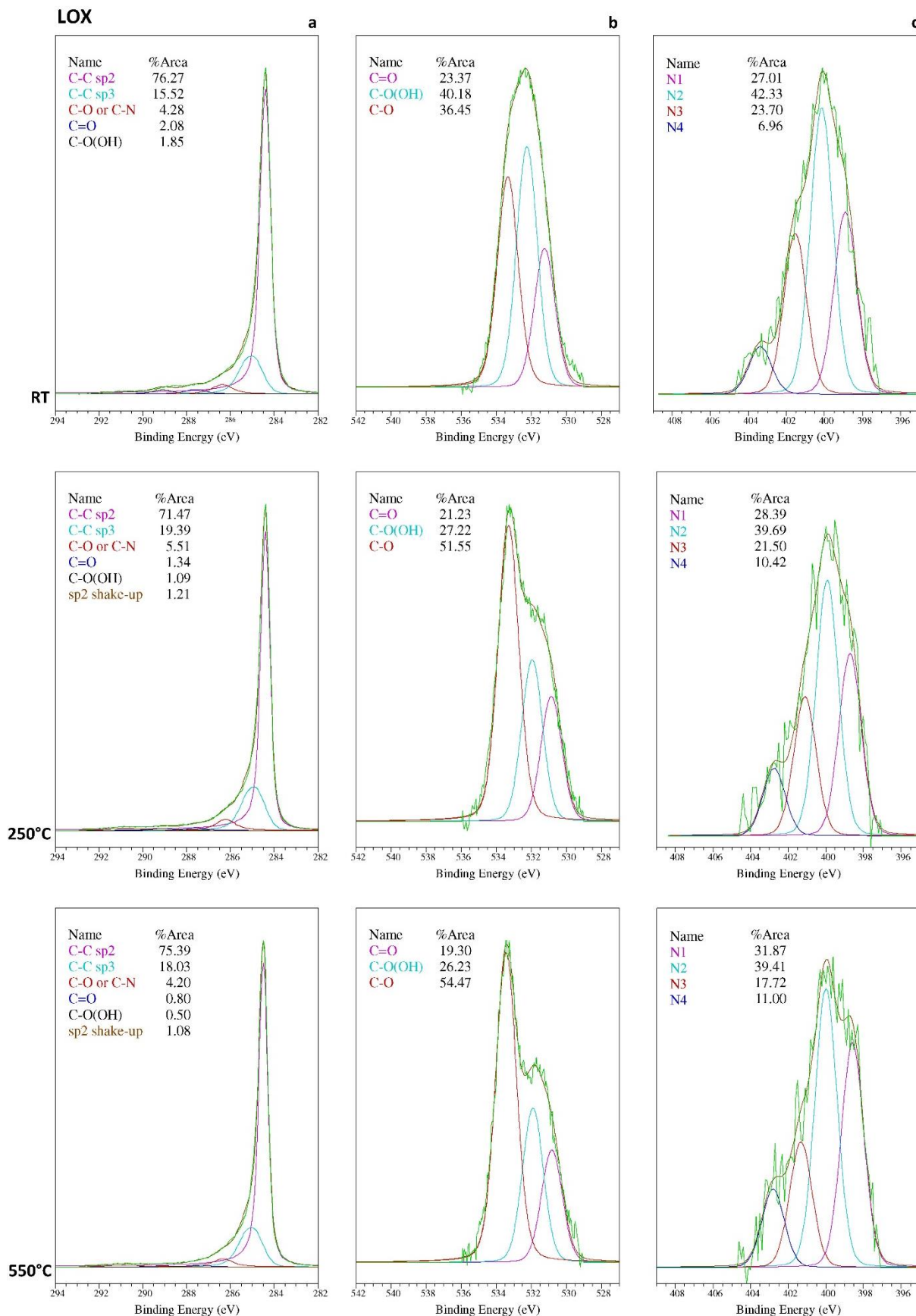


Figure 60. High resolution C1s (a), O1s (b), and N1s (c) XPS results and peak deconvolution for rGO sample LOX at room temperature (RT) and after further thermal reduction at 250°C and 550°C. The O1s and N1s spectra are not as smooth in the LO- materials (compared to HO-) because the lower oxygen and nitrogen content results in a smaller signal to noise ratio.

4.2.2.2.3 Results and discussion of N1s

The dopant bond type plays an important role in the properties exhibited by nitrogen containing carbon materials [228], particularly in regard to conductivity and reactivity, with more specific impacts on material properties outlined in Section Chemical composition 2.1.2.1 of the Literature Review. In the high resolution N1s spectra of rGO presented here, nitrogen-oxides are found at ≈ 403 eV and exhibit the smallest peaks (approximately 5% content) which represent a negligible contribution in the rGO material since the overall nitrogen content is less than 3%. The peak at ≈ 401 eV is attributed to quaternary nitrogen or nitrogen substituted in the graphitic lattice [86, 91, 93, 94, 99, 101, 217] and makes up about 20% of the nitrogen bonds. A slightly larger contribution of 30% is seen from the ≈ 399 eV feature, which is attributed to a two-coordinated nitrogen that is bound to at least one sp^2 carbon [79, 81, 101, 217, 229]. By far, the most prevalent nitrogen peak is at ≈ 400 eV (approximately 50%), which results from a three-coordinated nitrogen species with three sigma bonds (attached to sp^3 carbon) [82, 86, 97, 98, 100, 217] and, thus, will likely cause the rGO assembly to have lower Coulombic efficiencies [222]. These results are also very similar to the typical N1s peak ratios displayed for rGO materials prepared via hydrothermal reduction with urea [87].

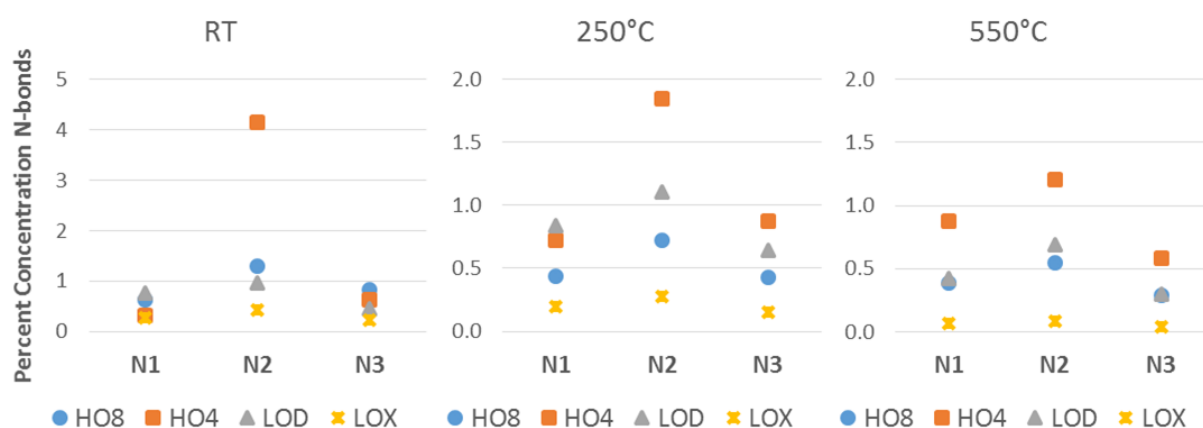


Figure 61. Results from the N1s high resolution XPS peak fitting showing the prevalence of associated nitrogen peaks within each rGO sample and the evolution of each species after heating to 250°C and then to 550°C. The N4 contribution is omitted from this comparison because it is only present in extremely small concentrations.

These results do not show a direct relationship between the oxygen content and nitrogen concentration. It is likely that the nitrogen doping is not directly related to the overall oxygen content in the material, but is instead related specifically to the presence of particular oxygen groups and reaction conditions in the initial GO. This is supported by the fact that HO8 and LOD have similar overall nitrogen content, so while the total oxygen content and/or prevalence of edges and defects along the carbon lattice does play a role, it may not be as significant as the impacts resulting from the long reaction time of Step 1: oxidation, which is thought to produce epoxy-rich, over-oxidized GO [57, 58]. Most studies on the nitrogen content in graphene materials have not been able to conclude if the enhanced N-bonding is due to an increase in oxygen groups or an increase in defects, because the two are often directly related.

Different types of nitrogen bonds are indicative of carbon regions that are either sp^2 or sp^3 hybridized, and the diagrams given in Figure 13 through Figure 15, as well as Figure 55, demonstrate the placement of specific nitrogen groups along the carbon sheet, which can either be bound to aliphatic or aromatic carbon. As shown in the N1s results presented in Figure 61, for all samples tested, the dominant bonding type is at the ≈ 400 eV peak, labelled N2. Further, the thermal reduction conditions have

shown this N2 species is most easily removed, even at low temperatures (< 250°C), as would be expected for particular amine-like functionalities [86, 95, 96]. This N2 feature could result from the ammonia treatment [87, 90, 95, 100] and/or hydrazine reduction [76, 79], as a slight loss of nitrogen at 150°C has been reported in one work on rGO reduced with hydrazine in the absence of the highly basic, hydrothermal conditions [81]. Since HO4 has a much higher initial nitrogen concentration, it shows greater losses during both thermal treatment steps, but in general the other nitrogen content observed for all samples is rather stable at these temperatures. Other than the instance of the N2 peak in HO4, only a very slight decrease in all nitrogen peaks is measured, and while trends can be observed, quantitative results for these very small changes after heating are not significant within error bounds for these measurements.

Taken together, these results indicate that the rGO materials examined here display very similar results to other work on rGO materials, exhibiting an overall nitrogen content of around 3% made up of nitrogen groups that remain largely stable at relatively high temperatures [99]. These groups appear to be a combination of “pyrrole-like” groups (such as pyrazoline [79-82] or hydrazone [73, 75, 76]) with some possible contributions from actual pyridinic, pyrrolic, and graphitic types [77, 83]. An exception to this is observed in HO4, where unstable amine-like moieties doubled the overall contribution from the N2 peak.

Based on these XPS results alone, no definitive conclusion can be made because multiple nitrogen groups exhibit a binding energy at ≈ 400 eV and many of these could be present in rGO based on the reduction methods employed. In spite of this, particular nitrogen species can be eliminated based on thermal reduction observations and features of the N1s spectra, especially when combined with details on the C1s spectra. Because the N2 peak of HO4 was greatly reduced at 250°C, it does not result from an aromatic species (cannot be pyrrolic), yet because it is not completely reduced at 250°C, it cannot result from residual hydrazine which is unstable at temperatures just over 100°C [76] and would exhibit a feature at a much lower binding energies (close to 396 eV [101]). Another possibility that can be eliminated is residual ammonia, because those peaks should again appear at lower binding energies of 398 eV [100], while ammonium ions appear at higher energies, reported at 402-406 eV [93, 96, 100, 217]. Based on reported work with nitrogen containing activated carbons, likely sources of the N2 peak could be chemisorbed ammonia [229], amide (shown to be present in rGO reduced with urea [87] and to fully convert or be decomposed by 400°C [96]), or secondary [100] and tertiary [96] amine groups (prevalent in low temperature activated carbons and decompose at low temperatures).

This then suggests the interaction with ammonia at acidic sites [90] is more likely be the source of the high N2 content in HO4, which may not be related to the hydrazine reduction process since this is known to produce more stable nitrogen species, as observed in the other rGO materials shown here. Further support for amine moieties in HO4 comes from the enhanced C1s features for HO4 (at 287 eV and 289 eV), which are characteristic of amine or pyridinium groups in carbonaceous solids [100, 217]. To fully evaluate the cause of this enhanced N2 feature, follow up work to compare HO3, HO4, and HO7 should be done in order to determine what impact the reaction time of Step 1 has on residual nitrogen content, if any.

4.2.2.2.4 Results and discussion O1s

Figure 62 shows the results for each type of oxygen group in the high-resolution O1s spectra for each rGO sample at RT and after heating to 250°C, and then to 550°C under high vacuum. As prepared, RT rGO shows the prevalence of carbonyl (O=C) is similar for rGO prepared from both high and low oxidized GO precursors. However, with increasing oxidation of GO, more carboxyl, hydroxyl, and epoxy (O-C sp³) groups are formed and these groups lead to more residual oxygen content in the rGO materials, even after hydrazine reduction. These results are consistent with what is known about the

formation [56, 59, 64] and reduction [65, 76, 228] of oxygen groups in GO, and indicates the HO samples have more carbon vacancies and edges as these residual oxygen groups are typically bound to dangling carbon bonds (aliphatic sp^3 carbon). The HO-rGO samples also have a higher amount of phenol groups ($O-C\ sp^2$), which are particularly observed in HO4, and this is again consistent with the over-oxidised conditions in *Step 1: oxidation* [57]. While this would have introduced more epoxy and hydroxyl groups to the basal plane, reduction with hydrazine effectively reduces the epoxy groups, leaving behind phenol which can be stabilized on the basal plane (hydroxyl groups have been shown to be unstable without epoxy neighbours and will migrate to edges or pair to form phenol [16, 62, 65]).

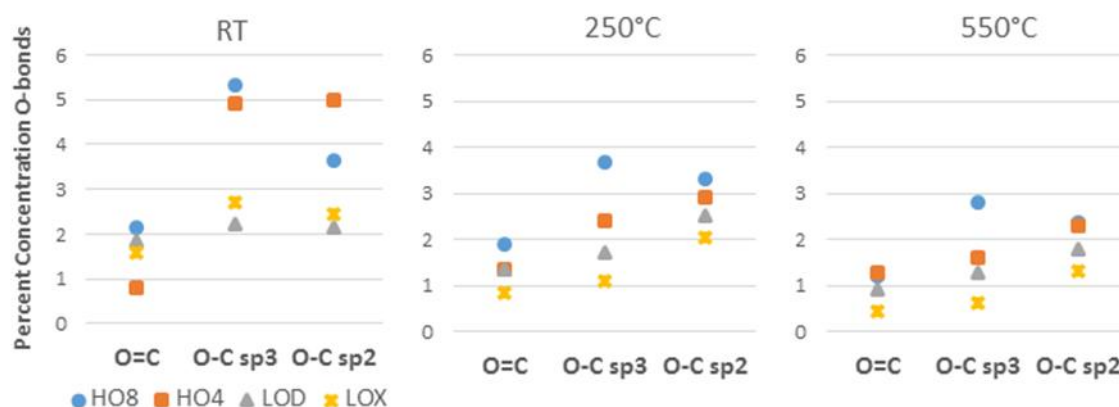


Figure 62. Results from the O1s high resolution XPS peak fitting which demonstrates the prevalence of specific oxygen bonding within each rGO sample and the evolution of each species after heating to 250°C, and then to 550°C.

The shape of the O1s spectra after further thermal treatment, as shown in Figure 57 to Figure 60, all assemblies except HO8 follow the same pattern, with the oxygen bound to aromatic carbon predominating at higher temperatures, while the two lower energy peaks for oxygen bound to aliphatic carbon and carbonyl groups are less prevalent. In this case, the largest loss of residual oxygen groups is with aliphatic bound oxygen, as would be expected, but the trend seen in HO8 clearly indicates there are more defects and edges present as aliphatic bonding on the edge, not on the basal plane, the latter being more stable at higher temperatures. This finding is significant in showing the *Step 2: hydrolysis* conditions do, in-fact, result in increased carbon vacancies, as proposed by Kang et al. [57] and that these structural features will also strongly impact the resulting rGO materials.

The evolution of specific oxygen groups upon further thermal reduction can be observed more clearly in Figure 63. Carbonyls bound to edges of rGO are not very prevalent, and it is possible to reduce their concentration slightly with further thermal treatment in all but the HO4 sample. It is likely that the removal of abundant nitrogen groups bound to sp^3 carbon sites in HO4, along with the increased epoxy content, facilitated the formation of additional carbonyls, causing the slight increase seen after 250°C, which is in support of some current models for the thermal reduction of GO [65, 66]. As discussed, the rGO samples prepared from high oxidized GO had almost twice the concentration of sp^3 carbon bound oxygen groups present at RT than low oxide rGO, and the results here follow the trend, showing that at temperatures of 200°C-400°C carboxyl and epoxide groups are removed. A more detailed account of these sp^3 carbon bound species is given below.

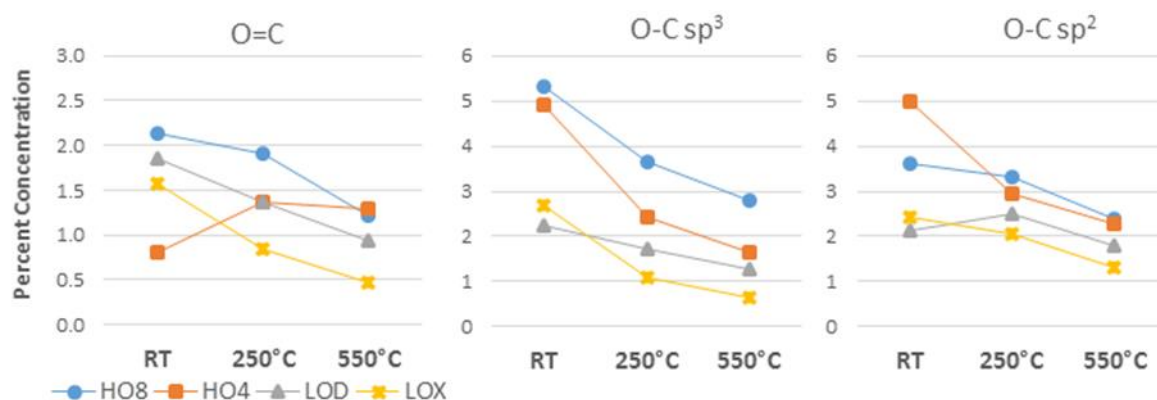


Figure 63. Results from the O1s high resolution XPS peak fitting showing the evolution of the specific oxygen functionalities at RT and after heating to 250°C and then to 550°C.

The fact that carboxyl, epoxide, and hydroxyl groups have very different thermal reduction behaviour can be used to differentiate between the hydroxyl and epoxide groups contributing to the aliphatic O-C peak. The rapid reduction seen after heating to 250°C results from removal of carboxyl and epoxide groups only, since hydroxyl is more stable (especially when bound at graphene edges) where it is not removed until over 400°C, and can persist up to 700°C. Thus, the final O-C aliphatic content is a good indication of how much edge-bound hydroxyl content is in the rGO assemblies. Differentiating between the hydroxyl and epoxide groups is useful, as it shows the rGO prepared from low oxidized GO does not have many epoxide groups bound to edge sites and consists of fairly equal parts carboxyl, carbonyl, and hydroxyl with negligible epoxy. All samples follow the accepted trend showing the hydroxyl edge groups are highly thermally stable, as evidenced by the dominance of the C-O peak in the thermally reduced spectra.

Further, the O-C aromatic bonding shows phenolic basal plane groups are also present, but unlike reports of thermally reduced GO, these groups are more easily removed in these pre-reduced hydrazine materials, most probably because epoxy groups are not present to stabilize them. Comparing this to GO reduced with thermal means only (no initial hydrazine treatment) temperatures of over 500°C are necessary to effectively reduce the hydroxyl and phenol groups because they will decompose only after all the epoxy groups are removed [66]. This conclusion is supported by the HO4 results, where there is a correlation between high epoxy content and more prevalent O-C aromatic bonds. This is a significant finding as it is highly desirable to minimize the amount of phenol in rGO materials, and it appears that first reducing GO with hydrazine can inhibit this formation and offers further support for suggesting a two-step hydrazine followed by thermal reduction procedure.

4.2.2.2.5 Results and discussion C1s

It is difficult to effectively isolate and quantify the lower intensity peaks of the C1s spectra related to the oxygen and nitrogen bonds because they overlap and the high intensity carbon to carbon bond peaks dominate. However, clear trends can be observed in the C1s spectra shown in Figure 56, Figure 57, Figure 58, Figure 59, and Figure 60. The C1s results support the conclusions drawn from the O1s profile and especially highlight the differences in the oxygen groups bound to sp³ carbon sites, specifically carboxyl, epoxy, and hydroxyl groups. C1s spectra are able to differentiate between these bond types, indicating both HO samples have a much higher residual content of all three of these groups than the LO samples do. Most notably, HO4 has a much higher carboxyl and epoxy content than the other materials, even after the 100°C hydrothermal reduction with hydrazine. This indicates it may be necessary to adjust the reduction conditions when using GO materials that have been over-oxidized in *Step 1: oxidation* by increasing the ratio of hydrazine to GO greater than the standard 7:10 ratio which is commonly reported [15], allowing the reduction to continue for longer periods or be

performed at higher temperatures to remove the additional carboxyl groups. Again, more prevalent sp^3 bonding sites indicates both HO-rGO assemblies have a higher defect density than LO-materials, and this finding combined with the residual sp^2/sp^3 content after heating to 550°C verifies many of the theories discussed in Section 2.1.2.1 of the Literature Review regarding the oxidation process [57, 64]. The results presented here clearly show that GO reaction conditions do in fact impact the structure of the resulting rGO sheets and should be considered in any analysis of rGO assemblies, especially when using low temperature reduction methods (< 400°C [96]).

The bonding within carbon (sp^2 and sp^3) is probably the most interesting feature of the C1s spectra. Figure 64 shows the atomic percentage of sp^2 carbon bonds in each of the rGO materials and how this is impacted by further thermal reduction. As expected, the rGO prepared from lower oxidized GO has more sp^2 carbon present in the initial RT materials. The large difference in the as-prepared, room temperature HO4 and HO8 materials with similar overall oxygen content show the large impact different oxygen functional groups will have on the aromaticity of the resulting rGO assembly. This is quite significant, as it shows the prevalence of sp^2 carbon bonding, which will determine the conductivity of the sheet. This is dependent on both the amount and type of oxygen groups remaining. Further, the evolution of sp^2 content upon further thermal reduction is an effective method to differentiate the sp^3 contribution from oxygen bonding, and from defects within the carbon lattice itself.

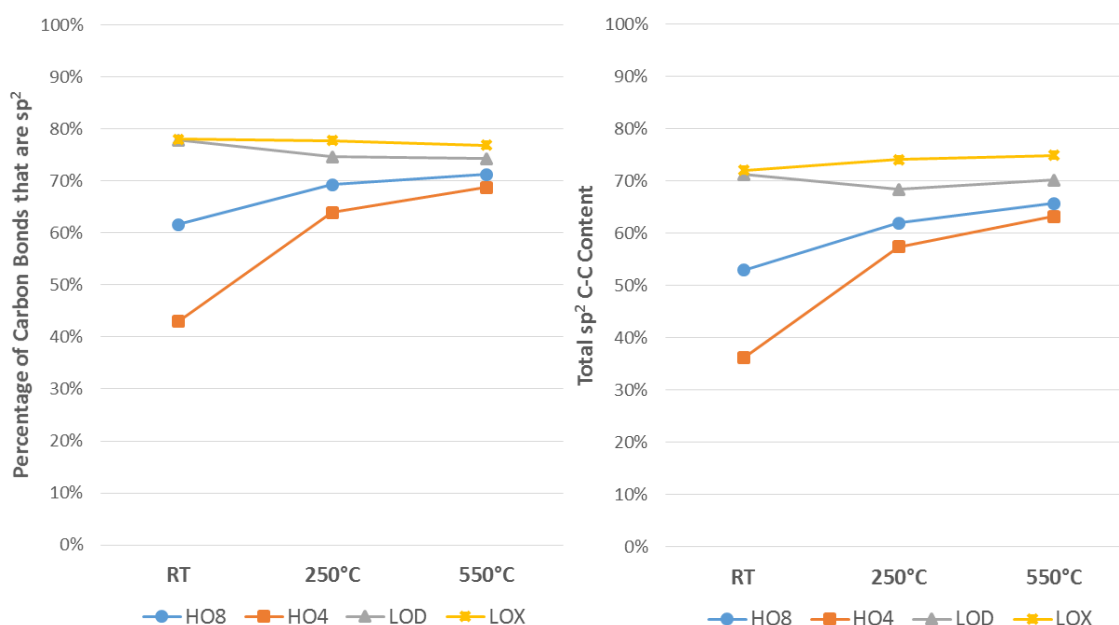


Figure 64. Percentage of sp^2 bonds as determined by fitting the C1s high resolution XPS spectra and the corresponding total sp^2 C-C content found from taking the sp^2 percentage of total carbon present in each sample.

The large difference between the sp^2 peak for HO8 and HO4 suggest the nitrogen content and epoxy groups highly impact the sp^2 fraction of the carbon lattice. Both HO- samples have the same initial oxygen content, but very different electronic conjugation within the carbon bonds. This residual oxygen bonding along the basal plane will have a large impact on the sp^2 domain size and also impact the corrugation along rGO sheets [59]. Since these 400 eV amine-like nitrogen species bond to sp^3 carbon and occur along the edges, the large increase in sp^3 and reduction in sp^2 regions for the HO4 material indicates the epoxy and nitrogen groups both act to reduce aromatic content in this sample. From Figure 53 and Figure 63, it is clear that HO4 loses a greater percentage of oxygen than HO8 after heating to 250°C, of which the sp^3 carbon group makes up a large portion. Knowing it is only basal plane bonds that are easily reduced at these temperatures, and because basal plane bonding has a

large influence on sp^2 carbon hybridization, the residual oxygen bonding of epoxy groups on the basal plane is most likely the cause for differences in the sp^2 carbon percentage within different samples, while the total amount of edges and defects is not as significant.

It can be concluded from this comparison of different GO processing conditions that, in order to ensure a high degree of sp^2 bonds, reducing the amount of amine-like nitrogen groups, as well as epoxy (most prevalent in HO4) and carboxyl (particularly in HO8) is necessary. Even though the total oxygen content of HO4 after the 250°C thermal reduction was equal to that of LOX and LOD at initial RT ($\approx 6.5\%$), there are pronounced differences in the amount of sp^2 carbon present. Correspondingly, both HO materials reach rather low oxygen and nitrogen contents after 550°C, but remain less sp^2 hybridized. These results indicate the processing conditions for the original GO material will have lasting impacts on the defects within the resulting rGO assemblies that are not directly related to the presence of oxygen groups. The harsher conditions applied during the *Step 2: hydrolysis* process for the HO assemblies must introduce significant and irreparable damage to the graphene lattice that carries over to rGO materials.

As expected, the sp^2 carbon content increases after thermal reduction, as shown in the total sp^2 carbon content of each material of Figure 64. However, it is interesting to note the LO samples had a higher percentage of initial sp^2 carbon bonds within the RT C1s spectra. This indicates the further thermal reduction of rGO prepared from low oxidized GO does not have much impact on restoring sp^2 carbon bonds, and in the case of LOD, it will actually decrease sp^2 content. If higher sp^2 content is desired for the rGO materials, because LOD and LOX have very few basal bound oxygen groups in the initial RT sample, additional reduction conditions would act only to remove edge groups (nitrogen or carboxyl), which will still leave behind a carbon edge that is not sp^2 hybridized. Thus, while the overall sp^2 content slightly increases in LOX, it is not likely additional reduction would significantly enhance the conductivity of these LO materials unless very high thermal treatment was applied to initiate graphitization. This would, in turn, significantly reduce the porosity and functionality of rGO assemblies as supercapacitors, but may be desirable for other rGO materials.

Another interesting result is that after thermal reduction, all samples seem to converge to an sp^2 atomic percentage just above 70%, which could be standard for rGO materials and be directly related to the defect density and folding along the sheet produced during the original oxidation conditions. LOX displays the highest sp^2 percentage, supporting the use of low temperature GO processing conditions if a more conductive rGO material is desired. While differences are less prevalent under high temperature reduction conditions, this again highlights the importance of controlling and accounting for the GO processing conditions in order for correct comparisons and conclusions about the performance of rGO materials to be made. This appears to be especially true for rGO materials prepared via reduction with hydrazine and ammonia (or urea), as the residual nitrogen content appears to have a large impact on sp^2 carbon content in the case of HO4. Thus, the percentage of sp^2 bonding is likely directly correlated with the sheet corrugation, prevalence of amine-like nitrogen species, and persistent phenol groups that are strongly bound along the basal plane, not solely because of edges or defects in the carbon lattice.

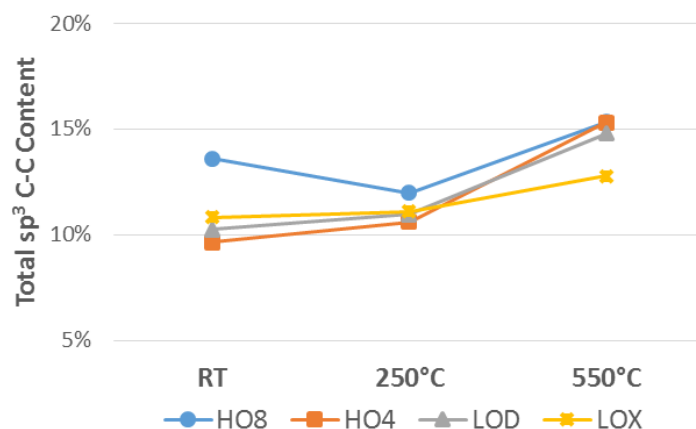


Figure 65. Percentage of total sp^3 C-C content present in each sample.

Similarly, looking at the total sp^3 content from Figure 65, it can be seen that there is a correlation between oxygen removal and increasing sp^3 C-C bonds. After 250°C thermal reduction, there is a slight decrease in aliphatic carbon in HO8, but for other materials, the composition is relatively constant. However, after the 550°C thermal reduction is applied there is an increase in sp^3 C-C bonds, which supports the conclusion that this condition results in modified oxygen bonding (increased phenol groups) and/or defects in the carbon plane resulting from epoxy and hydroxyl groups, as predicted by computational models [65]. Thus, it is likely that reduction at temperatures above 250°C will only translate to increased sp^3 carbon content and not improve the conductivity in rGO materials reduced using this combination of chemical and thermal procedures.

A final feature to note is the small ($\pi \rightarrow \pi^*$) shake-up satellite peak at high binding energies which is related to the highly ordered sp^2 bonds present. While the area is difficult to quantify because of the overlapping carbon-oxygen peaks and tail of the DS function, the presence of the sp^2 shake-up peak is directly related to the delocalized π conjugation in the aromatic carbon domains, indicating the prevalence of sp^2 regions and restoration of the lattice seen in highly ordered carbon materials (as in HOPG). The clear emergence of this peak in the RT LOX sample indicates a much higher ordering is present in this material. Even after further thermal reduction, when the overall sp^2 content for all assemblies is similar, the shake-up feature is not detectable in the HO materials.

4.2.2.3 High resolution valence band (VB) spectra

Valence-band XPS spectral scans for each sample were performed using beam energy of 150 eV over a range of 0-30 eV to determine the state of valence electrons and corresponding material properties related to bonding affinity and conductivity. The unique “signature” or “fingerprint” for the rGO materials analysed here are depicted in the VB spectra shown in Figure 66. While the precise features of a materials’ VB spectra are highly variable and still not well understood, the results here are a preliminary application of this method to rGO assemblies. Since it is the valence band itself that determines many of the properties of a material (conductivity, bonding affinity, etc.), it is worthwhile to develop methods to interpret the features present in rGO VB spectra and correlate them with material performance, and thus this analysis follows.

With regard to the VB spectra, the enlarged view close to the Fermi level shown in Figure 67 indicates the materials are all slightly shifted from zero (≈ 0.20 - 0.13 eV), with the magnitude of the shift related to the insulating nature of the material. The conductivity can also be characterized by the steepness of the VB spectra, just above the Fermi edge between 0-2 eV, which is directly related to the π -derived density of states (DOS). The first feature seen around 3eV is associated with $C2p-\pi$ bands in all carbon materials [220], and the peak intensity implies larger graphene domains. From this, it can be seen that of the as-prepared room temperature rGO samples without further thermal reduction, the LO-

assemblies have slightly better conductive properties, yet all samples other than HO4 have very similar DOS and C2p- π band intensity. The large difference seen in HO4 is related to the larger concentration of epoxy and nitrogen bonding.

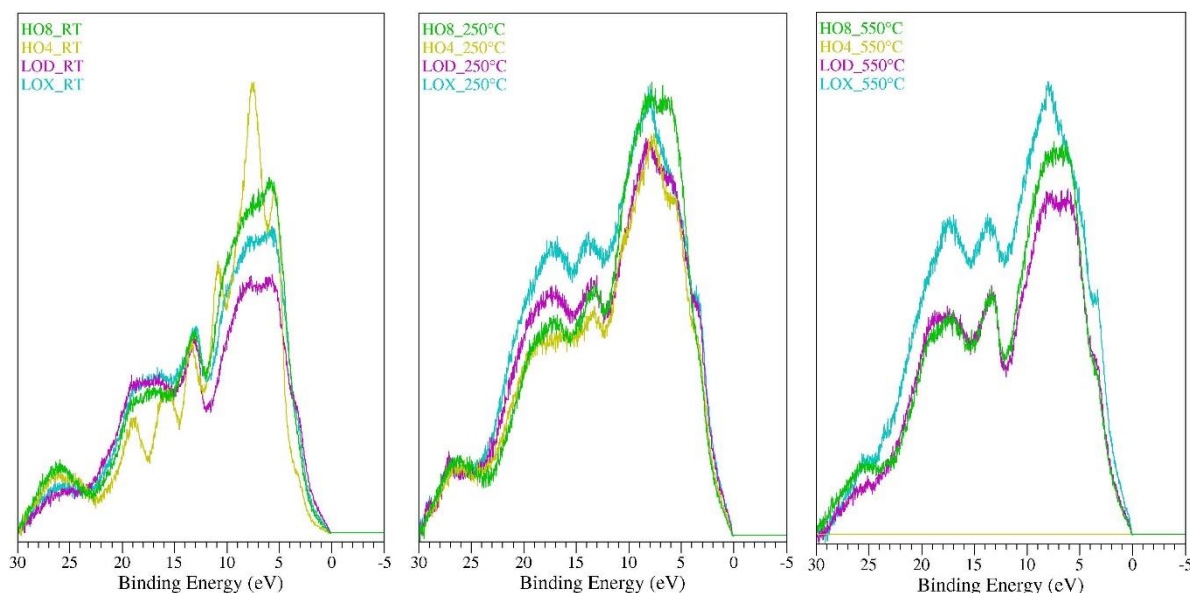


Figure 66. Valence band spectra showing a unique “signature” for each rGO sample at room temperature and after further thermal reduction at 250°C and 550°C. VB spectra here have been overlaid in order to compare peak intensities for different valence band energy regions described in the text, and the features are more clearly explained within the figures to follow (spectra for HO4 at 550°C is not available).

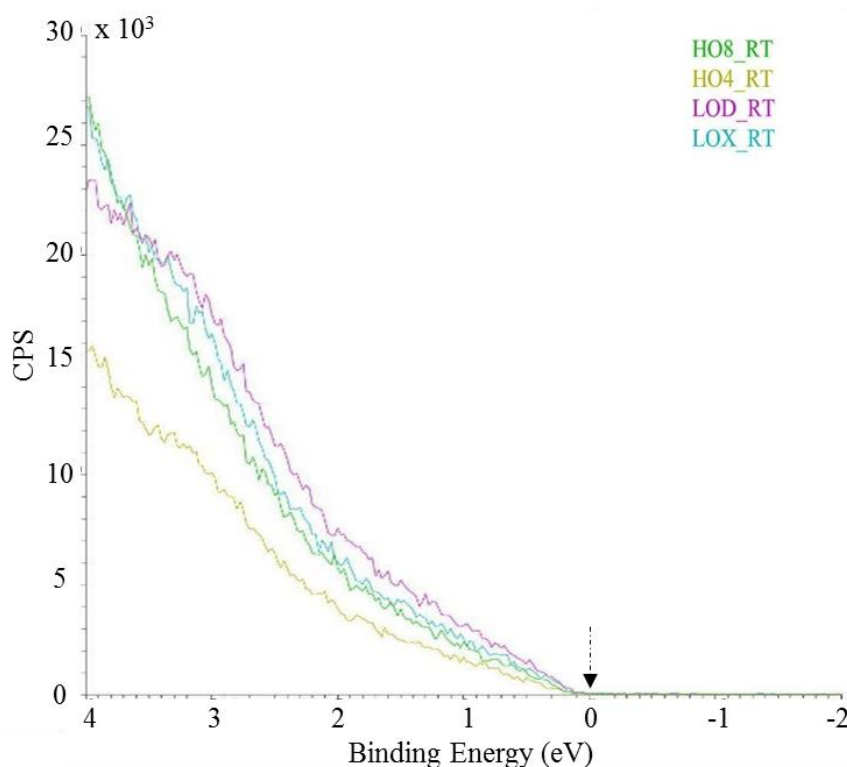


Figure 67. Enlarged view of the valence band spectra at the Fermi level for each sample at room temperature. The slope at 0-2 eV corresponds to the DOS, with the feature at 3 eV associated with C2p- π bands in all carbon materials. The black arrow highlights 0 eV and shows all spectra are slightly shifted to 0.20-0.13 eV.

The impact of further thermal reduction can be seen in Figure 68, where the increased slope and shift to take-off BE is closer to zero, and it is clear that conductivity increases in all rGO materials as they

are further reduced. There is no further increase in the slope for HO8 or LOD after 250°C, and it seems LOD even exhibits a decrease after heating to 550°C, which could be due to the introduction of additional hole-type defects and strain in the aromatic regions from forced removal of additional oxygen groups, as discussed in the previous section. These results support the findings discussed in the C1s spectral results presented previously, that imply disruption of this type is not restorable until graphitization occurs [46, 219, 220].

Combining these features seen in Figure 68 with the presence of the shoulder seen at 3 eV in Figure 66, it can be proposed that the LO- assemblies are more conductive than HO- because of the increased DOS. Further, LOX is the only material to show a very large enhancement in conductivity after 550°C, with a much higher DOS and extension of the valence band to the Fermi edge at 0 eV. This is likely related to larger aromatic domains and/or a higher degree of alignment within and between rGO layers – features that will be investigated in subsequent chapters. While the removal of oxygen and restoration of the sp^2 lattice will improve conductivity, it is likely to have a negative impact on the porosity of the assembly, which highlights the multitude of factors that should be considered when selecting rGO processing conditions for a given application.

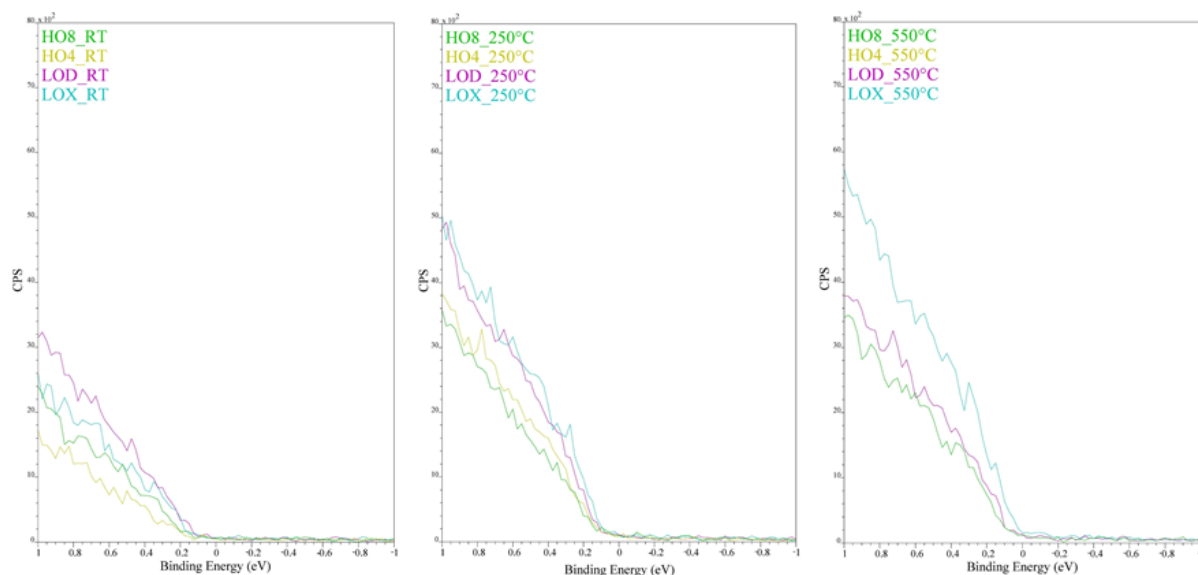


Figure 68. The evolution of valence band spectra at the Fermi Edge for all rGO materials at RT and after further thermal reduction at 250°C and 550°C. The ordinate axis is kept constant across each temperature, in order to highlight changes in the slope at low binding energy.

The valence band for oxidized carbon materials is most often broken into three characteristic regions for the major electron orbitals: i) C2p at 2-12 eV above the Fermi level, ii) C2s in the region of 12-22 eV, and iii) O2s from 22-30 eV. In addition, these regions can consist of hybrid p and s orbitals, as well as containing specific features for nitrogen-doped carbon materials. The full VB spectra for each material at room temperature and after further thermal reduction are shown in Figure 69 to Figure 71. It is clear that the VB for these rGO materials exhibits features that are characteristic of C2p, C2s, and O2s regions in carbon bonding.

The C2s and C2p regions are extremely important for carbon-based materials, and are best understood looking at the band structure of graphene and other carbon materials. In addition to the slope of the VB close to the Fermi Edge, the shoulder at 3 eV is related to the π - π bonds and can be correlated with other general features in the VB that describe structural properties of carbon materials depending on the type of carbon-carbon bonds present. The major spectral features depicted in Figure 69 to Figure 71 consist of two broad regions centred around 9 eV and 17 eV, and are typically associated with activated carbons, while the sharper feature at 13 eV is more pronounced in graphite [230].

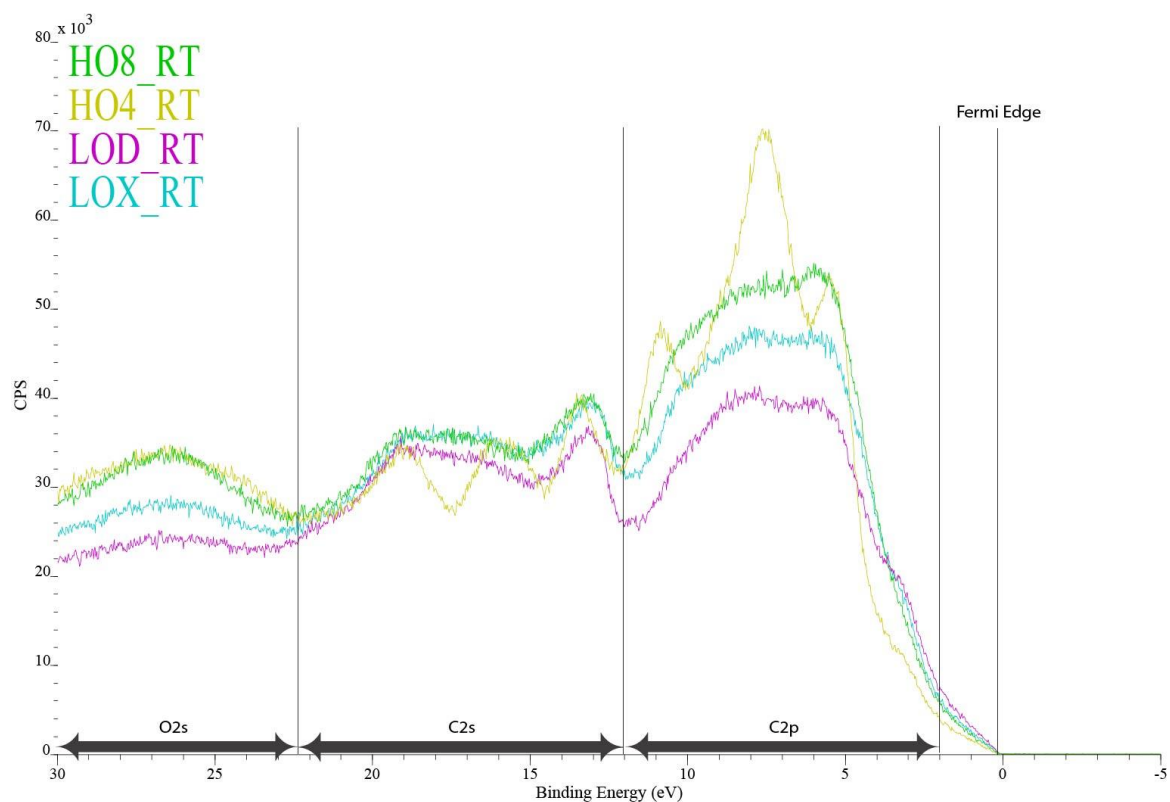


Figure 69. Overlapping valence band spectra for each of the rGO samples HO8, HO4, LOD, and LOX at room temperature to show the different “signature” patterns for each material.

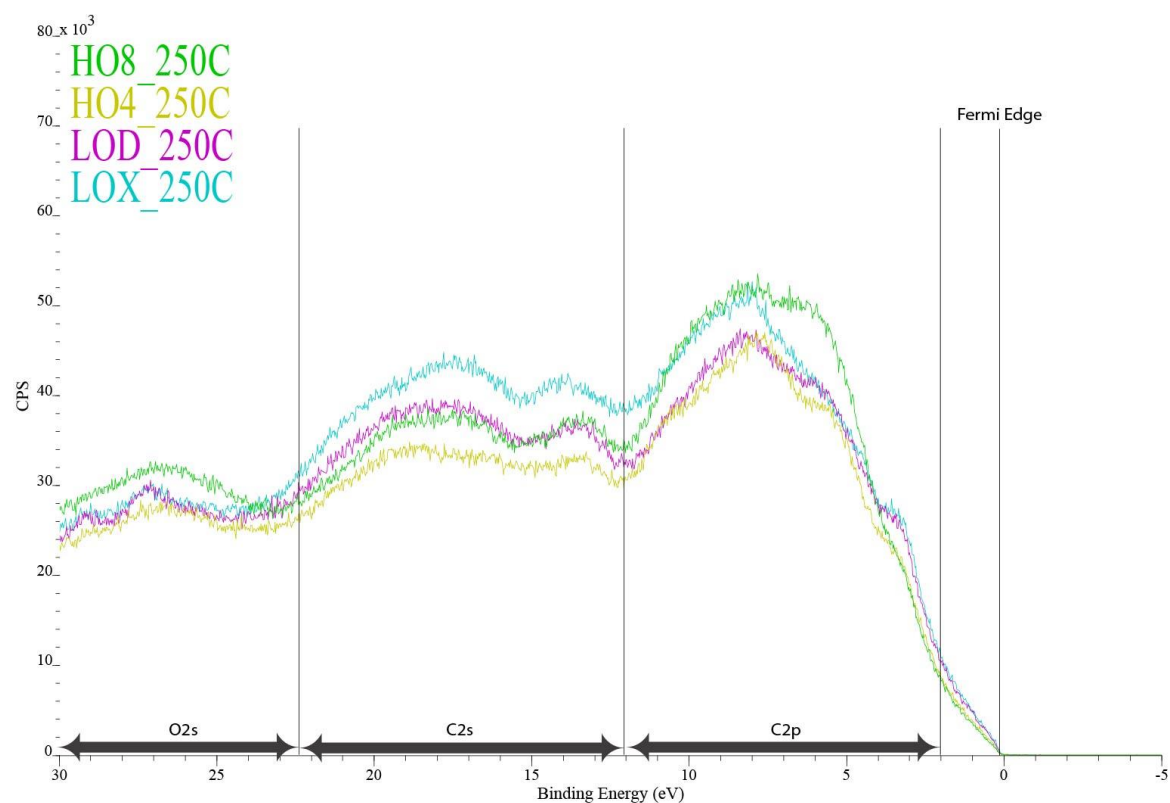


Figure 70. Overlapping valence band spectra for each of the rGO samples HO8, HO4, LOD, and LOX after further thermal reduction at 250°C, to demonstrate how the different “signature” patterns have changed after removal of oxygen and nitrogen groups.

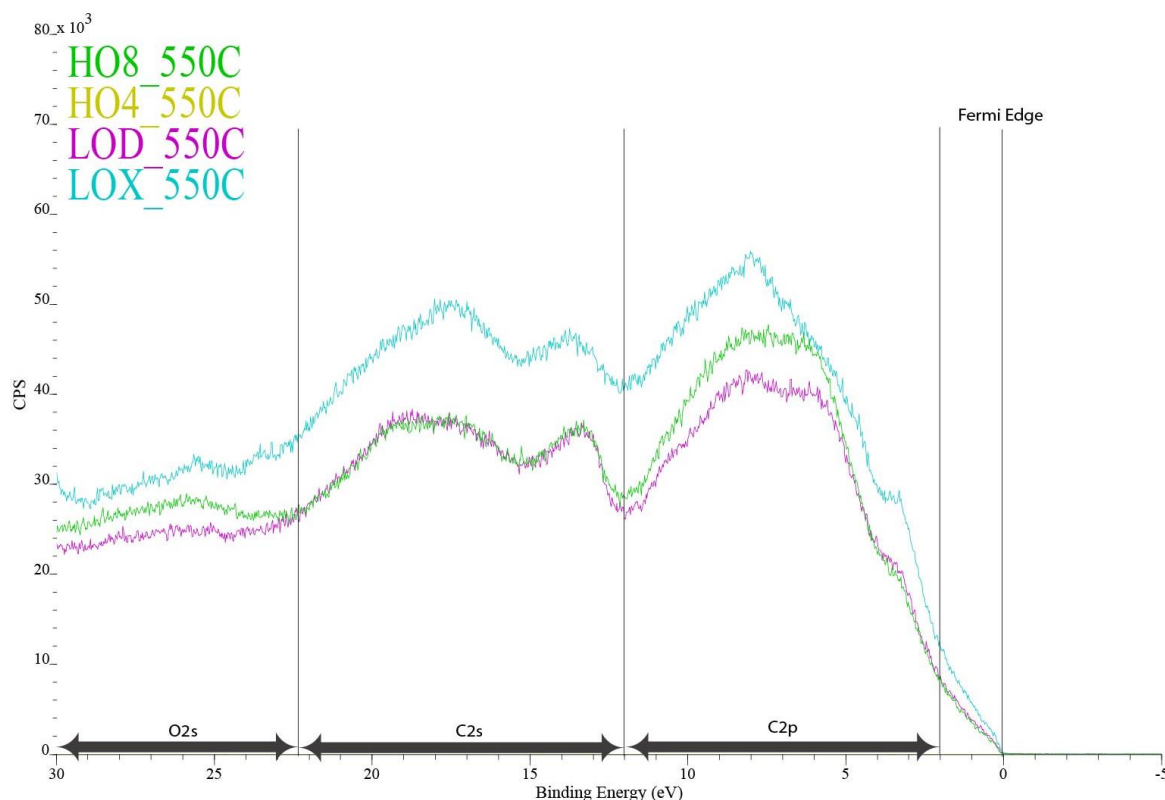


Figure 71. Overlapping valence band spectra for each of the rGO samples HO8, HO4, LOD, and LOX after further thermal reduction at 550°C to show how the different “signature” patterns have changed after removal of oxygen and nitrogen groups (spectra for HO4 at 550°C is not available).

While some VB spectral features are common in all rGO samples, HO4 has a very unique “signature,” most likely attributable to the higher prevalence of epoxy and nitrogen bonding previously identified in the high resolution XPS results. The distinct features of this sample can be used to identify more precise peak placement for the C2p and C2s spectral regions, markers which have remained elusive and limited VB spectra as a method to characterize carbon materials. Eleven distinct peaks could be identified in the HO4 VB profile and were fit using a deconvolution scheme built on knowledge of the band structure for various carbon materials, as shown in Figure 72. While it cannot be used as a quantitative method, the changes in specific peaks are more easily viewed after this peak fitting model is applied across the rGO assemblies with constrained peak widths and positions. The main features are marked A-K in an effort to de-code the VB “signature” of rGO and interpret the impacts of oxygen and nitrogen bonding on the C2s and C2p valence band. Comparison between the peak placement here and results from some notable works are listed in Table 6.

The C2p region, at about 2-12 eV, extends just above the Fermi level after the initial rise from the DOS. An increased π -peak intensity at 3 eV, combined with a steep rise in DOS reflects restoration of the π -conjugated aromatic structure. It is clear in Figure 69 to Figure 71 that the π -peak intensity is higher for rGO with lower oxygen content and this feature intensifies after further thermal reduction. The feature marked **A** in Figure 72 clearly shows that the π - π bonding becomes particularly prominent in LOX, after heating to 550°C. A shoulder at 8 eV has been associated with strong σ -bonding states in carbons [66], but other sources break this region into a C2p- σ component at 6-7 eV and C2s-C2p mixed component peak at 9-10 eV [231, 232]. The sharp peak intensity marked **C** is seen in all samples at 7 eV. This is most likely due to C2p- σ bands, as those in graphitic carbons, and indicates the presence of substantial sp^2 ordering [220]. Again, this feature is quite distinct in the thermally reduced LOX, where the nitrogen and oxygen content has been minimized. The combination of enhanced features at both 3 eV (C2p- π bands) and 7 eV (C2p- σ bands) implies larger aromatic domains with ordered stacking, and possible 3-fold coordination. This claim is supported by the feature marked **E** at 13 eV

that is characteristic of highly aromatic and graphitic carbons. McFeeley et al. [220] conducted an in-depth investigation on the VB of different types of carbon (diamond, graphite, and glassy carbon) and assigned the peak at 13.8 eV with a high density of states near P1 in the Brillouin Zone and the width of the valley representing the separation of sigma bands at symmetry point P.

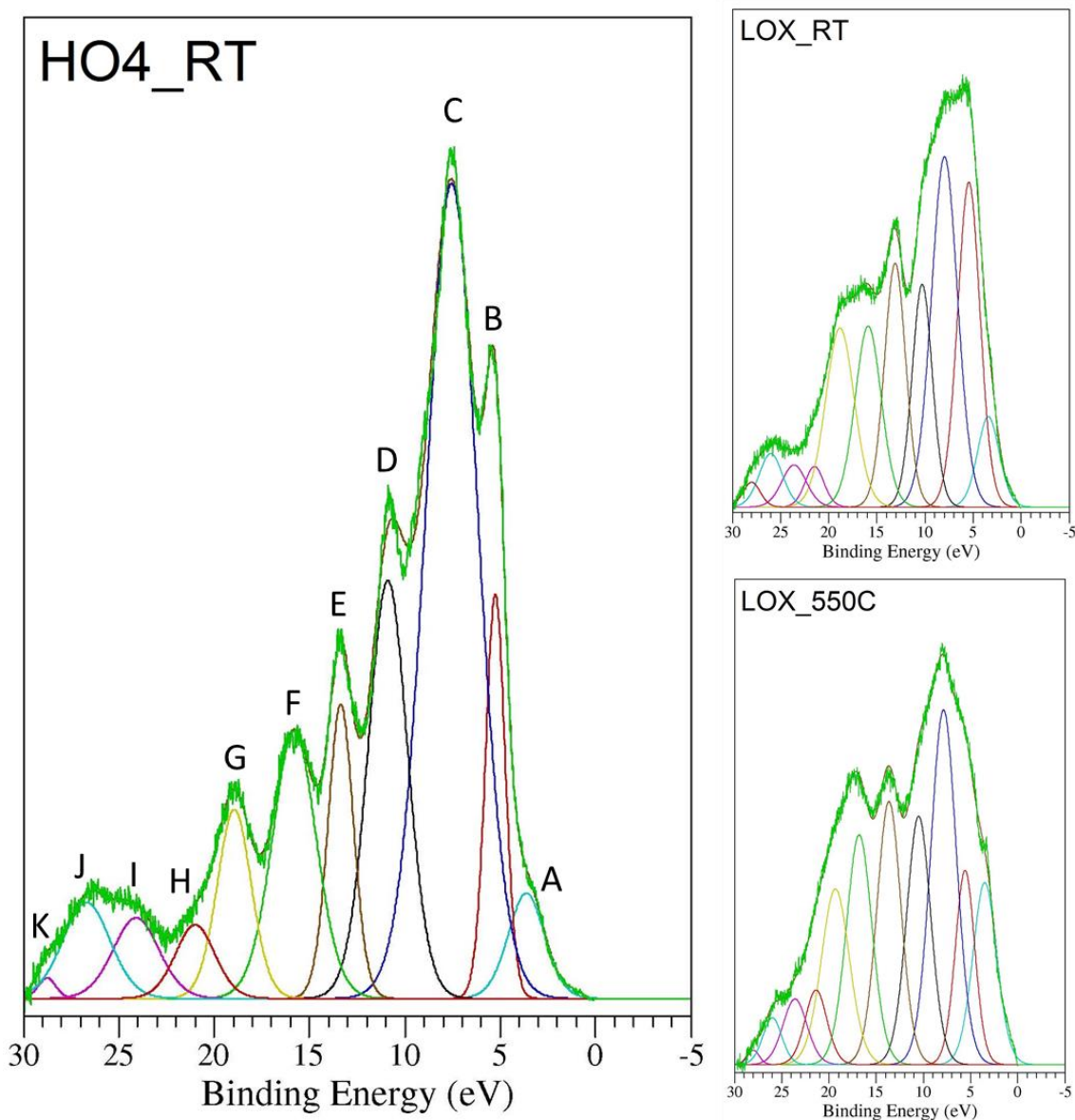


Figure 72. Deconvolution of the VB spectra for HO4 at room temperature, showing distinct peaks that are applied to LOX at RT and after heating to 550°C to highlight the features most strongly impacted by oxygen and nitrogen bonding which impact the electronic structure of the carbon lattice.

Using the peaks identified in HO4, it is clear the nitrogen content has a significant impact on the valence band and enhances the C2s and C2p features. The feature marked **B** in Figure 72 follows other results for nitrogen-functionalized carbon materials which show a shoulder or peak at 4.6 eV alongside a valley between this peak and the C2p- σ peak at 7 eV (marked **C**) that increases with higher nitrogen content [231]. This is further evident in the presentation of the VB after thermal reduction, where this 5 eV feature is not present in LOX once the nitrogen content fell below 1%. The enhancement to the RT HO4 peak at 7 eV can be attributed to C-N π -bonds and at 11 eV (marked **D**) from C-N σ -bonds [233]. These features are also present in the C2s region, with the 17 eV feature marked **F** being associated with nitrogen doped carbon materials. It is also associated with π - σ bonding in activated carbons, and is enhanced in LOX after thermal reduction. Thus, the nitrogen groups strongly impact the valence

structure in the carbon network if present at high enough concentrations. The features seen in HO4 are not as noticeable in the other rGO assemblies, which indicates the nitrogen bonding must be present in concentrations close to 5% before the effect on VB spectra can be observed.

Table 6. Bands identified in the VB spectra labelled A-K in Figure 20 are assigned with physical meaning and compared with literature values for binding energies in the C2s and C2p region for carbon materials.

BE (eV)	Bands in Figure 72		Reference [231]		Reference [230]		Reference [232]	
	Label	Assignment	eV	Assignment	eV	Assignment	eV	Assignment
3	A	π - π	4.6	π - π			3	π - π
5	B	Nitrogen			5	Nitrogen		
7	C	π - σ	7.2	π - σ			6.3	π - σ
10	D	Nitrogen hybrid s-p	9.6	hybrid s-p	10	Co-Nitrogen	10	hybrid s-p
13	E	C2s	13.5	C2s	13.5	C2s	13.5	C2s
17	F	Nitrogen π - σ	17	Nitrogen			17	Nitrogen
19	G	hybrid s-p						
21	H							
23	I	Oxygen						
26	J	-COOH						
28	K	Oxygen						

The O2s region is most readily evaluated by comparing the broad peak intensity to the amount of oxygen bonding in each material. As expected, this region has a higher intensity for rGO with higher oxygen content (as determined by the XPS results shown previously), with the differences in intensity clear in Figure 66. The loss of oxygen will yield a decrease in peak intensity within the O2s VB region and should correlate with an increased slope in the region 0-2 eV just above the Fermi edge, demonstrating that the presence of residual oxygen groups is related to the conductivity. This trend can be seen in data presented here, with the O2s region is virtually flat in the 550°C VB spectra. The HO- assemblies show a persistent peak closer to 25-26 eV, marked **J**, which is likely related to the increased carboxyl groups present in these materials. An interesting double-peak feature appears after heating to 250°C for the rGO prepared from low oxidized GO only and is likely due to the type of oxygen bonding present in those samples. This finding further supports the proposition that additional phenol groups have formed, as shown in Figure 63.

4.3 Energy Dispersive Spectroscopy

4.3.1 EDS applied to rGO assemblies

Energy Dispersive X-ray Spectroscopy (EDS, EDX or XEDS) is another useful tool to provide information on the composition of chemical elements present in GO and rGO materials. EDS can be used as both a qualitative and quantitative (if known standards are employed) technique for elements with an

atomic number greater than three ($Z > 3$). X-rays are produced via the incoming electron beam used in a scanning or transmission electron microscope (SEM or TEM). Within an SEM, the electron beam is focused on the surface of a sample and along with the backscattered and secondary electrons used for imaging, two types of X-rays also result from the interaction. The first type is a background signal (later subtracted) which is generated from continuum (Bremsstrahlung) X-rays resulting from the deceleration of electrons in the primary beam as they approach the sample. The spectra from Bremsstrahlung X-rays is subtracted for elemental analysis, as it is not useful for chemical identification because it contains a broad energy range up to that of the incoming electron beam. Characteristic X-rays are the second type of X-rays produced and can be used for qualitative and quantitative analysis, and elemental identification will depend on the accelerating voltage used and the interaction volume (dependent mostly to the mean atomic number and thickness of the sample but also related to beam resolution). In the SEM, EDS spatial resolution is usually on the order of microns.

When the energy of the incident electron beam is sufficiently greater than the ionization energy required to dislodge an electron from its shell, an electron from a higher shell will drop down to fill the vacancy and generate an X-ray with a specific energy characteristic of a particular element. An energy dispersive X-ray detector (typically a silicon drift detector (SDD)) records the number of X-rays generated at a given energy and the signal is displayed as a spectrum of intensity versus X-ray energy. The elements making up the GO and rGO samples are identified by the energy (KeV) of the Characteristic X-rays, while the concentrations of each element can be quantified by the intensity of the peaks (if compared to standards). The detection limit of EDS in the SEM is in the range 0.1-0.5 wt%, but is dependent on the type of sample being analysed. While EDS is effective for elemental analysis, large discrepancies can arise when fitting of the spectra, and this is why standards must be use for accurate background subtraction and quantitative peak fitting.

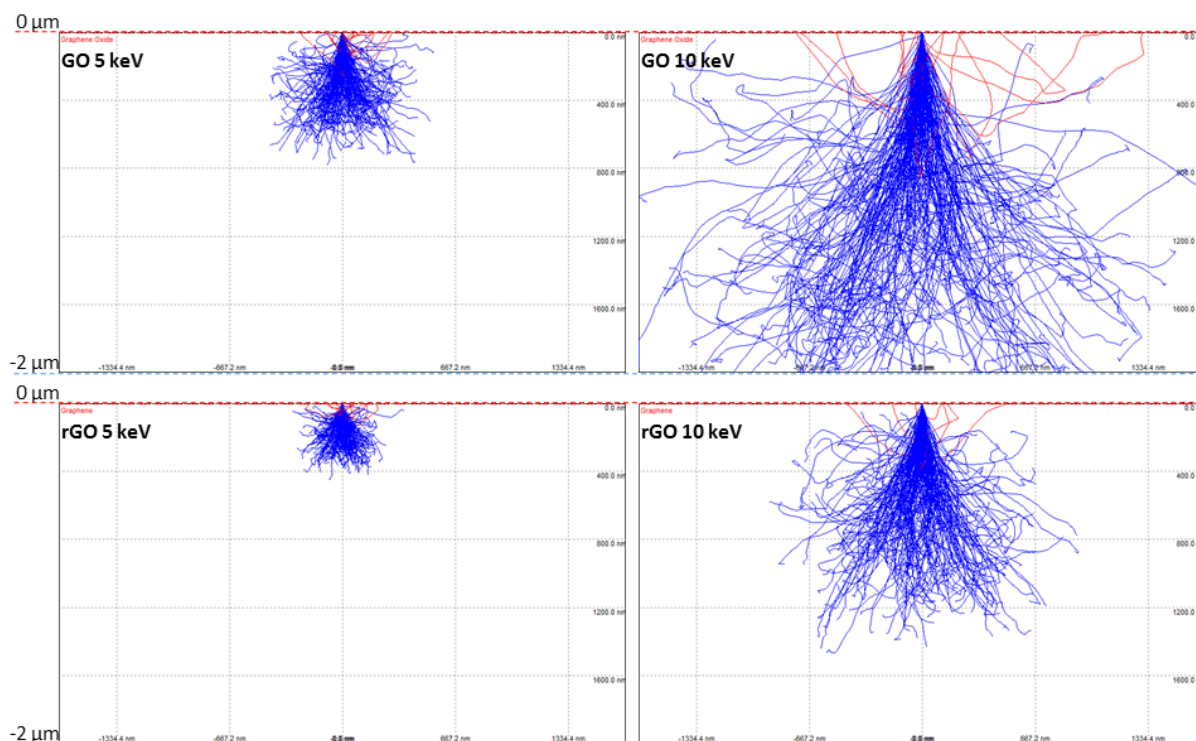


Figure 73. Monte Carlo simulations to estimate the interaction volume of the layered films for GO (top) and rGO (bottom) using an electron beam with accelerating voltage of 5 keV (left) or 10 keV (right). Each box has a height of 2 μm and length of 3 μm .

EDS is not able to differentiate between different types of chemical bonds or produce results with the quantitative precision of XPS for the light elements of interest here (carbon, nitrogen, and oxygen),

but it has the advantage of probing a much large interaction volume at depths in the micron range. Combining the enlarged interaction volume with the ease of data acquisition allows more area within the GO materials to be sampled to determine if the GO and rGO assemblies are relatively homogenous or contain any residual contamination from the initial oxidation procedure. To determine which portion of the material is contributing to the EDS signal, the penetration depth and interaction volume can be determined using a Monte Carlo simulation program [234], as shown in Figure 73. The interaction volumes are slightly different for GO and rGO because of the difference in density, but as seen in the results presented here, a 5 KeV beam will generate characteristic X-rays from up to 500 nm below the surface and a 10 keV beam will penetrate to depths well over a micron. Because the dried assemblies are about 6 μm thick, probing various sites along a sample with these interaction volumes should prove representative of these materials. Spectra from 10 keV and 5 keV showed no differences in the atomic percentage of species identified, thus in order to reduce charging or damage to the material, a 5 keV beam was used for analysis and imaging.

4.3.2 Results and discussion

The elements making up the GO and rGO samples are shown in Figure 74. Unlike the high precision of XPS, quantitative data from EDS for light elements can be problematic, as the peaks for carbon, nitrogen and oxygen overlap in this low energy range. Nevertheless, EDS is a useful tool to compare the relative carbon and oxygen content in GO, as well as in subsequent GO over a range of oxidation levels. The results from XPS are compared to those of EDS in Table 7, and it can be seen that the atomic percentage of oxygen differs by just under a factor of two (12% and 20% for EDS or 7% and 11% for XPS for low and high oxidized rGO, respectively). This is most likely due to the penetration depth differences of the two techniques. While XPS yields extremely precise quantitative data, it is only able to probe a small area at the very surface of the rGO assembly with a depth of a few nanometers. This small interaction volume may not be characteristic of the bulk, and it is possible that more oxygen functional groups are bound to the rGO sheets deeper within the layered assembly. EDS is able to generate characteristic X-rays in rGO assemblies from up to 500 nm below the surface with a 5 keV beam. Since the assemblies are less than 5 μm thick, this technique is able to probe a much larger percentage of the overall sample volume. In addition to this, there is likely to be some contribution from adsorbed water measured using EDS resulting from the small amount of water content at the surfaces throughout the assembly, or perhaps trapped within the bulk due to the filtration processing of the films. Because measurement is done under high vacuum conditions, adsorbed water content is minimal, and would not be near enough to explain the differences seen in XPS compared to EDS. Therefore, the main reason for these observed differences in oxygen content must be due to differences between the surface and the bulk of the material, where the surface species measured with XPS can be completely attributed to the chemical composition at the surface, while the species measured with EDS are attributed to the chemical composition of the bulk, which includes a slight contribution from adsorbed water at surfaces, as well as potential for small pockets of water that have been trapped between rGO layers (homogeneity of the bulk will be investigated in Chapters 5 and 6).

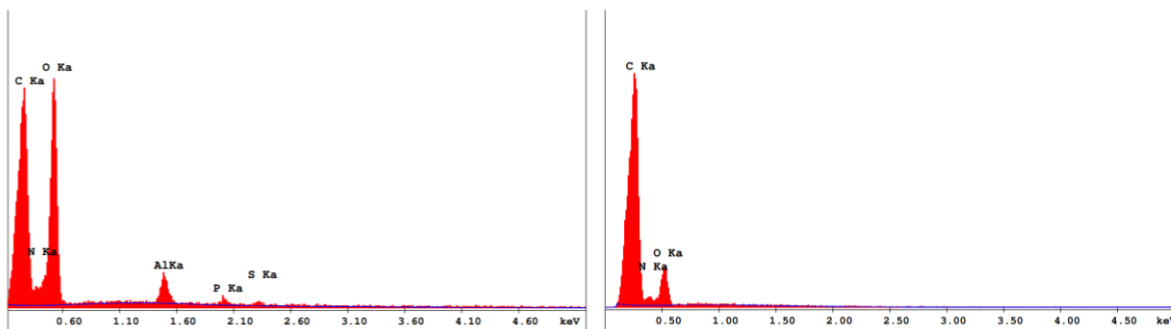


Figure 74. EDS for GO (left) and rGO (right) materials showing the elemental composition present.

Table 7. Comparison of XPS and EDS results for the rGO samples prepared from the highest and lowest oxidized GO. The table includes the atomic percentage calculated from spectra peaks of carbon and oxygen as well as the resulting C/O atomic ratio.

Sample	XPS			EDS		
	C1s %	O1s %	C/O Ratio	C %	O %	C/O Ratio
HO8	86	11.1	7.7	80	20.1	4.0
LOX	92	6.7	14	88	11.8	7.4

Due to the ease of data acquisition, a wider range of samples was evaluated, and spectra for assemblies consisting of the original GO along with the corresponding rGO assemblies were collected for comparison. EDS data was acquired and compared at three or more different sites along each sample, and it was found that within each assembly, all sites produced similar elemental ratios with a standard deviation in carbon and oxygen atomic percentages of less than 2%. These results indicate that all GO and rGO assemblies have homogeneously distributed elemental compositions. The atomic percentage for carbon and oxygen, as well as the corresponding elemental ratio, is given in Table 8 and the data shown graphically in Figure 75.

Table 8. Atomic percent concentrations of carbon and oxygen in GO and corresponding rGO assemblies prepared using GO synthesized with variations of the Hummer's method to modify oxidation degree.

Sample	GO			rGO		
	C %	O %	C/O Ratio	C %	O %	C/O Ratio
HO8	56.8	42.6	1.33 ± 0.03	79.9	20.1	3.98 ± 0.03
HO7	54.5	44.3	1.23 ± 0.01	81.2	18.8	4.31 ± 0.05
HO3	55.0	43.8	1.25 ± 0.02	80.7	19.3	4.18 ± 0.02
LOD	56.8	42.6	1.33 ± 0.01	81.3	18.8	4.32 ± 0.03
LOX	57.0	40.7	1.40 ± 0.05	88.1	11.8	7.44 ± 0.03

The trend in Figure 75 showing slight increases in atomic percentage of oxygen for the GO assemblies does not appear to hold for HO8, indicating there could be different types of oxygen groups present (as observed with XPS). However, the C/O ratio remains relatively constant for all GO materials, at a value of around 1.3. After reduction, all rGO assemblies contain an equivalent amount of oxygen, except for LOX which has significantly less. Again, results show the oxidation process used for LOX introduces oxygen species that can be more easily removed through reduction with hydrazine. LOX was synthesized from graphite with a larger mesh/sheet size and, similar to the XPS results, the much greater reduction seen in LOX is likely due to the difficulty in reducing edge-group located carboxyl and

hydroxyl moieties, which are less prevalent when low temperature chemical processing and larger graphite particle size is used.

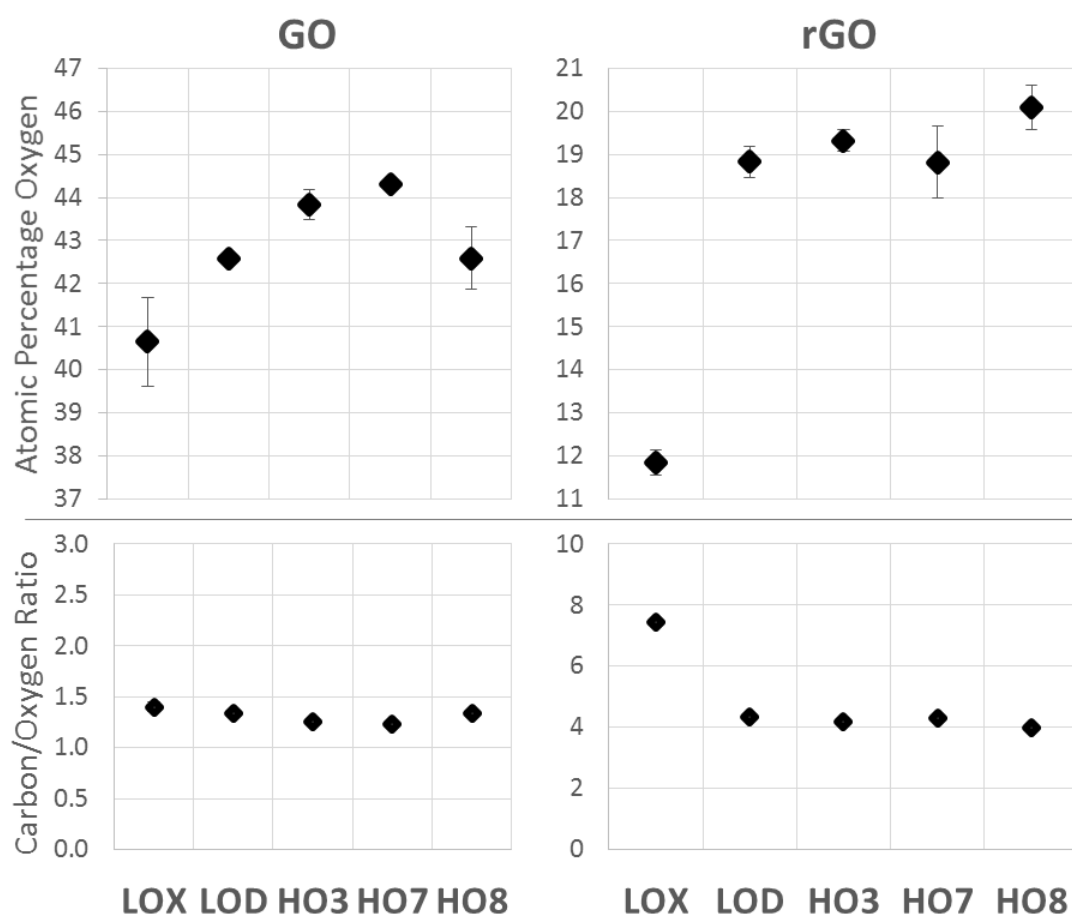


Figure 75. Atomic percent concentrations oxygen (top) alongside the carbon/oxygen ratio (bottom) for GO and rGO assemblies prepared from GO with modifications to the oxidation process

Other than LOX, the EDS data for both GO and rGO assemblies demonstrate that there does not appear to be substantial variance in the oxygen content of the GO materials synthesized using different conditions, nor does there seem to be large differences measured after the reduction process. The total oxygen content was reduced from an average of 43% in GO to 19% in rGO, indicating there are still many oxygen groups contributing to the mass and structure of rGO assemblies.

In addition to carbon and oxygen, EDS identified the presence of nitrogen in all rGO assemblies. Further, small amounts aluminium, phosphorus, and sulphur were present in the GO materials, as shown in Figure 74. Nitrogen content is difficult to evaluate quantitatively with EDS because the light elements in rGO produce a highly overlapped spectra, and the results that were acquired seemed to overestimate the nitrogen content at 10-12% for all rGO assemblies, a value significantly higher than the 3% identified with XPS. The aluminium seen in the GO spectra is a contaminant introduced during the membrane filtration process, which uses Anodisk aluminium oxide filters as the support the GO and rGO filters are built upon. It is only present in the resultant films, not in the GO or rGO solutions. In rGO assemblies, the dispersion of aluminium is not uniform across the surface and is present only in very small concentrations (<1%). High resolution SEM images indicate the contamination is due to small fragments of the filter breaking off onto the surface of the rGO assemblies. However, in the GO assemblies, the atomic percent of aluminium comprises 1-2% of the material and could be due to breakage at the surface, as well as doping from alumina ions resulting from corrosion caused by the

acidic GO solution. It was previously found these alumina ions act to stabilize the GO films [235] and it is possible to exploit this method of ionic doping in future work.

The other contaminants in GO assemblies are present at very small concentrations and this is residual contamination from the synthesis of the GO solution which was not entirely removed during the dialysis procedure. In most GO assemblies, phosphorus and sulphur contribute a total of 0.3 ± 0.1 atomic percent, which is not significant, but this value is much larger in LOX GO (1.3%). This indicates there are other differences resulting from the synthesis method for this solution. It can be seen that any phosphorus and sulphur contribution is removed during the reduction process, as no signal is visible in the rGO materials, and these elements will be neglected in future discussion on the chemical composition of rGO assemblies.

The XPS results were able to highlight differences in these materials that are not apparent using EDS (such as the type of nitrogen doping in rGO sheets and what oxygen functional groups remaining after further thermal reduction), and further work needs to be done to determine additional ways various synthesis methods for GO and reduction conditions of rGO can tailor the resulting surface chemistry. The main conclusions from the EDS results are: i) there is a significant amount of elemental oxygen remaining in rGO assemblies which falls within the range of 10-20%, with rGO from LOX containing substantially less oxygen content than the other materials; ii) the amount of nitrogen in rGO assemblies could be as high as 10% and may vary considerably between different rGO assemblies; iii) the rGO assemblies show a homogeneous surface chemistry and do not contain unexpected contaminants that would influence structural and/or transport results presented in future chapters of this work.

4.4 Conclusions

The findings in this chapter assist in determining if there are measurable differences resulting from variations in reaction conditions of GO on the chemical composition of the resulting rGO materials. These findings can then be used to deepen understanding on how these differences may impact the performance for rGO materials. Reports often overlook GO processing conditions when assessing the performance of rGO materials, and do not directly account for the specific chemical elements present, assuming that similar processing conditions will result in graphene-like sheets, without substantial differences. The results shown here indicate there are direct links between both the original GO synthesis procedures and reduction conditions on the resulting rGO sheets. It was also shown that it could be possible to tailor the chemistry of rGO across a wide range based on the original GO processing conditions and particular thermal reduction procedures applied following hydrothermal reduction using hydrazine. Further investigation along these lines, especially if combined with direct measures for material performance, should prove very useful for work on supercapacitors as the oxygen and nitrogen content, as well as what specific chemical species are present, will highly impact the performance [69].

Variations in the *Step 1: oxidation* and *Step 2: hydrolysis* process were expected to play a large role in determining the type of oxygen groups present in GO as well as the amount of damage to the carbon lattice. The results here verify that these conditions do carry over to the chemical composition of the rGO. This could be most clearly seen in the LOX assembly, which was the only sample to reach high purity, with room temperature C:O ratios comparable to other rGO materials undergoing thermal reduction at 1000°C. The low temperature conditions used in both oxidation steps should be highly advantageous in producing rGO with both low oxygen content and less defective graphene sheets, as much of the damage to the aromatic domains is a result of harsh oxidizing and reduction conditions that can be avoided in this combination of low temperature synthesis and hydrazine reduction. Because these conditions can be achieved without the need of further thermal reduction/annealing, processing conditions used for LOX would produce a high purity material that is able to retain high

porosity, as higher temperatures are known to cause the collapse of expanded regions in rGO materials [17].

There were also measureable differences in the oxygen and nitrogen content which seem to be most closely linked with the reaction time for *Step 2: hydrolysis* and *Step 1: oxidation*, respectively. LOD had the same reaction temperature as HO4 and HO8, yet the rGO had significantly less residual oxygen content. Limiting *Step 2: hydrolysis* to 15 minutes likely prevents over-oxidation of the GO and results in a much higher purity rGO material. Interestingly, it appears long reaction times for *Step 1: oxidation*, where HO4 was kept at this step for 8 hours, could be the cause of the much higher nitrogen content of this sample, which may relate to additional epoxy groups that formed during this over-oxidized step. Results indicate that these additional epoxy groups can act to both facilitate more edge bound nitrogen groups to form during reduction and stabilize oxygen groups bound to the basal plane – both of which will strongly impact the rGO sheet properties.

Since hydrazine reduction acts on the epoxy groups which are bound to the basal plane, the evolution of additional, more thermally stable basal plane groups seen in thermal reduction methods can be hindered, and thus the presence of epoxy is necessary to facilitate this reaction [66]. Further, the evolution of basal plane oxygen groups can result in the removal of carbon atoms, producing additional defects and reactive edge groups and/or facilitate the transition to strongly bound phenol groups [65]. Since hydrazine de-epoxidation and thermal de-hydroxylation act on different oxygen moieties at different temperatures, a combination of these techniques can be used to tailor the oxygen content and defect density of rGO sheets [27]. For low oxygen content, less defective materials, hydrazine treatment can be followed by thermal treatment, as demonstrated in hydrothermal methods producing rGO with exceptionally high conductance [75]. Conversely, if more defects and residual oxygen groups are desired, over-oxidation is attainable by increasing the reaction times during GO synthesis. High temperature GO processing combined with thermal reduction will produce a stable, yet highly defective rGO sheet that could prove more useful for functionalization or building composite materials.

Nitrogen content in rGO materials reduced using hydrazine in a hydrothermal solution with ammonia was clearly present, a feature that is important when evaluating impacts on the material performance of rGO assemblies. These amine-like moieties, bound to sp^3 carbon regions, were shown to dominate the N1s spectra, and these species are not likely to add to the desirable properties of graphene-based materials as the added resistance would likely impede performance. Thus, for these applications an alternative reduction route should be employed, or the rGO assemblies should be exposed to higher temperatures in order to remove these less stable groups and transition the remaining nitrogen species to aromatic moieties [79, 86, 94, 96, 99]. Further, acetic acid [60] and borohydride [236] are well-known alternatives that result in C:O ratios around 13:1, or another alternative is electrochemical reduction which is a less utilized, but promising, alternative that can produce high purity carbon (24:1) at 0.60-0.87 V [56].

The surface chemistry of rGO sheets will also impact the morphology, which then translates to impacts on the structure of the overall assembly. Not only will there be expansion in the interlayer-distance to adjust for the residual oxygen groups, the basal plane hydroxyl and phenol groups will induce more pronounced corrugation and strain along the sheet. This will have a significant impact on the aromatic domain size and electron transport in these materials. Further, residual oxygen groups will interact with the surrounding environment by drawing water and/or other species into the assembly, which has significant structural and performance considerations. These issues will be investigated in the next chapter which is focused on constructing a basic structural unit (BSU) for rGO assemblies that can account for differences in aromaticity and structural defects, as these rGO sheets come together to form hierarchical structures.

Chapter 5. The Basic Structural Unit of rGO Assemblies

5.1 Introduction: Concept of a Basic Structural Unit in the Microporous Region (<2 nm)

This chapter combines direct imaging with TEM with spectroscopy and diffraction in order to design a basic structural unit (BSU) for the rGO assemblies. Similar to the function of a unit cell for crystalline materials, the BSU serves to act as the most basic building block for describing the structure of more disordered materials. Since the BSU is *not* a 3D crystal, it is not a true unit cell (a term with very specific meaning in crystallography), yet it serves the same conceptual purpose, acting as a measure of the most basic repeating structural unit within the bulk material. Ascertaining an accurate model of the BSU is important as it serves as the base for designing all future structural models for rGO materials, and this basic unit can be more easily compared with other BSU models in layered or porous carbon materials [31, 32, 150, 237]. Further, the arrangement of these microstructural elements also plays a role in the electrical and chemical behaviour of carbon materials because graphitic segments have highly anisotropic properties. Thus, comparing features of the BSU for various rGO assemblies will allow for a deeper understanding of how structural features impact material performance. An example of this can be seen in the direct connection between the dimensions of a graphene layer and the oxidative reactivity of the material because the carbon atoms within basal plane sites are much less reactive than those at edge sites [32, 134, 228, 238, 239]. Thus, since graphitization results in an increase of defect-free graphene segments, it correspondingly leads to decreased reactivity; while increased disorder within the graphene segments correspondingly leads to increased reactivity. The specific features making up the BSU can therefore be directly linked to aspects of material performance.

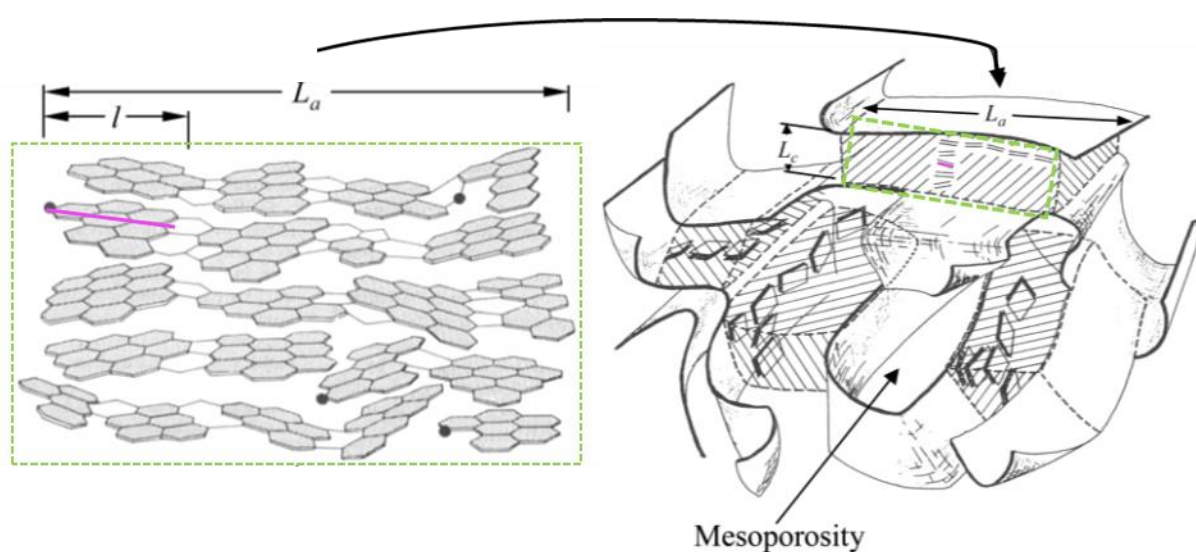


Figure 76. Diagram to represent the elements making up the basic structural unit for different types of carbons, as proposed by Oberlin et al. [156]. The BSU of total length, L_a , is composed of stacked, graphene-like layers with aromatic domain length (l , in pink) and corrugation from stacking faults, defects (white rings), and oxygenated edge groups (dots) which impact the stacking order along L_c (left). These units are assembled to form the larger, bulk carbon structure which may consist of larger meso- and macropores and contain a given degree of order between different BSUs (right).

Currently, no clear BSU model exists for rGO assemblies, but the rich scientific history of other carbon materials provides the general theory required to interpret experimental data by comparing the results for rGO materials to the BSUs developed for other bulk carbons [30-32, 150, 167, 168, 240, 241]. Many porous carbons fall into an intermediate region, somewhere between uniformly layered and highly disordered, containing aromatic domains and corrugation along the basal plane as well as oxygenated edge groups, as shown in Figure 76 [30, 150, 156]. Following this physical model developed by Oberlin

[156], this chapter utilizes a variety of experimental techniques to build a comprehensive picture of a BSU for rGO assemblies, comparing the features to that of other carbon bulk materials (such as graphite, coal, and pyrocarbons) where the structure has been better established due to the much longer history of research that has been well documented in textbooks [30-32, 45, 242]. Firstly, TEM provides a qualitative understanding of the structure by directly imaging the layered rGO sheets to sub-nm resolution. These images can then guide interpretation of Raman and XRD results, where data analysis can be somewhat ambiguous, and correct interpretation is highly dependent on the specific physical features of the carbon material under investigation [32, 170]. The sections presented here include a detailed critique and provide a best-practice approach to the analysis of Raman and XRD results for rGO materials, which, if applied, should prove to be a useful guide to those working with these materials.

As discussed in the Literature Review, pure graphite is a three dimensional atomic crystal structure, with ABAB stacking of the 2D graphene planes. Any deviation from the ABAB stacking order is a stacking fault that gives rise to a small increase in the interlayer distance ((002) plane). As greater disorder is introduced along the graphene sheets from defects/corrugation in the aromatic regions and/or binding of chemical groups to the carbon sheets, the stacking between sheets becomes more and more uncorrelated. It is known that turbostratic carbon (where graphene layers are rotated so the unit cell does not follow ABAB stacking), has an interlayer distance greater than 3.42 Å, and this is the value used to determine if the rotation of the graphene layers are completely uncorrelated (values between 3.35 Å and 3.42 Å are partially graphitized carbons [46, 168]). From this, the interlayer distance continues to increase in proportion to the stacking disorder, until eventually the material will become an amorphous carbon with completely random stacking.

It is necessary to quantify the disorder in rGO assemblies (as deviated from a perfect graphite crystal) in terms of: i) *intra*-layer carbon bonding (sp^2 , sp^3 , defects, and oxygen groups); and ii) *inter*-layer spacing and orientation (the (002) plane of graphene stacks). The size of the aromatic domains along the rGO sheet will influence the conductivity and corrugation of the sheets, and Raman spectroscopy is a well utilized tool to investigate bonding and disorder in carbon materials ranging from pure graphite to amorphous carbons [124, 125, 137, 170, 171, 243, 244]. In graphene-based materials, Raman spectroscopy can be used to quantify the size of the aromatic regions along the plane as well as determine the proportion of defective domains present along the sheet, leading to a more complete *intra*-sheet characterization of the BSU.

To support the choice of fitting and interpretation of the Raman results, generalizations made when interpreting the data are built on the real-space, high-resolution electron imaging also reported here. Further, the precise measurement of the *inter*-sheet spacing and alignment of the rGO sheets can be determined from the corresponding TEM selected area electron diffraction pattern (SAED) in reciprocal-space. Additionally, the layered, graphitic regions will contribute to XRD peaks produced by the periodicity between (*inter*) and within (*intra*) the graphene lamella, depending on the longer-range order and stacking of the graphene sheets. The shape and broadening of XRD line profiles provides microstructural information related to many structural properties including strain, aromaticity, and bonding type. These methods have long been applied to a variety of carbon structures ranging from coal [108] to pyrocarbons [32, 183] and, thus, provide a solid framework to expand these methods to application in graphene-based materials analysis.

5.2 Transmission Electron Microscopy

5.2.1 TEM applied to rGO assemblies

For dry assemblies, the rGO sheet alignment and other features in the microporous region ($< 2\text{ nm}$) can be investigated with TEM, as shown in Figure 77. To determine the structure of carbon layers, TEM imaging and the corresponding selected area diffraction pattern (SAED) have proven to be useful analysis techniques for dry and structurally stable carbon materials [131, 154, 183]. While dry rGO assemblies can be investigated and compared with other carbon materials using these methods, the sample preparation required for TEM imaging of rGO assemblies involves embedding in resin and then microtoming thin cross sections, which can distort the original structure. Furthermore, the small region within the assembly investigated with TEM may not be characteristic of the bulk, so this method alone is not appropriate for a full characterization of the rGO assemblies. Another large drawback is that without the use of cryo-microscopy facilities, this method cannot be applied to the hydrogel assemblies. In spite of these limitations, TEM remains a powerful characterization tool, and these TEM images along with the SAED pattern are integral parts of this initial investigation in order ensure the main parameters of the BSU are based on actual physical features. It is well known, and encouraged, that direct imaging and scattering techniques should be used in tandem, as the images are very complimentary to the more ambiguous data presented using other techniques.

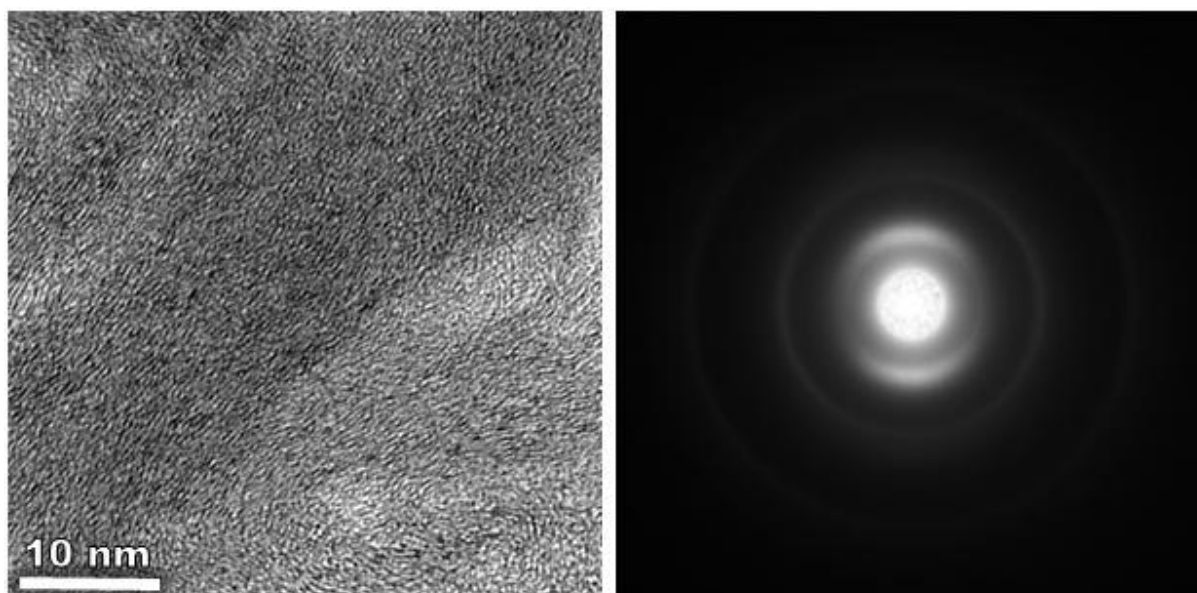


Figure 77. The TEM image (left) and SAED pattern (right) of the cross-section of a dry rGO assembly show crystalline coherent domains along with meso-scale disorder in inter-sheet alignment (radial intensity spread of (002) ring).

Lattice fringe analysis has long been used to evaluate the layered structure and graphitization of various carbons [245] and serves as a starting point for BSU design. High-magnification phase-contrast images are very useful in identifying ordered planes and interfaces within material, even in materials of uniform elemental composition. A slightly defocused TEM image (under-focus condition) will show atoms that appear dark relative to their surroundings. The regular spacing of layers, especially when they are parallel to the incident electron beam, allows these features to be seen directly in the TEM image because the electrons passing through the space between atomic columns retain their phase while those travelling down the column will be significantly inhibited. This dark-to-light pattern seen in Figure 77 indicates where the graphene planes are aligned. While this technique does not allow for a comprehensive evaluation of the alignment throughout the rGO assemblies, it does provide basic insight on some structural parameters.

Electron diffraction makes use of the wave properties of electrons and is effectively the same mechanism as that discussed with X-rays presented in Figure 33 [183]. The wavelength of the electron is determined by the de Broglie relation:

$$\lambda = \frac{h}{p} \quad 5.1$$

where p is the momentum, λ is the wavelength, and h is Planck's constant (4.136×10^{-15} eV·s). In a TEM, the electrons will be accelerated to a desired velocity:

$$v = \sqrt{\frac{2eU}{m_e}} \quad 5.2$$

where e is the elementary charge (1.602×10^{-19} C) accelerated by an electric field, U , and m_e is the mass of an electron (9.109×10^{-31} kg). Thus, the wavelength is dependent on the accelerating voltage used, and in a typical TEM (200 kV accelerating voltage) the electron will reach approximately 70% the speed of light, so it is necessary to take relativistic effects into account. Thus, the wavelength of an electron used for a typical SAED pattern can be defined by substituting $m_e v$ for momentum and combining the normal expression with the relativistic correction factor:

$$\lambda = \left(\frac{h}{\sqrt{2eUm_e}} \right) \left(\frac{1}{\sqrt{1 + \frac{eU}{2eUm_e}}} \right) \quad 5.3$$

which yields an electron with wavelength 2.5 pm. Comparing this to the Cu K α wavelength of 154 pm used in most X-ray diffraction measurements illustrates why the SAED is such a powerful tool in defining order and crystallinity at the atomic scale.

The two dimensional SAED is also much more efficient than techniques employing a point detector, as all forward scattering within a rather wide angular spread can be acquired at once. As shown in Figure 77, all crystalline features are revealed in one pattern, including those that are more diffuse, and these can all be analysed easily using radial and azimuthal intensity fluctuations. Further, the anisotropy of layered carbons can be quantified based on standard terminology and material properties applied to pyrocarbons [246]. Figure 78 shows the methods used to evaluate the orientation angle (OA) of a layered carbon by using the (002) plane in the SAED which has been well developed by Bourrat [31] and colleagues over the years.

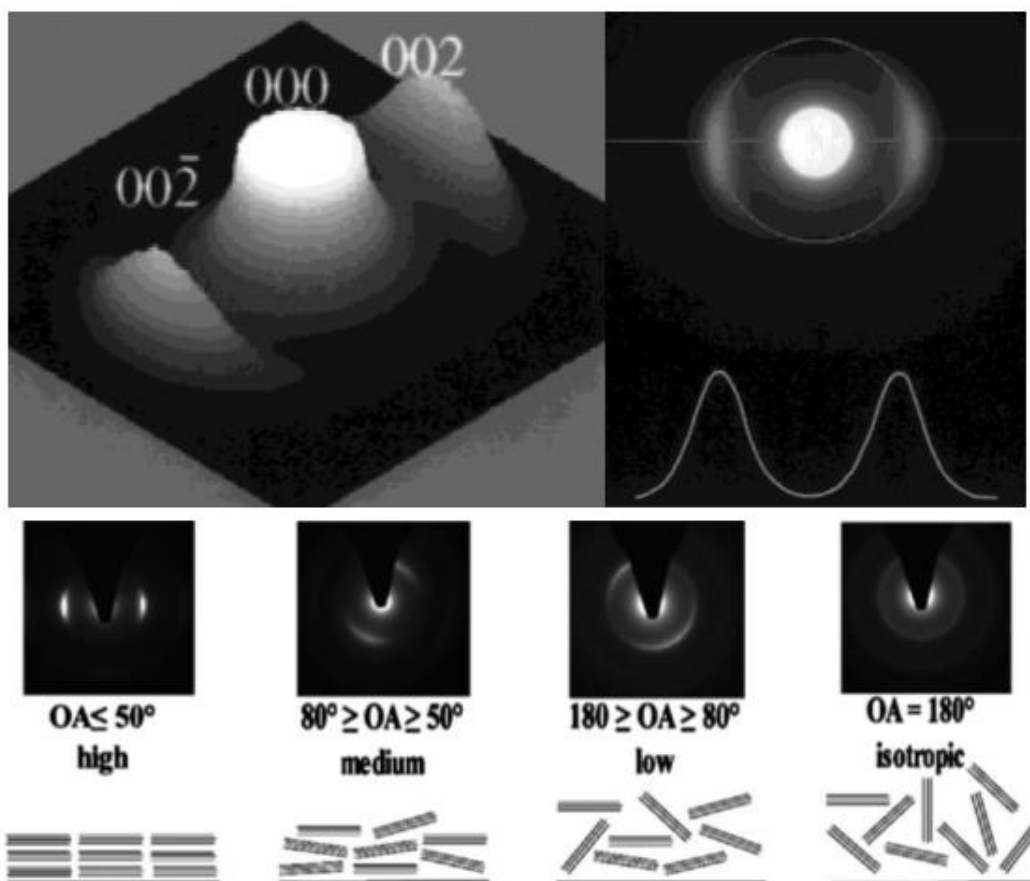


Figure 78. Method to measure the orientation angle (OA) of the (002) plane in layered carbons using the SAED, where the FWHM can be used to classify material into one of four levels of texture (from [247]).

5.2.2 Results and discussion

A lattice fringe analysis of a region in the HO3-rGO cross-section is shown in Figure 79, where the intensity fluctuations in the TEM image indicate regions where the graphene planes are more or less aligned. For reference, the precise details on the sample preparation procedure were given in Chapter 3. Areas where the edges of the carbon planes align create contrasting dark-light fringes, while the more amorphous areas appear grey. A region where the fringes appear can be used to create an intensity versus distance plot that measures the stacking distance of the (002) planes within the selected region. The region within the red box contains six distinguishable layers, with an average interlayer distance of 3.64 Å. Other methods, such as XRD, are better suited for obtaining a statistical average, but fringe analysis allows for added insight into the variations within each of the individual ordered regions. It is apparent that even within the highly ordered regions, the stacking is far from uniform, ranging from the lowest possible value of 3.34 Å (graphitic spacing) to 4.12 Å across a local selected area.

The TEM images presented here show that the structure of the dry rGO assemblies are very similar to many layered pyrocarbon materials [49], yet the rGO layers are clearly much more curved and disordered than most current literature about graphene-based materials assumes them to be. Since imaging alone does not provide the comprehensive information needed to build an accurate BSU model, the SAED pattern can be used to more quantitatively define the structure. As illustrated in Figure 80, the distinct diffraction rings demonstrate there is a high level of spatial order, and these features can be used to quantify the bond lengths and alignment within the rGO assembly. The two outer rings are produced by the crystallographic intra-sheet carbon bonds, depicted diffraction planes corresponding to the (100) plane at 0.213 nm and (110) plane at 0.123 nm which reconstruct to make the real space hexagon of graphene with $a_{C-C}=1.42$ Å shown in Figure 80. The inner ring corresponds

to the inter-sheet spacing of the (002) lamellar planes and shows an expansion from the π -stacking distance in crystalline graphite which is 3.35 Å. The distribution in the distance of the (002) ring from the beam centre (FWHM) can be attributed to the variation in inter-sheet spacing and/or strain present in the material, while the brighter spots are used to measure the longer-range of alignment of the layers.

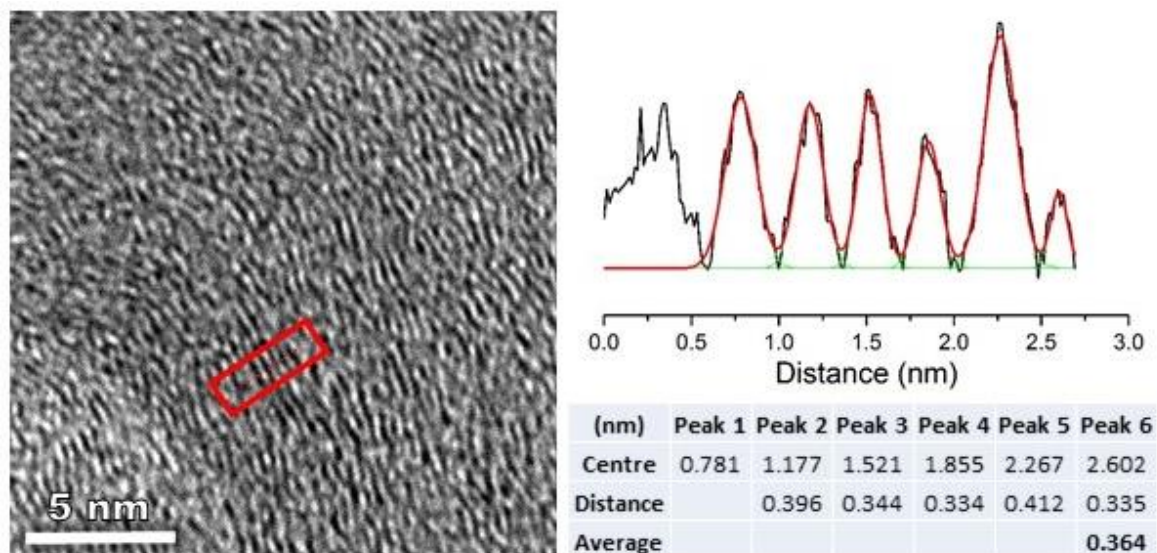


Figure 79. The fringe analysis technique measures fluctuations in intensity along a linear region of interest (shown in the red box on left image). A series of peaks is used to measure the distance between points of maximum intensity, which correspond to the interlayer distance (right).

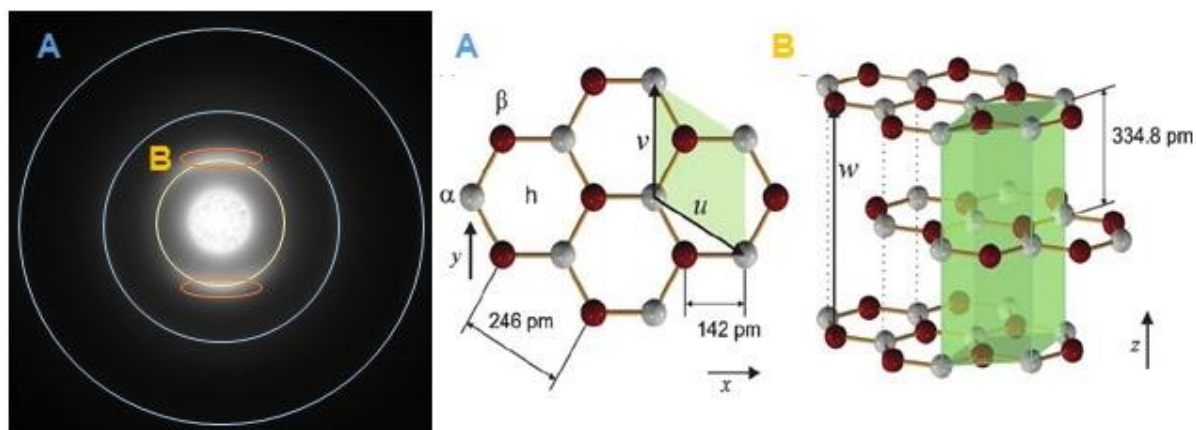


Figure 80. Diagram relating the rings seen in the SAED pattern to the unit cell of graphite (from [248]). The outer rings (marked A in blue) result from the intra-sheet carbon bonds while the inner ring and bright spots (marked B in orange) result from inter-sheet stacking of multiple basal planes.

Because the SAED pattern is anisotropic, it is best evaluated in sectors which correspond to the stacking direction in the rGO. As shown in Figure 81, a full 360° radial average is compared to the radial average within four sectors – two outlined in orange (1 and 3 where the (002) plane has highest intensity) and two outlined in blue (2 and 4 where the (002) plane has the lowest intensity). The bright regions in Figure 80(B) that are circled in orange exhibit the highest intensity and correspond to the stacking direction of the rGO sheets. There is a more defined, yet faint, ring extending across the full 360° which corresponds to a real-space periodicity measuring 4.0 Å (2.51 nm⁻¹). Even though this feature is close to the (002) ring region, it is an artefact produced from the carbon support film on the

TEM grid and is not a result of a physical feature within rGO assembly. After subtracting the background, a full 360° radial average, inter-sheet dominant orange sectors, and intra-sheet dominant blue sectors have each been fit with five peaks (A-E) to evaluate and compare the bond lengths, as reported in Table 9 and Table 10.

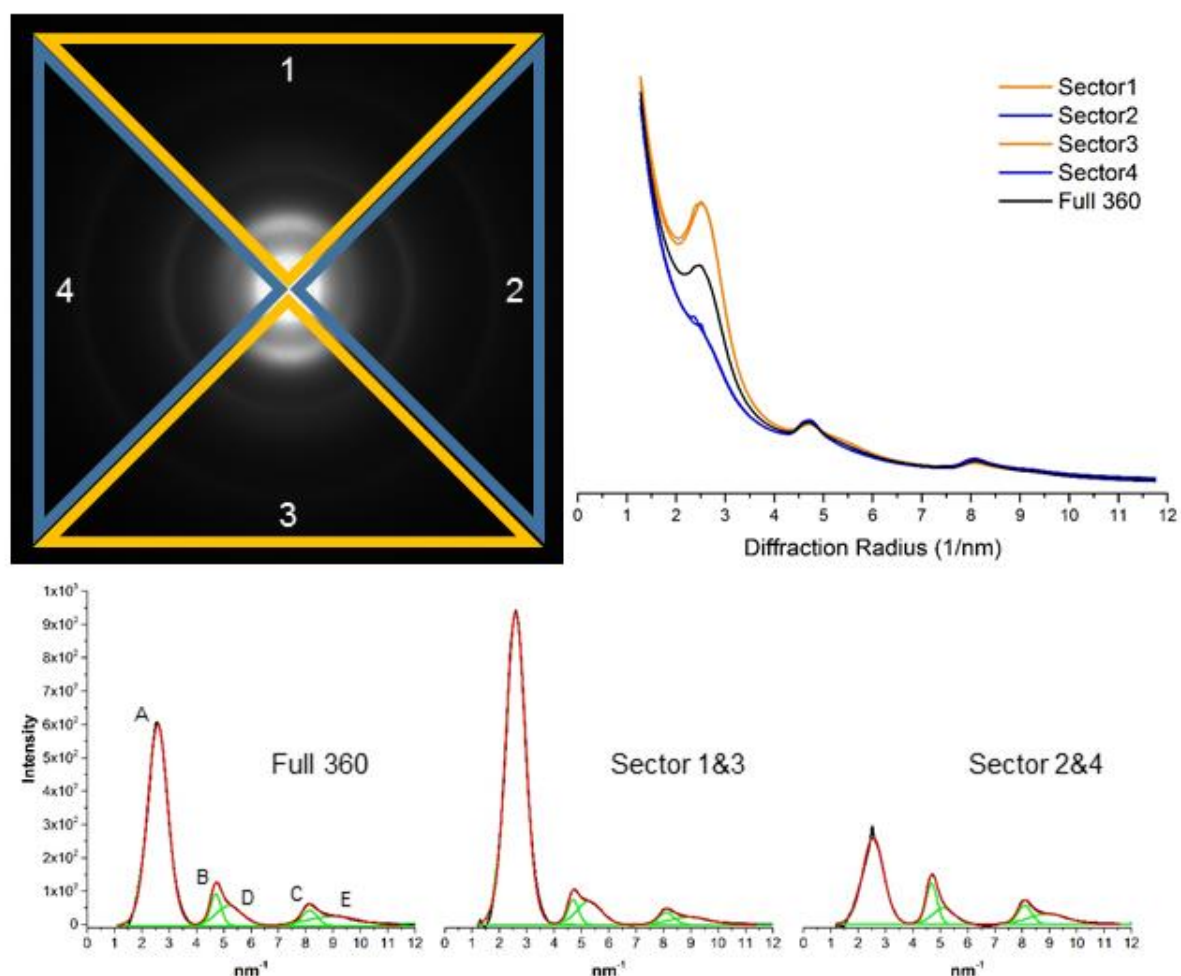


Figure 81. Inter-sheet lamellar stacking has enhanced intensity in sectors 1 and 3 (orange), while intra-sheet bonding is slightly enhanced in sectors 2 and 4 (blue). Radial intensity curves for each sector are plotted alongside the full 360° radial average to illustrate peak intensity is dependent on orientation. Peak fitting for the full 360° as well as sectors 1&3 and 2&4 was performed to obtain the values listed in Table 9.

Table 9. Results from fitting the SAED pattern to determine bond length, order, and alignment in the rGO assembly.

Peak (<i>hkl</i>)	Height (a.u.)			Centre (nm ⁻¹)			FWHM (nm ⁻¹)		
	360°	1 & 3	2 & 4	360°	1 & 3	2 & 4	360°	1 & 3	2 & 4
A (002)	605	938	261	2.59	2.59	2.55	0.868	0.837	0.906
B (100)	95	75	123	4.71	4.70	4.69	0.461	0.458	0.473
C (110)	47	37	57	8.14	8.12	8.10	0.647	0.649	0.598
D (004)	60	70	49	5.20	5.28	5.12	1.11	1.05	0.941
E (200)	29	23	32	9.03	8.97	8.95	2.21	1.69	1.68

Comparing the height of the peaks, shown in the first three columns of Table 9, indicates there is a strong preferential alignment within the rGO assembly, as would be expected in a layered carbon material. Comparing the difference in intensity values for sectors 1 and 3 versus sectors 2 and 4 make

it clear the inter- and intra- sheet bonds are relatively perpendicular to each other, with the (002) plane having a higher intensity within sectors 1 and 3, while the (100) and (110) planes are more pronounced in sectors 2 and 4. Further analysis of the SAED pattern can quantify the long-range alignment (curving of the layers) which produces the macro-disorder of the lamellar structure by measuring this radial intensity fluctuation along the (002) ring, as shown in Figure 82. This intensity spread is used to quantify what is referred to as the orientation angle (OA), and this value has been used to compare anisotropy relating to (002) plane fluctuations in different types of layered carbons [130, 131, 249, 250].

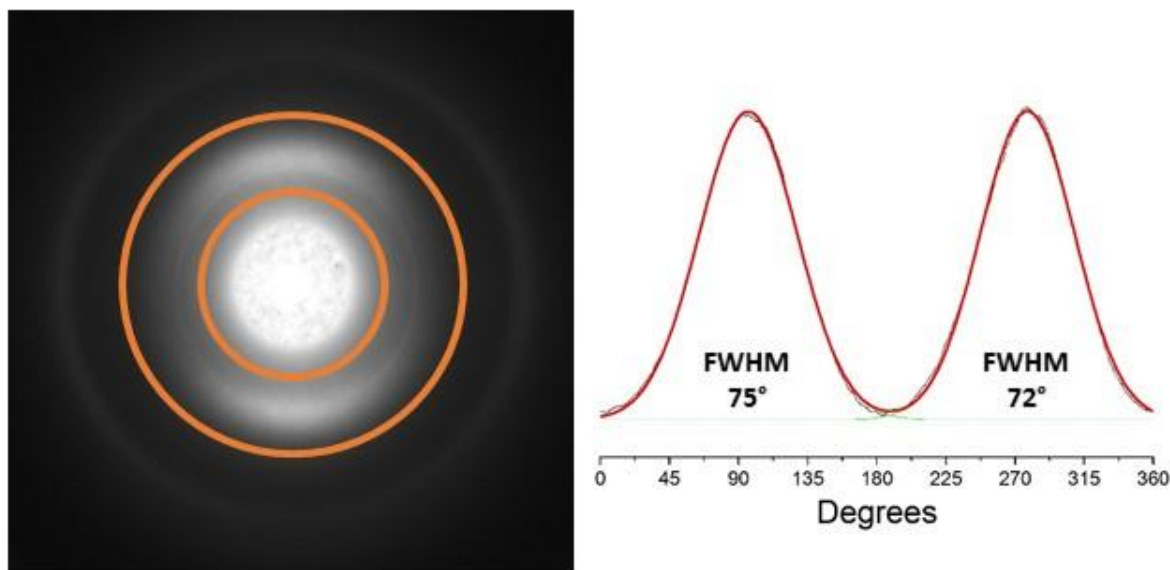


Figure 82. Measurement of intensity fluctuations along the (002) ring are used to classify the long-range alignment of the rGO layers (region between orange rings). This azimuthal intensity scan has been fitted with two Gaussians and the FWHM of 72° is a direct measure of the orientation angle (OA) used to classify layered carbon systems.

The OA is measured by taking an azimuthal intensity scan across the (002) ring of the SAED pattern, as depicted in Figure 82. Since the carbon sheets can be modelled as plates, or thin disks, a higher degree of alignment between the plates will produce two distinctly defined spots, while a purely disordered structure will produce an isotropic ring of constant intensity. If there is any alignment between the sheets, the (002) ring will be anisotropic and a plot of the azimuthal intensity will contain two peaks. From this, the FWHM can be used to categorize the carbon within the four assigned classes of high, medium, low, or isotropic [246]. For the rGO assembly tested here, the FWHM value of 75° shows it falls within the *medium* classification (OA values 50° to 80°).

The middle three columns in Table 9 compare the $(00l)$ and (hk) reflections of the diffraction radii, which is determined by the bond length for each indices, and these values remain fairly constant within all sectors. The SAED results are an average value of all the material probed in the viewing locus and are more representative of the whole than that measured with fringe analysis which samples only a very localized region over a few stacked clusters of rGO layers. The SAED pattern is also able to account for periodicity extending into regions of the image that visually appear disordered, and gives a more accurate measure of (002) spacing than using image analysis alone. This explains why the values in Table 10 are greater than the average interlayer spacing calculated from fringe analysis in Figure 79, and highlights these fluctuations in stacking height. It is clear that the more ordered regions achieve the minimum value for turbostratic stacking of 3.44 Å, yet the majority of the more disordered bulk consists of expanded interlayer spacing closer to 4 Å. The (100) and (110) reflections show the intra-sheet bonds between carbon atoms match those for graphite and pure graphene (hexagon with $a_c = 1.42$ Å and $\alpha = 120^\circ$), and these values are equivalent in Table 10. This supports the view that the

rGO sheets retain a high level of structural integrity *within the clusters*, with six-ring carbon bonds being the dominant bond-type making up the coherent domains even after reduction.

Table 10. Corresponding values for $d_{(hkl)}$ from the SAED pattern of rGO assemblies compared to those of graphite, with the L_c values highlighted for (002) and (004) reflections being the most accurate measurement for the coherence length of the BSU along the c-axis, as discussed in the text.

Peak (<i>hkl</i>)	d-space (nm)				Coherence Length (nm)		
	Graphite	360°	1 & 3	2 & 4	360°	1 & 3	2 & 4
A (002)	0.335	0.387	0.386	0.392	2.05	2.13	1.96
B (100)	0.213	0.212	0.213	0.213	7.98	8.04	7.78
C (110)	0.123	0.123	0.123	0.124	5.69	5.67	6.15
D (004)	0.168	0.192	0.189	0.195	1.60	1.70	1.89
E (200)	0.107	0.111	0.112	0.112	1.67	2.18	2.19

The Scherrer equation (equations 2.8 and 2.9) can be applied to the FWHM values in the later columns of Table 9 in order to estimate the lower bound for the length of the coherent domains, and these results are shown in Table 10. Initial analysis indicates the measure of layered stacking along the c-axis making up each coherent unit, L_c , extends for 2 nm, which equates to an average of 5 graphene sheets, given the average of 3.9 Å per interlayer spacing. The value for L_c is slightly reduced in the (004) peak, where the smaller domains equate to 4 layers, and because size broadening is independent of the diffraction angle, there must be a contribution from strain broadening present in the peak profile as well. Based on the Voigt fitting parameters, the peak shape for the (002) reflection is half Lorentzian (size broadening) and half Gaussian (strain broadening), and it is clear the Gaussian component plays a more dominant role in the (004) peak profile. Applying equation 2.10 to estimate the strain contribution to broadening, for spectra in the sectors for the direction perpendicular to the (001) plane (1&3), indicates strain could be contributing up to 30% of the peak broadening, which is expected in materials with sub-micron sized crystallites and stacking faults [45, 130, 251, 252]. Reevaluating the results for L_c with this in mind implies the coherent domains along the c-axis most likely consist of 7-8 rGO layers per stack.

The narrower (100) and (110) peaks suggests a much larger coherent region along the aromatic planes with L_a values of 6-8 nm. This is rather large for a porous turbostratic carbon, especially without annealing, as most materials have a typical L_a close to 1 nm in length [30, 170]. This could be a major reason for the improved performance of rGO assemblies (as compared to typical porous carbons), as it is known that larger values of L_a significantly contribute to increasing the conductivity in layered carbon materials [104, 133, 253]. Difficulties in accurately assessing these peak profiles arise because they overlap with the (004) and (200) reflections which are broadened further from the strain mentioned previously. It is clear there is significant asymmetry in the peaks from the (*hk*) reflections in rGO assemblies resulting from the two-dimensional crystallinity, which is expected for disordered carbons and/or nano-graphitic crystallites [31, 169, 183]. This was discussed in Chapter 2 (section 2.2.3.2 page 43), and lattice reflections of this type exhibit a sharp rise at the position of the Bragg plane that then falls off slowly toward large angles and is highly dependent on the alignment between the (*hk*) planes and incoming beam, as was detailed in Figure 32.

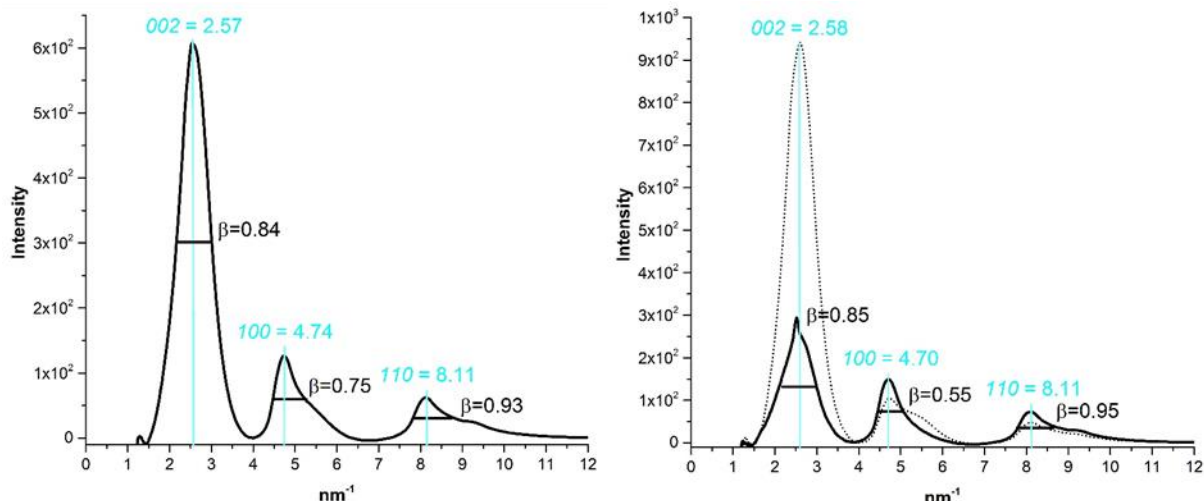


Figure 83. The maximum peak height was used to determine the location of the peak centre and breadth of the (002), (100), and (110) planes from the SAED pattern. The full 360° radial average is shown on the left and a comparison between sectors 1&3 (dotted) to sectors 2&4 (solid) is shown on the plot to the right.

For layered carbons that can be oriented with the layer planes parallel to the incoming beam (not powder diffraction samples), a simplified approach using the different sectors from the SAED is applied where the peak centre and broadening are directly measured from sectors within the curve itself [169, 183], as shown in Figure 83. As expected, in all cases, the peak centre is not significantly affected by the chosen method or by the sector analysed, but, there are pronounced differences in the values obtained for peak broadening depending on the method of measurement and the sector being analysed. This is related to the overlapping of the (100) and (004) peaks, as well as the broadening toward higher angles of the (*hk*) intensity distribution [183], and has large implications for determining the size of the coherence domains, as shown in Table 11. Sectors 2 and 4 are a direct measure of the (*hk*) indices, where the (100) reflection shows the largest difference in FWHM depending on the sector.

Table 11. Comparison of peak parameters and corresponding real-space values for data taken from the curve fitting or directly from the reduced SAED spectra, with the values in the final column being the most accurate assessment of L_a , as discussed in the text.

Peak (hkl)	Curve Fitting		Direct Spectra Figure 83				Figure 84
	Centre	FWHM	Centre	β 360°	Centre	β 2&4	β 2&4
A (002)	2.59	0.868	2.57	0.84	2.58	0.84	N/A
B (100)	4.71	0.461	4.74	0.75	4.70	0.55	0.60
C (110)	8.14	0.647	8.11	0.93	8.11	0.95	0.80
Real Space	D (nm)	L (nm)	D (nm)	L (nm)	D (nm)	L (nm)	L (nm)
L_c	0.386	2.05	0.389	2.12	0.388	2.09	N/A
$L_{a(10)}$	0.212	7.98	0.211	4.91	0.213	6.69	6.13
$L_{a(11)}$	0.123	5.69	0.123	3.92	0.123	3.87	4.60

In order to avoid more complicated fitting procedures [176], the anisotropic pattern allows that the SAED be analysed directly across the (*hk*) reflection eliminates the peak broadening contribution from the “fountain-like” spreading in these bands [183]. Measurement of the peaks across the narrowly

defined region shown retain the rod-like diffraction pattern, as shown by White and Germer [183] and reproduced in Figure 33. The resulting pattern from the narrow region selected in Figure 84 has more clearly defined (hk) bands, and the results shown in the last column Table 11 are thus most accurate in determining the length of the L_a coherence domain in this rGO assembly.

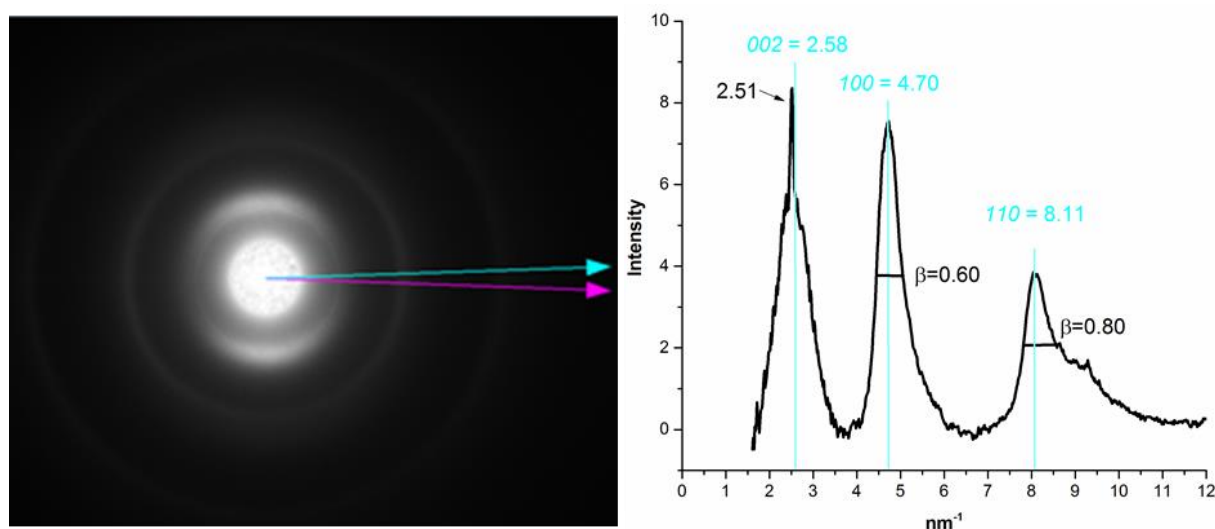


Figure 84. Measurement of the anisotropic SAED pattern across a very narrow range (5° spread between the pink and blue arrows) which corresponds to the (hk) reflections allows for the (10) and (11) peaks to be analysed without broadening due to the “fountain-like” spread from two-dimensional crystals. The sharp feature at 2.51 nm^{-1} is an artefact from the TEM support grid and is ignored in the rGO structural analysis.

To compare these calculations with direct imaging, the structure of the aromatic domains and stacked layers can be better visualized after modifying the TEM image using software such as ImageJ [254], as shown in Figure 85. Visual modifications that highlight the edges of the carbon planes (top right) make the ordered domains more clearly visible, and this shows a complex mix of ordered and disordered regions. Using the modified image (top right), eighty sites were used to measure the aromatic and stacked regions within the image, as demonstrated with the pink (stacking) and green (aromatic) lines denoting how the areas were measured (bottom left). It should be noted that this technique is to gain insight on the structure within the coherent domains, not to be used as a definitive measurement method. Nevertheless, the histograms in Figure 85 (bottom right) clearly show the most prevalent cluster size contains three to five layers and appear to have an aromatic domain just under 1 nm . The average values give slightly larger results, with ordered clusters having an average stacking height of $2.0 \pm 0.9 \text{ nm}$ (approximately 5 layers) and aromatic domain lengths of $1.1 \pm 0.4 \text{ nm}$.

Assessing these results in context to the model for porous carbons put forth by Oberlin et al. [156] shown in Figure 76, it appears the SAED results are a measure of the coherence length, L_c , while the measurements for the fringe length in the coherence domains appearing in the TEM images are representative of the smaller aromatic units, labelled as l . To verify this, and clarify the precise elements making up the BSU of rGO assemblies, an in-depth investigation into measuring the aromatic domain using Raman spectroscopy is presented in the next section, as it offers a more direct measure of the aromatic domain length, l , what is also termed the “inter-defect distance” in graphene sheets [107]. Further analysis on the aromatic domain length will continue throughout this chapter, and much discussion is devoted to this because there are many open questions regarding how to most accurately assign quantitative L_a values to the (hk) planes in rGO assemblies.

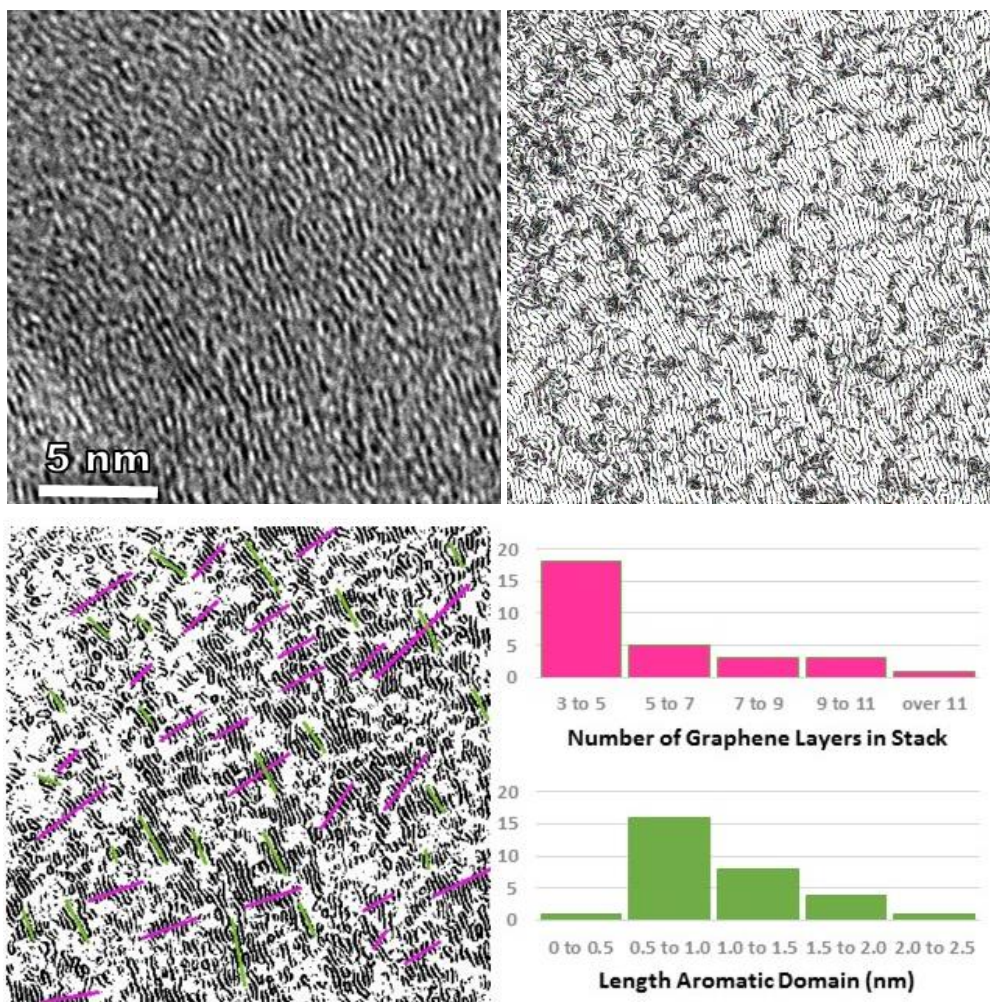


Figure 85. Original TEM image (top left) that was then modified using ImageJ [254] to highlight the stacked aromatic regions (top right). The image was further modified and then measurements were taken to quantify the domain length and number of stacked layers (bottom).

The TEM results indicate the dry rGO assemblies are very similar to other layered carbons and can be characterized using longstanding data interpretation methods to classify order within the material [30, 31, 150]. The results here also act as a guide for interpreting data presented in the following sections as it is clear there are no graphite nano-crystallites in the rGO assembly, and instead the material is made up of extended and roughly-aligned rGO sheets that assemble to form an continuous network with ordered, *mosaic cluster* regions surrounded by a more disordered carbon matrix (these elements are not referenced using the more common term, *mosaic crystal*, because they contain no three-dimensional crystallinity). Distortions within the mosaic clusters are due to perturbations in the sheets (corrugations) and translation, while the disordered matrix results from long-range misorientation produced by strain and variations in composition (defects or oxygen functionalities). The inter-sheet spacing of dry rGO assemblies within the coherent mosaic cluster domains is relatively constant, without much deviation from the expected values of a turbostratic structure, while the more disordered regions are slightly expanded to values closer to 4 Å. These stacked regions are not accessible to ions and will also block passage into expanded regions within the material – effectively diminishing overall surface area and decreasing accessible porosity.

Another aspect of interest is the general sheet size of the graphene making up the rGO assemblies, as this strongly contributes to the overall conductivity of the bulk material [133]. While the SAED pattern gives detailed information on the stacking distance, bond lengths, and overall orientation of the layers, it can only be used to estimate the length of the coherence (ordered) domains, as the highly distorted layers seen in the TEM image cannot be used to accurately measure the lateral sheet dimensions. As

shown in Figure 86, it is difficult to track each graphene layer outside of the coherent domains where fringes can be seen. It is not clear whether the sheets are highly corrugated but intact, or if they contain rips and defects that cleave the planes. High-resolution SEM imaging clearly shows the individual rGO sheets are indeed continuous, extending across hundreds of nanometres without any detectable rips or defects other than corrugation and wrinkling. This explains how the rGO assemblies remain stable as free standing films in the hydrated and dried condition, since the overlapping of large, corrugated layers facilitates many contact points. The combination of these two techniques leads to the conclusion that the defective areas appearing in the TEM image are due to corrugation and disorder which produce expanded stacking faults in the carbon network. The fringes in TEM are likely to correlate with the “aromatic regions”, I , along the rGO sheets, and this can be used to assist in the interpretation the results from Raman spectroscopy discussed in the next section.

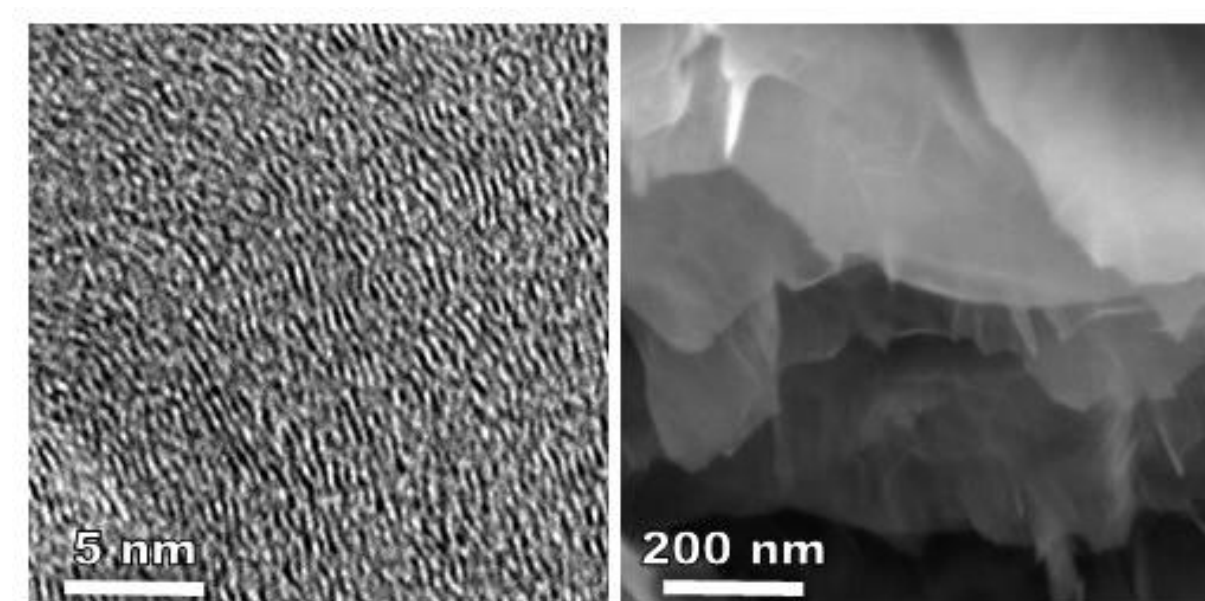


Figure 86. Edge-on images of rGO assemblies from TEM (left) can be better interpreted alongside high-resolution SEM (right) imaging which shows the very small lattice fringe lengths in TEM (< 5 nm) are due to disorder and stacking faults as SEM shows the size of rGO sheets extends to hundreds of nanometres.

5.3 Raman Spectroscopy

5.3.1 RMS applied to rGO assemblies

The author acknowledges this section is quite lengthy and detailed. There is good cause for this, as there is much confusion in the current literature on how best to interpret the results of Raman spectra from disordered graphene-based materials. Since RMS is one of the most widely applied methods used to understand the carbon bonding in rGO sheets, and because the parameters it identifies are of the utmost importance in determining fundamental causes of structure-property relationships in many carbon materials, the detailed analysis presented here is necessary to correctly interpret the results that follow. Further, within a broader context, this in-depth analysis aims to make a contribution toward understanding how the spectral features of various carbon forms can be directly tied to structural elements in rGO assemblies.

5.3.1.1 Raman spectra for graphene

Raman is a useful tool for characterizing bonding in carbon materials and has been extensively used to study the properties of graphene. First order Raman scattering involves phonons with wave vector $q \approx 0$ (G-band) while higher order Raman processes involve phonons with $q \neq 0$ (D-bands). Due to the high symmetry of sp^2 carbons, Raman spectroscopy is the most sensitive technique to characterize

disorder in the carbon network, providing information on any symmetry-breaking defects within the system. As shown in Figure 87, the main features in the Raman spectra of graphene and other layered carbon materials are commonly the G band, D band, D' band, 2D (also known as G') band, and the D+G (or D+D' depending on interpretation) band.

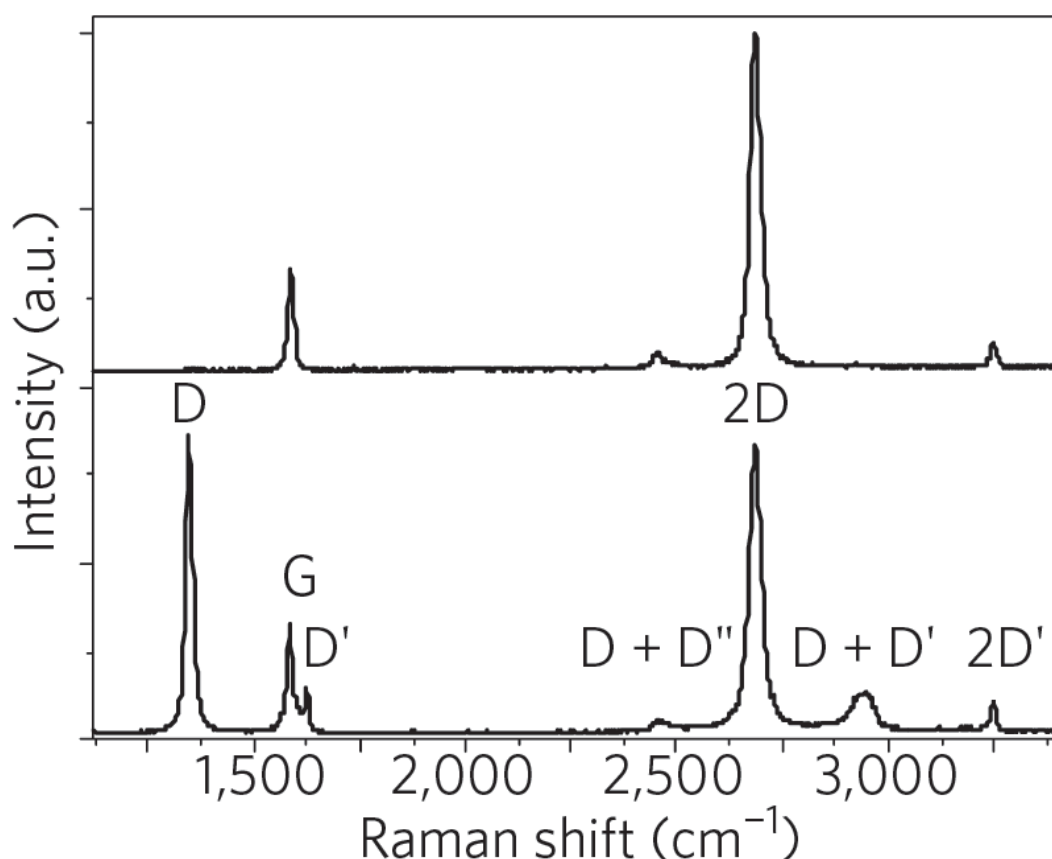


Figure 87. Example of Raman spectra for pristine graphene (top) and defective graphene (bottom), highlighting the main features used for structural analysis and interpretation (from [124]).

As shown in Figure 87, the Raman spectra for defective graphene materials can be described based on two main regions: one ranging from 1100 cm^{-1} to 1700 cm^{-1} (first-order) and another from 2400 cm^{-1} to 3200 cm^{-1} (second-order). The most prominent peak in monolayer graphene and graphite is the G peak, which is seen at 1580 cm^{-1} within the first-order region (graphite at 1580 cm^{-1} , GO at 1594 cm^{-1}). This band is directly related to sp^2 bond structure seen in graphene materials (six ring aromatic carbon sheets but is also active for chain-like bonding) and does not depend on the number of stacked graphene layers. Broadening of the G peak is directly related to the disorder along the graphene plane, and slight shifts in position (as small as $3\text{--}5\text{ cm}^{-1}$) are due to chemical doping or strain. The other peak in this region seen at 1350 cm^{-1} is the main D band which is directly related to disruption of the sp^2 symmetry in six ring aromatic bonding a pure G band material. Both the G and D bands result from six-member carbon rings, but the D band becomes active only when there is a disruption in the symmetry induced by an edge or a defect within the basal plane. Unlike the G band, the position of the D band is dependent on the laser excitation energy used. Graphene and graphite materials also exhibit a band that overlaps with G at 1620 cm^{-1} , termed D', which becomes active due to phonon confinement induced by edges only, and thus, is associated with finite-size graphitic crystals. In more disordered carbon materials, the D' band is masked by the much broader G band and cannot be used directly in the analysis of crystallite size.

The second-order region includes less prevalent features resulting from combinations of the other modes. The 2D (or G') band is often used in analysis of multilayered graphene materials, as it is Raman

active for crystalline aromatic domains in the graphitic material (π -states), and can be directly related to the number of stacked graphene layers [243]. Due to this method of activation, it is important to note that the absence of Bernal stacking between graphene layers (as in turbostratic graphite) will produce a 2D peak with shape and position equal to that of single layer graphene. Nano-graphitic crystals have a strong 2D peak because of the large edge to plane ratio, and bilayer graphene has a much broader and upshifted 2D band with respect to single layer. Thus, some aspects of stacking structure within layered carbon materials can be determined by the line shape of the 2D feature.

5.3.1.2 Raman spectra for carbon materials

While most of the recent publications on the structure and properties of graphene-based assemblies approach RMS results from a pristine graphene perspective, the nature of the defect induced bands in carbon materials is quite complex and has been an area of rigorous research for many years [125, 134, 170, 255-257]. Further, the more disordered the carbon material, the more difficult it is to clearly interpret the structural elements producing specific features in the spectra. This complexity increases as defective layers combine to form assemblies, and the Raman spectra for many porous carbons show even more features than those outlined in Figure 87. Only recently have there been in-depth studies that apply knowledge of these lesser-known Raman features to graphene oxide [258], and the analysis on rGO presented here aims to contribute to this field.

To begin the discussion on layered carbons, graphite is used as a standard because it is considered the most ordered, crystalline form while all other types will vary in both structure and composition. As previously discussed, the term 'crystallite' is often misused when describing the structure of porous carbons, as it should only be applied to three dimensional crystalline graphitic domains within the porous carbon material. Thus, using RMS to identify crystallite size refers to two separate crystallographic dimensions which are often uncorrelated. In the x-y plane, there is L_a used to define the length of the aromatic domain along the graphene sheet, while in the z direction there is L_c , defined by a precise number of Bernal stacked graphene layers with oriented stacking in the (002) direction. A detailed analysis of the 2D (also termed G') peak performed by Cancado et al. [259] resulted in a method to determine the out-of-plane lattice parameter from the Raman spectra and thus count the number of stacked graphene layers making up the crystallite structure. This can become confusing as the aromatic length defined by Raman spectra is defined as L_a in the literature, but it actually corresponds to the measure of l as defined by diffraction and image analysis contributing to Oberlin's model [156] shown in Figure 76. This section will hold to the typical RMS referencing of L_a in order to more clearly discuss and compare the results of existing literature, and then make a clear distinction between the two elements, L_a and l , in the concluding remarks.

While it is known that the 2D peak is indicative of highly ordered π -bonding and indicates the number of stacked graphene layers within the assembly, this is only true when crystallographic (002) plane Bernal stacking is present [125]. If the original graphite material is completely exfoliated during the oxidation process, no graphite remains and the restacked GO and rGO sheets within the assemblies will contain only turbostratic domains of stacked graphene layers. Thus, the resulting 2D peak will resemble that of single-layer graphene, as depicted in Figure 88. Turbostratic carbons and single layer graphene will have a single Lorentzian 2D band (centred at approximately 2780 cm^{-1} if using 2.41 eV), but turbostratic multi-layer graphene typically has decreased relative intensity and a much larger linewidth compared to that of single-layer (FWHM of $45\text{-}60\text{ cm}^{-1}$ and 24 cm^{-1} respectively). However, the intensity of the 2D band in different turbostratic materials provides insight on the prevalence of stacked regions, and the combination of X-ray diffraction analysis and Raman spectroscopy can be used to evaluate a corresponding coherence length from alignment along the (002) axis. Again, while the coherence domain is a measurement for the size of ordered structures composing the rGO assembly,

care should be taken to not label these regions as crystallites because no three dimensional crystallinity exists.

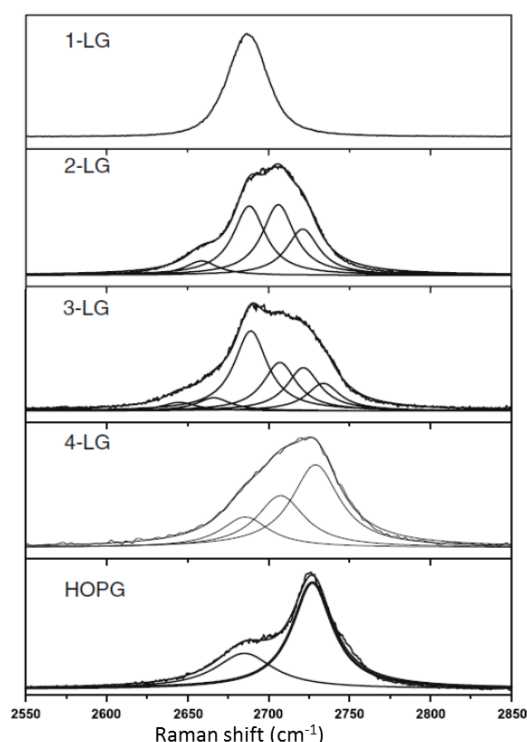


Figure 88. Comparison of the 2D (also termed G') Raman band taken with 2.41 eV laser energy for HOPG and 1-4 layers of graphene with Bernal stacking [125].

For all disordered carbons, regardless of the relative graphitic ordering, the Raman spectra is dominated by the D and G features resulting from sp^2 sites. While the G band is usually associated with 'graphitic' content, it is active with the motion of pairs of sp^2 atoms and *does not actually require the presence of sixfold aromatic rings*. As discussed, the D peak only becomes active in the presence of broken symmetry, however its intensity is *related to the presence of sixfold aromatic rings*. This fact can be easily misunderstood when conceptualizing the structure of disordered carbon from Raman results, with the aromatic domains are commonly defined incorrectly using the Tuinstra and Koenig (TK) model where the ratio of the D and G peak intensities is inversely proportional to the size of aromatic domains (L_a), or in-plane crystalline regions within the carbon network [255]. While the TK relationship holds for graphite clusters and other carbons with larger aromatic domains ($L_a > 10$ nm as in HOPG, graphene, etc.), the situation becomes more complex in disordered systems and warrants a more detailed discussion on interpretation of the features in rGO assemblies.

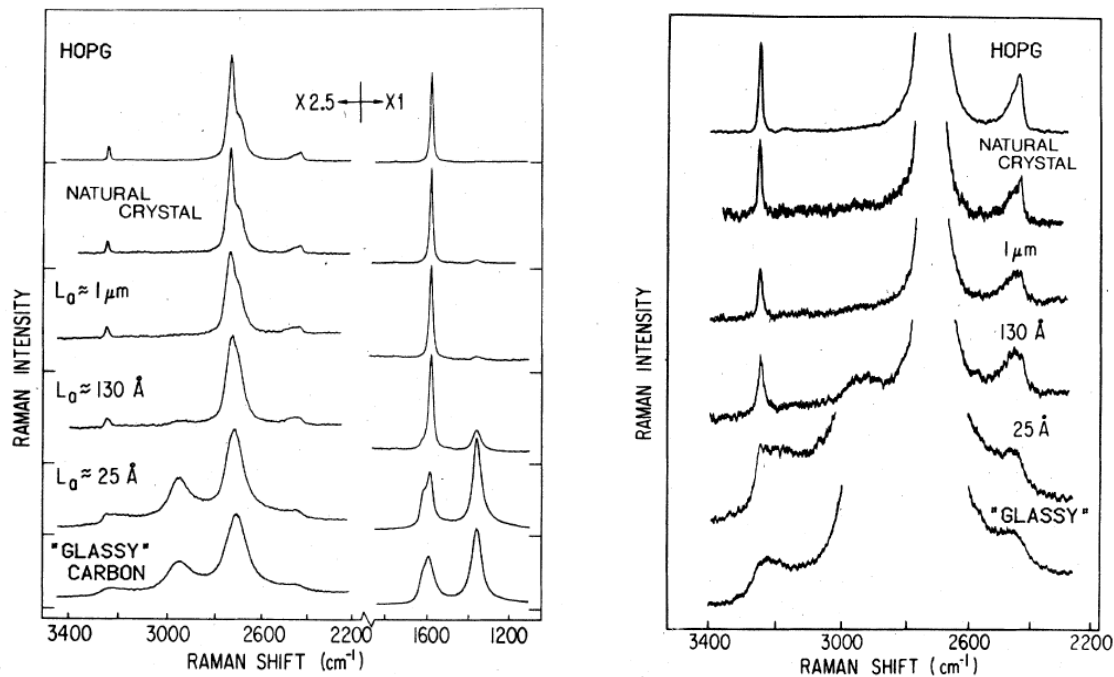


Figure 89. Evolution of first- and second-order Raman spectrum for HOPG and graphite crystallites of decreasing size, highlighting the presence of the D-band (1355 cm⁻¹) and broadening in second-order peaks as L_a decreases (from [260]).

Much work has been done using graphite and HOPG to show the effects of how the relative size of graphitic crystallites impacts both the first- and second-order spectral features, as shown in Figure 89. The spectra track the evolution from crystalline graphite and HOPG through nanocrystalline graphite to what they label “glassy” carbon [260]. It is clear that a transition takes place from the 13 nm to 2.5 nm crystallites, with the 2.5 nm material being much more closely related to glassy carbon – a characteristic also seen in rGO assemblies. These features were first explained in the work of Tuinstra and Koenig [255]. Not only were they the first to report the Raman spectra for graphite, Tuinstra and Koenig also correctly attributed the D band to the breakdown of the k -selection rule and correlated the relative intensities of the D and G peaks with the amount of ‘unorganized’ carbon and graphite crystal size. Quantitative values for the length of the crystallite, L_a , could then be found using the Tuinstra–Koenig (TK) relation:

$$\frac{I_D}{I_G} = \frac{C(E_{laser})}{L_a} \quad 5.4$$

where $C(E_{laser})$ is a constant that depends on the energy of the laser. Unfortunately, this equation is often incorrectly applied to more disordered carbon materials (as will be shown in detail throughout this section), and in spite of the much deeper understanding of Raman spectra of carbons available today, many authors continue to incorrectly apply the TK relation when evaluating graphene based assemblies and other porous, defective, or disordered carbons [170].

Knight and White [261] compared Raman spectral features across a broad range of carbon materials to discern relationships between peak profiles and real-space structural features, as shown in Figure 90. By examining materials with various types of carbon bonding and defects, they were able to correlate the peak width of the G-band with disorder, but found the TK relationship between the D/G intensity ratio and L_a did not hold for many types of graphitic and non-graphitic carbons. Further, the comparison of various graphitic carbons with different types of bonding allowed for insight on how various amounts of sp^2 and sp^3 regions influence the spectra. This work is especially valuable when assessing new types of carbon assemblies, such as the rGO investigated here, because the overall spectral shapes are a good guide in deciding what features are best suited for structural

characterization. For example, comparing the spectral shapes in Figure 90 to results of this work on rGO assemblies shows rGO is most similar to glassy carbon, a material that is not normally referenced when analysing Raman spectra for graphene-based assemblies. It should be noted that at the time of Knight and White's publication, it was thought glassy carbon was an amorphous carbon containing both sp^2 and sp^3 bonds, but now IUPAC designates it cannot be classed as amorphous and is known to be purely sp^2 consisting of a fullerene type structure [262].

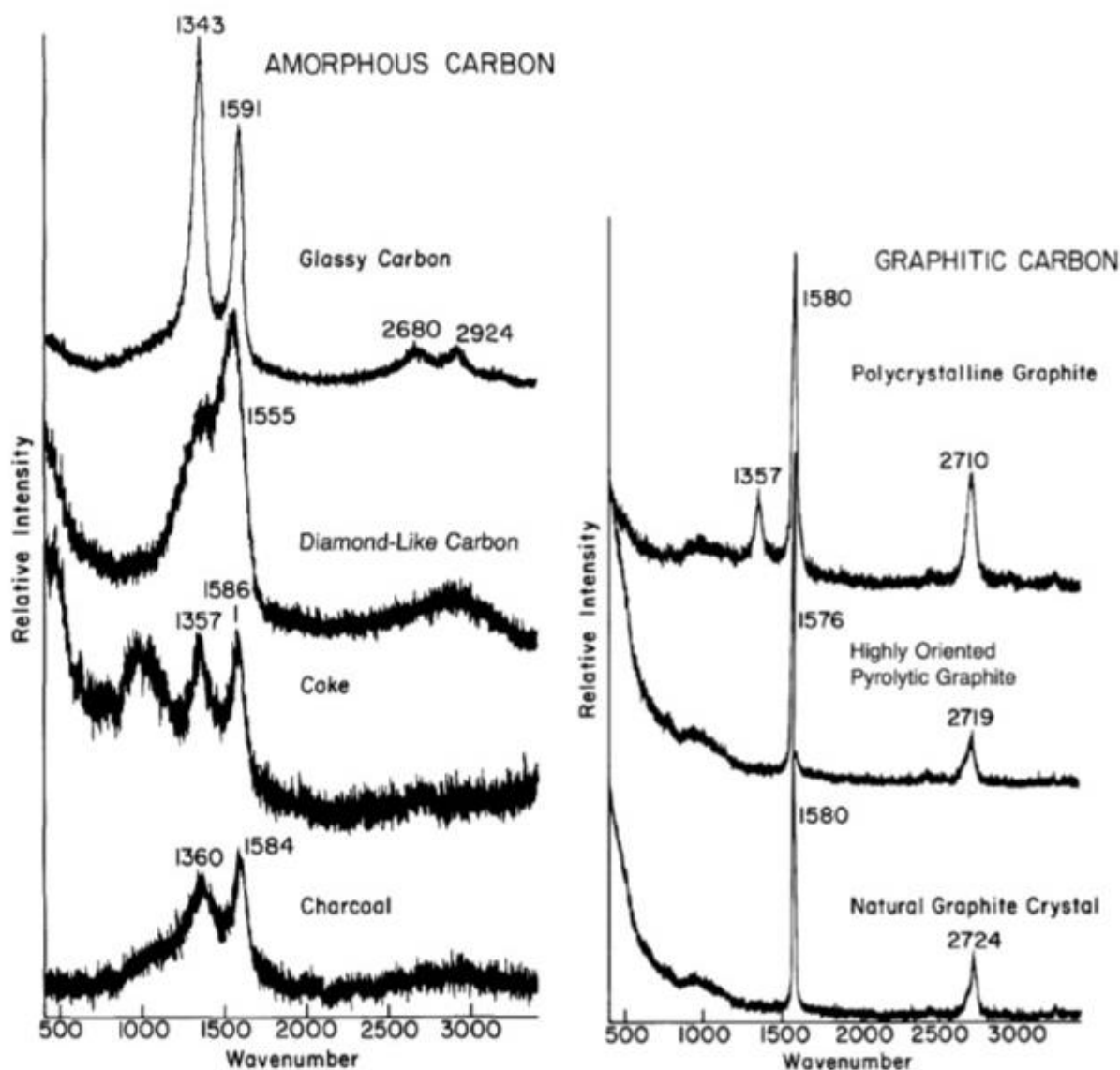


Figure 90. Raman spectra for various noncrystalline, mainly graphitic, amorphous carbons (left) compared with those for crystalline graphitic carbons (right) [261].

To clarify the origin of the D band, Wang et al. [256] published another detailed comparison between graphite and related sp^2 carbon materials including glassy carbon, single crystal graphite, varieties of HOPG, and 0.6% boron-doped HOPG (B-HOPG). The authors include a wide range of spectra alongside tables listing peak features for results taken with different laser wavelengths. This comprehensive report is extremely useful as it significantly reduced the ambiguity of analysis by presenting spectral features of diverse carbon materials in tandem. At the time, there was not a clear consensus of the origin of the D-band, with some authors attributing its appearance at 1360 cm^{-1} to specific vibrations at the edges of graphene layers. Wang's work [256] showed that the D-band is not directly related to carbon edges nor is it related to the presence of edge bonded functional groups, and instead fully

ascribed the D-band to vibrations in the hexagonal lattice alone. While the vibrations are impacted by edges, and in this case correlate with the size of aromatic regions (L_a), it was shown that this is not the only condition where the D-band is observed.

A comparison between HOPG and B-HOPG gave significant insight into how the nature and origin of the D band can be fully ascribed to symmetry breaking. Results showed the vibrational frequencies seen in HOPG are accompanied by previously unseen 'defect' bands at 1367 cm^{-1} (D), 1620 cm^{-1} (D'), 2950 cm^{-1} (D+G) for B-HOPG. Since the introduction of boron into the carbon lattice has no significant effect on the lattice parameters, nor does it create any edges, authors conclude the defect bands become optically active under any condition where the $K=0$ selection rule breaks down, not only because of edges or crystallite dimensions. Further evaluating the impact of oxidation, they show the D-band is not impacted by intercalated oxygen groups or oxidative edge groups, as this doesn't change the size of the aromatic domain. Further, results for carbons containing large amounts of oxygen bound along the basal plane were shown to be very similar to that of glassy carbon, a less-ordered carbon materials with minimal oxygen content – again supporting the assertion that the D-band can be fully ascribed to symmetry breaking vibrations in the hexagonal lattice.

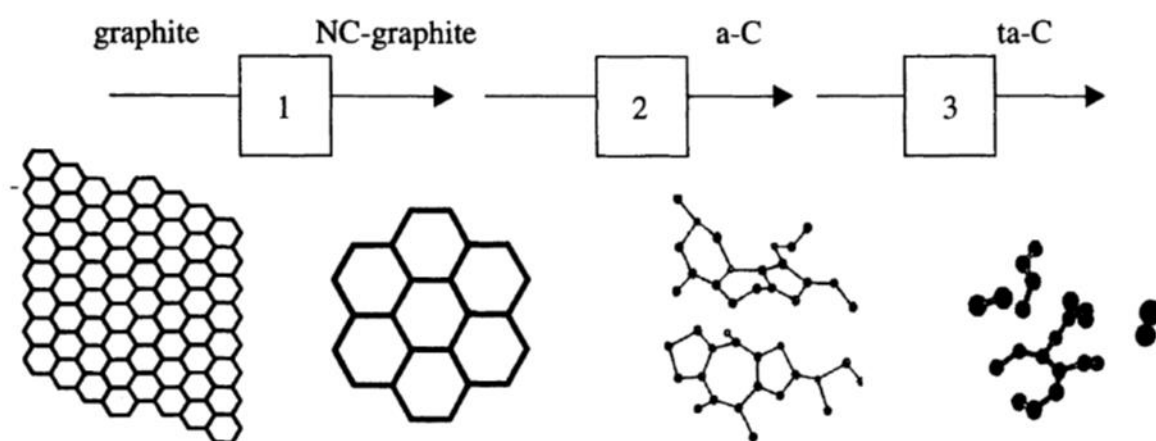


Figure 91. Graphic depiction of the sp^2 and sp^3 configurations in the three stage amorphization trajectory from graphite, to nanocrystalline graphite, to amorphous carbon (a-C) and tetrahedral amorphous carbon (ta-C) proposed by Ferrari and Robertson [171].

In 2000, Ferrari and Robertson, now longstanding experts in interpreting the Raman spectra of carbon materials, proposed the three-stage model depicted in Figure 91 to describe the amorphization trajectory from graphite (pure sp^2 bonding) to pure sp^3 amorphous carbon [170]. During Stage One, the graphite layers become smaller and the in-plane correlation length is reduced. As more topological disorder is introduced during Stage Two, the TK relation is no longer valid because while there are still aromatic rings, little long-range order exists along the graphene sheets. During the final stage, the sp^2 sites are converted from rings to chains, alongside a sharp increase in sp^3 bonding. Figure 92 shows how this model relates known physical processes to the size and position of the D and G peaks, and, under the restricted range of conditions given for the model, this method can be used to derive the sp^3 content in many different carbon materials containing various degrees of disorder. This work and future publications [171, 243, 263] not only provided useful models to understand the dynamic structural changes in various carbon systems, but it also showed how to use different aspects of the Raman spectra to determine the structure and composition of ordered and disordered carbon materials.

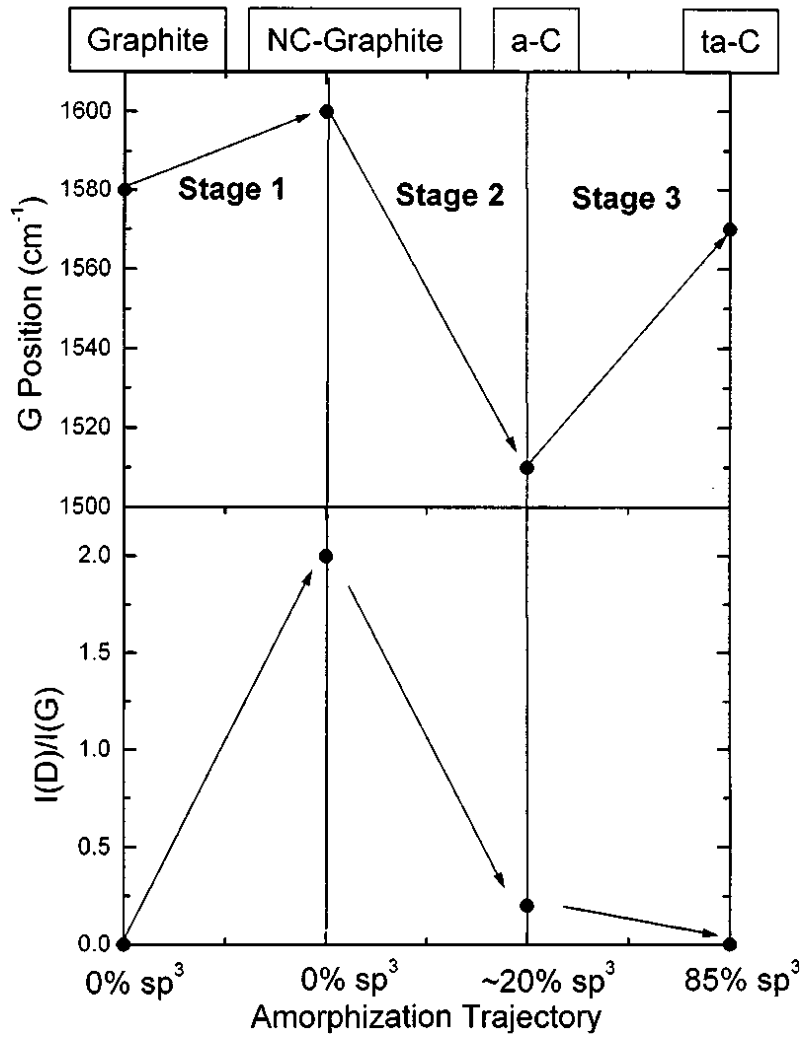


Figure 92. Three-stage model for the amorphization trajectory of carbons proposed by Ferrari and Robertson [170]. The position of the G band as well as the intensity ratio of the D to G band is related to the amount of sp^3 carbon present in graphite, nanocrystalline graphite, amorphous carbon (a-C), and tetrahedral amorphous carbon (ta-C).

In carbon materials with more disorder, the in-plane sp^2 clusters will become smaller and more distorted due to bond-bending, defects, and edges – lessening the number of sixfold aromatic rings contributing to the D peak. Even though the G peak is used to describe graphitic materials, it is related to the relative motion of carbon sp^2 atoms whether aromatic clusters are present or not. This is particularly relevant in amorphous carbons as the development of a D peak actually indicates ordering, a very different meaning than that seen with graphite. Thus, at a particular (L_a) during Stage Two, the TK relationship no longer holds and Ferrari and Robertson proposed I_D/I_G is instead proportional to L_a^2 for very small clusters, as shown in Figure 93 [170] and equation 5.5. Further, the broadening of the D peak can be correlated with the overall disorder resulting from the distribution of sp^2 clusters with different sizes and orientations.

$$\frac{I_D}{I_G} = C(E_{laser}) * L_a^2 \quad 5.5$$

All too often, publications on rGO misinterpret Raman spectra by making the assumption that a higher D peak intensity always equates to more defects. For example, a well-known work on the structure of GO and rGO materials by Stankovich et al. [71], which has been cited almost 8,000 times, does correctly interpret the increased intensity of the D peak to the presence of more aromatic domains, but then incorrectly claims the higher I_D/I_G ratio in rGO is due to a smaller L_a and an increase in sp^3 bonds. Without applying the work of Ferrari and Robertson and recognizing the difference for materials with

L_a less than 4 nm, the inverse dependence on I_D/I_G has not been considered. Further, as evidenced with glassy carbon, a pure sp^2 material, the large I_D/I_G peak ratio cannot be attributed to sp^3 bonding. Unfortunately, many other works have built upon this incorrect assumption that the removal of oxygen groups in GO increases the defect density in rGO [66].

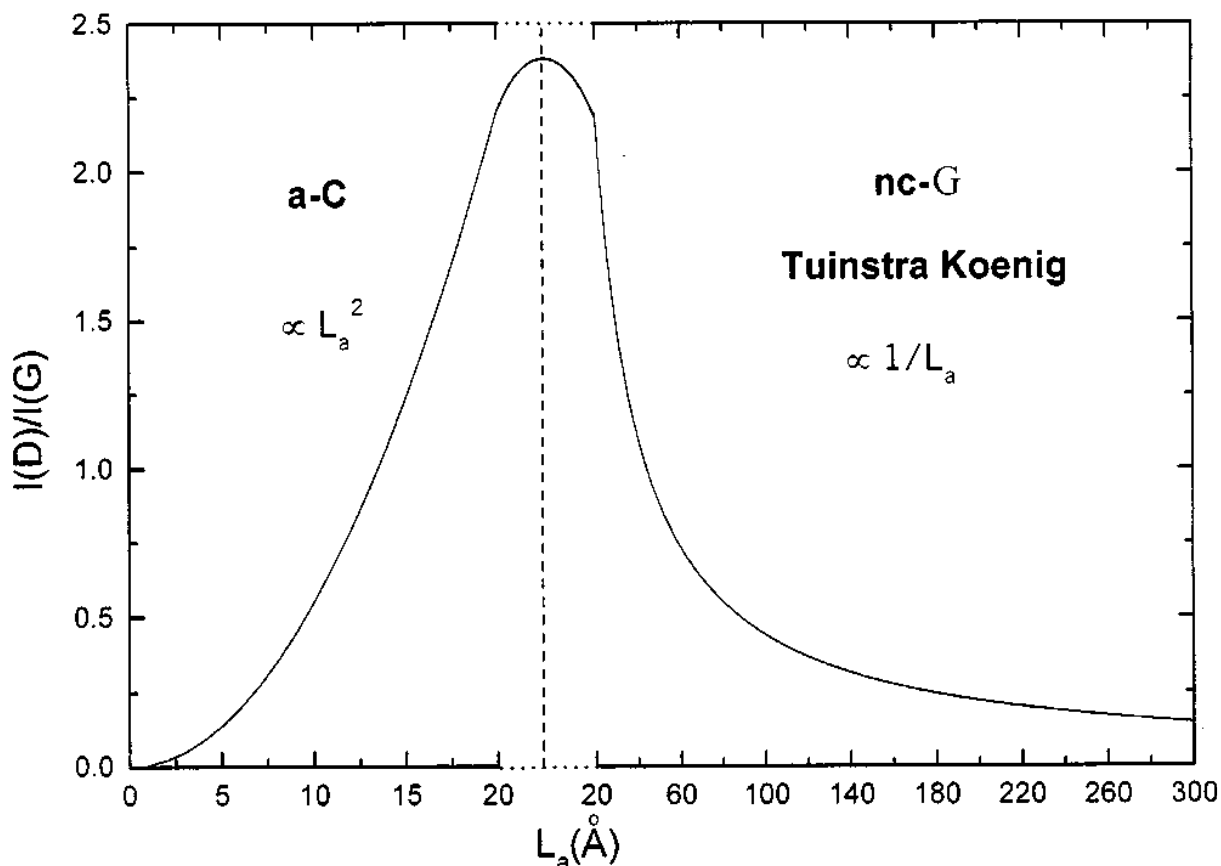


Figure 93. Relationship between the $I(D)/I(G)$ peak ratio and aromatic domain length, L_a , for graphitic material (labelled nc-G where the TK equation holds) and amorphous carbons (labelled a-C where the TK relationship is no longer valid) [170].

Ferrari and Robertson's model was the first to clearly outline the three specific size regimes where the I_D/I_G curve has distinguishable patterns. These initial L_a values have since been adjusted slightly to show that for L_a up to approximately 4 nm, I_D/I_G increases to a maximum value, and then decreases until L_a values of about 20 nm where it becomes rather flat. Much of the more recent work has focused on developing more accurate models for the regions where the TK relation fails ($L_a < 4$ nm and/or 4 nm $< L_a < 10$ nm). Understanding that Stage One and Stage Two carbons have different relationships between the D and G peak features, is paramount to calculating L_a . This conceptual model has been adjusted to account for two features that contribute to a defect: the defect itself and the extension due to electronic impacts from the defect. This extension, or activated region, is related to the 2 nm electron relaxation length in graphene (when using 2.4 eV excitation), and an exact measure of this region has been further supported by measurements on the coherence length of a photoexcited electron which was confirmed to be 3-4 nm [264, 265]. Thus, in carbon assemblies, when the aromatic regions become smaller than ≈ 4 nm because of a high density of defects, the D peak intensity breaks from the traditional T-K relation.

A much deeper understanding of how materials with $L_a < 4$ nm can be modelled became possible with experiments conducted on graphene. Lucchese et al. [266] measured the effect of disorder in Raman spectra of graphene bombarded with Ar^+ ions. As shown in Figure 93, two distinct regions are defined that give rise to the presence of the D band. The defect point itself (termed the 'structurally disordered' region, with radius r_s , shown in red) does not contain aromatic rings and, thus, does not contribute to

the D band intensity. The area surrounding r_s (termed the ‘activated’ region, with radius r_A , shown in green) is what contributes to the enhancement of the D band. A high density of defects leads to competing mechanisms, and when the inter-defect distance, L_D , becomes less than 4 nm, the activated regions are overtaken by the structurally disordered regions, resulting in the decrease of the I_D/I_G ratio. These measurements on graphene were compared with the TK relation [255] at larger L_D and the work of Ferrari and Robertson [170] for small L_D to produce a model that fits the entire length scale based on the new definitions for defective regions as shown below.

$$\frac{I_D}{I_G} = C_A \frac{r_A^2 - r_s^2}{r_A^2 - 2r_s^2} \left[\exp\left(-\pi \frac{r_s^2}{L_D^2}\right) - \exp\left(-\pi \frac{r_A^2 - r_s^2}{L_D^2}\right) \right] + C_S \left[1 - \exp\left(-\pi \frac{r_s^2}{L_D^2}\right) \right] \quad 5.6$$

While the proportionality constants (C_A and C_S) and the size of the activated region (r_A) are dependent on the excitation wavelength, data here (using $\lambda=514$ nm) was fitted with values for $C_A = (4.2 \pm 0.1)$, $C_S = (0.87 \pm 0.05)$, $r_A = (3.00 \pm 0.03$ nm), and $r_s = (1.00 \pm 0.04$ nm) [266].

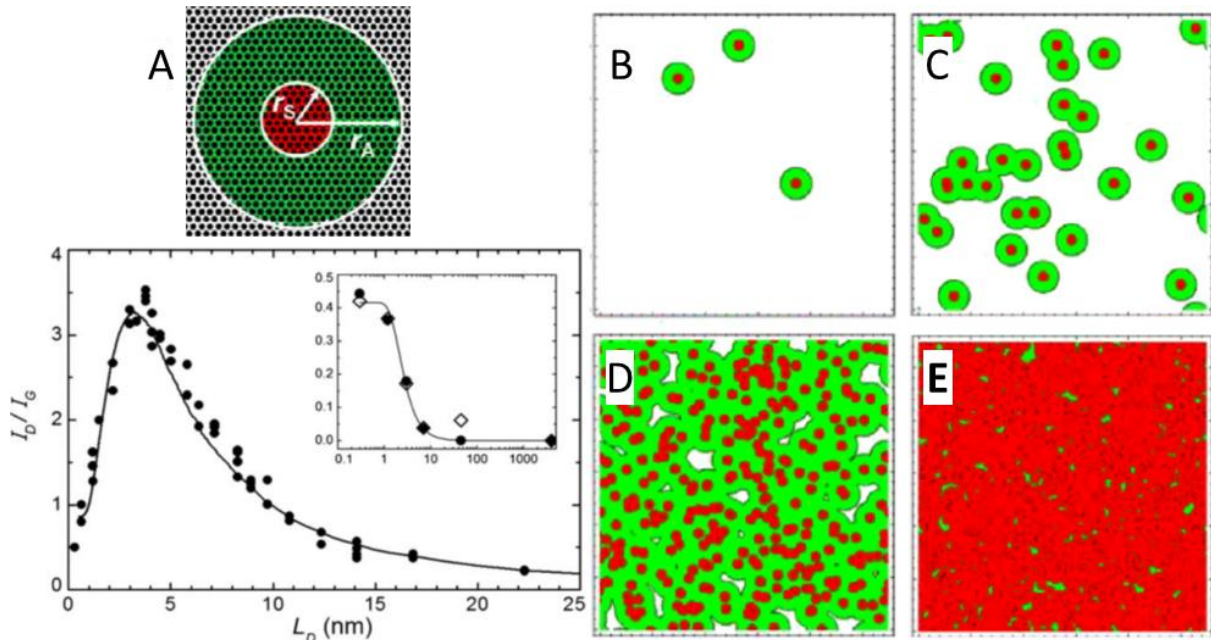


Figure 94. Work by Lucchese et al. [266] created a full model of the I_D/I_G dependence to the density of defects and inter-defect distance, L_D , from micro down to sub-nm scale. The new model defined both a “structurally disordered” region, r_s , alongside “activated” region, r_A , from which the D band arises (A). Depending on the defect density, the activated regions will overlap and the D band intensity will be influenced accordingly (B-E).

Cancado et al. [267] expanded on this model for application at different excitation energies. They approximate the relationship as:

$$\frac{I_D}{I_G} \cong C_A \frac{\pi(r_A^2 - r_s^2)}{L_D^2} \quad 5.7$$

with $r_A=3.1$ nm, $r_s=1$ nm, and the relation $C_A=(160 \pm 48)E_L^{-4}$. This model is meant to apply directly for graphene and graphitic materials with an L_D of 10 nm or larger, but the method to adjust the constant, C_A , is useful in applying to any equation in order to adjust the constant for spectra taken at different excitation energies. This work further compared the relationship between the FWHM of the D, G, and 2D bands with L_D across a range of excitation energies. These results are shown in Figure 95. In both models, the relations are based on the Raman spectra of ion-bombarded samples and adjustments for

other carbons or defect types have not been fully investigated. In spite of this, theories considering both the defect and activated area will always apply, and the equations should be valid for Raman active point defects, especially for larger values of L_D , where the nature of the defect will not have as strong of an influence on the I_D/I_G ratio. However, for the range of $L_D < 10$ nm (especially $L_D < 4$ nm), some uncertainty about the correct interpretation of Raman results remains, and, thus, alternative approaches are discussed here.

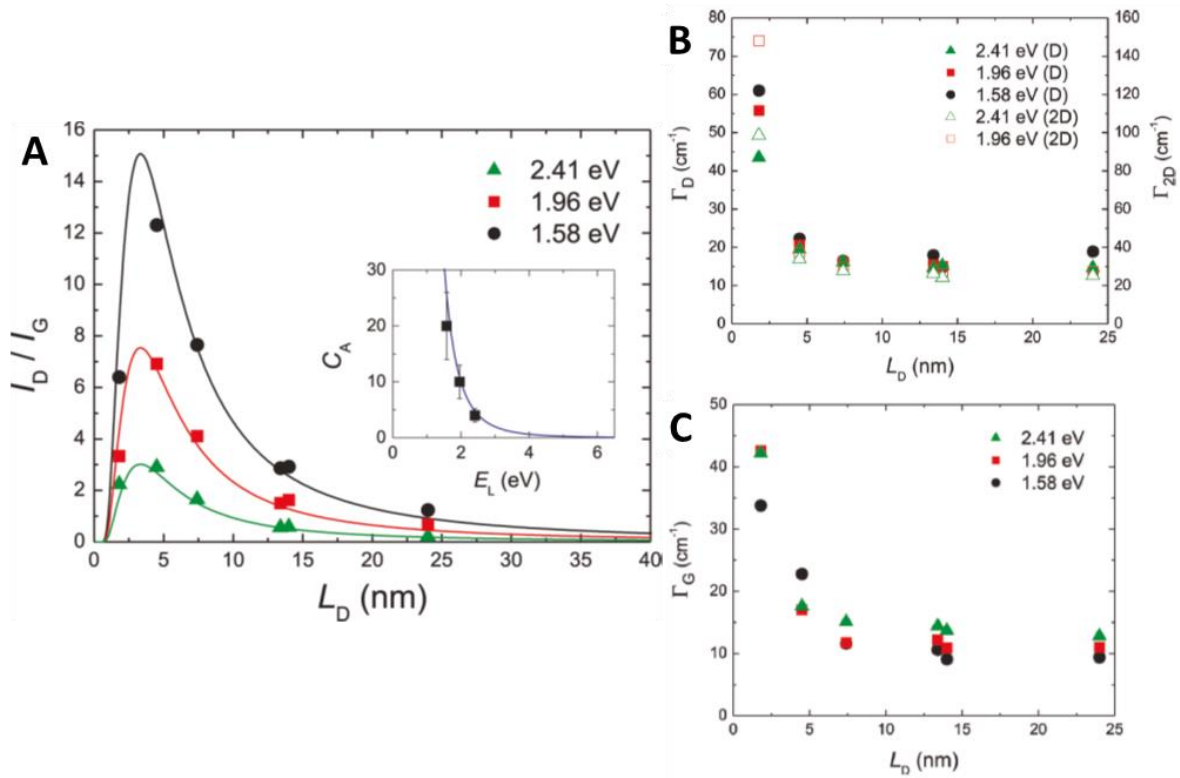


Figure 95. Cancado et al. [267] extended the model relating I_D/I_G with the inter-defect distance, L_D , to apply at different excitation energies by adjusting the coefficient, C_A , as shown in the inset with solid curve is given by $C_A = 160 \cdot E_L^{-4}$ (A). Relationship between the FWHM of the D and 2D bands to L_D at different excitation energies (B). Comparison of the FWHM of the G band to L_D at different excitation energies (C).

It has long been suggested that the width of the G band should be a more reliable means than the I_D/I_G ratio to determine the size of aromatic clusters. More recently other authors have come to a consensus that the width of the G band may be the most accurate way to describe the structure, especially when comparing diverse types of carbon materials [244, 268]. This is because the broadening of the G peak is a direct measure of disorder that increases continuously as the sp^2 grain size decreases [263], as shown in Figure 96. Further, discrepancies arising from dependence of the D band on the of excitation energy used are reduced because neither the position nor width of the G band is dependent on excitation energy, as shown in Figure 97. Mallet-Ladeira et al. [269] followed the work of Lucchese to investigate pyrocarbons with crystallite size in the 2-5 nm range. Results based on the I_D/I_G ratio were compared to an alternative approach using the HWHM of the G band. It was proposed, for L_a in the 2-10 nm range, less ambiguous results were obtained by using the relation below.

$$HWHM_G = (68 \pm 4) - (5.2 \pm 0.5) L_a \quad 5.8$$

However, actually plotting the results presented in Figure 97(B) shows a much larger discrepancy between the results and the proposed model, indicating Mallet's method is not as accurate as the

model proposed by Cancado. Further, the results of Mallet do not adequately address the region of $L_D < 4$ nm, which is of interest for oxidized and/or highly disordered carbon materials.

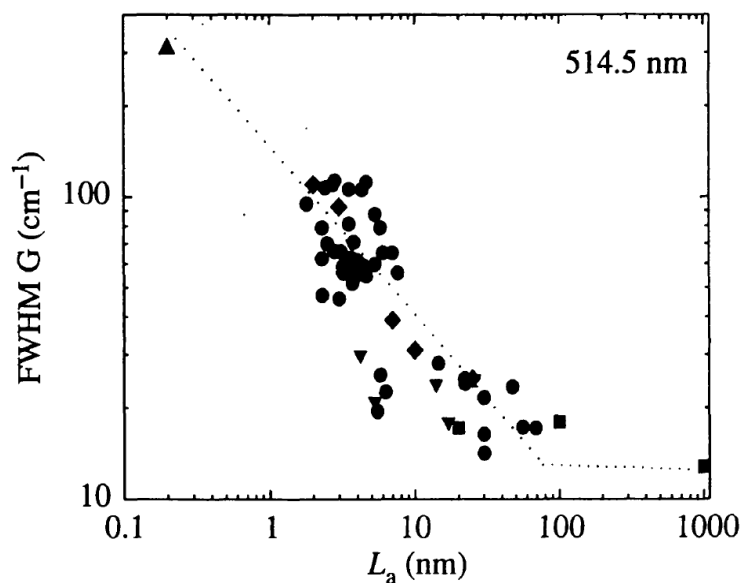


Figure 96. Early work of Ferrari and Robertson showing the relationship between the FWHM of the G band to known L_a values for a variety of carbon materials [263].

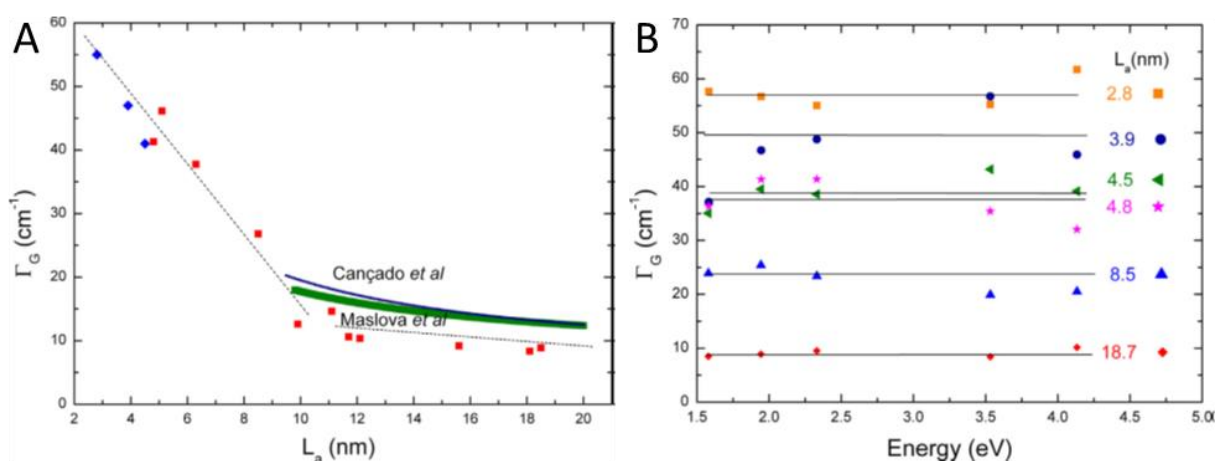


Figure 97. Mallet-Ladeira et al. [268] argue for using the HWHM of the G band to determine L_a in pyrocarbons and cokes, citing the distinct relationship in the 2-10 nm region (A) and independence from excitation energy (B) as advantages over the I_D/I_G ratio.

Published work on RMS analysis of carbon materials such as coal or activated carbon has often been overlooked by those focusing on graphene, GO, and rGO. Seong et al. [270] conducted a detailed analysis on soots of varied oxygen content and crystallite size and found neither the typical T-K relationship nor the empirical formulas of Knight and White [261] or Cancado [271] applied to disordered carbons like soot and carbon black with characteristically wide D bands. Ganesan et al. [216] effectively determined the structure of nano-graphitic carbons by using the broadening of the D and G bands to first determine if the carbon was in Stage One or Stage Two, and then applied the corresponding model to measure L_a . Correct measurement of the aromatic structural features was then able to explain why materials with the same I_D/I_G ratio exhibited large differences in chemistry and electronic properties.

Extending Raman theory from graphite and pure graphene to rGO assemblies requires important considerations because the defect types in rGO are significantly different from the uniform holes produced from Ar^+ ion bombardment in crystalline carbons. Only few recent publications have used

a more appropriate approach of comparing the structure and properties of reduced GO materials with amorphous, oxidized, or nano-structured carbons. Following the results from activated carbon shown in Figure 98 [137], interpreting the rGO spectra based on knowledge of disordered carbons [170, 171, 256], carbon black [272], and pyrocarbons [131, 268, 273] allows for a much more thorough understanding of the bonding and carbon structure in these materials. In addition to the main graphitic (G and 2D peaks at 1580 cm^{-1} and 2700 cm^{-1}) and disorder (D and D+G peaks at 1350 cm^{-1} and 2900 cm^{-1}) features discussed above, spectral fitting for rGO in the region between 1100 cm^{-1} to 1700 cm^{-1} should also include features related to the amount of disordered and amorphous sp^3 carbon present.

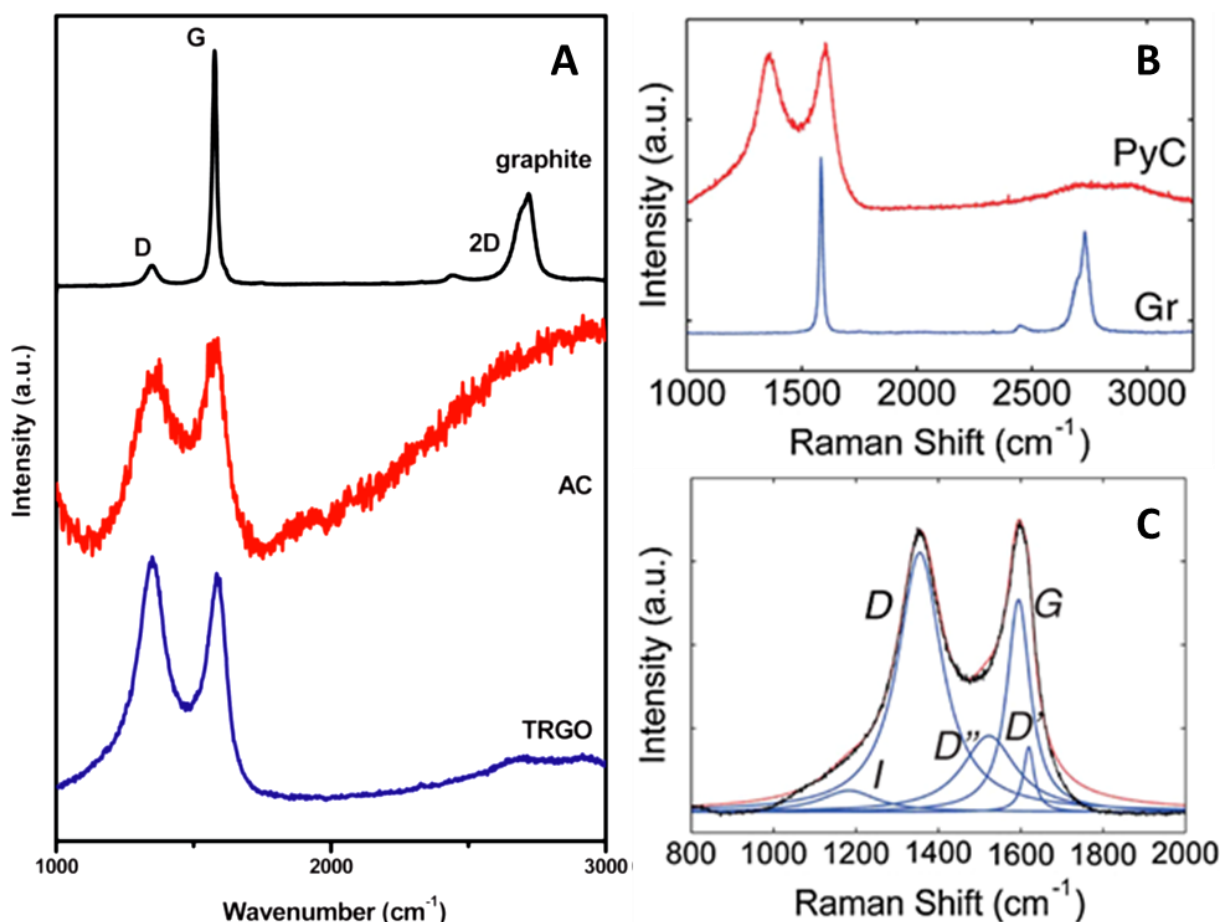


Figure 98. Typical Raman spectra features for graphite, activated carbon (AC), and thermally reduced GO (TRGO) (A) taken from reference [137]. A similar comparison of pyrocarbon (PyC) and graphite (Gr) Raman spectra (B) with the suggested curve fitting (C) taken from reference [273].

For a complete understanding of rGO materials, Schwan et al. [274] performed a detailed analysis on the spectral features in amorphous carbons which provides valuable insight on how best to combine Raman analysis of graphene with the disorder, defects, and chemical bonds in rGO. These additional features include the less characteristic peaks shown in Figure 98(C), with the broad peaks at 1150 cm^{-1} (I band) and 1480 cm^{-1} (D'' band) being reliable indicators for the amount of sp^3 (I) and disordered (D'') bonding present in various types of carbon [171, 270, 272]. In rGO assemblies, carbon groups bonded to nitrogen will also contribute to the features at 1150 cm^{-1} (I band) and 3200 cm^{-1} ($2\text{D}'$ band), and these peaks can be seen in all reports from nitrogen doped graphene materials [77, 78, 222, 275], although the cause was not fully understood. Combining knowledge of Raman features for disordered carbons [274] where these peaks have been attributed to sp^3 bonding resulting from hydrogen content in molecules like polyacetylene [170] helps to answer questions on the origin of peaks in nitrogen doped graphene. As the presence of nitrogen bonded to sp^3 carbon also enhances the I and 2D' peaks,

this can be interpreted with reference to the edge group bonding structure being similar to the hydrogen groups seen in molecules like polyacetylene.

5.3.2 Results and discussion

Now that a complete understanding of the structural features that contribute to the Raman spectra for various forms of carbon materials has been established, it is possible to accurately assess the results for rGO assemblies. After first establishing that the RMS results are reproducible across large areas of the surface (homogeneity) and that no artefacts have been introduced to these data from the laser, qualitative and quantitative results for the overall disorder and aromatic domains for rGO of different oxidation levels are presented and discussed in detail.

5.3.2.1 Consistency of results

To verify homogeneity across each sample surface, Raman maps of I_D/I_G peak ratios (shown in Figure 99) were used to determine if the defective and aromatic domains had any long range order and/or inconsistencies. As shown, the I_D/I_G peak ratio fluctuates from 1.3 to 1.9 with randomly dispersed domains, showing the sp^2 domains and defects are distributed homogeneously across the surface of rGO assemblies and no structural irregularities were observed. To prevent artefacts due to laser induced structural changes, spectra were taken at five different sites along each sample (across the total surface of the assembly with diameter ≈ 3.5 cm). It was found that spectral line shapes were identical at all five positions – thus, there are no variance values associated with the results. Extra precautions were taken for the GO assemblies, as the energy from the incident laser could remove the oxygen groups and impact data on the sp^2 domains and defects. Optical images of the surface showed a slight darkening at the laser site for GO prepared from HO8 and LOH (the two samples with highest oxidation) after interaction with the beam, but after rescanning the same spot, the spectrum did not change, indicating there was little to no laser induced damage influencing the results.

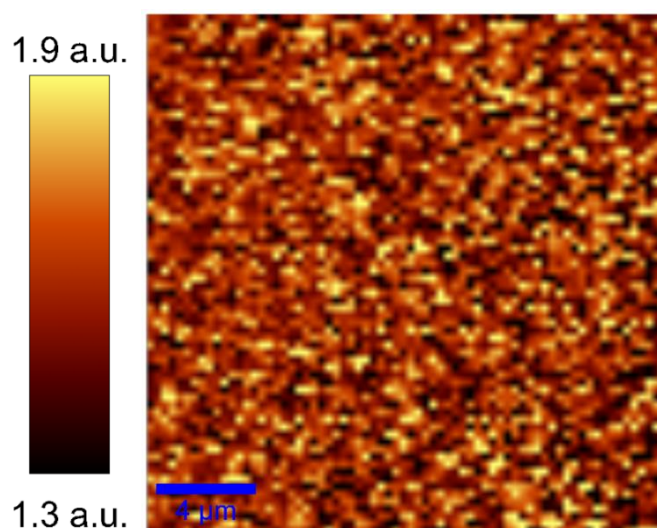


Figure 99. Raman map of D/G peak ratio across the surface of the HO8-rGO assembly, showing a homogeneous distribution of sp^2 domains and defects across the sample surface.

5.3.2.2 Comparison of spectral shapes for GO and rGO

The Raman spectra for the GO and corresponding rGO assemblies of varied oxidation degree are shown in Figure 100 after being normalized to the background and offset for visual clarity. All spectra contain features within the two main regions that are typical of porous carbons: The first-order features ranging from 1100 cm^{-1} to 1700 cm^{-1} and the second-order features ranging from 2400 cm^{-1} to 3200 cm^{-1} . Interestingly, the spectral shapes for GO are very similar to those of activated carbon [137],

charcoal [261], and soot [270], while the rGO spectra are more akin to glassy carbon [261], nano-graphitic carbons [216], and pyrolytic films [273].

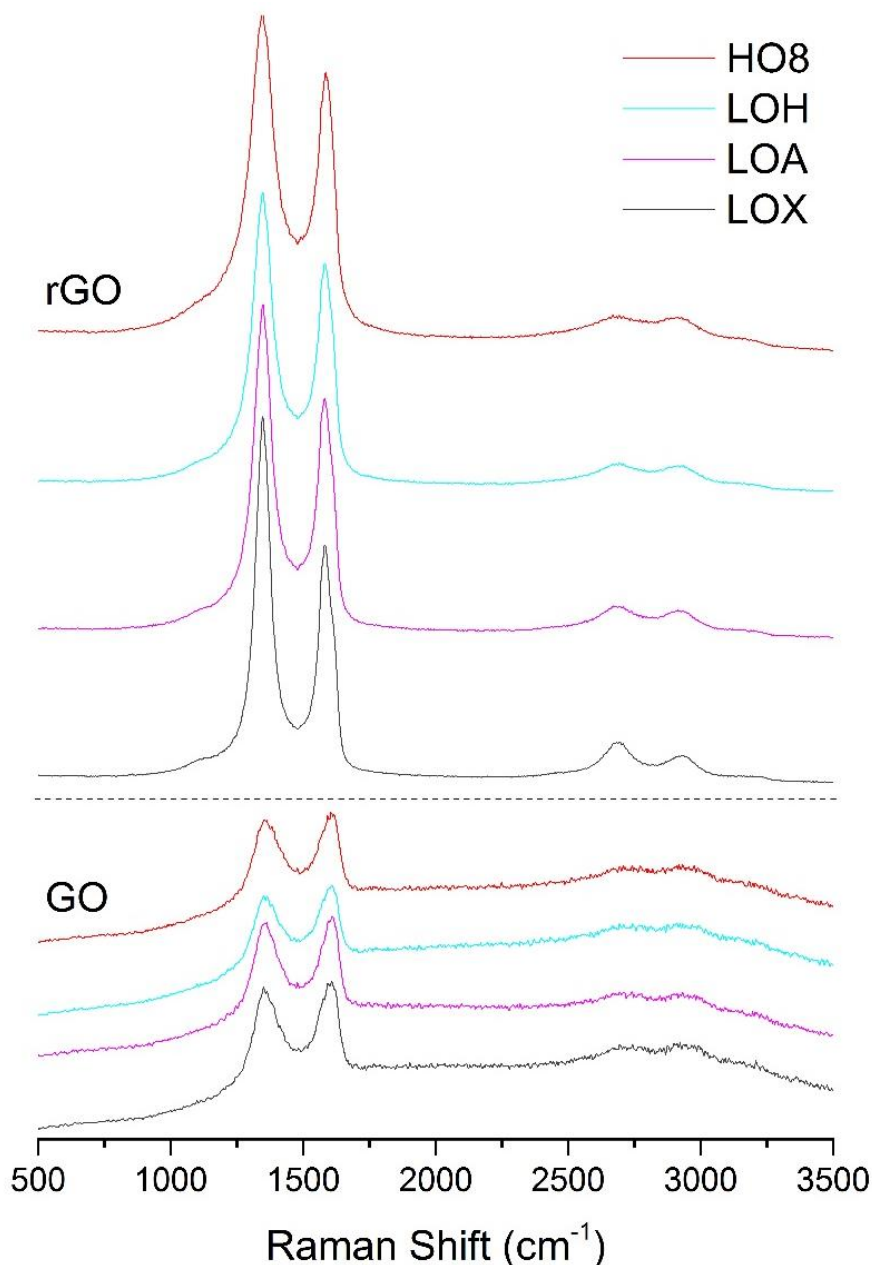


Figure 100. Raman spectra for GO (bottom) and rGO (top) samples prepared with various levels of oxidation.

The peaks for all GO assemblies are less pronounced, but after reduction to rGO, the peak intensity is clearly enhanced. The main peak parameters in the region from 1100 cm^{-1} to 1700 cm^{-1} , are displayed in Table 12 and shown visually for comparison in Figure 101. There are very clear trends in both GO and rGO assemblies which appear to be directly related to the amount of oxidation. The shifts in position for the D and G peaks are consistent with discussion related to oxidation, doping and strain mentioned previously. The lowest oxidized material, rGO LOX, has a G position closest to the 1582 cm^{-1} value expected for pure graphene and graphite, and the decrease in the FWHM_D values as the oxidation level goes down shows that disorder along the aromatic domain (graphene sheet surface) is directly related to oxidation.

The G peak parameters for the GO LOA sample do not follow the expected trend, and this is most likely due to the fitting procedure. The Raman spectra for the GO materials has a high level of noise and because low laser power must be used while acquiring results (to prevent reduction), this cannot be improved. Results for fitting the G peak in GO are highly variable depending on the chosen procedures,

and a less ambiguous approach compares results for both the FWHM_G and the I_D/I_G peak ratio to conclude all GO assemblies have very similar structural features.

Table 12. Comparison of the main peak parameters in the region from 1100 cm^{-1} to 1700 cm^{-1} for GO and rGO assemblies prepared from GO solutions with different oxidation levels.

Sample	Peak Position (cm^{-1})				Ratio		FWHM (cm^{-1})			
	D		G		I_D/I_G		D		G	
	GO	rGO	GO	rGO	GO	rGO	GO	rGO	GO	rGO
HO8	1356.0	1346.2	1602.0	1588.3	1.07	1.31	99.5	110.6	70.0	64.5
LOH	1355.0	1347.9	1601.4	1587.5	1.04	1.39	95.7	92.5	69.0	63.8
LOA	1354.8	1347.4	1604.1	1585.4	1.05	1.43	95.9	83.6	65.2	63.8
LOX	1354.8	1346.9	1601.0	1583.3	1.06	1.53	91.4	67.8	68.6	62.5

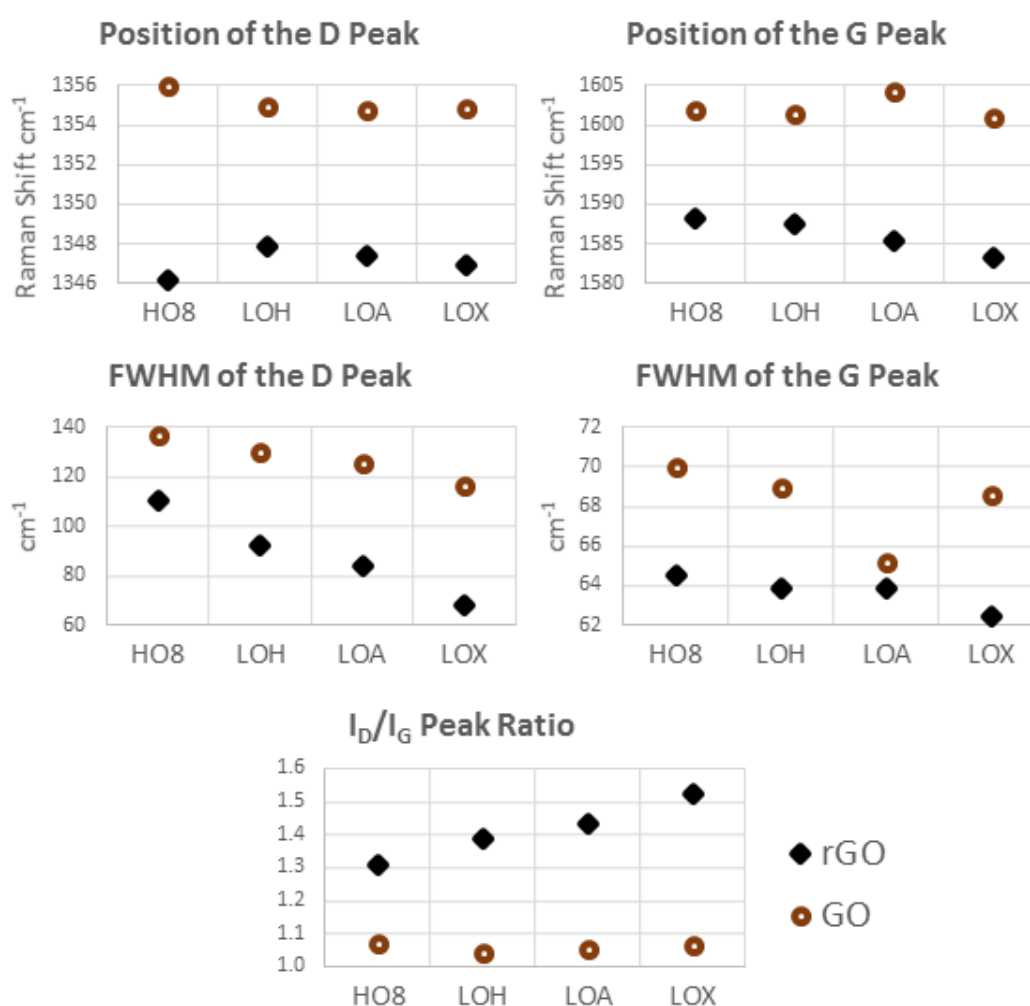


Figure 101. Comparison of the values from the table above, showing clear trends in the peak parameters for GO and rGO assemblies prepared from GO solutions with different oxidation levels.

While the D and G peak intensities are approximately equal for GO (I_D/I_G peak ratio ≈ 1), the D peak becomes dominant after reduction. This indicates the removal of oxygen groups during the reduction process results in an increase of the I_D/I_G peak ratio. In order to apply the correct models for interpreting the Raman spectra, the GO and rGO results are compared with the work of Knight and White [261] as well as Ferrari and Robertson [170, 171]. Knowing the chemical structure of GO and

rGO and that only basal plane oxygen bonding and defects will influence the D band, as shown by the work of Wang et al. [256] discussed previously, the increased D band intensity in rGO could be interpreted in three ways: there is a change in the size of the aromatic domains (I_D/I_G peak ratio), there is an increase in the prevalence of aromatic domains (D peak intensity), or there is a combination of both of these factors.

An analysis beginning with the G band is more easily correlated with physical features, because the broadening of the G peak is a direct measure of disorder that increases continuously as the sp^2 grain size decreases. The fact that rGO has only a slightly smaller $FWHM_G$ than GO but a much larger intensity, indicates that the sp^2 domains are not changing much in size, but the number of sp^2 bonds greatly increases after reduction. Further, knowing GO has many more basal plane oxygen groups than rGO, the increased $FWHM_G$ supports the rationality that L_a should be smaller in GO than it is in rGO. As assumed with the XPS results, it again appears that all GO materials reach a saturation point where all available basal plane sites are bonded to oxygen functionalities. Using the amorphization trajectory of Ferrari and Robertson [170], this would place both GO and rGO assemblies in Stage Two, where the TK relation should not be used to determine the size of the aromatic domains present in rGO. Instead, these materials are better analysed using methods applied to defective and amorphous carbons, where the models for L_a smaller than 4 nm presented by Lucchese et al. [266] should be applied. This follows along with conclusions drawn from XPS, showing much more oxygen and nitrogen was present in GO8 compared to LOX after reduction.

Based on this additional insight, it is now clear that the increased D peak intensity for lower oxidized samples is largely attributed to the increased prevalence of aromatic domains, with only slight differences in the size of L_a for each sample. Here, being a Stage Two carbon, the increasing I_D/I_G ratio does not imply more defects and in fact relates to slightly larger aromatic domains. A more complete analysis of all the peak features in the rGO assemblies will now be discussed with exact measurements of L_a to follow.

5.3.2.3 Raman peak fitting

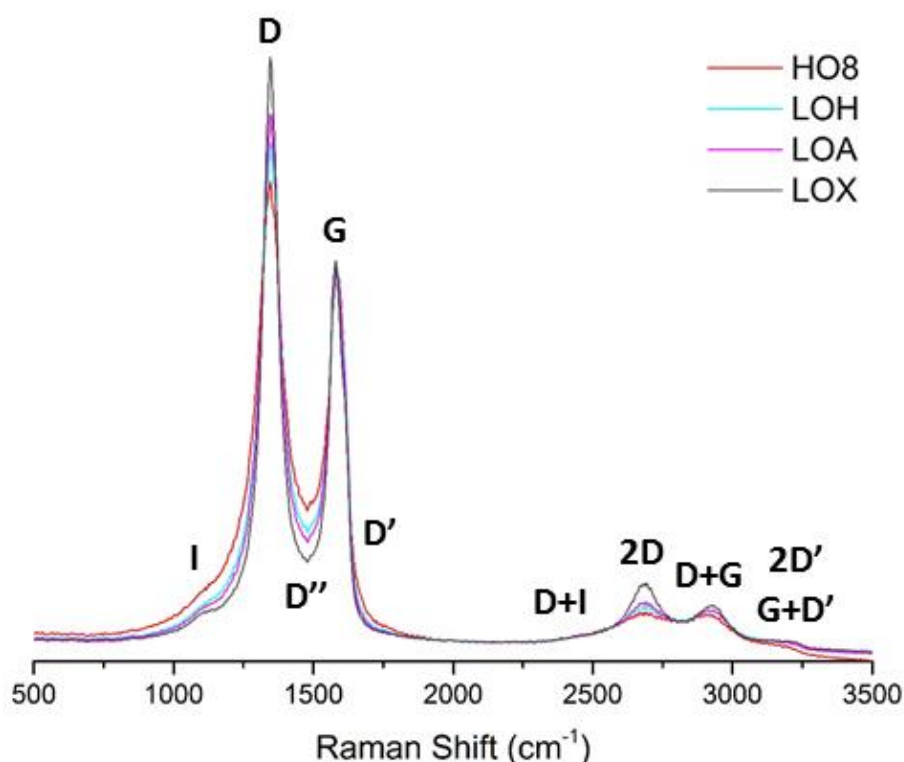


Figure 102. Raman spectra for rGO assemblies normalized to the G-peak intensity highlights the differences in all other peaks directly relates to the oxidation level.

To more clearly highlight the differences in rGO assemblies, overlaid spectra are presented in Figure 102. It is clear that if the intensity of the G peak is kept constant, the intensity of all other peaks increases as the oxidation level decreases. In addition, the valley between the D and G peaks deepens with lower oxidized rGO, indicating the broad I and D'' peaks that results from chemical doping and/or sp^3 bonding are correlated with the level of oxidation. It is also interesting to note the much more pronounced 2D peak in LOX. In order for these spectral features to more precisely interpreted, correct peak fitting methods specific for more disordered porous carbons must be applied.

The fitting methods and data interpretation for the Raman spectra of rGO assemblies are based on an extensive literature review to find the best methods applicable for more complex and/or disordered carbon materials [257, 261, 270, 273]. Ideally, the high intensity G and D peaks should be fitted with a BWF and Lorentzian line pair no matter the carbon type [170]. This BWF component was also applied for the XPS fitting of the sp^2 carbon component in Chapter 4. While this does give the best fit of the spectral line, the BFW line parameters cannot be used to directly extract the useful G peak parameters, namely the FWHM and intensity. Therefore, the most suitable approach is to first use two Lorentzians to fit the D and G peaks alone in order to directly compare and interpret features related to the FWHM and intensity ratios (as was done in the section above comparing GO and rGO), and then follow this with a more complex fit to include all the features outlined in Figure 87 and Figure 98(C).

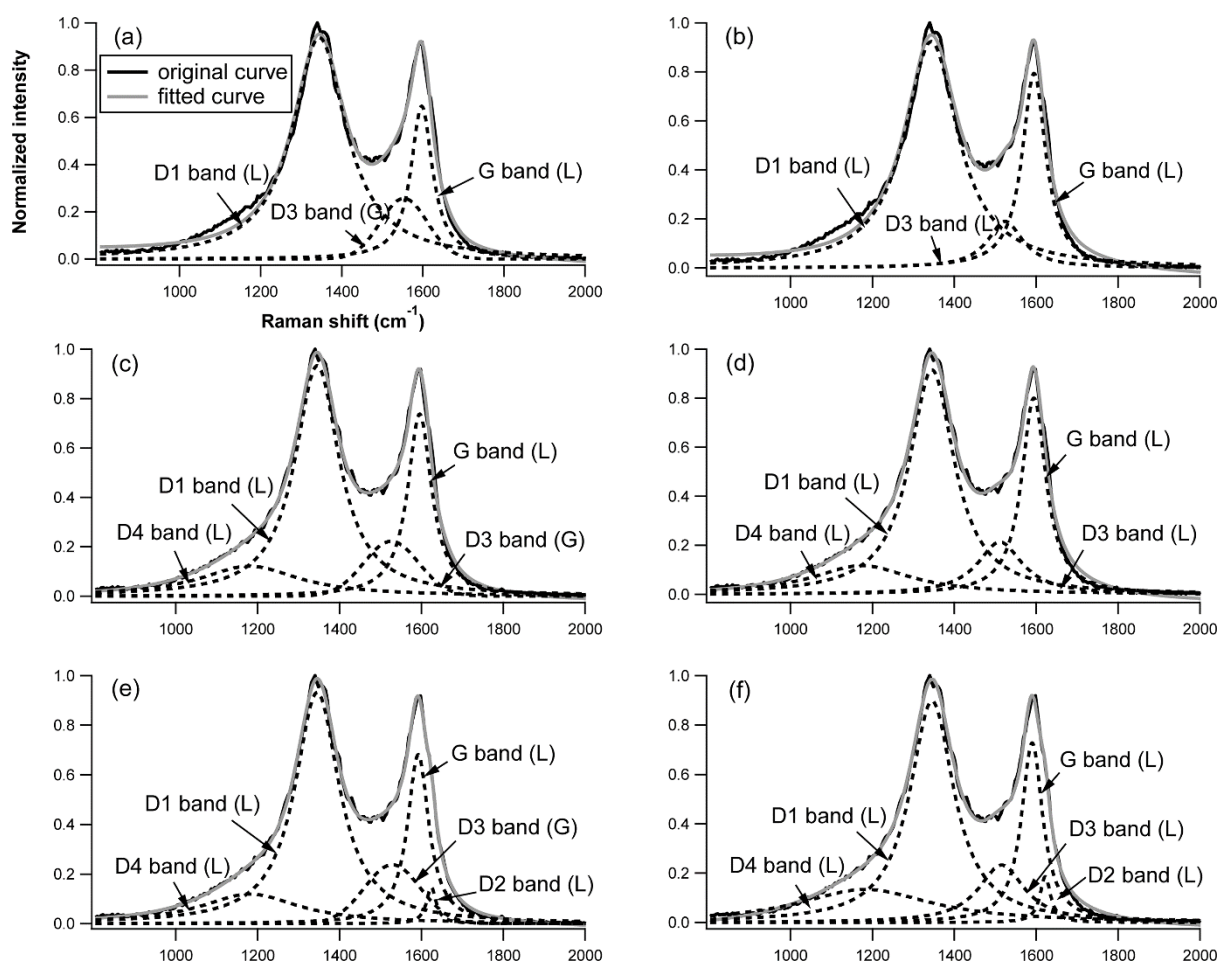


Figure 103. Summary of curve fitting options outlined by Seong on spectra of soot: (a) 2 Lorentzian and 1 Gaussian, (b) 3 Lorentzian, (c) 3 Lorentzian and 1 Gaussian, (d) 4 Lorentzian, (e) 4 Lorentzian and 1 Gaussian, (f) 5 Lorentzian [257].

The full spectral fitting combines the BFW with up to four Lorentzians (and/or one Gaussian) in the region from 1100 cm^{-1} to 1700 cm^{-1} and another four Lorentzians (and/or one Gaussian) in the region from 2400 cm^{-1} to 3200 cm^{-1} . This method will account for all features of interest in most porous carbons, and the fitting methods discussed here have been analytically compared in many Raman

investigations on carbon materials – with notable work related to rGO assemblies being that of Seong to investigate the reactivity of soot [270], Sadezky to compare features of carbonaceous materials [273], Knight and White to determine bonding in disordered carbons [261], Vallerot to measure coherence domains in pyrocarbons [131], and Mallet on measuring aromatic domains in nanocrystalline pitch coke [269]. Mallet suggested an alternative method to that presented here, and instead uses two Lorentzians for D and G along with a broad Gaussian to account for all the disordered peaks.

Correctly choosing a fitting method depends on what information needs to be obtained and the specific features present in the spectra, and as shown earlier in Figure 90, this varies greatly depending on the carbon material. A comparison of possible fitting methods conducted by Seong [270] is shown in Figure 103. It is clear from a visual inspection of the spectra for rGO in Figure 102 that the I and D' features are present, and the shoulder on the outer side of the G peak results from the D' feature. Accounting for these additional peaks can yield valuable insight into the material structure and are often overlooked in current publications. Thus, the analysis follows the approach shown in Figure 103(e), except the BFW shape is used for the G peak because the asymmetric broadening accounts for the physical process of coupling a discrete mode to a continuum as is the case for the sp^2 feature. The BFW also reduces overestimation of the I and D' features. A Gaussian is used for the D' feature because this shape is expected for a random distribution of phonon lifetimes as is the case in disordered bonding seen in amorphous sp^2 and sp^3 carbon materials. A final step is to extend this procedure for all first order features into the second-order region as shown in Figure 104.

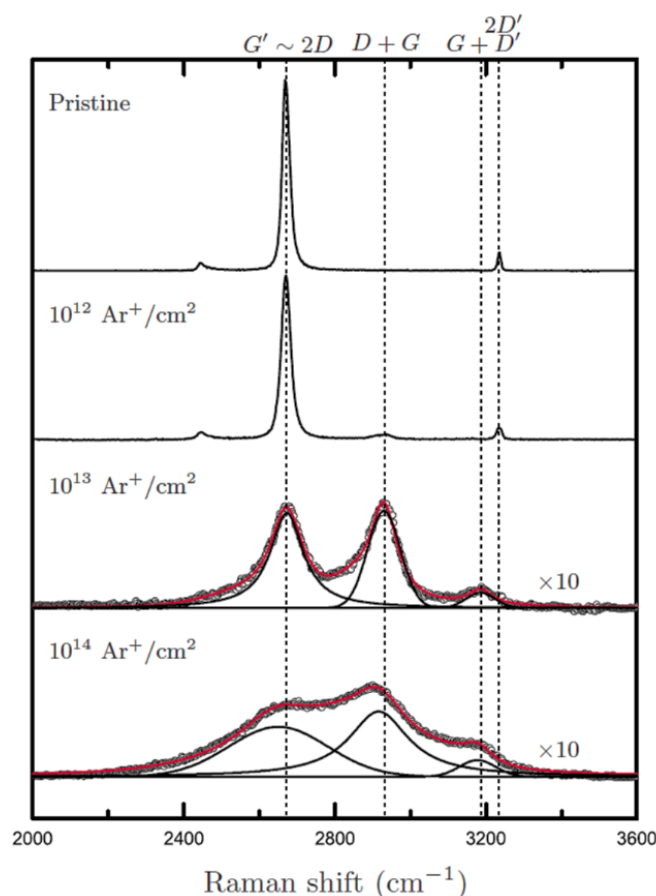


Figure 104. Example of fitting second-order spectral features for graphene materials with various degrees of defects and disorder (from [276]).

The fitting approach applied to the rGO assemblies is shown for LOX in Figure 105, along with the corresponding peak labels for the first- and second-order regions. It is clear that the additional

features are necessary for a good spectral fit. This method of combining a BFW (G), Gaussian (D''), and three Lorentzian (I, D, D') peaks for the first-order spectral region one Gaussian (combination of $2D'$ and $G+D'$) with and three Lorentzian ($D+D''$, $2D$, $D+G$) peaks for the second-order spectral region was applied to all rGO assemblies and is shown in Figure 106. The significant extractable parameters are listed in Table 13 and relevant peak ratios are compared in Table 14 – both will be used to guide discussion in the following sections.

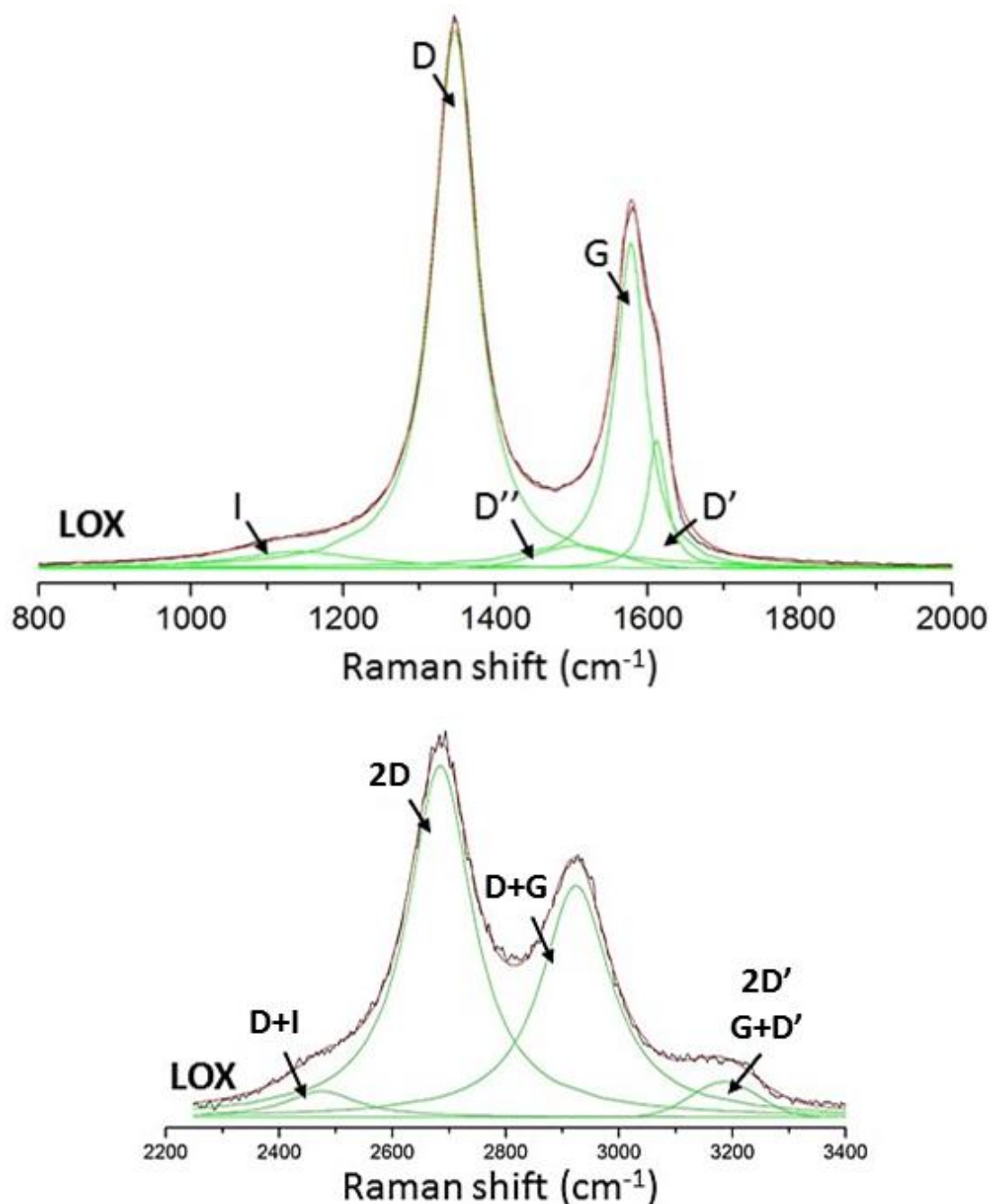


Figure 105. Details of the fitting procedure are labelled for the LOX assembly showing the BFW (G), Gaussian (D''), and three Lorentzian (I, D, D') peaks for the first-order spectral region (top) and the three Lorentzian ($D+I$, $2D$, $D+G$) and one Gaussian (combination of $2D'$ and $G+D'$) peaks for the second-order spectral region (bottom).

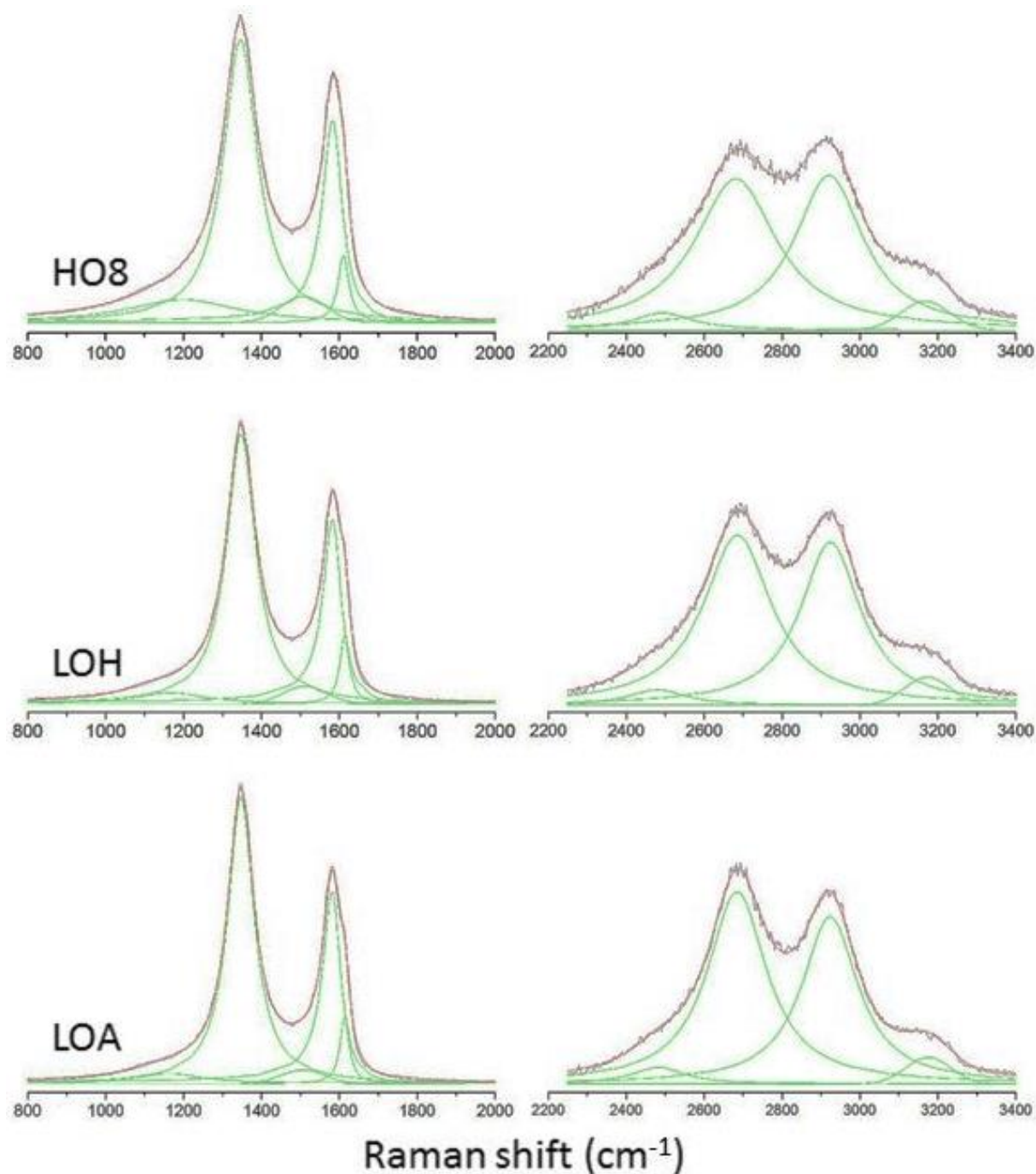


Figure 106. Peak fitting for the first- (left) and second-order (right) regions of the Raman spectra for rGO assemblies. All fits converged with a χ^2 tolerance value of $1\text{E-}6$ reached (reduced χ^2 ranged from $8.9\text{E-}6$ to $4.4\text{E-}5$ and adjusted $R^2 > 0.999$).

Table 13. Relevant parameters extracted from the peak fitting procedure applied to all rGO assemblies.

Sample	Peak Position (cm^{-1})			FWHM (cm^{-1})			Area (cm^{-2})			
	D	G	2D	D	G	2D	D	G	I	D''
rGO HO8	1346.2	1588.3	2681.6	110.6	64.5	255.7	202	89.8	50.5	15.4
rGO LOH	1347.9	1587.5	2685.6	92.5	63.8	187.8	187	93.0	18.7	11.7
rGO LOA	1347.4	1585.4	2684.7	83.6	63.8	175.3	180	95.8	15.7	9.02
rGO LOX	1346.9	1583.3	2684.5	67.8	62.5	149.4	163	98.3	15.5	8.91

5.3.2.4 Interpretation of peak fitting

5.3.2.4.1 Position of the dominant bands

The position of the D peak is the same for all samples, and matches the expected value for defective carbons. The placement of the G band for both graphite and single sheet graphene is centred at 1582 cm^{-1} and is unaffected by the number of stacked layers. Oxygen-containing carbons have a G band that is typically upshifted, with a frequency closer to the 1600 cm^{-1} usually reported for GO. Since the G band only shifts due to lattice strain or in-plane doping, the trend observed in Figure 107 clearly indicates the peak position correlates with the oxidation degree. Thus, the G-peak position in rGO assemblies can be used to indicate the amount of residual oxygen groups, and this, in turn, gives rise to additional lattice strain within the material. The G peak position is highly dependent on stress and measurements on strained graphene sheets show the G peak can drop up to 20 cm^{-1} after the stress is removed [274]. Results here indicate as more oxygen is removed, the rGO sheets become less strained, and the G position approaches that of graphite and graphene.

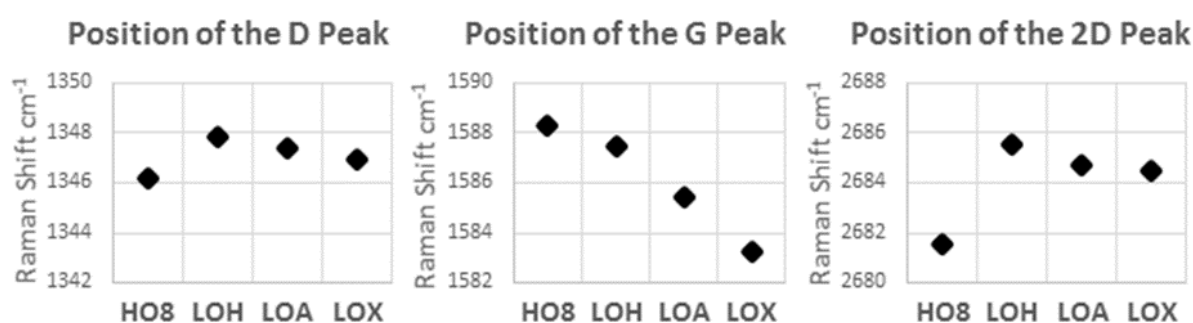


Figure 107. Comparison of D, G, and 2D peak positions for all rGO assemblies.

This shift in G peak position can be attributed directly to dopant concentration in nitrogen-doped graphene [221]. Because both doping and strain contribute to the shift, these effects can be distinguished using the 2D peak position, as nitrogen doping causes a shift to lower frequencies. The results here indicate that HO8 is impacted by both strain and nitrogen doping while the LO- assemblies differ solely due to different levels of strain in the material. Further, the position and shape of the 2D band is directly related to the number of Bernel stacked layers in carbon materials. The single, yet broadened, Lorentzian centred close to 2685 cm^{-1} indicates all the rGO assemblies consist of turbostratic graphene layers. The enhanced intensity of the 2D band for LOX indicates there is a larger interplanar coherence length in this material, which would be expected as the removal of oxygen groups and strain allows for more uniform stacking between aromatic domains.

5.3.2.4.2 Broadening of the dominant bands

The width of the Raman peaks also provides useful insight on the structure of rGO materials and how this relates to oxidation level, and clear trends are visible in Figure 108. If the aromatic domains in disordered carbon materials are considered as small clusters of ordered regions [274], the broadening of the D and G bands can be attributed to differences in cluster size, cluster distribution, cluster orientation, and/or the influence of stress and chemical bonding. The G peak is a direct measure of disorder in sp^2 clusters and increases continuously as the disorder increases, but it is important to recognize this signal results from both aromatic and chain-like bonds where the D peak is a measure of only intact aromatic rings. The high variability in the FWHM_D compared to that of the FWHM_G indicates that while rGO assemblies contain sp^2 clusters of relatively similar size ($\text{FWHM}_G \propto L_a$), there

is a direct correlation between higher oxidation and the ordering of the aromatic clusters ($\text{FWHM}_D \propto$ staking of the planes).

It has been shown that in disordered soots and carbon blacks, materials with vastly different oxidative reactivity properties will have identical FWHM_G values solely because the bond lengths and angle distortions in the sp^2 clusters are similar [270]. Therefore, even though the broadening of the G peak is a direct measure of disorder, the FWHM_G for all assemblies is rather consistent, a trait often seen in defective and activated carbons [107], and indicates aromatic domains of roughly the same size, with the more defined G peak in LOX indicating the slightly larger L_a which would be consistent with less residual oxygen groups remaining in the lowest oxidized sample. Combining this conclusion with the comparative intensities in Figure 102, shows the increasing D peak intensity pairs with decreasing FWHM_G , indicating aromatic regions are both more prevalent and slightly larger in less oxidized material.

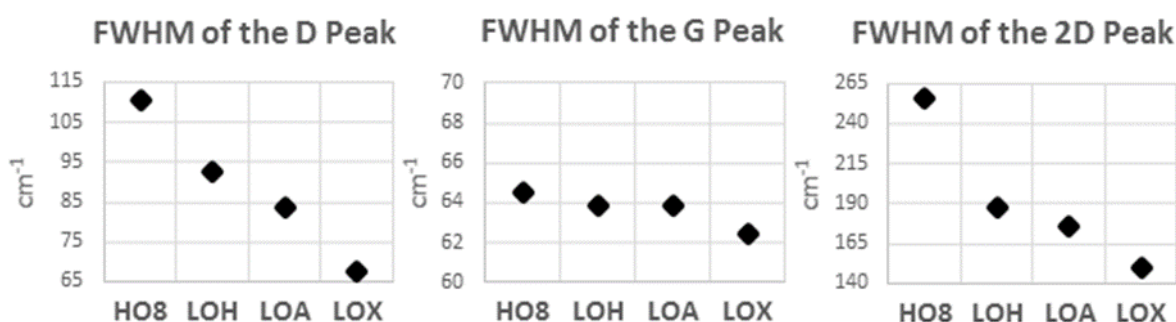


Figure 108. Comparison of D, G, and 2D FWHM values for all rGO assemblies.

It has also been shown that for almost every type of carbon material (from nano-graphitic crystallites to glassy carbon), a FWHM_D that is more than three times that of the FWHM_G indicates very small aromatic domains where $L_a < 4$ nm [107]. Further, it has also been shown that the D peak broadening becomes even more significant in highly defective carbon materials because the phonon coherence length becomes extremely small [276]. Therefore, for rGO assemblies, it appears the disorder is more directly comparative with the FWHM_D , and there is a distinct trend between decreasing FWHM_D and decreasing oxidation, similar to that seen in soot [270]. This indicates that the aromatic clusters in assemblies with less oxidation are more uniformly oriented, and this enhanced alignment is also reflected in the 2D peak which also shows more intense and less broadened peaks as the oxidation level decreases.

From this, it can be concluded that the oxidation level of the rGO contributes to the size and prevalence of aromatic clusters, which then directly impacts on the stacking of graphene sheets in the assembly. This supports the previous statements linking oxidation with levels of strain in the assemblies.

5.3.2.4.3 Area of the dominant and less prominent bands

There is a clear and direct trend between the total area of both the D and G peaks with the oxidation level. At lower oxidation levels, the area of the D peak decreases, while the area of the G peak increases. This trend follows the much more traditional thinking about Raman spectra of graphitic materials, and the D band indicates defects and disorder while the G band is associated with graphitic domains. Using the area of the D and G bands as a direct qualitative measure of structural order in rGO assemblies appears to be the most direct parameter. However, care should be taken not to draw conclusions from this alone, and converting the area to an overall percentage reveals there are differences in the type of disorder present in the different assemblies.

In line with discussion on the increased prevalence of aromatic domains in LOX, graphitic regions (G band) have a larger overall percent contribution in lower oxidized assemblies. Further, the relatively constant contribution from defect regions (D band) is consistent with Ferrari and Robertson's amorphization trajectory for disordered carbons [170] and Lucchese's model of high density of activated regions in defective graphene proposed by [266], since it is clear from the other peak features that rGO assemblies have L_a in the unique length scale of less than 4 nm, where the defect density is extremely high and the crossover from sp^2 to sp^3 is initiated. The slight increase in percent area of the D peak follows the expected trend for oxidation in the LO- materials, but the decrease seen in HO8 indicates some of the aromatic domains contributing to the D peak signal are lost, as would be expected if the defects were contributing to sp^3 bonds. Support for this is seen in the I band and is discussed below.

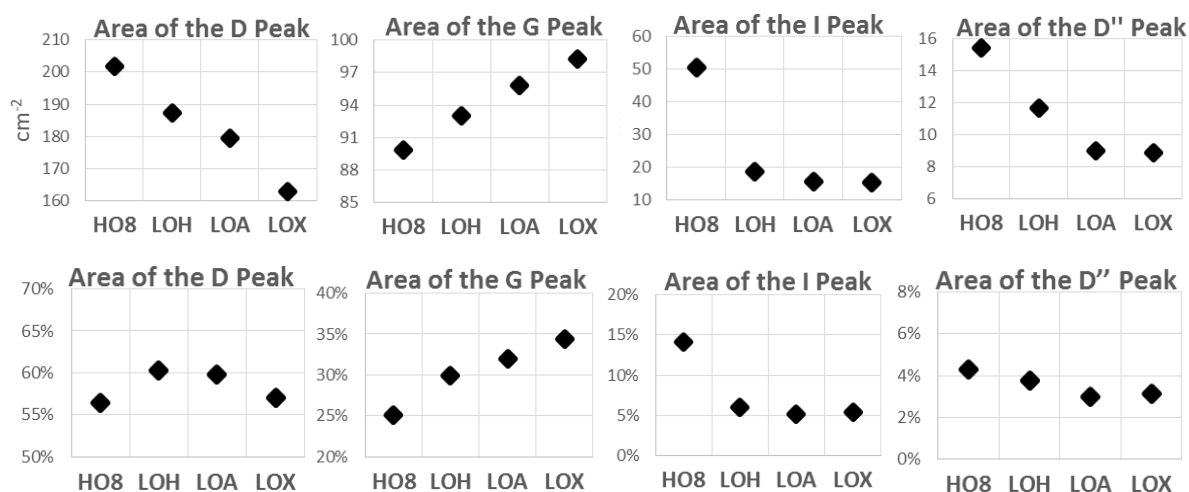


Figure 109. Comparison of the D, G, D', I, and D'' peak area values for all rGO assemblies.

Analysis of the less prominent spectral peaks provides additional structural information and it is clear from data in Figure 109 that these peak features are correlated with oxidation levels. As discussed, these additional peaks include the I peak ($\approx 1180 \text{ cm}^{-1}$) and D'' peak ($\approx 1500 \text{ cm}^{-1}$). The I peak is directly related to the amount of sp^3 carbon present. This can result from C-C bonds in diamond-like carbons or be a measure of impurities, and in soots it has been attributed specifically to C-O bonding [277]. The results here show a clear distinction between HO- and LO- preparation methods and this correlates strongly with the XPS results identifying twice as much oxygen remains in HO-rGO, with HO8 containing more residual epoxy and carboxyl oxygen groups. It appears there is only one, more recent published work on rGO that utilizes the I band Raman feature to identify structural elements [258], even though it is a simple and straightforward approach to assess the presence of residual oxygen groups. The I band can also act as a measure of the sp^2/sp^3 bond ratio, and these results indicate sp^3 bonding is present in all materials, but only at very small levels for all LO- assemblies. This is very constant with the interpretation of the D band discussed above.

Expressing the area as a total percentage, the I band indicates there is 2-3 times more sp^3 bonding in HO8 than the low oxidized samples, again consistent with chemical measurements presented in the previous chapter. Thus, it can be assumed that for higher oxidized rGO, the additional basal plane oxygen groups present in HO- materials, as identified in XPS, increase the amount of sp^3 bonding by disturbing the aromatic regions. This is also evident in the decreased area of the G peak, linking the I feature with G peak properties through the physical formation of basal plane epoxy and/or residual hydroxyl functionalities to in-plane defects that combine with wrinkling and strain to decrease the sp^2 content. All of these structural features are similar to observations in other types of porous and layered carbons [66, 130, 273].

The D'' band has been shown to correlate well with the amount of amorphous sp^2 carbon [171], C-H vibrations[274], and oxidative reactivity [270] even in materials with identical L_a . As expected, there is a stronger D'' signal in the higher oxidized assemblies. However, the overall contribution of the D'' peak is quite small for all materials (3-5%), signifying rGO assemblies contain disordered, but not amorphous, structural regions. This further validates why the rGO spectra are so similar to that of glassy carbon. While glassy carbon can be considered a disordered carbon with very small aromatic domains, it is not actually amorphous and contains purely sp^2 bonding.

5.3.2.4.4 Peak Ratios

Various peak ratios can be used to unveil the exact nature of defects present in graphene materials, and those most widely applied for studies on carbon materials are listed in Table 14 and shown graphically within the discussion to follow. These ratios play an important role for both qualitative and quantitative assessments. Important considerations are required when interpreting the results because correct judgement regarding the defect type and amorphization stage of the carbon is necessary to obtain accurate structural parameters.

Table 14. Relevant peak ratios extracted from the fitting procedure applied for all rGO assemblies.

Sample	Related to rGO			Related to defect		
	I_D/I_G	I_{2D}/I_{D+G}	I_{2D}/I_G	$I_{D'}/I_G$	$I_D/I_{D'}$	$A_D/A_{D'}$
rGO HO8	1.31	0.98	0.09	0.33	4.2	13.1
rGO LOH	1.39	1.04	0.10	0.37	3.9	11.9
rGO LOA	1.43	1.15	0.11	0.35	4.3	12.5
rGO LOX	1.53	1.52	0.16	0.39	4.2	9.3

D/D'

To compare differences between boundary, vacancy, and sp^3 defects, it was found that the $I_D/I_{D'}$ ratio can be used to evaluate the nature of the defects in graphene and HOPG [278]. The results are shown in Figure 110, for specific types of carbon defects in graphene, and the trend relating the $I_D/I_{D'}$ ratio is easily distinguishable in Stage One carbons (three separate dashed lines on the figure), but at the crossover into Stage Two where there is an extremely high concentration of defects, the nature of the defect can be lost and the parameters no longer show a clear relation to a specific type of defect (cluster of data points at top right). While the $I_D/I_{D'}$ value for rGO assemblies shown in Figure 111 (values of 3.9-4.3) is closest to that of boundary defects (figure inset showing ratio of 3.5 is indicative of boundary defects in HOPG), comparing it to data for defective graphene sheets plotted in Figure 110, the rGO results fall closely in line with the red data, especially that of oxidized graphene. This intermediate value of ≈ 4 has been reported for other nano-graphitic carbons [216] and is attributed to contributions from both boundary-like defects (majority) and other vacancy-like defects (minority). It has been established that sp^2 carbon bonds are dominant in the rGO assemblies, and this indicates that besides the residual oxygen groups (more prevalent in HO8 which also shows highest sp^3 content), the majority of defects preserve the sp^2 structure. It follows that boundaries resulting from basal plane defects (5-7-7-5 and 5-8-5 clusters) [279] and corrugation resulting from graphene wrinkling [48] are the larger contributors to the high defect density. Of these, knowing the rGO retains a large sheet size (low edge to basal plane ratio), it is most probable that wrinkling is the dominant defect present. A

highly corrugated structure is supported by both the TEM and Raman analysis and can be used to explain the presence of strain in the rGO assemblies as well as correlate with material properties such as mechanical strength [280] and reactivity [281, 282].

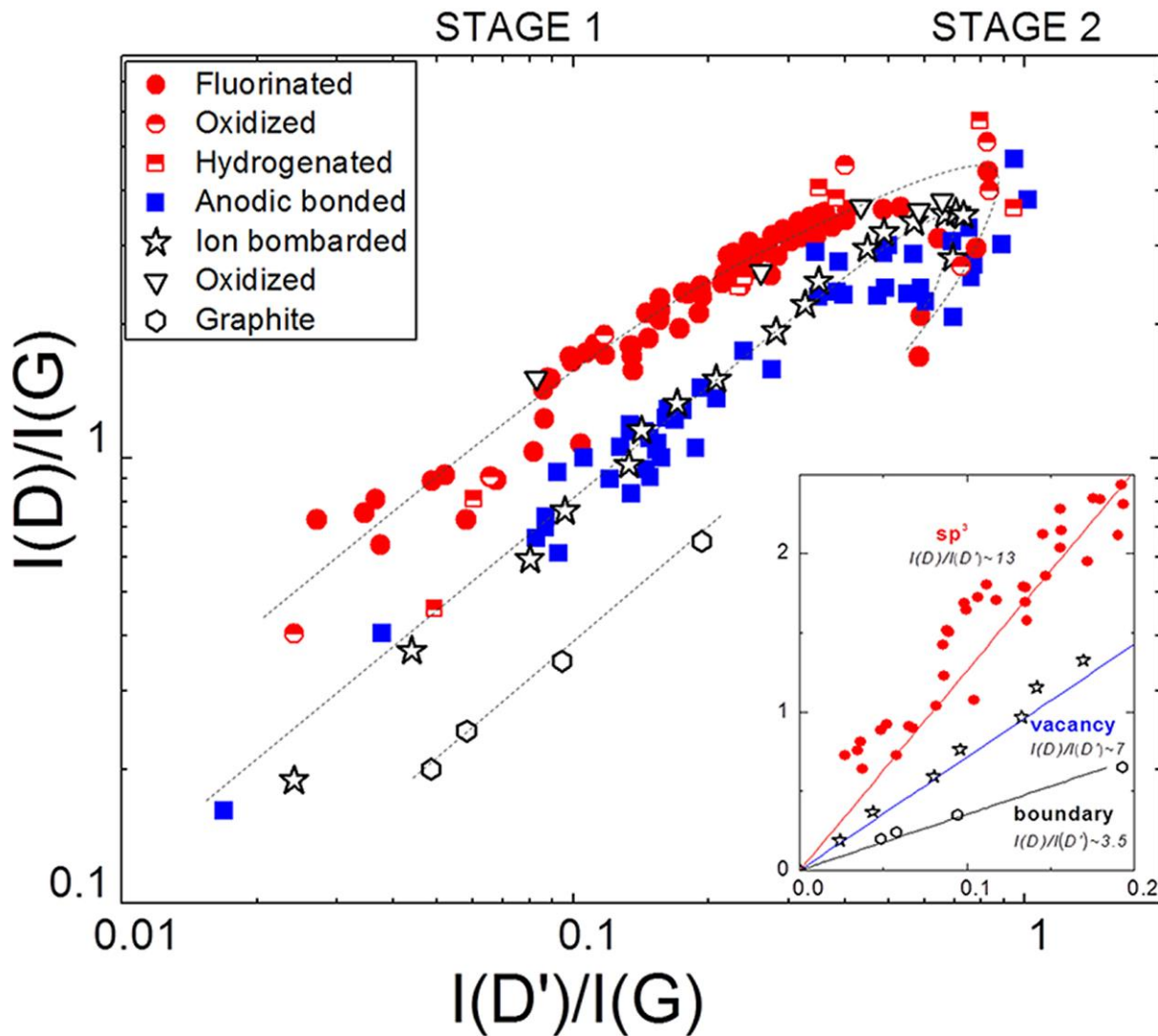


Figure 110. Graphene and HOPG with different types of defects are compared to show a relationship between $I_{D'}/I_G$ and I_D/I_G that translates into $I_D/I_{D'}$ values that can differentiate boundary-, vacancy-, and sp^3 -like defects – each shown by the data points of black hexagons (graphite edge), stars (ion induced holes), and red dots (chemical bonding), respectively (from [278]).

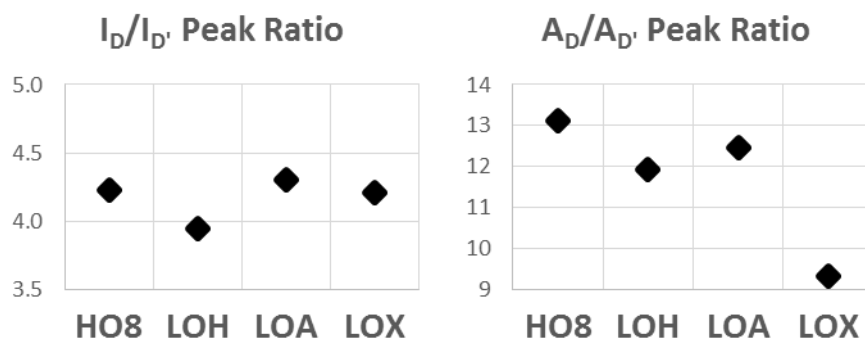


Figure 111. Comparison of the $I_D/I_{D'}$ and $A_D/A_{D'}$ peak ratios for all rGO assemblies.

For Stage Two carbons, it has been suggested the integrated area is a better parameter to apply in this case because at high defect concentrations the D band can become extensively broadened [258, 269, 270, 276]. Using $A_D/A_{D'}$, the linear trend distinguishing defect types can be preserved when crossing

from Stage One to Stage Two carbons, and the $A_D/A_{D'}$ ratio is able to highlight differences in sp^3 like defects between samples. The trend follows what would be expected in regard to bonding from oxygen, nitrogen, and hydrogen groups on higher oxidized materials, as discussed with the XPS results presented in Chapter 4.

It should also be noted that the D' peak has been found to be more prominent in nitrogen doped graphene as it is highly dependent on defects along edges [221]. Since all rGO samples prepared using the hydrazine method will contain nitrogen as well as edge bonded oxygen groups, it is expected this will be the most significant contribution to the D' peak signal. It is probable that the rGO assemblies exhibit a combination of effects resulting from edges and edge bonded functional groups (nitrogen and oxygen) as well as basal plane defects and wrinkling, which can be seen in the $A_D/A_{D'}$ and $I_D/I_{D'}$ ratios respectively. Considering this, data is in line with the XPS results of the previous chapter which showed the basal plane oxygen content and level of nitrogen doping is significantly lower in LOX.

D/G

One of the most relevant parameters resulting from the Raman spectra is determination of L_a . As discussed, there have been many approaches suggested for determining this for carbon materials, and applying the most relevant model for carbons with small aromatic domains, like rGO assemblies, is still an area of ongoing research. Decisions on how to approach the problem can be guided based on a qualitative understanding of the particular carbon or graphene system being analysed. The meaning of the I_D/I_G peak ratios for GO and rGO materials could be interpreted differently depending on assumptions about the nature and density of the defects. Materials with a high degree of amorphous carbon will require a different approach than a nano-graphitic carbon, and it is not yet known which methods are best suited for analysis of rGO assemblies. For example, depending on the choice of model and assumptions made about the structure, an I_D/I_G peak ratio of 1 could result from L_a of 1 nm, 10 nm, or 40 nm [170, 266].

Table 15. Results for L_a based on different calculation methods. Three are based on the I_D/I_G ratio, including the original Tuinstra-Koenig model [255], modified T-K relation for Stage Two carbons from Ferrari and Robertson [170], and the graphene activation area model developed by Lucchese [266]. These are compared to results from an alternative model using the broadening of the G-band proposed by Mallet [268].

		Method to Calculate L_a (nm)			
Sample	I_D/I_G	T-K	Ferrari	Lucchese	Mallet
GO (avg)	1.06	4.76	1.30	0.86	3.94
rGO HO8	1.31	3.84	1.44	1.09	6.87
rGO LOH	1.39	3.63	1.49	1.14	6.94
rGO LOA	1.43	3.52	1.51	1.16	6.94
rGO LOX	1.53	3.30	1.56	1.22	7.07
Based on		I_D/I_G Ratio			$FWHM_G$

Due to the large variability in methods used to calculate L_a , the results here are based on a comparison of different approaches in the literature and highlight how applying the incorrect model will strongly impact the results – both qualitatively and quantitatively. Table 15 lists the results for L_a based on different calculation methods these are compared graphically in Figure 112. The first three columns use methods based on the I_D/I_G peak ratio while the fourth makes use of the broadening of the G band

as an alternative approach. All calculations using the I_D/I_G ratio include constants that have been adjusted for energy dependence [267, 271].

Among the first three models listed, the traditional T-K relation [255] is most widely reported in GO and rGO literature, even though it does not account for differences due to the amorphization trajectory. It is clear that if assuming GO and rGO are in Stage One (where T-K holds), all samples have aromatic domains of over 3 nm which is over twice that calculated using other models and much larger than TEM results indicate. Further, the T-K results do not qualitatively align with what is known to be true regarding the disorder and chemical bonding in the materials. The T-K model is the only one that assigns smaller aromatic domains to lower oxidized materials, implying oxidation creates a more ordered material. Conversely, the models of Ferrari, Lucchese, and Mallet all align with the conceptual understanding that higher oxidation material is more defective, a claim that is further validated by other Raman features as well as the XPS results reported in Chapter 4.

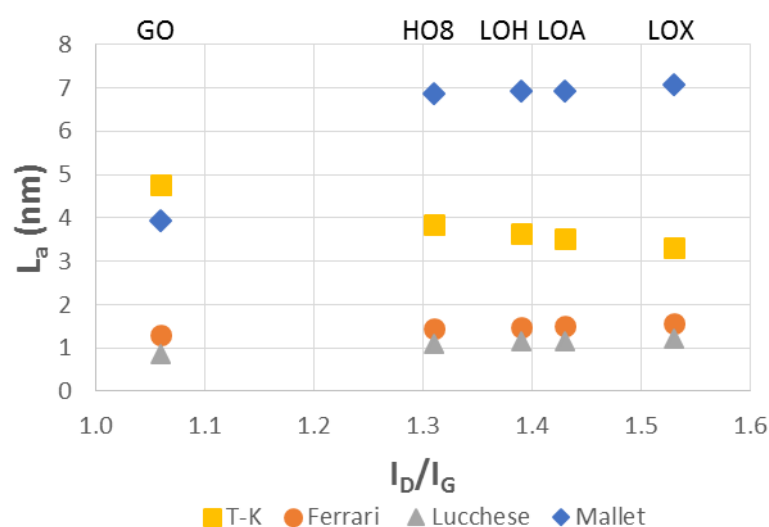


Figure 112. Comparison of the calculated L_a results, based on different models for GO and rGO assemblies.

Showing the T-K relation is invalid for rGO assemblies, and instead applying the knowledge that Stage Two carbons have an I_D/I_G ratio that is proportional to L_a^2 , as shown by Ferrari and Robertson [170], the size of the aromatic domains using Ferrari's model comes very close to that from the TEM fringe length measurements (1.3-1.5 nm compared to the TEM estimated length of 1.1 ± 0.4 nm). This length of ≈ 1 nm also matches values that would be expected for highly disordered sp^2 carbon materials [107]. The trend of decreasing L_a with increasing oxidation level is also in line with what is expected, further supporting the conclusion that rGO assemblies fall within Stage Two of the amorphization trajectory. This relation does not depend on specified size for the activated region (r_A) or defect type (r_S) as the Lucchese [266] model does and is suggested as the most straightforward approach to measure L_a in Stage Two carbons, especially when the defect parameters are not known.

Lucchese's model [266] allows for greater precision when measuring L_a , especially when comparing carbon materials with different types of defects. Again, the results here account for the conceptual understanding that the aromatic domains in LOX should be larger than those in HO8 and GO. L_a values in Table 7 result from adjusting the proportionality constants and activated region in equation 5.6 to account for 2.33 eV excitation energy [267] ($C_A = 4.81$, $C_S = 0.996$, and $r_A = 3.43$ nm), while the size of the defect (r_S) was kept at 1 nm. As the defect size in rGO materials has not been directly measured by STM or AFM like with Ar+ experiments, it is estimated the defect size is similar based on the analysis of the I_D/I_G ratio discussed above along with the TEM images. The disordered regions in the TEM image analysis from Figure 85 would imply the defects may be smaller, but definitely not larger, than 1 nm.

Placing the values in Table 7 as the upper limit and adjusting r_s to 0.75 nm causes L_a to decrease by 0.2 nm. Combining this with the results using Ferrari and Robertson's model, a safe approximation of ± 0.2 nm was added in Figure 113 for variance in the measurement.

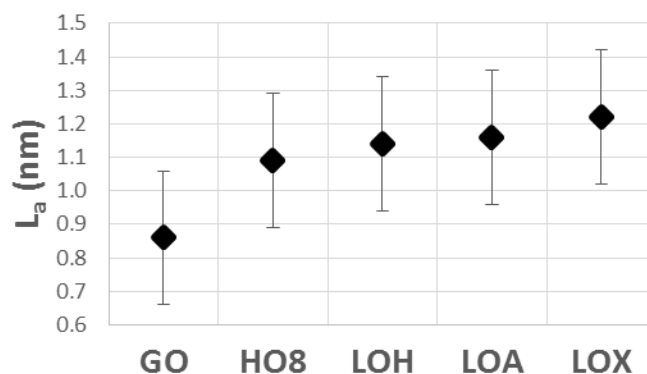


Figure 113. Calculation of L_a based on Lucchese's model [266] with error bars to account for possible variance due to estimation of defect size.

It should be noted that while the exact measurement of L_a as determined by Lucchese's method does depend on the type of defect, it is a systematic variance and the trend, as well as the relative difference, measured in GO and rGO materials will not be impacted by this. Thus, all L_a values are indeed unique for each rGO assembly, but they all fall within the range of 1.2 ± 0.3 nm. Further, incorporating the fluctuations in the I_D/I_G peak ratio across the rGO sample surface (1.3 to 1.9 as shown in the Raman map from Figure 99) does not require additional variance to be added to these values as this range falls within the tolerance provided. Conversely, GO assemblies do not exhibit unique measures of L_a , despite the varied oxidation levels, and again it appears that GO materials reach a saturation point where all available basal plane sites are bonded to oxygen functionalities. The chemical structure was detailed in the Literature Review, and based on the bond configuration of GO, the distance between basal plane oxygen groups should be less than 1 nm, supporting the results shown here.

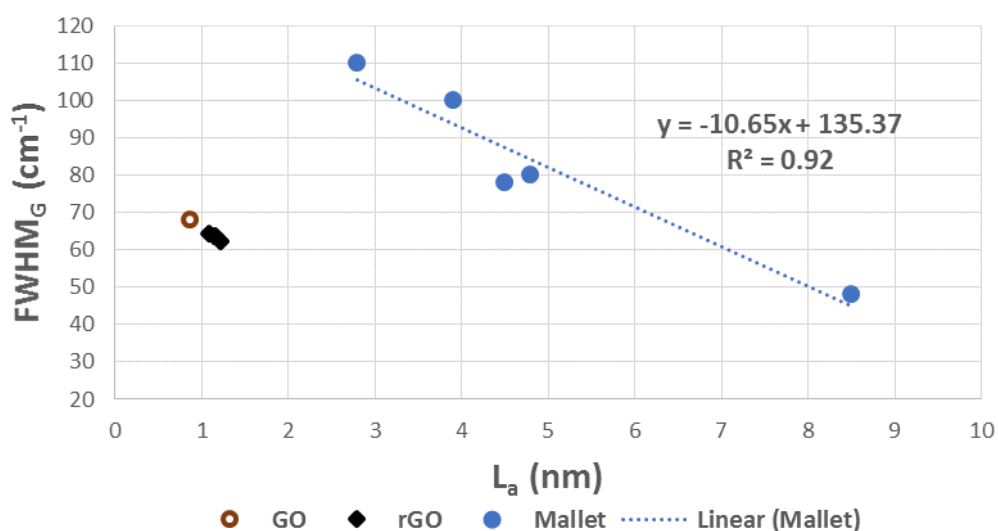


Figure 114. Data and linear fit that Mallet's model [268] is based on compared with results for rGO and GO using L_a values resulting from Lucchese's model [266].

The use of the $FWHM_G$ to determine L_a has been suggested as a less ambiguous approach, and the results from the I_D/I_G peak ratio are compared to the model proposed by Mallet [268, 269]. While this

method follows the expected trend of decreasing L_a with increasing oxidation level, it greatly overestimates the size of the aromatic domains when compared to TEM results and the other Raman based models, as shown in Figure 114. Because the $FWHM_G$ is a direct measure of disorder, it appears there are different mechanisms impacting the disorder, not only the size of the aromatic domains.

It has been shown that for amorphous carbon, the crossover point where the TK relation no longer occurs (I_D/I_G ratio shifts from being proportional to $1/L_a$ to L_a^2) when the $FWHM_G$ becomes greater than 50 cm^{-1} and corresponds to L_a values close to 1 nm [274]. Even though no data in Figure 115 is from amorphous carbon, it clearly follows this model, and again emphasizes the need to distinguish between carbons in Stage One or Stage Two. This behaviour can also be related to the specific disorder in the material as seen in Knight and White's work investigating spectral shapes for graphitic, amorphous, and glassy carbon [261].

Because Mallet designed this model based on nano-graphitic carbons with suspected L_a in the $2\text{--}10\text{ nm}$ range, he did not account for differences between Stage One and Stage Two carbons. As discussed, there is a pronounced shift in Raman spectral features when carbons are extremely disordered and/or have aromatic domains of less than 4 nm . Assuming the independent measurements for L_a are correct, Mallet's material appears to retain a Stage One nano-graphitic structure with L_a as small as 2.8 nm , which can be the case in highly crystalline carbon materials (pyrocarbons and graphite) [171] where only edge defects are present and nano-graphitic domains are undisturbed. Figure 115 combines Mallet's data with Ganesan's work [216] on both Stage One and Stage Two nano-graphitic carbons in a similar size regime. With this, a trend appears that indicates a modification should be applied between Stage One and Stage Two carbons, similar to the approach using the I_D/I_G ratio.

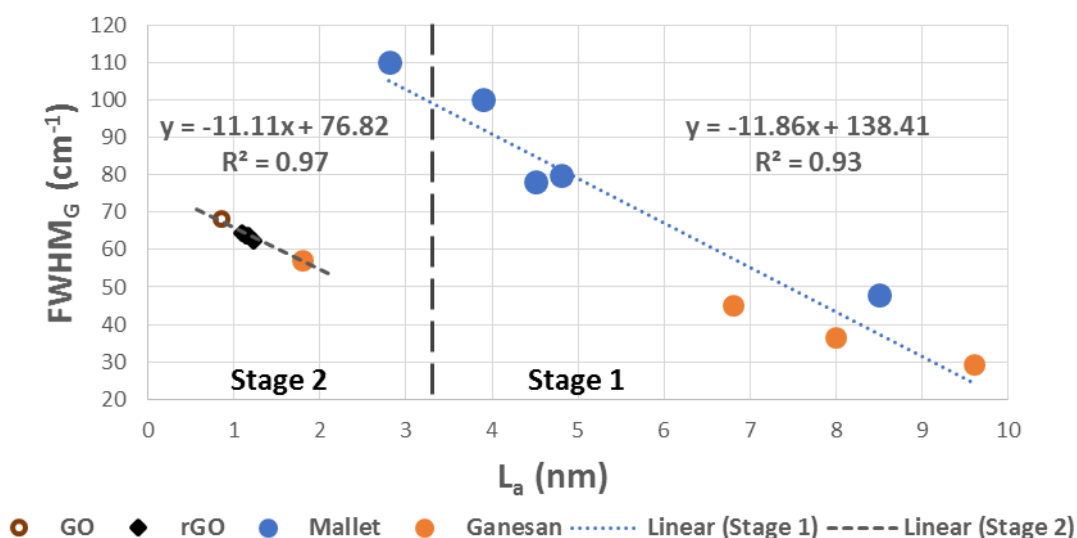


Figure 115. Comparison of GO and rGO assemblies with nano-graphitic carbons investigated by Mallet [268] and Ganesan's work [216] on both Stage One and Stage Two nano-graphitic carbons in a similar size region.

A direct comparison between the original $FWHM_G$ model presented by Mallet and the linear fits for data in Stage One and Stage Two from Figure 115 is compared below:

$$\text{Mallet: } FWHM_G = (136 \pm 8) - (10.4 \pm 1.0) L_a$$

$$\text{Stage one: } FWHM_G = (138) - (11.9) L_a$$

$$\text{Stage two: } FWHM_G = (77) - (11.1) L_a$$

These results indicate the model holds for other types of Stage One nano-graphitic carbons with L_a in the $4\text{--}10\text{ nm}$ range. More data is needed to predict the behaviour of specific carbons at the cross-over region between Stage One and Stage Two (L_a of $2\text{--}4\text{ nm}$), and it is clear another relationship develops

for Stage Two carbons. Interestingly, the slope of the trendlines for Stage One and Stage Two are equivalent, it is only the intercept that requires adjustment by a factor of approximately one-half. This indicates that depending on the type and density of defects, a maximum FWHM_G is reached during Stage One and once a material's level of disorder passes this, there is a distinct change in the shape of the G peak feature. It seems possible to calculate L_a using the FWHM_G as long as two distinct models were applied for Stage One or Stage Two carbons, but more results are needed to ensure the validity.

2D/D+G and 2D/G

The higher order peaks can also be used to evaluate strain and disorder within the rGO assemblies. Comparing the 2D peak with the G and D+G features provides a clear insight into the aromatic structural order. The 2D peak is related to the edge to plane ratio of nano-graphitic carbons and relates to the overall dimensions of the ordered domains in rGO. As seen in Figure 116, both of these ratios follow almost identical trends related to the oxidation level of the materials. The I_{2D}/I_G ratio is only affected by disorganization within the hexagonal network, so a decrease seen here is directly related to increased disorder [276]. Because the 2D peak will become more pronounced if larger ordered regions are allowed to form (more edges surrounding coherent domains), these ratios are highly dependent on the geometry of the defect, where strain related corrugation and protruding bonds (such as with the nitrogen and oxygen present in rGO) will strongly attenuate the 2D signal [221].

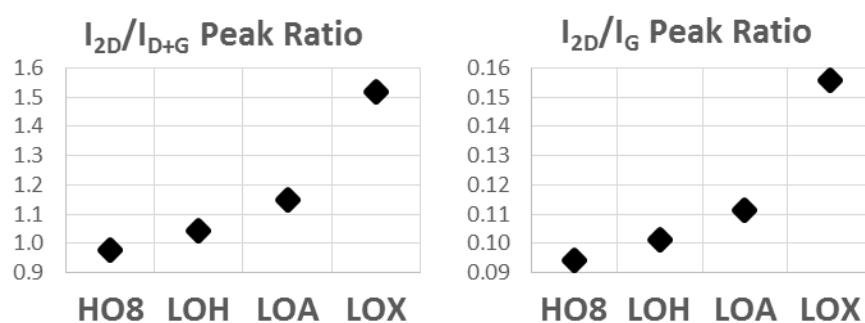


Figure 116. Comparison of the I_{2D}/I_{D+G} and I_{2D}/I_G peak ratios for all rGO assemblies

Further, since the I_{2D}/I_{D+G} ratio relates the aromatic structural order (2D) with lattice disorder (D+G), it can be a direct indicator of electronic conjugation [126]. This ratio has been shown to increase upon annealing when aromatic structure is restored after heating [66], as was seen with the XPS results for rGO assemblies. Thus, this ratio is clearly linked with the amount of residual oxygen groups and sheet corrugation, with the results here showing the aromatic regions in lower oxidized materials are able to form larger, ordered units with interplanar coherence domains, with an exceptionally high degree of stacking in LOX. Translating this to probable material performance indicates that while LOX is likely to have higher conductivity, much of the surface will not be accessible because of more the aromatic domains are stacked together. Also of interest is to notice while the I_D/I_G ratio follows a linear trend, the I_{2D}/I_{D+G} values do not, showing the overall order (as related to the ability of rGO to form larger stacked regions) is not solely dependent of the size of L_a and is most likely related to the specific oxygen and nitrogen groups present, as revealed with XPS.

5.3.2.5 RMS of rGO hydrogel assemblies

RMS is an extremely applicable tool to investigate the structure of the hydrated rGO assemblies because it does not require vacuum conditions and can easily probe structural changes *in situ* as the material dries. In this current section, the methods described above used on dried rGO assemblies are applied to wet hydrogel films prepared at the standard 100°C reduction temperature and also a

hydrothermal assembly prepared at 180°C. As discussed in the Literature Review, hydrated and hydrothermally prepared materials are presumed to have different pore structures than the dried rGO assemblies, as demonstrated by electrochemical and permeation experiments conducted on them [17, 22, 25]. While the unique properties of these materials have been observed, direct measurement of the structural features determining this has not yet been reported, these results aim to better understand the role of water and hydrothermal processing in determining rGO assembly performance.

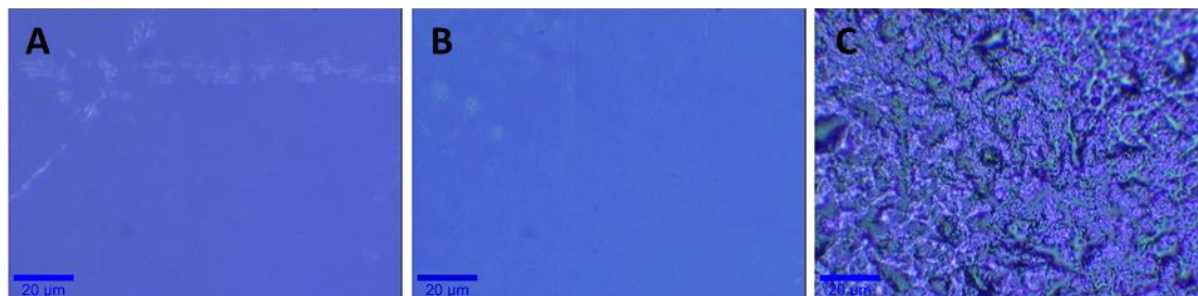


Figure 117. Optical images of the rGO hydrogels used for Raman analysis, showing both of the hydrated films prepared at 100°C (A) and 180°C (B) have a very smooth surface which becomes very rough as the water evaporates (C). The blue scale bars indicate 20 μm .

Both hydrogel assemblies were prepared from HO4-GO solutions and were reduced with hydrazine, like those of the dried materials discussed previously. The rGO solutions were then vacuum filtered, as outlined in Methods, to produce free-standing films, but not allowed to dry and kept hydrated by submerging them in water until RMS testing. As shown in Figure 117, the surface of both hydrogel assemblies is very smooth. As the water is removed, a high level of roughness is observed which indicates that the level of hydration and drying conditions will have a significant impact on the resulting pore structure of the material. While the pore network itself will be better characterized in the following chapter, it is first appropriate to determine if the hydration and/or hydrothermal treatment has significant impacts on the rGO sheets themselves. It is not known if the drying process causes changes to the size of the aromatic domains of the rGO sheets. Thus, the method developed for the dry rGO assemblies has been applied to hydrogels with the following results.

The full RMS spectra for two rGO hydrogels is shown in Figure 118 and exhibit a very similar profile to the dried rGO assemblies in Figure 100, suggesting hydrogel materials also fall into Stage Two of the amorphization trajectory. The comparison shown in Figure 119 highlights the only obvious differences are seen in the higher order region where the D+I feature has a much more pronounced peak at 2450 cm^{-1} and additional enhancement of the G+D' feature at 3200 cm^{-1} . It can also be seen that the intensity of the D+G peak is higher than the 2D peak, a different relationship than that seen in the dry assemblies where the I_{2D}/I_{D+G} ratio was greater than or equal to one. Looking back at Figure 89, it is clear that the 2450 cm^{-1} feature is more pronounced in graphitic materials with decreasing aromatic domain size, signalling the presence of crystalline order and/or pronounced edge groups. If this were the case, it is expected that the D' feature would also be enhanced, and this is supported by the correspondingly enlarged D+D' feature. In order to make a direct measure of the D' peak itself, the first order region has been deconvoluted and is discussed below.

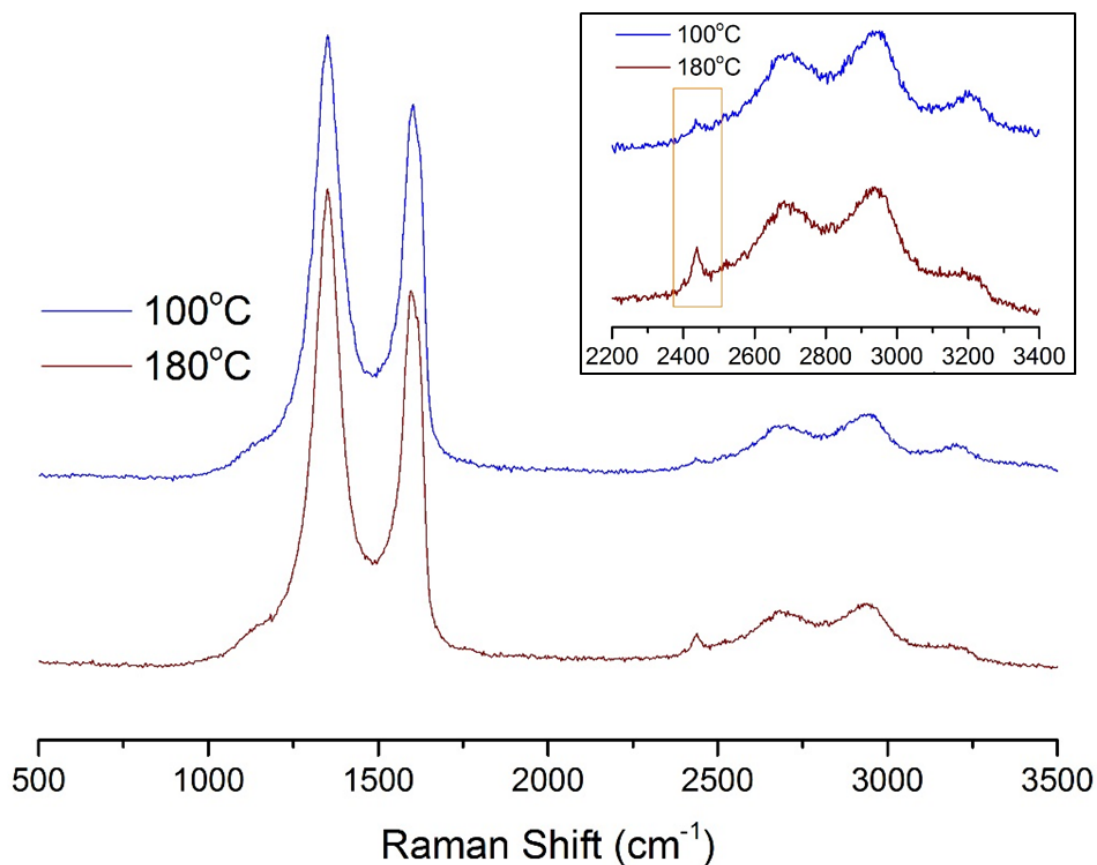


Figure 118. Full Raman spectra for HO4 rGO hydrogel assemblies prepared at different reduction temperatures. The inset highlights the higher order region which exhibits different properties than the dried assemblies, most notably the enhanced feature at 2450 cm^{-1} .

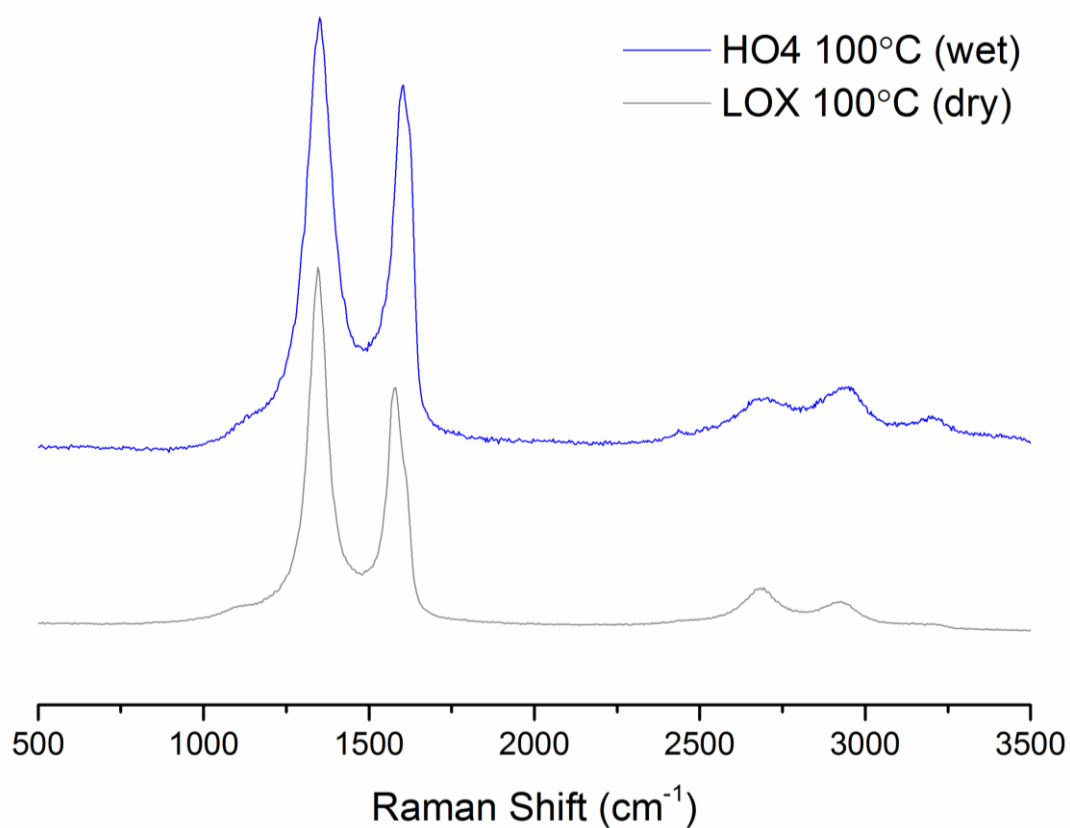


Figure 119. Comparison of the Raman spectra for the HO4 hydrogel and LOX pump dried assembly, both reduced at 100°C , to highlight the dry and hydrogel assemblies show very similar spectral features.

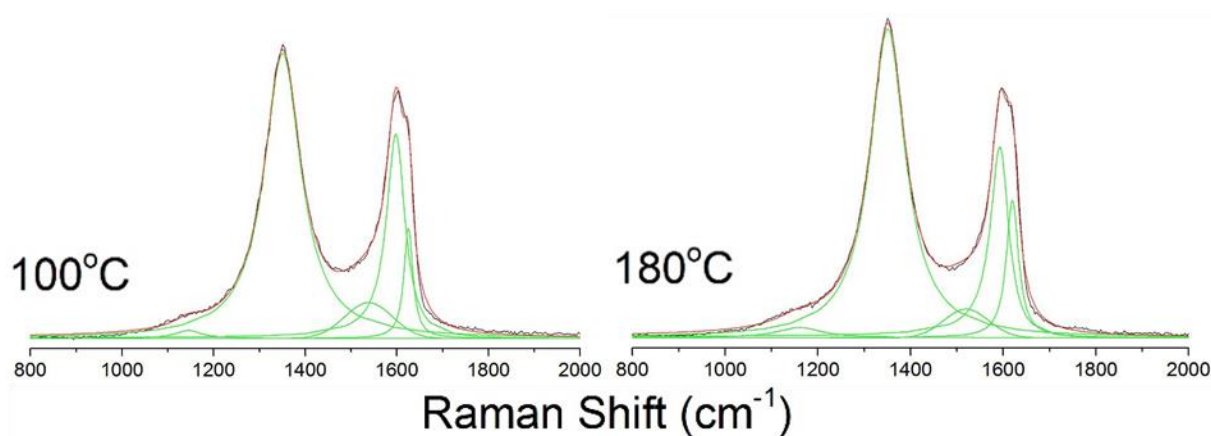


Figure 120. Fitting procedure applied to the first order RMS region for HO4 hydrogel assemblies prepared at the different reduction temperatures of 100°C and 180°C.

After applying the peak fitting procedure, the resulting first order RMS profiles are shown in Figure 120. Again, the enlarged D' feature is detected, especially in the hydrogel reduced at 180°C. From the XPS results, HO4 rGO has a much higher nitrogen content than other materials (5.2% in HO4, < 3% for HO8, LOD, and LOX), and as discussed, this edge-bound species is known to enhance the D' feature [263]. The other relevant spectral features are listed in Table 16, and they indicate the structure of rGO sheets making up the hydrogels is quite similar to the dried materials and is also consistent with the previous discussion about common structural features seen in disordered porous carbons. The main difference is seen in the position of the D and G peaks, which both show a shift to higher values (as compared to $\sim 1347\text{ cm}^{-1}$ and $\sim 1588\text{ cm}^{-1}$ dried rGO assemblies displayed in Table 12) – both factors indicative of strain and oxidation. These values are similar to the dry HO8 assembly with highest oxygen content, and this suggests the Raman shift is likely due to the increased basal plane oxygen groups present in HO4, which is supported by the XPS results from Chapter 4. The fact that the G band falls back toward expected values for low oxidized rGO when reduced at the higher, 180°C, temperature supports that this strain is due to oxidation.

Table 16. Relevant parameters extracted from the peak fitting procedure applied for all rGO assemblies.

Sample	Peak Position (cm^{-1})		FWHM(cm^{-1})		Area(cm^{-2})				(nm)
HO4	D	G	D	G	D	I	D''	I_D/I_G	L_a
100°C	1350.7	1597.9	98.3	65.8	177	3.6	18.9	1.28	1.07
180°C	1350.8	1592.7	93.4	65.0	181	7.7	13.9	1.49	1.20

Since the hydrated rGO sheets are largely separated by intercalated water molecules, they have not been stacked back into dense turbostratic layers, and these results indicate the strain and disorder present in rGO results from the chemistry, not the drying process or constricted entanglement from surrounding sheets. The FWHM and area values for the D and D'' peaks fall directly in line with the trends presented in the discussion on dried assemblies relating the disorder to the oxidation level of the original GO, and implying that the amount of aromatic carbon present is similar to that in dry materials. The area of the I peak is much less than would be expected with this HO- material, and indicates the presence of water may play a role in reducing the amount of sp^3 carbon bonds, however more work would need to be done to investigate this.

Applying equation 5.6 (Lucchese et al. [266]) to the I_D/I_G ratio, the length of the aromatic domain in the HO4 hydrogel reduced at 100°C is directly in line with the oxidation trend seen in the dry samples,

indicating neither hydration nor drying plays a role in determining the length of these regions. Interestingly, the L_a measured for HO4 reduced at 180°C has larger aromatic regions, close to that of the LOX sample. This indicates that the increased temperature applied during the hydrothermal reduction effectively removes many of the basal plane oxygen groups, as was shown during the thermal reduction process applied in the XPS results, as discussed in Chapter 2 [76]. The hydrothermal processing is believed to increase the corrugation along the rGO sheets [22], a feature investigated in the next chapter, but it appears this increased structural disorder has no impact on the aromatic domain size.

These findings are relevant to current work on rGO, as it appears all rGO materials prepared by hydrazine reduction at 100°C will likely exhibit these same general structural features regardless of the hydration level or individual chemistry, and can be easily characterized using the analysis methods presented here. In addition, the results for the hydrothermally reduced rGO assembly made it possible to eliminate increased corrugation as the cause of disruption to the aromatic domains. Further, while all assemblies will have aromatic domains of about 1 nm, the difference in L_a is directly related to the presence of residual oxygen groups bonded to the basal plane, traits that are determined by the processing conditions of the original GO and reduction conditions. Thus, care should be taken when comparing results from rGO assemblies prepared using even slightly different processes because, as shown, these parameters can impact the size of aromatic regions by up to 20%.

5.3.3 Concluding remarks

Combining together the results and discussion of this chapter, it can be seen that dry and hydrogel rGO assemblies fall within Stage Two of the three-stage amorphization trajectory proposed by Ferrari and Robertson, shown in Figure 121 [170]. The major physical process occurring in Stage Two is a bond-bending disorder that results in significant changes to the vibrational density of states (VDOS) so that the carbon is no longer considered graphitic, yet it is not necessarily amorphous. This would be expected in a material like rGO that is a purely turbostratic carbon with plentiful structural perturbations along the basal plane. The main impacts on the Raman spectra in this stage are a decrease in the position of the G peak from the maximum value of 1600 cm^{-1} and a decrease in the I_D/I_G ratio from the maximum values just over 2 seen for most Stage One carbons with small aromatic domains. Instead of comparing rGO assemblies with pure graphene and graphite, analysing the structure based on knowledge of a range of carbonaceous materials clearly show that they follow well-known trends where steady-state values are reached at high levels of disorder [107]. Most notable of these are d-space greater than 3.5 Å, aromatic domains less than 2 nm, and broad RMS peaks that quantify the particular type of disorder.

A major conclusion from Ferrari and Robertson's work was that for Stage One carbons, I_D is directly proportional to the defect concentration, while in Stage Two this relationship shifts to be inversely proportional. The TK equation is no longer valid in Stage Two, and L_a must be interpreted using alternative models which account for competing mechanisms in carbons with an extremely high defect density. It is suggested that application of Luchesse's model [266] provides the best method to measure L_a in rGO assemblies, even though it is necessary to allow for a somewhat large variance because the precise measurement of defects size in rGO is not known as precisely as that for ion induced defects. Additionally, broadening of the D and G bands can be used to measure disorder and distinguish between Stage One and Stage Two carbons. A potential model to calculate L_a from the FWHM_G in Stage Two carbons has been proposed, but this requires independent measurements of L_a in rGO materials as well as data from a wider set of Stage Two carbon structures.

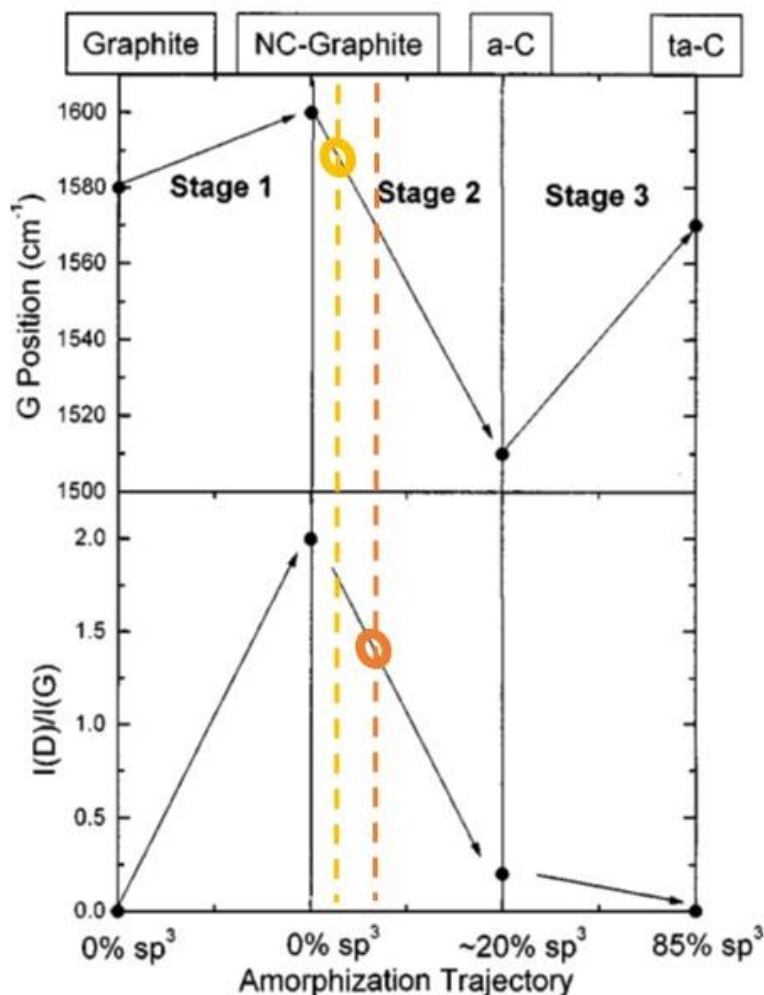


Figure 121. Raman results from the rGO assemblies are marked on the three-stage model for the amorphization trajectory of carbons proposed by Ferrari and Robertson [170] showing rGO materials are most likely in Stage Two and contain 5-10% sp³ bonds.

5.4 X-ray Diffraction

5.4.1 XRD applied to rGO assemblies

X-ray diffraction is a widely applied and well-known characterization tool that has been in use for over one hundred years. The detailed aspects of diffraction in carbons discussed in Section 2.3.2.2 of the Literature Review have not often been applied to the more recent work on rGO, and XRD results are often misinterpreted as containing graphite crystallites (when they do not) and/or inaccurately assign the XRD peak as a measure for total interlayer spacing (especially with layered rGO materials) [20, 25, 77, 101]. Clearly, both the designation of crystallite and of expanded layers are not represented by the broad, low intensity peak produced by rGO, which actually results from the nano-turbostratic coherent domains within the assembly and is not related to the larger pores that are present. The slight shift in the position of the diffraction peak is indicative of stacked turbostratic layers making up the 'mosaic clusters', not a measure of interlayer expansion, since turbostratic carbon is known to have a larger interlayer spacing than graphite. As such, these clusters are representative of inaccessible space, providing no information on the disordered regions surrounding these turbostratic regions larger, nor does it provide a measure of any micro- or meso- porosity in the material. Thus, while useful in identifying structural aspects making up the mosaic clusters, care should be taken in putting any value into reports that use XRD to as the only method to evaluate the structure of the assembly as a whole.

Even though the information gained from XRD is limited, it remains widely reported and commonly used, most likely due to the long history of applying XRD to evaluate more ordered carbon forms (graphitizing and non-graphitizing) [46]. However, applying quantitative XRD methods to more disordered carbons requires a much more detailed analysis to elucidate the important structural parameters [108, 175, 176, 250, 283]. In order to align with the more simplified approach and allow for wider adoption of these methods, some results for rGO will be present here along with suggestions for integrating some insights gleaned from the rich history of research into the structural characterization of other types of carbonaceous materials – similar to the demonstration in the RMS section above. Application of these methods can be used to uncover valuable information related to the structure of the nanoscale ordered domains, as well as insight on chemical functionalities such as oxygen content. XRD is an extremely accessible tool, and thus if clear methods can be developed which can aid researchers in easily analysing the acquired data, this would be a useful contribution to the field. An overview of these methods is discussed here in order to outline a “best-practice” approach for XRD analysis of rGO materials.

As discussed in the literature review, geometric considerations play a large role in what information can be gathered from layered carbons. While most work is done on powder samples with random orientation of crystal planes, rGO assemblies consisting of (001) and (hk) planes are perpendicular to each other, and with the traditional reflection geometry (Bragg-Brentano) only the inter-layer (001) plane will contribute to the reflected intensity. Further, because the rGO assemblies are disordered and quite rough (at the atomic scale), higher order reflections or rocking curve scans cannot normally be acquired as supplementary data needed to construct a structural model. Therefore, any useful information is confined almost exclusively to the structure of the broad (002) peak.

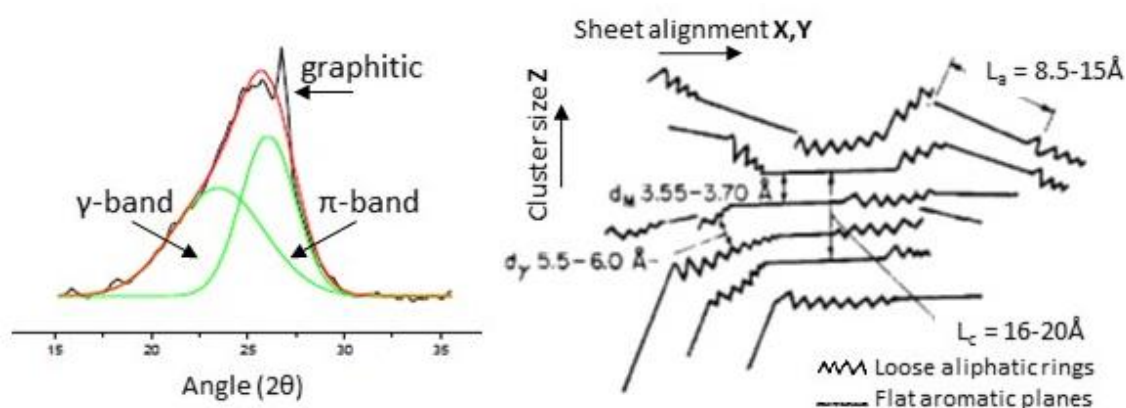


Figure 122. Example of fitting the (002) peak for XRD in coal to quantify aromatic and aliphatic contributions to the inter-layer reflection from [284] and corresponding structural diagram developed in 1961 by Yen et al. [109]

Coal analysis has long used the (002) peak to distinguish between three types of inter-layer bonding within the microcrystalline carbon domains [109]. As illustrated in link Figure 122, the sharp peak at 26.6° indicates the presence of graphitic layering (AB stacking at 3.34 Å), the main broad peak centred around 25° is characteristic of the aromatic sp^2 turbostratic (π -band) regions, and the low intensity hump around 21° that broadens toward lower angles is a measure of aliphatic sp^3 saturated (γ -band) regions. This method has since been applied in studies on various coals [108, 284] and soot [270]. The area under the π -band and γ -band can then be used to assess the aromaticity (f_a) of the carbon, and is defined as:

$$f_a = \frac{A_\pi}{A_\pi + A_\gamma} \quad 5.9$$

The aromaticity of carbon particles is a useful measure for predicting the material performance as the number of active sites depends on the carbon structure – especially in regard to desirable properties such as conductivity, combustion, and reactivity. It is interesting to notice the diagram and dimensions given for the proposed structure of coal shown in Figure 122 by Yen et al. from 1961 [109] is very similar to the parameters extracted for rGO assemblies from TEM and RMS discussed previously – again confirming the structure of rGO is very similar to that seen in other disordered and porous carbons, and implying the same correlations between material properties and structure could be applied here.

5.4.2 Results and discussion

Comparing rGO assemblies from GO of different oxidation levels, Figure 123 shows differences in the shape of the (002) peak profile for assemblies from both high and low oxidation levels. It is clear that no sharp graphitic peaks are present (at least in a large enough concentration to be resolved), and rGO also exhibits the mixed π -band and γ -band components that represent the aromatic and aliphatic components in coal and soot particles. The π -band is dominant for all rGO assemblies, and it is likely the same structural processes described for lamellar pyrocarbons, where the majority of disorder is induced by sp^2 curvature and arch-like features, with minimal contributions from small aliphatic species [111], is present here. The γ -band is more pronounced in the highest oxidized sample (HO8) and virtually non-existent in the extra-low oxidized sample (LOX), and is able to act as a measure for aromaticity in rGO.

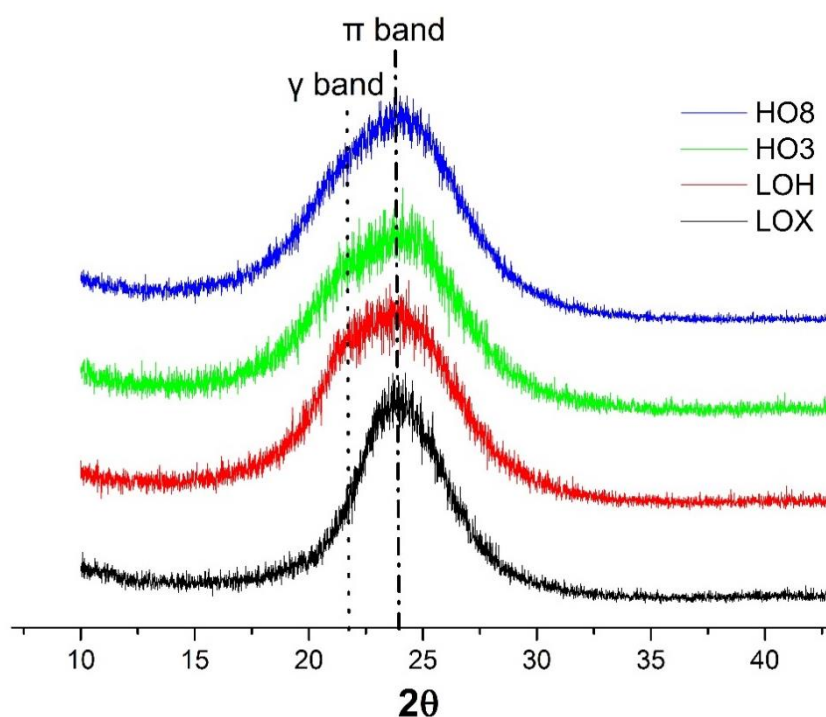


Figure 123. Peak profile of the (002) reflection for pump-dried rGO assemblies. To emphasize differences in peak shape, the spectra have been normalized to give peak height of one and offset for clarity.

A comparison was made between Lorentzian, Gaussian, and Voigt functions to test the best fit for the (002) peak profile of rGO assemblies. As expected, the Voigt profile was best suited for all samples [181, 182]. The fitting for each (002) peak profile is shown in Figure 124, with all assemblies having π -band and γ -band components except for LOX, which exhibits purely aromatic layering. Corresponding peak parameters are listed in Table 17, and these show that while the average inter-sheet spacing for the π -band stays the same in all materials, the aromatic component does relate to the oxidation degree

of the original GO, as shown previously with XPS. Correspondingly, the FWHM_γ increases with oxidation level, however the FWHM_π remains constant except for LOX, indicating the difference in aromaticity (f_a) seen in XPS and Raman is also detected here. The FWHM values for the π -band were approximately 70-90% Gaussian, again indicating strain plays a role in peak broadening, and the results for L_c were found using the Scherrer equation (equations 2.8 and 2.9) after a deduction in the FWHM for strain was accounted for (to compare, without strain $L_c=1.3$ nm for all assemblies other than LOX where $L_c=1.8$ nm). A lower bound of five layers defines the small (002) coherent domains for all assemblies other than LOX, where at least seven layers make up the average stack height. This shows LOX is likely to have superior performance in strength applications and as a barrier film, since the coherent domains are more numerous and 30% larger than assemblies made from other rGO materials. Further, these results are similar to those found using TEM, reinforcing the common nature of rGO materials and also verifying the sample preparation methods used did not have a large impact on the SAED data.

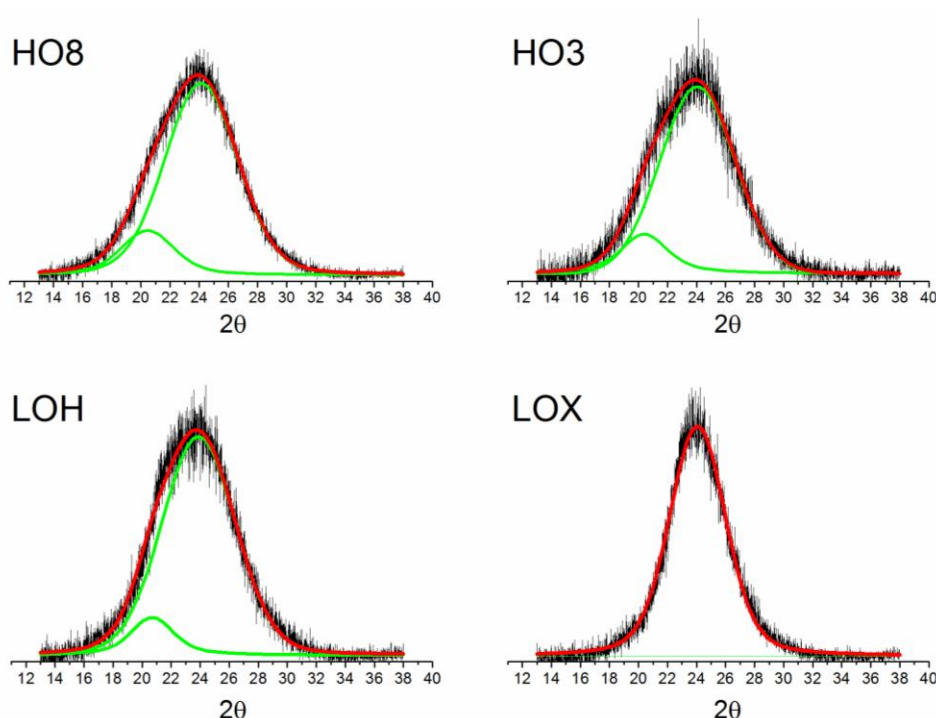


Figure 124. Fitting results for the XRD (002) peak profile, consisting of the π -band and γ -band components. All fits converged with a χ^2 tolerance value of $1\text{E-}6$ reached (reduced χ^2 ranged from 62 to 142 and adjusted $R^2>0.97$).

Table 17. Results of the XRD (002) peak fitting for π - and γ -band components in rGO assemblies to assess the aromaticity of the material and determine the length of the coherent domains.

Sample	$d_{(002)}$ (nm)	f_a	FWHM_γ (°)	FWHM_π (°)	L_c (nm)	Layers
HO8	0.369	0.84	4.35	5.91	1.81	5
HO3	0.370	0.85	3.89	6.09	1.76	5
LOH	0.372	0.89	3.53	5.97	1.79	5
LOX	0.370	1.00	0	4.57	2.34	7

The impact of drying method on the resulting rGO assemblies has remained an open question in the study of rGO material properties [285]. Usually, this element of processing is not discussed, and the large impact it has on the resulting rGO structure has been neglected in most reports. The large difference in the degree of order present in the coherent domains for the original GO and resulting rGO that has either been pump dried or air dried is shown in Figure 125. Clearly, the coherent domains are greatly diminished in rGO, resulting in very few ordered regions being present at all. The drying method impacts the amount of ordered layering within the (002) plane, and it appears that the small contribution from coherent domains in rGO is a direct result of the processing, where pump drying provides additional force to pull the rGO sheets into close contact. It is expected that controlling the drying process can help tailor material properties for specific applications. For example, applications requiring low permeability would benefit from pump drying and annealing, while applications requiring higher amounts of accessible surface area would want to minimize inter-sheet stacking through controlling the humidity or air drying. This also appears to have a large impact on the mechanical strength of rGO dried paper [20], but the significance of the XRD peak profile was not fully analysed in this work in order to equate physical structure with the strength of the materials.

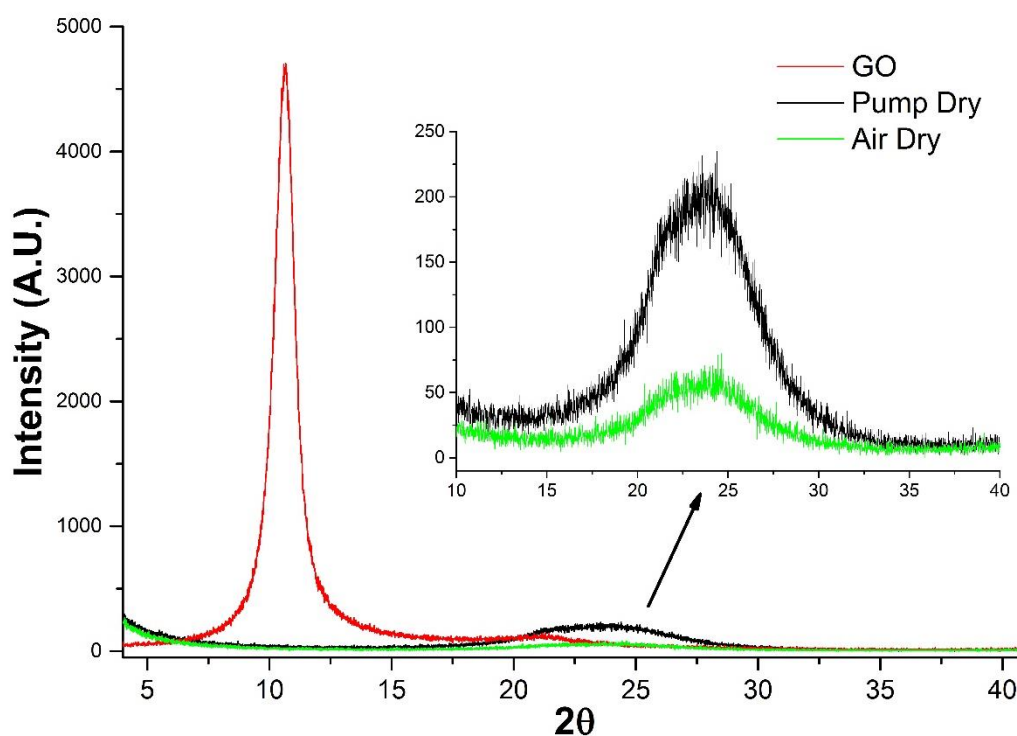


Figure 125. XRD profile for the LOH GO and rGO assemblies highlighting the marked change in (002) peak depending on the drying method used.

There is also a pronounced difference in the (002) peak for hydrogel films, as shown in Figure 126 for the highest oxidation HO8 material. Higher oxidized GO assemblies have a less pronounced peak, indicating the sheets are also more disordered before reduction. The pump-dried rGO assembly has the characteristic π -band and γ -band components, but the hydrogel film which has never been dried, shows no (002) reflections present. The broad hump extended to higher angles is typical of scattering from liquid water at room temperature [286, 287], which is present in bulk form throughout the hydrogel and adsorbed at the surfaces of the rGO sheets. These results show the coherent domains, or clusters, are produced during the drying process, and hydrated films are held together only through the disordered entangling of the layers and/or extremely small regions of inter-layer π -stacking, consisting of less than three layers of rGO sheets.

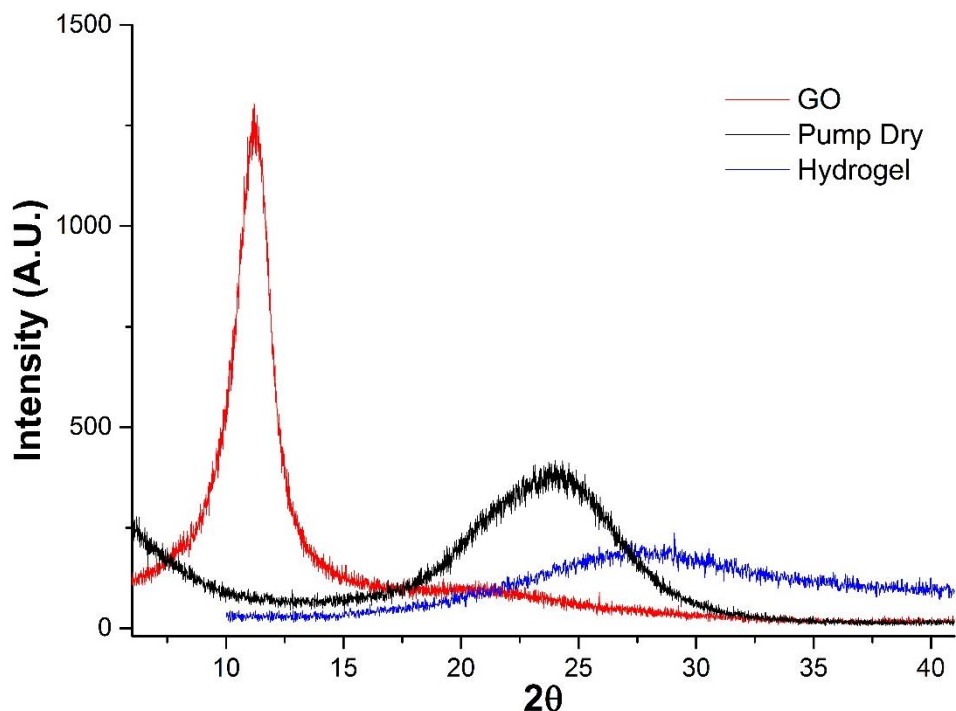


Figure 126. XRD profile for the HO8 GO and rGO assemblies showing the non-existent (002) peak for hydrogel assemblies.

It is clear that the structural information gained through the typical XRD analysis is quite limited, and a more detailed analysis of diffraction peak profiles for various dried and hydrogel rGO assemblies is presented in the following chapter using WAXS. In spite of this, the work here shows that by incorporating a few additional steps to the XRD peak fitting procedure, insight on both the chemistry and physical structure is easily obtained through the analysis of peak features that account for aromaticity and size broadening. To conclude this chapter, the qualitative and quantitative parameters extracted from these XRD results are combined with the insight gained through the detailed RMS and TEM analysis to construct a working model for the BSU of rGO assemblies presented in the concluding remarks.

5.5 Conclusions

The findings in this chapter make it possible to now understand the structural parameters making up the basic structural unit (BSU) for rGO assemblies. The results allowed the specific micro-scale structural features in rGO materials of different oxidation degrees and levels of hydration to be determined. The work presented here proposes and makes use of an integrated approach to collective data interpretation of the three most commonly used experimental techniques applied to carbon materials – TEM, RMS, and XRD. Following this, it has been shown that simple, yet specific, additions to the peak fitting procedures provide a significant amount of useful information on both the chemistry and structure of the rGO assemblies. Longstanding questions regarding the structural elements of rGO materials thus were able to be addressed using existing experimental methods and an in-depth analysis of work done on other carbon forms [131, 170, 257]. It was found that many of the discrepancies (most commonly being incorrect interpretation of the I_D/I_G ratio and overlooking the meaning of the interband features) in the current literature result relate to inappropriate data interpretation. A more successful approach for characterising rGO materials is presented in this chapter.

It is clear from these results that the major structural elements shown in Figure 76, as developed by Oberlin et al. [156], can be applied in the structural characterization of rGO bulk materials. The TEM

images show that the rGO assemblies are fairly disordered at the micro-scale, with the carbon matrix consisting of turbostratic mosaic clusters that are surrounded by disordered, porous regions. The pump dried sample investigated showed that no clearly defined mesopores are present, with the majority of the more disordered bulk consisting of expanded interlayer spacing, with an average value about 4 Å. These results depict the structure as widely inaccessible because of the widespread stacked regions surrounded exclusively by very narrow, sub-nm micropores.

Applying the Scherrer equation to the selected area electron diffraction (SAED) results to assess the length of the coherent domains yielded values of L_c just over 2 nm and L_a just over 6 nm. Considering the additional peak broadening is related to strain (estimated to contribute 30% based on the results shown here), this implies the coherent domains along the c-axis most likely consist of 7-8 rGO layers per stack. The measurement for L_a based on diffraction results is very different from that measured via TEM fringe analysis and RMS. A comparison of these techniques makes clear that the value obtained through the Scherrer equation corresponds to the L_a parameter from Figure 76, while that obtained through direct measurement on the TEM image and assessment of the I_D/I_G peak parameter is associated with the smaller structural element, l . This shows how important it is to clarify exactly what element of the 'aromatic domain' is being measured, reported, and correlated with specific aspects of material performance.

In regard to the overall orientation of these clusters, the pump dried films, which are expected to contain the highest level of order for all the different drying methods, fall in to the *medium* texture classification (OA values 50° to 80°). Based on this, it is expected that rGO materials dried under other conditions (air, vacuum, etc.) would fall at the cusp of the *low* ordered class, since the processing methods apply less pressure to pull the layers firmly into alignment. Correspondingly, in rGO materials with lower texture, smaller and less ordered clusters and additional disorder between clusters, would lead to an increase in the overall microporous volume. The stability of the free standing hydrogel films can thus be explained by combining this insight on high levels of disorder at the micro- and mesoscale with the results from high-resolution SEM imaging which showed the individual rGO sheets are indeed continuous and extend across hundreds of nanometres. This explains that the stability of the bulk materials is directly attributable to this disorder, since the overlapping of large, corrugated layers results in a great amount of entanglement, ensuring even hydrogel assemblies (where contact points and stacked clusters are scarce) remain intact. It is only through the drying process that the stacking of turbostratic contact points occurs, adding more stability, albeit decreasing accessible surface area, due to the van der Waals forces within the clusters.

Along with defining a BSU for rGO assemblies, the results in this chapter showed how much additional information can be gained by analysing the inter-band features in both the first- and second-order RMS regions and applying the three-stage amorphization trajectory model developed by Ferrari and Robertson [170]. This method of combining a BFW (G), Gaussian (D''), and three Lorentzian (I, D, D') peaks for the first-order spectral region one Gaussian (combination of $2D'$ and $G+D'$) with and three Lorentzian ($D+D''$, $2D$, $D+G$) peaks for the second-order spectral region was able to elucidate structural information about the aromatic domains and overall disorder (including differences in strain, cluster size, cluster distribution, and cluster orientation), while also quantifying chemical differences (including oxygen content, dopant concentration, nature of defects, and sp^3 content). Further, it was found that the T-K relation [255] is invalid for rGO assemblies, and the model for Stage Two carbons where the I_D/I_G ratio is proportional to L_a^2 [170] is suggested as the most straightforward approach to measure the aromatic domain length, l , especially when the explicit defect parameters are not known. Specifically related to the structural difference in the rGO materials tested here, the RMS results showed aromatic regions are both more prevalent and slightly larger in less oxidized material. However, while rGO assemblies contain sp^2 clusters of relatively similar size ($FWHM_G \propto L_a$), there is a direct correlation between higher oxidation and the ordering of these aromatic clusters ($FWHM_D \propto$

staging of the planes). Further, analysis of the I-band indicates there is 2-3 times more sp^3 bonding in HO8 than the low oxidized samples, and the additional basal plane oxygen groups present in HO-materials (supporting the XPS results of Chapter 4) increase the amount of sp^3 bonding by disturbing the aromatic regions through basal plane epoxy and/or residual hydroxyl functionalities and in-plane defects that combine with wrinkling and strain to decrease the sp^2 content.

It was also found that expanding the peak fitting parameters can be easily applied to the γ -band component of the XRD peak profile to assess the aromaticity of dried rGO assemblies as long as the coherent domains produce a (002) peak profile with adequate amplitude and a sufficiently defined shape. The XRD results aligned well with those of XPS in Chapter 4, with an oxygen content of 15% being assigned to HO- materials and 10% to the LOH, while no γ -band was detectable in the extra-low oxidized sample, LOX. Further, the values obtained for L_c based on the FWHM of the π -band matched closely to that measured using SAED, without requiring the advanced sample preparation methods. It was also determined that of all the materials tested, the only sample to have a significantly larger number of stacks making up the mosaic clusters was LOX, with a lower limit of 9 rGO layers compared to 7 for the other assemblies tested (this layer number was adjusted from the direct measure of 7 and 5 to account for strain contribution determined via SAED).

For all rGO assemblies tested, the aromatic domain length, l , can be directly linked with the oxidation level and processing conditions of the original GO material. While all GO assemblies showed $l \approx 1$ nm, indicative of a saturation value for fully oxidized graphene sheets, rGO assemblies had aromatic domain lengths within the range of 1.2 ± 0.3 nm, with the samples of lowest oxidation level (LOX and HO4-180°C) having significantly larger aromatic regions. It was not known if hydration, the drying process, or the corrugation level would also cause changes to the size of the aromatic domains of the rGO sheets, and the results from the RMS spectra for two rGO hydrogels reduced at different temperatures showed that none of the processing methods related to hydration, drying, or corrugation was the determining factor for the size of l . Both hydrogels exhibited very similar profiles to the dried rGO assemblies, suggesting all rGO assemblies fall into Stage Two of the amorphization trajectory and should be analysed using the models proposed by Ferrari [170] or Lucchese [266].

These results are important for standardizing research in the field of rGO materials, as the RMS results clearly indicate the difference in the aromatic domain size is directly related to the presence of residual oxygen groups bonded to the basal plane – a trait that is determined by the processing conditions of the original GO and reduction conditions. Thus, care should be taken when comparing results from rGO assemblies prepared using even slightly different processes.

Combining the results from TEM, RMS, and XRD, a full structural picture begins to emerge, and this can be used to address the previously unanswered questions underlying aspects of performance for rGO assemblies. From the results presented here, it can be concluded that the oxidation level of the rGO contributes to both the size and prevalence of aromatic clusters which influence the stacking of graphene sheets and resultant porosity in the assembly. This supports the earlier discussion within linking oxidation with levels of strain in the assemblies, and results are very similar to investigations on pyrocarbons which directly relate processing conditions to the carbon micro-structure [131] where the OA and $FWHM_D$ are used to distinguish between rough laminar (RL), smooth laminar (SL), and regenerative laminar (ReL) structure – all highly anisotropic carbons, yet each exhibits very different mechanical properties [130, 131, 241]. Making this connection allows for a comparison between rGO and pyrocarbons, where rGO assemblies would classify as a low defect density SL carbon [152].

The general progression during heat treatment of pyrocarbons clearly shows that three stages can be distinguished along the graphitization trajectory, where each is related to the structure and texture of the carbon layers. Bourrat et al. [130-132] have established that a sharp decrease in the $FWHM_D$ is observed when heating to 1600°C that is followed by a further, steady decrease until 2000°C where RL,

SL, and ReL all reach a constant value of 40cm^{-1} . Above 2000°C , the ultimate stages of graphitization occur in RL and ReL, but the high anisotropy and trapped curvature prevent SL from being fully graphitizable. Annealing up to 2000°C facilitates a straightening of the graphene layers, yet these small aromatic domains ($L_a \approx 1\text{ nm}$) do not increase much in size. Rather, it is the inter-planar ordering that improves, increasing the anisotropy (smaller OA and more pronounced (002) peak), which translates to additional long-range order and larger cluster size (L_c).

This increased L_c correlates with a decreased porosity and less accessible surface area which explains the decreased capacitance seen in annealed rGO assemblies [17]. As shown here, the inter-sheet spacing of dry rGO assemblies within the mosaic clusters is relatively constant, without much deviation from a bulk turbostratic carbon, and only small micropores ($< 1\text{ nm}$) exist within the disordered regions. This explains why the pump dried rGO assemblies display poor capacitance [17], which is even further diminished after annealing, since these stacked regions are not accessible to ions and also increase tortuosity by blocking passage into the small amount of microporous regions that are present – effectively densifying the carbon [242], diminishing accessible surface area, and decreasing porosity. L_c can also be directly linked to mechanical properties in porous carbon materials [20], as the pores and voids act as stress concentration sites, reducing the overall strength of the bulk material [242]. Processing methods that can effectively smooth the texture in the material (heat treatments, or other processing reduces stress and increases strength) with enhance the mechanical performance, however there is a crossover point where this eventually leads to a brittle nature [242].

To expand these conclusions and tie aspects of material performance to the specific features making up the BSU of the rGO assemblies investigated here, some common generalizations can be made. In addition to the loss of accessible surface area mentioned above, the size of both L_c and L_a will have direct impacts on the bulk material's conductivity, reactivity, and permittivity. Making the distinction between L_a , as measured by diffraction (6.2 nm), and l , as measured by RMS (1.2 nm), could be a major reason for the improved performance of rGO assemblies as electrode materials, as it is known that larger values of L_a significantly contribute to increasing the conductivity in layered carbon materials [104, 133, 253]. However, it is also true that because these larger layer planes contain fewer carbon defects and edge sites, any processes that induces more order along the layer planes will also decrease the carbon's reactivity because the carbon atoms within basal plane sites are much less reactive than those at edge sites [32, 134, 228, 238, 239]. Correspondingly, there is a clear link between decreased reactivity and increased crystallinity for carbon materials [242].

Work here clearly shows that even when materials have same I_D/I_G ratio, the large differences in chemistry and electronic properties [216] can be understood based on the broadening of the D and G RMS bands. Further, since the I_{2D}/I_{D+G} ratio relates the aromatic structural order (2D) with lattice disorder (D+G), it can be a direct indicator of electronic conjugation. Translating this to probable material performance indicates that while LOX is likely to have higher conductivity, much of the surface will not be accessible because of more aromatic domains are stacked together. Also of interest is to notice while the I_D/I_G ratio follows a linear trend, the I_{2D}/I_{D+G} values do not, showing the overall order (as related to the ability of rGO to form larger stacked regions) is not solely dependent of the size of L_a and is most likely related to the specific oxygen and nitrogen groups present. Combining these results indicate LOX is likely to have the least amount of accessible surface area, but exhibit superior performance as a conductive additive, in strength applications, and as a barrier film, since the coherent domains are both larger (longer L_c and L_a) and more numerous.

Combining this insight with the ability to functionalize and tailor both the individual rGO sheets and resulting bulk assemblies through rather simple variations in processing conditions (slight temperature differences, reaction time, drying method, filtering method, etc.) shows why there have been so many published reports detailing remarkable performance across very diverse forms of rGO bulk materials. In general, the microscale results from this chapter are strongly aligned with the work of Farbos et al.

[49] who created atomistic models to reconstruct the main structural features in laminar pyrocarbons based on experimental results from HRTEM and neutron diffraction with radial distribution analysis. This model is shown on the left in Figure 127, where light grey regions are aromatic domains, dark grey regions carbon-bond defects, and the coloured dots represent different functional groups. Comparing this to the ‘through-the-surface’ and ‘through-the-edge’ SEM images of a pump dried rGO assembly make it clear why it has been (incorrectly) assumed that these rGO materials contain very aligned, and ordered, rGO layers. The results from this chapter were able to show that while the essential elements making up the BSU of rGO assemblies are the same as those shown in the models for laminar pyrocarbons, the different processing conditions used for rGO materials allow for a much larger amount of structural disorder to be introduced at the mesoscale. Thus, the next chapter specifically investigates the structural features within this size regime, to complete the analysis of rGO bulk materials.

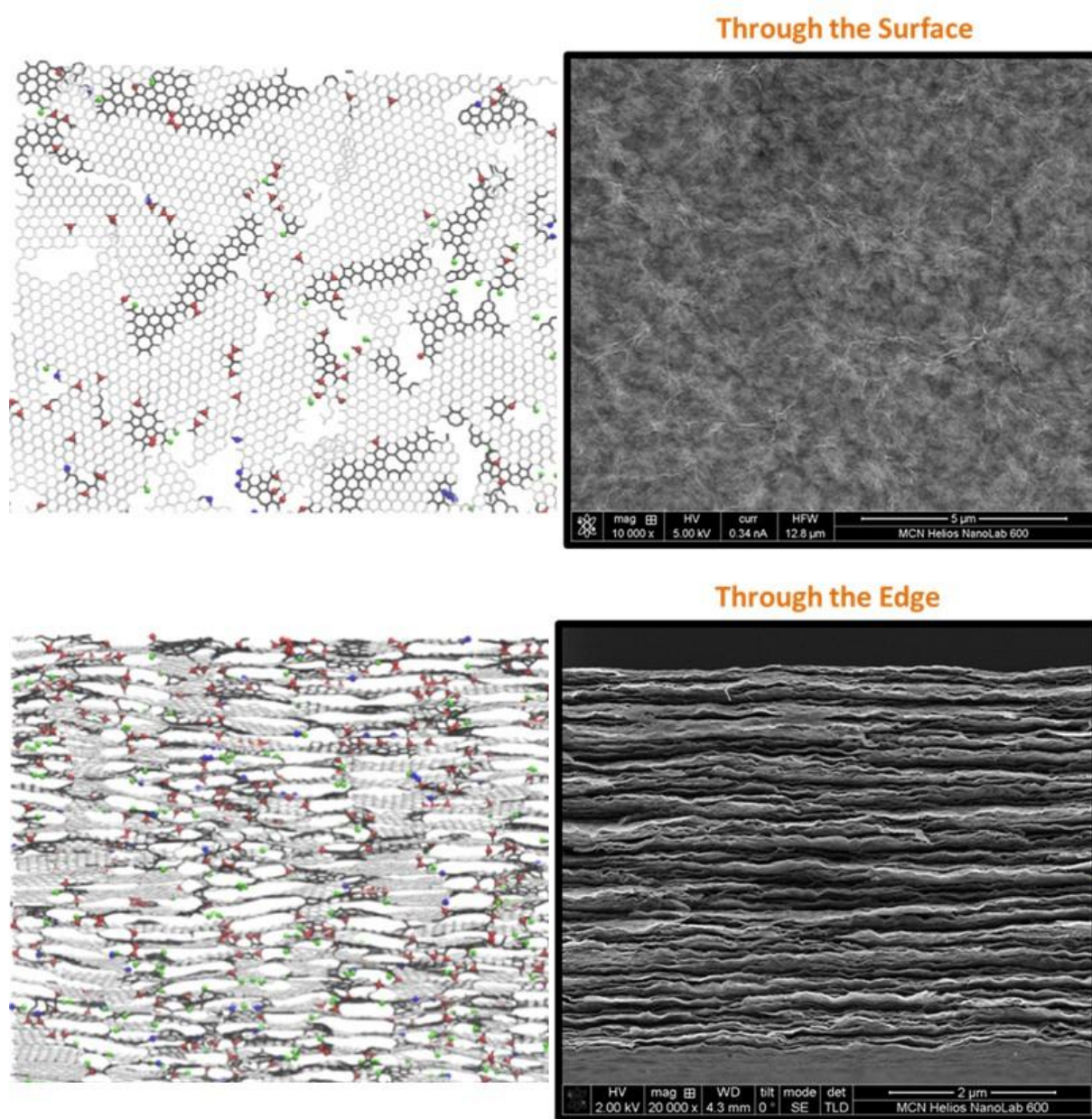


Figure 127. The elements of the BSU for dried rGO assemblies fit well with the micro- to mesoscale structural model for a lamellar pyrocarbon developed by Farbos et al. [49] which are shown on the left and compared to SEM images of pump dried rGO assemblies showing the macro-scale features as seen “through-the-surface” and “through-the-edge”.

Chapter 6. rGO Assemblies as Bulk Porous Carbons

6.1 Introduction: rGO Assemblies as a Bulk Porous Carbon Material

The work presented in this final experimental chapter builds on the information gathered in the previous chapters about the chemistry and aromatic sheet structure, in order to extend a structural model into the meso- and macroscale regions. The results here focus on the main structural differences that are presumed to influence material properties, as identified in the Literature Review. A comparison of rGO assemblies with varied oxidation levels, heat treatment, drying methods, and pore size (using EM-rGO) is made in order to reach a better understanding of how these processing factors impact the pore network. This chapter includes a comparison of EM-rGO materials in order to determine what effects the additional processing step of incorporating non-volatile liquid (sulfuric acid) into the assembly before it is dried has on the structure of rGO assemblies. Further, the impact of hydration is then studied in detail, comparing hydrogels prepared with different pore structures (as tuned by the sulfuric acid electrolyte method discussed in Chapter 3) as well as monitoring the structural changes as the rGO assemblies are dried *in situ*. The physical structure of the rGO pore networks has not been directly visualized to date, therefore the results in this chapter are expected to be particularly useful in the field. In addition, this work also provides critical insight into how wide- and small-angle scattering can be used to answer key structural questions in the field, especially as related to layered hydrogel assemblies and investigation into transport behaviour using *in situ* sample environments.

Since the models used to fit SAS data are not unique, with various structural elements resulting in data that has very similar features, a conceptual understanding of the major structural elements is necessary to interpret the scattering curves. This chapter therefore begins with direct imaging using optical and electron microscopy in order to gather the most relevant structural features and assess the homogeneity of the rGO assemblies. Anticipating what physical features will give rise to the scattering patterns observed allows for a more accurate interpretation of data and ensures the models used for fitting the curves are sound.

In terms of the bulk material, the main features of interest include: i) the overall homogeneity (presence of large voids or other structures that may influence the performance of the bulk materials); ii) the distribution and size of aromatic clusters within the ab-plane (based on the BSU parameters identified in Chapter 5); iii) the inter-lamellar pore size/shape and overall alignment of the pores in the ac-plane. The rGO assemblies are expected to have a complex pore network that is contained between the defective graphene sheets which stack into the ordered lamellar structure along the c-axis. As with the discussion on layered carbons and carbon fibres presented in the Literature Review, because of the anisotropic nature of the materials, the shape of the features along the surface of adjacent graphene layers (situated laterally along the surface of the sheets), is not expected to have the same features as the pore network between the sheets (synonymous with interlayer distance), so measurement using different geometric arrangements will be necessary to determine the structure as a bulk, 3D material. As shown in Figure 128, because the features of individual rGO sheets, as well as features of the bulk material, differ depending on if the structure is being assessed through-the-surface or through-the-edge, information from both the ab-plane and ac-plane needs to be assessed independently and then combined for the complete model.

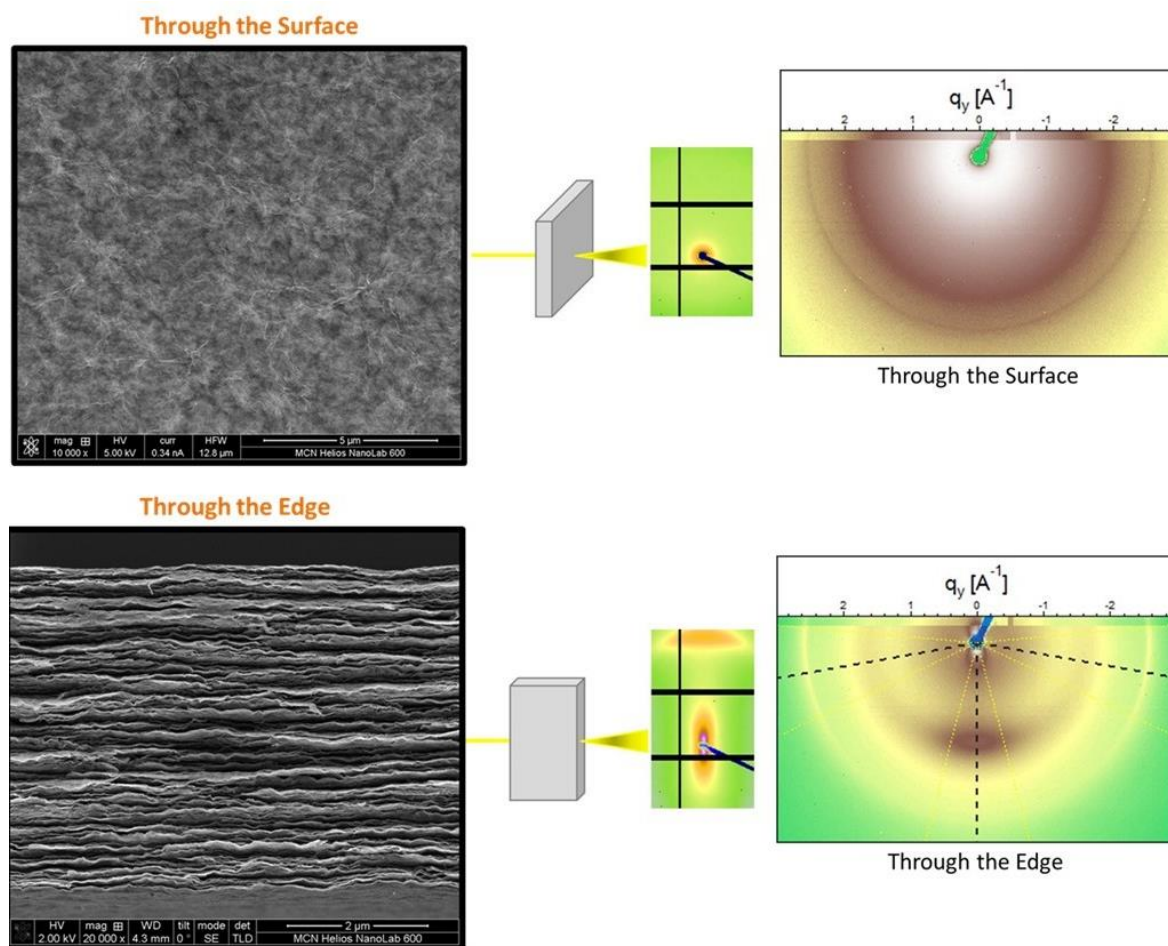


Figure 128. General description of how the different structural elements of the rGO sheets will influence the scattering pattern, depending on if the wide- and small- angle scattering measurements are taken through-the-surface or through-the-edge of the assembly. The SEM images and schematic of the scattering geometry indicate how the sample is oriented with respect to the incoming beam to produce the 2D scattering results shown at right.

The terminology of “through-the-surface” and “through-the-edge” is made clear schematically in Figure 128 and the geometry will be referred to in this way throughout the chapter in order to describe scattering from the ab-plane and ac-plane, respectively. It is noted that because of the random, turbostratic layering, the features along the surface of the graphene sheets along the a-axis or b-axis are taken to be equal, as evidenced by the results of Chapter 5 and the isotropic scattering from the ab-plane presented in this chapter (for details, reference Figure 36). Therefore, to simplify discussion, the two scattering planes of interest are referred to as the ab-plane (intra-sheet features and pores) and the ac-plane (inter-sheet features and pores), excluding any reference to the bc-plane. The resulting WAXS patterns clearly demonstrate that scattering through-the-surface is isotropic, while scattering through-the-edge is anisotropic, and the details of these features is the main focus of this chapter. WAXS and SAXS data is later combined to uncover the structure of the carbon-pore network across a large length scale for a full description of the main features making up the carbon matrix and resulting pore network across the meso- and macroscale. This chapter concludes with combined neutron diffraction, SANS, and USANS curves for rGO assemblies taken through-the-surface in order to extend the q -range even further, assessing bulk structural elements at the micron scale.

6.2 Direct Imaging

6.2.1 Optical imaging

Optical imaging provides the largest field of view and has the advantage of acquiring images in ambient conditions. While it is not able to provide information on chemical or microstructural elements like differences in oxidation levels or pore size, there were clear differences in macroscopic features depending on the drying method used, as shown in Figure 129. A comparison was made between rGO assemblies that were left on the vacuum pump after filtering (pump dried) to those dried in air and placed in a low temperature oven (50°C) and fully wet hydrogels.

At low magnification, as shown in Figure 129, the pump dried surface appears to have many small agglomerates at the surface, however when the magnification is increased, it is clear that these are not particles but look more like circular shaped collapsed regions. Along with these pitted features, the pump dried assemblies have a much rougher surface, with a high level of corrugation, especially compared to the air dried assembly and hydrogel. The collapsed pits are absent in the other materials, and while the air dried sample does have a wavy topology, both have a very smooth surface overall. It is likely that the strong capillary forces cause the rGO pore network to collapse when the water is forcibly removed from the rGO assemblies, as it is during the pump and vacuum drying procedures. It also appears that the air drying method is able to better preserve the expanded pore network in the original hydrogel materials. There were no heterogeneities seen in the wet or dry films, and the waves and corrugation in the dry material extended uniformly across the entire surface.

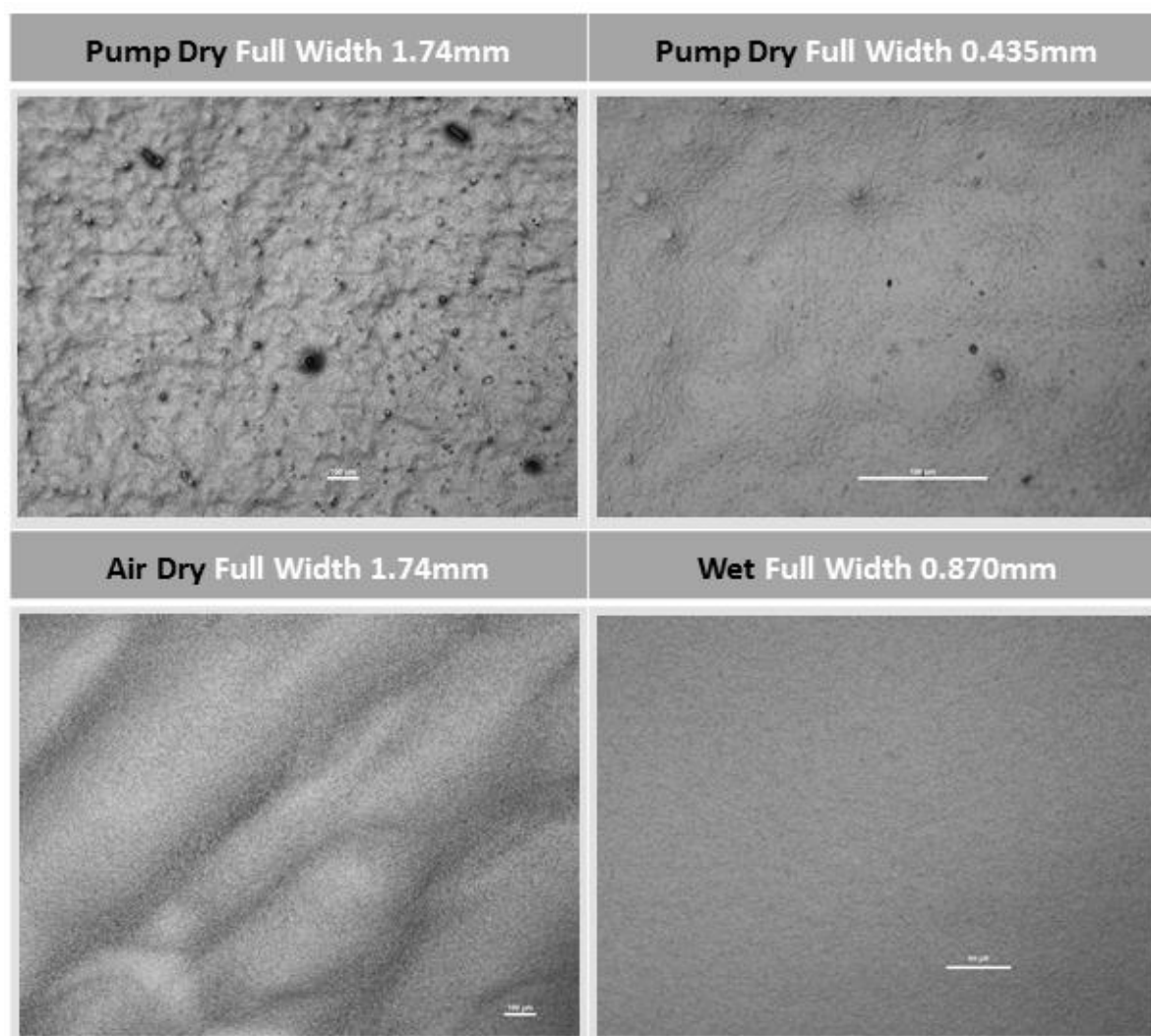


Figure 129. Optical images comparing the surface topology of HO3 rGO assemblies dried under different conditions (all scale bars are 100 µm).

It should also be noted that the pump dried assemblies always have a uniform, pearly lustre (similar to that of pure graphite or other layered, reflective material), while air dried and wet films are an opaque black. The lustre of the pump dried materials is indicative of more uniform stacking which is able to directly reflect the light, while the opaque surface would be typical of more disorder and larger inter-sheet spacing/pores that would cause a more diffuse reflection [247]. Thus, while the air dried and hydrogel materials appear to have a smoother surface at the macroscale, the microscale structure seems to have the opposite trend.

It is also very desirable to have a conceptual understanding of the macroscale topological changes that occur upon drying. A hydrogel assembly was allowed to dry under the optical microscope to see if any major structural changes could be observed. As seen in Figure 130, the wet hydrogel has a very smooth and uniform surface which is retained upon drying. Neither the pits nor rough corrugation seen in the pump dried rGO assembly appeared anywhere along the surface of the dried hydrogel. The larger scale waviness seen in the air dried sample in Figure 129 did appear as the hydrogel dried, with the change being pronounced and rapid. The wavy topology was visible almost immediately after the water evaporated (within a few seconds) and was accompanied by an overall shrinkage of the film, similar to what would be seen in dried paper. Once fully dry, the surface remained in the wavy state. It appears there are no measureable intermediate steps that occur as the water is removed from the material, and instead the hydrogels remain stable in a completely hydrated state until they reach a critical drying point, at which point they can curl up into a more fragile form.

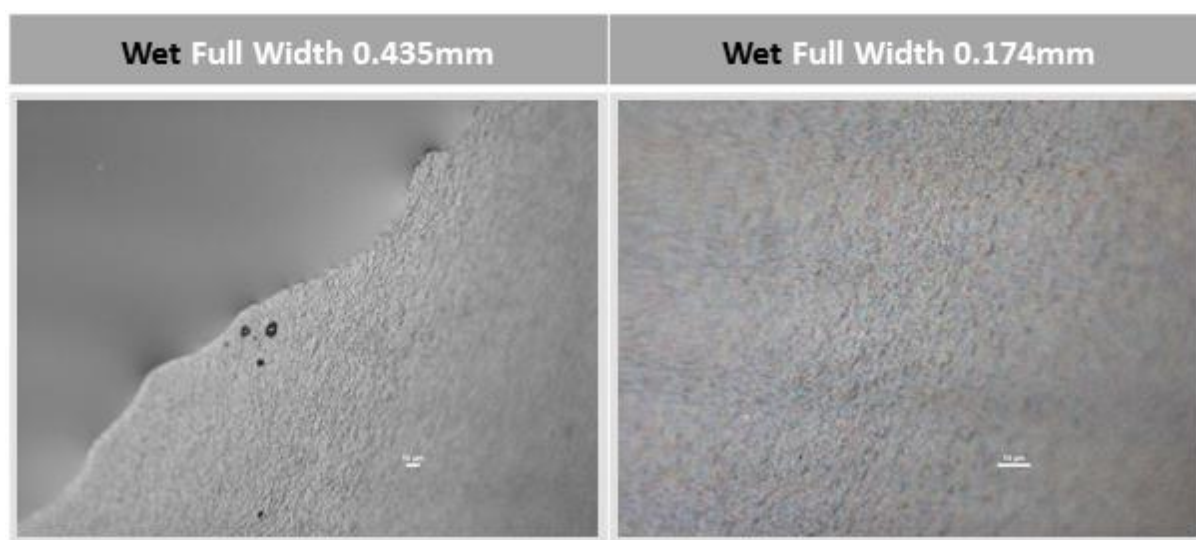


Figure 130. Optical images showing the surface topology of a wet HO3 rGO hydrogel (all scale bars are 10 μm).

Obvious macroscale structural differences exist in the electrolyte-mediated samples (both as compared to other rGO assemblies and between EM-rGOs), and the optical images show pronounced differences that will be discussed here. The methods and reasoning for intercalating the rGO hydrogels with non-volatile sulfuric acid at different concentrations is described in detail in Chapters 1 and 2, but the current interpretation is that the acid prevents the graphene layers from restacking while the water is removed from the assembly using a vacuum drying method [24]. It has been assumed (through measuring changes in the overall thickness of the film) that this process is able to tune the interlayer spacing between the graphene layers to a rather uniform height, thus controlling the density and pore size in the rGO materials. The residual acid is then washed from the rGO assembly and it is kept hydrated for future use, allowing the water to prevent the pores from restacking. The images presented here are taken after the EM-rGO assembly has been dried, but before it has been washed to remove the acid.

The EM-rGO surface topology can be seen in Figure 131, where an obvious inhomogeneity is present in the materials. There appears to be a combination of smoother sections interspersed with rough, chunky clusters, and a large amount of surface cracks become noticeable when the concentration of the original sulfuric acid treatment is 1.0 M or above. These features are quite important, as no consideration to how the inhomogeneity or surface cracking could be impacting the material performance of EM-rGO has been presented to date in the literature. From these initial images, it appears there could be at least two distinct domains within the material, each of them composed of different structural elements. Looking back at the surfaces of air dried and hydrated assemblies, the smooth regions of the EM-rGO look very similar, except that these smooth regions become cracked with higher concentrations of acid. It appears the intercalation of the acid is not uniform within the rGO assemblies, but it is not known if these features remain to impact the structure and/or performance after rehydration. To evaluate these small domains, which appear to range in size across a few hundred microns, a small beam size would need to be used in order to differentiate the features. Thus, this inhomogeneity should be able to be observed in WAXS and SAXS data, as the beam diameter is only about 200 μm . However these distinct features will not appear in neutron data because a much large beam size (2 cm or more) is needed to generate enough scattering events for measurement. The SAS results addressing these questions about homogeneity and hydrated EM-rGO assemblies are presented subsequently in this chapter.

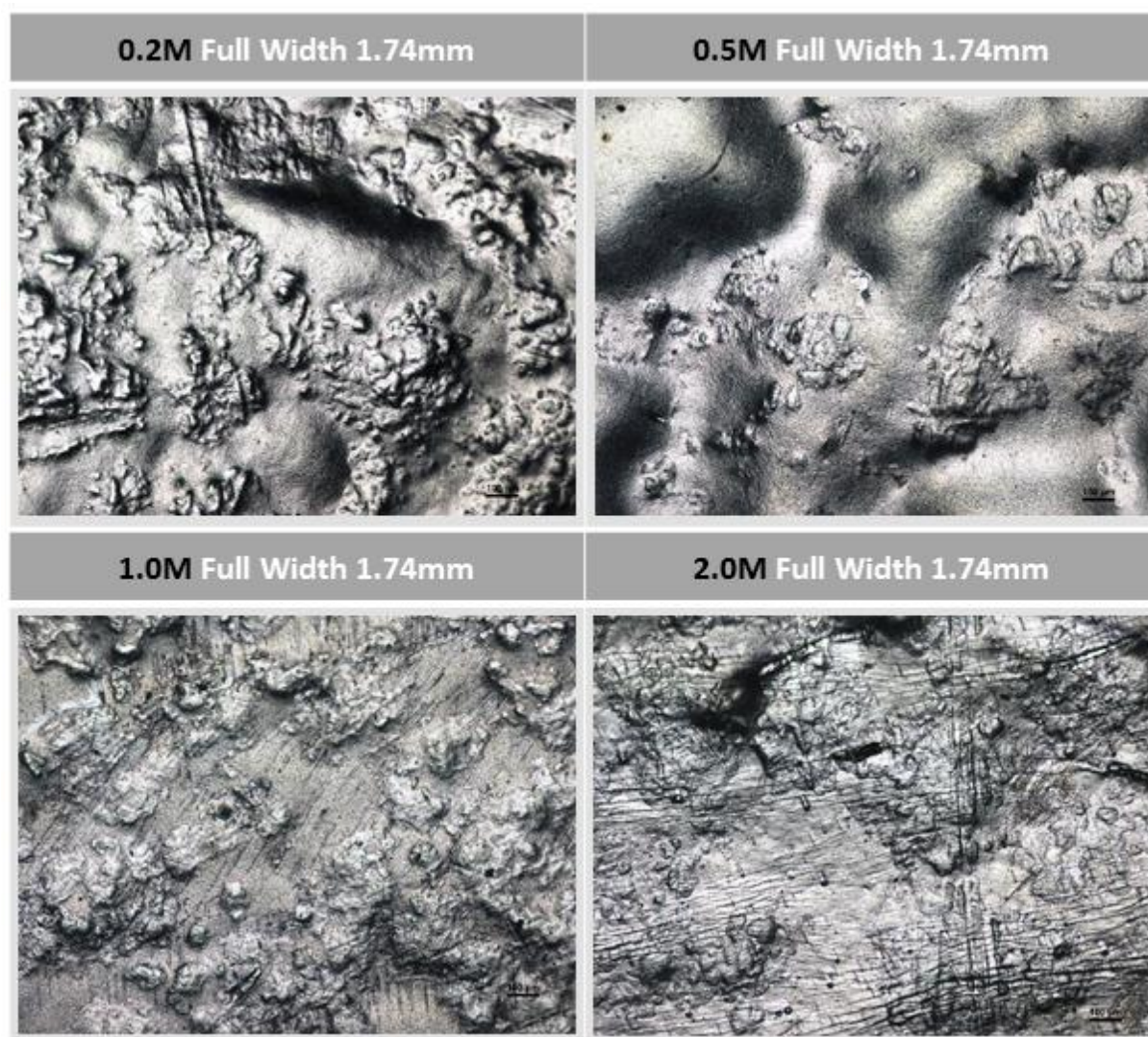


Figure 131. Optical images of EM-rGO assemblies treated with different concentrations of sulfuric acid (0.2 M, 0.5 M, 1.0 M, and 2.0 M) as indicated.

Figure 132, magnified four times from that of Figure 131, compares the surface of pump and air dried rGO assemblies to the EM-rGO materials, in order to more clearly assess the effects of the acid. The 0.2M image clarifies that the large clusters seen in Figure 131 are actually more like the collapsed regions seen in the pump dried sample. This indicates that there could be regions where the acid is not present, allowing the graphene sheets to easily restack as the water is removed during the vacuum drying process. Correspondingly, the regions where the acid remains are more able to retain the porous structure, with an appearance more like the air dried and hydrogel surfaces. However, too high an acid concentration seems to degrade the structural integrity of the graphene layer network. As mentioned, materials treated with higher concentrations of acid had a higher prevalence of surface cracks than those treated with a low concentration of acid. These were especially prevalent in the assembly treated with a 5 M solution, and the appearance of streaks, or surface cracks, was not seen in any regions of assembly prepared with a 0.2 M solution.

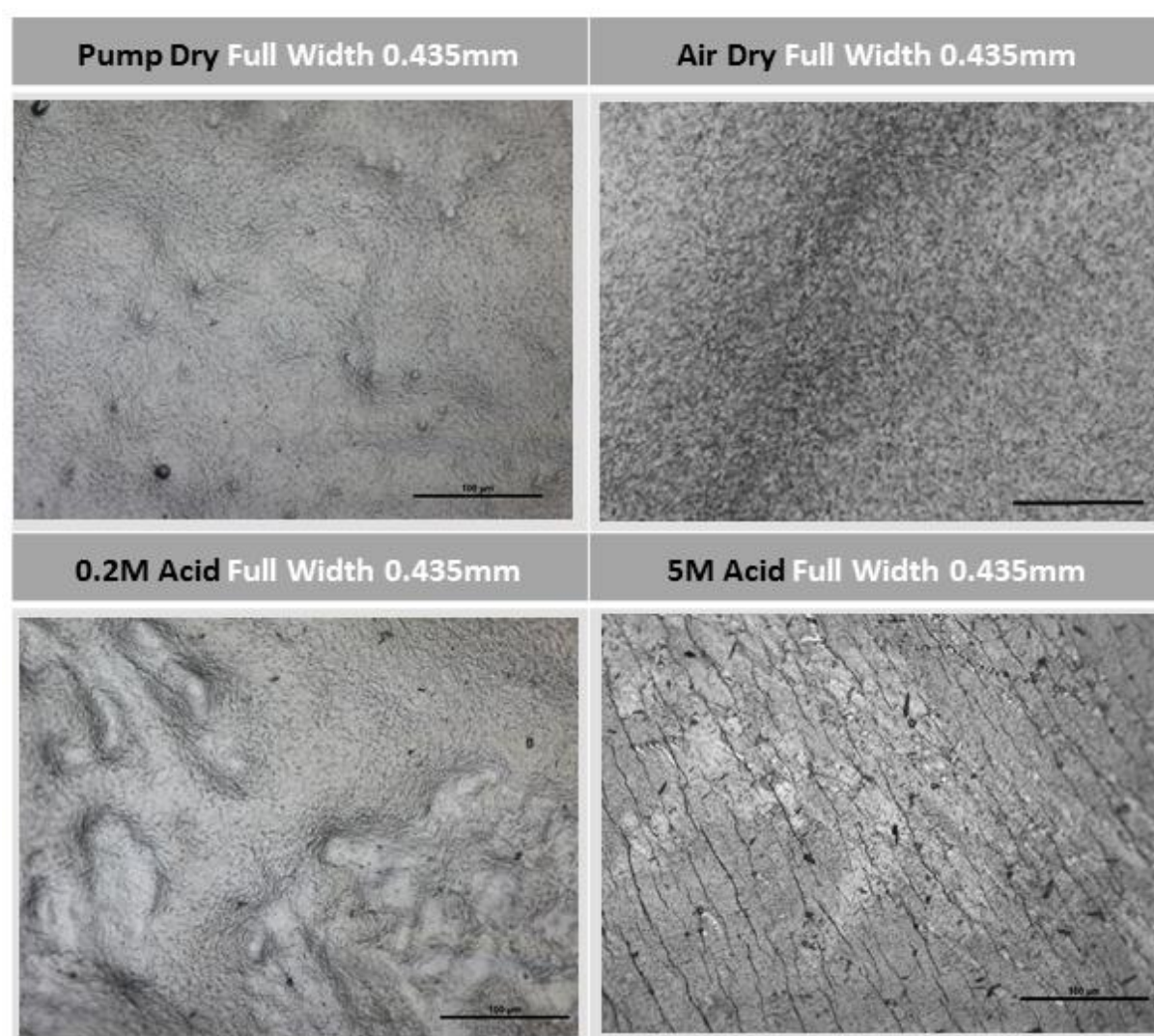


Figure 132. Optical images comparing the surface topology of HO3 rGO assemblies dried under different conditions to EM-rGO prepared with different concentrations of intercalated sulfuric acid and then vacuum dried (all scale bars are 100 μm).

6.2.2 Electron imaging

The GO and rGO prepared in the oxidation series were investigated using low energy, high resolution SEM to see if there were structural features and/or inhomogeneities at the macro- and mesoscale. This section is brief, as it is not possible for SEM imaging to resolve all the fine structures, but is meant to assess the structural integrity of the assemblies and build a sound foundation for interpretation of subsequent scattering data. To obtain the best images possible, a low accelerating voltage was used for all samples (5keV or less) and a through lens detector was used for the high resolution images to accentuate the surface features. Further details of the imaging protocol are given in Chapter 3, but some necessary information is provided here in order to clarify parameters that could otherwise distort the interpretation of data. Because the interaction volume is so large in carbon materials (discussed in the EDS section of Chapter 4), SEM images can be distorted by the secondary electrons emitted from material quite far below the surface, diminishing the topological contrast. Therefore, the use of low accelerating voltage and the through lens detector (most sensitive to surface signals) assists in ensuring that subtle surface features are represented in the images. A widely-used Everly-Thornhart detector (ETD) was used for surface imaging at lower magnification for improved depth of field, and it should also be mentioned that no discernible elemental differences were detected in backscattered electron images (thus not included here). Since the surface features are the main area of interest, no metal deposition or coating was applied before imaging. It should be noted that the GO assemblies are not conductive, so there can be a significant amount of charging occurring while imaging, even at low voltage. This is why the contrast varies more in the GO images, and further differences in brightness are not due to the material itself, but relate to the location of the secondary electron detector in relation to the incoming beam and surface of the material. For both the GO and rGO materials, beam damage to the samples was not a factor in these images, as new locations were selected at the first sign of hydrocarbon contamination. Further, all images were taken from characteristic surfaces and the bulk assembly was scanned across a wide area to ensure these features were uniform and representative of the bulk.

Beginning with discussion on the through-the-surface plane (ab-plane), Figure 133 and Figure 134 show SEM images of the surface of GO and rGO assemblies, respectively. The sample materials presented here of LOX, LOD, HO3, and HO8 were selected because they were most widely tested using other techniques in this thesis, but it should be mentioned here that a wider range of assemblies were imaged and none showed any measurable differences (also tested were LOA, LOH, HO7). The most characteristic feature of the GO surfaces are the deep crevices or folds, somewhat resembling the surface of the brain. The alignment of these features are quite random, with an average width between the folds being about 10 μm . These are not actual folds that penetrate the film, only curves and wrinkles along the film's surface, and they become more pronounced when charging, indicating the structure is quite delicate and responds dynamically to the influx of electrons. It is not clear what link these features have to the structure and performance of GO assemblies, and this is suggested as a possible avenue for future research.

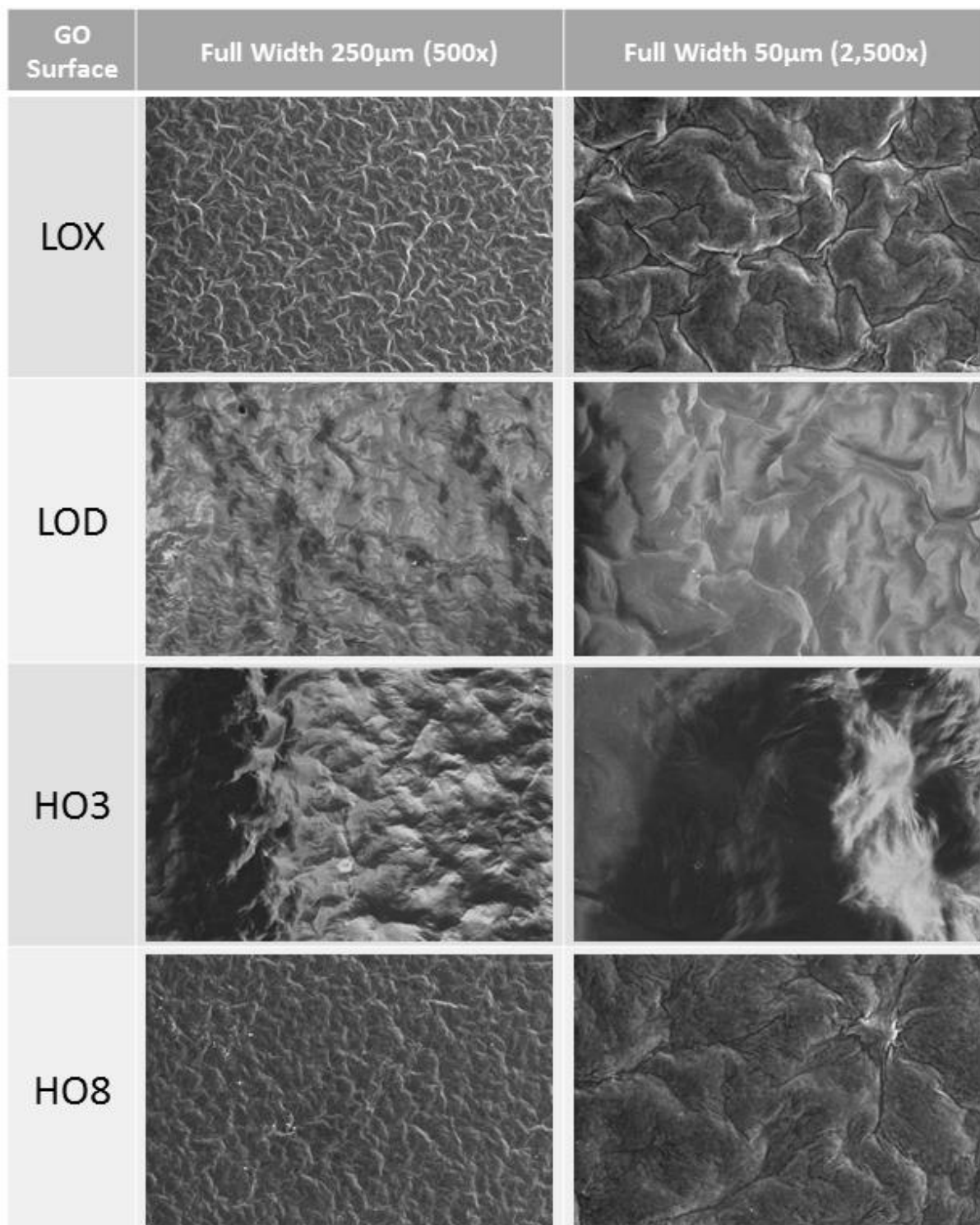


Figure 133. SEM images of the surface of GO assemblies of different oxidation levels.

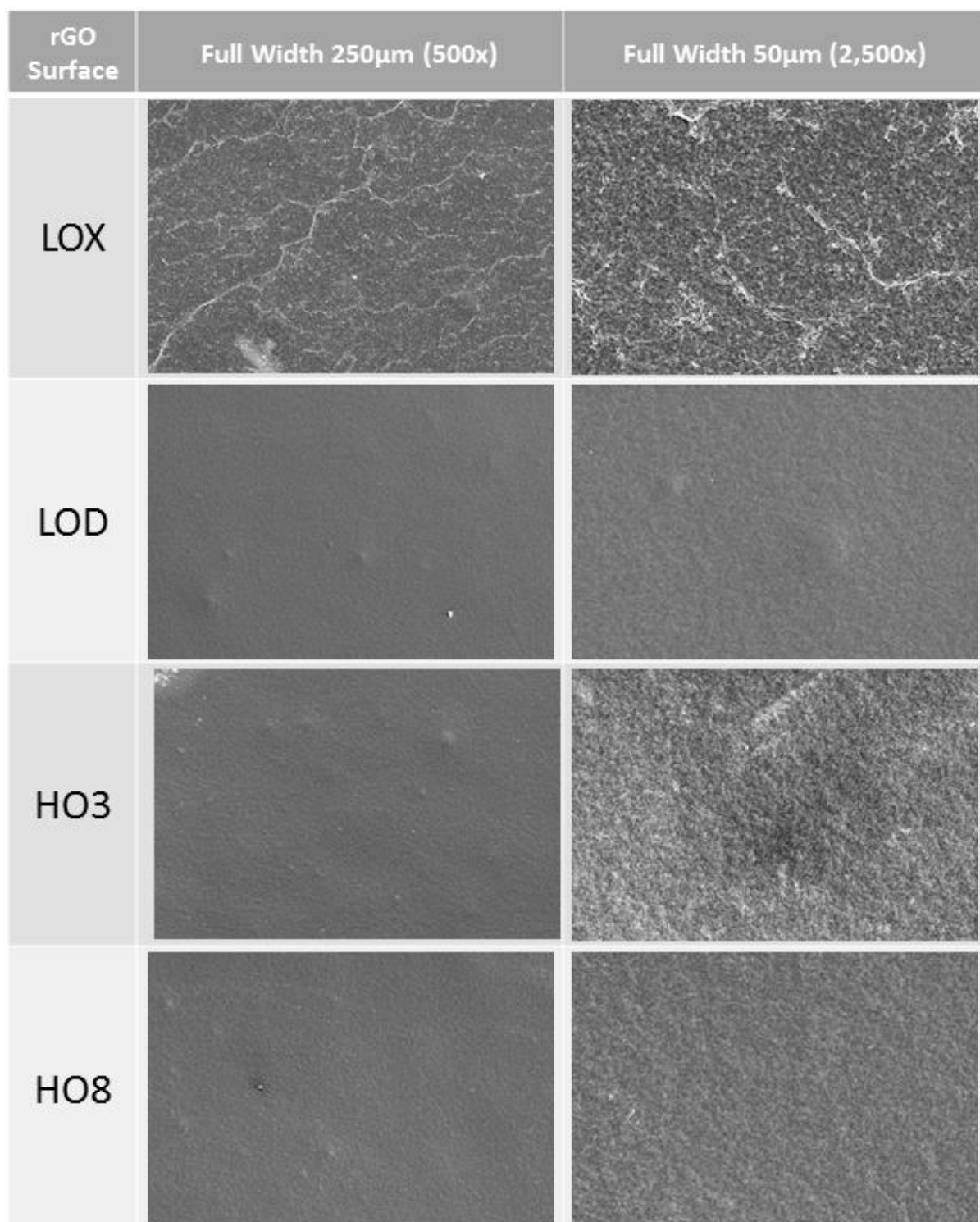


Figure 134. SEM images of the surface of pump dried rGO assemblies prepared from GO precursors of different oxidation levels.

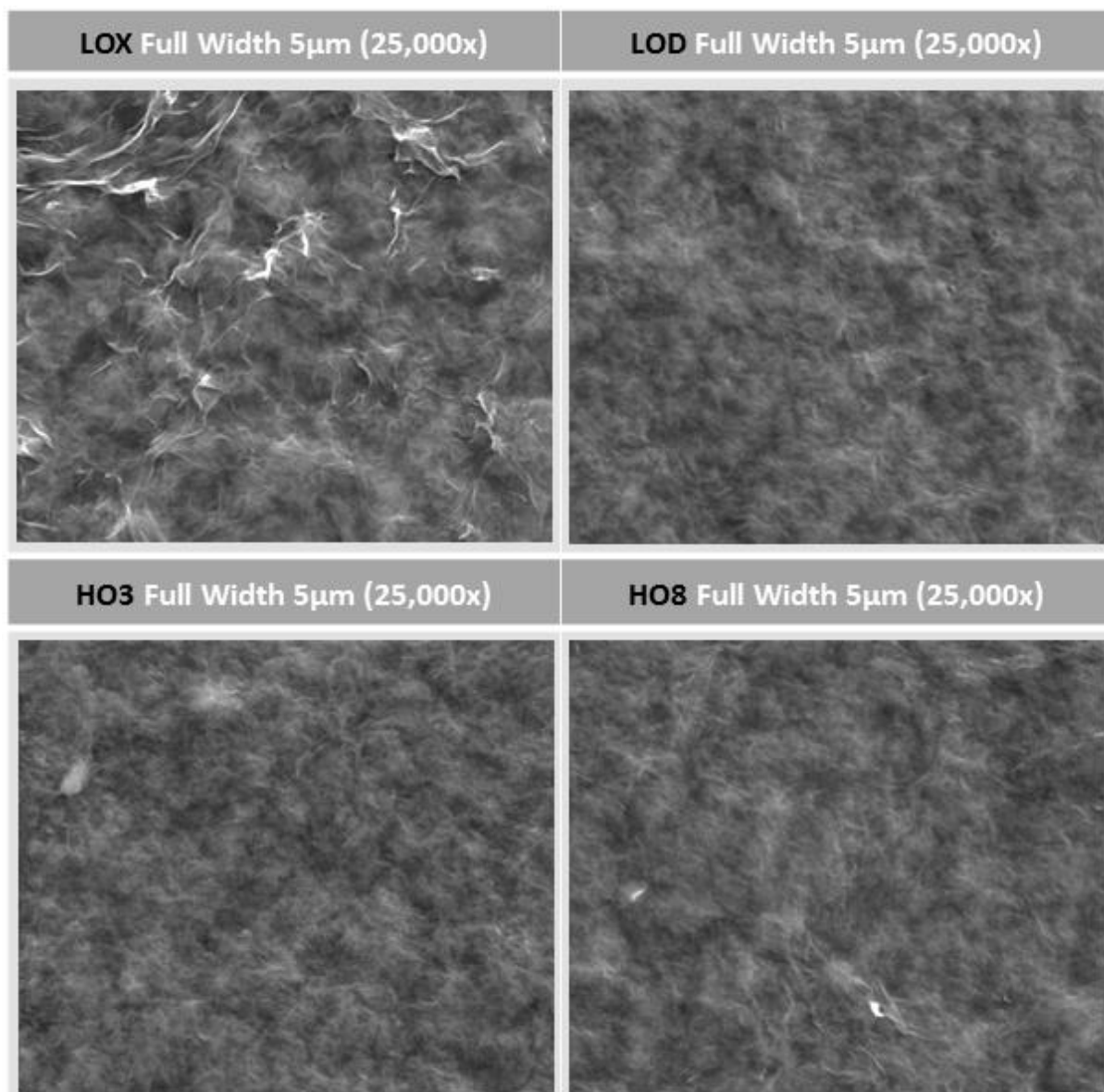


Figure 135. Higher resolution SEM images of the surface of pump dried rGO assemblies prepared from GO precursors of different oxidation levels, showing density fluctuations along the surface.

The rGO structure is the main focus of this thesis, so the attention is now directed there. Unlike the GO surface, rGO has a smooth topology overall, with the exception of a few circular collapsed areas as seen in the optical images, shown in Figure 129. The LOX assembly presented a higher degree of wrinkling at the surface, but overall the structure appears uniform and free from large defects that could dominate scattering data and/or performance of the materials. At this lower magnification, there are not any obvious structural elements that can be identified, which could help conceptualize what features will contribute to the scattering curves. However, the higher magnification images presented in Figure 135 indicate there are density fluctuations within the ab-plane, as measured by the change in contrast seen across the surfaces. While these fluctuations cannot be evaluated quantitatively with SEM, these images do highlight what features the shape of the density distribution and pore network is likely to have, serving as a visual guide in interpretation of the through-the-surface isotropic scattering pattern.

From Figure 136, where the smaller surface features are resolved, it is clear there is a high degree of wrinkling, folding, and corrugation along the ab- plane, as well as density fluctuations caused by differences in restacked regions when compared to areas with oxidized and/or more disordered layers. These features are dispersed quite randomly, again supporting the assertion that SAXS and SANS are

necessary techniques to evaluate the overall size, shape, and statistical distribution of these features both on the surface and in the interior of the sample. Based on these SEM images, there are no clear, macroscopic differences in structure attributable to the various oxidation levels.

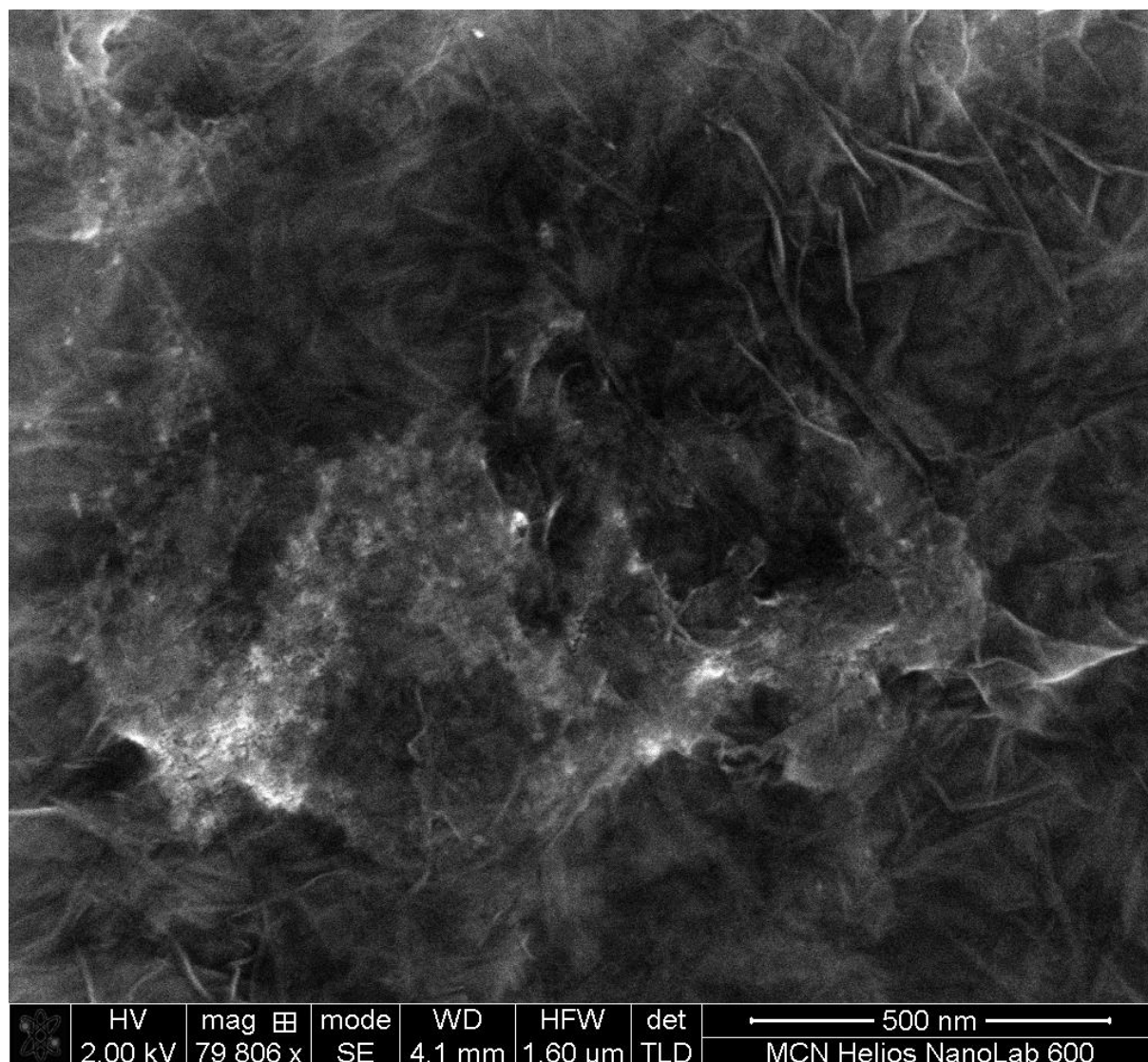


Figure 136. High resolution SEM image of the surface of the HO3 rGO assembly, showing density fluctuations as well as wrinkles, folds, and corrugation along the surface.

A final aspect in relation to the physical features contributing to the pore structure and carbon matrix within the ab-plane is shown in Figure 137. The dual-beam FIB-SEM allows for concurrent electron imaging (minimal to no damage to the sample) and ion milling (controllable ablation and machining), and here, the surface of the rGO assembly was exposed to a low dose of high energy gallium ions for different lengths of time. The progression of ablation is shown from region 1, where the rGO surface has not been exposed to the ion beam, through to areas of progressive damage in areas 2, 3, and 4, as indicated by the arrows. The penetration depth of the ions is related to the density of the material, and further, less dense material is more easily removed. These images provide an indication of what the structure of the pore network in the ab-plane. These features are quite random, but the pores appear at first to form rather uniform size specks that arrange into elongated coils, being separated by denser regions of a larger width. While these images would measure the features at length scales of 10 to 100 nm, referencing back to the results of the aromatic domain and micro-structure discussed in Chapter 5, it is likely that these features of aromatic domains and stacked clusters show self-similar

features at larger length scales, as would be expected in a fractal structure. This idea is expanded on later when presenting the results from small angle scattering.

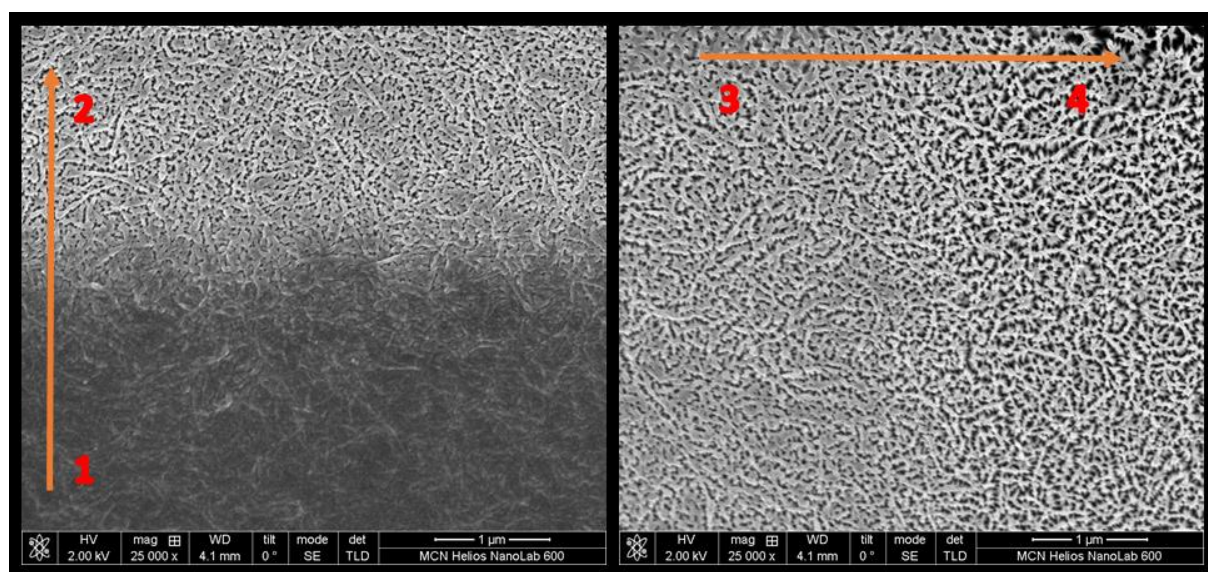


Figure 137. SEM image of the surface of the HO3 rGO assembly after low-dose ion irradiation to selectively ablate regions of the carbon matrix depending on the density of the bulk. The images show progressive damage to the surface, where area 1 has not been exposed to the ion beam while areas 2, 3, and 4 have been irradiated for increasing amounts of time.

The remainder of this section moves to discussion on the through-the-edge structural elements in the ac-plane. The high resolution SEM image in Figure 138 shows the structure along the edge of an rGO assembly that has been cut with a blade. Within this size range covering about 100nm up to 1 μm , there is clearly an overall alignment in the horizontal direction, which is wavy and becomes more disordered at smaller length scales. The corrugation and wrinkling is quite pronounced throughout the bulk, and it appears the structure of graphene sheets in the mesoscale region is highly disordered and distorted, as was demonstrated with the TEM results at the microscale. Again, SAS will play an important role in determining if the structure at the microscale carries over to exhibit similar levels of alignment in the bulk. However, from this initial direct assessment, it appears the overall alignment of the graphene layers at the macroscale is less disordered than that measured at the microscale.

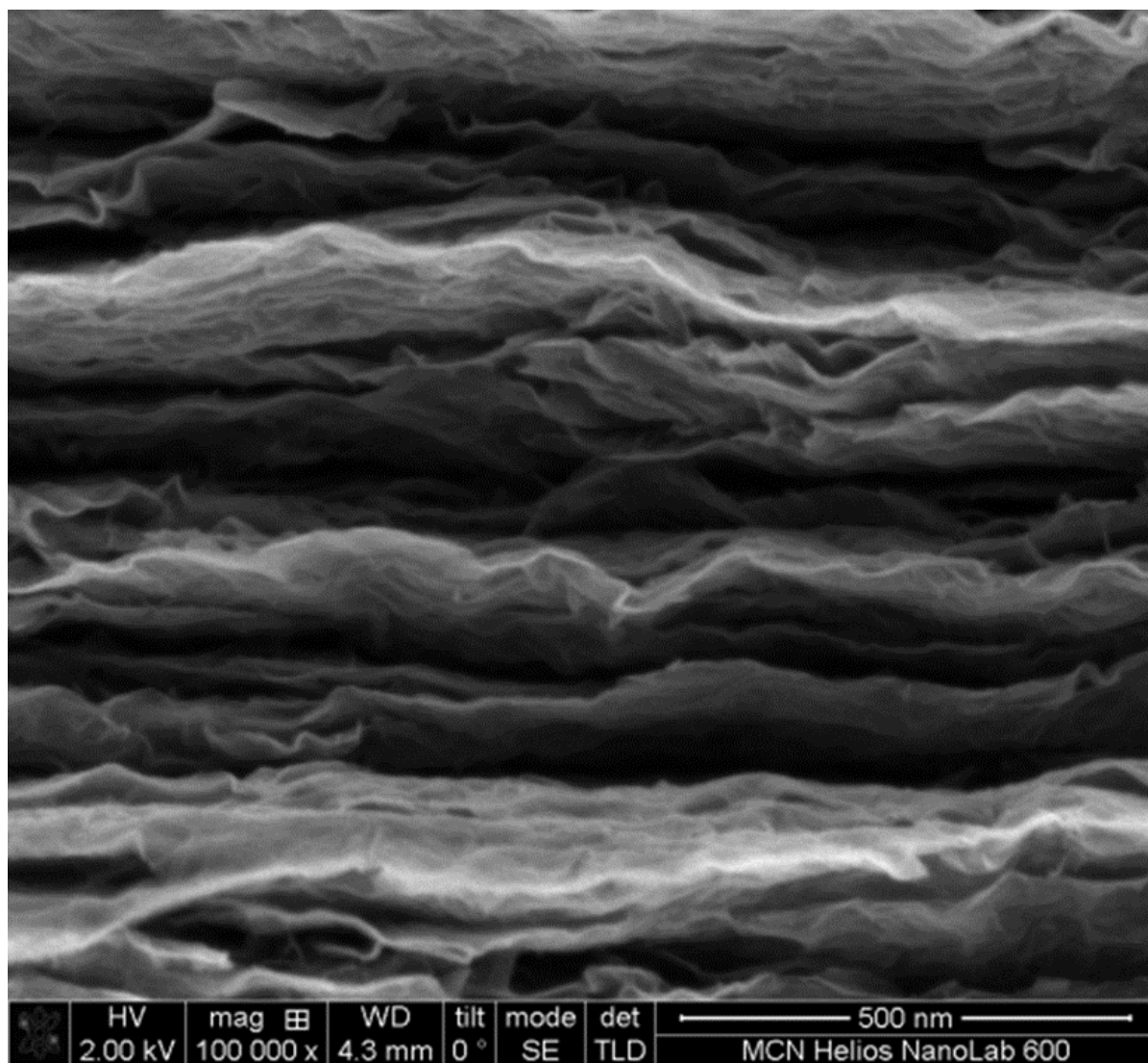


Figure 138. High resolution SEM image of the edge of the HO3 rGO assembly, showing a high degree of corrugation and waviness within the stacked graphene layers.

To gain insight on the intermediate, mesoscale region, the TEM image of the assembly cross-section in Figure 139 is able to resolve the edge of the graphene sheets, again appearing as fringes in the image. At this scale of 2-50 nm, the alignment of the layers is much more disordered than what might be originally postulated based on SEM images alone. These results are quite important, as until now it has been assumed that these rGO assemblies consist of very well aligned planes and computational models have been designed based on this assumption [26, 131, 288]. The findings here strongly suggest that the mesoscale features are very curled and turbulent, at least within the pump dried materials. This image also indicates that the porous structure and density differences are rather uniform and random throughout the bulk, with all the pores shown here being less than 1 nm, as expected based on previous reports and processing conditions [131, 152]. This again confirms there are no graphitic crystallites dispersed within the material, or visible agglomerates of any kind, and overall the structure appears to have a homogeneous density distribution even with this high degree of mesoscale disorder, again very similar to published results for numerous pyrocarbon materials. This result could support the validity of using the results from many years investigating pyrocarbon performance to interpret the performance of rGO assemblies. It would suggest that if the structure of the dried rGO films is not fundamentally different, enhancements to performance are most likely due to the elongated rGO-sheets which are preserved using solution processing methods, since many pyrocarbons have relatively short graphene layers [32, 133, 242], as was discussed in more detail within Chapter 2.

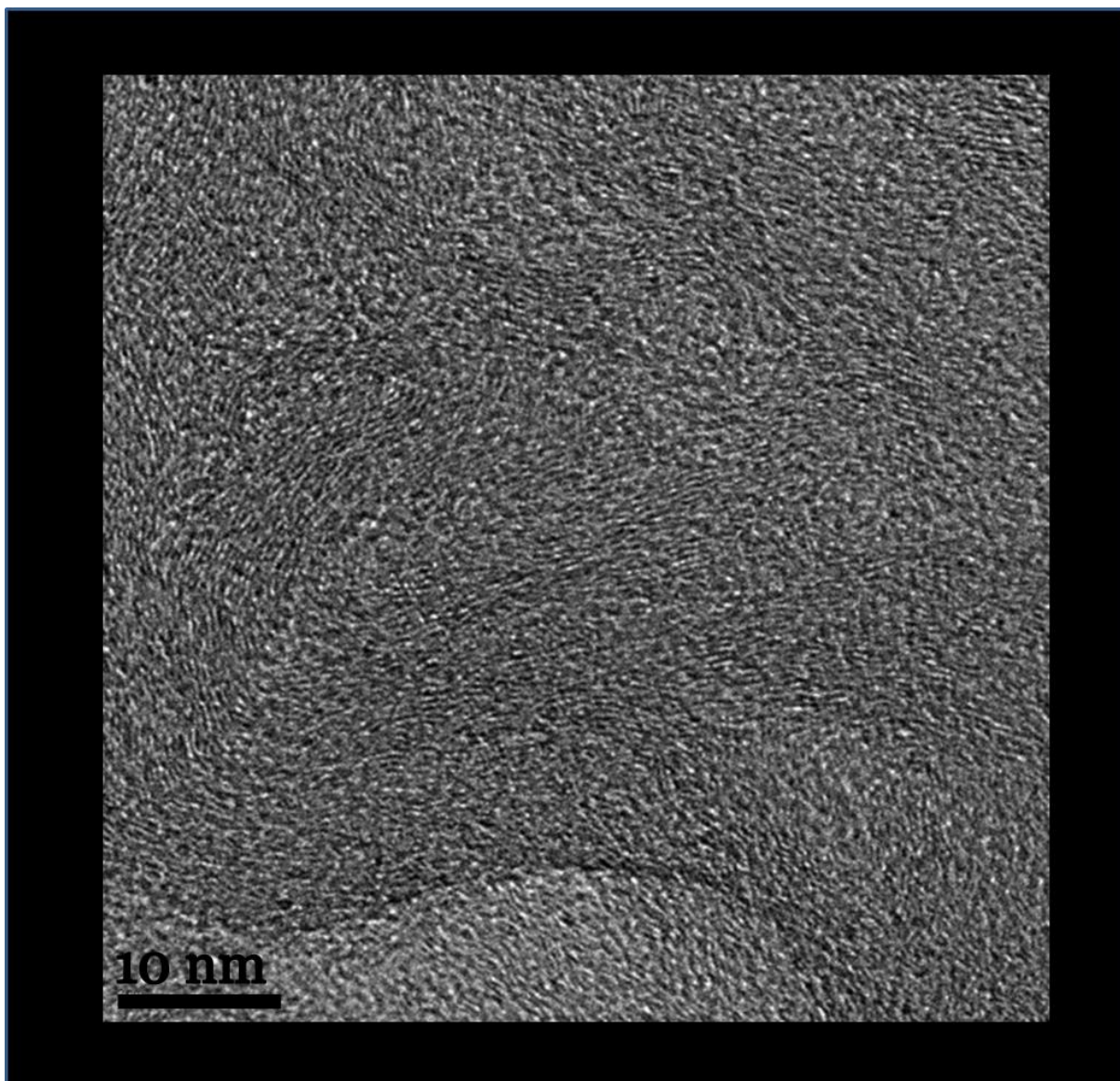


Figure 139. TEM image of the edge of the HO3 rGO assembly, showing the graphene layers are much more turbulent at the mesoscale than that indicated from microscale features in SEM.

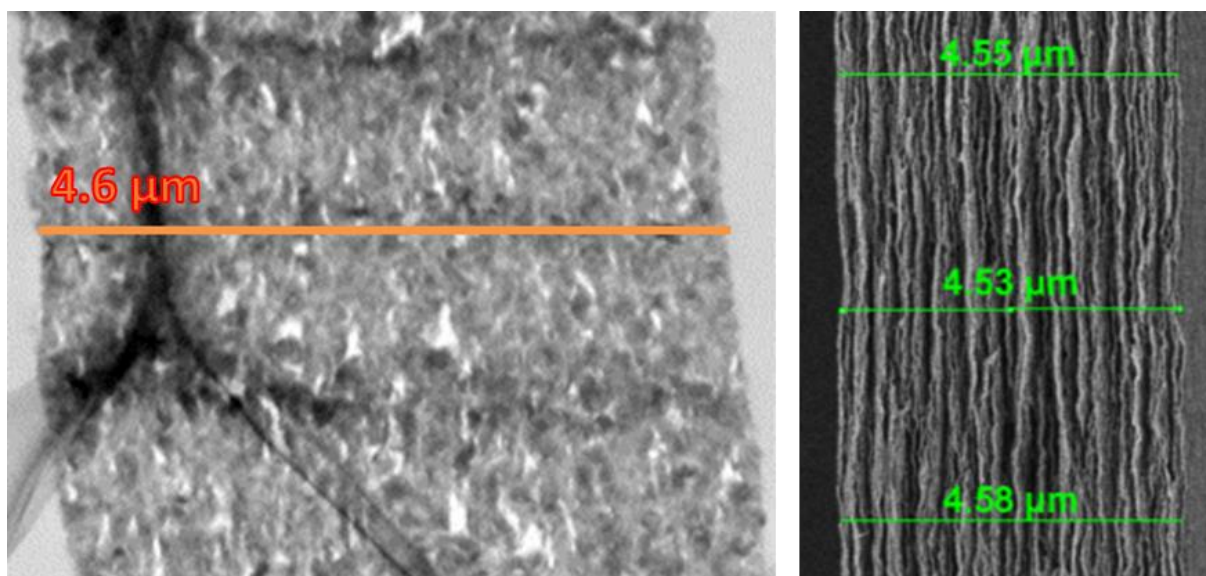


Figure 140. Comparison of TEM (left) and SEM (right) images of the total cross section of the HO3 rGO assembly at the macroscale.

The final structural question to be addressed through direct imaging is to determine if any large voids or agglomerates are present in the bulk materials at the microscale. From Figure 138, it is not clear if any large voids are present, as the cutting process leaves graphene sheets protruding from the edge at different depths. The lower resolution TEM image shown in Figure 140 indicates there could be many larger voids of size up to about 100 nm within the bulk. It was not clear if these voids were actual features in the rGO assemblies, or an artifact produced during the embedding and microtoming sample preparation methods required to obtain the thin cross section necessary for TEM imaging. To cross check, the overall thickness of the assembly cross section measured in the TEM slice was compared to that measured for the bulk edge of the SEM sample in order to ascertain if any swelling or contraction could have caused damage. As shown, both cross sections exhibited equal values for the overall thickness, indicating the voids seen in the TEM image were actual physical features in the original films. This could be the cause of the pitting seen in the optical images, as large voids close to the surface would result in such features.

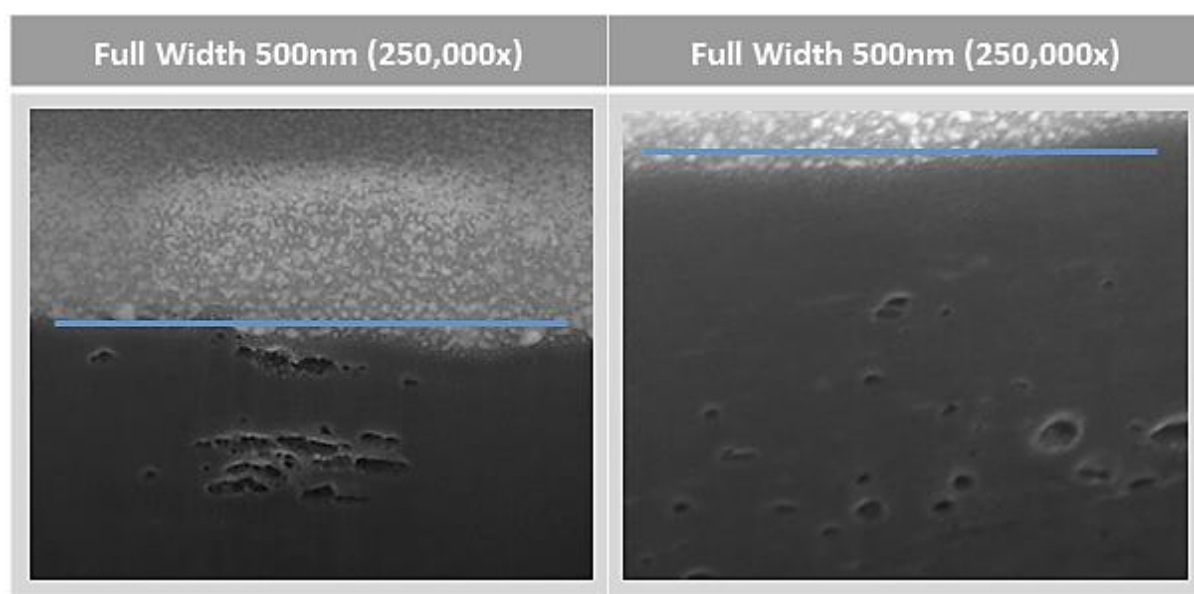


Figure 141. High resolution SEM images of the cross section of two pump dried HO3 rGO assemblies from within the bulk, where a focused ion beam was first used to cut away the bulk material in thin sections and resulted in a smooth surface of the carbon matrix that is imaged with the electron beam. The blue line represents the horizontal surface of the rGO assembly with the area below it being the carbon matrix and voids, and the area above it being a layer of platinum deposited to protect the bulk material during the ion milling process.

The presence of meso- and macro-scale voids would be a significant finding because all current research on these bulk rGO assemblies does not incorporate these features into structural models or interpretation of data [21, 24-26]. Until now, the material has been assumed to be homogeneous based on the SEM images of the cross section. To validate if there are actually voids within the bulk material, a dual-beam FIB-SEM was used to cut a cross section within the bulk of different pump dried rGO films and then image the resulting surface. Voids ranging in size of up to 100 nm were again visible, as shown in Figure 141. While the limits of resolution do not allow imaging of individual sheets as with fringe analysis in TEM, FIB-SEM is a powerful tool for gaining structural information on the bulk materials. While overall, the carbon matrix appears rather homogeneous, there were areas within the assemblies that exhibited these these bubbles or pores which seemed to range in size across the mesoscale, even approaching 100 nm in length. It should be noted these features were not present in all areas explored with FIB-SEM (many were uniform without larger pores), and did not seem to be as prevalent as the TEM image in Figure 140 would suggest. It is possible to perform high resolution series sectioning using FIB-SEM and reconstruct the images to form a 3D rendition of the bulk volume

sampled, and this is suggested as a possible area for future work, alongside comparing these results with materials dried under different conditions.

6.3 X-ray and Neutron Scattering

6.3.1 WAXS, SAXS, and SANS applied to rGO assemblies

In addition to the fundamental concepts and theories outlined in the Literature Review, this section outlines the main aspects of wide- and small-angle scattering as related to carbon materials with structural features similar to rGO assemblies. This outline is then used to interpret the results presented later in the chapter. Scattering experimentation and theory is very broad and complex, so the content presented here, as well as the methods applied to the scattering results, will be limited to the aspects most integral to determining the structural parameters of interest in the rGO assemblies.

More specifically, the focus here is limited to the structural features that will have large impacts on performance, where a quantitative and accurate description of the morphology of rGO assemblies in the dried and hydrated state is necessary to explain transport behaviour. These results aim to address: i) polydispersity and density fluctuations in the bulk, ii) the shape, size, and alignment of the pores, iii) the structure of the pore surface, and iv) the structure of the pore network and total porosity. Additionally, experimental methods that can be used to uncover the mechanisms behind the dynamic processes related to the hydration level are suggested based on innovative options for *in situ* measurements in ambient conditions. This work attempts to simplify the procedures and analysis in order for the methods to be adopted and more widely applied by researchers without extended expertise in scattering theory.

Starting from the most general case, knowing scattering arises due to contrast differences in the material, a porous system is considered monodisperse when it consists of two phases (two scattering length densities) and the dispersion medium of pores in the carbon matrix is similar in size, shape, and internal structure. Thus, $\Delta\rho$ results from a difference in density between the pores and the solid, and the scattering intensity, $I(q)$, is proportional to this contrast. However, there are many cases where the pores are not monodisperse and this requires further considerations when evaluating data, most generally like that discussed by Beaucage and Schaefer in their studies of complex carbon systems with multiple size-scale structures [289]. Polydispersity is an important consideration for analysing scattering results of rGO materials, and as seen in the results from Chapter 5 and SEM imaging in the previous section, it appears different structural features dominate at different length scales. Additionally, knowing that there is chemical inhomogeneity in the rGO sheets, as shown in Chapter 4, the impacts this can have on the scattering length density of the carbon matrix and smoothness of the carbon/pore interface merits investigation.

Quickly referencing back to content in the Literature Review, the Guinier plots for rGO assemblies is best separated into two regions because of the varied dimensions of graphene layers and pores, as described in Figure 40. It is likely that scattering through-the-surface, as shown using transmission geometry in Figure 33(A), may be similar to the network of branched pores (as shown in the green region of Figure 39, similar to the network seen after ion bombardment in Figure 137 and scale across the surface of each rGO sheet, which, from previous published works using atomic force microscopy, measure the dimensions to approximately 1 μm in length. The graphene sheets are in the form of a flat disk, with a length/diameter in the *ab*-plane much larger than the thin edge extending along the *c*-axis ($L \gg t$), measurement through-the-edge of the rGO assemblies is similar to the reflectance geometry in Figure 33(C) which exhibits very different features than those shown using transmission geometry through the *ab*-plane. From the edge, the thin disks of graphene layers will appear more like rods, needles, or ellipses with the clustering of the layers, which assemble to become like a

branched network that also exhibits highly aligned features, as the carbon fibre shown in Figure 42(B). Thus, the two different geometric configurations for rGO assemblies, the ab-plane and the ac-plane, cannot be characterized using a single shape to interpret the form factor. It is expected that density fluctuations among and between coherence domains (as defined by the BSU in Chapter 5) due to corrugation, wrinkling, pores, and stacking will be the main source of scattering from the ab-plane, and these features will be randomly oriented across the graphene sheets, resulting in an isotropic scattering pattern. Conversely, the graphene layers and resulting pore structure will be highly oriented in the ac-plane, producing a more distinctive anisotropic scattering pattern. Because of this, the two major alignments of through the layers or through-the-edge will require independent models to quantify the structure.

Scattering patterns acquired using a 2D detector have large benefits over a point detector, as data across a very large solid angle can be acquired simultaneously (much more rapidly for all radial directions and across a large scattering range). A 2D scattering pattern can quickly be analyzed for pronounced features, the most obvious being if the pattern is isotropic or anisotropic. Crystalline or well-ordered samples produce defined spots or ring patterns, while a diffuse isotropic pattern is characteristic of more disordered systems with no easily discernable alignment or structural periodicity. It is typical for porous carbons to exhibit an isotropic scattering pattern because the pores are aligned randomly across all orientations and often have pores of non-uniform size. However, for bulk layered carbons (not powder samples), the resulting scattering pattern is quite different than that of isotropic porous carbon particles such as activated carbon and coal [183] [30, 136] or purely disordered carbon such as glassy carbon [290]. This anisotropic feature of the mesoscale pore network in rGO assemblies thus requires a similar approach to the microscale experimental analysis applied to the SAED pattern presented in the TEM results.

When selecting procedures to best execute and interpret scattering experiments on rGO assemblies, carbon fibers again appear to represent a bulk carbon with properties most like those expected in rGO materials. Figure 142 compares two carbon fibres, the first producing an isotropic scattering pattern, which is typical of randomly oriented pores, while the other shows distinct alignment as evidenced by the anisotropic scattering pattern [136]. Because it is expected that rGO assemblies will exhibit both isotropic (through the sheets) and anisotropic (through-the-edge) scattering patterns depending on the geometric orientation, the analysis of the different types of patterns requires two slightly different approaches. The following discussion addresses them both, beginning with the isotropic pattern.

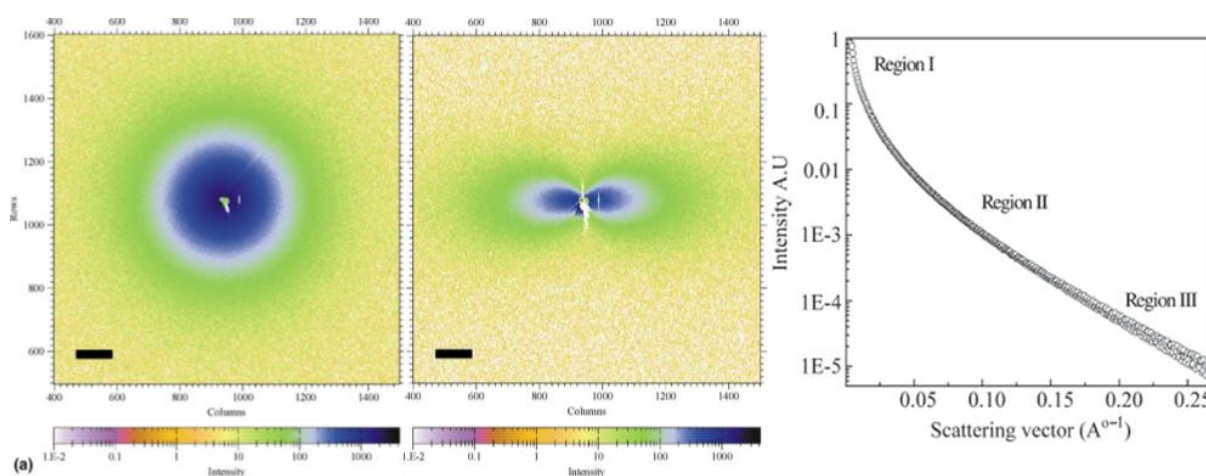


Figure 142. A comparison of isotropic and anisotropic scattering patterns from carbon fibres with different pore structures. The result of reducing the scattering pattern by taking a radial average of an isotropic sample is also highlights the fact that many porous carbons have rather featureless curves (from [136]).

An isotropic pattern can be manipulated, by taking a radial average, to produce a curve similar to the generic scattering curve shown in Figure 142, where the intensity scales with the scattering vector, q . Even though there are often no pronounced features in the isotropic scattering pattern of porous carbons because of the rough surface, density fluctuations, and non-uniform pore sizes, the reduced curve is still able to provide information about the structure of the material. The structural features of interest are usually represented in three distinct regions according to the q -range corresponding to specific length scales within the material. Generally, the low- q region marked Region I ($q < 0.01 \text{ \AA}^{-1}$) gives an idea of grain size and shape of the clusters/aggregates formed while Region II ($0.05 \text{ \AA}^{-1} < q < 0.15 \text{ \AA}^{-1}$) provides information about the interface between the carbon matrix and pore where a power relationship can be defined using Porod's Law. In Region III ($0.2 \text{ \AA}^{-1} < q$), the correlation length of the individual particles or pores is evaluated and eventually reaches the scale for Bragg peaks in the wide angle region if periodic structures or atomic crystallinity exists. The main theories underlying these interpretations were discussed in the Literature Review.

Deviation from Porod's law (where the slope at higher- q does not reach the value of -4 expected for a smooth interface) is always exhibited in porous carbon materials to a greater or lesser extent [28, 30, 34]. Typically, a value of -3 is reported for glassy carbon [290] while most porous carbons of various type (coal, activated carbons, etc.) fall within the range of -3 to -4 [291]. There has been much work done in this area to investigate the dimensionality of the interface in both disordered bulk carbons and porous carbons and relate it to material properties, as discussed in the Literature Review. In general, taking the dimensionality as D , the deviation from Porod's law is typically due to a combination of: i) unoriented amorphous carbon, which occurs in three dimensions resulting in $D=3$, ii) fluctuations in the spacing of basal planes, which occurs in only one dimension, resulting in $D=1$, and iii) surface roughness and density fluctuations along the pore surface from corrugation and elemental impurities [30, 290]. By subtracting out the contributions from both the amorphous content ($D=3$) and fluctuations in layer spacing ($D=1$) and then applying a Fourier transform to the remaining data, Perret and Ruland [240, 290] were able to obtain the pore distribution function $g(r)$ in real space for a variety of porous carbon materials.

Building on this range between amorphous and perfectly stacked carbons, another way to interpret the deviation from Porod's law is describing the interface as fractal [199, 292]. This has been done for many different carbon materials and presented as either a mass fractal [293, 294], surface fractal [193], or pore fractal [34], as well as combinations of these [203, 295], each of which requires some understanding of the physical structure and a sound argument for why these properties are present in that particular carbon system [296]. Typically, surface fractals result in a slope between -3 and -4, indicating surface roughness along a two dimensional interface, while mass fractals result in a slope between -2 and -3, indicating there are fluctuations in three dimensions.

On work with carbon fibres, Tang et al. [296] expanded the fractal dimensionality across two length scales, where higher- q contained information about the surface fractal dimension of the pores ($q^{-(6-D)}$) and the intermediate- q range described the mass fractal dimension of the carbon aggregates (q^{-D}), similar to the methods used for analysing multiple size-scale structures [289]. In general, this fractal property can describe a roughness, branching, and/or aggregation within different size regimes (as measured by Δq), and extends along the entire length scale where the slope of the scattering curve holds constant (q_{\max} and q_{\min}). Bale and Schmidt [193] point out that different features within various q -ranges are to be expected in carbon materials since larger fractal objects/aggregates do not scatter in the same way smaller pores/surfaces with fractal boundaries will. Pfeifer et al. clearly demonstrated that systems with fractal boundaries will have many features that are similar to porous systems with a pore-dimension distribution (akin to PSD) that follows a power law [200]. These features can also be linked with the properties of individual graphene sheets, where the fractal dimension of graphene

clusters can be related to the solvent accessible surface area [116], as discussed in the Literature Review.

The fact that layered rGO assemblies exhibit a distinct anisotropic pattern when measured through the edge provides a large advantage in more clearly identifying the structural elements of the pores compared to the featureless curves for many isotropic carbon particle assemblies. The ability to evaluate structural features in the ab-plane and ac-plane independently, leads to much less ambiguous results solely due to the enhanced distinction of discrete scattering features. Without more defined features in scattering data or an alternative, direct measurement of the size and shape of the pore structure, a fair amount of ambiguity is left when setting parameters for data fitting. As many different models will often fit well to a featureless scattering curve, results may be based on erroneous assumptions and lead to conclusions with no basis in physical reality. Thus, the more defined scattering pattern resulting from the layered structure of lamellar carbons can lead to more consistent conclusions, especially when combined with direct imaging and an independent assessment of physical features making up the BSU, like that reported previously in this work. Consequently, the approach to data analysis of the rGO assemblies closely follows that suggested for anisotropic carbon fibre materials, specifically as laid out by Tang et al. [296], Lozanno et al. [28], and Dresselhaus [30] along with the more general principles used for analysis of isotropic scattering carbons [34, 290, 295, 297].

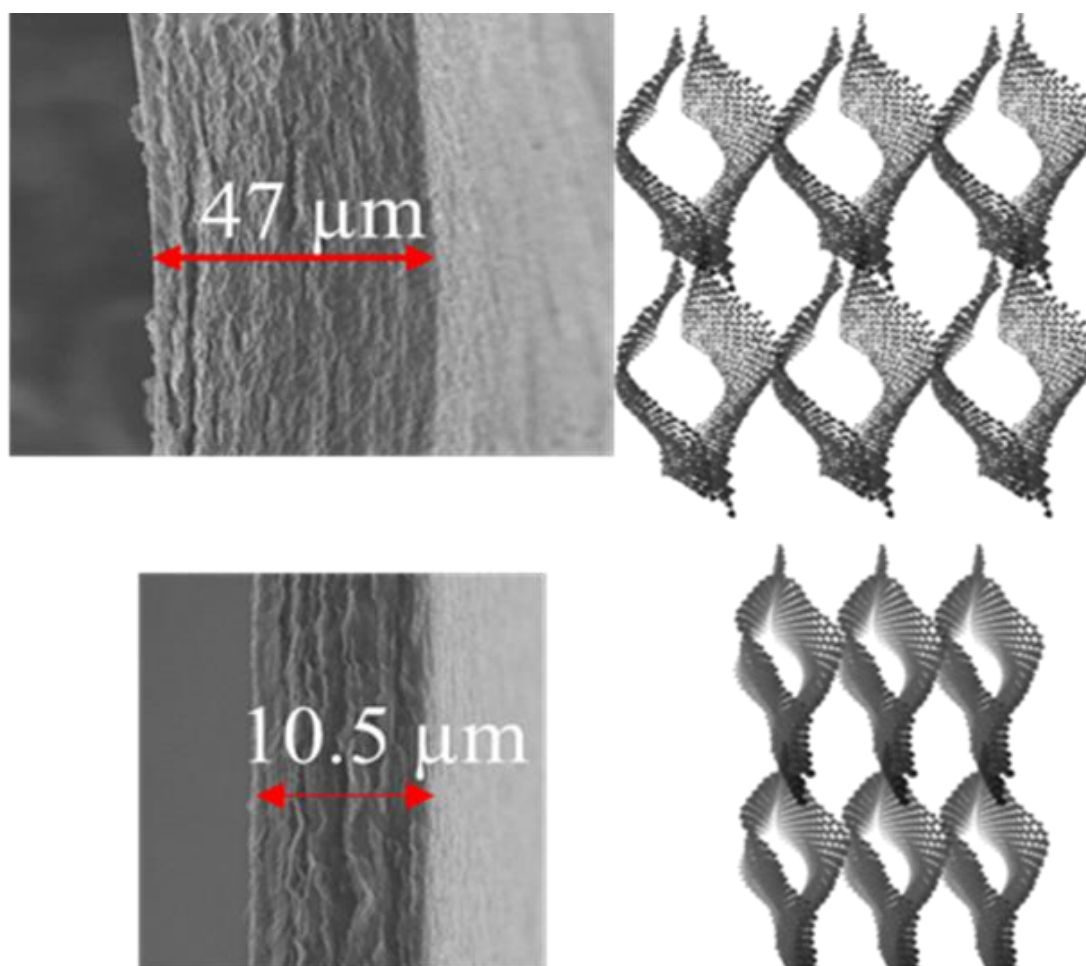


Figure 143. SEM image and assumed structural model for EM-rGO materials tuned with sulphuric acid of different concentrations. Reproduced from [17].

Figure 143 shows the assumed cross-sectional structure of EM-rGO assemblies with different pore sizes, which was based on dynamic electrosorption analysis [17] without any measure of actual physical features in the material other than the SEM images shown. While the mass of the rGO

assemblies is equal, there is a large difference in the overall thickness of the films. It has been assumed that this thickness increase equates to larger pores, but retains a uniform PSD, as shown in the schematic [17, 24]. As discussed in the Literature review, because of the highly aligned, layered structure in these materials, any differences in interlayer spacing would not be quantifiable from surface scattering patterns through the ab-plane. This adds another element of technical complexity when analysing rGO assemblies because the edge is quite thin, ranging from about 6 μm for pump dried films to 150 μm for hydrogels. Another advantage of performing WAXS and SAXS measurements with a high intensity beam, such as those produced by synchrotron sources, is that the beam size is significantly smaller than that of typical lab-based X-ray sources. Thus, this small size beam is able to probe thin samples, such as that of carbon fibres and the edge of rGO assemblies. This was not possible with SANS because the number of interaction events is lessened due to the weaker interaction and lower flux of the neutron beam. SANS typically employs a beam with spot size of a few centimetres in diameter compared to a few hundred microns or less with SAXS, and is why through-the-edge SANS data was not acquired for use in this work.

Wide angle scattering will provide information on the structure of the carbon matrix at the atomic scale (like that seen with TEM and XRD in Chapter 5) along with identifying the pore structure in the lower mesoscale size regime. The scattering at small angles is able to extend this range to give information on the structure of pores throughout the mesoscale as well as characterize the larger structures such as the overall pore network, voids, and/or agglomerates. The analysis of the WAXS data follows a very similar procedure to that used with TEM, where the (002) peak is used to quantify the inter-sheet distance of the stacked clusters, orientation angle, and estimate the size of the layered clusters (L_c). If there are uniform pores of a distance size (small PSD), these will also appear, but with a Bragg peak at smaller angles than that of the (002) peak. However, if there is a distribution of pore sizes, the scattering will broaden across a large angular range, as shown schematically in Figure 144.

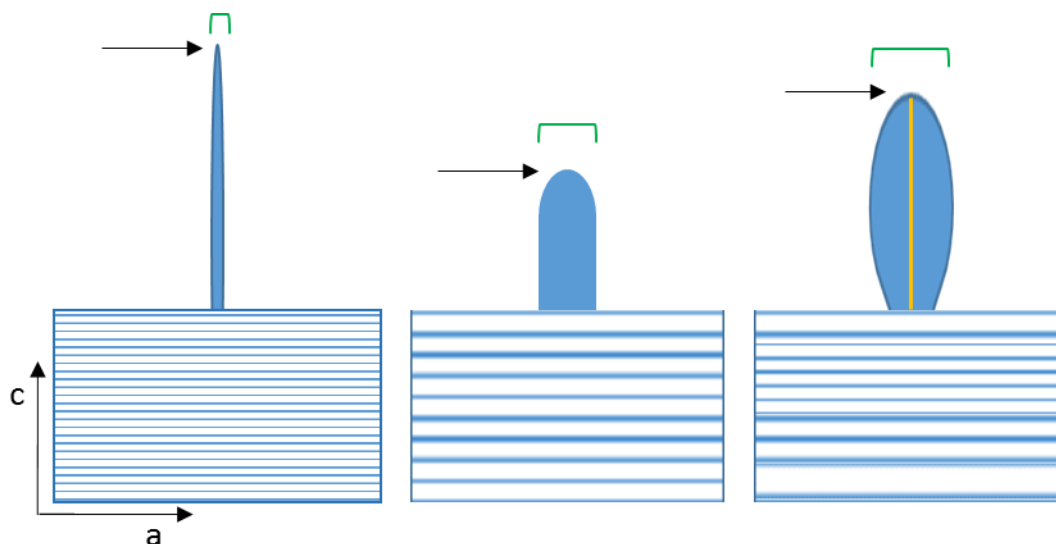


Figure 144. Schematic of the effect of sheet layering on the shape of the SAS curve when the incident beam is parallel to the layering plane (through-the-edge). The striped boxes represent the layers and the solid elongated objects represent the SAS pattern. The length of the scattering feature (black arrow) indicates the smallest periodic size in the c-axis, while the widening (green bracket) is related to the extension of periodic order along the a-axis. Periodicity creates a more uniform width while size distribution decreases long-range ordering and results in a fan-shaped pattern where the intensity spread (orange line) is related to the prevalence of scatterers within a given range.

Building on this concept, the anisotropic SAXS patterns are analysed in a similar way to that of the (002) peak, where the ‘fan-like’ intensity spread is measured as both a distance from the beam centre to ascertain the size of the scattering features (height of the pore along the c-axis as a function of scattering vector, q), as well as a radial orientation at set values of q to ascertain the alignment of these

features (function of the azimuthal angle, ϕ). Further, the widening of the SAS pattern is related to the width of the periodic layering (length of the pore along the a-axis). These factors combine to describe the shape and size of the pores in the ac-plane. The more direct analysis of the through-the-edge scattering pattern, combined with the structural understanding of a BSU developed in Chapter 5 can be used to better interpret the more ambiguous, through-the-surface, features. A combination of these results then allows for qualitative understanding of the surface homogeneities that build the overall pore network and lead to differences in material properties of rGO assemblies.

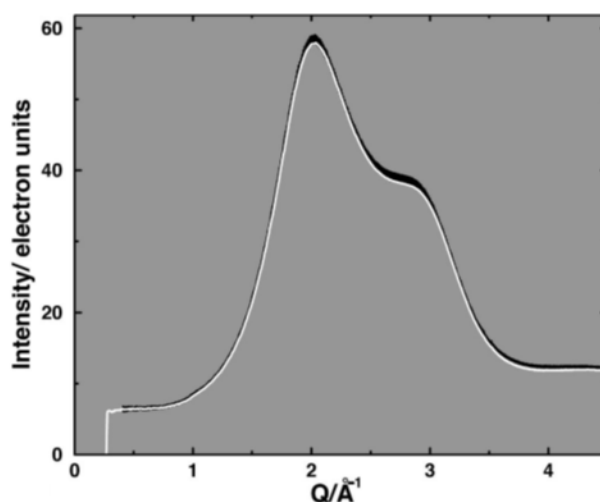


Figure 145. WAXS results for bulk water in ambient conditions showing two characteristic features (reproduced from [286]).

To interpret the isotropic pattern, the slope of the rather featureless SAS curve can be understood based on the information obtained from the anisotropic pattern and structural models from other porous carbon systems mentioned here and in the Literature Review. In general, there are two main features to consider when assigning a physical meaning to the Porod region of the rGO assemblies:

1. In the ab-plane, there is a constant, characteristic density fluctuation that can be measured independently by fitting the Porod region of through-the-surface curves. The power law relating q to the intensity is in the range of -2 to -3, and is indicative of mass or pore fractals. Extension of this range in q is directly related to the size scale of the scatterers (q_{\min} at L_{\min} and q_{\max} at L_{\max}) which encompasses the individual scattering features at high- q and carries across the network to low- q , with porous carbons exhibiting one of the most extended fractal networks known [34]. This surface scattering is related to the mosaic clustering of the BSUs and pore network produced by the graphene-sheet structure (aromatic domains, functional groups, defects, corrugation, and restacking), remaining relatively constant across the entire length of the graphene sheet.
2. In the ac-plane, specific features related to the inter-layer spacing and resulting pores can be measured independently using the diffraction peak at wider angles (turbostratic domains) and the pronounced hump at smaller angles (BSU cluster size). The overall alignment can be characterized as the sample is rotated, and if there is additional periodicity within the expanded layers, or constant pore dimensions, there will be another defined Bragg peak correlated with it. These features combine with the constant roughness running along the surface of the rGO sheets (corrugation and defects), which is characterized by the slope of the Porod region at low- q measured to be in the range of -3 to -4.

In the case of the hydrated assemblies, there is information that can be gathered based on the structure and amount of water present in the materials. In this case, the scattering results from the

interface between the rGO sheets and the liquid, and this can then be correlated with the total surface area. Further, a measure of the amount of water present can be deduced from the intensity of the scattering features of the liquid and correlated with the total accessible porosity within the assembly, as it would be completely filled by the liquid. The structure of water has been long investigated using X-ray and neutron diffraction techniques [286, 287, 298-300], and the main structural features are shown in Figure 145, where the distribution function is dominated by the oxygen–oxygen bonds because the bulk of the electron density in water is centred near the oxygen nucleus [286]. The first peak corresponds to a real space feature at 3.5 Å, which equates to that of turbostratic carbon.

6.3.2 WAXS and SAXS results and discussion

6.3.2.1 General analysis of WAXS and SAXS features in GO and rGO assemblies

The presentation of WAXS and SAXS data begins with comparison and evaluation of basic GO and rGO scattering curves in order to outline the major features of interest. Following this, assemblies that underwent heat treatment (hydrothermal or annealing) as well as those dried under different conditions are presented in more detail because they show the largest variance in structure which can serve as a guide when outlining how the data analysis process is applied in order to compare and quantify the pore structure in these materials. Overall, the same procedures are followed for all materials, continuing from the dry assemblies to compare features from the rGO oxidation series, as well as hydrogels and EM-rGO assemblies. To better streamline the discussion, the in-depth explanation is only provided in the first section and the following sections report and discuss the results, unless new methods are applied that deserve particular mention. For these initial sections, examples using LOD rGO are shown, but all rGO samples have the same features, and discussion turns to the specifics of other rGO samples later in section 6.3.2.3.

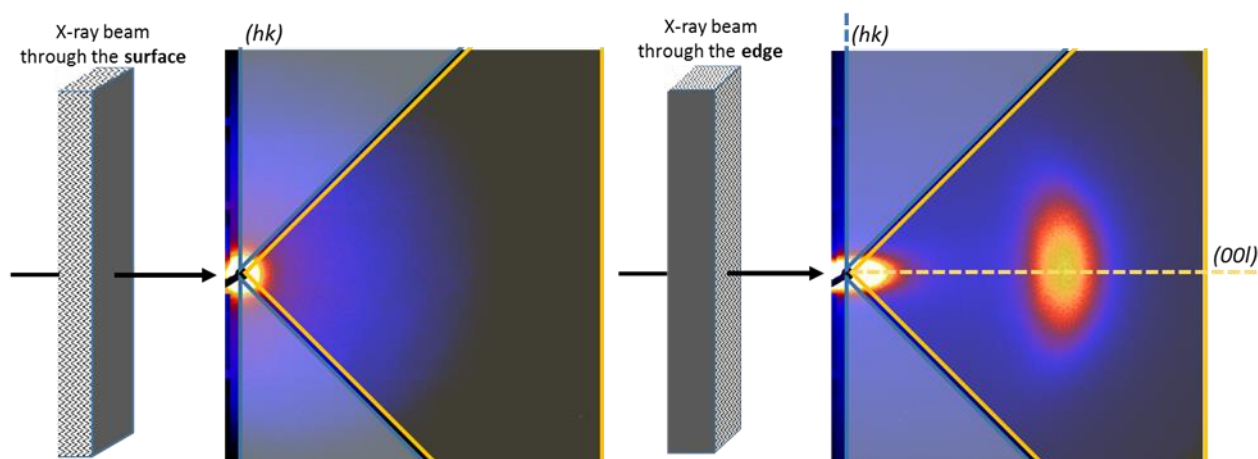


Figure 146. Schematic of how the rGO assemblies are placed in respect to the incoming X-ray beam in order to produce isotropic (through surface) and anisotropic (through edge) WAXS patterns. The wavy lines represent the edges of layered rGO sheets and the solid plane represents the surface. The 2D image is evaluated in sectors, where the blue region corresponds to intra-sheet features along the *ab*-plane and the yellow region can evaluate the inter-sheet stacking and pores along the *ac*-plane independently as the sample is rotated from 0° to 90° to align through-the-edge.

Because of the anisotropic structure of rGO assemblies, Figure 146 provides a schematic of how the materials were aligned with the incoming X-ray beam. As discussed, this alignment allows differentiation of the WAXS scattering patterns resulting from the (hk) or $(00l)$ lattice reflections. Differing from the SAED results, in data presented here, the (11) and (10) peaks are not included in the analysis and the regions shown in blue are instead related to the overall structure of the intra-layer surface of the graphene sheets and pore network in the *ab*-plane. The region indicated in yellow is

related to the inter-layer stacking and inter-sheet pores within the ac-plane, where the (002) peak resulting from the turbostratic coherent domains is clearly visible when the assembly is oriented through-the-edge. While there is high scattering intensity at small angles close to the beam-stop, the purely isotropic, featureless pattern produced when the X-ray beam goes through-the-surface is evidence of random ordering along the ab-plane, with no pores or clusters of a uniform size. In comparison, the pattern produced by scattering through-the-edge clearly identifies the presence of periodic layering within the turbostratic domains, as was the case with SAED, and also exhibits an elongated small-angle feature. No defined peak or ring is evident in the intensity spread of the small angle region in these images, suggesting the inter-sheet pores and layer spacing must contain variance in size. Further, the elongated intensity spread ranging into wider angles in the (001) direction is suggestive of more prevalent structural features that extend to smaller sizes within the inter-sheet direction. A similar sector analysis is applied for the data reduction of the SAXS patterns, using two regions with 90° range and these are then combined to form a full scattering curve extending across a q-range of 0.003 Å⁻¹ to 3 Å⁻¹.

Figure 147 shows the 2D scattering patterns taken with a camera length of 45 cm (at 20 keV) to obtain the WAXS results and a camera length of 7,250 cm (at 12 keV) to obtain the SAXS results for GO and rGO assemblies. This abundant range allows for the structure to be evaluated across three orders of magnitude, which is necessary for porous carbon materials with such an extended pore network. The WAXS pattern shows the same trends for GO and rGO reported in the XRD results, where the inter-layer spacing of GO is much larger (peak shift) and the inter-sheet stacking is more ordered (higher intensity and smaller OA as indicated by the spread of the Bragg peak). However, it is interesting to notice that the SAXS patterns demonstrate these differences in micro-scale order do not have an equal impact on the meso-scale, where the scattering patterns taken through-the-edge show a high degree of alignment for both GO and rGO assemblies. The mesoscale alignment along the c-axis, ϕ , will be quantified and compared for different samples later in this chapter, but the SAXS patterns alone show there are two distinct levels of orientation, where the OA measured from the (002) peak at wide angles shows more fluctuations are present at the microscale than at the mesoscale ($OA > \phi$).

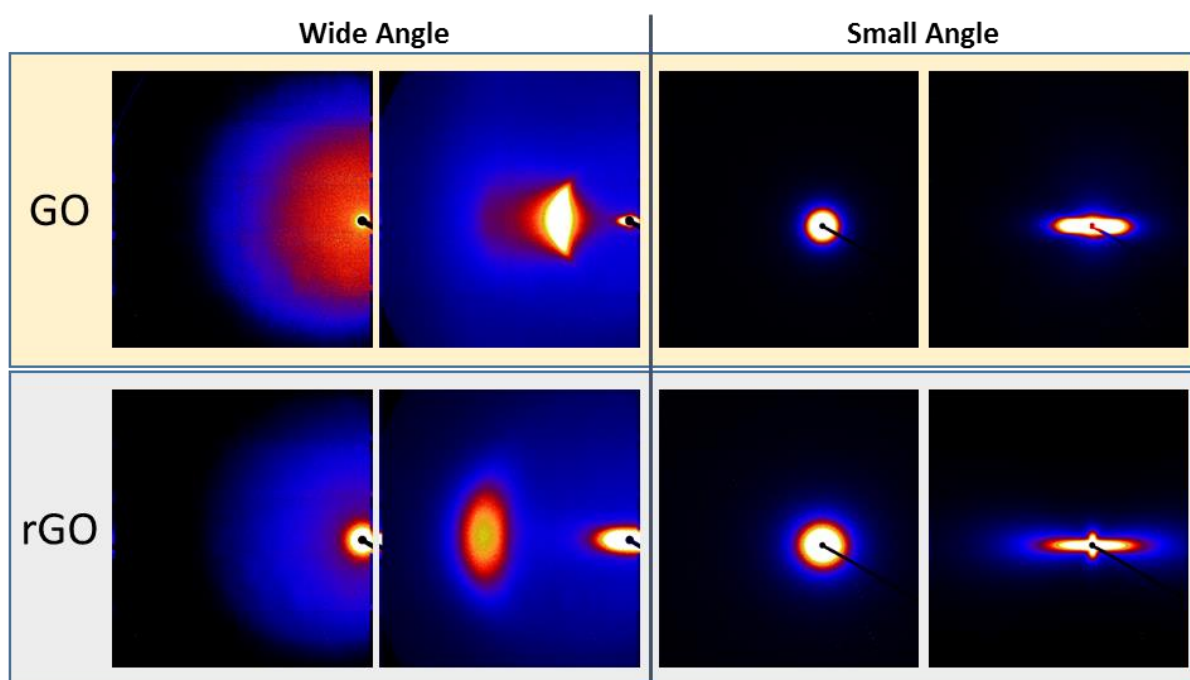


Figure 147. WAXS and SAXS patterns for pump dried GO and LOD rGO layered assemblies probed through-the-surface (isotropic patterns) or through-the-edge where the Bragg peak and pore alignment are clearly visible in the anisotropic patterns.

To more clearly examine the scattering features and alignment of pump dried GO and rGO assemblies, a mask is applied to the 2D scattering pattern in order to independently evaluate sectors related to specific geometric planes in the material (by including only the area shown in blue or the area shown in yellow), similar to that discussed with TEM SAED data. Figure 146 shows which regions are used for analysis in the horizontal or vertical sectors. Reduced scattering curves from the horizontal sector of the GO and rGO scattering patterns taken through-the-surface and through-the-edge are shown in Figure 148. The main features of the curves used throughout this analysis are shown on the figure.

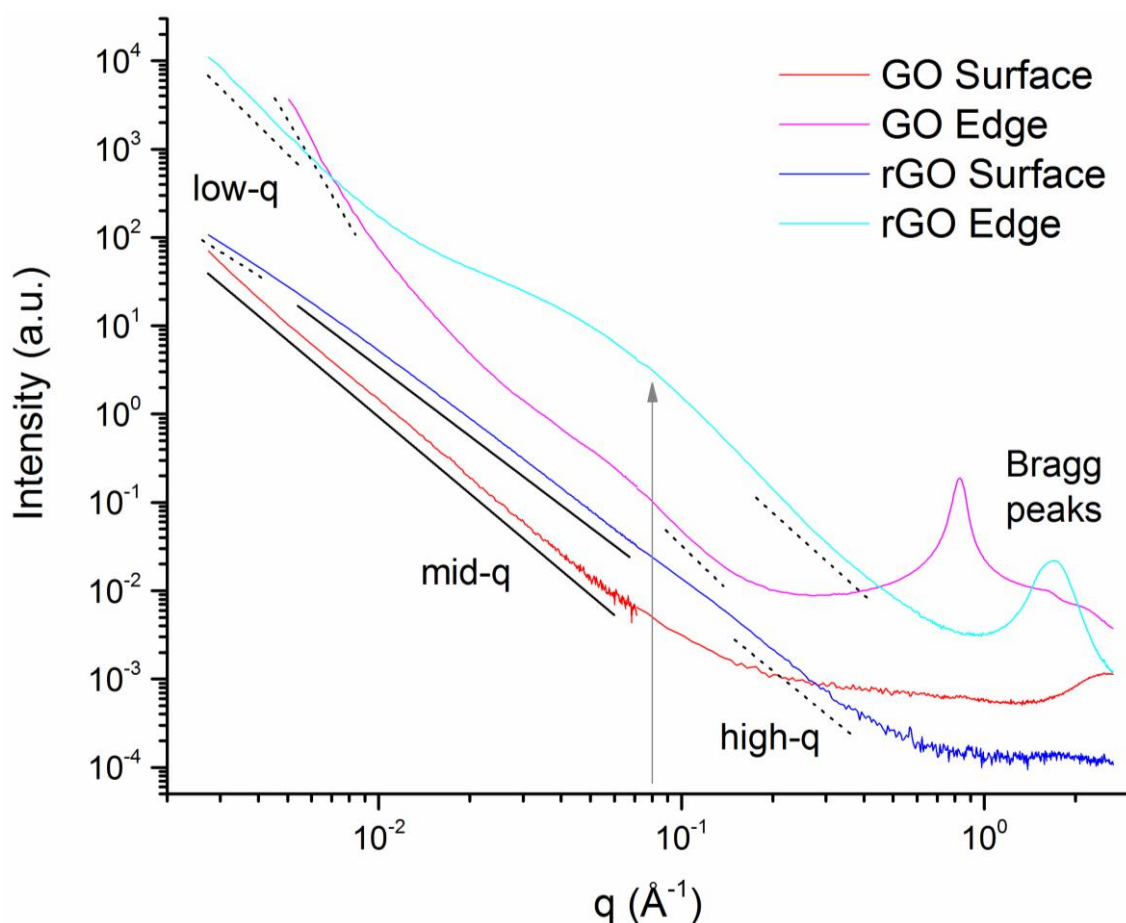


Figure 148. Reduced scattering curves for pump dried GO and rGO taken from the horizontal sector shown in yellow in Figure 146 where the Bragg peak emerges when the X-ray beam is aligned through-the-edge. The main features of the curve used for analysis are marked on the figure, where the dotted and solid lines indicate which regions are used to calculate the slope (Porod region) and the arrow indicates the scattering feature associated with a larger inter-sheet structure.

The GO and rGO samples were rotated across the full 90° (from surface to edge) to assess the overall alignment of the graphene layers and resulting pore structure in the ac-plane with the results given in Figure 149. To clarify some of the geometric references in this section, looking back at Figure 146, the horizontal sector includes scattering from the inter-sheet (ac-plane) features while the vertical sector includes scattering from the intra-sheet (ab-plane) features. For rotation measurements, scattering through-the-edge is labelled at 90° and scattering through-the-surface is labelled 0°. Thus, scattering within the horizontal sector is expected to become more pronounced with rotation from 0° to 90° as the features in the ac-plane align. This is clearly seen in the reduced scattering curves for the horizontal sector plotted Figure 149, where the (002) Bragg peak for pump dried rGO appears at about 1.8 Å⁻¹ along with a broad hump centred around 0.1 Å⁻¹, both appearing after a rotation of 30° and then becoming more pronounced. This can be compared with the reduced scattering curves in the vertical

sector, where the change is much less pronounced, indicating the surface scattering along the ab-plane is constant across a full angular rotation. Overall, the same trends appear in the pump dried GO, but less inter-layer fluctuations result in a more pronounced Bragg peak, while the flatter sheets (less corrugation and defects) result in an extended Porod region where no structural features are visible until rotations above 75°. The bulge in the 90° rotation of both the horizontal and vertical sectors for the GO sample is at a smaller q-value than that of rGO and more pronounced, suggesting a larger degree of order which is expected. The steep upturn in the low-q region of the 90° GO curve could indicate a second order correlation peak, but further extension of the range would be necessary to confirm this.

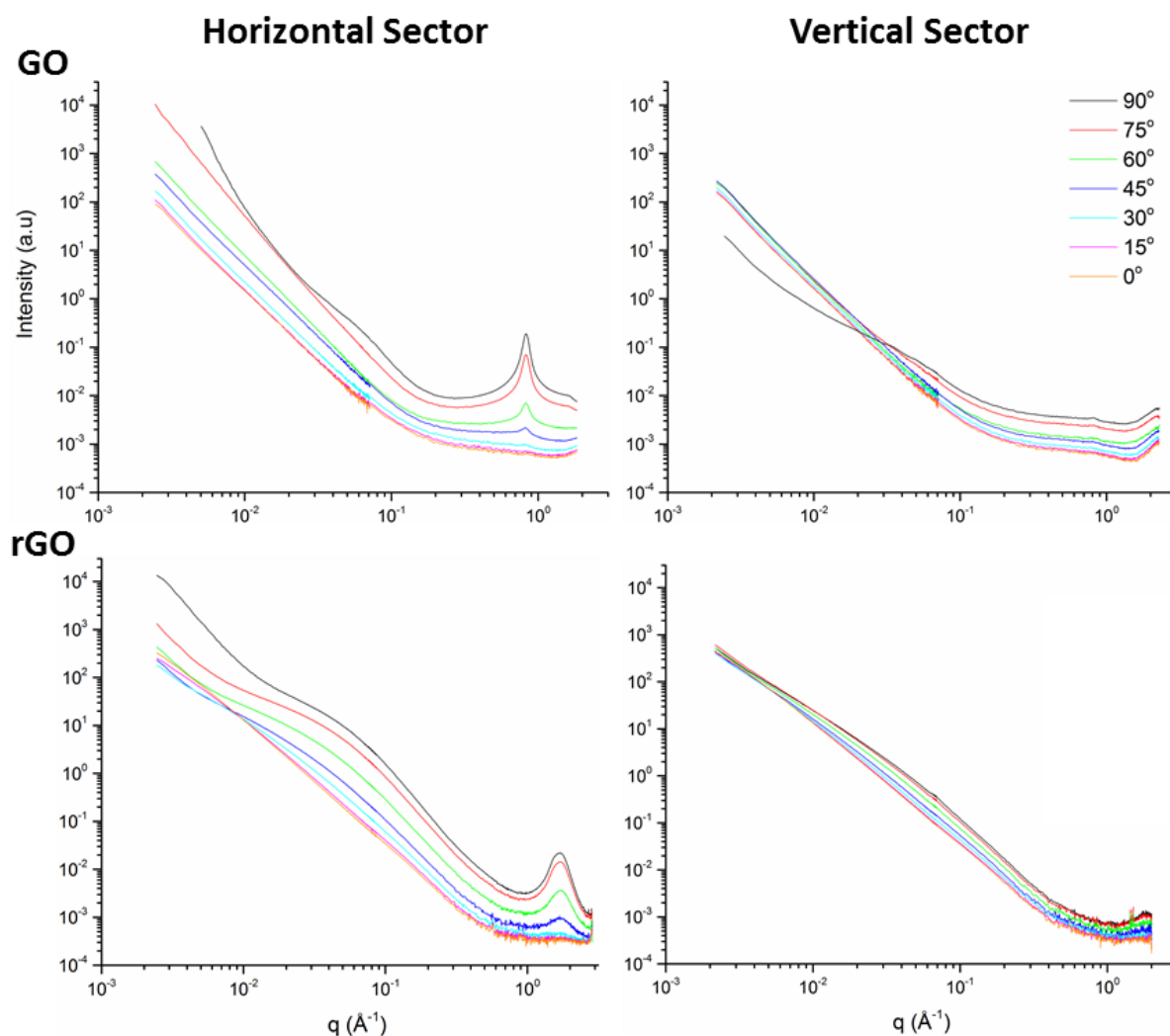


Figure 149. Sector analysis in the horizontal and vertical sections of the 2D scattering pattern for pump dried GO (top) and the resulting rGO (bottom) assembly across a full 90° rotation.

The Porod regions of the curves, where the scattering relationship follows a power law, can be found by fitting the linear regions on the intensity vs q plot plotted with a log-log scale, as indicated in Figure 150. The q-range of each Porod region is correlated with the length scale that the scattering features extend across, and the numeric value of the slope provides information on the interface between the two phases and the overall nature of density fluctuations in the materials, as described in the Literature Review. Figure 150 indicates which portions of the curves were used to extract values for the slope reported in Table 18. An extended linear region is observed for through-the-surface scattering curves, especially for the rGO sample. From the through surface plots in Figure 148, it can be seen that the small angle scattering begins at a q-value of about 0.4 Å⁻¹ or 0.5 Å⁻¹ for rGO and 0.2 Å⁻¹ for GO and

extends over the entire small-angle range. The relative size/scale of the scattering feature causing the intensity change across a Porod region can be estimated by $q_{\min} \approx \pi/l_{\max}$ and $q_{\max} \approx \pi/l_{\min}$. This indicates the through-the-surface scattering originates from features of approximately 7 Å in rGO and 15 Å in GO, equating to twice the interlayer stacking distance (turbostratic layering in rGO of 3.5 Å and 7 Å for GO). This is quite significant, as the scattering curves show that along the ab-plane, the structure of pump dried assemblies is uniform without pronounced features across the entire micro- and mesoscale range. The broad hump separating the linear regions of the rotated and through edge curves correspond to the radius of gyration of a physical structure present in the ac-plane, most likely resulting from the layer stacking and resulting in inter-sheet clusters and pore network, likely corresponding to the BSU identified in Chapter 5.

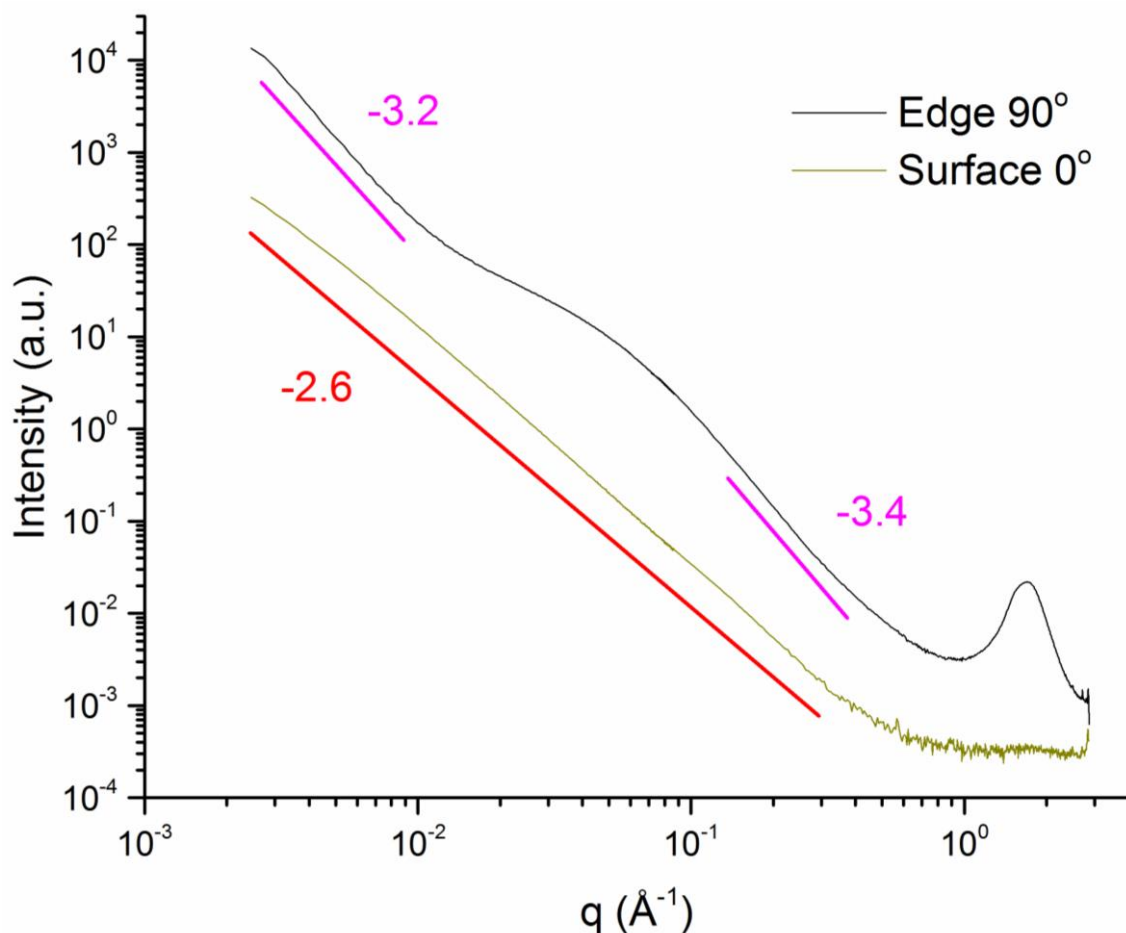


Figure 150. A comparison of the Porod regions in the reduced scattering curves for pump dried rGO taken in the horizontal sector show very different power law relationships for through-the-edge (ac-plane) and through-the-surface (ab-plane) with the value of -3 to -4 being characteristic of a rough interface and the value of -2.6 relating to a fractal dimension describing the density distributions and features of the pore network in the bulk (a mass or pore fractal).

The GO assemblies have a constant slope all the way down to 0.2 Å^{-1} which steepens as the sample is rotated. This indicates there are two scattering components, one from the surface of the sheets which becomes more pronounced at larger rotations (approaches -4) and one from the bulk material measured through-the-surface of the sheets (mass fractal with dimensionality 2.85). The sharp upturn at low- q in the 90° rotation of GO is a negative deviation (more negative than -4) from Porod's law which is indicative of a diffuse boundary or interface layer [191]. This feature is explained by the two domains making up GO assemblies where the carbon layers are separated by an oxygenated layer. For the other regions, the slope lies between -2 and -3. A slope of -3 is common in glassy carbon [290], which correlates with uniform space filling (three dimensional fractal), and comparing the 0° results

for GO and rGO support that GO is more planar with defined stacking, as a higher fractal dimensionality signals an extended L_a which results from straightened carbon layers, as shown in various pyrocarbons investigated by Bourrat [133]. Comparing this with rGO assemblies exhibiting a mass fractal dimension of about 2.6, shows rGO has more disorder within the stacked domains caused by corrugation and resultant surface roughness. This dimensionality can be related to the work of Cranford and Buehler presented in the Literature Review [116] where the ideal fractal dimension of a stacked/crumpled graphene sheet is close to 2.3 in order to achieve a maximum accessible surface area (ASA). Values higher than this (between 2.3 and 3) correspond to increased stacking of the layers (expected for longer and more planar L_a), decreasing the ASA and overall porosity in the bulk. While it is not yet known if this model can be used quantitatively, it will be applied qualitatively and compared with other theories on pore and mass fractals throughout discussion on different rGO assemblies as a means of tying the scattering results to the material properties of the bulk. Knowledge of the structure and performance of the different assemblies can be used to establish the validity of this fractal model in these complex systems.

Table 18. Comparison of the slope of the linear regions for pump dried GO and rGO assemblies with values of high-q and low-q regions in rGO listed individually, while GO is measured across the full q-range (*90° rotation is the only GO curve with two Porod regions and the value listed is at high-q).

	Sector	90°	75°	60°	45°	30°	15°	0°
GO full-q	Horizontal	-6.13*	-3.45	-3.10	-2.95	-2.88	-2.85	-2.85
	Vertical	-2.88*	-2.81	-2.85	-2.82	-2.82	-2.83	-2.84
rGO high-q	Horizontal	-3.42	-3.26	-3.07	-2.92	-2.82	-2.70	-2.67
	Vertical	-2.85	-2.82	-2.79	-2.75	-2.68	-2.66	-2.67
rGO low-q	Horizontal	-3.21	-2.71	-2.40	-2.24	-1.91	-2.12	-2.46
	Vertical	-1.97	-2.06	-2.11	-2.19	-2.27	-2.38	-2.42

With the absence of any other defined structure besides that of fractal scaling, it would be expected that the 0° rotation should show no differences between the horizontal and vertical sectors at both high-q and low-q slope. However, there is slight variance in the rGO assembly, but because this feature is so diffuse, it is most likely a result of misalignment within the corrugated and curvy sheets, where the large hump seen clearly with the 90° rotation carries over into the ab-plane to some degree. This is clearly the case when looking at the plots of Figure 149 where the high-q Bragg peak and broadened lower-q feature follow a clearly defined pattern where both features diminish with equal relative intensity. As this diffuse feature would result in a more negative slope at high-q and a less negative slope at low-q, a close estimate for the scattering resulting from the ab-plane features alone lies between the two values, and this simplified average will be used when comparing the fractal dimension of different samples (about -2.56 in the case of the pump dried rGO).

In order to more clearly identify the features of interest within the scattering curves, a Kratky plot [301] where the intensity is multiplied by q^2 and shown on a linear-log scale is shown in Figure 151. Here, the through edge curve shows the Bragg peak at high-q is quite dominant, and the broad hump is more clearly centred around 0.05 \AA^{-1} with a broad, Gaussian-like distribution which indicates size distribution in the physical feature. The increased scattering at low-q remains constant, with no additional features discernible. In contrast, the through-the-surface scattering curve exhibits very slight structural elements, with a slight increase in scattering at lower-q setting in at about 0.06 \AA^{-1} , within the q-region where the broad hump seen in the through-the-edge curve appears. The lowest-q region may indicate another region of curvature, perhaps defining the large-scale scattering structure which is likely

linked to the total length of the graphene sheets, which would define the largest elements of the branched pore network.

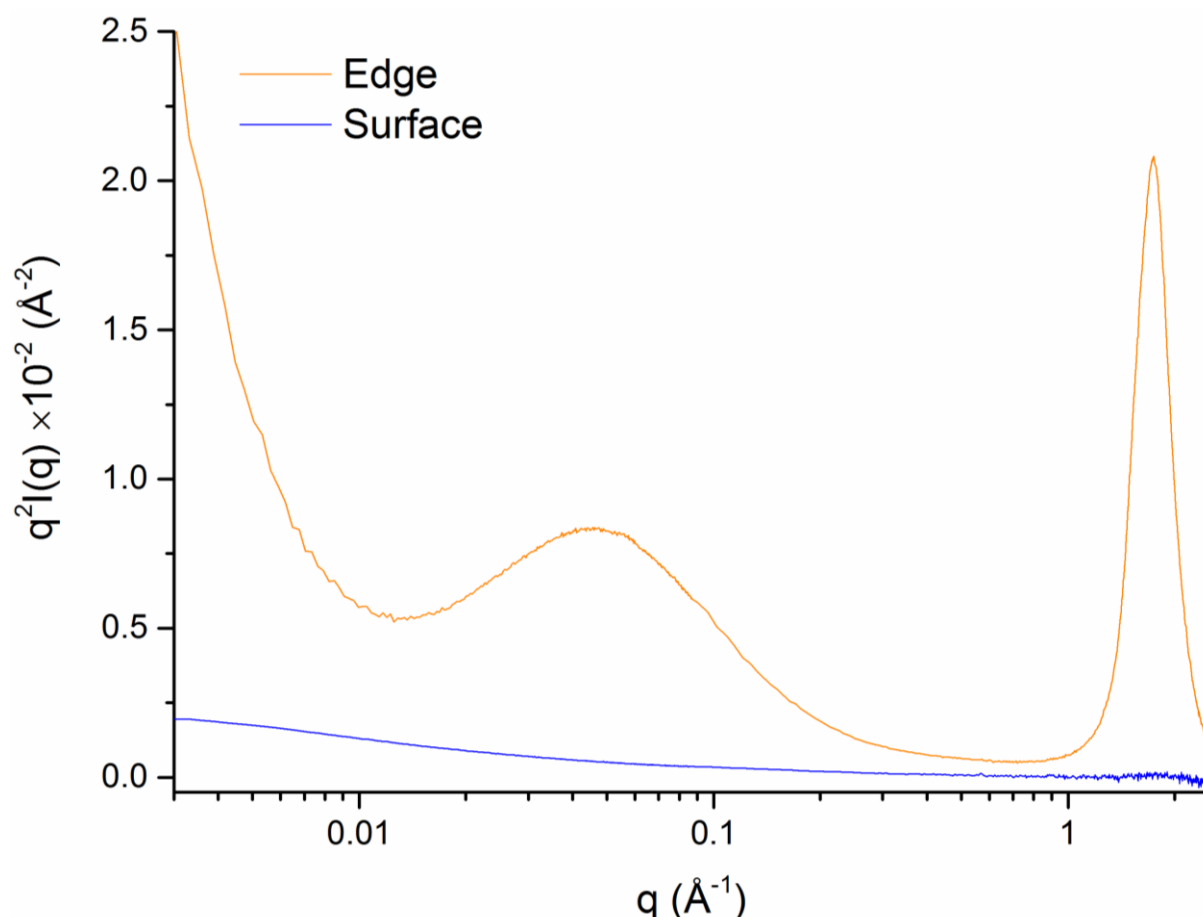


Figure 151. Kratky plot of the pump dried rGO assembly which more clearly identifies scattering features within the edge and surface curves.

As a final step in determining what aspects are contributing to the SAS curves in order to apply the best model for fitting, Perret and Ruland [240] performed extensive scattering experiments on various carbons, ranging from amorphous [175], graphitized [184], and non-graphitizable [175, 297] and showed that by plotting $I(q)$ multiplied by q^3 as a function of q^2 would provide insight on what portion of the scattering results from slight differences in the interlayer stacking within the carbon clusters. The linear regions of this curve would have a slope of q^{-1} , which would result from scattering from one dimensional structures with the edges of the carbon planes in these slacked regions effectively acting as rods. This is shown in Figure 152, where the slope of the linear region of the edge and surface plots are similar, indicating the amount of scattering resulting from these one dimensional features is likewise similar. However, the scattering range that these features extend across varies greatly, depending on the orientation. The scattering due to interlayer fluctuations does not occur until about 0.005 \AA^{-2} ($q \approx 0.070 \text{ \AA}^{-1}$) when measured through-the-edge, but extends to about 0.002 \AA^{-2} ($q \approx 0.045 \text{ \AA}^{-1}$) when measured through-the-surface, and even then the deviation is quite small. This shows the one dimensional fluctuations act across a much longer region for through-the-surface scattering, most likely due to the small density differences in stacking height extending broadly along the rGO sheets – a result of surface roughness and corrugation. In the through edge curve, the deviation from the linear fit at lower- q values indicates the scattering in this region must be due to 2D and/or 3D structural elements. These features can also be correlated with likely material performance, as the through-the-edge curve is similar to that of high modulus carbon fibres, while the through-the-surface plot is similar to that of high strength fibres [30, 240].

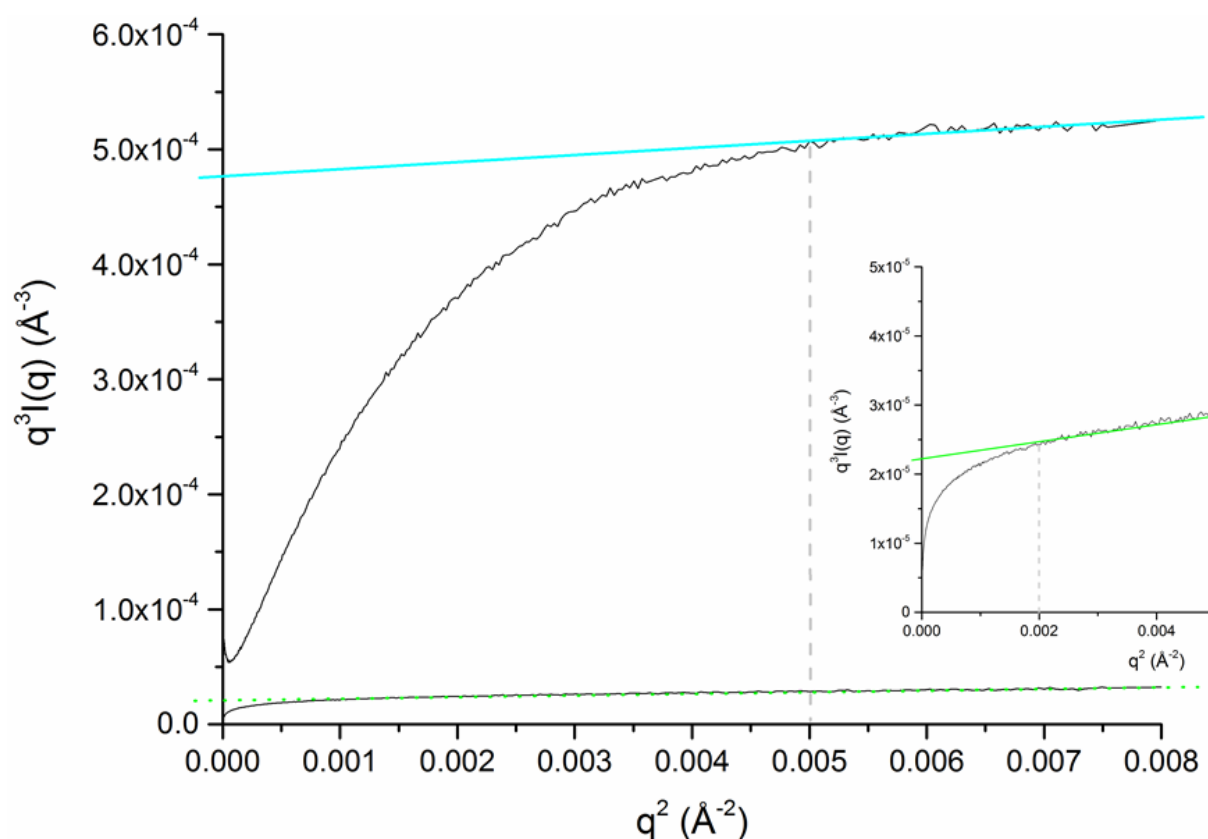


Figure 152. Fit of the liner region in a plot of $q^3I(q)$ versus q^2 for the through-the-edge curve (blue) and the through-the-surface curve (green) and dotted lines indicating the onset of scattering resulting from interlayer fluctuations in the stacking distance between graphene planes (note maximum q^2 of $0.008 \text{ \AA}^{-2} \approx 7 \text{ nm}$).

The evaluation of the Porod plot, Kratky plot, and onset of one dimensional scattering correlates well with the previous discussion of layered carbon materials and ties in with what is known about the BSU based on the results of Chapter 5. Based on this, it is proposed that the rGO layers form cluster aggregates with turbostratic layering which are randomly dispersed across the ab-plane and with general layered ordering within the ac-plane. The aromatic domains restack to form these clusters, and the presence of the horizontal sector of the through-the-edge scattering pattern show a Bragg peak which identifies the average interlayer spacing and acts as a measure of the minimum number of layers making up the clusters, as determined by the Scherrer equation. These clusters then act as the next order of structure (as the BSU) which appears as the large hump in the mid q -range. Scattering is then dominated by the surface of these clusters, causing the deviation from linear behaviour seen in Figure 152. The lowest- q region, at a size range larger than the clusters, the Porod slope between -3 and -4 signals surface roughness is dominating the scattering along the longer-ranging rGO sheet, and it is expected this feature continues to q -values corresponding to the length of the rGO sheets and overall thickness of the assembly (outside of this range, but this claim is later investigated with USANS). Most of these features are only distinguishable in scattering patterns with the incident beam through-the-edge of the assemblies, and the through-the-surface plot is dominated by scattering related to one dimensional fluctuations due to slight differences in interlayer stacking and density differences amongst the clusters and disordered pore network surrounding it. This is consistent with the fractal model proposed for crumpled graphene sheets [116] where the fractal dimension measured with SAS can be used to as a measure of accessible porosity (portion of the assembly not consisting of the stacked clusters with collapse of the pore space due to van der Waals forces), which was also shown through experimental work comparing the fractal dimension to L_a in different types of carbon black [133].

This leads the discussion directly to choosing a model to fit the through-the-edge scattering curves of the rGO assemblies in order to quantify these structural elements. As discussed in the Literature Review, a full scattering model usually contains a form factor to describe the shape and size of the scattering features which is combined with a structure factor describing the interaction within and between these scattering entities. The incoherent background scattering for carbon materials can be easily subtracted by fitting the flat region of the high- q through-the-surface curves [173]. This was then adjusted to account for the different volume illuminated by the beam as the samples were rotated from 0° through to 90° and subtracted from scattering data. The rather featureless through-the-surface curves and the low- q through-the-edge curve can be quite simply characterized by applying a constant linear fit to the data, of the form:

$$I(q) = c * q^{-\alpha} \quad 6.1$$

where c is a constant and α is defined 6-D for surface fractals or $\alpha=D$ for mass fractals.

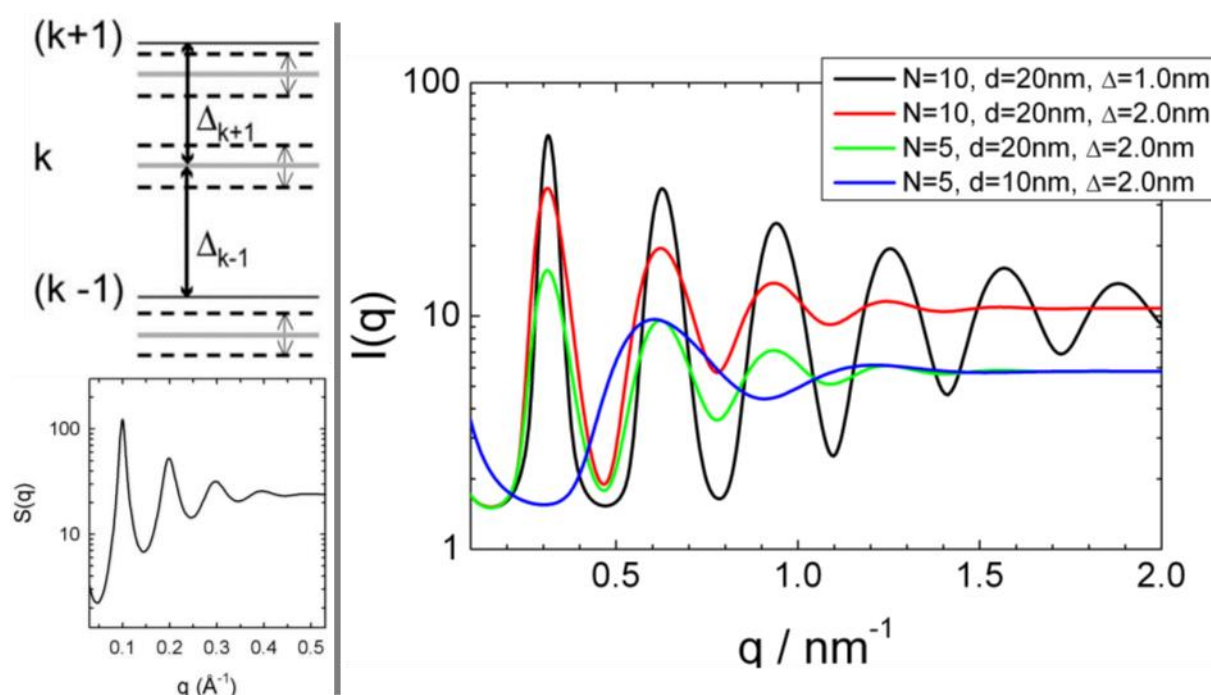


Figure 153. Schematic of the stacking disorder described by paracrystalline theory where the displacements in the layer positions result in a structure function that decays across longer-range order (left). The structure factor applied here is displayed in the plot on the right, showing how different physical parameters (number of layers, N , layer spacing, d , and the variance in layer spacing, Δ) impact the resulting function (right). Reproduced from the SASfit user guide [214].

As for the through-the-edge features, knowledge of the physical structure was combined with a review of the literature for various scattering models, with the focus of finding the simplest function to apply to the system (limited number of assumptions and terms). After attempting various spherical, elliptical, and combined Guinier-Porod unified fit combinations, the best results were acquired using a model developed for multi-lamellar structures, specifically as described within paracrystalline theory (PT) [214, 302], described in Figure 153.

As the BSU has already been identified as a “cluster object”, these clusters are used to define the form factor making up the carbon matrix, which are surrounded by a more disordered, porous region. Essentially a fractal aggregate [214], these clusters are lamellar paracrystals with individual, fluctuating layers. In these systems, a Bragg peak is observed because there is a large amount of short-range order, however, the large variance in layer spacing causes long-range order to be lost. The structure factor derived from paracrystalline theory is of the form [302]:

$$S_{PT}(q, N, d, \Delta, N_{diff}) = N_{diff} + \sum_{N_k=N-2\sigma}^{N+2\sigma} x_k S_{k,PT} \quad 6.2$$

with a polydispersity of layer sizes given by:

$$x_k = \frac{1}{\sigma\sqrt{2\pi}} e^{-\frac{(N_k-N)^2}{2\sigma^2}} \quad 6.3$$

with StdDev defined by $\sigma = \begin{cases} \sqrt{N} & \text{for } N \geq 5, \\ 0.5(N-1) & \text{for } N < 5 \end{cases}$

and:

$$S_{k,PT} = \left(N_k + 2 \sum_{N_k=N-2\sigma}^{N+2\sigma} (N_k - m) \cos(mqd) e^{-\left(\frac{m^2 q^2 \Delta^2}{2}\right)} \right) \quad 6.4$$

where N is the number of layers making up the clustered stacks, d is the average interlayer distance within the clusters, Δ is the stacking disorder parameter, and N_{diff} accounts for an additional diffuse background resulting from a number of uncorrelated scattering bilayers. This additional diffuse term is used in systems with a high degree of lattice defects. The decay of the structure function depicted in Figure 153 shows the decrease in peak height is accompanied by broadening which is related to the diffraction order. This loss of order results in diffuse background scattering. The impact of the stacking number, interlayer distance, and polydispersity are also shown in Figure 153, and the fit applied using SASfit [214] accounts for polydispersity by applying a series with varied number of bilayers, as noted in the definition of x_k above, and is symmetrical around the mean number of layers, N .

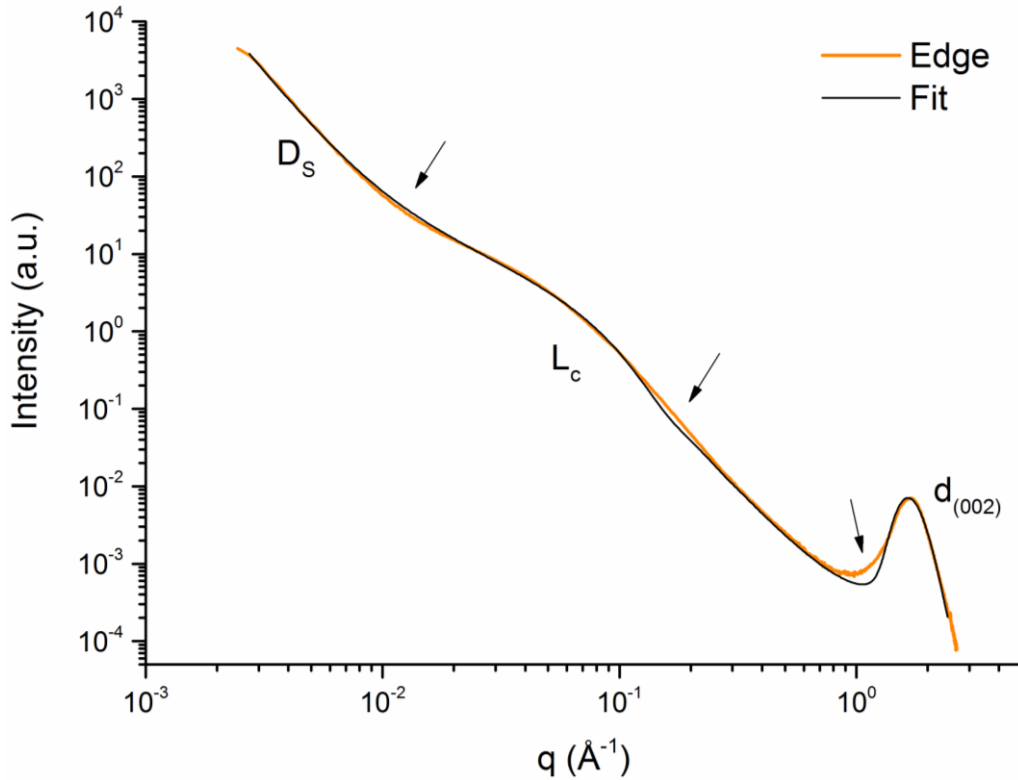


Figure 154. Full fit of the through-the-edge scattering pattern of the pump dried rGO assembly with the raw data in yellow and the black line is the fit to data after applying a paracrystalline, multi-lamellar structure factor combined with a power law at low- q . The portions of the curve related to surface scattering, D_s , cluster height, L_c , and interlayer distance, $d_{(002)}$ are labelled on the curve along with arrows highlighting deviations from the raw data discussed in the text.

The results of applying a combination of the power law function at low- q and the PT model at mid- to high- q are shown in Figure 154. This choice of fitting is simple, makes limited assumptions, and is an accurate representation of the actual physical structure within the rGO assemblies. The main features of interest are indicated on the graph, where the surface fractal dimension, D_s , representing the roughness (corrugation) of the rGO sheets dominates at length scales larger than the size of cluster aggregates, L_c , which appear in the mid- q range and are linked to the size and shape of the Bragg peak at high- q , $d_{(002)}$. The fit describes the main features quite well, providing quantitative information on the interlayer spacing and the number of sheets making up the clusters, a value that can be compared with the lower limit of N found with the Scherrer equation. The arrows highlight deviations from data, which are easily explained and do not detract from the validity of the quantitative results. The two arrows at either side of the L_c feature are a result of the high polydispersity in cluster size, which is not fully accounted for by this simplified model, but does not impact the value for the average cluster height. The arrow to the left of the Bragg peak highlights the broadened feature which is a result of the radial averaging across the whole horizontal sector, since the broad OA ensuing from varied stacking domains spreads the peak shape at larger azimuthal angles (away from the peak centre) and this broadening is a result of the radial averaging procedure, as discussed in the Literature Review. Even though only the horizontal sector is used, this region is still quite broad, and plotting the intensity from a very narrow sector, or line directly through the centre of the (002) peak feature does not display the broadening and has a shape like that of the black PT fit function. However, reducing the scattering pattern from the entire horizontal sector is much more easily applied across the range of samples and large data sets while also proving a much higher overall intensity for fitting. Thus, the broadening to the left of the Bragg peak is not a necessary parameter to include in the rGO structural analysis.

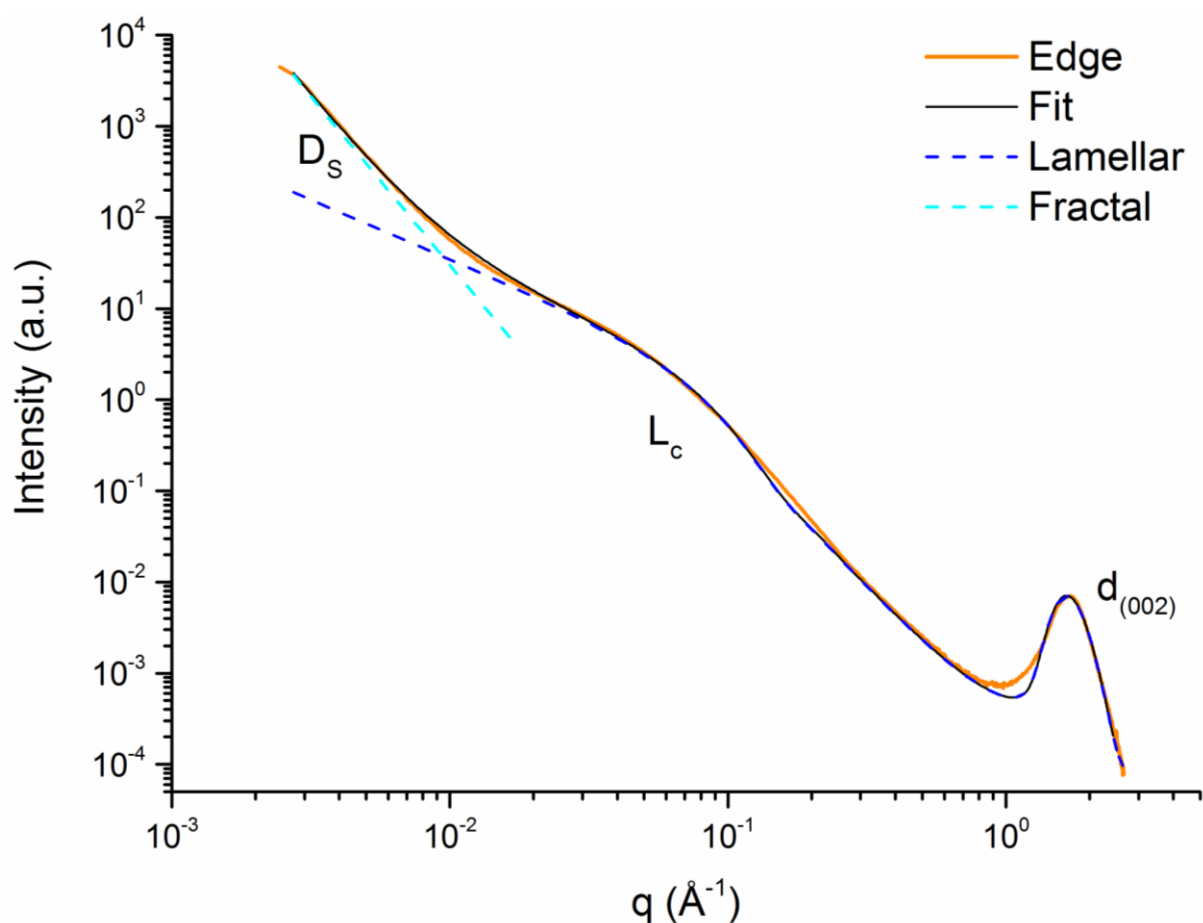


Figure 155. Results of the surface fractal and lamellar models shown individually on the through-the-edge scattering curve.

For added clarity, Figure 155 shows the two model elements separately, overlaid on the regions they correlate with on the curve. The final fit for the pump dry rGO results in the values listed in Table 19. The PT structure is defined by an interlayer distance of 3.6 Å, matching the values established using other methods and the value for N gives an average value of 8-9 rGO layers making up the cluster aggregates. This is slightly above the value obtained with the Scherrer equation, which is expected since it provides a lower limit of the coherent domain height. Multiplying N with $d_{(002)}$ gives a value of 3.1 nm which translates to a q value of 0.2 Å^{-1} and clarifies that the scattering slope from this point through to the minimum intensity (previously determined to extend to length scales down to 7 Å which is a single bilayer) is a result of the rGO edges making up the stacked clusters. This also correlates with the slight shift in the slope of the through-the-surface Kratky plot in Figure 151, indicating it is these density differences from within the cluster and the more disordered region surrounding them that contribute to the scattering from the ab-plane. A Δ value of 0.49 confirms that there is not much variance in the interlayer stacking distance within the turbostratic clusters, and the small value of N_{diff} indicates there is a small number of uncorrelated scattering bi-layers.

Table 19. Results of the surface fractal and paracrystalline lamellar model applied to the through-the-edge scattering curve of the pump dried rGO assembly. Colours match the individual components which fit the curve in Figure 155.

Surface Fractal		Fractal Aggregate		Paracrystalline Lamellar Structure			
c	α	c	α	N	D	Δ	N_{diff}
$1.2(10^{-6})$	3.7	$2.5(10^{-3})$	1.4	8.5	3.6 Å	0.49	0.4

The surface fractal component extends all the way down and would intersect at a value of q or about 0.4 Å^{-1} , which is the same value for L_{min} as the through-the-surface fractal component. This shows the corrugated surface roughness extends across the entire length of the rGO sheets and is rather constant across a huge size range (sub-nm to micron range). Values for α of 3.8 in the low- q range are standard for many porous carbon materials [34], and because a surface fractal is defined by $\alpha=6-D_s$, the fractal dimensionality, D_s , is 2.3 in this assembly. In order to determine if the low- q region reaches a steady asymptote, holds a continuous slope of -3.7, or has another scattering feature at even larger sizes, the scattering curve would need to be extended to ultra-small angles, and this aspect is investigated later in this chapter using USANS.

The through-the-surface fractal component yields an α value between 2 and 3, exhibiting a constant mass fractal feature across a very large q -range. This is common of porous fractal systems in nanostructured carbons, and is understood by the interpreting the high- q value as the size of the fractal object (in this case, the interlayer space of the turbostratic clusters) which extends all the way across the network, with a typical dimensionality of 2.8 [34], which is close to the value of 2.6 measured for pump dried rGO. In addition, the absence of humps or knees in the scattering results for rGO show there are neither defined pore sizes nor large voids in the bulk assemblies. Thus, the small voids seen in the FIB/SEM results from the previous sector are not prevalent enough to be detected in the scattering results.

The fractal dimension can be related to the overall porosity, ϕ , by either interpreting the system as fractal pores within a bulk or a fractal mass consisting of pores. As either can be done according to Babinet's principle (the scattering pattern from the solid is identical to that from a hole of the same size and shape), the fractal dimension is related to the small length components present and how much space is filled by them. In a network that fills space, $D=3$, so if the scattering is interpreted as resulting from the voids (pores), an α value of 3 would be a completely uniform porous volume, while values closer to 3 are more porous, and values closer to 2 are less. While some work interprets this value to

represent the pore space [34], an equivalent analysis could be done assuming the fractal dimension represented the mass, where the same equation applies, but would be interpreted as representing the mass, or space not filled by the pores. A simple check to verify which interpretation applies best to rGO materials is to determine if more porous assemblies have α values closer to 3 (which would indicate pore fractal interpretation) or closer to 2 (would indicate mass fractal interpretation). This will be tested in the following section when comparing rGO materials prepared with different drying conditions.

6.3.2.2 *Drying conditions and heat treatment*

The methods developed in the previous section are now applied to a series of rGO assemblies dried under different conditions or treated with higher temperatures. It is expected that pump dried assemblies would have more aligned and closer packed layers, while those which are air dried would have higher porosity. Further, assemblies prepared from hydrothermal rGO reduced at 180°C and pump dried samples that were later heated to 250°C are expected to contain less oxygen groups than those reduced under the typical conditions at 100°C. In addition, the hydrothermal assemblies are thought to contain more corrugated rGO sheets which would contribute to increased stacking disorder. All of the material investigated in this section was prepared with the LOD original GO precursor and is fully dried (not in hydrogel form). It should be noted that rGO materials prepared from other GO precursors were also tested, but, as the purpose of this section is to highlight differences due to drying and temperature conditions, discussion is limited to LOD. As with the SEM results, no measureable differences were seen between samples other than impacts from oxidation level, already discussed in the XRD results section, 5.4.2. Following this, a detailed look at rGO materials of varied oxidation is the focus of the next section, 6.3.2.3.

The sector plots within the horizontal region (across the (002) reflection) for each rGO assembly rotated through-the-edge (90°), at 45°, and through-the-surface (0°) are shown in Figure 156 through Figure 160. They clearly show the differences in alignment of the structural features depending on the processing conditions applied. The most pronounced difference is in the Bragg peak region, with this feature rapidly diminishing in samples with more alignment within the layered clusters (smaller OA). Ranking the samples of more-to-less alignment, yields annealed, pump dry, vacuum dry, air dry, to hydrothermal, as would be expected. The corresponding WAXS patterns oriented at 90° and 0° show the shape of the Bragg peak and relative intensity of these features, indicating the micro- and mesoscale features are correlated with the amount of disorder present, but in all cases the mesoscale features are more aligned than those at the microscale (OA at wide angles more disperse than the SAS). SAXS patterns at 90° and smaller rotation to 75° are shown in order to indicate how quickly the scattering diminishes, as a measure of the alignment of the larger features within the bulk materials. Assemblies with a higher degree of alignment give a characteristic cross-shaped SAS pattern, while the more diffuse fan-shape is seen in samples with mid-range ordering, and a very broad oval is produced for the most disordered, hydrothermal assembly which showed no anisotropic shape at rotations smaller than 75° (60° to 0° were circular in shape).

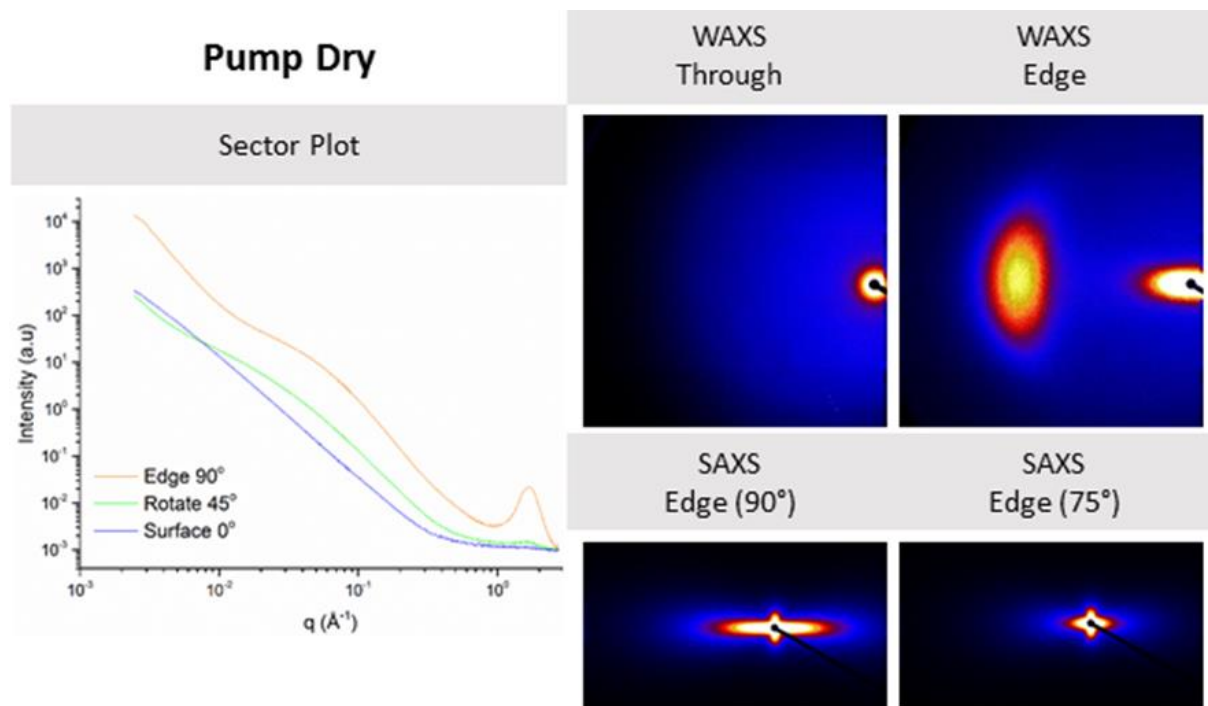


Figure 156. Sector plot of the horizontal region (across the (002) reflection) when the assembly is rotated through-the-edge (90°), at 45°, and through-the-surface (0°). The corresponding 90° and 0° WAXS patterns are shown above the SAXS patterns at 90° and smaller rotation to 75° for the pump dried rGO assembly.

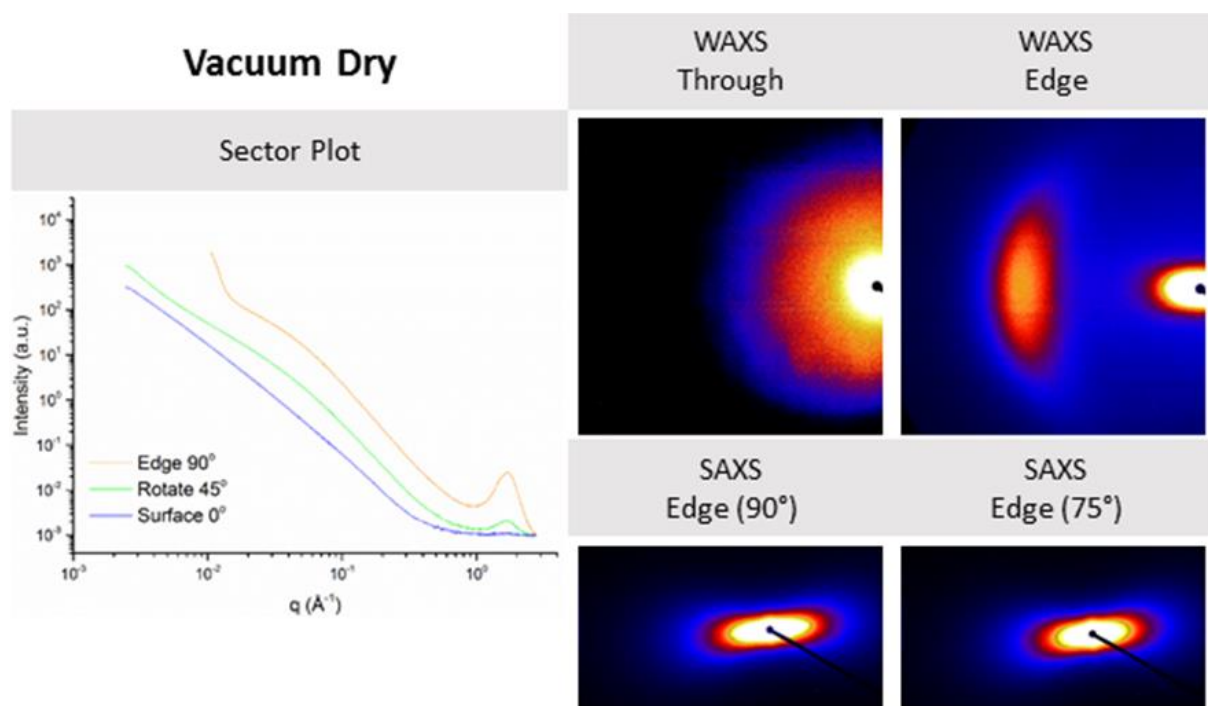


Figure 157. Sector plot of the horizontal region (across the (002) reflection) when the assembly is rotated through-the-edge (90°), at 45°, and through-the-surface (0°). The corresponding 90° and 0° WAXS patterns are shown above the SAXS patterns at 90° and smaller rotation to 75° for the vacuum dried rGO assembly.

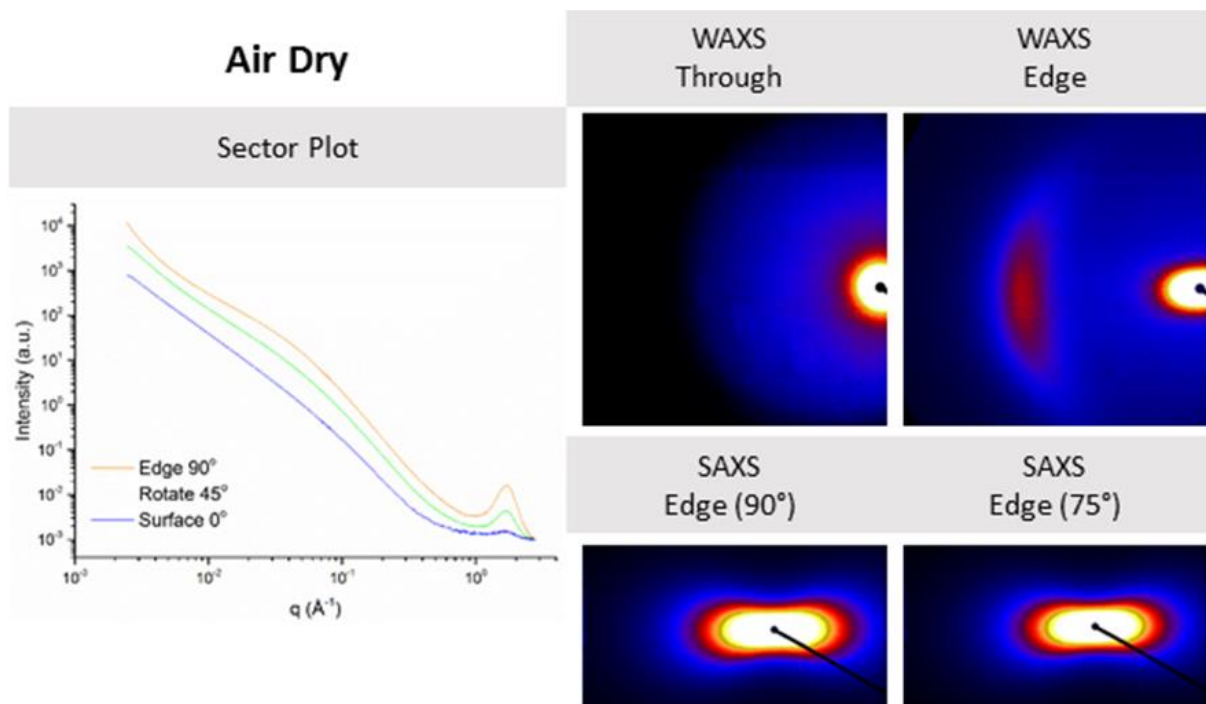


Figure 158. Sector plot of the horizontal region (across the (002) reflection) when the assembly is rotated through-the-edge (90°), at 45°, and through-the-surface (0°). The corresponding 90° and 0° WAXS patterns are shown above the SAXS patterns at 90° and smaller rotation to 75° for the air dried rGO assembly.

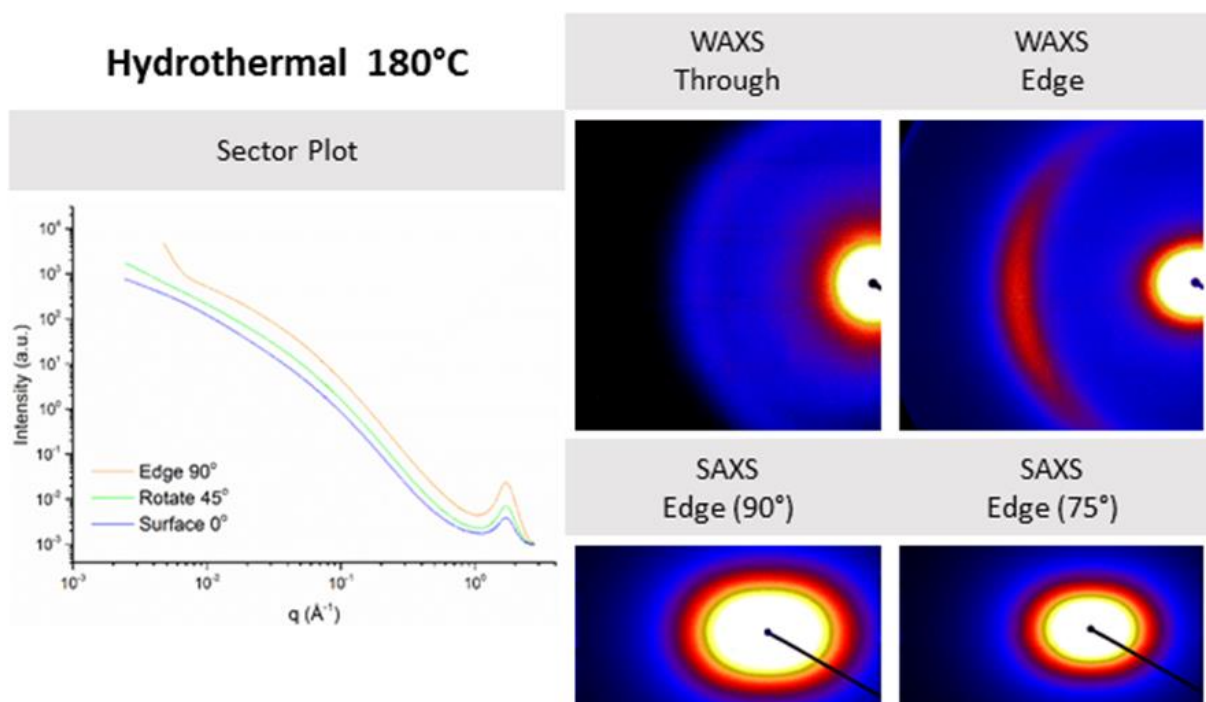


Figure 159. Sector plot of the horizontal region (across the (002) reflection) when the assembly is rotated through-the-edge (90°), at 45°, and through-the-surface (0°). The corresponding 90° and 0° WAXS patterns are shown above the SAXS patterns at 90° and smaller rotation to 75° for the hydrothermal rGO assembly.

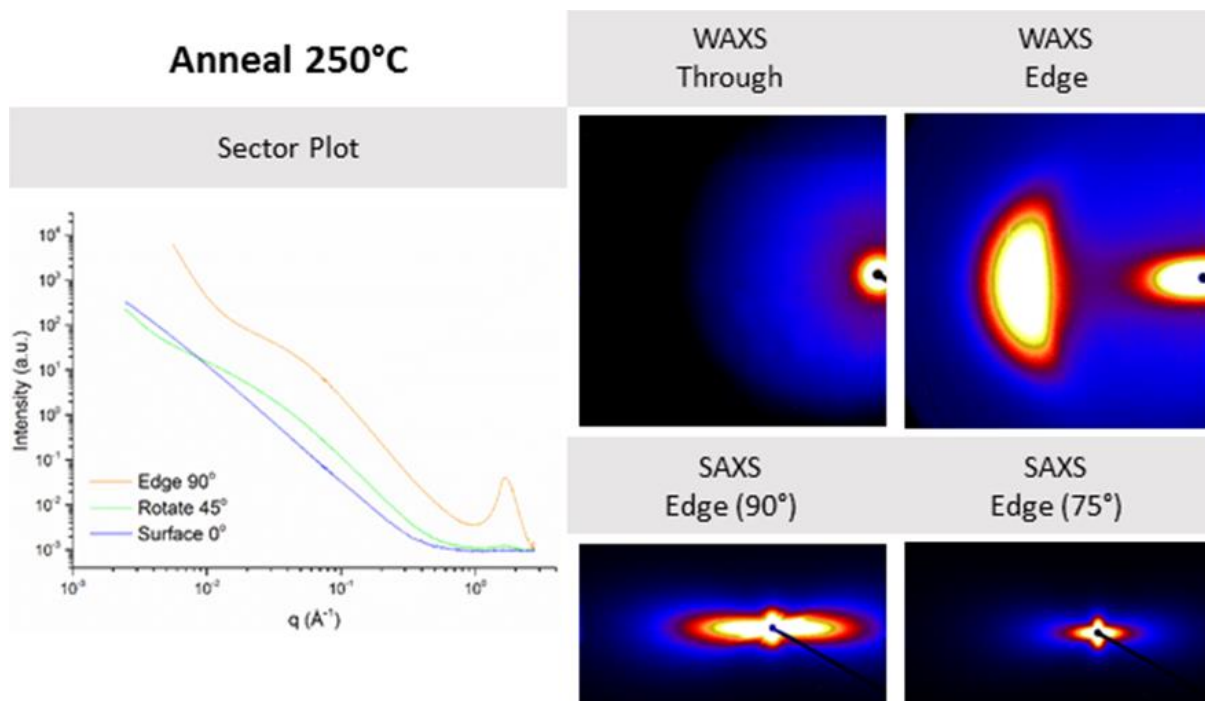


Figure 160. Sector plot of the horizontal region (across the (002) reflection) when the assembly is rotated through-the-edge (90°), at 45°, and through-the-surface (0°). The corresponding 90° and 0° WAXS patterns are shown above the SAXS patterns at 90° smaller rotation to 75° for the annealed rGO assembly.

The (002) coherence domains from the WAXS patterns were evaluated using the same procedures discussed in the results for the SAED from TEM and the aromaticity evaluation from XRD. The horizontal sector was used to acquire a peak profile for the (002) reflection, which was then fit in order to obtain: i) a general comparison of the shape and maximum intensity of the peaks (prevalence of restacked clusters), ii) the π -band peak centre (stacking distance within the turbostratic coherence domains), iii) the FWHM of the π -band contribution (average length of the coherence domains), and iv) the relative contributions from the π -band and γ -band (aromaticity). These general features are shown in Figure 161, where there is a clear difference in both the shape and intensity of the peaks that underwent heat treatment, compared to those reduced under typical 100°C conditions without further annealing. All of the low-temperature assemblies have the characteristic γ -band indicating oxygen groups are present and contributing to the diffraction peaks of the (002) coherence domains. These bands are absent in the heat treated assemblies, indicating many more oxygen groups have been removed, as discussed in the Literature Review and Chapter 4.

The annealed assembly has a much higher scattered intensity than the other rGO assemblies. While the scattering is not on an absolute scale, the same amount of material is irradiated by the beam for all samples tested, so differences in intensity are related to the amount of material scattering at that q -range. This indicates there are more restacked clusters in the annealed material, as presumed by previous work where a decrease of capacitance was correlated with more pronounced (002) peaks measured by XRD [20]. There are also other pronounced differences that appear in the WAXS results after annealing the pump dried material at 250°C, which have not been reported before. There is a pronounced shift in the main (002) band accompanied by the characteristic skew commonly seen in graphitic materials. Accompanying this is a small, sharp peak (indicated with arrow) at a Bragg spacing of 3.34 Å, which demonstrates that some small regions have begun to graphitize at these temperatures. This would be expected for graphitizable carbons since 200°C to 250°C is the Wigner energy release peak for defects in graphite, where it has been shown the sheet defects can recombine resulting in increased crystallinity and reduced strain within the bulk material [303-305].

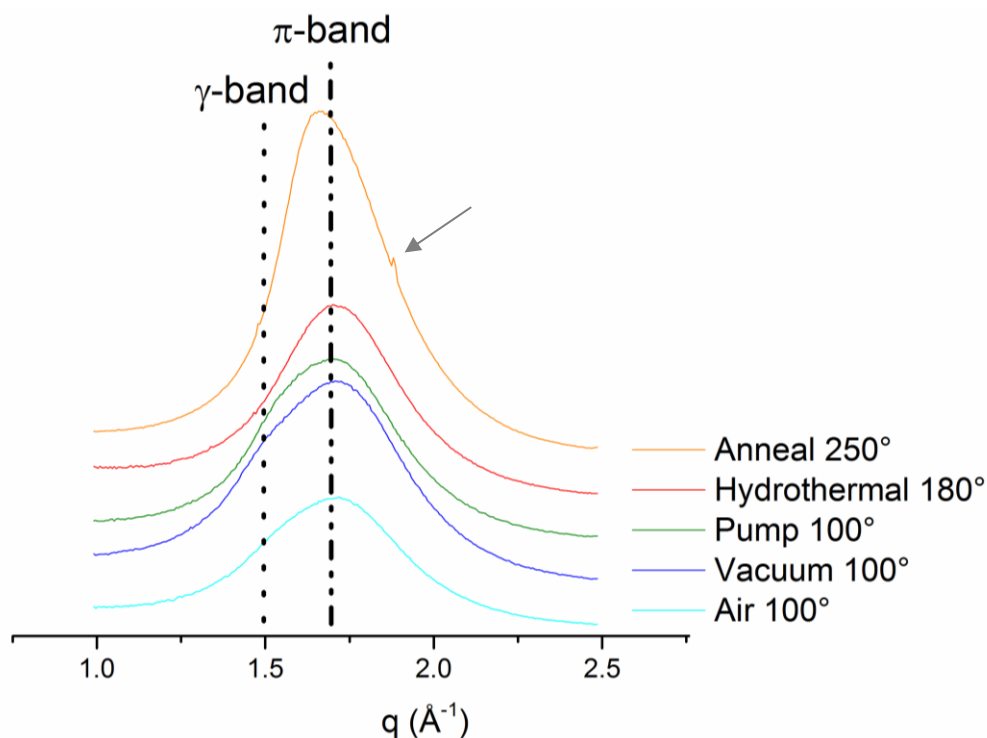


Figure 161. Comparison of the (002) peak profiles for rGO assemblies that underwent heat treatment (annealing or hydrothermal) or various drying conditions (pump, vacuum, or air). The π -band and γ -band components are indicated by the dotted lines and the small arrow highlights the emergence of a graphitic peak in the annealed assembly.

The aromaticity of the 100°C rGO assemblies was 93%, a value between the LOH (89%) and LOX (100%) samples tested with XRD in Chapter 5, as would be expected with the LOD-GO processing conditions. This correlates well with the expected oxidation trend for these materials. To obtain the other parameters of interest, the FWHM for each π -band was used in the Scherrer equation to calculate the coherence length along the c-axis, L_c , and the average number of graphene layers as determined by dividing L_c by the average interlayer spacing. Finally, a measure of the azimuthal intensity spread across the (002) peak was taken as a measure of the alignment of the coherence domains along the layer plane. These values are shown in Table 20.

For the SAXS analysis of the pore network and cluster aggregates, the slope of the linear Porod region for the through-the-surface curves was compared within the low-to-mid q -range of 0.002 \AA^{-1} to 0.05 \AA^{-1} . The through-the-surface fit for the hydrothermal sample is not included because there is no clear linear region in the curve, indicating the high degree of corrugation and misorientation makes the mid- q aggregate feature prevalent across all rotations. The PT model developed for the pump dried rGO was applied to the other assemblies for comparison of cluster size and sheet roughness.

Table 20. Structural parameters evaluated directly from the Bragg peak taken from WAXS curves for the rGO assemblies as measured through-the-edge along the (002) peak profile.

	Anneal 250°C	Hydrothermal 180°C	Pump Dry 100°C	Vacuum Dry 100°C	Air Dry 100°C
d_{002} (nm)	0.379	0.366	0.368	0.365	0.365
L_c (nm)	3.18	2.78	2.59	2.56	2.59
N_{layers}	8-9	7-8	7	7	7

Table 21. Structural parameters evaluated using SASfit software to fit the combined SAXS and WAXS reduced scattering curves of the rGO assemblies with a fractal or paracrystalline model, as measured through surface or edge, as indicated.

Sample	Through-the-Surface	Through-the-edge							
		Surface Fractal		Fractal Aggregate		Paracrystalline Structure			
	α	c	α	c	α	N	D	Δ	N _{diff}
Pump Dry	2.5	1.2(10 ⁻⁶)	3.7	2.5(10 ⁻³)	1.4	8.5	3.6 Å	0.49	0.4
Vacuum Dry	2.3	2.7(10 ⁻¹¹)	7.0	3.3(10 ⁻³)	1.5	8.5	3.6 Å	0.55	0.5
Air Dry	2.2	1.8(10 ⁻⁵)	3.4	1.3(10 ⁻³)	1.8	6.8	3.6 Å	0.47	1.0
Hydrothermal	N/A	4.6(10 ⁻⁷)	4.3	2.8(10 ⁻³)	1.9	6.0	3.6 Å	0.41	1.1
Annealed	2.5	2.6(10 ⁻⁷)	4.6	3.9(10 ⁻³)	1.4	8.5	3.6 Å	0.39	0.2

The results in Table 21 show the differences between the drying methods for the through-the-surface curves, as well as the through-the-edge curves. The α value for the through-the-surface fit indicates that values closer to two have more disordered aggregates, which is likely due to a more porous structure, while values closer to three indicate a greater order within the rGO layers which likely results in a greater number of cluster aggregates. The surface fractal region for through-the-edge scattering gives α values higher than 4, indicating there is multiple scattering resulting from these features [175]. The fractal aggregates are also instructive in probing the structural differences in the materials, where values closer to one are typical of more aligned material, while values closer to two are seen in those with more disorder (larger OA). This would be expected, as the scattering from perfectly aligned edges would result in an α value of one [175]. The PT model produces results quite similar to that from the Scherrer equation alone, and the Δ term shows there is a relatively small deviation in the stacking distance within the turbostratic clusters themselves. The disorder surrounding the clusters produces the accessible surface area and porosity, with the most useful term gained from applying the PT model being N_{diff}, which accounts for an additional diffuse background resulting from a number of uncorrelated scattering bilayers. This term indicates there is a much larger contribution from disordered stacking in the hydrothermal and air dried assemblies, which would result in more overall porosity.

Combining this information on the overall structural elements leads to the diagram in Figure 162. The reduced through-the-edge scattering curves, and the shape of the SAXS and WAXS patterns are used to design a physical representation of how these elements combine within the bulk assemblies. Within the coherent domains of turbostratic clusters (shown in green), the interlayer space, $d_{(002)}$, shows up with maximum intensity of the Bragg peak, while the overall, average orientation of these stacks is described by the angular spread (OA). Over longer distances, the larger volumes within the assembly (shown in the overall box and grey bracket) contribute to the small angle scattering as a measure of the overall order of the clusters themselves and the porous space surrounding them. Stacks with smaller dimensions (fewer rGO layers) will diminish the intensity and broaden the Bragg peak while also extending/broadening the SAS hump resulting from the cluster aggregates. Loose stacking leads to more disorder among the rGO layers, smaller cluster sizes, and more surrounding porosity. The pink line shows how L_a is measured with Raman, where any slight deviation in symmetry (corrugation, oxygen group, vacancy, etc.) will act as a defect and limit the size of the aromatic domain measurement. Thus, the annealed rGO will have a longer L_a measured by Raman because there are fewer oxygen groups present (as in LOX). The blue line represents how L_a is measured with XRD, where the longer range periodicity of the intrasheet carbon-carbon bond lengths is not as sensitive to defect detection, with the long, relatively intact rGO sheets containing comparatively long (hk) coherence domains. This

is useful information, as it shows this combination of experimental methods can distinguish between structural features related to periodicity and phonon effects. Again, the annealed rGO will have a longer L_a measured by XRD, but this is now because there is a higher degree of order and reduced corrugation along the sheets with the reduction of defects that have recombined to increase crystallinity and reduce strain within the bulk.

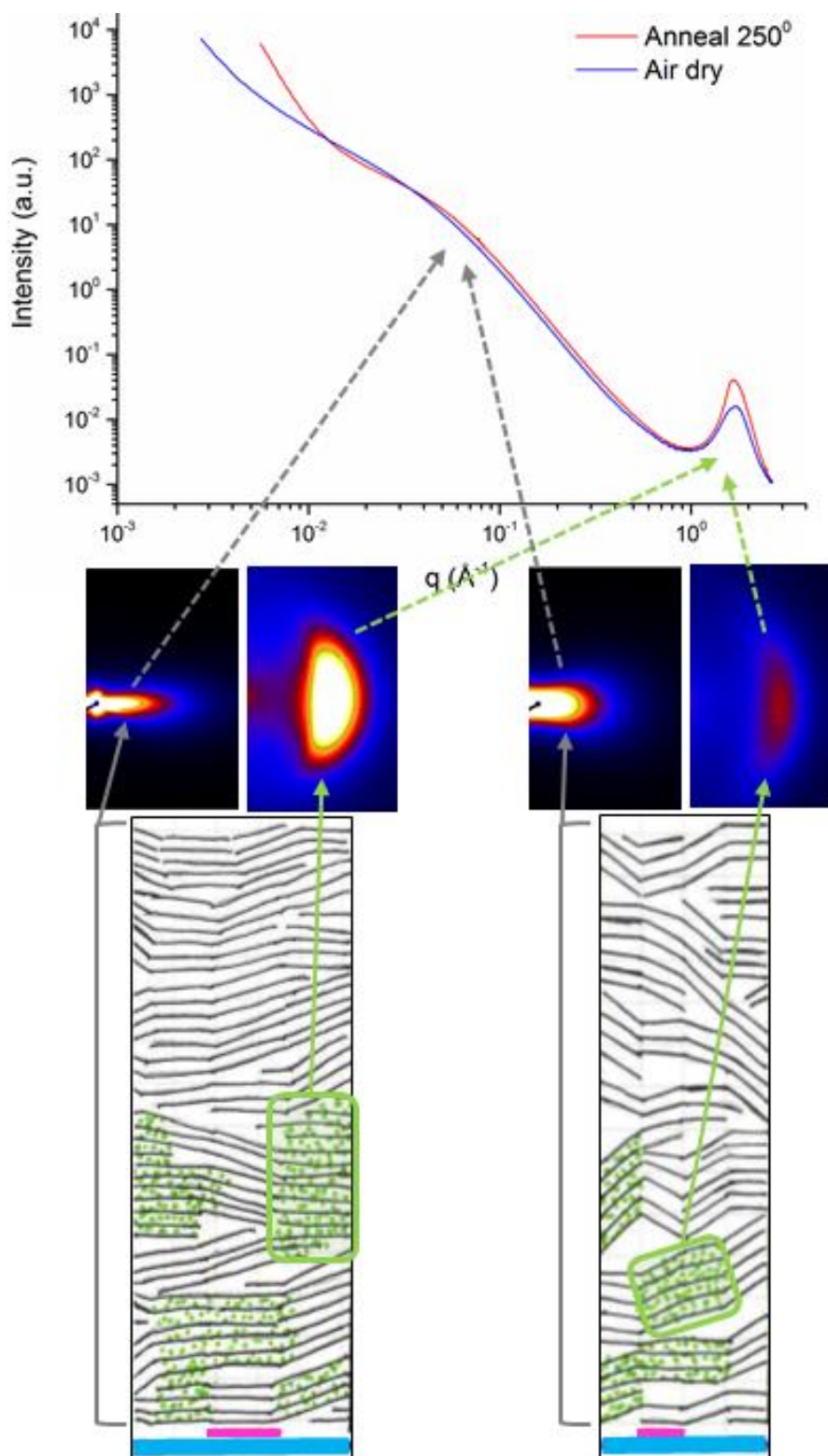


Figure 162. The reduced through edge scattering curves and shape of the SAXS and WAXS patterns (top) are used to design a structural diagram of ordered and disordered domains within the annealed and air dried assemblies (bottom), indicating how these structural elements can impact the pore network surrounding these turbostratic clusters. The grey brackets and arrows highlight that the larger volumes within the assembly contribute to the small angle scattering, and these regions consist of both open pore space and also the coherent domains of turbostratic clusters, as indicated in green. The interlayer space, $d_{(002)}$, within the clusters is the source of the wide-angle peak (green arrows). The pink line shows how L_a is measured with Raman and the blue line represents how L_a is measured with XRD.

6.3.2.3 Oxidation level

The differences in the Bragg peak features and L_c for the oxidation series has been presented in detail within Chapter 5. This section focuses on identifying if these structural changes carry over to SAS results. As shown in Figure 163, the density and aromaticity differences are not detectable at the meso- and macroscale when looking at density fluctuations along the ab-plane in the through-the-surface scattering curves. This shows that the chemical differences act almost exclusively on the micro-scale, and will mostly influence material properties related to conductivity, reactivity, and the ability to functionalize the remaining oxygen groups. These micro-scale differences do not impact the larger structural features in the assemblies, except in the case of LOX where it has been shown there is a slight increase in the number of stacked layers. This difference is visible only very weakly in the Porod slope, where there is an increase in the fractal dimension from 2.6 to 2.7 (listed in Table 22), indicating a loss of accessible surface area as this space is more uniformly filled. This finding is important because it suggests it is possible to tune the chemical functionalities while holding the physical structure rather constant.

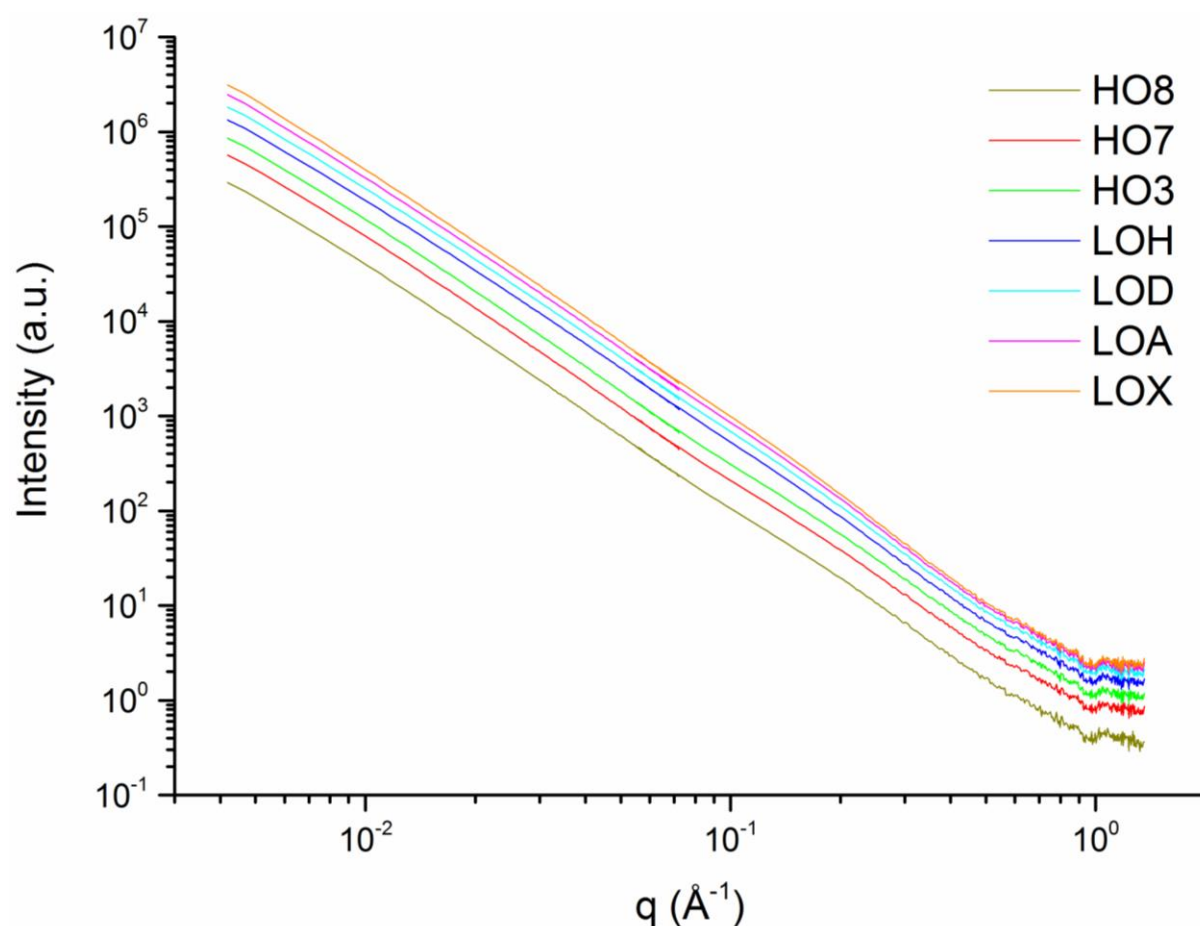


Figure 163. Plot of the through-the-surface combined WAXS and SAXS results for pump dried rGO assemblies of varied oxidation level. Curves are offset for clarity with arbitrary intensity values.

Table 22. Fit of the Porod region for through-the-surface SAXS results for rGO assemblies of varied oxidation level

Sample	HO8	HO7	HO3	LOH	LOD	LOA	LOX
α	-2.6	-2.6	-2.6	-2.5	-2.6	-2.6	-2.7

6.3.2.4 Electrolyte-mediated-rGO

This section compares the scattering results of EM-rGO materials in order to determine what effects the additional processing step of incorporating non-volatile liquid (sulfuric acid) into the assembly before it is dried has on the resulting pore structure. The EM-rGO assemblies were tested as-prepared (freeze-dried with the sulfuric acid still within the layers), after-washing (removing the acid and soaking in water before allowing to air dry), and as hydrated films (after washing and keeping hydrated for 24 hours). The as-prepared and after-washing materials help assess the impact of processing conditions on the bulk assembly, while the hydrogel results best represent what the structure is like within an actual device, as the EM-rGO materials are used as supercapacitor electrodes while in a hydrated state. All assemblies shown here were prepared with HO3 and HO4 GO precursors, with no measureable difference observed between the two. Thus, they are referred to only as EM-rGO without reference to the slight difference in oxidation.

Similar to the optical images presented earlier in this chapter, it was first necessary to determine if the structure of EM-rGO assemblies was homogeneous. Figure 164 compares the surface scattering patterns of 2.0 M (top) and 0.1 M (bottom) EM-rGO assemblies. It is clear that there are distinct structural features present within the 2.0 M EM-rGO, resulting in an inhomogeneous structure, as seen in the optical images. Comparatively, the 0.1 M EM-rGO did not show any variance and indicates that sulfuric acid is uniformly distributed and/or does not have detrimental impacts on the surface of the rGO sheets.

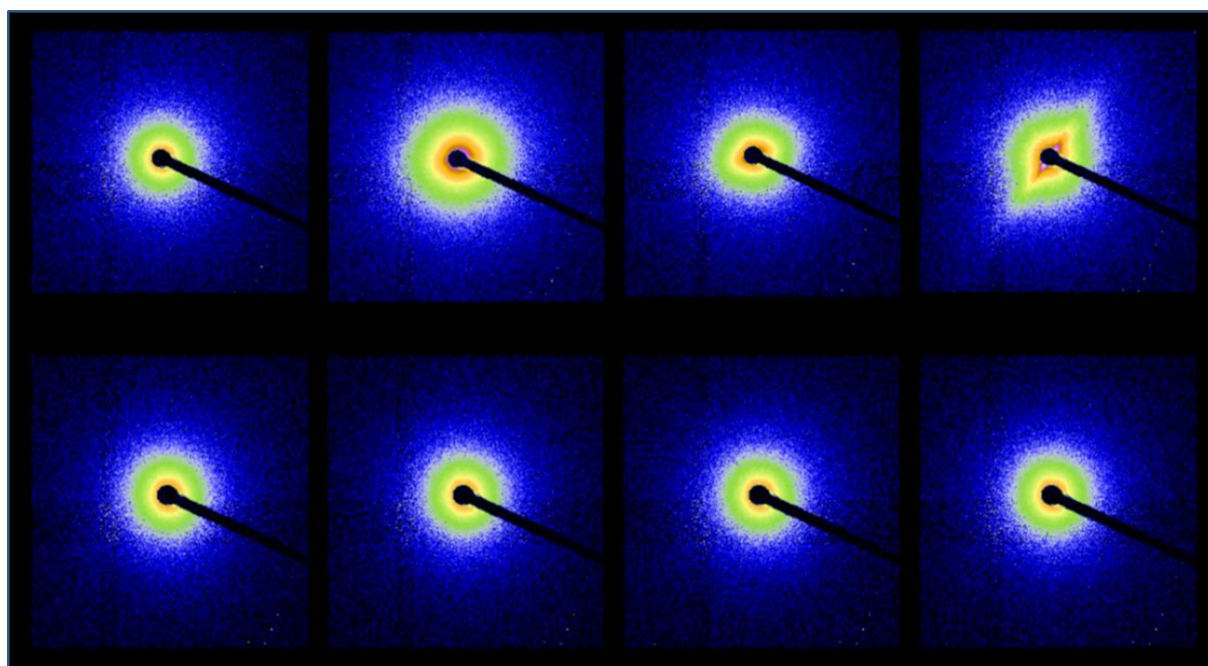


Figure 164. SAXS results for as-prepared EM-rGO assemblies taken at different locations along the surface of 2.0 M (top) and 0.1 M (bottom) samples.

As the EM-rGOs undergo a freeze drying process, comparing the impact of this drying method on rGO assemblies without any intercalated acid, to that of the after-washing EM-rGO (no sulfuric acid is contributing to the scattering pattern) and rGO assemblies dried under vacuum, but without freezing, can provide insight on what features are a result of the drying method and what is directly related to the incorporation of the EM-rGO pore-tuning process. Through edge SAXS patterns comparing these conditions are shown in Figure 165 at different rotations, and are also compared with the annealed rGO because it has the most oriented, and least porous, carbon matrix.

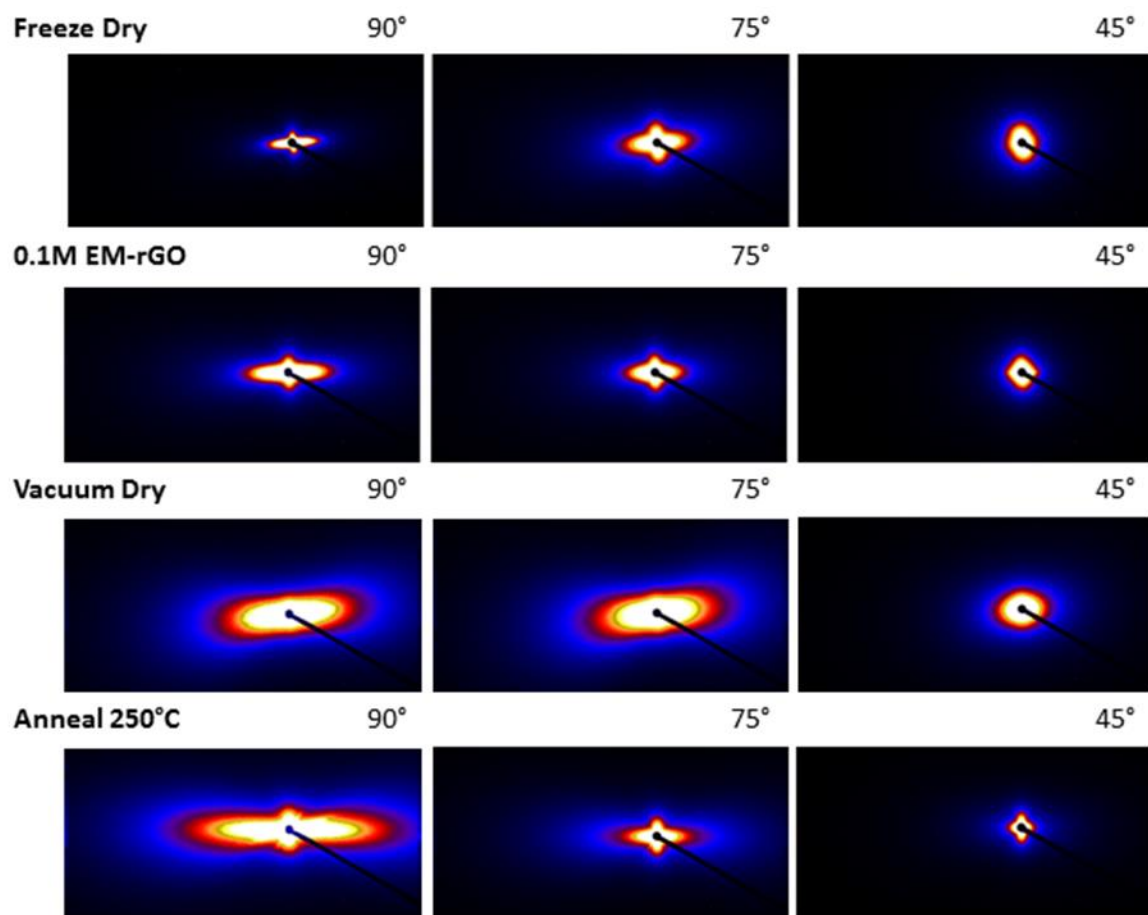


Figure 165. Comparison of through edge SAXS patterns of the freeze dried method (with and without pre-treatment of 0.1 M sulfuric acid) to other drying methods which produced more aligned rGO sheets.

From the scattering results, it can be seen that both the freeze drying process and the incorporation of sulfuric acid impact the pore structure within the rGO assemblies. The freeze drying process produces a highly aligned SAXS pattern, with a very pronounced cross shape, the intensity concentrated almost exclusively at smaller angles (closer to the beam stop). The vacuum dried assembly has a much more distributed scattering pattern, indicating more distribution of sizes, and the much broader SAXS pattern, especially in the 75° rotation, is representative of broader pore features with more disorder and larger PSD along the ab-plane. Compared to the annealed rGO, the freeze drying process seems to preserve the high degree of order present (evidenced by the retention of features throughout the rotation curves), but the ac-plane scattering does not extend as far into wide angles.

A comparison of the SAXS patterns for hydrated EM-rGO assemblies is shown in Figure 166. It is clear that the defined pore structure is retained after the materials are washed and rehydrated, with the assemblies tuned with sulfuric acid of concentration 1.0 M or less having very distinct scattering patterns. These differences would not be noticed if only scattering through-the-surface were measured, as the distinct cross and fan shaped patterns only appear at angles greater than 45°. The 45° pattern is very interesting in itself, as the symmetrical shape of the 0.1 M and 0.5 M materials show the pore structure is quite similar in the ab-plane and the ac-plane, suggesting the pores have a more defined morphology both between and along the rGO sheets. As the concentration of acid is increased, more surface area within the assembly is expected to remain accessible, as the intercalated acid produces regions that resist restacking of the rGO sheets. This is clearly evident in the 1.0 M and 5.0 M patterns, where the scattering is elongated and fan-shaped, indicating expansion between the layers is more prevalent and there are wider slits/pores between the rGO sheets.

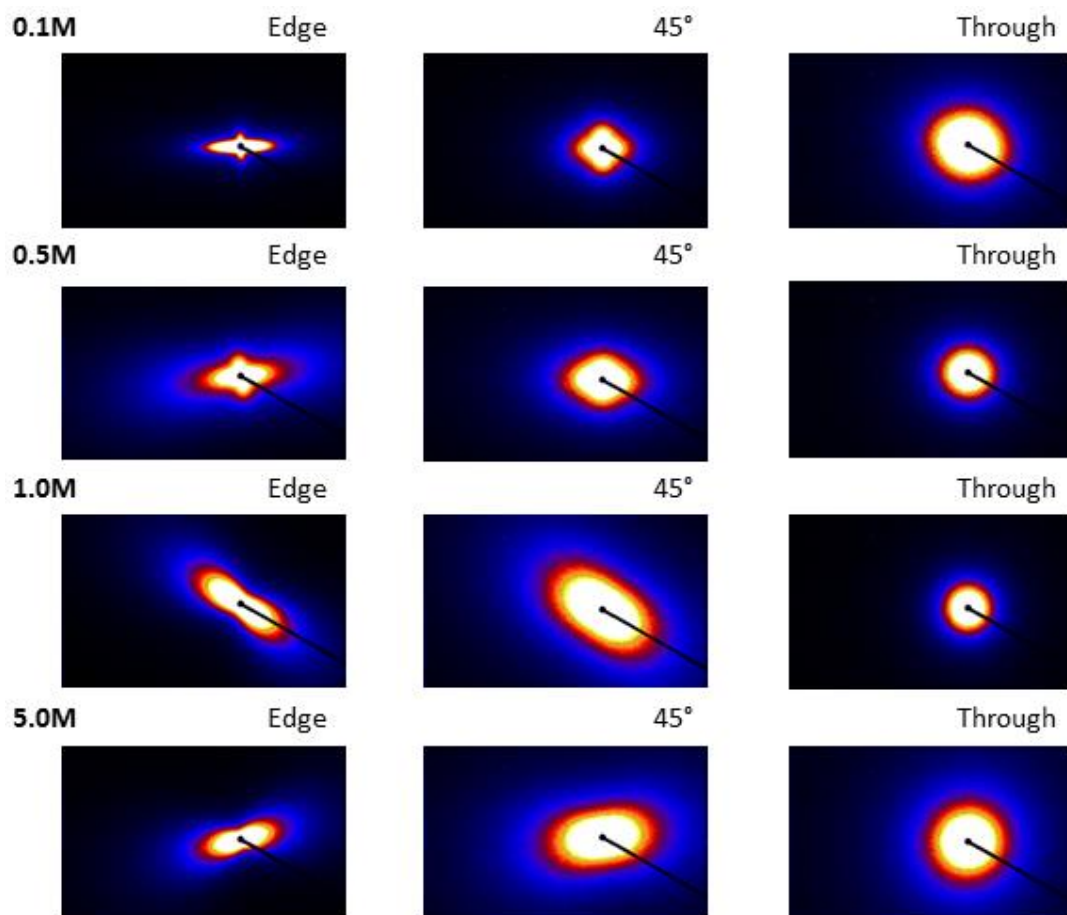


Figure 166. Comparison of through-the-edge SAXS patterns for hydrated EM-rGOs prepared with different concentrations of sulfuric acid at 90° (edge), 45°, and 0°(surface).

The WAXS patterns of Figure 167 are adjusted to show the same intensity range across all the images. There is a high degree of order present in the EM-rGO materials, exhibiting the well-defined (002) peak similar to that seen in pump dried assemblies. The alignment (OA) of the 1.0 M, 0.5 M, and 0.1 M Bragg peak is rather constant, but the intensity diminishes with higher sulfuric acid concentrations, indicating the amount of turbostratic clusters present in the bulk is reduced depending on how much acid is intercalated before drying. Correspondingly, the presence of fewer cluster aggregates would indicate there is more accessible surface area present in the assembly. It can also be seen that the EM-processing limits the amount of water within the rGO layers, as the scattering from water seen at high- q (along the Bragg peak and beyond) is most prevalent in the rGO hydrogel and 5.0 M EM-rGO, while remaining quite low in materials tuned with concentrations of 1.0 M or less.

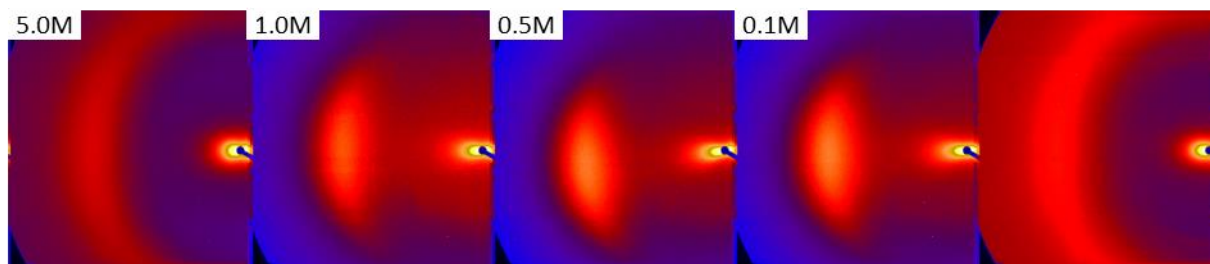


Figure 167. Through-the-edge WAXS patterns for hydrated EM-rGOs and a typical rGO hydrogel (far right) with identical intensity scaling. The intensity at the highest q -values (at and beyond the Bragg peak shown in diffuse red) is due to scattering from water.

The structure of water within rGO assemblies is interesting in its own right, and it can also be a very useful tool in investigating the structure and accessible surface area within rGO assemblies. With the hydrated assemblies, the scattering interface is between the rGO sheets and water, compared to the dried assemblies where there is scattering between the rGO sheets and air. As seen in the results presented with the dried materials, the small pore features can be overshadowed by the larger turbostratic agglomerates, making it difficult to discern what elements of the scattering result from the small pores and which result from the density fluctuations within the carbon matrix. In the hydrated materials, the easily-detected water background (measured directly from the intensity differences at high- q , see the features at $q=1 \text{ \AA}^{-1}$ and $q=3 \text{ \AA}^{-1}$) can be used as a direct measure of how much of the liquid is incorporated within the assembly, equating with the accessible surface and total pore volume. Figure 168 shows the structural elements of the carbon matrix and water are discernible in the reduced through-the-edge WAXS patterns from Figure 167. The high background at maximum- q is a result of bulk water, as scattering from water alone exhibits the double feature broad peak at a q -value just above that of the (002) rGO peak, as expected from the typical ambient water peak shape presented in Figure 145.

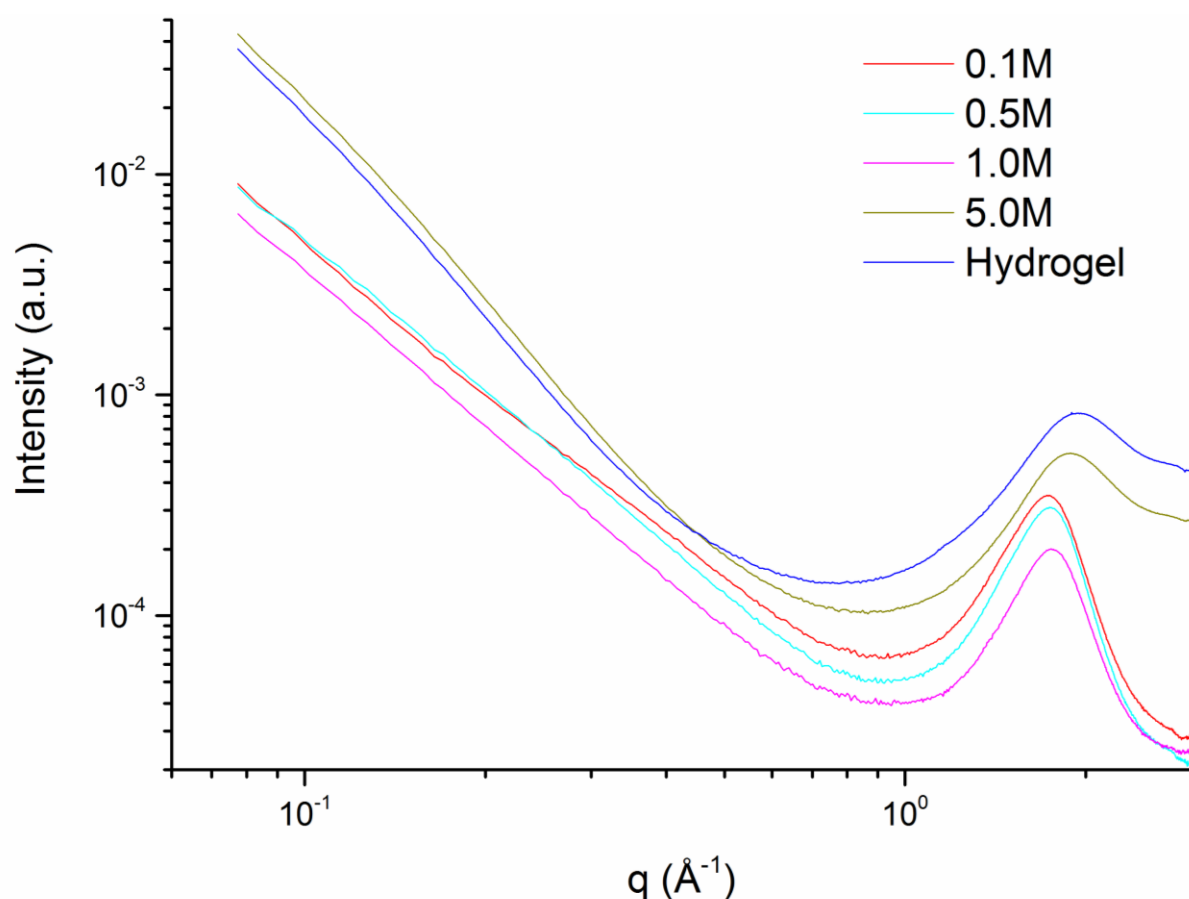


Figure 168. Reduced through-the-edge WAXS patterns for the EM-rGO materials tuned with different amounts of sulfuric acid as compared to a hydrogel assembly without modification.

From Figure 168, bulk water is clearly present in the 5.0 M and in the hydrogel assemblies. The lack of a measureable feature from bulk water in the 1.0 M, 0.5 M, and 0.1 M scattering curves is quite significant and will be a focus of future work, to be discussed in the Chapter 7. While the bulk water peaks are absent, the amount of water within the assembly can be directly calculated from the background scattering, and the relative difference between samples can be determined by the intensity values at $q \approx 1 \text{ \AA}^{-1}$. A full analysis with all data measured in absolute intensity is also a focus of future work, but the current results show the volume of water within each assembly scales directly

with the concentration of acid used to tune the pore network, and the amount of acid left within the materials after freeze drying will determine the volume of water within the washed, hydrated EM-rGO assemblies.

The onset of the scattering just below the Bragg peak coming from structural elements of a larger size (at onset of the typical ‘small-angle’ region below $q \approx 1 \text{ \AA}^{-1}$), occurs at approximately the same q -value for all EM-rGO materials ($0.7\text{-}0.8 \text{ \AA}^{-1}$), indicating the features are again due to the restacked clusters with fluctuations ranging all the way down to the initial interlayer distance between the rGO sheets. The PT model was applied to the WAXS results for the EM-rGO assemblies and the results are shown in Table 23. There is a slight decrease in the number of rGO layers making up the restacked clusters, but overall this value remains consistent for materials tuned with a sulfuric acid concentration of 1.0 M or below. The α values are also very similar for the 0.1 M, 0.5 M, and 1.0 M materials and the fan pattern observed in the small angle region of the images in Figure 167 are characteristic of slit-like pores between the rGO sheets, with the 1.0 M sample having a slightly wider distribution which is indicative of longer slits. In contrast, the specific features of the clusters cannot be obtained from the 5.0 M and hydrogel assemblies because that region of the curve is dominated by scattering from the bulk water. However, the WAXS images show there is some amount of turbostratic alignment present, as slight intensity differences are detectable across the ring for the mixed water and carbon (002) peak profile. The lack of any defined (002) feature shows there is a much smaller amount of restacking of the rGO sheets within the hydrogel materials and EM-rGO tuned with a high concentration of sulfuric acid. Further, a comparison of the α values for the hydrated assemblies in Table 23 to the dried ones in Table 21, follow the proposed trend of larger values for more porous materials.

Table 23. Structural parameters evaluated from WAXS of the EM-rGO assemblies as measured through-the-edge along the (002) peak profile.

	0.1 M	0.5 M	1.0 M	5.0 M	Hydrogel
d_{002} (nm)	0.367	0.365	0.359	Dominated by bulk water	
L_c (nm)	2.47	2.17	2.25		
N_{layers}	7	6	7		
α	2.28	2.25	2.34	3.07	3.07

To see how the structure differs within the pore network along the surface of rGO sheets, features of a through-the-surface scattering curve are compared to those resulting from the through-the-edge scattering reported above. The curves in Figure 169 are also quite interesting, as they demonstrate how the amount of bulk water is quite different in the ab - and ac -planes. Because the through surface scattering is thinner, the scattering curve is of lower intensity, as is was with all the dried assemblies presented previously. However, a pronounced difference is seen at high- q , where the bulk water feature is clearly visible, indicating water is present in bulk-form within the long, slit-shaped pore network which extends along the ab -plane, and is not detected in the ac -plane. The small, sharp peak at $q \approx 2.1 \text{ \AA}^{-1}$ is the (hk) carbon-carbon peak.

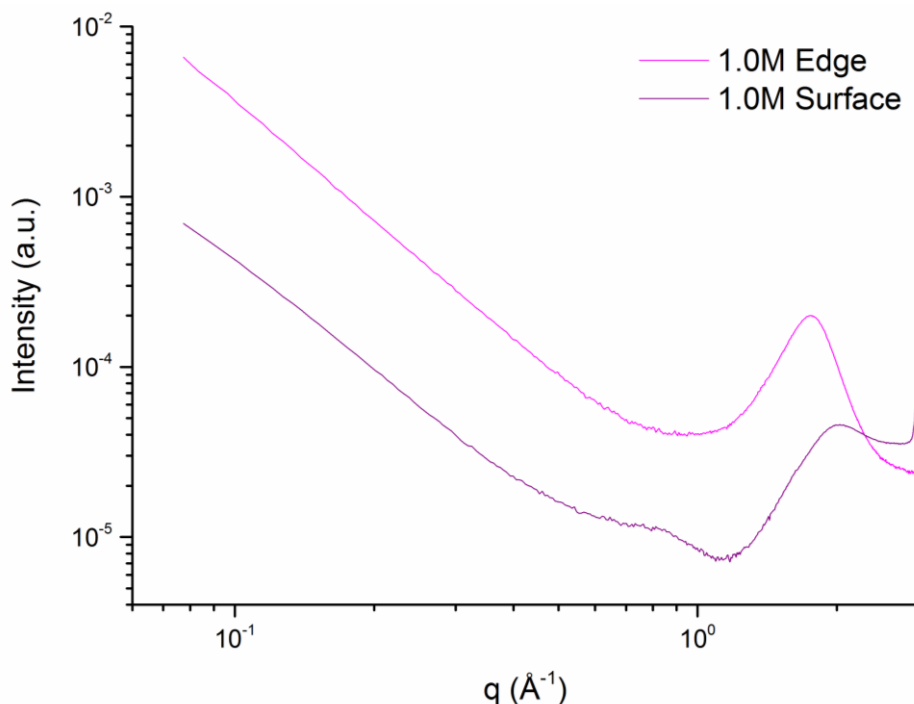


Figure 169. Comparison of the through-the-edge and through-the-surface WAXS results for 1.0 M EM-rGO.

Comparing the through-the-surface scattering curves for 1.0 M and 5.0 M EM-rGO assemblies shows that bulk water is present within the ab-plane for both samples, even though it was detected in the ac-plane for the 5.0 M assembly. Again, the (hk) carbon-carbon peak is observed, and the slope in the lower- q range of $0.08 \text{ \AA}^{-1} < q < 0.3 \text{ \AA}^{-1}$ is 2.15 for the 1.0 M sample and 2.28 for the 5.0 M sample. These values are slightly less than the more porous air dried assemblies reported previously, following the trend of a fractal dimension closer to 2 is related to more accessible surface area. The intensity is again directly related to the water content in the assembly, and this will be evaluated using detailed absolute scaling in the proposed future work discussed in Chapter 7, correlating the results to real-space features and total porosity of the materials.

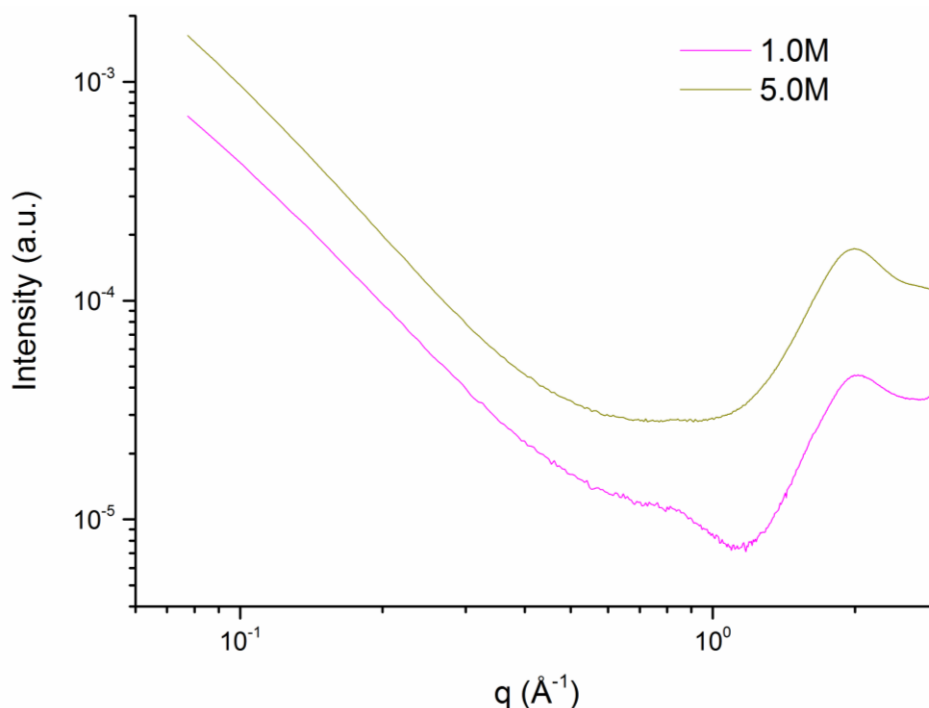


Figure 170. Through-the-surface scattering curves for 1.0 M and 5.0 M EM-rGO show the presence of bulk water at high- q .

6.3.2.5 Hydration level

A closer examination of the role of water in rGO assemblies has been investigated using *in situ* WAXS and SAXS to observe the structural changes that occur as the hydrogels are dried. The original hydrogel was prepared with the filtration method, but removed while fully hydrated and kept in water until testing. The hydrogel assemblies are very stable in water over long periods of time, indicating there are some restacked regions in the materials and/or a large amount of disorder which keep the individual rGO sheets together as an intact assembly.

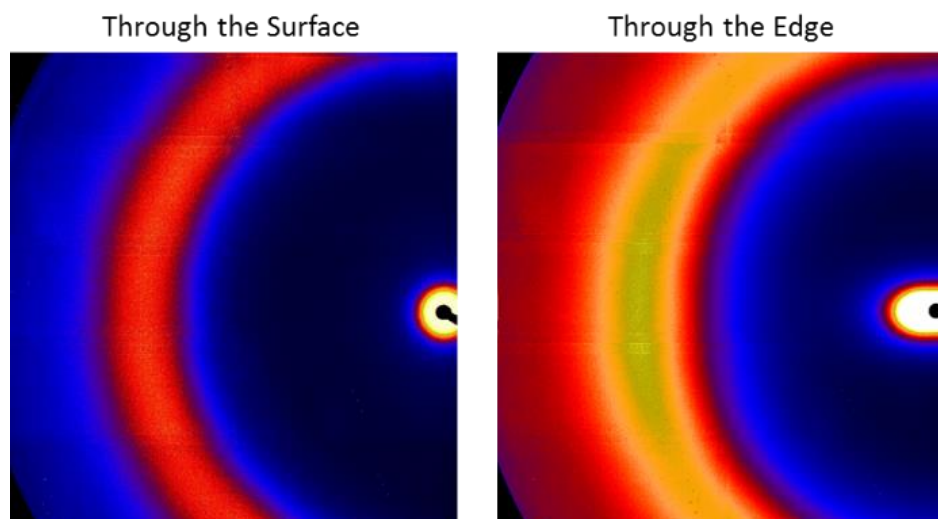


Figure 171. WAXS patterns for rGO hydrogels showing the peak for bulk water is present in both through-the-surface and through-the-edge images, where a faint (002) feature is visible in the latter.

Figure 171 shows the general WAXS features present in the rGO hydrogel materials. Again, the bulk water is clearly present in both the *ab*- and *ac*-plane. The faint (002) peak is detectable, indicating there are small turbostratic clusters consisting of a few rGO layers within the wet films, as well. The elongated small angle region of the through-the-edge pattern again indicates a slit-like expanded region between the rGO layers.

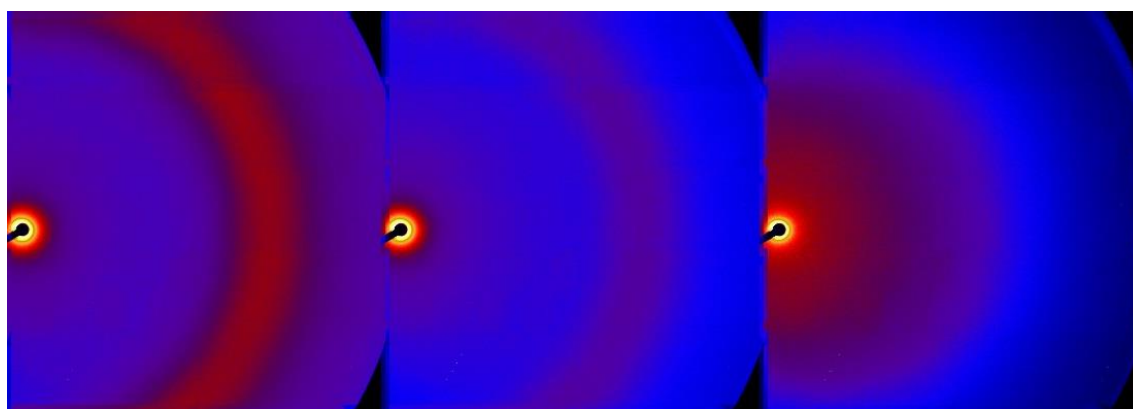


Figure 172. Through-the-surface *in situ* WAXS patterns for hydrogel assemblies from a fully wet to a fully dry state (left to right), with the intermediate structure undergoing a pronounced transition, as referenced in the text.

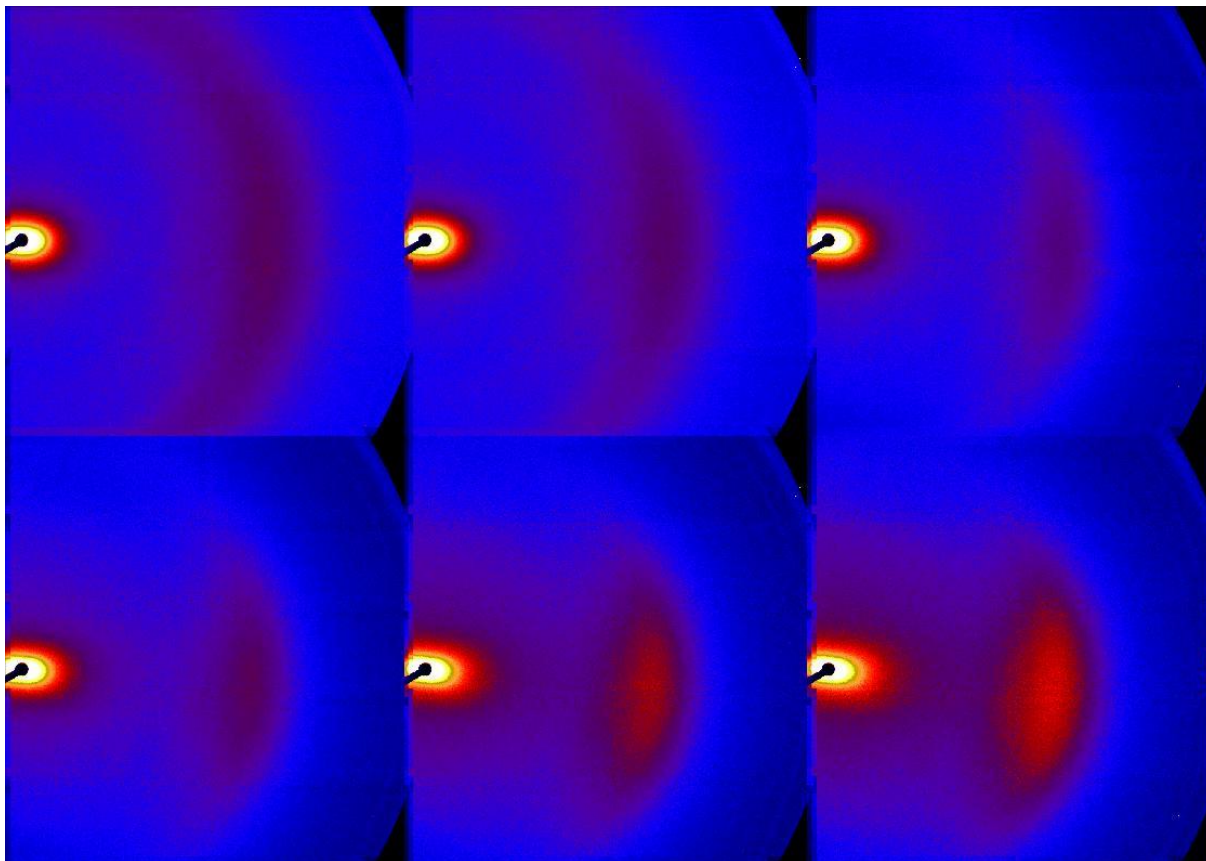


Figure 173. Through-the-edge *in situ* WAXS patterns for hydrogel assemblies from a fully wet to a fully dry state (top left to bottom right), with the intermediate structure undergoing a pronounced transition, as referenced in the text.

The hydrogel assembly was allowed to dry while collecting WAXS patterns every ten seconds. Data collection continued until there was no noticeable change in the scattering results, indicating the fully dried assembly reached steady state. The WAXS images shown in Figure 172 and Figure 173 have been adjusted to have equal intensity scaling, and show the main features detected in through-the-surface and through-the-edge scattering patterns as the material goes through a distinct transition. The structural states are more clearly represented in the reduced through-the-edge curves plotted in Figure 174. Here, it can be seen that the completely hydrated assemblies contain a large amount of bulk water, which is evident in the higher intensity black curves, where a small amount of water evaporates as time goes on. With a lower water content, a second lower intensity, broad feature at $q \approx 1.3 \text{ \AA}^{-1}$ emerges (indicated with arrow). Shortly following this, there is a pronounced decrease in the bulk water signal, and the (002) Bragg peak feature quickly becomes more pronounced (indicated with arrow at $q \approx 2.5 \text{ \AA}^{-1}$). This initial, collapsed state, is highlighted by the darkened black line. Looking at only the curves in black, it can be seen that up until this point, the slope at smaller angles is relatively constant, following a predictable and constant decrease in intensity which is directly related to the volume of water in the hydrated assembly. The high- q region also followed this trend until a critical drying point was reached and all bulk water was expelled from between the layers. This could be expected as the aromatic domains of the rGO sheets are highly hydrophobic, and water confined within small nano-pores would be quickly expelled from regions with strong surface forces dominating over the bulk.

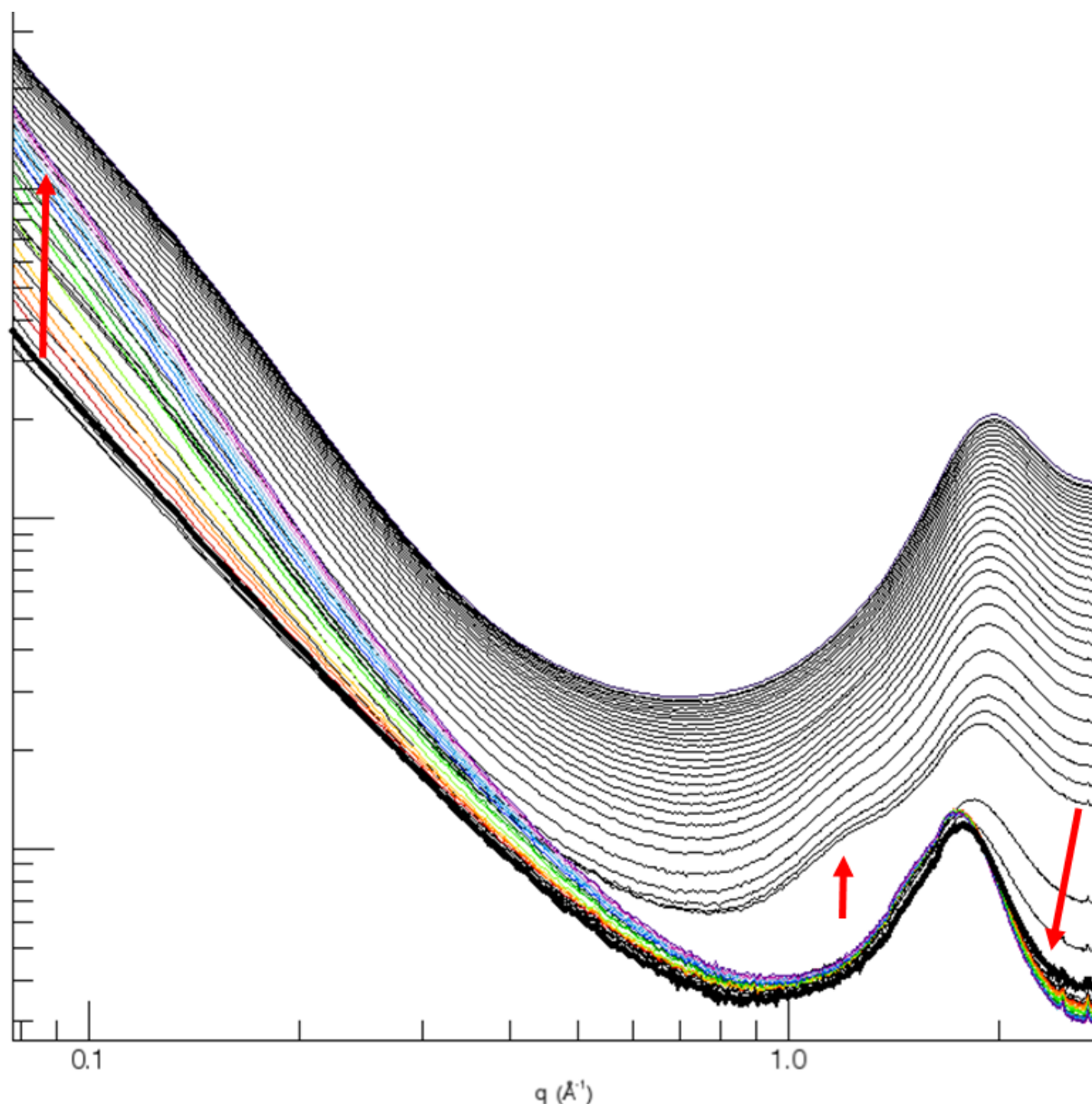


Figure 174. Reduced horizontal sector for the through-the-edge WAXS results of an rGO hydrogel as it goes from a completely hydrated ($V_{\text{rGO}}:V_{\text{H}_2\text{O}}$ of 1:20) (top, black curves) to a completely dry ($V_{\text{rGO}}:V_{\text{H}_2\text{O}}$ of 1:0.05) (lower, rainbow curves) state. The arrows indicate the major structural changes that are discussed in the text.

After the drying point is reached at the final black curve shown in bold, the Bragg peak feature stays relatively constant, while a pronounced change occurs in the lower- q region (shown with arrow along the rainbow coloured curves). Again, interpreting these features as part of the paracrystalline lamellar aggregates, the FWHM of the (002) peak is a measure of how many layers make up each cluster while the growing broad peak at lower- q is a measure of the aggregate form itself. While there is a slight narrowing of the (002) peak, no measureable difference is detected in L_c , which remains at a value of 2.2 nm, corresponding to a stacking of six rGO layers (after applying the Scherrer equation). This leads to the conclusion that as the water is removed from the rGO layers, there is a point where the structure collapses to form aggregates of about 6 rGO layers, yet much of the extended pore network is still preserved in this state. As the residual adsorbed water is removed, the aggregated clusters do not grow in size, but they do become more numerous. This is the cause of the increased slope within the higher- q SAS region (area indicated by dotted lines in Figure 148).

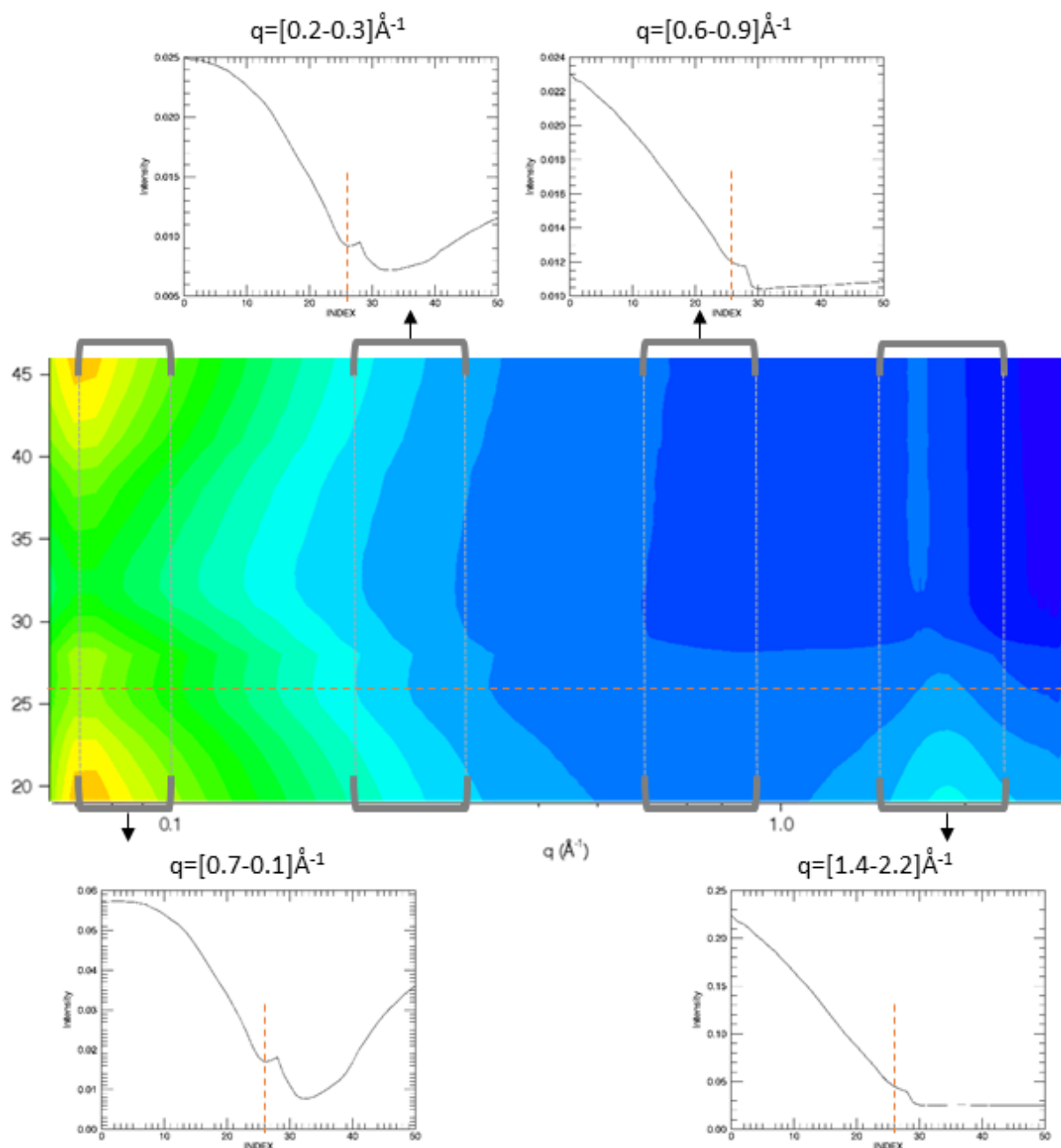


Figure 175. Plot of the reduced *in situ* hydrogel curves from Figure 174 with the number index on the y-axis and the colours corresponding to the relative intensity (orange highest, dark blue lowest). The insets correspond with q -ranges of interest discussed in the text (shown with grey brackets and black arrows pointing to the q -range indicated), with orange dashed lines corresponding to the index number where a pronounced shift occurs.

Looking specifically at the region where the bulk water is expelled from the network, Figure 175 shows a contour plot where the peak from bulk water diminishes and the (002) Bragg peak emerges. Specific q -ranges were chosen and the insets of the regions shown in grey clearly mark where pronounced changes in intensity occur. In all q -regions chosen on the graph, the change occurs at index number 26 and continues through to number 30. After this point, the intensity is constant within the high- q region and starts to increase in the low- q region. This again supports the claim that the additional scattering comes from larger structures in the rGO assemblies, while the individual turbostratic clusters have a constant interlayer distance and stacking height.

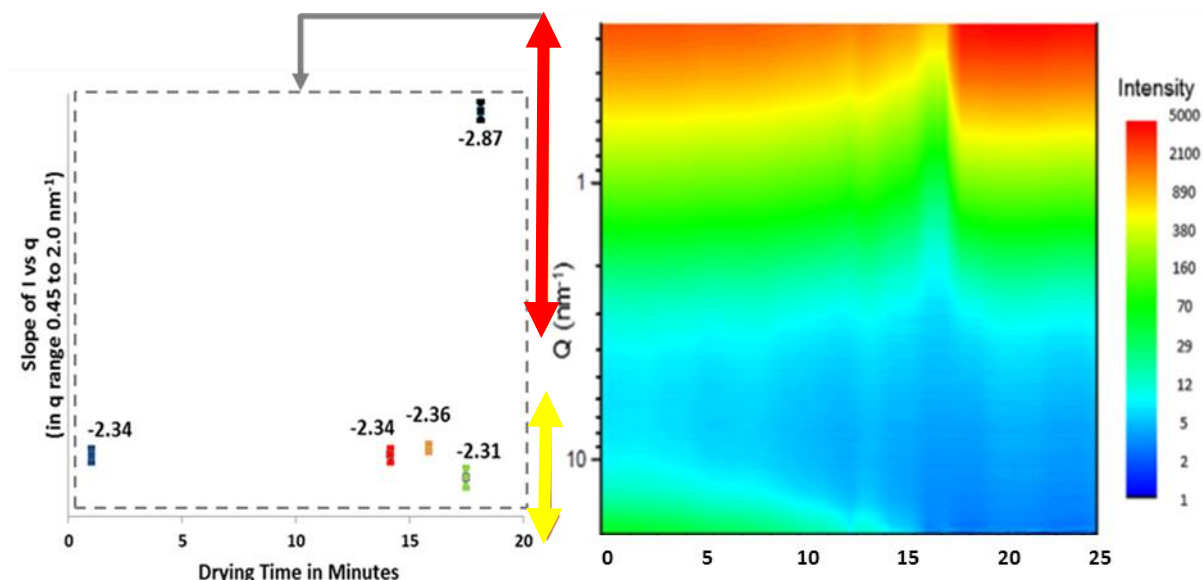


Figure 176. Reduced through-the-surface SAXS results for an rGO hydrogel as it goes from a completely hydrated (drying time of zero) to a completely dry (drying time >18 minutes) state with the slope of the low-q SAS range (red arrow) plotted to show the transition over time (on left).

The through-the-surface reduced SAXS curves are shown in a contour plot in Figure 176, in this case with the drying time (in minutes) given on the horizontal axis and q (in nm^{-1}) referenced on the vertical axis. The slope of the reduced scattering curves at smaller angles (indicated by the range of the red arrow) is plotted to the left of the contour plot to highlight the abrupt structural change discussed here. In this data, the same decreased intensity at high- q can be seen as the bulk water evaporates from the assembly (indicated with the range of the yellow arrow), and the pronounced shift in slope at lower- q (indicated with range of the red arrow) has the same pattern of holding steady at -2.3 for the entire time bulk water is present and then quickly decreasing slightly before abruptly increasing to -2.87, a value much closer to -3, which would be expected if all the pores were collapsed (uniform amorphous-like carbon [297]). This fits well with the description of graphene as fractal crumpling of sheets [116], where the fully hydrated rGO materials have optimal stabilization with a fractal dimension equal to 2.3, as suggested in the computational models. As restacking increases due to van der Waals forces, the fractal dimension increases as the accessible surface area decreases, and the experimental results shown here match the values proposed by the model.

This result can explain why, as supercapacitors, the performance of hydrogels has been shown to be far superior to dried materials [17, 20, 21, 25], and this exceptional performance is linked to both an increased accessible surface area along with lower ionic resistance within the enlarged pore network. These investigations into the role of water in rGO produced quite insightful results, and Chapter 7, discussing future work, goes in to detail on how the work presented here will be expanded upon.

6.3.3 Neutron results and discussion

While the larger size of the beam limits the experimental small angle neutron data to an investigation of scattering through-the-surface in the ab -plane, additional insights can be gained using neutron scattering, especially in relation to extending the q -range with USANS. Figure 177 shows the results of a combined USANS, SANS, and neutron diffraction plot for a pump dried rGO assembly. It should be noted that the USANS and SANS results are taken through-the-surface of the materials (ab -plane), while the diffraction results will display features predominantly from the ac -plane, so this curve is not a true representation of an individual surface or edge curve, and the PT model cannot be applied to fit

the small-angle region of the curve because measurement for through-the-edge scattering is possible with these techniques. Nevertheless, this curve does show the main features of the rGO assemblies and provides needed insight on the behaviour at ultra-low- q .

The SANS and USANS results significantly extend the range from the SAXS data, and it can be seen that the broad hump is slightly visible in the through-the-surface scattering as well. Further, this overall scattering feature ranges across an extensive q -range, even larger than that reported for porous carbons with what was already recognized as one of the widest reported ranges [34]. Again, interpreting the main features of the curve as representing an extended, porous fractal network, the low- q region indicated by the orange line at $q \approx 7(10^{-5}) \text{ \AA}^{-1}$ corresponds to L_{max} and the high- q region indicated by the orange line at $q \approx 0.3 \text{ \AA}^{-1}$ corresponds to L_{min} . This would indicate the pore network extends from the sub-nm level up to over 4.5 \mu m , larger than the size of the individual rGO sheets. Again this low- q upturn, or negative deviation from Porod's Law (as the value of α is 4.4), can indicate diffuse scattering is present. Because the pump dried rGO assemblies have a thickness of 4.5 \mu m (see Figure 140), this feature is likely to be indicative of the edge of the bulk assembly, as six layers were stacked together for the neutron measurements. In this case, the actual scattering curve can be assumed to level off to a horizontal asymptote, indicating the total scattering surface from the 'particle' (in this case the entire rGO assembly) has been measured. Future work will subtract this diffuse component from the curve and thus allow for the total surface area to be calculated, following the calculations outlined in Chapter 2.

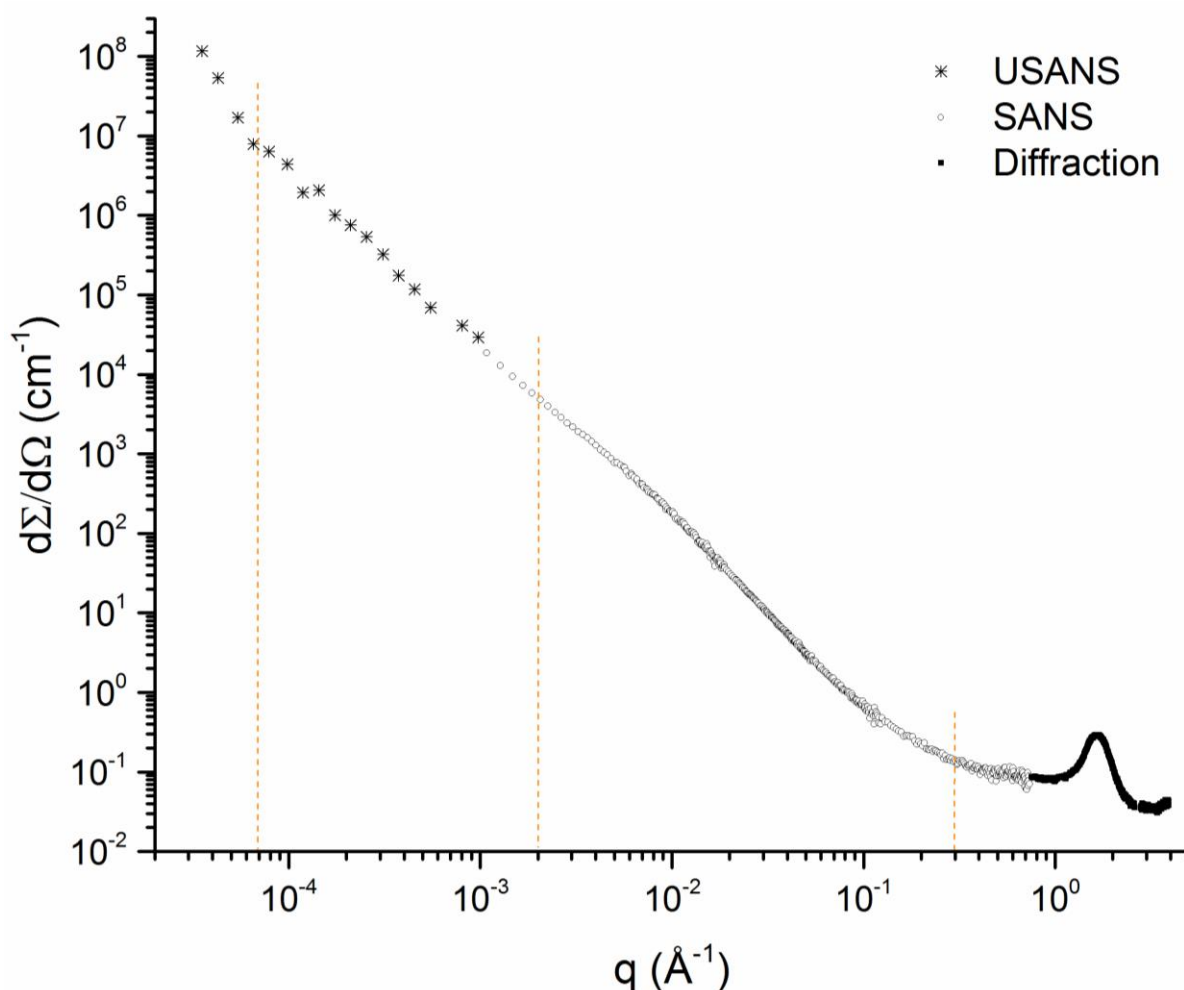


Figure 177. Combined USANS, SANS, and neutron diffraction plot on an absolute intensity scale for HO3 rGO. Defined structural regions are indicated with orange lines on the plot and are referenced in the text.

To determine which features of within the combined neutron curve are of most significance, a Kratky plot is shown for this extended curve in Figure 178. There are three clear features indicated with the arrows, where the (002) Bragg peak is again prominent at high- q and is preceded by the hump appearing at $q \approx 10^{-2} \text{ \AA}^{-1}$. There is then a long, flatter section before the pronounced intensity increase at ultra-low- q . The region below the orange line at $q \approx 2(10^{-3}) \text{ \AA}^{-1}$ in Figure 177 is at the same q -value as the upturn seen in through-the-edge scattering in the SAXS data. The broad hump below this value is enhanced with the Kratky plot and is most likely related to the cluster aggregates.

Comparing the through-the-surface neutron Kratky plot with the through-the-edge SAXS Kratky plot in Figure 151, the through-the-surface SANS and USANS results add clarity on what features are contributing to the scattering in the ab -plane. The SAXS results showed the broad hump related to the agglomerate clusters centred at about 0.07 \AA^{-1} with a range from $10^{-2} \text{ \AA}^{-1} > q > 0.6 \text{ \AA}^{-1}$, in the SANS results, a minimum is seen on of Kratky plot close to 0.07 \AA^{-1} which extends upward in a similar range of $10^{-2} \text{ \AA}^{-1} > q > 1 \text{ \AA}^{-1}$. The high intensity low- q feature in the SAXS plot was ascribed to the surface roughness, and in the SANS/USANS results, this feature is also detected in the through-the-surface scattering extending across a range of $7(10^{-4}) \text{ \AA}^{-1} > q > 10^{-2} \text{ \AA}^{-1}$. The SANS results confirm a structural feature is detected across this entire range, starting at the same position as that seen with the SAXS results, with the Kratky plot in Figure 178 clearly showing a higher level structure does exist as a separate feature from the agglomerate clusters. This suggests that within this region, scattering is dominated by features of the rGO sheet roughness which can be analysed separately after removing the scattering from the collapsed agglomerate clusters and this will then can act as a direct measure of the accessible scattering surface area. This analysis is ongoing and is left for a focus of future work.

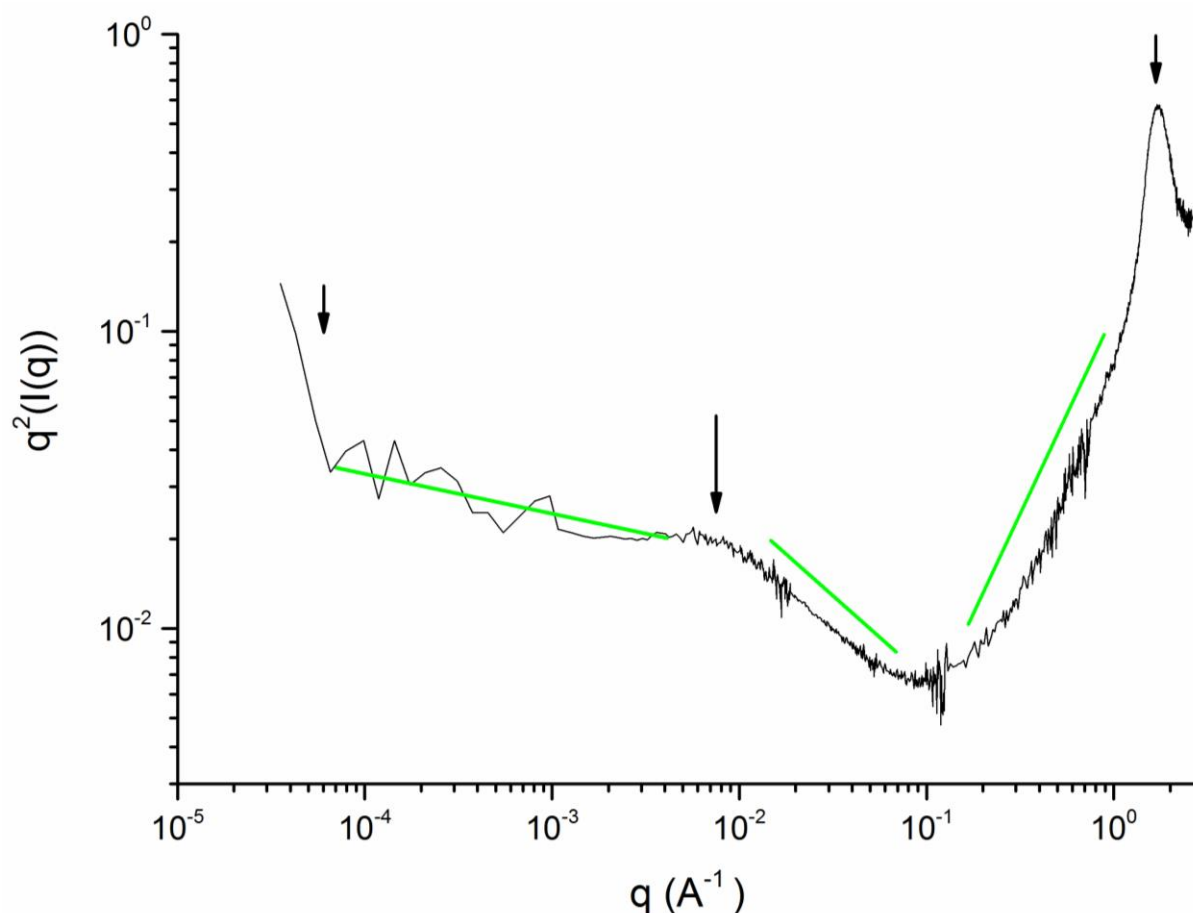


Figure 178. Kratky plot of the combined USANS, SANS, and neutron diffraction results for HO3 rGO with the regions of interest highlighted in green and defined features indicated with the arrows.

To estimate the size of the scattering feature causing the broad hump in the mid-q region in Figure 177, the Guinier plot for a q-range of $qR_g < \sqrt{3}$ was used. The slope of the linear region in the q-range correlating with the feature can be used to obtain the effective size of the scattering particle, and the result is shown in Figure 179, with a slope of -367. Assuming a simple spherical shape, the slope in the Guinier region is equated to $R_g^2/3$, which yields a value for R_g of 3.3 nm. Again assuming a spherical shape, the radius would be found with $\sqrt{((5/3)R_g)}$ resulting in a particle with radius 2.3 nm. As the through-the-surface scattering relates to features in the ab-plane, this feature is most likely attributable to the misaligned aromatic clusters that are distributed out-of-plane, as indicated by the large OA and medium-to-low texture of the rGO materials, as discussed in Chapter 5. The 2.3 nm measurement matches with that of the L_c component of the clusters shown previously, again signifying an average of six rGO layers are stacked in each cluster.

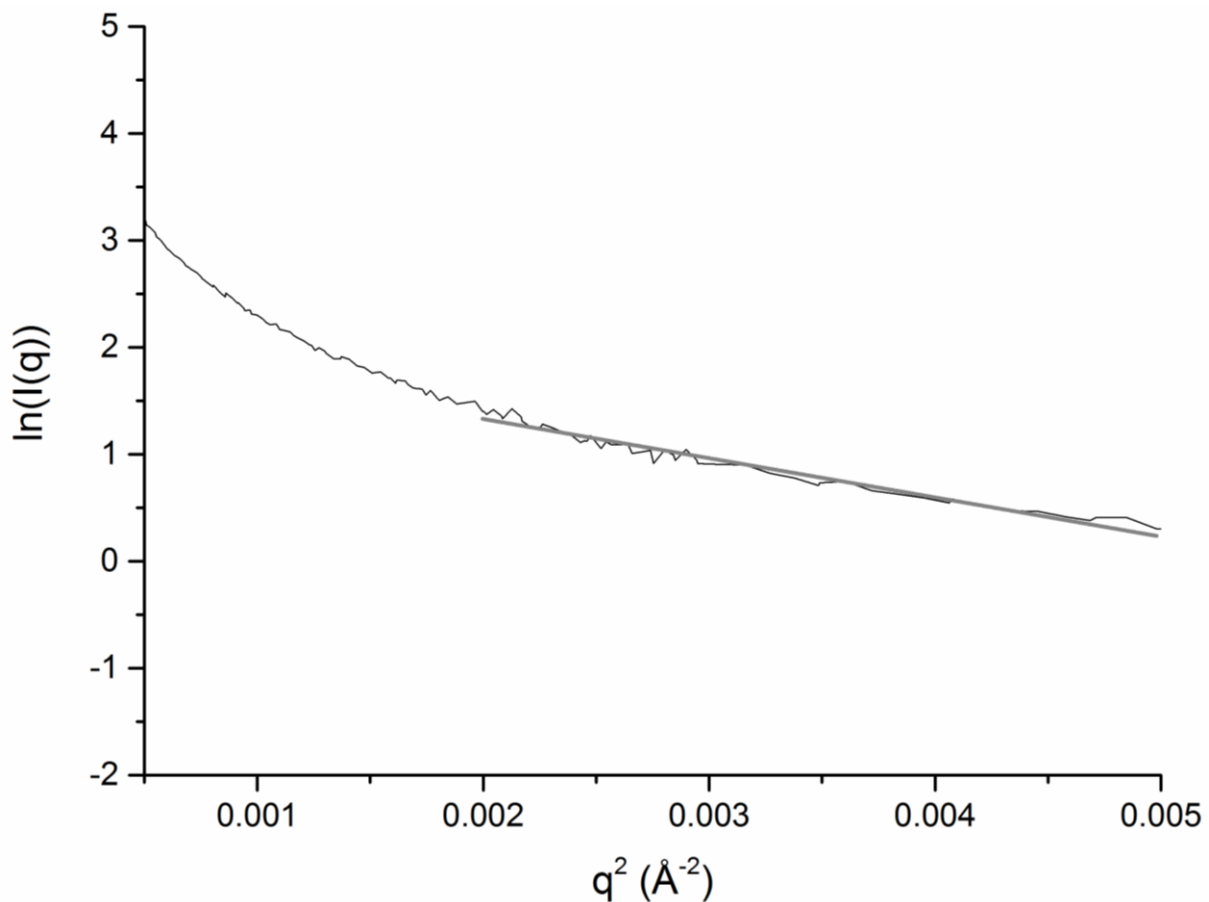


Figure 179. Guinier plot of the SANS region corresponding to the feature seen in the mid-q range for HO3 rGO with a fit of the linear region to obtain the slope which can be related to the radius of gyration of the scattering particle.

More work is needed to fully quantify the rGO scattering results, but the discussion here provides the initial steps in interpreting data. The slope across this whole region yields a fractal dimension of 2.25, and interpreting the results as a porous fractal network and applying the methods used to interpret the pore length in porous carbons exhibiting this long-range fractal region, Pfeiffer et al. [34] showed the minimum q-value represents the smallest size of the pore while the maximum q-value represents the most extended pore length. With the USANS results it is possible to say that the fractal range goes from just under 1 nm up to 4.5 μm , which equates to the entire thickness of the dried films. Applying the pore fractal method to estimate porosity [34]:

$$\varphi = \frac{V(L_{min})}{V(L_{max})} = \left(\frac{(L_{max}/L_{min})^{3-D_p} - 1}{3 - D_p} + 1 \right)^{-1} \sim \left(\ln \left(\frac{L_{max}}{L_{min}} \right) \right)^{-1} \quad 6.5$$

When $L_{\max} \gg L_{\min}$, a result of a porosity of 12% is determined, which is lower than that measured for porous carbon particles (19% to 46% reported by [34]). Without the extended q -range for comparison of other rGO materials, it is not yet clear if this fractal scaling method is justly applicable in these systems, but further work will apply this method to compare results for assemblies dried under different conditions.

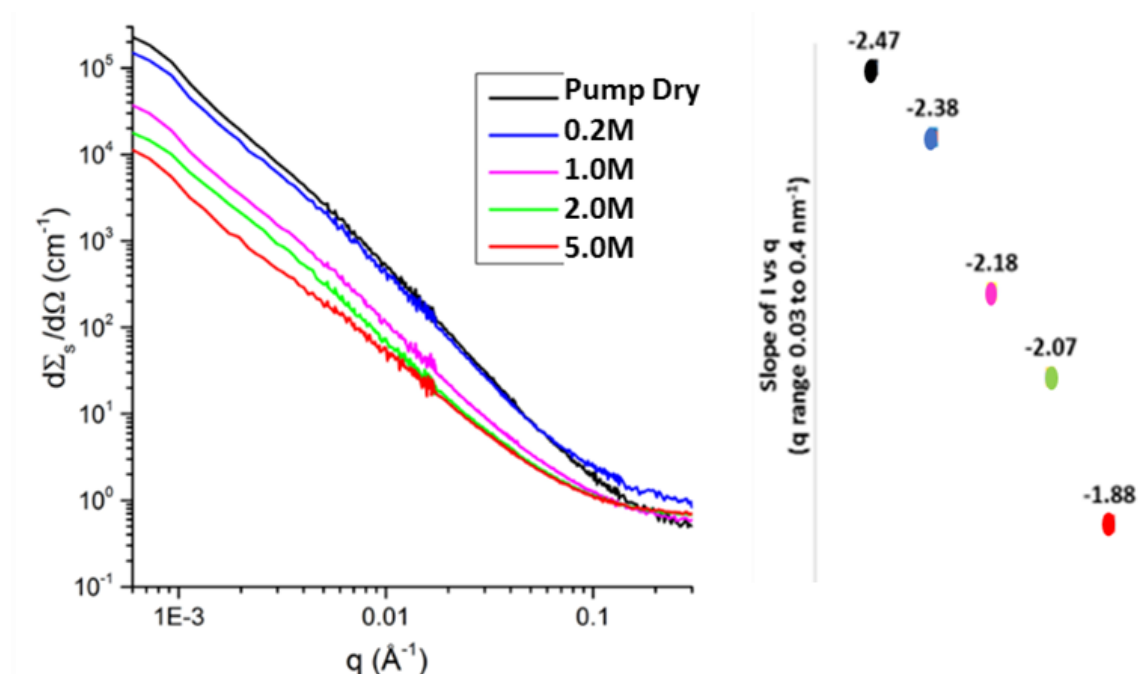


Figure 180. SANS curves for as-prepared, dried EM-rGO assemblies as compared to a pump dried sample that was not tuned with sulfuric acid.

Another interpretation applies the concept of a planar invasion percolation cluster, which has a fractal dimension of 1.9 [306]. A stack of these percolation clusters results in a dimension of 2.9 [197], and these concepts would apply to what is known about the physical structure of the rGO as well as match well with data for EM-rGO assemblies shown in Figure 180. In this case, materials that are fully exfoliated, with aligned sheets and limited aggregates show a structure more like that of a planar percolation cluster, with a slope close to 1.9, and this value would scale as more of these planar clusters are stacked, following the behaviour seen in EM-rGO assemblies with more/less aggregate clusters. In any case, the SANS results on the absolute intensity scale show that there is more scattering surface per unit volume in the pump dried assembly and this decreases as higher concentrations of sulfuric acid are used to tune the pore size. This information is however limited, as these values also include the scattering from the cluster aggregates which will not contribute to the accessible surface area. The pump dried assembly has more scattering per unit volume because it is much denser with the close packed, often restacked, rGO layers. Hence, the fractal interpretations provide more insight on the structure of the pore network and how that is likely to effect the material performance.

6.4 Conclusions and Future Work

This chapter built upon the concepts developed at the chemical (Chapter 4) and macromolecular (Chapter 5) level in order to deliver a comprehensive interpretation of the chief aspects influencing the structure and resulting material performance of rGO bulk materials. The results presented here make progress in understanding the features present at the mesoscale, a region that has remained

relatively unexplored in rGO assemblies until now. Combining turbostratic clusters and OA factors measured with diffraction at the microscale with the mesoscale features that were revealed using TEM, HRSEM, and SAS, clearly showed there are different levels of order present within the rGO assemblies, with the mesoscale features having a much more tortuous, disordered network than previously assumed [26]. Assessment of the bulk material was further extended into the macroscale region using direct imaging, where it was shown there are likely to be more complex and heterogeneous features present in the EM-rGO materials.

While the results presented here are not wholly quantitative, there have been many noteworthy findings presented which aid in determining the structure of rGO assemblies at the meso- and macroscale. This work supports that the main structural components of rGO assemblies are well defined by the BSU concept put forth by Oberlin et al. [156] for pyrocarbons (see Figure 76) and that of Wood et al. [119] for graphene oxide papers (see Figure 22). These components consist of a BSU cluster with dimensions L_a (composed of l) and L_c at the microscale that are joined to form larger lamellae (clusters) and super-lamellae extending up through the micron scale. The results for rGO differ from Wood's structural model for GO [119] in that GO is much more planar in nature, causing the clustered features to be more disk-like (lamellae) in shape with an identifiable diffuse layer (interlayer resulting from attached oxygen groups yielding the slope with negative deviation from Porod's Law), while the rGO sheets have a much rougher surface and form polydisperse cluster agglomerates consisting of an average of 7 stacked layers.

It was clearly demonstrated that different aspects of processing will impact the resulting rGO assemblies within explicit size domains. For example, while the drying methods do not have impacts on the chemical or macromolecular scale (aromatic domain size, l), they are main determinants in the resulting meso- and macroscale features which play large roles in defining the overall pore network and pore accessibility. Correspondingly, the oxidation level and processing conditions of the GO precursor had the largest impact on the structure at the microscale, yet appears to have a minimal influence on the essential meso- and macroscale features of the bulk assembly.

The results here support the findings in Chapter 5, where the mid- q scattering feature identified in SAXS results corresponds to the turbostratic clusters which are well characterized using models developed for multi-lamellar structures, specifically as described within paracrystalline theory (PT) [214, 302], described in Figure 153. By comparing the results of applying the PT model to the through-the-edge scattering curves to the results of Chapter 5, in both cases it was determined that overall stacking height of the clusters is very similar for all processing conditions, with the cluster height averaging around 2.5 nm, corresponding to an average of 6-7 rGO layers. The only exception to this is with the annealed sample, where the higher temperature removes oxygen groups and smooths the carbon lattice by reducing corrugation and stacking faults [303], resulting in densification of the carbon matrix due to increased cluster prevalence and size (more rGO layers per cluster).

The through-the-surface SAS measurements showed that the rGO bulk assemblies have very consistent structure along the ab -plane, with density differences ranging across an extended length scale, with scattering features being detected at very low- q and continuing all the way up to $q \approx 1 \text{ \AA}^{-1}$. This equates to physical features with size ranging from the 3.5 Å interlayer distance within the turbostratic clusters across the length of the rGO sheets ($\approx 1 \text{ }\mu\text{m}$) up to the total thickness of the assembly ($\approx 5 \text{ }\mu\text{m}$), suggesting the pore fractal models developed for nanoporous carbons [34] can be applied to quantify the pore dimensions and overall porosity. The rather featureless scattering curves present difficulties in interpretation, and the results here show that much of the through-the-edge scattering observed is due to the restacked turbostratic clusters, not a well-defined pore network. In spite of this, it is possible to move forward with a more in-depth and quantitative analysis of the rGO materials, comparing the theories and models developed here to the material performance and absorption data for rGO assemblies prepared using different processing conditions.

The through-the-surface scattering patterns are very similar to that seen in coal [307], and the next step would be to isolate the scattering components from that resulting from roughness along the surface of the rGO sheets and that resulting from the cluster aggregates – most likely following Beaucage and Schaefer in their studies of complex carbon systems with multiple size-scale structures [289]. Additional steps will include attempts to subtract the contributions from both the amorphous content ($D=3$) and fluctuations in layer spacing ($D=1$) in order to convert data specifically related to the porous surface to real space and obtain the pore distribution function $g(r)$, as performed by Perret and Ruland [240, 290]. This method allows for quantitative determination of slight sub-nm deviations in stacking which are characteristic of these dense, porous carbon materials.

A detailed analysis of the orientation parameters, both the OA at wide angles, and ϕ at small angles, as shown in Figure 181, would facilitate a quantitative comparison of the dimensions of the micropores within the rGO assemblies. The OA analysis procedure used on the SAED results in Chapter 5 can also be applied to the through-the-edge WAXS results shown here to quantify the texture for the different rGO materials. Further, the broadening of the anisotropic SAS feature can be used to determine the relative dimension of the pores, using the approach applied to carbon fibres with elongated pores wedged between well aligned planes [28, 30, 136], as discussed in Chapter 2.

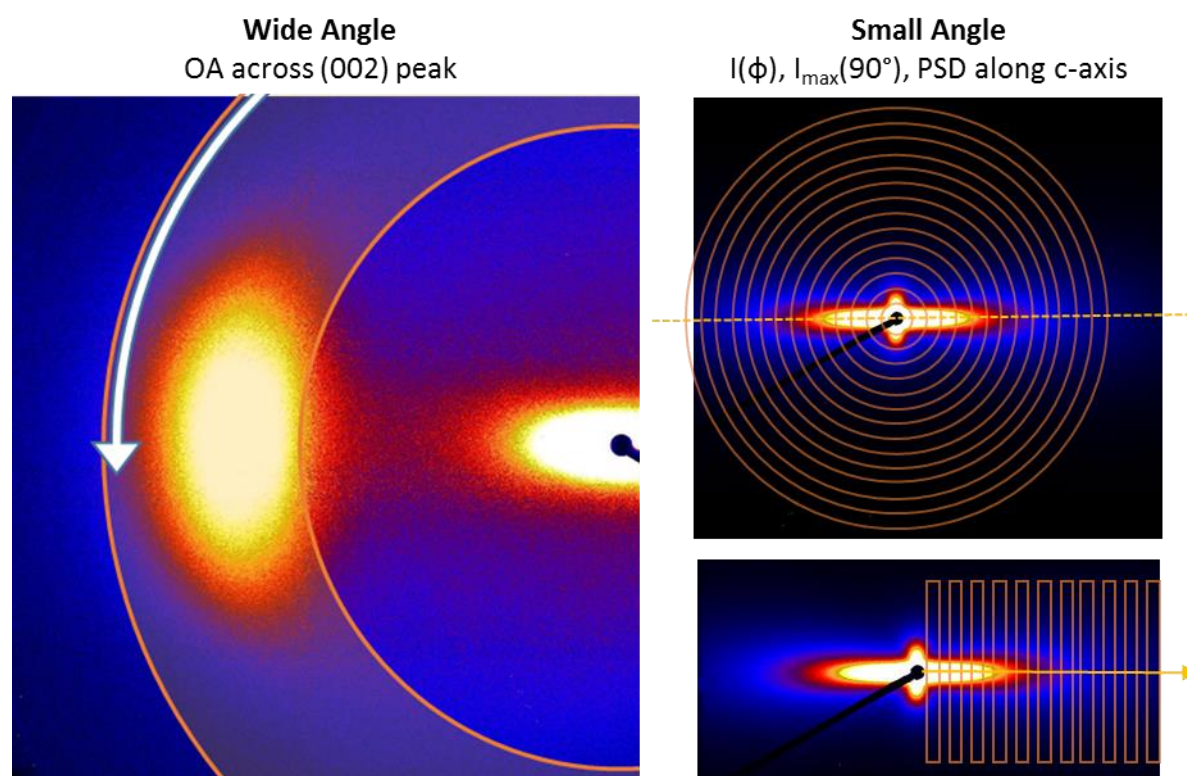


Figure 181. Depiction of how carbon orientation and pore alignment can be measured at the microscale (wide angle at left) and mesoscale (small angle at right) based on the approach for pore characterization via WAXS and SAXS analysis in carbon fibres as outlined by Dresselhaus [30] and discussed in Chapter 2.

The results for the hydrogel assemblies are quite promising and these show that *in situ* SAXS is a powerful tool in understanding how the structure of rGO materials is impacted by hydration. The results shown here clearly indicate there is a critical drying point where bulk water is expelled quite abruptly from the assembly, and at this point the cluster agglomerates form. Further, the structural progression shows that the width of the Bragg peak stays relatively constant while the slope in the small-angle region continues to increase. This trend sheds light on how the mosaic cluster network is formed within the rGO bulk, and it can be seen that while the size of the clusters does not change, the overall prevalence of these restacked domains continues to increase as the water evaporates. The

results show that as more rGO sheets assemble to form clusters, the increased stacking (prevalence of van der Waals bonding) can be measured by an increase of the slope in this mid- q region, which further supports the previous reports using the fractal dimensionality as a measure of available surface area [116, 133]. Furthermore, this method shows that the water background is in itself a useful feature, as it can quantitatively measure the total porosity and distinguish between assemblies with pore sizes large enough to hold bulk water (the 5.0 M EM-rGO materials) or only adsorbed water (all EM-rGO materials prepared using sulfuric acid concentration of 1.0 M or less).

Chapter 7. Conclusions and Future Work

7.1 Overall Outcome: rGO Assemblies as a Unique Type of Porous Carbon

The wet processing methods used to fabricate rGO assemblies, along with their unique lamellar geometry, makes them quite promising materials for a wide variety of applications [11, 12, 29, 308]. However, the same complex structural elements that make rGO so promising also present experimental difficulties when attempting to fully characterize the multitude of elements impacting the performance elements of the bulk material. This work has taken a comprehensive approach to elucidate the structure of rGO assemblies, from the sub-nm level all the way through to the macroscale, and has been able to identify many specific structural elements that are thought to influence structure-performance relationships in these materials. As the key features of porous carbons fall within the two main areas of *chemical bonding within the carbon matrix* and *the pores contained within it*, quantitative chemical differences were first identified in Chapter 4 and then combined with the results for structural elements identified in Chapters 5 and 6 to achieve the aim of elucidating the structure of rGO assemblies.

The main purpose of this study has been two-fold:

- i) **To explore the application of radiative experimental techniques in order to determine how chemical and structural data for rGO assemblies can be best obtained and interpreted**
- ii) **To use these results in order to define the chemical and structural make-up of dried and hydrated bulk rGO materials prepared by filtration of aqueous dispersions reduced via hydrazine**

The first aim has been achieved through the application of widely used experimental methods, and the gap in knowledge was able to be addressed by outlining how these methods can be best applied to understand structure-property relationships in rGO assemblies. Specifically, there have been a number of enhancements to data interpretation suggested, such as highlighting the relevance of the valence band to identify oxygen and nitrogen functional groups and detailing how more thorough fitting procedures can be applied to the XRD and RMS peaks to extract a wealth of important information on defect concentration, aromaticity, and overall disorder at the microscale. Further, the anisotropic features WAXS and SAXS patterns were analysed to determine the separate structural elements in rGO assemblies along the *ab*- and *ac*-planes.

The second aim has been achieved by using the results from the aforementioned techniques to answer many of the open questions regarding the structure of rGO materials. Specific questions outlined in the Introduction were:

- Do the processing conditions of the original GO precursor impact the chemical composition of the resulting rGO?
- What is the chemical composition and physical structure of the rGO sheets?
- What is the structure of the carbon matrix and pore network within the rGO assemblies?
- What roles do drying and hydration play in determining the structure of the bulk materials?

All have been addressed in this work, providing much insight into the relationship between structure and processing conditions, while also suggesting areas of further research. Overall, the main aspects contributing to the structure of rGO assemblies are outlined in Figure 182, with details related to each feature discussed in the sections to follow. This highlights the fact that structural elements within different length scales have unique impacts on the formation of the overall carbon matrix and resulting material performance.

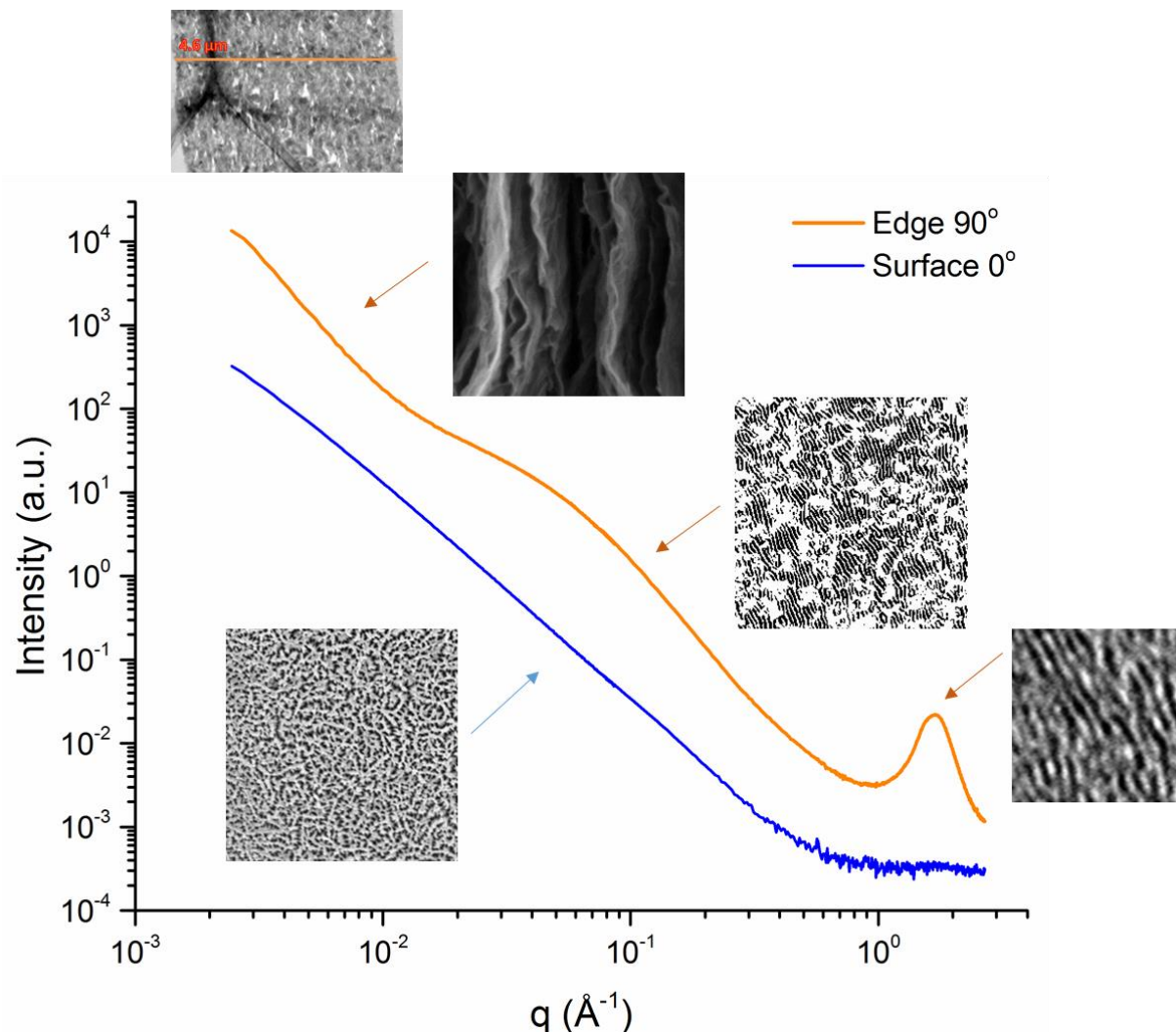


Figure 182. Depiction of the individual structural elements making up the scattering curve for rGO assemblies. This figure highlights the findings of this work, showing the influence of orientation and scale on the particular structural element within the rGO assembly. The through-the-surface fractal network is consistent throughout the bulk, while the through-the-edge lamellar structure is composed of different size entities. From right to left: the Bragg peak at high- q measuring the interlayer distance between the stacked aromatic domains; the broad feature at mid- q relating to the size of the turbostratic clusters; the Porod region at low- q arising from the surface roughness of aligned and elongated rGO sheets; these features continue across the entire 4.5 μm length of the bulk assembly.

7.2 Main Findings

7.2.1 Chemical composition of rGO sheets

One outcome of this work was to show a link between the processing conditions of the original GO precursor and the chemical and structural features of the resulting rGO sheets and assemblies. This work provided the experimental evidence to show that the parameters of reaction time and temperature within *Step 1: oxidation* and *Step 2: hydrolysis* [57] did result in differences in chemical composition of the rGO assemblies, with measured differences observed in the specific type of basal and edge bound oxygen and nitrogen moieties in the reduced materials. These results indicate that longer reaction times for *Step one: oxidation* result in rGO sheets with more residual epoxy groups, which likely leads to increased nitrogen doping during hydrothermal reduction, where both hydrazine and ammonia could react with these oxygen functional groups. It was also found that longer reaction times for *Step two: hydrolysis* are likely to result in rGO sheets with more carbon defects and sp^3 bonded oxygen species. Correspondingly, shorter reaction times and lower reaction temperatures

result in rGO with significantly less epoxy, hydroxyl, and carboxyl groups, with the extra-low oxidized rGO (LOX) even achieving levels of high purity (>95% carbon) after further thermal reduction.

It was found that rGO produced via hydrazine hydrothermal reduction at 100°C results in nitrogen groups that are almost exclusively bound at sp^3 carbon sites. Precisely which nitrogen species are present in rGO materials is an area of current research, and further investigation is needed to more clearly identify these nitrogen groups. However, the results of this work indicate these “amine-like” moieties do have a large impacts on the valence band of rGO materials. Based on the results from HO4, it seems possible that the amount of the amine-like nitrogen introduced to the rGO sheets could be enhanced via modifications to the original GO oxidation process, where the over-oxidized basal plane resulting from holding the reaction in *Step 1: oxidation* for an extended period introduces abundant basal-bound oxygen groups, increasing the reaction sites for both hydrazine and ammonia. Further, these results indicate aromatic nitrogen species are not prevalent in the rGO assemblies examined in this work, and the overall nitrogen content largely diminished upon further thermal reduction.

It was determined that the prevalence of residual phenolic basal plane groups in rGO can be minimized using a hydrazine reduction method compared to that of thermal reduction alone, where it is thought that the lack of epoxy groups destabilizes basal-bound hydroxyls [76], facilitating a more complete reduction. This is an important finding as applications that require high conductance require a minimal amount of basal-plane phenol groups in rGO materials, and these results offer further support for a two-step reduction process using hydrazine followed by thermal reduction procedure [75, 76]. Thus, this work shows there is a high likelihood that tailoring GO processing conditions can be used to impact the resulting rGO assemblies, resulting in specific types of residual oxygen and nitrogen groups, allowing the material to be better tailored for specific conductive and pseudocapacitive properties.

The valence band (VB) spectra proved to be a valuable tool in uncovering unique attributes of rGO assemblies with slight variations in chemistry. Differences in conductivity for rGO of varied oxidation level were reported based on the behaviour of the VB spectra close to the Fermi energy. Further, this work was able to assign specific bond-types to the unique “signature” of rGO VB features, where eleven distinct features were identified, as shown in Figure 72 and labelled in Table 6. It was found that the nitrogen XPS feature in HO4-rGO appearing at ≈ 400 eV has a significant impact on the VB of rGO materials if the total nitrogen concentration is above 5%, but this impact was diminished at lower levels of nitrogen content.

7.2.2 Microscale features and properties

This work provided a detailed analysis of how the XRD and RMS peak profiles for rGO assemblies can be interpreted to quantify many useful structural parameters. The importance of the RMS inter-band features was shown, and by employing these peak fitting parameters, RMS alone is able to provide a significant amount of information related to the oxygen content, aromatic domain length, defect type, and overall disorder. Further, by interpreting the rGO results in the context of Ferrari and Robertson’s three stage amorphization trajectory [170], it is possible to correctly interpret the structural meaning behind the peak features, and this work found that GO and rGO are high defect-density materials warranting use of the model developed by Lucchese et al. [266] to determine the aromatic domain length based on the I_D/I_G peak ratio. Thus, it was determined the aromatic domain length, l , contributing to the basic structural unit (BSU) model for rGO materials, is directly related to the oxidation level, not due to other factors such as corrugation. The aromatic domains were shown to be quite small for all samples, with an average size of just over 1 nm.

Further expanding the concept of the BSU, it was determined that the porous carbon structural models developed by Oberlin et al. [156] proved to be a very valuable reference which allows for a more direct

comparison to other carbon forms. This then allowed for associations to be made between specific structural elements and performance, where the elongated L_a is the likely cause of the high conductivity in rGO assemblies. The detailed parameters of the BSU for rGO assemblies, along with the links between these structural elements and material performance, were found to consist of turbostratic clusters with average interlayer space of 3.7 Å and an average of 6-8 stacked rGO layers. The close-packed elements of these clusters have an aromatic length, l , of just over 1 nm (as shown in TEM images and RMS analysis), but there also exists a longer (hk) domain length, L_a , that extends to over 6 nm. The shorter l units and residual oxygen groups were found to be the cause of disordered stacking, which results in a pore network almost exclusively of sub-nm micropores extending throughout the bulk of the dried assemblies.

It was shown that if the correct peak fitting methods are applied, a combination of XRD and RMS is a very accessible and simple experimental approach that can provide extensive insight on both the microstructure and chemistry. Quantification of the γ -band feature in the XRD profile readily allowed measurement of the aromaticity of rGO materials, and further analysis with RMS and SAED found there is a high level of strain present in the dried rGO assemblies, which is directly attributable to the oxidation level. This micro-strain is quite a significant structural parameter, accounting for 30% of peak broadening, and this plays a key role in the mechanical properties rGO assemblies. Thus, this work has shown how tailoring the residual oxygen groups present on the rGO sheets will directly impact porosity, reactivity, and mechanical performance.

7.2.3 Mesoscale features and properties

This work has shown that the structural features within the mesoscale region were an important missing link in the full characterization of rGO assemblies. Until now, it was assumed that the layers within the rGO bulk material were rather well ordered, and the structural models proposed were based on a combination of XRD results at the microscale and SEM at the macroscale, both of which imply a lamellar structure with rGO sheets laying within the ab -plane and forming a porous network of “cascading nanoslits” [21, 24, 26, 29]. While this work found that there is a rather high level of orientation within individual turbostratic clusters (diffraction peak profile) and in the overall bulk layering as shown via SEM (Figure 138), at the mesoscale there are highly disordered features (shown via TEM Figure 139 and Figure 140) and this work has been the first to identify these features.

The BSU clusters are surrounded by a more disordered, porous region that varies in structure depending on the reduction temperature and drying method used. It was found that the relative size of these clusters and the features contained within them (interlayer distance, $d_{(002)}$, and aromatic length, l), remain fairly constant for all materials, but the drying method can be used to tailor the disorder which results in pore networks that are more or less accessible. Pump dried and annealed materials had the most order and least porosity, while air dried and hydrothermal assemblies were more disordered and showed increased porosity, as depicted in Figure 162. It was further found that standard methods for characterizing the texture of pyrocarbons could be applied to rGO materials, leading to the conclusion that the pump dried films can be classified as medium textured carbon materials [131].

It was found the individual BSUs combine to form a bulk system like that of a *mosaic cluster*. The BSUs are dispersed throughout the bulk, consisting of turbostratic, corrugated, and distorted layers that are then surrounded by a more disordered carbon matrix. This work has shown that the more tightly stacked these clusters become, along with their prevalence, will limit the accessible surface area by decreasing the overall porosity and also increasing the overall tortuosity due to blocked passage within the pore network. Further, the results suggest that the fractal interpretation of SAXS results allows for a simplified approach to compare the relative amount of accessible surface area in different rGO

materials. The results of this work provide experimental evidence that supports the model of optimized graphene crumpling (where a fractal dimension of 2.3 signifies the maximum solvent accessible surface area, and values larger than this are linked to prevalence of restacked regions [116]). These findings have implications for graphene-based supercapacitors, as it poses an upper limit on the accessible surface area that is significantly less than the theoretical maximum.

While the oxidation level has large impacts on the structure of the rGO sheets at the microscale, the SAXS data showed that the chemical composition does not carry over to have large impacts on meso- and macroscale features. This should prove to be useful insight, as it shows the processing conditions have distinctive impacts within discrete size regions (oxidation and reduction at the microscale and drying at the mesoscale). There was a slight difference seen in the LOX assembly, where the slope of the Porod region in the through-the-surface SAXS curve was slightly more negative (-2.7 comp -2.6) than other rGO materials. Based on the results showing LOX has significantly less oxygen groups present, and hence less disorder within the restacked clusters due to the elongated aromatic domain length, l . This result also supports assumption that fractal dimensions closer to 3 are correlated with less accessible surface area. In terms of material performance, it is clear that LOX is likely to offer superior performance as an additive for conductive or barrier films, and future work would be able to more unequivocally verify this.

Based on the shape of the SAS features, the WAXS and SAXS results clearly show that EM-rGO has a much more defined pore structure than the typical dried assemblies. However, for all rGO assemblies, it was found that the pore network in these materials is not as precisely defined as previous literature would suggest [24, 26]. Results here indicate that pore network of EM-rGO materials tuned with sulfuric acid concentrations of 1.0 M or less is composed of relatively disordered and narrow slit-like pores that have relatively equidistant interlayer dimensions (height along the c-axis). If this is the case, the difference in the performance of these materials is probably due to the length of these pores, as the EM pore-tuning process (details given in the Literature Review and Chapter 3) allows for wider regions along the rGO sheets to remain exfoliated and reduces the amount of turbostratic clusters formed. Further, it was found that for the EM-rGO materials tuned with highly concentrated acid, there is a larger impact on the pore network that results in a greater amount of increased porosity (evidenced by the SAXS results showing bulk water is present) and distinct macroscale features which are addressed in the following section.

7.2.4 Macroscale features and properties

Optical images microscopy showed the EM-rGO assemblies do not have homogeneous surfaces. This was especially apparent in the materials prepared with higher concentrations of acid, where additional ripping was identified across the exterior. These features could contribute to the enhanced performance of these materials as supercapacitors [24], as there would be more accessible surface area and enlarged pores along the ab-plane (prevention of restacking and expansion) as well as additional pathways created along the ac-plane (lateral tears), decreasing the tortuosity of the pore network to facilitate more rapid ion transport through the bulk [14, 35, 37, 39, 120].

The SAXS results for rGO hydrogels and hydrated EM-rGO assemblies provided unprecedented insight on the structure of rGO materials as well as the amount of water confined within the pore network. By monitoring the drying process *in situ*, it was revealed that there is a critical drying point where all bulk water is expelled from the carbon matrix, yet the remaining adsorbed water prevents the rGO sheets from forming restacked clusters immediately. As the water continues to evaporate, the clusters (again ≈ 7 layers) begin to form, becoming more numerous as the water content lessens.

7.3 Future research directions

7.3.1 Impacts on rGO sheet chemistry resulting from GO processing conditions

More variations in GO processing conditions, as well as additional reduction methods, should be examined in order to more thoroughly verify the reaction mechanisms and increase the control and scalability for bulk processing of rGO materials. Further, the XPS results on the rGO materials presented here would be better supported in combination with angle-dependent X-ray absorption near edge structure (XANES) in order to reveal the orientation of each of the carbon-oxygen and carbon-nitrogen bonds identified by XPS. With XANES, the X-rays are used to determine the direction of chemical bonds of the specific atomic species by its absorption edge, and this technique offers opportunities to explore the configuration of the unoccupied orbitals with σ and π symmetry, as there is unique orientation in regard to the aromatic ring plane. Analysis of the XANES profiles can be combined with the high resolution XPS and VB results to further verify the assignment of chemical bonding reported here and allow for a more definitive understanding of the bond types and alignment in rGO sheets.

7.3.2 Quantitative analysis of the pore network

It was shown that the mesopore structure is difficult to characterise with SAS because the scattering is dominated by the larger, BSU cluster aggregates. Further methods to more quantitatively analyse SAS data for rGO assemblies were outlined in Chapter 6, and included application of the pore fractal model [34] and orientation parameters used to calculate the pore length in carbon fibres [30, 136, 240]. Future work to directly compare the fractal dimension, as measured from the Porod region of the SAXS curves, to surface area and porosity as measured with water sorption and dynamic electrosorption analysis [17] for different rGO materials, would make it possible to directly link these structural features with material performance.

7.3.3 Homogeneity of the bulk material

TEM (Figure 140) and FIB/SEM images (Figure 141) found that there are larger voids present within the rGO assemblies. These findings could be explored further via a serial-milling process where the FIB is used to ablate a very thin region of the bulk and then the surface is imaged with the electron beam (FIB-tomography). This process continues to collect a series of images which can then be reconstructed using image processing software to reconstruct a 3D rendition of the bulk. Adjustments to the FIB/SEM machining and imaging parameters should be explored in an attempt to improve the resolution of the rGO carbon matrix, and it is likely that using a helium ion beam in combination with EDS and STEM imaging/diffraction would be very successful at characterizing various dried rGO assemblies with extreme precision.

7.3.4 Hydration and water transport

Future work to more quantitatively analyse SAXS data like that presented here would be of great benefit, as the scattering signal from the water can be used to determine the total porosity as well as measure the amount of water present when this critical drying point is reached. Quantifying the minimum amount of water necessary to prevent restacking is a valuable piece of information when designing rGO materials for applications requiring minimal volume (increased volumetric capacitance [35, 37, 144]) or tailoring permeation behaviour (water treatment [309] or separation science [12, 141]). Future to correlate material performance from water sorption and gas permeation experiments at controlled levels of relative humidity with SAXS data would aid in fundamental studies on the water dynamics [299, 310] within rGO assemblies would facilitate the design of many innovative materials.

In future neutron scattering experiments, contrast matching using D₂O/H₂O mixtures can be used along with *in situ* measurements using controlled humidity to better quantify the surface structure and total porosity using the extended q-range and absolute intensity scale. Additional work using quasielastic neutron scattering (QENS) would be able to directly measure water structure and dynamics within the hydrated rGO assemblies. These proposed research areas, in combination with the work suggested in the following section, should largely contribute to the understanding of both rGO materials as well as the structure of water and/or ions confined in micropores particular surface properties [299, 311-314].

7.3.5 Further *in situ* investigations on ion transport in rGO assemblies

At this time, there is a large research effort focused on understanding of the fundamental processes influencing the performance of carbon-based supercapacitors. Experimental results are needed to determine the behaviour of ions in confinement and the overall dynamics of charging at the carbon interface, which can then be combined with knowledge on surface chemistry and conductivity in order to significantly advance developments of higher-performing energy storage materials [123]. Advanced materials design would combine these insights into the chemistry and structure of the carbon matrix with a tailored pore network and particular electrolyte formulation, allowing the creation of a hybrid, nanostructured carbon-electrolyte system with enhanced properties [24, 35, 36, 39, 41, 42, 123]. As discussed in Chapter 2, *in situ* SAXS and SANS provides opportunities to probe the dynamics within these systems and gain remarkable insight into ion transport and energy storage processes within porous carbon materials [163, 165, 312].

Using the *in situ* cell design discussed in Chapter 3, and shown in Figure 49, experiments were carried out at the SAXS/WAXS beamline of the Australian Synchrotron to determine if the experimental procedures and results reported by Prehal et al. [163] (on activated carbon particles with average pore size of 1-2 nm) could be reproduced using EM-rGO supercapacitor electrodes. An initial analysis of these data showed that the design of the *in situ* cell needs further optimization, yet results from cyclic voltammetry using lower charging rates were able to show measureable differences in ion transport properties. Modes of inquiry such as this allow for unique insights on how these materials function as energy storage devices.

7.3.6 Suggestions for innovative rGO bulk materials

Extensive proposals focused on potential applications for rGO materials continue to be widely reported [4, 8, 10-12, 14, 27, 37, 38, 52, 74, 103, 104, 222, 308, 309, 315], with additional interest in solvated graphenes and hydrogel assemblies for biological applications [29]. Because these dedicated reviews are so abundant, comments regarding new applications for these materials will not be detailed here. However, it is noted that the results of this thesis established that rGO assemblies are extremely similar to SL pyrocarbons, and it would be expected that they would perform as well as SL and be relevant in similar applications. Also, because of the added benefits resulting from the highly adaptable processing conditions, it is likely that rGO can offer unique opportunities to enhance the performance of materials traditionally constructed with SL pyrocarbons. Following this, one area that has not yet been reported on is within the arena of nuclear energy. Because nuclear fuels and moderators [316, 317] make use of pyrolytic graphite and water (and/or D₂O), the fact that rGO hydrogels contain both of these elements within in one material (with the added ability to functionalize the sheets with various dopants) could suggest novel advancements and new functional materials. Combining this with the outstanding performance of rGO-based energy storage devices, these materials will be sure to play an important role in helping to shape a sustainable energy future – with the ability to understand the fundamental properties of these systems being key to successful development.

References

1. Novoselov, K.S., et al., *Two-dimensional atomic crystals*. Proc Natl Acad Sci U S A, 2005. **102**(30): p. 10451-3.
2. Novoselov, K.S., et al., *Electric field effect in atomically thin carbon films*. Science, 2004. **306**: p. 666-669.
3. Gao, H., Liu, Z., and Feng, X., *From 2004 to 2014: A fruitful decade for graphene research in china*. Small, 2014. **10**(11): p. 2121.
4. Randviir, E.P., Brownson, D.A.C., and Banks, C.E., *A decade of graphene research: Production, applications and outlook*. Mater Today, 2014. **17**(9): p. 426-432.
5. Boehm, H.P., *Graphene--how a laboratory curiosity suddenly became extremely interesting*. Angew Chem Int Ed Engl, 2010. **49**(49): p. 9332-5.
6. Wu, Y.H., Yu, T., and Shen, Z.X., *Two-dimensional carbon nanostructures: Fundamental properties, synthesis, characterization, and potential applications*. J Appl Phys, 2010. **108**(7): p. 071301.
7. Luo, J., Kim, J., and Huang, J., *Material processing of chemically modified graphene: Some challenges and solutions*. Acc Chem Res, 2013. **46**(10): p. 2225-2234.
8. Geim, A.K. and Novoselov, K.S., *The rise of graphene*. Nature Materials, 2007. **6**: p. 183-191.
9. Rao, C.N.R., et al., *Graphene: The new two-dimensional nanomaterial*. Angew Chem Int Ed, 2009. **48**(42): p. 7752-7777.
10. Zhong, Y.L., et al., *Scalable production of graphene via wet chemistry: Progress and challenges*. Mater Today, 2015. **18**(2): p. 73-78.
11. Whitby, R.L.D., *Chemical control of graphene architecture: Tailoring shape and properties*. ACS Nano, 2014. **8**(10): p. 9733-9754.
12. Edwards, R.S. and Coleman, K.S., *Graphene synthesis: Relationship to applications*. Nanoscale, 2013. **5**(1): p. 38-51.
13. Schaefer, D.W., *Engineered porous materials*. MRS Bull, 1994. **19**(4): p. 14-19.
14. Su, D.S. and Schlogl, R., *Nanostructured carbon and carbon nanocomposites for electrochemical energy storage applications*. ChemSusChem, 2010. **3**(2): p. 136-68.
15. Li, D., et al., *Processable aqueous dispersions of graphene nanosheets*. Nat Nanotechnol, 2008. **3**(2): p. 101-5.
16. Gao, X., Shao, Y., and Zhongfang, C., *From graphene to graphene oxide and back*, in *Graphene chemistry: Theoretical perspectives*, D. Jiang and Z. Chen, Editors. 2013, John Wiley & Sons, Ltd.: West Sussex, United Kingdom. p. 291-317.
17. Cheng, C., et al., *Dynamic electrosorption analysis: A viable liquid-phase characterization method for porous carbon?* J Mat Chem A, 2013. **1**(33): p. 9332.
18. Boehm, H.P., et al., *Das adsorptionsverhalten sehr dünner kohlenstoff-folien*. Z Anorg Allg Chem, 1962. **316**(3-4): p. 119-127.
19. Boehm, H.P., et al., *Thin carbon leaves*. Z Naturforsch, 1962. **17b**: p. 150-153.
20. Chen, H., et al., *Mechanically strong, electrically conductive, and biocompatible graphene paper*. Adv Mater, 2008. **20**(18): p. 3557-3561.
21. Yang, X., et al., *Ordered gelation of chemically converted graphene for next-generation electroconductive hydrogel films*. Angew Chem Int Ed Engl, 2011. **50**(32): p. 7325-8.
22. Qiu, L., et al., *Controllable corrugation of chemically converted graphene sheets in water and potential application for nanofiltration*. Chem Commun, 2011. **47**(20): p. 5810-2.
23. Wang, Y., Zhang, X., and Li, D., *Dynamic configuration of reduced graphene oxide in aqueous dispersion and its effect on thin film properties*. Chem Commun, 2015. **51**(100): p. 17760-3.
24. Yang, X., et al., *Liquid-mediated dense integration of graphene materials for compact capacitive energy storage*. Science, 2013. **341**(6145): p. 534-7.

25. Yang, X., et al., *Bioinspired effective prevention of restacking in multilayered graphene films: Towards the next generation of high-performance supercapacitors*. Adv Mater, 2011. **23**(25): p. 2833-8.
26. Cheng, C., et al., *Ion transport in complex layered graphene-based membranes with tuneable interlayer spacing*. Sci Adv, 2016. **2**.
27. Tang, Q., Zhou, Z., and Chen, Z., *Graphene-related nanomaterials: Tuning properties by functionalization*. Nanoscale, 2013. **5**(11): p. 4541-83.
28. Lozano-Castelló, D., et al., *Porous texture of carbons*, in *Carbons for electrochemical energy storage and conversion systems*, F.B.a.E. Frackowiak, Editor. 2009, CRC Press: Boca Raton, FL. p. 115-162.
29. Cheng, C. and Li, D., *Solvated graphenes: An emerging class of functional soft materials*. Adv Mater, 2013. **25**(1): p. 13-30.
30. Dresselhaus, M.S., et al., *Graphite fibers and filaments*. 1988, Berlin Springer Berlin Heidelberg.
31. Bourrat, X., *Structure in carbons and carbon artifacts*, in *Sciences of carbon materials*, H. Marsh and F. Rodriguez-Reinoso, Editors. 2000, Universidad de Alicante: Alicante. p. 1-97.
32. Marsh, H. and Rodriguez-Reinoso, F., *Activated carbon*. 2006, Oxford: Elsevier.
33. Calo, J.M. and Hall, P.J., *The application of small angle scattering techniques to porosity characterization in carbons*. Carbon, 2004. **42**: p. 1299-1304.
34. Pfeifer, P., et al., *Nearly space-filling fractal networks of carbon nanopores*. Phys Rev Lett, 2002. **88**(11): p. 115502.
35. Borchardt, L., Oschatz, M., and Kaskel, S., *Tailoring porosity in carbon materials for supercapacitor applications*. Materials Horizons, 2014. **1**(2): p. 157-168.
36. Forse, A.C., et al., *New perspectives on the charging mechanisms of supercapacitors*. J Am Chem Soc, 2016. **138**(18): p. 5731-44.
37. Frackowiak, E., *Carbon materials for supercapacitor application*. PCCP, 2007. **9**(15): p. 1774-85.
38. Jiang, L. and Fan, Z., *Design of advanced porous graphene materials: From graphene nanomesh to 3d architectures*. Nanoscale, 2014. **6**(4): p. 1922-45.
39. Salanne, M., et al., *Efficient storage mechanisms for building better supercapacitors*. Nature Energy, 2016. **1**(6): p. 16070.
40. Merlet, C., et al., *On the molecular origin of supercapacitance in nanoporous carbon electrodes*. Nat Mater, 2012. **11**(4): p. 306-10.
41. Kondrat, S., et al., *Effect of pore size and its dispersity on the energy storage in nanoporous supercapacitors*. Energy Environ Sci, 2012. **5**(4): p. 6474.
42. Kondrat, S., et al., *Accelerating charging dynamics in subnanometre pores*. Nat Mater, 2014. **13**(4): p. 387-93.
43. Bianco, A., et al., *All in the graphene family – a recommended nomenclature for two-dimensional carbon materials*. Carbon, 2013. **65**: p. 1-6.
44. Suarez-Martinez, I., Grobert, N., and Ewels, C.P., *Nomenclature of sp² carbon nanoforms*. Carbon, 2012. **50**(3): p. 741-747.
45. Drits, V.A. and Tchoubar, C., *X-ray diffraction by disordered lamellar structures*. 1990, Berlin: Springer-Verlag.
46. Franklin, R.E., *Crystallite growth in graphitizing and non-graphitizing carbons*. Proceedings of the Royal Society A, 1951. **209**(1097): p. 196-218.
47. Ahmed, E.M., *Hydrogel: Preparation, characterization, and applications: A review*. J Adv Res, 2015. **6**(2): p. 105-21.
48. Meyer, J.C., et al., *The structure of suspended graphene sheets*. Natur, 2007. **446**(7131): p. 60-3.
49. Farbos, B., et al., *Nanoscale structure and texture of highly anisotropic pyrocarbons revisited with transmission electron microscopy, image processing, neutron diffraction and atomistic modeling*. Carbon, 2014. **80**: p. 472-489.

50. Alcalde, H., et al., *Market uptake potential of graphene as a disruptive material*. Proc IEEE, 2013. **101**(7): p. 1793-1800.
51. *Research and markets: Global market for graphene to 2025: Market size, production volumes, applications, products, prospects, research and companies*, in Business Wire. 2015: New York.
52. Shapira, P., Gök, A., and Salehi, F., *Graphene enterprise: Mapping innovation and business development in a strategic emerging technology*. J Nanopart Res, 2016. **18**(9): p. 269.
53. Avouris, P., *Graphene: Electronic and photonic properties and devices*. Nano Lett, 2010. **10**(11): p. 4285-94.
54. Brodie, B.C., *On the atomic weight of graphite*. Philosophical Transactions, 1859. **149**: p. 249-259.
55. Hummers, W.S. and Offeman, R.E., *Preparation of graphite oxide*. J Am Chem Soc, 1958. **80**: p. 1339.
56. Dreyer, D.R., et al., *The chemistry of graphene oxide*. Chem Soc Rev, 2010. **39**(1): p. 228-40.
57. Kang, J.H., et al., *Hidden second oxidation step of hummers method*. Chem Mater, 2016. **28**(3): p. 756-764.
58. Shao, G., et al., *Graphene oxide: The mechanisms of oxidation and exfoliation*. JMatS, 2012. **47**: p. 4400-4409.
59. Szabo, T., et al., *Evolution of surface functional groups in a series of progressively oxidized graphite oxides*. Chem Mater, 2006. **18**: p. 2740-2749.
60. Moon, I.K., et al., *Reduced graphene oxide by chemical graphitization*. Nat Commun, 2010. **1**: p. 73.
61. Staudenmaier, L., *Verfahren zur darstellung der graphitsäure*. Berichte der deutschen chemischen Gesellschaft, 1898. **31**(2): p. 1481-1487.
62. Lerf, A., et al., *Structure of graphite oxide revisited*. J Phys Chem B, 1988. **102**: p. 4477-4482.
63. He, H., et al., *A new structural model for graphite oxide*. Chem Phys Lett, 1998. **287**(1-2): p. 53-56.
64. Gao, W., et al., *New insights into the structure and reduction of graphite oxide*. Nat Chem, 2009. **1**(5): p. 403-8.
65. Bagri, A., et al., *Structural evolution during the reduction of chemically derived graphene oxide*. Nat Chem, 2010. **2**(7): p. 581-7.
66. Ganguly, A., et al., *Probing the thermal deoxygenation of graphene oxide using high-resolution in situ x-ray-based spectroscopies*. J Phys Chem C, 2011. **115**(34): p. 17009-17019.
67. Nakajima, T. and Matsuo, Y., *Formation process and structure of graphite oxide*. Carbon, 1994. **32**(3): p. 469-475.
68. Boukhvalov, D.W. and Katsnelson, M.I., *Modeling of graphite oxide*. J Am Chem Soc, 2008. **130**: p. 10697-10701.
69. Chen, C.-M., et al., *Structural evolution during annealing of thermally reduced graphene nanosheets for application in supercapacitors*. Carbon, 2012. **50**(10): p. 3572-3584.
70. Gomez-Navarro, C., et al., *Electronic transport properties of individual chemically reduced graphene oxide sheets*. Nano Lett, 2007. **7**(11): p. 3499-3503.
71. Stankovich, S., et al., *Synthesis of graphene-based nanosheets via chemical reduction of exfoliated graphite oxide*. Carbon, 2007. **45**(7): p. 1558-1565.
72. Yang, D., et al., *Chemical analysis of graphene oxide films after heat and chemical treatments by x-ray photoelectron and micro-raman spectroscopy*. Carbon, 2009. **47**(1): p. 145-152.
73. Ren, P.G., et al., *Temperature dependence of graphene oxide reduced by hydrazine hydrate*. Nanot, 2011. **22**(5): p. 055705.
74. Shi, J.-L., et al., *The nanostructure preservation of 3d porous graphene: New insights into the graphitization and surface chemistry of non-stacked double-layer templated graphene after high-temperature treatment*. Carbon, 2016. **103**: p. 36-44.

75. Wang, R., et al., *Facile one-step hydrazine-assisted solvothermal synthesis of nitrogen-doped reduced graphene oxide: Reduction effect and mechanisms*. RSC Adv, 2013. **3**(4): p. 1194-1200.
76. Gao, X., Jang, J., and Nagase, S., *Hydrazine and thermal reduction of graphene oxide: Reaction mechanisms, product structures, and reaction design*. J Phys Chem C, 2010. **114**(2): p. 832-842.
77. Hassan, F.M., et al., *Pyrrolic-structure enriched nitrogen doped graphene for highly efficient next generation supercapacitors*. J Mat Chem A, 2013. **1**(8): p. 2904.
78. Xinran Wang, X.L., Li Zhang, Youngki Yoon, Peter K. Weber, Hailiang Wang, Jing Guo, Hongjie Dai, *N-doping of graphene through electrothermal reactions with ammonia*. Science, 2009. **324**: p. 768-771.
79. Park, S., et al., *Chemical structures of hydrazine-treated graphene oxide and generation of aromatic nitrogen doping*. Nat Commun, 2012. **3**: p. 638.
80. Ellis, A.V., et al., *Structural determination of thermally and hydrazine treated graphene oxide using electron spectroscopic analysis*. J Phys Chem C, 2013. **117**(41): p. 21312-21319.
81. Dennis, R.V., et al., *Near-edge x-ray absorption fine structure spectroscopy study of nitrogen incorporation in chemically reduced graphene oxide*. J Vac Sci Tech B, 2013. **31**(4): p. 041204.
82. Scardamaglia, M., et al., *Nitrogen implantation of suspended graphene flakes: Annealing effects and selectivity of sp² nitrogen species*. Carbon, 2014. **73**(Supplement C): p. 371-381.
83. Govindaraj, A. and Rao, C.N.R., *Doping of graphene by nitrogen, boron, and other elements*, in *Functionalization of graphene*, V. Georgakilas, Editor. 2014, Wiley-VCH Verlag GmbH & Co.
84. Jeong, H.M., et al., *Nitrogen-doped graphene for high-performance ultracapacitors and the importance of nitrogen-doped sites at basal planes*. Nano Lett, 2011. **11**(6): p. 2472-7.
85. Zhang, J., Xia, Z., and Dai, L., *Carbon-based electrocatalysts for advanced energy conversion and storage*. Sci Adv, 2015. **1**.
86. Li, X., et al., *Simultaneous nitrogen doping and reduction of graphene oxide*. J Am Chem Soc, 2009. **131**: p. 15939-15944.
87. Sun, L., et al., *Nitrogen-doped graphene with high nitrogen level via a one-step hydrothermal reaction of graphene oxide with urea for superior capacitive energy storage*. RSC Adv, 2012. **2**(10): p. 4498-4506.
88. Huang-Minlon, *A simple modification of the wolff-kishner reduction*. J Am Chem Soc, 1946. **68**(12): p. 247-2488.
89. Wang, X., et al., *N- doping of graphene through electrothermal reactions with ammonia*. Science, 2009. **324**(5928): p. 768-771.
90. Gadipelli, S. and Guo, Z.X., *Graphene-based materials: Synthesis and gas sorption, storage and separation*. Prog Mater Sci, 2015. **69**(Supplement C): p. 1-60.
91. Guo, H.-L., et al., *Synthesis and characterization of nitrogen-doped graphene hydrogels by hydrothermal route with urea as reducing-doping agents*. J Mater Chem, 2013. **1**(6): p. 2248-2255.
92. Montes-Morán, M.A., et al., *On the nature of basic sites on carbon surfaces: An overview*. Carbon, 2004. **42**(7): p. 1219-1225.
93. Pietrzak, R., *Xps study and physico-chemical properties of nitrogen-enriched microporous activated carbon from high volatile bituminous coal*. Fuel, 2009. **88**(10): p. 1871-1877.
94. Kelemen, S.R., et al., *Xps and 15n nmr study of nitrogen forms in carbonaceous solids*. Energy Fuels, 2002. **16**(6): p. 1507-1515.
95. Shafeeyan, M.S., et al., *A review on surface modification of activated carbon for carbon dioxide adsorption*. J Anal Appl Pyrolysis, 2010. **89**(2): p. 143-151.
96. Jansen, R.J.J. and van Bekkum, H., *Xps of nitrogen-containing functional groups on activated carbon*. Carbon, 1995. **33**(8): p. 1021-1027.
97. Ishitani, A., *Application of x-ray photoelectron spectroscopy to surface analysis of carbon fiber*. Carbon, 1981. **19**(4): p. 269-275.

98. Proctor, A. and Sherwood, P.M.A., *X-ray photoelectron spectroscopic studies of carbon fibre surfaces—ii: The effect of electrochemical treatment*. Carbon, 1983. **21**(1): p. 53-59.
99. Pels, J.R., et al., *Evolution of nitrogen functionalities in carbonaceous materials during pyrolysis*. Carbon, 1995. **33**(11): p. 1641-1653.
100. Latham, K.G., et al., *Synchrotron based nexafs study on nitrogen doped hydrothermal carbon: Insights into surface functionalities and formation mechanisms*. Carbon, 2017. **114**(Supplement C): p. 566-578.
101. Long, D., et al., *Preparation of nitrogen-doped graphene sheets by a combined chemical and hydrothermal reduction of graphene oxide*. Langmuir, 2010. **26**(20): p. 16096-16102.
102. Gomez-Navarro, C., et al., *Atomic structure of reduced graphene oxide*. Nano Lett, 2010. **10**(4): p. 1144-8.
103. Stankovich, S., et al., *Graphene-based composite materials*. Natur, 2006. **442**(7100): p. 282-6.
104. Mattevi, C., et al., *Evolution of electrical, chemical, and structural properties of transparent and conducting chemically derived graphene thin films*. Adv Funct Mater, 2009. **19**(16): p. 2577-2583.
105. Mkhoyan, K.A., et al., *Atomic and electronic structure of graphene-oxide*. Nano Lett, 2009. **9**(3): p. 1058-1063.
106. Erickson, K., et al., *Determination of the local chemical structure of graphene oxide and reduced graphene oxide*. Adv Mater, 2010. **22**(40): p. 4467-72.
107. Cuesta, A., et al., *Comparative performance of x-ray diffraction and raman microprobe techniques for the study of carbon materials*. J Mater Chem, 1998. **8**: p. 2875-2879.
108. Lu, L., et al., *Quantitative x-ray diffraction analysis and its application to various coals*. Carbon, 2001. **39**(12): p. 1821-1833.
109. Yen, T.F., Erdman, J.G., and Pollack, S.S., *Investigation of the structure of petroleum asphaltenes by x-ray diffraction*. Anal Chem, 1961. **33**: p. 1587-94.
110. Lehtinen, O., et al., *Atomic scale study of the life cycle of a dislocation in graphene from birth to annihilation*. Nat Commun, 2013. **4**: p. 2098.
111. Bourrat, X., et al., *The role of pentagons in the growth of laminar pyrocarbon*. Carbon, 2001. **39**: p. 2369-2368.
112. Zang, J., et al., *Multifunctionality and control of the crumpling and unfolding of large-area graphene*. Nat Mater, 2013. **12**(4): p. 321-5.
113. Chang, C., et al., *How graphene crumples are stabilized?* RSC Adv, 2013. **3**(8): p. 2720.
114. Plimpton, S., *Fast parallel algorithms for short-range molecular dynamics*. J Comput Phys, 1995. **117**(1): p. 1-19.
115. Brenner, D.W., et al., *A second-generation reactive empirical bond order (rebo) potential energy expression for hydrocarbons*. J Phys: Condens Matter, 2002. **14**(4): p. 783.
116. Cranford, S.W. and Buehler, M.J., *Packing efficiency and accessible surface area of crumpled graphene*. PhRvB, 2011. **84**(20).
117. Radovic, L.R., *Surface chemical and electrochemical properties of carbons*, in *Carbons for electrochemical energy storage and conversion systems*, F.B.a.E. Frackowiak, Editor. 2009, CRC Press: Boca Raton, FL. p. 163-220.
118. Futaba, D.N., et al., *Shape-engineerable and highly densely packed single-walled carbon nanotubes and their application as super-capacitor electrodes*. Nat Mater, 2006. **5**(12): p. 987-94.
119. Wood, C.D., et al., *Hierarchical structure and properties of graphene oxide papers*. Journal of Applied Mechanics, 2013. **80**(4): p. 040913.
120. Zhang, L., et al., *Porous 3d graphene-based bulk materials with exceptional high surface area and excellent conductivity for supercapacitors*. Sci Rep, 2013. **3**: p. 1408.
121. Orazem, M.E. and Tribollet, B., *Electrochemical impedance spectroscopy*. 2008, Hoboken, NJ: John Wiley & Sons, Inc.

122. Wang, S., et al., *Correlation in structure and properties of highly-porous graphene monoliths studied with a thermal treatment method*. Carbon, 2016. **96**: p. 174-183.
123. Simon, P. and Gogotsi, Y., *Capacitive energy storage in nanostructured carbonelectrolyte systems*. Acc Chem Res, 2013. **46**(5): p. 1094-1103.
124. Ferrari, A.C. and Basko, D.M., *Raman spectroscopy as a versatile tool for studying the properties of graphene*. Nat Nanotechnol, 2013. **8**(4): p. 235-46.
125. Malard, L.M., et al., *Raman spectroscopy in graphene*. PhR, 2009. **473**(5-6): p. 51-87.
126. Zhan, D., et al., *Electronic structure of graphite oxide and thermally reduced graphite oxide*. Carbon, 2011. **49**(4): p. 1362-1366.
127. Siegel, D.A., et al., *Many-body interactions in quasi-freestanding graphene*. Proc Natl Acad Sci U S A, 2011. **108**(28): p. 11365-9.
128. Rozp łocha, F., Patyka, J., and Stankowski, J., *Graphene bonding forces in graphite*. Acta Phys Pol, A, 2007. **112**(3): p. 557-562.
129. Mintmire, J.W., Dunlap, B.I., and White, C.T., *Are fullerene tubules metallic?* Phys Rev Lett, 1992. **68**(5): p. 631-634.
130. Bourrat, X. *Pyrocarbon performances and characterization*. in *World Conference on Carbon*. 2009. Biarritz, France.
131. Vallerot, J.-M., et al., *Quantitative structural and textural assessment of laminar pyrocarbons through raman spectroscopy, electron diffraction and few other techniques*. Carbon, 2006. **44**(9): p. 1833-1844.
132. Bourrat, X., et al., *Low temperature pyrocarbons: A review*. Journal of Brazillian Chemical Society, 2006. **17**(6): p. 1090-1095.
133. Bourrat, X., *Electrically conductive grades of carbon black: Structure and properties*. Carbon, 1993. **31**(2): p. 287-302.
134. Dresselhaus, M.S., Dresselhaus, G., and Eklund, P.C., *Science of fullerenes and carbon nanotubes*. 1996, San Diego: Academic Press.
135. Ding, N., et al., *Influence of carbon pore size on the discharge capacity of li-o₂batteries*. J Mat Chem A, 2014. **2**(31): p. 12433.
136. Lozano-Castell , D., et al., *Isotropic and anisotropic microporosity development upon chemical activation of carbon fibers, revealed by microbeam small-angle x-ray scattering*. Carbon, 2006. **44**(7): p. 1121-1129.
137. Wong, C.H., Ambrosi, A., and Pumera, M., *Thermally reduced graphenes exhibiting a close relationship to amorphous carbon*. Nanoscale, 2012. **4**(16): p. 4972-7.
138. Bennett, S.C. and Johnson, D.J., *Strength-structure relationships in pan-based carbon fibres*. JMatS, 1983. **18**: p. 3337-3347.
139. Didusko, R., Swiatkowski, A., and Trznadel, B.J., *On surface of micropores and fractal dimension of activated carbon determined on the basis of adsorption and saxs investigations*. Carbon, 2000. **38**: p. 1153-1162.
140. Nair, R.R., et al., *Unimpeded permeation of water through helium-leak-tight graphene based membranes*. Science, 2012. **335**(6067): p. 442-444.
141. Raghav, N., Chakraborty, S., and Maiti, P.K., *Molecular mechanism of water permeation in a helium impermeable graphene and graphene oxide membrane*. PCCP, 2015. **17**: p. 20557-20562.
142. Boukhvalov, D.W., Katsnelson, M.I., and Son, Y.W., *Origin of anomalous water permeation through graphene oxide membrane*. Nano Lett, 2013. **13**(8): p. 3930-5.
143. Hsieh, W., et al., *Facile simulation of carbon with wide pore size distribution for electric double-layer capacitance based on helmholtz models*. J Mat Chem A, 2015. **3**(32): p. 16535-16543.
144. Simon, P. and Gogotsi, Y., *Capacitive energy storage in nanostructured carbon electrolyte systems*. Accounts of chemical research 2013. **46**(5): p. 1094-1103.

145. Barbieri, O., et al., *Capacitance limits of high surface area activated carbons for double layer capacitors*. Carbon, 2005. **43**(6): p. 1303-1310.
146. Largeot, C., et al., *Relation between the ion size and pore size for an electric double-layer capacitor*. J Am Chem Soc, 2008. **130**(9): p. 2730-2731.
147. Raymundo-Piñero, E., et al., *Relationship between the nanoporous texture of activated carbons and their capacitance properties in different electrolytes*. Carbon, 2006. **44**(12): p. 2498-2507.
148. Biggs, M.J., Buts, A., and Williamson, D., *Molecular simulation evidence for solidlike adsorbate in complex carbonaceous micropore structures*. Langmuir, 2004. **20**: p. 5786-5800.
149. Mezei, M., *A cavity-biased (t , v , μ) monte carlo method for the computer simulation of fluids*. Mol Phys, 1980. **40**(4): p. 901-906.
150. Oberlin, A. and Bonnamy, S., *A realistic approach to disordered carbons*, in *Chemistry and physics of carbon: Volume*, L.R. Radovic, Editor. 2012, CRC Press. p. 1-84.
151. Oberlin, A., *Carbonization and graphitization*. Carbon, 1984. **22**(6): p. 521-541.
152. Goma, J. and Oberlin, A., *Characterization of low temperature pyrocarbons obtained by densification of porous substrates*. Carbon, 1986. **24**(2): p. 135-142.
153. Lafdi, K., Bonnamy, S., and Oberlin, A., *Anisotropic pitch-based carbon fibers - carbonization and graphitization*. Carbon, 1992. **30**(4): p. 533-549.
154. Oberlin, A., *Application of dark-field electron microscopy to carbon study*. Carbon, 1979. **17**(1): p. 7-20.
155. Oberlin, A. and Terriere, G., *Graphitization studies of soft carbons and anthracites by electron microscopy*. Carbon, 1973. **11**(6): p. 672.
156. Oberlin, A., Villey, M., and Combaz, A., *Influence of elemental composition on carbonization: Pyrolysis of kerosene shale and kuckersite*. Carbon, 1980. **18**(5): p. 347-353.
157. Chmiola, J., et al., *Anomalous increase in carbon capacitance at pore sizes less than 1 nanometer*. Science, 2006. **313**(5794): p. 1760-1763.
158. Frackowiak, E., *Carbon materials for supercapacitor application*. PCCP, 2007. **9**(15): p. 1774-1785.
159. Hollamby, M.J., *Practical applications of small-angle neutron scattering*. PCCP, 2013. **15**(26): p. 10566-10579.
160. Melnichenko, Y.B. and Wignall, G.D., *Small-angle neutron scattering in materials science: Recent practical applications*. J Appl Phys, 2007. **102**(2): p. 021101.
161. Mileeva, Z., et al., *The use of small angle neutron scattering with contrast matching and variable adsorbate partial pressures in the study of porosity in activated carbons*. Carbon, 2012. **50**(14): p. 5062-5075.
162. Milner, E.M., et al., *Structure and morphology of charged graphene platelets in solution by small-angle neutron scattering*. J Am Chem Soc, 2012. **134**(20): p. 8302-8305.
163. Prehal, C., et al., *Tracking the structural arrangement of ions in carbon supercapacitor nanopores using in situ small-angle x-ray scattering*. Energy Environ Sci, 2015. **8**(6): p. 1725-1735.
164. Ruch, P.W., et al., *A dilatometric and small-angle x-ray scattering study of the electrochemical activation of mesophase pitch-derived carbon in non-aqueous electrolyte solution*. Carbon, 2010. **48**(7): p. 1880-1888.
165. Boukhalfa, S., et al., *In situ small angle neutron scattering revealing ion sorption in microporous carbon electrical double layer capacitors*. ACS Nano, 2014. **8**(3): p. 2495-2503.
166. Bañuelos, J.L., et al., *Densification of ionic liquid molecules within a hierarchical nanoporous carbon structure revealed by small-angle scattering and molecular dynamics simulation*. Chem Mater, 2014. **26**(2): p. 1144-1153.
167. Warren, B.E., *X-ray diffraction in random layer lattices*. Phys Rev, 1941. **59**(9): p. 693-698.
168. Franklin, R.E., *The structure of graphitic carbons*. Acta Crystallogr, 1951. **4**: p. 253-261.

169. Biscoe, J. and Warren, B.E., *An x - ray study of carbon black*. J Appl Phys, 1942. **13**(6): p. 364-371.
170. Ferrari, A.C. and Robertson, J., *Interpretation of raman spectra of disordered and amorphous carbon*. Phys Rev B, 2000. **61**(20): p. 14095-14107.
171. Ferrari, A.C. and Robertson, J., *Raman spectroscopy of amorphous, nanostructured, diamond-like carbon, and nanodiamond*. Philosophical Transactions: Mathematical, Physical and Engineering Sciences, 2004. **362**(1824): p. 2477-2512.
172. Bragg, W.H. and Bragg, W.L., *The reflection of x-rays by crystals*. Proceedings of the Royal Society of London Series A, 1913. **88**(605): p. 428-438.
173. Franklin, R.E., *The interpretation of diffuse x-ray diagrams of carbon*. Acta Crystallogr, 1950. **3**: p. 107-121.
174. Ergun, S. and Tiensuu, V.H., *Determination of x - ray absorption coefficients of inhomogeneous materials*. J Appl Phys, 1958. **29**(6): p. 946-949.
175. Ruland, W. and Smarsly, B., *X-ray scattering of non-graphitic carbon: An improved method of evaluation*. J Appl Crystallogr, 2002. **35**(5): p. 624-633.
176. Faber, K., et al., *Investigation of the microstructure of disordered, non-graphitic carbons by an advanced analysis method for wide-angle x-ray scattering*. Z Anorg Allg Chem, 2014. **640**(15): p. 3107-3117.
177. Ruland, W. and Tompa, H., *The effect of preferred orientation on the intensity distribution of (hk) interferences*. AcCrA, 1968. **24**(1): p. 93-99.
178. Darwin, C.G., *Xxxiv. The theory of x-ray reflexion*. Philosophical Magazine Series 6, 1914. **27**(158): p. 315-333.
179. Langford, J.I. and Wilson, A.J.C., *Seherrer after sixty years: A survey and some new results in the determination of crystallite size* Journal of Applied Crystallography, 1978. **11**: p. 102-113.
180. Stokes, A.R. and Wilson, A.J.C., *The diffraction of x-rays by distorted crystal aggregates*. Proc Physical Soc, 1944. **56**: p. 174-181.
181. Balzar, D., *Voigt-function model in diffraction line-broadening analysis*, in *Microstructure analysis from diffraction*, R.L. Snyder, H.J. Bunge, and J. Fiala, Editors. 1999, International Union of Crystallography.
182. Langford, J.I., *A rapid method for analysing the breadths of diffraction and spectral lines using the voigt function*. Journal of Applied Crystallography, 1978. **11**: p. 10-14.
183. White, A.H. and Germer, L.H., *The structure of black carbon*. The Journal of Chemical Physics, 1941. **9**(7): p. 492-497.
184. Fourdeux, A., Perret, R., and Ruland, W., *The effect of preferred orientation on (hk) interferences as shown by electron diffraction of carbon fibres*. J Appl Crystallogr, 1968. **1**(4): p. 252-254.
185. Benecke, G., et al., *A customizable software for fast reduction and analysis of large x-ray scattering data sets: Applications of the new package to small-angle x-ray scattering and grazing-incidence small-angle x-ray scattering*. J Appl Crystallogr, 2014. **47**(Pt 5): p. 1797-1803.
186. Hammouda, B. *Probing nanoscale structures - the sans toolbox*. 2016.
187. Lozano-Castello, D., et al., *Characterization of pore distribution in activated carbon fibers by microbeam small angle x-ray scattering*. Carbon, 2002. **40**: p. 2727-2735.
188. Newbloom, G.M., et al., *Mesoscale morphology and charge transport in colloidal networks of poly(3-hexylthiophene)*. Macromolecules, 2011. **44**(10): p. 3801-3809.
189. Guinier, A., *La diffraction des rayons x aux tres petits angles; application a l'etude de phenomenes ultramicroscopiques*. Ann Phys 1939. **12**(161-237).
190. Porod, G., *Die röntgenkleinwinkelstreuung von dichtgepackten kolloiden systemen*. Kolloid-Zeitschrift, 1951. **124**(2): p. 83-114.
191. Sinha, S.K., et al., *X-ray and neutron scattering from rough surfaces*. PhRvB, 1988. **38**(4): p. 2297-2311.

192. Mitropoulos, A.C., et al., *Scattering by curved and fractal surfaces*. J Colloid Interface Sci, 1998. **203**(1): p. 229-230.
193. Bale, H.D. and Schmidt, P.W., *Small-angle x-ray-scattering investigation of submicroscopic porosity with fractal properties*. Phys Rev Lett, 1984. **53**(6): p. 596-599.
194. Teixeira, J., *Small-angle scattering by fractal systems*. J Appl Crystallogr, 1988. **21**(6): p. 781-785.
195. Mildner, D.F.R. and Hall, P.L., *Small-angle scattering from porous solids with fractal geometry*. J Phys D: Appl Phys, 1986. **19**(8): p. 1535.
196. Martin, J.E. and Hurd, A.J., *Scattering from fractals*. J Appl Crystallogr, 1987. **20**(2): p. 61-78.
197. Pfeifer, P. and Avnir, D., *Chemistry in noninteger dimensions between two and three. I. Fractal theory of heterogeneous surfaces*. J Chem Phys, 1983. **79**(7): p. 3558-3565.
198. Avnir, D., Farin, D., and Pfeifer, P., *Chemistry in noninteger dimensions between two and three. II. Fractal surfaces of adsorbents*. The Journal of Chemical Physics, 1983. **79**(7): p. 3566-3571.
199. Pfeifer, P., *Fractal dimension as a working tool for surface-roughness problems*. Appl Surf Sci, 1984. **18**: p. 146-164.
200. Avnir, D., Farin, D., and Pfeifer, P., *Molecular fractal surfaces*. Natur, 1984. **308**(5956): p. 261-263.
201. Cherny, A.Y., et al., *Small-angle scattering from the deterministic fractal systems*. Journal of Surface Investigation X-ray, Synchrotron and Neutron Techniques, 2010. **4**(6): p. 903-907.
202. Cherny, A.Y., et al., *Deterministic fractals: Extracting additional information from small-angle scattering data*. Phys Rev E Stat Nonlin Soft Matter Phys, 2011. **84**(3 Pt 2): p. 036203.
203. Cherny, A.Y., et al., *Small-angle scattering from multiphase fractals*. J Appl Crystallogr, 2014. **47**(1): p. 198-206.
204. Marcano, D.C., et al., *Improved synthesis of graphene oxide*. ACS Nano, 2010. **4**(8): p. 4806-4814.
205. Lorenz, C., von Pelchrzim, F., and Schroeder, R., *Genomic systematic evolution of ligands by exponential enrichment (genomic selex) for the identification of protein-binding rnas independent of their expression levels*. Nat Protocols, 2006. **1**(5): p. 2204-2212.
206. Hirata, M., et al., *Thin-film particles of graphite oxide 1*. Carbon, 2004. **42**(14): p. 2929-2937.
207. Studer, A.J., Hagen, M.E., and Noakes, T.J., *Wombat: The high-intensity powder diffractometer at the opal reactor*. Physica B: Condensed Matter, 2006. **385–386, Part 2**: p. 1013-1015.
208. Gilbert, E.P., Schulz, J.C., and Noakes, T.J., *'Quokka'—the small-angle neutron scattering instrument at opal*. Physica B: Condensed Matter, 2006. **385–386, Part 2**: p. 1180-1182.
209. Kline, S., *Reduction and analysis of sabs and usans data using igor pro*. J Appl Crystallogr, 2006. **39**(6): p. 895-900.
210. Rehm, C., et al., *Kookaburra: The ultra-small-angle neutron scattering instrument at opal*. J Appl Crystallogr, 2013. **46**(6): p. 1699-1704.
211. Bonse, U. and Hart, M., *Tailless x-ray single-crystal reflection curves obtained by multiple reflection*. Appl Phys Lett, 1965. **7**(9): p. 238-240.
212. Pedersen, J.S., Posselt, D., and Mortensen, K., *Analytical treatment of the resolution function for small-angle scattering*. J Appl Crystallogr, 1990. **23**(4): p. 321-333.
213. Lake, J., *An iterative method of slit-correcting small angle x-ray data*. Acta Crystallogr, 1967. **23**(2): p. 191-194.
214. Kohlbrecher, J., *Sasfit: A program for fitting simple structural models to small angle scattering data*, in *User Guide for SASfit Software*. 2014, Paul Scherrer Institute.
215. Konno, H., *X-ray photoelectron spectroscopy*, in *Materials science and engineering of carbon*, M. Inagaki and F. Kang, Editors. 2016, Butterworth-Heinemann. p. 153-171.
216. Ganesan, K., et al., *A comparative study on defect estimation using xps and raman spectroscopy in few layer nanographitic structures*. PCCP, 2016. **18**(32): p. 22160-7.

217. Titantah, J.T. and Lamoen, D., *Carbon and nitrogen 1s energy levels in amorphous carbon nitride systems: Xps interpretation using first-principles*. Diamond Relat Mater, 2007. **16**(3): p. 581-588.
218. Schultz, B.J., et al., *X-ray absorption spectroscopy studies of electronic structure recovery and nitrogen local structure upon thermal reduction of graphene oxide in an ammonia environment*. RSC Adv, 2014. **4**(2): p. 634-644.
219. Xie, Y. and Sherwood, P., *X-ray photoelectron spectroscopic studies of carbon fiber surfaces. 13. Valence-band studies of oxidized fibers interpreted by x-alpha calculations*. Chem Mater, 1991. **3**: p. 164-168.
220. McFeely, F.R., et al., *X-ray photoemission studies of diamond, graphite, and glassy carbon valence bands*. PhRvB, 1974. **9**(12): p. 5268-5278.
221. Zafar, Z., et al., *Evolution of raman spectra in nitrogen doped graphene*. Carbon, 2013. **61**: p. 57-62.
222. Wang, H., Maiyalagan, T., and Wang, X., *Review on recent progress in nitrogen-doped graphene: Synthesis, characterization, and its potential applications*. ACS Catalysis, 2012. **2**(5): p. 781-794.
223. Lai, L., et al., *Exploration of the active center structure of nitrogen-doped graphene-based catalysts for oxygen reduction reaction*. Energy Environ Sci, 2012. **5**(7): p. 7936.
224. Qu, L., et al., *Nitrogen-doped graphene as efficient metal-free electrocatalyst for oxygen reduction in fuel cells*. ACS Nano, 2010. **4**(3): p. 1321-1326.
225. Fairley, N. and Carrick, A., *The casa cookbook*. Part 1: Recipes for xps data processing. 2005, Cheshire, UK: Acolyte Science.
226. Christ, B.V., *Critical review of xps data-banks*. Surfaces and Interface Analysis, 2007. **39**: p. 1-53.
227. Yamada, Y., et al., *Nitrogen-containing graphene analyzed by x-ray photoelectron spectroscopy*. Carbon, 2014. **70**(Supplement C): p. 59-74.
228. Terrones, H., et al., *The role of defects and doping in 2d graphene sheets and 1d nanoribbons*. Rep Prog Phys, 2012. **75**(6): p. 062501.
229. Stohr, B., Boehm, H.P., and Schlogl, R., *Enhancement of the catalytic activity of activated carbons in oxidation reactions by thermal treatment with ammonia or hydrogen cyanide and observation of a superoxide species as a possible intermediate*. Carbon, 1991. **29**(6): p. 707-720.
230. Chen, Z.Y., et al., *Valence band electronic structure of carbon nitride from x-ray photoelectron spectroscopy*. J Appl Phys, 2002. **92**(1): p. 281.
231. Ray, S.C., et al., *Electronic properties of a-cn[_x] thin films: An x-ray-absorption and photoemission spectroscopy study*. J Appl Phys, 2005. **98**(3): p. 033708.
232. Bhattacharyya, S., Spaeth, C., and Richter, F., *Valence band spectra of nitrogen incorporated amorphous carbon films*. J Appl Phys, 2001. **89**(4): p. 2414.
233. Mansour, A. and Oelhafen, P., *Effects of defects on the electronic structure of ion-irradiated graphite* Appl Phys A, 1994. **58**: p. 437-440.
234. Drouin, D., et al., *Casino v2.42 - a fast and easy-to-use modeling tool for scanning electron microscopy and microanalysis users*. Scanning, 2007. **29**: p. 92-101.
235. Yeh, C.N., et al., *On the origin of the stability of graphene oxide membranes in water*. Nat Chem, 2014. **7**(2): p. 166-70.
236. Shin, H.-J., et al., *Efficient reduction of graphite oxide by sodium borohydride and its effect on electrical conductance*. Adv Funct Mater, 2009. **19**(12): p. 1987-1992.
237. Bourrat, X., *Structure of pyrocarbons*, in *World of carbon*, P. Delhaes, Editor. 2003. p. 159-187.
238. Sharma, R., et al., *Anomalously large reactivity of single graphene layers and edges toward electron transfer chemistries*. Nano Lett, 2010. **10**(2): p. 398-405.
239. Vander Wal, R.L., et al., *Carbon nanostructure examined by lattice fringe analysis of high-resolution transmission electron microscopy images*. Appl Spectrosc, 2004. **58**(2): p. 230-237.

240. Perret, R. and Ruland, W., *The microstructure of pan-base carbon fibres*. J Appl Crystallogr, 1970. **3**(6): p. 525-532.
241. Harris, P.J.F., *Structure of non-graphitising carbons*. Int Mater Rev, 2013. **42**(5): p. 206-218.
242. *Composite materials: Processing, applications, characterizations*. 1 ed. 2017, Berlin Heidelberg: Springer-Verlag.
243. Ferrari, A.C., et al., *Raman spectrum of graphene and graphene layers*. Phys Rev Lett, 2006. **97**(18).
244. Sood, A.K. and Chakraborty, B., *Understanding graphene via raman scattering*, in *Graphene: Synthesis, properties, and phenomena*, C.N.R. Rao and A.K. Sood, Editors. 2013, Wiley-VCH Verlag & Co.: Weinheim, Germany. p. 49-90.
245. Egerton, R.F., *Tem specimens and images*. 2016: p. 89-120.
246. Reznik, B. and Huttinger, K.J., *On the terminology for pyrolytic carbon*. Carbon, 2002. **40**: p. 617-636.
247. Bourrat, X., et al., *Pyrocarbon anisotropy as measured by electron diffraction and polarized light*. J Mater Res, 2011. **15**(01): p. 92-101.
248. Hembacher, S., et al., *Revealing the hidden atom in graphite by low-temperature atomic force microscopy*. Proceedings of the National Academy of Sciences, 2003. **100**(22): p. 12539-12542.
249. López-Honorato, E., et al., *Deposition of triso particles with superhard sic coatings and the characterization of anisotropy by raman spectroscopy*. Journal of Engineering for Gas Turbines and Power, 2009. **131**(4): p. 042905.
250. Weisbecker, P., et al., *Microstructure of pyrocarbons from pair distribution function analysis using neutron diffraction*. Carbon, 2012. **50**(4): p. 1563-1573.
251. Marrow, T.J., et al., *In situ measurement of the strains within a mechanically loaded polygranular graphite*. Carbon, 2016. **96**: p. 285-302.
252. Qin, W. and Szpunar, J.A., *Origin of lattice strain in nanocrystalline materials*. Philos Mag Lett, 2005. **85**(12): p. 649-656.
253. Jafri, S.H.M., et al., *Conductivity engineering of graphene by defect formation*. J Phys D: Appl Phys, 2010. **43**(4): p. 045404.
254. Rasband, W.S., *Imagej*. 1997-2016, U. S. National Institutes of Health: Bethesda, Maryland, USA.
255. Tuinstra, F. and Koenig, J.L., *Raman spectrum of graphite*. The Journal of Chemical Physics, 1970. **53**(3): p. 1126.
256. Wang, Y., Alsmeyer, D.C., and McCreery, R.L., *Raman spectroscopy of carbon materials: Structural basis of observed spectra*. Chem Mater, 1990. **2**: p. 557-563.
257. Sadezky, A., et al., *Raman microspectroscopy of soot and related carbonaceous materials: Spectral analysis and structural information*. Carbon, 2005. **43**(8): p. 1731-1742.
258. Claramunt, S., et al., *The importance of interbands on the interpretation of the raman spectrum of graphene oxide*. J Phys Chem C, 2015. **119**(18): p. 10123-10129.
259. Cançado, L.G., et al., *Measuring the degree of stacking order in graphite by raman spectroscopy*. Carbon, 2008. **46**(2): p. 272-275.
260. Nemanich, R.J. and Solin, S.A., *First- and second-order raman scattering from finite-size crystals of graphite*. PhRvB, 1979. **20**(2): p. 392-401.
261. Knight, D.S. and White, W.B., *Characterization of diamond films by raman spectroscopy*. J Mater Res, 1989. **4**(02): p. 385-393.
262. *Iupac compendium of chemical terminology - the gold book*. 2005-2017, International Union of Pure and Applied Chemistry.
263. Ferrari, A.C., Rodil, S.E., and Robertson, J., *Interpretation of infrared and raman spectra of amorphous carbon nitrides*. PhRvB, 2003. **67**(15): p. 155306-155326.
264. Casiraghi, C., et al., *Raman spectroscopy of graphene edges*. Nano Lett, 2009. **9**: p. 1433.

265. Beams, R., Cancado, L.G., and Novotny, L., *Low temperature raman study of the electron coherence length near graphene edges*. Nano Lett, 2011. **11**(3): p. 1177-81.
266. Lucchese, M.M., et al., *Quantifying ion-induced defects and raman relaxation length in graphene*. Carbon, 2010. **48**(5): p. 1592-1597.
267. Cancado, L.G., et al., *Quantifying defects in graphene via raman spectroscopy at different excitation energies*. Nano Lett, 2011. **11**(8): p. 3190-6.
268. Mallet-Ladeira, P., et al., *A raman study to obtain crystallite size of carbon materials: A better alternative to the tuinstra-koenig law*. Carbon, 2014. **80**: p. 629-639.
269. Mallet-Ladeira, P., et al., *Behavior of raman d band for pyrocarbons with crystallite size in the 2–5 nm range*. Appl Phys A, 2013. **114**(3): p. 759-763.
270. Seong, H.J. and Boehman, A.L., *Evaluation of raman parameters using visible raman microscopy for soot oxidative reactivity*. Energy Fuels, 2013. **27**(3): p. 1613-1624.
271. Cançado, L.G., et al., *General equation for the determination of the crystallite size l_a of nanographite by raman spectroscopy*. Appl Phys Lett, 2006. **88**(16): p. 163106.
272. Jawhari, T., Roid, A., and Casado, J., *Raman spectroscopic characterization of some commercially available carbon black materials*. Carbon, 1995. **33**(11): p. 1561-1565.
273. Kaplas, T. and Svirko, Y., *Direct deposition of semitransparent conducting pyrolytic carbon films*. Journal of Nanophotonics, 2012. **6**(1): p. 061703.
274. Schwan, J., et al., *Raman spectroscopy on amorphous carbon films*. J Appl Phys, 1996. **80**(1): p. 440.
275. Wang, T., et al., *Interaction between nitrogen and sulfur in co-doped graphene and synergetic effect in supercapacitor*. Sci Rep, 2015. **5**: p. 9591.
276. Martins Ferreira, E.H., et al., *Evolution of the raman spectra from single-, few-, and many-layer graphene with increasing disorder*. PhRvB, 2010. **82**(12).
277. Liu, Y., et al., *Structural and hygroscopic changes of soot during heterogeneous reaction with $o(3)$* . PCCP, 2010. **12**(36): p. 10896-903.
278. Eckmann, A., et al., *Probing the nature of defects in graphene by raman spectroscopy*. Nano Lett, 2012. **12**(8): p. 3925-30.
279. Araujo, P.T., Terrones, M., and Dresselhaus, M.S., *Defects and impurities in graphene-like materials*. Mater Today, 2012. **15**(3): p. 98.
280. Jhon, Y.I., et al., *The mechanical responses of tilted and non-tilted grain boundaries in graphene*. Carbon, 2012. **50**(10): p. 3708-3716.
281. Kim, K., et al., *Selective metal deposition at graphene line defects by atomic layer deposition*. Nat Commun, 2014. **5**: p. 4781.
282. Long, F., et al., *Characteristic work function variations of graphene line defects*. ACS Appl Mater Interfaces, 2016. **8**(28): p. 18360-6.
283. Petkov, V., et al., *Atomic pair distribution functions analysis of disordered low-z materials*. PCCP, 2013. **15**(22): p. 8544-8554.
284. Manoj, B., *Investigation of nanocrystalline structure in selected carbonaceous materials*. International Journal of Minerals, Metallurgy, and Materials, 2014. **21**(9): p. 940-946.
285. Park, S. and Ruoff, R.S., *Chemical methods for the production of graphenes*. Nat Nano, 2009. **4**(4): p. 217-224.
286. Hura, G., et al., *A high-quality x-ray scattering experiment on liquid water at ambient conditions*. The Journal of Chemical Physics, 2000. **113**(20): p. 9140-9148.
287. Amann-Winkel, K., et al., *X-ray and neutron scattering of water*. Chem Rev, 2016. **116**(13): p. 7570-7589.
288. Bruneton, E., Narcy, B., and Oberlin, A., *Carbon-carbon composites prepared by a rapid densification process ii: Structural and textural characterizations*. Carbon, 1997. **35**(10–11): p. 1599-1611.

289. Beaucage, G. and Schaefer, D.W., *Structural studies of complex systems using small-angle scattering a unified guinier power-law approach*. J Non-Cryst Solids, 1994. **172**(2): p. 797-805.
290. Perret, R. and Ruland, W., *X-ray small-angle scattering of glassy carbon*. J Appl Crystallogr, 1972. **5**(3): p. 183-187.
291. Reich, M.H., et al., *The application of saxs to determine the fractal properties of porous carbon-based materials*. J Colloid Interface Sci, 1990. **135**(2): p. 353-362.
292. Schmidt, P., *Small-angle scattering studies of disordered, porous and fractal systems*. J Appl Crystallogr, 1991. **24**(5): p. 414-435.
293. Reiker, T.P., Moisono, S., and Ehrburger-Dolle, F., *Small-angle x-ray scattering from carbon blacks: Crossover between the fractal and porod regimes*. Langmuir, 1999. **15**: p. 914-917.
294. Beaucage, G., *Small-angle scattering from polymeric mass fractals of arbitrary mass-fractal dimension*. J Appl Crystallogr, 1996. **29**(2): p. 134-146.
295. Beaucage, G., *Approximations leading to a unified exponential/power-law approach to small-angle scattering*. J Appl Crystallogr, 1995. **28**(6): p. 717-728.
296. Tang, M.Y., et al., *X - ray scattering studies of graphite fibers*. J Appl Phys, 1986. **60**(2): p. 803-810.
297. Perret, R. and Ruland, W., *X-ray small-angle scattering of non-graphitizable carbons*. J Appl Crystallogr, 1968. **1**(5): p. 308-313.
298. Bosio, L., Johari, G.P., and Teixeira, J., *X-ray study of high-density amorphous water*. Phys Rev Lett, 1986. **56**(5): p. 460-463.
299. Iiyama, T., et al., *Study of the structure of a water molecular assembly in a hydrophobic nanospace at low temperature with in situ x-ray diffraction*. Chem Phys Lett, 1997. **274**(1): p. 152-158.
300. Narten, A.H., Danford, M.D., and Levy, H.A., *X-ray diffraction study of liquid water in the temperature range 4-200c*. Discuss Faraday Soc, 1967. **43**(0): p. 97-107.
301. Porod, G., *Small angle x-ray scattering / edited by o. Glatter and o. Kratky*, ed. O. Kratky and O. Glatter. 1982, London ; New York: Academic Press.
302. Guinier, A., *X-ray diffraction: In crystals, imperfect crystals, and amorphous bodies*. 1963, San Francisco: Freeman.
303. Wigner, E., *On the quantum correction for thermodynamic equilibrium*. Phys Rev, 1932. **40**(5): p. 749-759.
304. Telling, R.H., et al., *Wigner defects bridge the graphite gap*. Nat Mater, 2003. **2**(5): p. 333-337.
305. Ewels, C.P., et al., *Metastable frenkel pair defect in graphite: Source of wigner energy?* Phys Rev Lett, 2003. **91**(2): p. 025505.
306. Zhang, Y., *The fractal volume of the two-dimensional invasion percolation cluster*. Commun Math Phys, 1995. **167**: p. 237-254.
307. Radlinski, A.P., et al., *Application of saxs and sans in evaluation of porosity, pore size distribution and surface area of coal*. Intl J Coal Geo, 2004. **59**(3-4): p. 245-271.
308. Li, D. and Kaner, R.B., *Materials science. Graphene-based materials*. Science, 2008. **320**(5880): p. 1170-1.
309. Li, R., Zhang, L., and Wang, P., *Rational design of nanomaterials for water treatment*. Nanoscale, 2015. **7**(41): p. 17167-94.
310. Iiyama, T., Ruike, M., and Kaneko, K., *Structural mechanism of water adsorption in hydrophobic micropores from in situ small angle x-ray scattering*. Chem Phys Lett, 2000. **331**(5-6): p. 359-364.
311. Futamura, R., et al., *Negative thermal expansion of water in hydrophobic nanospaces*. PCCP, 2012. **14**(2): p. 981-986.
312. Iiyama, T., et al., *In situ small-angle x-ray scattering study of cluster formation in carbon micropores*. Colloids Surf Physicochem Eng Aspects, 2004. **241**(1-3): p. 207-213.

- 313. Qomi, M.J., et al., *Anomalous composition-dependent dynamics of nanoconfined water in the interlayer of disordered calcium-silicates*. J Chem Phys, 2014. **140**(5): p. 054515.
- 314. Sakuma, H., et al., *Structure of hydrated sodium ions and water molecules adsorbed on the mica/water interface*. J Phys Chem C, 2011. **115**(32): p. 15959-15964.
- 315. Kumar, N.A. and Baek, J.B., *Doped graphene supercapacitors*. Nanot, 2015. **26**(49): p. 492001.
- 316. Bokros, J.C. and Schwartz, A.S., *Pyrolytic graphite and nuclear fuel particles coated therewith* 1968, Atomic Energy Commission USA.
- 317. *Nuclear fuel cycle science and engineering*. 2012: Woodhead Publishing.